Cranfield University

School of Mechanical Engineering

Ph.D

Qing-ping Zheng

Soot Production in a Tubular Gas Turbine Combustor

Supervisor: Professor J.B. Moss

January 1994

This thesis is submitted for the degree of Doctor of Philosophy

To my father and mother

Abstract

Soot production in gas turbine combustors is not desirable since it is the major source of exhaust smoke emission and its thermal radiation to the combustor liner deteriorates the liner durability. Soot formation involves comparatively slow chemistry and equilibrium can not be applied to soot modelling in the combustor flow field. The exact sooting process in the combustor is poorly understood given both the complexity and the limited experimental data available. The work reported in this thesis seeks to first develop in-situ techniques for retrieving spatially-resolved soot properties, mainly soot particle volume fraction, from within the combustor and also to apply the measured results to comparisons with predicted soot concentrations.

Two probing methods have been demonstrated which also incorporate a laser absorption technique. The sight probe proves to be more reliable in the present measurements. The evaluation of the physical probing techniques in sooty laboratory flames reveals that the flame structure will not be substantially distorted by the probe. The disturbance caused by the probe is localised, a feature which is evident in the reported water flow visualization test. The necessary inert gas purge can be minimised to reduce the local aerodynamic perturbation. The measured soot volume fraction distributions are comparable with sooting levels reported in flame studies in the literature. The peak soot volume fractions are located off-axis, characteristic of the fuel atomization. The measurements in the primary zone are restricted by the multi-phase character of the flow, where soot absorption can not be readily discriminated from fuel droplet scattering. Measurements are reported over a range of air-fuel ratios, inlet pressures and temperatures.

Time-averaged scalar distributions at the nominal dilution section have been obtained in addition to the soot measurement using probe sampling and standard gas analysis. Correlations of carbon dioxide with mixture fraction reveal a clear relationship at overall lean conditions consistent with widely used modelled assumptions. There are less well-correlated relationships between temperature and mixture fraction, possibly due to the influence of scalar fluctuations and also of the scalar dissipation rate. Soot loading in the present flow conditions is characteristically low, based on the mixture fraction and soot volume fraction data. Thermal radiation in the visible spectrum shows a distinct narrow band spectra in addition to the soot continuum, which is believed to arise from C_2 radical emission. The mean radiation intensities, predicted by using the measured temperature and soot concentration results, are in general lower than the measured mean intensities. Temperature fluctuation levels may be particularly influential in some of these calculations.

Soot modelling in the combustor has been undertaken by applying an extended laminar flamelet concept. The two-equation soot formation model has been primarily developed on laminar flames. The comparison of the computation and measurement suggests that this soot model holds promise in the context of prediction in the combustor. In the absence of a satisfactory theoretical description of the fuel-air burning in the combustor, where the liquid kerosine employed is replaced by gaseous propane, the computed scalar profiles are inconsistent in some important respects with the measured ones. This exerts a major effect on the soot prediction in terms of the quantitative detail in the computation, which is however crucial for the soot model development. The original flow field modelling needs to be improved for the purpose of further soot model refinement.

Acknowledgement

I would like to thank my supervisor, Prof. J.B. Moss, for his patience and guidance during the past three years. His valuable advice in the study has substantially expanded my understanding of combustion science and technology. The helpful assistance of my colleagues, Mr. C.D. Stewart and Dr. K.J. Young (now of Sheffield University) are greatly appreciated. Thank are also due to Mr. S. Alizadeh (now of Computational Dynamics Ltd, London) for his help in the CFD work.

I am very grateful to the Committee of Vice-Chancellors and Principals of the Universities of the United Kingdom, London, for the award of an Overseas Research Studentship. The initial research programme was sponsored by the Phase One BRITE/EURAM project from the European Commission. SNECMA of France extended the loan of a fuel injector which made the subsequent scalar and radiation measurements possible. The support of these bodies are acknowledged with thanks.

My wife, Ning, and my boy, Liang, deserve my wholehearted thanks for their encouragement and love during the whole study period. I would also like to thank my family for their continuous care and support.

Contents

Figure List

Nomenclature

a	radiation calibration constant (Eq. 5-7)
AFR	air-fuel-ratio
b	radiation calibration constant (Eq. 5-7)
C_1, C_2	Plank's first and second constant
D	combustor liner diameter
e	blackbody emission intensity
f_v	soot volume fraction
F	complex function of refractive index
h	enthalpy
H	height above the burner
I	transmitted laser intensity
I_e	thermal radiation intensity
I_o	laser source emission intensity
k	extinction coefficient
L	optical length
m	complex refractive index
$\dot{m}$	mass flow rate
n	number density
P	pressure
$P(\zeta)$	probability distribution function (of ζ)
Q_{abs}	absorption efficiency
Q_{ext}	extinction efficiency
Q_{sca}	scattering efficiency
r	particle radii
R	combustor radial position
T	temperature
u	velocity
V	voltage output on photon-detector
x	radial position
Y	mass fraction

Greek symbols

α,β	exponents in the beta function
α,δ	nucleation terms in the soot model (Eq. 2-8)
β	coagulation term in the soot model (Eq. 2-8)
γ	surface growth term in the soot model (Eq. 2-8)
ϵ	emissivity
η	carbon conversion rate

θ	radiation solid angle
λ	wavelength
μ	viscosity
ζ	mixture fraction
ρ	density
σ	transmittance
ϕ	general variable
ω	oxidation rate

Subscripts

d	dilution zone
HC	hydrocarbon
mix	mixture
s	soot
RMS	root-mean-square

Superscripts

$\bar{}$	Reynolds (time) average
$'$	Reynolds (time) fluctuation
$\sim$	Favre (mass weighted) average
$''$	Favre (mass weighted) fluctuation

Soot properties in CFD calculation (Figures 6-7 ~ 6-9)

FORM	formation rate (mass), kg m^{-3} s^{-1}
OXIM	oxidation rate (mass), kg m^{-3} s^{-1}
SOON	number density, $1/m^3$
SOOV	volume fraction

Chapter 1 Introduction

Soot particles formed inside gas turbine combustors are the major precursor of exhaust smoke emission. Smoke emission reduction in gas turbine combustion has attracted increasing research in recent years. The most immediate concern is the environmental impact of particulate emission. Even though gas turbine engines contribute only slightly to the overall problem of smoke atmospheric pollution, their contribution is significant in and around the local applications, for example the power plant or airport. The more demanding challenge currently is NO_x emission reduction to limit and minimise the depletion of stratospheric ozone layer. This has led to the development of low emission combustion technologies, like that of overall lean mixture-burning strategies, which will also tend to further reduce smoke levels. Other approaches however - for example, those incorporating rich burn/rapid quench/lean burn designs - enhance very substantially soot production in the now enlarged richer burning zones and require particularly effective burn-out subsequently. The trade-off between the smoke and NO_x emissions is critical to combustion technology development in terms of engine performance. The further disadvantage of smoke emission from the engine exhaust plume in the military aircraft is its visibility and thus is an easy target.

Particulate soot is an effective radiator and plays an important role in the thermal radiation from the combustion products to the combustor liner, especially as a continuum in the visible spectrum. Excessive radiation to the combustor wall will reduce the combustor durability and life and therefore increase the overhaul cost of the gas turbine engine. Currently, liner cooling is primarily effected by annular films of air introduced in discrete stages down the length of the combustor. Such films are essentially transparent however to thermal radiation from the luminous combustion zone. It is anticipated from current trends in combustor design that the percentage of cooling air flow will decrease in order to permit increases in the combustion air flow to enhance fuel-air mixing and combustion. Under these constraints, it is desirable to reduce the radiation source, or more specifically the soot production, in the combustor.

The better utilization of existing oil feedstock suggests that the fuel composition of future aviation kerosine could involve an increase in its Carbon/Hydrogen ratio and, in consequence, a tendency for its combustion to emit more soot. All these factors suggest that, in order to effectively control the unwanted soot production in the combustors, it is necessary to fully understand the mechanisms associated with the sooting processes in gas turbine

combustion.

From the combustion viewpoint, soot production reflects poor overall combustion and consequently a loss in combustion efficiency. Analytically there are two distinct combustion modes, one is premixed combustion and the other is non-premixed, or diffusion combustion. In the premixed flame, as in the petrol engine, the fuel and oxidizer, normally air, are well mixed prior to ignition. The mixture can in principle be considered to be homogeneous prior to combustion. When the mixture fraction of the fuel-air reactant mixture is beyond a certain range, typically around the value of 0.1, no soot will be formed in the flame and the problem of smoke emission will not be encountered. The advantages of premixed burning are impaired by its instability, auto-ignition and flashback, characteristics which may significantly restrict its adoption in aero-gas turbine combustors.

More commonly, practical combustion devices, like the gas turbine combustor, diesel engine and furnace, employ diffusion type combustion with simultaneous mixing and burning within an overall fuel-lean environment. The fuel, normally kerosine for the application in aircraft engines, and the air are initially separated and combustion takes place at the interface where they mix. Whether the local mixture in the flow field is lean or rich depends on the fuel and air mixing process, there usually exists a range of mixture in the flow from pure fuel (at the fuel injection exit) to pure air (at the air entrance). The mixing rate in a gaseous-fuelled flame is usually lower than the chemical-reaction rate and the combustion process is therefore mass diffusion controlled, or mixing controlled. In liquid fuel-air combustion, the fuel undergoes evaporation and the fuel vapour subsequently mixes with air and the burning is essentially dominated by physical diffusion. In the combustor the liquid fuel-air mixing is achieved by various ways, for example by establishing a highly turbulent flow field using multi-swirling flows in the dome, introducing primary and dilution jets to augment the local mixing. Even under these conditions, there still exist fuel rich domains, especially near the fuel injector region. These are potential sources of soot formation, although the sooting process also depends on the local temperature field and aerodynamic parameters, eg. turbulence and pressure.

The detailed sooting mechanism inside gas turbine combustor chambers is poorly understood. Studies on the sooting process in the past few years have mainly concentrated on laboratory flames of simple geometry. Most of these studies have focused on obtaining a phenomenological understanding which characterises the soot formation/oxidation mechanism for different combustion schemes rather than on establishing theoretical models to describe the sooting steps. Among these, very limited investigations are directly related to soot from gas

turbine combustion, reflecting in part the difficulties of obtaining diagnostic access into the combustor under representative operating conditions. On the other hand, detailed experimental data is crucial to the validation of computer-based soot models developed for the purpose of combustor theoretical analysis and design evaluation.

Early combustor design is based on empirical data from extensive testing and their correlation with models of gross features which essentially outline the potential combustor performance. This approach has been utilised successfully for gross aerodynamic properties such as the exit plane temperature uniformity, combustion efficiency etc. (Lefebvre (1983)). Attempts in relation to emission predictions, especially of those with slow chemical process like NO_x and smoke, are less satisfactory as these species are not locally equilibrated and the detailed production mechanism inside the combustor chamber is usually required. Gas turbine combustion in current generation designs employs non-premixed type burning, where inlet air and liquid fuel are initially fed in separately. The internal flowfield is particularly influenced by the combustor geometry and fuel injection scheme. From the standpoint of global flame structure and as outlined earlier, the combustion is mixing rate controlled. The fuel-air turbulent mixing can be characterised by the distribution of local equivalence ratio, or mixture fraction. Mixture fraction is widely used as the key conserved scalar to which other scalars, for example temperature and species concentrations, are related by unique state relationships. This forms the basis for a number of detailed theoretical approaches (Peters (1984)).

The laminar flamelet concept has shown considerable potential as a means of resolving turbulent reacting flows where the chemistry can be considered to be fast (Bilger (1976) and Peters (1984)). In dealing with the slow soot formation/oxidation in turbulent diffusion flames, Moss and co-workers have extended this flamelet approach to soot source term modelling in laminar flames (Moss et al. (1988)), buoyant fires (Syed (1991)) and jet flames (Young (1993)). The soot model comprises essentially two equations, for particle number density and volume fraction, characterising the global sooting mechanism. The formation rates in the model are assumed to be simply dependent on local mixture fraction and the detailed chemistry/turbulence interaction is thus simplified. The strategy has been demonstrated for a combustor flow field calculation, however without direct comparison with experimental data for soot concentration profiles (Alizadeh (1993)). A highly turbulent flow, in a complex geometry with swirl, typical of those in a combustor, is thus required for the soot model validation. The aim of this thesis work is primarily to develop appropriate diagnostic techniques for soot concentration measurement inside the combustor and also to show comparisons between laminar flamelet soot modelling and the measured data.

The present study is mainly driven by the investigation of in-situ techniques for spatially-resolved soot concentration measurement in a tubular gas turbine combustor of conventional design. Properties of the local flow field, like temperature and species concentrations have been obtained to complement to the soot information. Spectral thermal radiation was also measured and compared with predictions based on the temperature and soot concentration profiles. Numerical predictions of this combustor flow field using the extended laminar flamelet approach are also presented.

The thesis has the following structure:

Chapter 2 describes the background on the sooting process, including its formation and oxidation in the gas turbine combustor. The application of computational fluid dynamics to combustor flow field evaluation is briefly discussed and numerical models for soot production during combustion are analyzed.

Chapter 3 discusses the development of optical techniques for in-situ soot volume fraction measurement. Two techniques are first evaluated in laboratory jet flames, for which there exists a data base of soot profiles from other independent measurements. Following their evaluation, spatially resolved soot concentration distributions were measured from within a tubular combustor, operating at modestly preheated air inlet temperatures and elevated pressures up to 4 bar.

Chapter 4 describes the characterisation of additional combustor flow field properties, mainly temperature and species concentration profiles. Mixture fraction profiles, the critical conserved scalar in the flamelet approach, are also measured by a sampling method developed from studies of simple laboratory flames (Moss et al. (1988)). The state relationships for time-averaged soot volume fraction, temperature and CO_2, as the major combustion product, against mean mixture fraction are reported for the combustor flow.

Thermal radiation, directly related to soot production, is measured in Chapter 5. From this experiment, methods of optical temperature determination are assessed first in laminar diffusion flames. Modifications for the instrumetations were made for radiation detection in the combustor following conclusions from the laminar flame experiment. The measured radiation in the combustor is compared with the prediction from measured mean properties including temperature and soot volume fraction reported in Chapters 3 and 4.

Numerical predictions of the combustor flow field are described in Chapter 6 based on

a commercial CFD package, PHOENICS, which is modified to incorporate a laminar flamelet approach. The flamelet library, essential for turbulent flow calculations, is constructed from predictions using a one dimensional counter flow code. The computational results for temperature and CO_2 profiles are compared with the measurements reported in Chapter 4. Further calculations of soot production in the combustor use an extended laminar flamelet method, adopted from that initially developed for an ethylene-air diffusion flame which has also been evaluated for laminar and turbulent pre-vaporized kerosine-air diffusion flames (Moss et al. (1991)). The predicted soot volume fraction profiles are compared with the measured data from Chapter 3.

The final Chapter 7 reviews the overall study, sets out summary conclusions and highlights recommendations for future investigations.

Chapter 2 Soot Formation and Oxidation in Turbulent Flames

2.1 INTRODUCTION

The production of particulate carbon (soot) during combustion occurs when there is incomplete conversion of carbon elements in the fuel to CO. The presence of soot is not desirable in many combustion situations, like those involved in gas turbine combustors, diesel engines and fires. In other circumstances, like furnace combustion however, soot acts as a major radiant source and contributes most of the heat transfer from the flame. Similarly, the candle flame also depends on the luminosity of soot radiation. Whether the objective is to promote or to suppress the soot production in a particular application one needs to have a thorough understanding of the detailed sooting mechanisms inside the flame.

The combustion of liquid and gaseous hydrocarbons are of practical interest as most of the presently utilised fuels - for example kerosine, diesel and natural gas - fall into this category. Once it is formed from these fuels, soot is often difficult to burn out. Whilst other types of fuel, like coal and wood, also tend to emit smoke, they are comparatively less problematic in terms of soot formation. This is because their combustion usually takes place in large chambers permitting more control, both spatially and temporally, than in other systems.

Sooting behaviour in premixed and non-premixed flames provides the theme for different research topics. In premixed flames, physical mixing at the molecular level is assumed to be perfectly achieved and the combustion of a homogeneous mixture is controlled by both chemical kinetics and heat transfer. Chemistry related to soot formation can in principle be resolved in more detail, eg. the influences of temperature, parent fuel properties and chemical pathways to soot formation. The sooting dependence on other flame parameters, for example pressure and temperature, can also be investigated. Although the general sooting mechanism in premixed flames is similar with that in diffusion flames, the detailed processes in the two flames are however quite different.

In diffusion flames, the sooting chemistry is always coupled with fuel-oxidizer mixing. The finite kinetic rate of soot formation is, unlike many other gaseous combustion products, comparable with the physical mixing rate and therefore the formation process may not be simplified as mixing limited. There the soot formation is more associated with the combustion process and local flame variables thereof such as mixture fraction, temperature and sometimes

residence time.

Co-flowing laminar diffusion flames are one of the popularly used burning configurations for establishing reliable soot models which embrace the formation rates responsible for each sooting stages. Soot in laminar diffusion flames is formed in a region on the fuel side, roughly parallel to the reaction zone. Soot particles diffuse very slowly, so the structure of this region is determined by convection of the particles from the fuel rich side to the reaction zone interior of the flame. As the particles flow to the upper regions of the flame, oxidation takes over and the balance of formation and oxidation rates determines the final production. In turbulent flames, soot is formed on the fuel side of the peak temperature contour after the initial pyrolysis products. The soot formation rate is sensitive to initial conditions, for example fuel type and inlet temperature. Soot burnout begins to occur very close to the peak in temperature where O_2 starts to penetrate (Haynes and Wagner (1981) and Kent and Wagner (1984)).

The theoretical models developed from laminar flames are ultimately to be applied to soot predictions in turbulent flames. The soot formation mechanism is a quite complex issue and various approaches have been demonstrated to quantify this mechanism. Early reviews on soot by, for example Tesner (1979), Calcote (1981) and Haynes and Wagner (1981), gave some fundamentals on soot production which outlined that the governing stages includes qualitatively four steps, namely (1) particle nucleation, (2) surface growth, (3) coagulation and (4) oxidation. Each step has its own distinct characteristics in terms of the evolution of soot particle size and number density. The accumulation of kinetic and mechanistic descriptions in recent years in relation to soot formation has led to some progress in developing soot models which may be applicable to practical combustion systems, for example those including detailed sooting chemistry or employing global mechanism (Jander and Wagner (1990) and Bockhorn (1993)). In the more specific areas, Glassman (1988) provided an overview of the sooting chemistry in various burning configurations - pre-mixed flames, normal and inverse co-annular, Wolfhard-Parker and counter-flowing diffusion flames, and shock tubes. Charalampopoulos (1992) focused on the morphology and dynamics of particulate soot in combustion systems by using laser scattering techniques.

The intention of this chapter is to outline briefly the basics of soot formation/destruction in combustion processes, with particular emphasis on gas turbine combustion generated soot particles. Theoretical approaches to its formation and oxidation are also presented, together with the strategies for numerical modelling of combustor flowfield including soot particles.

2.2 SOOT IN COMBUSTION

2.2.1 Soot formation/consumption

The four governing steps mentioned above represent the whole sooting process regardless of the burning modes and flow conditions. Formation and oxidation may coincide in the flame, depending on the temperature and mixing progress history. When the reactants are pre-mixed, the onset of soot generation theoretically occurs with the C/O ratio (in mole) of the homogeneous mixture exceeds unity. Experimental results from different burning configurations, eg. Bunsen burner, flat flame and stirred reactor (Haynes and Wagner (1981) and Glassman (1988)), suggest that this critical C/O ratio is around the value of 0.5. In their model primary zone, notionally simulating gas turbine combustion, Holderness and Macfarlane (1973) found the threshold of equivalence ratio to be 1.4 to 1.5 for kerosine spray burning, or C/O ratio from 0.52 to 0.56. The output of soot in premixed flames increases rapidly with increasing C/O ratio up to the rich flammable limit. The range of critical equivalence ratio, or mixture fraction, in diffusion flames is however much narrower. Soot in diffusion flames is discussed here since gas turbine combustion insofar employs this scheme.

Nucleation

The combustion of hydrocarbon-air mixtures undergoes fuel pyrolysis in the absence of oxygen. The intermediate products usually include unsaturated hydrocarbons, particularly acetylene and its higher analogues and more important polycyclic aromatic hydrocarbons (PAH). The gas phase condensation of these soot precursors at high temperatures, which includes the chemical and physical growth of the precursors, will eventually result in the formation of small particle nuclei - the first appearance of soot. The temperature for soot onset is believed to be around 1400 K (Glassman (1988)). Weiner and Harris (1988) proposed that soot particle inception is due to coalescent collisions between very large hydrocarbons, like those of 1000 amu (atomic mass unit). Although this route is widely accepted, there exist other views arguing against this radical mechanism. Calcote (1981) has suggested that reactions of neutral species cannot possibly explain the fast growth rates of the intermediate species and that soot formation is controlled by ionic mechanisms. However the experimental evidence by Bertrand and Delfau (1985) indicated that ions have very small, if any, effect on the production of soot. The dependence of soot formation on the radical character of PAH formation is supported by many experimental results like those of Mckinnon and Howard (1992) and D'Alessio et al. (1992) and also by kinetic modelling (Frenklach and Wang (1990)).

The elementary soot particles formed during nucleation have broadly the same physical and chemical characteristics regardless of the fuel precursor or combustion process (Palmer and Cullis (1965)). The mature soot collected from the diffusion flames of various hydrocarbons by Saito et al. (1991) shows the same morphology as reported by Megaridis and Dobbins (1988) from an ethylene flame. These particles are spherical and the average diameter is typically in the range of 20~40 nm. The smallest particles that are documented are about 8 nm (Harris and Weiner (1983)). These spherical units are made up of graphite type layers where the inter layer spacing is somewhat greater than that of graphite. They have a hexagonal structure similar to graphite, characterising the aromatic ring structure of its PAH precursor, and have a carbon-to-hydrogen (C/H) atomic ratio of about 8:1 ~ 12:1 (Calcote (1981)). The soot density is close to that of graphite at about 2000 kg/m^3.

Surface growth

The chemical composition of soot, though mainly carbon, differs with the time history of its formation. The earliest soot may contain hydrogen up to 10% by mole. Once the solid phase soot emerges, its reaction with surrounding gas, particularly acetylene, takes place appreciably on the surface of the particle. The higher reactivity of H in the soot gradually leads to the reduction in mass percentage of hydrogen content. Accompanying this H-abstraction is the decomposition of C_2H_2 on the surface of soot which leads to the increase of the soot C/H ratio. Besides the C_2H_2 participation, recent analysis by Frenklach and Wang (1990) and the experimental observation by Mckinnon and Howard (1992) suggested that PAH condensation onto soot particles also contributes to the surface growth at the early stage. Along with this surface growth reaction is a diminishing of the radical nature of soot (the phenomenon known as soot aging) under the influence of gas phase species collision. As the soot activation declines, the surface growth will cease at some point. According to Harris et al. (1986) surface growth is responsible for at least 90% of the ultimate soot loading in most systems, with particle inception responsible for the rest.

Coagulation

Particle coagulation is the only physical step without chemical reaction involvement. The aggressive young particles are subject to coalescence and essentially grow together, filling the space inbetween the particles with material from the gas phase. When they are old enough, with less reactivity, they do not continue growing then only agglomerate and stick together to form aggregates of several possible shapes such as clusters, straight chains and randomly branched chains. The coagulation has a strong influence on the morphology (structure and size

distribution) of soot and in consequence its optical properties. The initial soot number density is determined by nucleation, typically ranges from $10^{18} \sim 10^{19}$ 1/m^3. The coagulation results in lower number density and bigger size without affecting the soot volume (mass) fraction. The aggregate number density in the burned gases of a variety of combustion processes is remarkably similar and lies between $10^{15} \sim 10^{16}$ 1/m^3 (Jander and Wagner (1990)). The upper limit of the particle diameter, however depends on the combustion configuration. In laboratory flames the size can reach up to about 200 nm (Kent and Wagner (1983)). A maximum size, about 250 nm of the similar magnitude, was observed in a gas turbine combustor (Eckerle and Rosfjord (1988)). After reaching the maximum size discretely, the burn out of individual soot aggregates follows.

Oxidation

Soot particles undergoing oxidation are relatively mature with respect to the formation processes. The most important soot oxidizing agents are oxygen molecules, oxygen atoms and hydroxyl radicals, depending on the local flame conditions. It is also conceivable that the major combustion products carbon dioxide and water oxidise soot to some extent. Laurendeau (1978) has suggested, based on char gasification, that these reactions would only be significant under rather fuel-rich conditions.

The most acclaimed particulate oxidation mechanism is that proposed by Nagle and Strickland-Constable (1962). They investigated the oxidation of artificial carbon, graphite and pyrographite by the oxygen molecule at the pressure of about 20 kPa and temperatures above 2000 K, where the oxidation rate becomes reasonably constant. The burnout process of soot is very close to that of graphite and thus the Nagle and Strickland-Constable model has been applied directly to soot (Appleton (1973)). Their semi-empirical formula has been shown to yield accurate oxidation rates for partial pressures of oxygen from 10^{-5} to 1 atm, and temperatures from 1100 to 2500 K. The role of O_2 in soot oxidation was also supported by Lee et al. (1962), however within narrower oxygen partial pressure range ($0.04 \sim 0.1$ atm).

The oxidation by O_2 using such rates, notably the Nagle and Strickland-Constable expression, underestimated the oxidation step in some cases and the addition of particle oxidation by hydroxyl radical seems appropriate (Neoh et al. (1981) and Garo et al. (1990)). The OH attack on soot surface was considered by Millikan and Foss (1962) and later formulated by Fenimore and Jones (1967). Recently Neoh et al. (1981, 1984) studied the kinetics and mechanism of soot oxidation at temperatures between 1575 and 1865 K and oxygen partial pressure of 10^{-5} to 0.05. They found that hydroxyl radical is the principal oxidant under these

conditions, characteristic of fuel rich flames. The reaction probability, or collision efficiency, of soot with oxygen atom and hydroxyl radical is expected to be higher than with oxygen molecule. Under fuel rich conditions the oxygen concentration on the other hand may be comparable to the O concentration and even less than the OH concentration. The rate of soot oxidation by these species, especially hydroxyl radical, will thus be higher than that by oxygen when their concentrations increase. The formulae associated with oxidation rates by O_2 and OH are presented in a later section 2.3.3.

The combustion of soot ceases at about 1300 K. The effect of oxidation on the physical structure of soot under fuel-lean conditions was found to be an increase in number density together with the decrease of size and volume fraction (Neoh et al. (1984)). The increase of number density is interpreted to mean that soot aggregates or particles break up during oxidation due to internal burning by oxygen molecules. For fuel-rich conditions the restricted hydroxyl radicals attack gives much less internal burning. The balance of the formation rate and burn out rate determines the final smoke emission level from the flame.

2.2.2 Gas Turbine Combustion Generated Soot

Diffusion flames, specifically turbulent diffusion flames, are the practical form of combustion in which soot problems most readily manifest themselves. Gas turbine combustion is usually maintained by a spray of fuel entering the dome of the combustor, into which air is gradually fed along the full length of the combustor, featuring a globally non-premixed flame. The combustion products must then be diluted with excess air to a uniformly lower temperature level acceptable to the turbine and also to oxidize the particulate soot effectively to reduce the exhaust smoke emission level.

The heterogeneous air-liquid fuel burning proceeds concurrently with mixing, which makes the physico-chemical processes more closely coupled. The two-phase gas turbine combustion, or sometimes multi-phase in the presence of solid particles, is one of the most complicated spray combustion systems, especially in relation to soot formation. The flow field is often highly turbulent, in order to augment the intimate fuel-air mixing and thereafter to achieve high combustion efficiency, normally above 99%. Unlike many laboratory flames, which are often two dimensional, the flame inside the combustor is three-dimensional and the flame front is difficult to define due to the complex aerodynamic flow pattern, determined by spray atomization. As a result, defining the soot formation regime is also a complicated task but this is crucial in developing methods to reduce soot production.

The comparatively recent application of air blast atomizers has the distinct advantage over the previous pressure jet atomizer that it generates a relatively finer spray, (mean droplet sizes of about 40 μm from airblast atomization and 80 μm from pressure atomization), whose spray is leaner due to the air addition in the injector and the structure (mainly cone angle) is less sensitive to the change of combustion chamber pressure. Its soot emission related performance is evidently much better than its pressure jet counterpart (Lefebvre (1983)). Spray combustion has been the subject of a number of comprehensive reviews by, eg. Chigier (1976), Faeth (1983, 1987) and Williams (1990). In the initial regions of the spray, near the atomizer exit, both the temperature and oxygen concentration levels are too low to allow combustion in the dense spray. When the bulk liquid is dispersed into a droplet cloud, the individual droplets undergo evaporation at temperatures substantially lower than the flame temperature (Chigier (1976)). Presser et al. (1993) observed from their swirling spray flames with pressure-jet atomization that large droplets are transported downstream relatively unperturbed by the surrounding gas stream while smaller ones are entrained by the recirculating aerodynamic pattern. Most of the droplets in the spray do not burn individually but their vapour clouds mix with air and subsequently burn in the flame front interfaced by fuel vapour and air in a diffusion flame manner. This is generally plausible, especially for the description of group combustion of droplets. In their confined air-blast atomizer spray flames, McDonell and Samuelsen (1991) have found that the general structure of the flame is consistent with the group combustion theory, although it is noted that individual small drops still exist outside of the reaction zone. For very small (say, 10μm) droplets of a high-volatility fuel, the evaporation may be complete in the heat up process, so that the flame structure is only mildly influenced by the effect of two-phase flow. When the fuel-air mixing has a comparable rate to the reaction, the flame may be premixed-like (Kuo (1986)). Nevertheless, the mass (or volume, which is proportional to the cube of the diameter) percentage of small droplets in a spray is usually low and their impact on the whole spray combustion will not be significant.

The vapour-air combustion in the convective environment inside gas turbine combustors takes place along the droplet trajectory. The flame is anchored in the combustor recirculation zone where unburned mixtures are entrained and ignited by the recirculating burned hot gases. Part of the ignited reactants burn inside the recirculation zone acting as new ignition source whilst the rest leave the recirculation zone and subsequently burn downstream. The combustion products from the upstream primary zone are mixed and cooled later, in modern engines by dilution air. The primary zone which includes high temperature and rich mixture eddies is the main soot formation region. The low velocity, increased residence time, recirculation zone is favourable for the slow sooting process. Combustors of different design may have quite different flowfield or recirculation zone structure, depending on the primary jet penetration and

flow split. Deeper jet penetration and strong air swirling, for example, may result in shorter recirculation zones. Therefore the soot formation domains in combustors are often strongly geometry-dependent.

Experimental data from laminar diffusion flames suggest that the soot formation region is very narrow, typically centred on a mixture fraction around 0.1 and temperatures above 1400 K (Glassman (1988)). Mixture fraction measurement inside the combustor liner presents a formidable task at present due to the lack of a reliable technique. From the soot reduction point of view, the primary zone has to be designed to operate near stoichiometric and to eliminate rich pockets, within the constraints of combustion stability, ignitability and NO_x emission.

The soot formed in the primary zone is subject to oxidation downstream. Burn out by O_2 and OH, which is evident in laboratory flames, is expected to hold true in the combustor as well. The lack of experimental data, especially OH concentration, makes it difficult to judge which is the dominant oxidizer. At present, the limited soot modelling campaigns in combustors continue to treat O_2 as the main contributor to soot oxidation (Alizadeh (1993) and Srivatsa (1982)).

2.3 MODELLING SOOT PRODUCTION IN THE COMBUSTOR FLOW FIELD

2.3.1 Equations for turbulent reacting flows

The basic equations governing turbulent reacting flows are based on the continuity and Navier-Stokes equations. When chemical reaction is involved in the flow, extra balance equations are required to address the heat release and chemical species conservation. The mass-weighted balance equations for mass, momentum, energy and chemical species concentration in steady flows, for example those in gas turbine combustions, assume the form -

mass continuity

$$\frac{\partial}{\partial x_j}(\bar{\rho}\tilde{u}_j)=0 \qquad (2\text{-}1)$$

momentum conservation

$$\frac{\partial(\bar{\rho}\tilde{u}_i\tilde{u}_j)}{\partial x_j}=-\frac{\partial \bar{p}}{\partial x_i}+\frac{\partial}{\partial x_j}(\bar{\tau}_{ij}-\overline{\rho u_i'' u_j''}) \qquad (2\text{-}2)$$

enthalpy

$$\frac{\partial(\rho\tilde{u}_j\tilde{h})}{\partial x_j} = \tilde{u}_j\frac{\partial\bar{p}}{\partial x_j} + \frac{\partial}{\partial x_j}[\mu\overline{\frac{\partial h}{\partial x_j}} - \overline{\rho u_j'' h''}] - \frac{\partial\dot{q}_j}{\partial x_j} \tag{2-3}$$

chemical species

$$\frac{\partial(\bar{\rho}\tilde{u}_j\tilde{Y}_k)}{\partial x_j} = \frac{\partial}{\partial x_j}(\rho D\overline{\frac{\partial Y_k}{\partial x_j}} - \overline{\rho u_j'' Y_k''}) + \bar{S}_k \tag{2-4}$$

To solve the equations for a turbulent flow field, a scalar effective-viscosity turbulence model is usually employed (Launder and Spalding (1974)). This two-equations model is initially for simple thin shear layer type flows where velocity gradient and scalar gradient each have only one single significant component. Such gradients in the combustor flow field, especially in the recirculation zone, usually have more than one significant component and turbulent transport are dominant which can not be described in eddy viscosity terms. According to the experimental data analysis reported by Heitor and Whitelaw (1986), the eddy-viscosity turbulence model should be adequate for the flow in the dilution section of the combustor since the production of turbulent kinetic energy is largely due to the interaction of shear stress with shear strain. In the upstream recirculation zone, the flow is characterized by a large mean radial pressure gradient. Since the production of turbulent kinetic energy is not accounted for by mean gradient mechanisms, the k-ϵ model would underpredict the turbulent energy levels, and is unlike to provide correct trends for the turbulent transport of scalar quantities in the primary zone.

The two-equation model has nevertheless been used extensively for the complex three-dimensional flows in combustors. Its wide applications in combustion are owing to the simplifications in the numerical approaches where the detailed solutions of the Reynolds stresses and turbulent scalar flux are presented by the more efficient first order closure. It is by far the best compromise between accuracy and computational cost. Alternative second moment closures offer a possible means of removing some of the uncertainties in the use of k-ϵ model. The solutions in this approach for the dissipation rate equation together with the 6 Reynolds stresses and turbulent scalar flux balance equations are not well developed yet (Jones and Whitelaw (1984)). Hence most of the computational fluid dynamics (CFD) codes, notably PHOENICS, FLUENT, etc. are primarily based on the two equation turbulent model.

2.3.2 Chemical source term closure

Closure of the mean chemical source term $\overline{S_\alpha}$ from the averaging of Eq. 2-4 poses one

of the most difficult tasks in combustion modelling. The source term is typically a linear function of species concentrations but exponential function of temperature. This highly non-linear form introduces considerable difficulty as the mean rate of reaction cannot be calculated from the mean temperature and the property fluctuation has to be taken into account. Decomposition of the source term S_α contains a number of cross-correlations of scalar variables which need further balance equations (Libby and Williams (1980)).

To avoid this disadvantage in tackling turbulent reacting flows, simplified models have been proposed which are based on the fast chemistry assumption. For non-premixed flames it is essential that the rate of chemical reaction is much faster than the rate of turbulent transport and the combustion is then mixing controlled. A chemistry-independent conserved scalar variable, mixture fraction ζ, is introduced to describe the turbulent inter-diffusion. All other scalars are assumed to be uniquely related to the mixture fraction. Such state relationships can be established from either chemical equilibrium or laminar flamelet calculations (Bilger (1980)) and experimental data from laminar flames. With equal diffusivities for all species, the balance equation (2-4) for the mixture fraction has no source term and hence greatly simplifies its solution. Equilibrium calculations of arbitrary complexity can be performed on the computer for adiabatic reactions of fast, reversible chemistry (Gordon and McBride (1971)). Most practical combustion however does not attain equilibrium everywhere and equilibrium prediction tends to overestimate, for example CO and H_2 in turbulent diffusion flames (Liew et al. (1984)) and gas turbine combustors (McGuirk (1987)). One approach to the departure from equilibrium is addressed in the recently developed laminar flamelet model.

In the laminar flamelet concept, a turbulent flame is considered to comprise microscopic laminar flamelets whose characteristic dimension is smaller than the principal turbulent length scales. Each flamelet may be subject to hydrodynamic strain and the scalar state relationships $\phi_\alpha=\phi_\alpha(\zeta;\chi)$ are then functions of the two parameters, mixture fraction and a measure of the local strain, χ. The latter denotes the scalar dissipation rate which is characteristic of the reciprocal strain field. The inclusion of the stretch implies that libraries of flamelet profiles have to be generated for a range of strain rates through either laborious experiments or numerical calculations, which in turn needs full understanding of the chemical reaction mechanisms. Reactions of fuels, as large as C_8-hydrocarbons (octane), and air combustions have been well described at the elementary level (Westbrook and Pitz (1991)). For the practical multi-components fuels, like diesel and kerosine, the relevant detailed chemical kinetics are however poorly understood. Attempts to formulate simplified kerosine-air reaction mechanisms in the present programme are illustrated in Appendix E, which is based on sub-kinetic models involving elementary reactions up to C_4, the sub-models are primarily limited by the employed

numerical code capability.

The instantaneous state relationships between the conserved scalar - mixture fraction ζ - and other scalars ϕ are in general non-linear and the statistics of the mixture fraction are required to calculate the mean and higher moments of these thermochemical variables. For each spatial location x, the first and second moments of the scalars may be obtained from the probability distribution $p(\zeta;x)$:

$$\tilde{\phi}(x) = \int_0^1 \phi(\zeta)\tilde{p}(\zeta;x)d\zeta \tag{2-5a}$$

$$\widetilde{\phi''^2}(x) = \int_0^1 [\phi(\zeta) - \tilde{\phi}(x)]^2 \tilde{p}(\zeta;x)d\zeta \tag{2-5b}$$

where the density (Favre) weighted pdf may be defined as

$$\tilde{p}(\zeta;x) = \rho p(\zeta;x)/\overline{\rho} \tag{2-6}$$

The pdf is often determined by adopting a standard n-parameter distribution function and relating the first n statistical moments to these parameters. The beta-function distribution has been most widely used since it has the advantage that its two parameters can be related algebraically to the first two moments of the scalars (cf. Peters (1984)). The normalised beta-function for mixture fraction has the form

$$p(\zeta) = \frac{\zeta^{\alpha-1}(1-\zeta)^{\beta-1}}{\int_0^1 \zeta^{\alpha-1}(1-\zeta)^{\beta-1}d\zeta} \tag{2-7}$$

Another widely used prescription of the shape of the pdf is the clipped-Gaussian but this is mathematically less tractable in CFD applications. The beta-function has been used in the present study.

In turbulent flames the state relationships are often functions of more than one variable, for example local strain rate and the kinetic rate of chemical reaction in the case of slow chemistry like NOx and soot formation. Extra independent variables have to be introduced and the subsequent multivariate pdf, or joint pdfs based on statistical independence, does not yet provide satisfactory solutions. Evidence from laminar flame experiments indicates that soot formation rates, rather than the soot concentration itself, are functions of mixture fraction only (Kent and Honnery (1990) and Moss et al. (1991)). The mean formation rates have been established in this manner and incorporated as source terms in the balance equations for soot parameters. The laminar flamelet approach has therefore been extended to the soot modelling in turbulent flames without further major computational complexity. The strategy will be outlined in the next section.

2.3.3 Soot model

Soot formation

By comparison with the fast chemistry of the heat release mechanisms, soot formation is characterized as a typically slow chemical process and the controlling steps in the formation mechanisms have to be precisely identified. Detailed kinetic modelling by Frenklach and Wang (1990) for the individual steps, for example nucleation and surface growth outlined in section 2.2.1, have showed good agreement with measurements. However the number of independent composition variables which such models invoke lies far beyond that which can be incorporated in practical combustion calculations for the foreseeable future.

A number of simplifications have been made in which the sooting steps are restricted to global mechanisms. Khan and Greeves (1974) investigated soot formation in diesel engines and derived a correlation which suggested that the rate of soot production is a function of equivalence ratio (mixture fraction), unburned fuel concentration and temperature. Similar one-step expressions have been used in gas turbine combustors by Naegeli et al. (1983) and, more generally, by Mullins et al. (1987). A more mechanistic formulation, via a two-step process, was introduced by Tesner et al. (1971) and, based on the early work of Gilyazetdnov (1972), by Moss et al. (1987, 1988). The later model centred on two variables, the particle number density, n and the volume fraction, f_v. The perceived critical processes of nucleation, surface growth and coagulation are incorporated in rate expressions of the form

$$\frac{d}{dt}\left(\frac{n}{N_0}\right) = \alpha - \beta\left(\frac{n}{N_0}\right)^2, \quad m^{-3}s^{-1} \qquad (2\text{-}8a)$$

(nucleation) (coagulation)

$$\rho_s \frac{df_v}{dt} = \gamma f_v^{\frac{2}{3}} n^{\frac{1}{3}} + \delta, \quad kg\,m^{-3}s^{-1} \qquad (2\text{-}8b)$$

(surface growth) (nucleation)

where

$\alpha \equiv C_\alpha \rho^2 T^{1/2} Y_{HC} \exp(-T_\alpha/T)$	$m^{-3}\,s^{-1}$
$\beta \equiv C_\beta T^{1/2}$	$m^3\,s^{-1}$
$\gamma \equiv C_\gamma \rho T^{1/2} Y_{HC} \exp(-T_\gamma/T)$	$kg\,s^{-1}$
$\delta \equiv C_\delta \alpha$	$kg\,m^{-3}\,s^{-1}$

ρ_s and N_0 denote an assumed soot density (1800 kg/m^3) and Avogadro's number (6×10^{26}) respectively, whilst Y_{HC} is a representative fuel fraction. The comparisons of predicted and measured soot volume fraction distributions in laminar diffusion flames showed that this model

can satisfactorily predict the soot properties by identifying appropriate constants for the above rate expressions. The two-step model can yield better predictions in turbulent flames than the one-step counterpart owing to its more detailed prescription for the physical processes (Coelho et al. (1993)). The disadvantages of all these empirical models lie in the fact that the constants evaluated for one flame configuration may need to be re-calibrated for different flames (Moss et al. (1988)). Furthermore, the rate constants C_α,C_β,C_γ,C_δ and especially the activation energy (temperature T_α and T_γ), are highly fuel type dependent. This is clearly demonstrated in the results of a laminar pre-vaporised kerosine flame where the rate constants are quite different from that of methane and ethylene flames (Stewart et al. (1991)). Nevertheless the experimental effort in model validation is small and simplified global mechanisms are broadly compatible with the computational demands of turbulent flame predictions.

Soot oxidation

The rate of soot destruction has received less attention than the formation rates. The process is comparatively straight forward, where mature soot particles are subject to oxidative attack by gaseous species. As mentioned in section 2.2.1, the major oxidation species of engineering importance are oxygen molecules and hydroxyl radicals. Even though there are differences between the graphite and soot with respect to their respective chemical compositions, the burnout rate of graphite by O_2 is widely used to predict the soot oxidation. The semi-empirical oxidation rate by O_2 formulated by Nagle and Strickland-Constable (1962) takes the form:

$$\omega = 120[(\frac{k_A P_{O_2}}{1+k_z P_{O_2}})\chi + k_B P_{O_2}(1-\chi)], \quad kg \cdot m^{-2} s^{-1} \tag{2-9}$$

where

$$\chi = [1 + k_T/(k_B P_{O_2})]^{-1}$$

$k_A = 20.0 \times \exp(-15{,}100/T)$ kg m^{-2} s^{-1} atm^{-1}

$k_B = 4.46 \times 10^{-3} \exp(-7{,}640/T)$ kg m^{-2} s^{-1} atm^{-1}

$k_T = 1.51 \times 10^{5} \exp(-48{,}800/T)$ kg m^{-2} s^{-1}

and

$k_z = 21.3 \times \exp(2{,}060/T)$ atm^{-1}

Another, often cited, rate expression is that proposed by Lee et al. (1962) which was developed on the basis of soot particle destruction on a laminar diffusion flame and generally gives a relatively higher oxidation rate than the Nagle and Strickland-Constable one (Appleton (1973)).

The role of the hydroxyl radical in soot oxidation has been emphasised recently by Neoh

(1981) and Bradley et al. (1984) and experimentally investigated by Garo et al. (1990) using laser induced fluorescence for OH radical concentration measurement. The long-standing expression due to Fenimore and Jones (1967),

$$\omega = 1.27 \times 10^3 \times \alpha \times P_{OH} / \sqrt{T}, \quad kg \cdot m^{-2} s^{-1} \tag{2-10}$$

has been adopted, where α is the collision efficiency and is found experimentally to assume the value of 0.13 ~ 0.28 (Neoh et al. (1981) and Bradley et al. (1984)) or up to 0.1 as reported by Garo et al. (1990)). Similar level has also been reported by Roth and von Gersum (1990) where the collision efficiency is estimated to be 0.2.

A typical comparison of oxidation rates from Eqs. 2-9 ~ 2-10 is illustrated in Figure 2.1, where a laminar flamelet data set for propane-air combustion is used at the initial temperature for air and fuel of 473 and 300 K, respectively, at 1 bar pressure. The collision efficiency α is chosen as 0.1. Both these expressions are incorporated in the present combustor soot predictions and the results will be shown in Chapter 6.

Turbulent closure of the source terms for soot properties in Eq. 2-4 is achieved by averaging over the mixture fraction probability density function, P(ζ), namely

$$\overline{S}_{soot} = \int_0^1 S(\overline{\phi}, \zeta) P(\zeta) d\zeta \tag{2-11}$$

and neglecting the more complex correlations between soot properties and mixture fraction (Moss et al. (1991)). The time-averaged soot number density N and soot volume fraction f_v can then be implemented to the balance equation 2-4 following the forms

$$\frac{\partial}{\partial x_i}(\overline{\rho}\,\tilde{u}_i\tilde{\phi}_n) - \frac{\partial}{\partial x_i}\left(\frac{\mu_t}{\sigma_\phi}\frac{\partial \tilde{\phi}_n}{\partial x_i}\right) = \overline{\alpha} - \overline{\rho}^{\,2}\,\overline{\beta}\,\tilde{\phi}_n^{\,2} - N_0^{\,1/3}\,\overline{\rho}\,\overline{\epsilon}\,\tilde{\phi}_n^{\,4/3}\,\tilde{\phi}_m^{\,-1/3} \tag{2-12a}$$

$$\frac{\partial}{\partial x_i}(\overline{\rho}\,\tilde{u}_i\tilde{\phi}_m) - \frac{\partial}{\partial x_i}\left(\frac{\mu_t}{\sigma_\phi}\frac{\partial \tilde{\phi}_m}{\partial x_i}\right) = \overline{\delta} + N_0\overline{\rho}\,\overline{\gamma}\,\tilde{\phi}_n - N_0^{\,1/3}\,\overline{\rho}\,\overline{\epsilon}\,\tilde{\phi}_n^{\,1/3}\,\tilde{\phi}_m^{\,-2/3} \tag{2-12b}$$

where

$$\tilde{\phi}_n = \frac{\overline{n}}{N_0\,\overline{\rho}} \qquad \tilde{\phi}_m = \frac{\rho_s \overline{f_v}}{\overline{\rho}} \tag{2-13}$$

and the oxidation term in Eq. 2-12

$$\epsilon = \left(\frac{36\pi}{\rho_s^{\,2}}\right)^{\frac{1}{3}}\omega \tag{2-14}$$

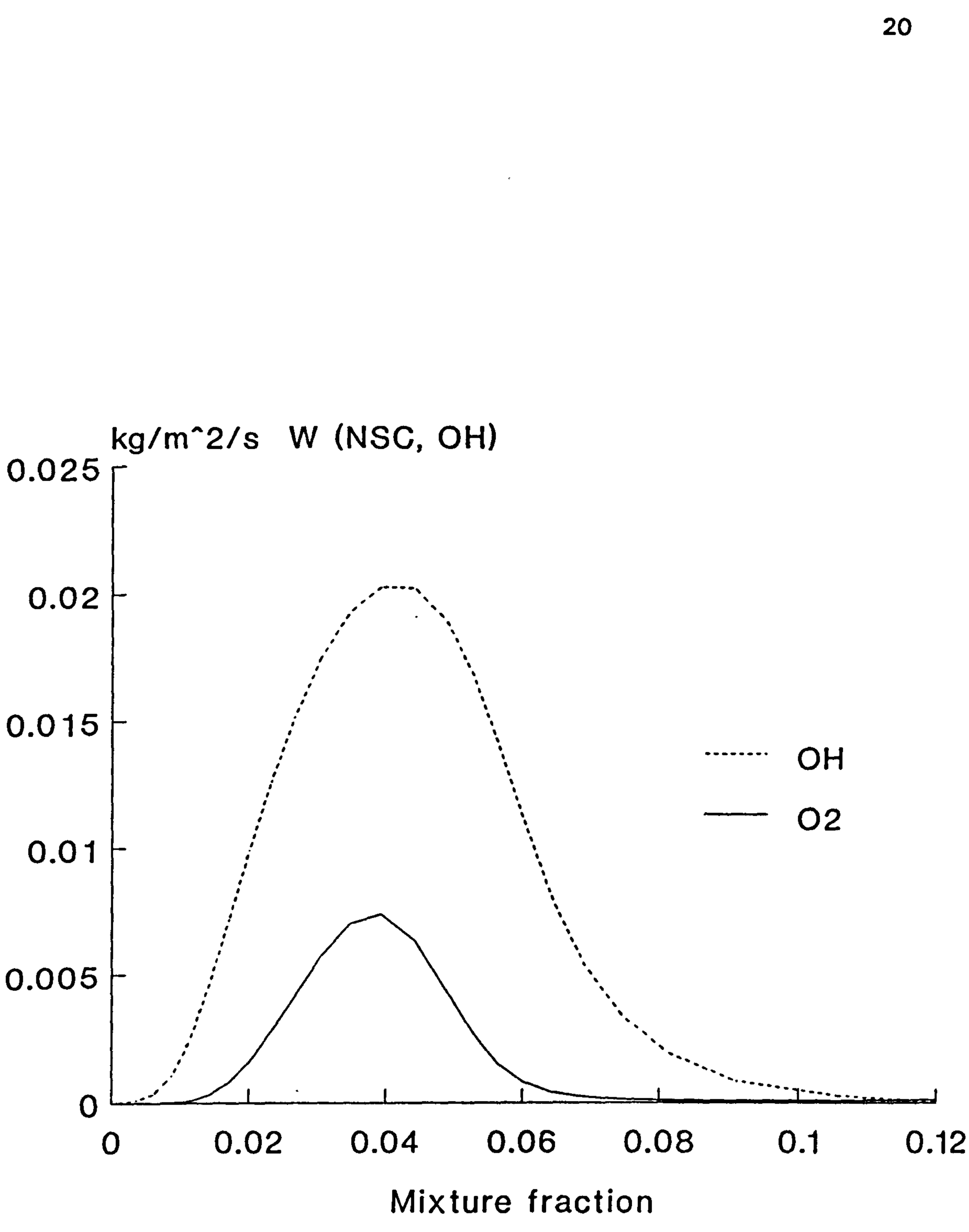

Figure 2.1 Oxidation rates of soot by O_2 (Eq. 2-9) and OH (Eq. 2-10)

Chapter 3 Spatially Resolved Soot Volume Fraction Measurement by an in-situ Probing Technique

3.1 INTRODUCTION

Soot measurements are traditionally restricted to the combustor exhaust and involve techniques of sample extraction and their subsequent analysis. Exhaust smoke level is a function of combustor operating conditions, eg. air inlet temperature, pressure and total air-fuel-ratio, and smoke emission is often controlled at the expense of other performance parameters, like NOx emission, etc. The detailed soot formation and consumption mechanisms inside the combustor chamber remain poorly understood and modelling soot production in simpler turbulent flames is still a challenge. For purposes of detailed and more mechanistic combustor design analysis, however, spatially resolved measurements are required from within the combusting zones, employing techniques constrained to minimise the perturbations to both the flow field and to the measured sample.

Experimental options for soot parameter measurement generally fall into the following categories,

1) probe sampling,
2) optical absorption/scattering and
3) planar laser imaging

The first two have been involved in applications on many practical combustion systems. The third is in principle a qualitative analysis method like those LII (Laser Induced Incandescence (Dec (1992) and Greenhalgh (1993))) and elastic scattering (Dasch and Heffelfinger (1991)), and it normally needs large optical access for the laser sheet and as well as imaging. Sampling techniques usually include extracting the soot particles out of the flame and collecting the particles by sampling filters, followed by subsequent analysis. The analytical procedure involves either simply weighting the deposits to obtain mass fraction (Nakanishi et al. (1981), Babikian et al. (1990)), or visual observation on various optical equipments, eg. SEM (Scanning Electron Microscope) (Saito et al. (1991)), TEM (Transmission Electron Microscopy) (Megaridis and Dobbins (1988)) and by DMPS (Differential Mobility Particle Sizing) (Kerdy et al. (1983)) for size and number density measurement. Sampling experiments are relatively straight forward but attention needs to be concentrated on the deposit analysis procedure, as soot is very likely to deposit on the wall of a sample probe. Babikian et al. (1990) eliminated that possible mass loss by weighing the soot particles on the filter as well as

recording the weight of the probe before and after sampling. For optical post processing, particle losses on the probe surface will obviously disturb the sizing information but no satisfactory improvement has been achieved yet. In its application to heavily sooting flames, the probe sample passage will normally be blocked by soot and that limits the potential application of sampling to the high cost gas turbine combustor measurement.

In-situ optical alternatives are therefore more attractive in relation to combustor measurement. Following Mie/Rayleigh scattering theory, light scattered from soot particles is directly related to the particle size and number density (Kerker (1969)). Light scattering has been employed extensively on laboratory flames where there is often ready optical access (D'alessio et al. (1992)), but very limited data have been reported from within gas turbine combustors. Wood and Samuelsen (1985) performed laser particle scattering in a model axisymmetric combustor with specially designed windows for laser beam incident and scattered signal detection, but the experiment was restricted to low pressure operation with respect to the window strength. Eckerle and Rosfjord (1988) made scattering measurements in a generic gas turbine combustor, using sequential removal of liner louvres to expose the measuring volume to the optics. The resulting local combustion flow field was however different from the original pattern. Of the optical techniques absorption measurement is simple to establish compared with scattering, but generally provides volume fraction only without size and number density information, and often only the integrated line of sight property is available rather than a point-by-point distribution. To overcome this spatial distribution problem, tomography is a useful tool to retrieve spatial information by deconvolution (Eckbreth (1988), Hall and Bonczyk (1987)). The deconvolution application requires a comparatively large cross section of optical access and sometimes, though not essential, a symmetric flow field. Typically industrial gas turbine combustors, which are usually of a three dimensional asymmetric type and with limited optical access, do not meet this requirement.

Similar soot measurements have been made in quite different combustion environments. Physical probing in pool fires (Markstein, (1984), Fischer et al. (1987)) and jet flames (Sivathanu et al. (1991), Klassen et al. (1992)), for example, have shown a potential way of retrieving local soot properties from light extinction measurements, where soot volume fraction f_v is directly related to the soot spectral emissivity ϵ_λ (or spectra absorption coefficient τ_λ) from the Beer-Lambert law. ϵ_λ can be determined from flame radiation or absorption measurements.

Radiation and laser extinction are common in-situ experimental techniques for soot volume fraction measurement. Radiation from soot clouds depends on both soot concentration and its temperature, therefore soot at low temperatures (cold soot) may be easily ignored, and

it will provide an underestimate of soot volume fraction (Klassen et al. (1992)). Laser extinction is only dependent on the soot concentration, and has been applied to measurement on various flames. Integral line of sight soot measurements have been demonstrated on gas turbine combustors at high pressures from spectral radiance (Norgren (1971)), from an operating engine gas turbine combustor by multi-wavelength extinction technique (Koch et al. (1991)) and in a model combustor by absorption/emission (Bowden et al. (1984)). Most of the detailed soot properties are obtained using probe sampling method (cf. Clark (1982)). To date, spatially resolved information on soot particles inside gas turbine combustors using optical techniques has not yet been reported, reflecting in part the difficulty of gaining optical access to the combustor, especially at high pressure conditions. In the present application, the introduction of a physical probe is envisaged for local property measurement given the limited optical access to the industrial gas turbine combustor and the asymmetry of the flow field in the combustor.

Combined probing and optical techniques have been employed in some open flame studies by Souil et al. (1986) and Makstein (1984). However probing measurements of spectral absorption over a reduced flame zone path length, exposed between the limbs of a water-cooled fibre optic probe may be masked by spurious signals generated by thermal stresses in the probe and by optical component contamination (Makstein (1984)). These are recurring problems for in-situ soot measurements which seek to combine the benefits of probes, in relation to spatial resolution, together with an optical technique which leaves the distribution of local property substantially undisturbed. The objective of this study is to investigate options for mapping soot concentration in the rich burning zones of a research gas turbine combustor, typical of tubular designs used in gas turbine engines, and to demonstrate suitable techniques via measurements in the combustor over a range of operating conditions. Two schemes, permitting transverse and axial access to the liner, have been developed. They are combined with laser extinction techniques, employed successfully in laboratory flames, to perform the experiments in the combustor. Preliminary validation tests of the probing techniques were carried out on jet flames of simple geometry and easy optical access and compared with non-intrusive tomographic measurements. Results to be reported here are local soot volume fraction distributions at atmospheric and elevated pressures up to 4 bar inside the tubular combustor.

3.2 LASER ABSORPTION THEORY APPLIED TO SOOT VOLUME FRACTION MEASUREMENT

The fundamentals of the laser absorption technique for soot concentration measurement

are based on the fact that when a monochromatic beam passes through an absorbing aerosol, the transmitted intensity, I_i, is related to the initial beam intensity, I_o, from the Beer-Lambert law by

$$I_i = I_o \exp \int_0^{x_i} -k_i \, dx \tag{3-1}$$

where x_i is the optical path length, k_i is the extinction coefficient of the medium within the path length x_i, defined as (Kerker (1969))

$$k_i = \int_0^{\infty} N(r) Q_{ext}(\lambda, m, r) \pi r^2 dr \tag{3-2}$$

where N(r) is the particle distribution function such that $\pi N(r) r^2 dr$ is the particle concentration in the size range dr about r, and Q_{ext} is the particle extinction efficiency, a function of the complex refractive indices of the soot particle, m ($m = n - i\kappa$, n: refractive index, κ: absorptive index), particle size r and the light wavelength λ. The light extinction arises from both scattering and absorption, in the well known Rayleigh limit where $\alpha = 2\pi r/\lambda < 1$, α is the particle size parameter, the efficiency factors are approximately

$$\begin{aligned} Q_{ext} &= Q_{abs} + Q_{sca} \\ &= 24 F_{abs}(\lambda) \alpha + \frac{8}{3} F_{sca}(\lambda) \alpha^4 \end{aligned} \tag{3-3}$$

with

$$F_{abs}(\lambda) = \frac{n\kappa}{(n^2 - \kappa^2 + 2)^2 + 4n^2\kappa^2} \tag{3-4}$$

and

$$\begin{aligned} F_{sca}(\lambda) &= \left| \frac{m^2 - 1}{m^2 + 2} \right|^2 \\ &= \frac{[(n^2 - \kappa^2 - 1)(n^2 - \kappa^2 + 2) + 4n^2\kappa^2]^2 + 36 n^2 \kappa^2}{[(n^2 - \kappa^2 + 2)^2 + 4n^2\kappa^2]^2} \end{aligned} \tag{3-5}$$

The absorption efficiency Q_{abs} is proportional to the 1st power of the size parameter α, and the scattering efficiency Q_{sca} depends on the 4th power of α. If the particle size is smaller than the light wavelength, ie. $\alpha \ll 1$, then α^4 is negligible, and the evaluation of extinction efficiency is less complicated. For small particles in the Rayleigh region,

$$Q_{ext} \simeq Q_{abs} = 24 \alpha F_{abs}(\lambda) \tag{3-6}$$

The red line of the Helium-Neon laser is a commonly used radiation source for extinction measurement due to its relatively long wavelength (632.8 nm) in the visible region thus giving a small α value for typical soot particles in laboratory flames. Soot particle sizes

in laminar diffusion flames are typically from 15 to 70 nm (Vandsburger et al. (1984)), while in turbulent flames the range extends from 20 - 120 nm (Kent and Wagner (1983)); very limited soot particle size information has been retrieved from gas turbine combustors due to the lack of optical access. Wood and Samuelsen (1984) reported the size range in an axisymmetric swirling combustor from 80 to 380 nm, an unusually high upper limit. The fuel, blended isooctane, used by Wood and Samuelsen (1984) is different from aviation kerosine with regard to the chemical composition and smoke point. Combustion of different fuels will form soot particles in different time history. As a result the particle sizes, related to the particle growth and coagulation, depend on the parent fuel.

A more interesting case relevant to gas turbine combustion is that reported by Eckerle and Rosfjord (1988) of the measurement in a modified JT12 combustor with Jet A as fuel. There the centre line soot particle diameter lies between 200 - 250 nm. No particulate soot size information from any other source is available insofar for the combustor studied here. A demonstration of error for the small particle assumption for α is shown in Figure 3.1, where the exact solution of Q_{ext} (Eq. 3-3) is compared with the Rayleigh limit Q_{ext} (Eq. 3-6). $\pi r^2 Q_{ext}$ and $\pi r^2 Q_{abs}$ are also referred to as the effective extinction (absorption) cross section, as they have the dimension of area (m^2) and may be considered as the projected area of the particle to the incident light.

The Beer-Lambert law in Eq. 3-1 is only valid when

1. the soot particles are spherical in shape
2. the soot constitutes monodisperse aerosol

For the first assumption, it is evident from electron microscope photographs that young soot formed from droplet combustion consists of fine particles having nearly spherical shape (Nakanishi et al. (1981)). Vandsburger et al. (1984) report scattering measurements which suggested the ratio of the horizontal depolarized component over the vertical polarized component of scattered light from soot is of the order of 2%, such a ratio is a good indicator of their spherical shape. Nevertheless, agglomeration and chain formation in the sooting process will inevitably reduce the aspect ratio of the soot cloud and hence its shape will depart from spherical. Quantitatively, the fractal concept analysis on soot aggregates by Charalampopoulos and Chang (1991) indicated that Mie analysis for spherical soot yields diameters differing only by 1.8% or less from the agglomerate diameters, however the Rayleigh analysis underestimates the inferred optical diameter by 9% and overestimates the number density by 34%.

In general, soot particles in an aerosol are polydisperse and the exact particulate size

distribution depends on the particular system studied. The size distribution however is usually relatively narrow and the one often used is (Tien and Lee (1981))

$$N(r) = ar^3 \exp(-3r/r_m) \tag{3-7}$$

where r_m is the most probable radius and a is a constant. The soot volume fraction, which is the volume of soot per unit volume of space is defined as

$$fv_i = \int_0^\infty \frac{4}{3}\pi r^3 N(r)\,dr = 1.38\,a r_m^7 \tag{3-8}$$

The spectral extinction coefficient for a polydisperse aerosol is then given from Eqs. (3-2), (3-6) to (3-8) by

$$k_i = 2.28 \frac{fv_i}{r_m^7} \int_0^\infty r^5 \exp(-3\frac{r}{r_m}) Q_{ext}\,dr$$

$$= 36\pi F(\lambda) fv_i / \lambda \tag{3-9}$$

the f_{vi} can then be estimated based on Eqs. (3-1) to (3-9). Here f_{vi} denotes the volume fraction distribution of soot along the path length x_i. The distribution in a practical combustion system is typically spatially inhomogeneous, however, and the f_{vi} is then only a path length integrated property. The recovery of local spatially resolved soot data thus requires deconvolution of the measured data.

By varying the path length with finite steps Δx_i to next length x_{i+1} ($x_{i+1} = x_i + \Delta x_i$), the transmitted intensity, I_{i+1}, is

$$I_{i+1} = I_o \exp(\int_0^{x_i} -k_i\,dx + \int_{x_i}^{x_{i+1}} -k_{\Delta x_i}\,dx) \tag{3-10}$$

Combining Eqs. (3-1) and (3-10), we can integrate the absorption over the path length from x_i to x_{i+1}

$$\int_{x_i}^{x_{i+1}} -k_{\Delta x_i}\,dx = -(\ln\frac{I_o}{I_{i+1}} - \ln\frac{I_o}{I_i}) \tag{3-11}$$

when the length interval Δx_i is so small that the soot property, ie. the spectral extinction coefficient $k_{\Delta xi}$, along this region can be reasonably treated as homogeneous, then from Eqs. (3-9) and (3-11) the local soot volume fraction within the region Δx_i can be expressed as

$$fv_i \simeq fv_{\Delta x_i} = \frac{\lambda}{36\pi F(\lambda)} \frac{\ln(I_0/I_{i+1}) - \ln(I_0/I_i)}{\Delta x_i}$$

$$= \frac{\lambda}{36\pi F(\lambda)} \frac{d[\ln(I_o/I_i)]}{dx_i} \quad (\Delta x_i \to 0) \qquad (3\text{-}12)$$

Eq. 3-12 is virtually an expression for determining local (point) volume fraction of soot. When the laser source is selected, λ and $F(\lambda)$ are independent constants, and I_o is also a system constant associated with laser itself, local f_{vi} is only a function of the spatial distribution of the transmitted laser intensity I_i, or more specifically $Ln(I_o/I_i)$. The $Ln(I_o/I_i)$ distribution can be measured by systematically varying the optical length x_i in the flame. As only limited optical access is available in the combustor, attention in this study has been focused on probe-borne optical approaches without modifying the combustor chamber itself. To have more insight into the problems of probing measurements in sooty flames, preliminary tests have been conducted on jet flames.

3.3 PROBING TECHNIQUE EVALUATION ON LABORATORY FLAMES

3.3.1 Probe configurations

Two probe configurations have been developed with respect to the application in a research tubular combustor; one is described as a sight tube probe, the other as a reflecting probe.

Sight probe

The sight probe is to be inserted through the side of the combustor liner, with the laser beam shielded within the central core of the probe. Water cooling together with inert gas purge, normally nitrogen gas with no chemical effectiveness, have to be employed to protect the probe itself and to ensure that the optical path is free of particle contamination. To achieve this, three stainless steel tubes were assembled concentrically, with the probe inside and outside diameters 3.28 and 7.0 mm respectively (Figure 3.2). A quartz window, 10 mm in diameter and 20 mm in length, was mounted at the end of the tube, outside the combustor, as a pressure sealing to prevent gas mixture leaking from inside the combustor chamber, especially at high pressure conditions. When the laser beam is kept stationary, the traversing radial position of probe tip will determine the exposed beam length, or the optical path length, x_i and absorption intensity profiles are systematically measured. The detailed measurement procedure is outlined later in this section.

It is anticipated that such probe intrusion to the combustion flow field is inevitably

aerodynamically disturbing, since the probe is physically exposed inside the combustor. The main aerodynamic effect of introducing a probe into a flame, as indicated by Heitor and Moreira (1993), is the disturbance of the scalar concentration gradients in the vicinity of the probe as a result of the streamline distortion. Soot measurement by probing techniques in the literatures, such as Markstein (1984), Sivathanu et al. (1991) in open flames estimated that the discrepancy in the local flow field caused by probe presence could be about 5 K in temperature, and 25% in soot volume fraction respectively. The probes applied by the above researchers comprised two tubes of fixed separation distance defining the optical path length, between 5 - 10 mm. The single tube sight probe designed in this study obviously has the advantage of less aerodynamic perturbation in relation to the half exposure of probe itself in the flame, but the field to be investigated is also rather smaller. It was observed that when the sight probe was traversed in the combustor for a certain period of time, coke was formed on the probe outside surface. The coke might be the product of liquid kerosine pyrolysis on the hot metal surface. This implied that the temperature of probe surface was not far away from the gas temperature even though it was water cooled. The local temperature field can not be substantially disturbed hence the soot formation/burnout process will not be affected from the temperature effect. Images of the combustor flow field with the probe presence have been obtained in an isothermal water visualization test; the images are described in Section 3.4 together with analysis of probe aerodynamic disturbance to the combustor flow.

Reflecting probe

To improve the aerodynamic performance of the probing technique in the gas turbine combustor, a second option is to introduce the probe from the exit plane of the combustor, with the probe parallel to the combustor axis, therefore only the tip of the probe is exposed in the immediate vicinity of the measuring regime and the overall flow disturbance is reduced (Figure 3.3). Two optical arrangements are envisaged, one is to shine the laser beam from the tip of the probe, with the aid of optical fibre introducing the laser beam from outside the probe (or combustor) to the fibre outlet at the tip of the probe. Fibre optics can only perform with the outlet paired to a converging lens, such a system is typically of the minimum size of a few millimetres. To accommodate the fibre optics the probe would have an outside diameter of the order of, say larger than 9 mm, the size of the present reflecting probe, including water cooling and inert gas purge. Given the inside diameter of the combustor chamber about 100 mm, it would be of no advantage to use fibre optics given this geometric aspect. The second option, which is employed in this study, is to use the probe as a reflector, such that when the transverse position changes, the absorbing optical path length varies as well. An ordinary mirror is not feasible in this application as beam steering makes it difficult to control the laser beam path.

A retro-reflector (or so called "corner cube") was therefore chosen as it has the distinctive characteristics that any ray entering its effective aperture will be reflected and emerge from the entrance (exit face parallel to itself, but with opposite direction of propagation) and substantially independent of incident angle. This reduces the impact of beam steering in a combustion field. A 3 mm reflecting diameter was chosen as a compromise to offer easy optical alignment - obviously the bigger the diameter the better from the effective area point of view - while keeping the possible flowfield disturbance small.

In this configuration, with the probe outside diameter limited to 9 mm, the design of the probe is complicated in comparison with the sight probe. At the first time of operation, cooling water leaked inside the probe due to manufacturing difficulties. The reflector was specially made by Optical Works Ltd for the specific dimension required. The length of the probe is determined by the measurement requirement in the primary zone, while in its application in the dilution station an extra wafer, of the thickness identical to the distance between primary and dilution hole stations, can be inserted between the probe flange and the pressure casing.

The probes are both actuated by an electrical motor on the combustor rig, whilst the spatial traversing was determined by linear transducer. Prior to the combustor experiment, tests of these probes were conducted on laboratory jet flames. The sight probe was evaluated on a pre-vaporised kerosine jet flame inside a pressure vessel, whereas the reflecting probe was tested on an open ethylene jet flame in ambient still air. The actuating system for the actual combustor was not compatible with the jet flame vessel and the ethylene open flame provided much easier optical access.

3.2.2 Pre-vaporised kerosine and ethylene jet flames

Both these jet flames have been experimentally studied previously (Young (1993)) in relation to soot production mechanisms and detailed soot volume fraction profiles have been mapped using non-intrusive tomographic line-of-sight technique. It is thus possible to compare the probe measurement with an existing data base.

Table I. Jet flame flow conditions
(atmospheric pressure)

	Kerosine	Ethylene
Flow type	Confined	Unconfined
Fuel exit velocity (m/s)	22.3	24.5
Air exit velocity (m/s)	0.234	0
Fuel exit Reynolds No.	9500	8600
Fuel exit temperature (K)	598	300
Air exit temperature (K)	288	300

Kerosine jet flame - sight probe

The kerosine flame was generated by a nozzle from which pre-vaporised aviation kerosine (Avtur) was issued in to a confined cylindrical chamber. The pressure vessel which confines the jet flame incorporates large diameter quartz windows. These windows are symmetrically mounted for easy optical access. Room temperature air flows through the surrounding area as a co-flowing stream (Figure 3.4 (a)). To vaporize the kerosine, liquid kerosine is first sprayed in to a brass chamber, heated to 673~773 K, and then expelled out of the chamber, normally at a temperature of 600 K. This high temperature was maintained along the rest of the passage by external heating wire, until the fuel is out of the nozzle. The flow rate of kerosine and air were monitored by a ¼" Fischer & Porter 1/4-20-G-5/81 tube with stainless steel float and FP 3/8-27-G-5/81 tube with GNSVGT 59 float respectively. Detailed fuel and air flow conditions are listed in Table I. The sight probe was inserted horizontally from an existing probing port in the pressure vessel wall (primarily designed for thermocouple temperature measurement).

Ethylene jet flame - reflecting probe

Since the mounting system of the reflecting probe, in particular the flange configuration, was designed for the combustor application and was incompatible with the above pressure casing, an ethylene jet flame was chosen to evaluate the reflecting probe. The ethylene flow rate was measured by a FP rotameter comprising a 1/8-25-G-5/81 tube with stainless steel float. The ethylene jet emerged vertically from a stainless steel tube, of inside diameter 3.1 mm into stagnant room air (Figure 3.4 (b)). The probe axis was set perpendicular to the flame axis. The laser beam in this configuration traversed the flame twice, backwards and forwards from laser tube to reflector through the absorbing medium, the optical path length x_i used in the f_v calculation is therefore twice the spatial length. Detailed flow conditions can be found in Table I.

3.3.3 Data collection and analysis

The mass flow rates of the kerosine, ethylene and air (in the co-flowing kerosine flame) were monitored with an accuracy of about $\pm 2\%$. Further uncertainty, as will be found in the measurement results, arises from the procedure of controlling the valves which regulate the flow rate.

A red He-Ne laser (wavelength 632.8 μm, Melles Griot model 05 LHR 121, with beam

diameter of 0.59 mm at e^{-2} point) was used as a radiation light source. The laser beam was first colliminated by a pair of lenses to reduce the beam size, preventing undesired beam attenuation by the probe inside surface. The transmitted laser intensity was detected by a 444-12-12-171 type photodiode from the Silicon Detector Corp. The voltage output of the photodiode was then recorded by a BBC computer via an OASIS 12R type Analog-to-Digital Converter at the acquisition frequency of 14 kHz and absorption signals were averaged over 8 seconds. The error which arises from the fluctuation of both laser source and photodiode dark current is about 3%. The refractive index of soot at the wavelength 632.8 nm was selected as m=1.92-0.45i (Mullins and Williams (1987)) to be consistent with previous laser extinction measurements (Moss et al. (1987), Stewart et al. (1991) and Young (1993)) although perhaps not directly applicable to both the fuels employed here. The choice of soot optical properties from various published data will introduce uncertainties in the measured data, since the complex function of refractive index is not consistent among these data (cf. Appendix A: Refractive Index of Soot). The present selection lies roughly in the middle level of most of these values.

When the sight probe traverses across the symmetrical jet flame, the accompanying transmitted laser intensity I_i has the profile shown in Figure 3.5, where the signal is described as $Ln(I_o/I_i)$ rather than I_i alone for analysis convenience. From Eq. 3-12, it is the slope of $Ln(I_o/I_i)$ which determines the local soot volume fraction. In common with all techniques, practical measurement can not perfectly describe physical phenomenon partly because experimental quality depends on the signal to noise ratio. Any scatter in the transmitted intensity $Ln(I_o/I_i)$ profile would lead to an unphysical f_v distribution. To improve data quality, the transmitted intensity profile was smoothed prior to calculation using a least square cubic spline curve fitting from the NAG mathematical library (subroutine E02 BAF (NAG library (1987), Hopkins and Phillips (1988))). The radial position and $Ln(I_o/I_i)$ are treated as x, y values respectively in the curve fitting. Interior knots, or x values of the joins between each experiment position, are pre-selected and a best fit is achieved by trial and error of usually not more than three attempts. The curve fitting shown in Figure 3.5 is the best fit of the raw data. The first derivative of the mathematical curve was then calculated by subroutine E02 BBF and E02 BCF, from which the soot volume fraction is estimated, following Eq. 3-12.

3.3.4 Results and discussion - jet flames

<u>Sight Probe - Kerosine flame</u>

These measurements were conducted at the flame heights of 260 mm and above where the soot absorption level is high and thus any discrepancy due to reproducibility of flow

conditions may be reduced. The observed discrepancy, relative to the line of sight absorption through central axis, is about 4% at heights over 300 mm and 28% at 260 mm (cf. Table II).

Table II Comparison of Soot Concentration Measurements in the Kerosine Jet Flame
(Line of sight through central axis absorption $Ln(I_o/I_i)$, peak soot volume fraction f_v)

		H=260 mm		H=300 mm		H=350 mm		H=406 mm	
		Ln	fv	Ln	fv	Ln	fv	Ln	fv
Probe	0.23			1.108	71	.880	53	.702	32
V_{N_2} (m/s)	0.07	1.222	59	.981	63	.860	51	.693	31
Tomographic		.960	77	1.020	93	.890	70	.709	42
%(Probe/Tomo)		127.2	77	96.2	68	96.6	73	97.7	74

The absorption $Ln(I_o/I_i)$ data and f_v profiles inferred from $Ln(I_o/I_i)$ based on Eq. 3-12 are illustrated in Figures 3.5 and 3.6. Distributions of absorption $Ln(I_o/I_i)$ showed the noise level below 3% as estimated in Section 3.3.3, comparing the data points with the fitted curve. The sight probe was inserted from the '+' side. When the soot concentration distribution at the '-' side was folded to the '+' side, the profiles are surprising symmetrical with no corresponding distortion generated by the probe. It was first expected that the probe might introduce some distortion on the local flow field, causing flame to lean towards the opposed '-' side. The measured profiles reveal that since the jet flame is a parabolic flow and the sight probe was introduced from the side of the flame, the field occupied by the probe is certainly aerodynamically stretched. But the boundary layer and wake associated with the probe perturbation appears negligible at the measuring volume since they are remote from each other. The local soot concentration in consequence is considered to be little affected by parabolic flow pattern.

The nitrogen purge is more likely to exert some disturbing effect on the measurements but this can be minimised by choosing an "optimum" purge velocity, or flow rate, when no influence is observed in the f_v profile. The jet flame does not necessarily have a constant velocity profile across the radius and since it is the relative velocity, or purge velocity over local flame flow velocity, that controls the purge effect, the "optimum" purge rate should follow the detailed velocity profile. However such a detailed velocity profile was not experimentally available and only a universal figure could be established. Under the present flow condition of the jet flame, the critical purge velocity was found to be about 0.23 m/s (Figure 3.7 (c), (d)), regardless of flame velocity profile.

The comparisons of the probe and tomographic results cited in Figure 3.7 give good agreement in the general shape of the soot volume fraction profiles, but there is a large discrepancy in the peak f_v. From Table II the discrepancies at all these different vertical heights range from 32 to 23 percent. This is not considered to be the product of aerodynamic perturbation, since if the discrepancy in the central part f_v is caused by nitrogen purge, eg. at 0.07 m/s, then with about three times purge rate of 0.23 m/s, the momentum of the nitrogen is increased, and thereafter more soot particles will be blown away from the probing path length, especially near the region of the probe tip. The results in Figures 3.7 (c), (d) do not show such trend. It might be that the two different techniques do provide different results. It is arguable that the probe will develop a nearly 30 percent error since Sivathanu et al. (1991) estimated the uncertainty associated with a similar probe to be about 25 percent in soot volume fraction of 1 ppm in the application of a two-tube probe and the sight probe should have a better performance. The exact probe perturbation level remains unclear. Qualitative analysis of the probe disturbance from water visualization test will be described later.

Reflecting probe

The results from the reflecting probe are less encouraging (Figure 3.8) then the sight probe data and appear to be substantially noisier. The $Ln(I_o/I_t)$ distribution at the 350 mm height is better than the other three positions, indicating the high noise level and lower absorption in these regions. The main contribution to the signal noise is the laser beam steering in the large density gradient flow field with accordingly large refractive index gradient. Since the effective radius of the reflector is about 1.5 mm, compared with the laser beam diameter of about 0.6 mm, it is extremely difficult to guide the reflecting probe traverse within the 0.45 mm ((1.5-0.6)/2) flexible range. Soot volume fraction profiles at the same horizontal positions are shown in Figure 3.9. Only at 350 mm where the absorption level is the highest does the probing data agree well with that from the tomographic measurement (Figure 3.9 (d)). Data at the other three heights in Figures 3.9 (a), (b), (c) showed poor agreement both in peak values and profile shapes.

Owing to the poor mixedness in these jet flames, the soot concentration level is of order of several ppm. In the gas turbine combustor where mixing is enhanced in the highly turbulent flow and there are relatively higher flow velocities (or shorter residence time), the soot level may be lower than encountered in the jet flame, in which case the performance of the reflecting probe might be even worse.

Soot volume fraction measurements by the probing technique have confirmed the

applicability of Eq. 3-12 to flames of either 2 or 3 dimensions, since no symmetric assumption is necessary, unlike the simple tomographic deconvolution. The sight probe data is more consistent and admits more satisfactory data interpretation. The comparison with the non-intrusive technique is encouraging, but the reflecting probe provides data contaminated with high noise levels and provides sensible data only in very sooty regions.

3.4 SOOT CONCENTRATION MEASUREMENT IN THE TUBULAR COMBUSTOR

3.4.1 Test rig and the tubular combustor

Test rig

The combustor test rig is illustrated schematically in Figure 3.10. A steady air flow is supplied by Screw type Howden compressors capable of delivering 3.8 kg/s at pressures up to 16 bar. The air mass flow rate is metered using a BS1042 type orifice plate and, by adjusting an in line spill valve, a required flow rate can be sustained. Prior to entering the combustor, the air is heated by an electrical heater, with an outlet air temperature up to 260 °C. A pressurising tail pipe is positioned downstream from the exit of the combustor. By closing or opening the pintle throat on the tail pipe, elevated combustor pressures can be achieved. Avtur (aviation kerosine) was used as fuel with a hydrogen-to-carbon atomic ratio of 1.95. The fuel flow rate was regulated by a Fischer & Porter ¼" variable area tri-flat flowrator tube with precision bore (No. FP ¼-25-G-5/81) and titanium spherical float. The flowmeter is of ±2% accuracy. To achieve accurate control of the fuel and air flow is difficult by manually adjusting the flowmeter and spill valve. The flow conditions during the experiment were monitored separately via combustor exit gas temperature and combustor duct metal wall temperature. These time-mean measurements indicated steady flow conditions with less than 3% uncertainties. Determination of the instantaneous deviation from the assigned conditions is not possible in the highly turbulent flow because the instantaneous flow properties, for example temperature, are fluctuating. The latter proved to be less problematic in the present soot volume fraction measurements since only time-mean distributions are sought and the mean absorption profiles showed good repeatability. In the latter chapters 4 and 5 where instantaneous properties are required for scalar correlations and radiation predictions, the repeatability of instantaneous flow conditions will have an important effect. This will be discussed in the relevant chapters.

Although the rig can be operated at higher pressure and temperature, flow conditions

up to 4 bar and 200 °C was selected for the soot measurement. The main reason is that the cost of running at higher pressure and temperature is much more expensive and therefore it is considered not appropriate for the purpose of probing development.

Tubular combustor

The model combustor is of a SNECMA design, manufactured by Volvo Flygmotor for an EC BRITE/EURAM collaborative project. The project theme was "Low emission combustor technology", under which optical experiments were to be explored for temperature, fuel spray and soot measurements. This tubular combustor is also used by SNECMA to perform preliminary thermal resistance tests on the injection systems (Desaulty (1991)). The combustor has a conventional tubular style, and can be considered to consist of three regions, an upstream dome, a primary zone and a dilution zone (Figure 3.11). The mixing holes at both primary and dilution locations are symmetrically positioned in the combustor liner; the dimensions of the holes can be found in Table III. A single swirler in the centre of the combustor head has the function of generating a recirculation zone for stabilizing the flame. There are film cooling holes between each reaction zone, with a substantial portion of the air flow rate dedicated to cooling. The film cooling flow is very high and comprises 58% of the total. The flow rate distribution for each location is shown in Figure 3.12. An air blast injector of SNECMA design served as the fuel spray atomizer.

Table III SNECMA combustor geometry

	Air impingement hole diameter (mm)	Diameter of cross-section (mm)	Number of holes	Distance from injector exit (mm)
Primary	9.9	89	4	42.5
Dilution	9.1	98.6	4	82.5

The combustor was accommodated inside a stainless steel pressure casing, fitted with a windowed slot for optical access to the primary zone and a port for the dilution zone (Figure 3.13). Laser access to the combustor field was then achieved through windows in these ports on the pressure casing and the existing primary and dilution holes. These windows were purged by air on the inner surface. Thermal radiation from the flame inside the combustor onto the photodiode is checked and identified as negligible relative to the absorption signal. A uncooled stainless steel duct, aligning the combustor chamber exit, is assembled down stream of the combustor. Three thermocouples were welded on the outside surface of this duct to monitor the temperature of the metal wall, partly to limit the flow conditions to prevent the duct being overheated.

3.4.2 Experimental detail

Sight probe

The configuration of the laser optics was arranged to be similar to that employed in the vaporised kerosine jet flame. The probe is inserted through the existing holes, with laser and photon detector at the two opposite sides out of the rig (Figure 3.14 (a)). The approach to absorption data reduction was also the same as in the jet flame. The problem of thermal expansion associated with the combustor rig, typically about 1 ~ 2 mm, made it necessary to re-align the optics during each run after ignition to make sure that the beam passes through the centre of the probe, within the core diameter of 3.28 mm (Figure 3.2). Dummy traversing of the probe provided a $Ln(I_o/I_i)$ variation of less than $\pm 0.5\%$ in the absence of absorption. The noise arises mainly from laser source instability, photodiode dark current level and inhomogeneous window transmission.

One further possible error arises from the time mean of the recorded intensity, since

$$\overline{Ln(I_o/I_i)} = Ln(\overline{I_o/I_i}) - \overline{Ln(1+I_i'/\overline{I_i})} \neq Ln(\overline{I_o/I_i})$$

the $Ln(I_o/I_i)$ in Eq. 3-12 is actually referred to the left side component, whilst in experiments it is the far right side component that was measured. The discrepancy between these two values will depend on the local fluctuation level. One solution to this difficulty is to first record the instantaneous value of $Ln(I_o/I_i)$ and average this log arithmetic value. An alternative solution might have been to record both the mean and fluctuation component of I_i simultaneously.

Reflecting probe

The reflecting probe is introduced from the exit of the combustor, parallel to the combustor axis (Figure 3.14 (b)). The incident laser beam first passes through a beam splitter, and the reflected light from the probe is collected by the beam splitter and guided onto the photodiode. The alignment of the optics is straight forward in relation to collecting the reflected laser beam whilst positioned in the combustion field where high refractive index gradients prevail, showing the merit of corner cube, but the small effective area of the reflector suffered from laser beam steering and the signal noise was inevitably high. The peak-to-peak level typically exceeded the mean value in some cases.

Flow conditions

The flow function of the combustor, $\dot{m}\sqrt{T/P}$, was kept at 2.6 at 1 bar and 2.3 ($kgK^{1/2}/s$ bar) at 4 bar. This is close to the normalised design value of 2.6 according to SNECMA and thus the combustor flow field is representative of the designed flow. The air inlet temperature was mostly set at 473 K, near to the gas turbine engine idle condition, with an air mass flow rate of 0.12 kg/s at atmospheric pressure operations, and 0.46 kg/s at a pressure of 4 bar. The flow conditions at which experiments are performed are outlined in Table IV.

Table IV Combustor Conditions for Soot Volume fraction Measurement

	Inlet Air Temperature	Pressure (bar)	AFR
Primary	~ 200 °C	1	12~45
Dilution	~ 200 °C	1	12~45
	~ 130 °C	~ 4	25~30

During the experiments the variation of air fuel ratio was achieved by fixing the air mass flow rate and adjusting the kerosine flow rate. The smoke emission level from aero-engines is typically high at conditions of low inlet air temperature and high pressure (Lefebvre (1983)). Combustors in these applications normally operate at Air-Fuel-Ratio of higher than 50. Gas turbine combustors operated near this AFR at low pressure exhibit little smoke emission. The flame of AFR about 45 in the SNECMA designed combustor shows 'appreciably' little yellow luminosity on the basis of combustion performance (Figure 3.15), however it is sooty flame that is required for probing technique development. Under the constraint of the operating cost, the AFR range in this study reached overall stoichiometric value (AFR=14.6) to promote soot formation. Under these unusually rich flow conditions, the combustion zone has expanded from the normal primary zone to, in the case of AFR<14.6, the whole combustor. Figure 3.16 clearly shows the flame expansion at the overall rich condition. The selection of operating conditions here for the probing investigation reflected the compromise necessary to enhance soot production for a limited pressure rise, as a demonstration of the probing technique, and to be substantially free from the multi-phase flow ambiguity described below.

The laser absorption technique is sensitive to the scattering effects of fuel droplets, which may not be distinguishable from soot particle absorption despite differences in their relative size and number density. There are significant differences in both particle size and number density between characteristic soot ($\leq 0.2\ \mu m$, $\sim 10^{15}\ m^{-3}$) and fuel droplet ($\leq 50\ \mu m$, $\sim 10^{6}\ m^{-3}$). It was suggested that large droplet particles might lead to discernible high frequency extinction (scattering) whilst small soot particles of relatively large number density might lead to low frequency extinction (absorption). The time series of integrated laser

extinction from different regimes have therefore been analyzed with a view to establishing whether they exhibit characteristics which would permit discrimination between the effects of soot and fuel droplets. Spectrum analysis of the transmitted laser intensity, based on DFT technique (Discrete Fourier Transform) was performed using OASIS VIS software, with a recording time of 0.01 second at an acquisition frequency 51.2 kHz. As the VIS program can only work at input voltages between ± 0.1 V, the input voltage corresponding to the photon intensity was adjusted by an amplifier to suit this range. The calculation of the DFT is fully described in Appendix B: Discrete Fourier Transform of Absorption Signal. Normalised power spectrum density was calculated by averaging 10 series of discrete recordings to smooth the spectra distribution. The results will be discussed in the result section.

3.4.3 Flow visualization of the sight probe in a full scale replica perspex combustor

Aerodynamic disturbance to the combustor flow field as a consequence of the probe intrusion is of primary importance to the measurement quality. The previous jet flame test revealed that no asymmetry will be introduced in the soot concentration distribution by the probe itself. To visualise the combustor flow pattern in the presence of the probe, isothermal water visualization tests were conducted with a replica perspex combustor.

Comprehensive details of the combustor flow visualization are described by Join-Lambert (1992) and will only briefly described here. For this combustor, a water flow rate excess of 10 gal/min (0.758 kg/s) has to be maintained in order to generate a turbulent flow pattern similar to the combustion flow. Below this figure, small perturbed eddies are claimed to start to appear in the region of the primary zone, indicating the increasingly dominant role of fluid viscosity over aerodynamic force at low Reynolds number. During the experiment, the model was operated at the lower bound flow rate to keep the water velocity low enough for satisfactory tracing of the streaks of the tiny seeding air bubbles by conventional photography.

The combustor flow field was observed to be asymmetric, due to the configuration design. The mounting bolts, joining the combustor (flame tube) to the pressure casing generated eddies of considerable turbulence which strongly affected the downstream flow pattern. In particular the impingement depth of the primary jets was strongly affected since the primary holes are very close to these bolts (Join-Lambert (1992)). To eliminate uncertainties in relation to that uneven assembling of the combustor liner might cause an uneven flow field as stated above, further flow visualization tests in this study indicated that the flow field inside the combustor chamber is insensitive to the rig assembly. This is concluded from that when the combustor was slightly asymmetrically positioned in the enclosure (equivalent to pressure

casing), the flow pattern inside the combustor was unchanged.

The particular emphasis of the present study was the impact of the optical probe on the internal flow patterns. The probe simulation focused on the sight probe, since its application is more robust than the reflecting probe and was expected to provide more meaningful data inside the combustor. A brass bar of 7 mm diameter, identical to the outside diameter of the probe, was inserted into the perspex combustor in the dilution station with its tip at the radial position R=-35 mm.

Compared with the original flow field, the dilution jet was significantly reduced by the blockage of the probe (Figure 3.17), whereas local flow field (near the probe tip) was not largely affected. The comparison suggested that local flow field properties will not be disturbed by the probe itself, but along the path of the dilution jet, more significant disturbances result. From Figure 3.17 (a) the dilution jet is seen to penetrate the path length along the opposed dilution holes from about -49.8 mm (end side of dilution station) to -35 mm. Therefore experimental data at radial positions R> -35 mm will be more close to real flow.

It is clear from these tests that local flowfield near the probe tip is not subject to disturbance caused by the probe itself in the highly turbulent flow but the blockage of mixing holes does significantly change the dilution station flow structure. This effect is localised and the gross influence to the combustor is of little importance. The problem of dilution hole blockage can possibly be overcome by punching extra holes in the combustor. With regard to introducing the sight probe these extra holes should be sealed against any air flow into the combustor such that the measurement will be at conditions closer to the original combustor characteristics than that using the existing holes. Since the present study is focused on technique development, and in particular the feasibility of a probing measurement inside the combustor, the above consideration was of second priority. Nevertheless it does point out the direction for improvement of the measurement technique.

Figure 3.18 shows different flow patterns in the dilution zone in the presence of the probe, reflecting the highly turbulent features of the combustor flow field and their changes against time. The other dilution jet holes, namely 6 & 8 were not influenced by the partial blockage of the neighbouring hole, namely 5 (Figure 3.19).

3.4.4 Results and discussion - combustor

Sight probe

Illustrative $Ln(I_o/I_i)$ data is shown in Figure 3.20. The repeatability shown in the profiles, generally over 4 minutes for several recordings, implies reasonably constant flow conditions over this time period and high signal quality both in primary and dilution zone. Before commencing the measurement, a preliminary study of probe purge effects is undertaken to minimise experimental error from this source. The nitrogen purge could possibly reduce the soot concentration level to some extent. As shown in Figure 3.21, the soot volume fraction measured with a purge velocity of 49.5 m/s is only about 59% of the peak value observed with that using a purge velocity of 21.4 m/s. The "optimum" velocity was established by reducing the purge rate still further to about 9.0 m/s. This rate was maintained throughout the experiments.

When the shielding probe was fully retracted to the laser side, ie. the laser beam was fully exposed to the sooty aerosol inside the combustor, a path integrated absorption can then be obtained (Figure 3.22). The integrated $Ln(I_o/I_i)$ against the air fuel ratio indicates the expected decline in the soot concentration level when air fuel ratio is increased, or the fuel mass flow rate is reduced. Conventional measurements of combustor exit smoke number against air fuel ratio have the same trend, for a combustor fuelled by air blast fuel atomization (Shown in Figure 3.22, from Norster and Lefebvre (1972)) under the test conditions of up to pressure 9 bar and inlet temperature 900 K. This trend is also supported by the correlation between SAE smoke number and AFR in a CJ805 (J79) engine low smoke combustor (Blazowski (1978)). At higher AFR conditions, less fuel is fed and thus less fuel rich eddies are generated. As a result soot formation domains are depressed. Another reason might lie in the fuel atomization. Lower fuel throughput for fixed air flow rate is usually accompanied with smaller spray initial size (or pre-filming thickness), this will result in subsequent smaller droplet size. The configuration of the air blast injector used here determines that the liquid kerosine is already in the droplet state at the exit of the injector. In general, the decreased fuel mass flow, giving rise to the AFR, tends to reduce the co-flow momentum of the liquid fuel with the surrounding gas in air blast atomization, and therefore increases the relative velocity between the air and droplet, or with the effect of increased Weber number. As the aerodynamic Weber number has a profound influence on fuel atomization quality, enhanced atomization will lead the rich mixture rapidly to stoichiometric levels and thus reduce the number of fuel rich eddies, thereafter reduce the soot formation probability.

The sooting process includes both formation and burnout stages (Haynes and Wagner (1981)); soot is normally formed in the high temperature, fuel rich primary zone and oxidised in the following leaner zones. Thermal radiation flux in the gas turbine combustor, a key function of soot concentration, increases from the primary zone to the intermediate zone,

reaching its peak level and then reducing in the dilution zone (Norgren and Ingebo (1976)). Prado et al. (1977) describe a soot mass concentration map which first increases and then decreases along the combustor axis. Soot particles in the regime downstream from the dilution zone would normally be in the oxidation stage, and the soot volume fraction in the dilution zone can be a direct indication of combustor exhaust smoke levels, although the quantitative relation of soot (smoke) concentration between these two stations will differ with combustor design. Gas turbine combustors are normally operated at overall air fuel ratio of about 50 with the primary zone burning at richer than stoichiometric level. Some AFRs in the present measurement are exceptionally low, eg. AFR=12, which suggests that the whole combustor is actually burning at rich conditions. In consequence the soot formation region expands to the whole combustor field.

A spatially resolved distribution of soot volume fraction is shown in Figure 3.23, it can be interpreted in terms of mass fraction, introducing a soot density of 1800 kg/m^3 consistent with previous work (Moss et al. (1987)). The figure shows distinct double peak profiles. Since soot is formed in the fuel rich pockets, the peaks are therefore expected to follow the fuel trajectory. The asymmetry in the profiles demonstrates the influence of the probe blockage on local mixing, as the probe blocks about 51% of the hole area for dilution impingement on the '-' side, local dilution is substantially reduced, leading to a correspondingly high soot concentration. The combustor flow field is asymmetric as mentioned in section 3.4.3, but the mixture fraction distribution at an axial position 5 mm upstream from the dilution zone, where the flow is free from the dilution effect, shows a less asymmetrical profile. The mixture fraction measurements will be discussed in more detail in Chapter 4. As stated in section 3.4.3, the blockage problem might be solved by inserting the sight probe through an extra punched hole. No action had been taken in respect of this problem under the constraint of time. Subsequent measurements of related properties, for example, temperature and mixture fraction, were also conducted using geometrically similar probing methods, maintaining a consistent configuration.

Ferguson and Mellor (1979) reported major disagreements between measured and predicted soot concentration, based on measurements of flame radiation intensity. To resolve the discrepancy, they speculated that the peak soot concentration could occur off the combustor axis, and that the centre line data might not be a good indication of the soot concentration along a diametral radiation path. Clark (1982) measured soot mass concentration by probe sampling, indicating a peak level at a radial off-axis position. The results here confirmed that the peak position would follow the fuel atomization trajectory, which in gas turbine combustors usually introduces the peak between the combustor axis and wall.

Air inlet temperature has a profound influence on soot concentration in the dilution zone, the soot volume fraction declining with increased inlet air temperature (Figure 3.24). One explanation for this lies in the fact that although the high temperature will promote both soot formation and oxidation rate (Moss et al. (1991)) the enhanced droplet atomization will also augment the destruction of fuel rich pockets and reduced the sooting tendency in rich mixture regime, normally in the primary zone. At AFR=28, the actual primary zone in this combustor would extend from the designed "physical" primary zone to the downstream. Higher inlet temperature is shown to substantially increase soot formation rate in the primary zone in computational predictions by Alizadeh (1993). The net effect of increased air inlet temperature from 50 °C to 500 °C in a propane fuelled jet flame was observed to reduce the final soot concentration (Nishida and Mukohara (1982)). A critical difference between gaseous fuel and liquid fuel combustion is the fuel preparation. As long as the liquid evaporates into the gaseous state, the subsequent flame structure will be much the same in a kerosine spray flame and a propane diffusion flame as reported by Onuma and Ogasawara (1975) and Onuma et al. (1977). Therefore the total effect of increasing air temperature in a kerosine-fuelled combustor is likely to be a reduction in exhaust soot concentration as reported by Norster and Lefebvre (1972).

Babikian et al. (1990) reported line of sight soot volume fraction levels from 0.164 to 1.01×10^{-7} at different nozzle air fuel ratio, under the overall air-fuel-ratio of 49 at 1 atmospheric pressure. The present study give a local peak value of about 0.8×10^{-7} at AFR=45, a value of a similar magnitude although the absolute level must depend on the individual combustor flow field. The soot volume fraction rises sharply at elevated pressure, reflecting that soot formation rate increases with pressure but also the increased gas density under high pressures (Figure 3.25). The peak soot volume fraction at 4 bar is about 2 times higher than that at 1 bar. The peak soot volume (mass) fraction at elevated pressures (Figure 3.26 (a), (b)) compared favourably with the sampling result of 330 mg/m^3 reported by Clark (1982). Some reduction in inlet air temperature accompanies higher pressure operation in the system employed at Cranfield in this study, making it complicated to make direct comparisons between the detailed soot distributions. It is evident from Figure 3.26 (a), (b) that considerable broadening of radial profiles and increased soot levels along the axis of the liner results from enhanced mass transfer due to the higher turbulence at elevated pressure. Soot formation rates and burnout rates are strong functions of flame temperature and mixture fraction and these have been extensively investigated but the pressure effect on sooting processes in spray flame is still a complex issue. In general, high pressures promote soot formation in gaseous diffusion flames (Haynes and Wagner (1981)). Furthermore it is experimentally observed for this SNECMA designed atomizer that fuel drop sizes at high pressures are bigger than that at lower pressures (Jasuja and Tam (1992)). This inevitably creates more fuel rich eddies and also promotes soot

formation. In view of the complex inter-dependence between flow field and soot formation, the change of mixture fraction and temperature profiles with increased pressure will have a substantial effect on sooting processes and might lead to the quite different soot concentration profiles as shown in Figure 3.26. More details with regard to the mixture fraction and temperature distributions are clearly required for a better understanding of the sooting mechanism inside the combustor. This will be addressed in Chapter 4.

Soot production in the dilution zone of gas turbine combustor is generally in the post formation stage, the formation process in the primary zone will be of more importance in understanding the sooting mechanism in a combustor. The path integrated extinction in the primary zone is about 2.5 times that in the dilution zone (Figure 3.27), although during the experimental procedure no correspondingly high flame luminosity is observed. It is concluded that light extinction in the primary zone results from both liquid droplet scattering and particulate soot absorption. Within the constraints of the experimental facility and cost, further significant increases in air pressure and inlet temperature were impractical. Improving kerosine atomization will certainly reduce the droplet lifetime, and so help eliminate the droplet interference in the soot absorption measurement. A marginal change in the balance of sooting behaviour in the primary zone has been achieved by fuel pre-heating. In Figure 3.28, at an air-fuel-ratio of 50, directly heating the liquid kerosine from room temperature to about 115 °C prior to injection substantially reduced the primary station extinction level. As the fuel flow rate increased to AFR=22, convective heat transfer to the kerosine reduces and little effect was observed. A "false" particulate volume fraction in Figure 3.28 demonstrates the sensitivity of the probing technique, although the distributions do not have an unambiguously quantitative meaning, since the method of data analysis treats both scattering from droplet and soot absorption by simply using Eq. 3-12.

Another method of improving atomization is to preheat the inlet air to promote droplet evaporation. As discussed previously in relation to Figure 3.24, increasing the inlet air temperature will lead the rich mixture towards stoichiometric, thereby inhibiting soot production as well. At AFR=30 the primary zone extinction reduces with increased air inlet temperature, but as fuel flow rate increased to overall AFR=14, little reduction was achieved over the temperature range from 160 °C to 260 °C. With high fuel mass flow rate, or equivalently high fuel velocity, the Weber number of atomization is reduced because of the decrease of gas-liquid relative velocity, leading to comparatively large droplet size. Mizutani et al. (1977) suggested that preheating the gas had a large effect on small droplets, as is found here for AFR=30. On the other hand, the modest changes in flame properties with preheating observed by Katsuki et al. (1976) and Hubbard (1957) suggested that comparatively large droplets ($\approx 100\ \mu m$) are less

influenced by the preheating level. The droplets at the exit of the injector in this SNECMA combustor typically have the initial size about 100 μm (Jasuja and Tam (1992)). Vranos (1974) estimated that the evaporation time of 100 μm droplet is 3.6 ms based on d^2 theory in his combustor geometry under normal operating conditions. The droplet velocity in the combustor, typically less than 20 m/s as reported by McDonell and Samuelsen (1991) from their measurement, is generally lower than the gas velocity due to the aerodynamic drag force on the liquid. Referring to these characteristic figures, it is expected that the drop transport distance may not cover the length from injector exit to dilution zone, about 82.5 mm (cf. Table III). This implies that the dilution station may be largely free from droplets at to combustor operating conditions, for example AFR=45, whilst the primary zone is predominantly a multi-phase flow feature. The thermal radiation measurements in Chapter 5 support such assumption.

As indicated earlier the fact that soot measurement in the primary zone is hampered by the difficulty of differentiating the droplet scattering from soot absorption in the extinction signal prompted further analysis. The real time signal of line-of-sight integrated absorption intensities are illustrated in Figure 3.30. The power spectrum density profiles of these path integrated soot absorption show a large percentage of low frequency fluctuation spanning the range up to 10 kHz (Figure 3.31). The sequential analysis in the primary zone from droplet dominant flow (AFR=12) to droplet and soot co-existing flow (AFR=45) suggested that there is no discernible high frequency from large droplet scattering, indicating the insensitivity of the comparatively big laser beam diameter, about 1.0 mm, to the typical droplet (Figure 3.31 (a)). Some difference in terms of slope between these flow conditions is obvious, and further comparison of sooty flame and droplet contaminated flame in Figure 3.31 (b) might indicate that particles of high number density, eg. soot, have a broader spectrum than droplets have and as a consequence the soot spectrum will drop less sharply, ie. the slope is smaller. The frequency response of different water droplet sizes reveals that the slope of a 1 μm aerosol is smaller than that of 5 μm in point scattering measurement (Domnick (1992)). One further ambiguity is that in Figure 3.31 (b) the sooty flame is promoted by high pressure, where the increased turbulent intensity at high pressure will also contribute to the high frequency fluctuation. This spectrum analysis does not therefore give a satisfactory solution for the discrimination of droplets from soot, and attempts to understanding the detail of soot formation in the two-phase primary zone still remains challenging.

Soot formation in the fuel rich region is restricted to a comparatively narrow range of mixture fraction (0.07 - 0.20) in laminar flames (Moss et al. (1991)), and in turbulent flame the lower limit is of the order of equivalence ratio 2.8 for kerosine (mixture fraction 0.16) (Prado et al. (1977)). Peters and Haumond (1990) suggest an equivalence ratio range of around 1.4

(mixture fraction 0.087) for soot formation in gas turbine combustor. These rich mixtures can only be generated within the wakes of fuel trajectories in the combustor. The mixture fraction profile in combustor chambers is characteristically high in the regime near the centre line, inside the recirculation zone (Jones and Wilhelmi (1989)) where the gas velocity is also low, and so promotes maximum soot formation since this is a slow process. Despite the reservation introduced earlier, the extinction data of the primary zone have been interpreted as particle absorption to compare with that in the dilution zone. Figure 3.32 suggests that the central part is free from particles, as can be imagined from combustor streamlines in this region which lies at the edge of the recirculation zone, where the axial velocity is around zero or reversal to upstream, and no particle can be transferred to the centre line. The peak position qualitatively indicates the main kerosine volume flux in the combustion flow.

Reflecting probe

As reported earlier, the application of the reflecting probe suffered from substantial laser beam steering in the high gradient field. The soot concentration level is much lower than that of the ethylene jet flame investigated in the initial evaluation and the noise arising from beam steering becomes a controlling factor. Sensible results can be obtained for only half the length across the dilution zone at AFRs higher than 14 (Figure 3.33). The front reflecting surface of the corner cube is 2.0 mm away from the probe outer diameter, limited by the external probe diameter, and has to be purged by nitrogen at a rate twice as high as that applied in the sight probe measurement to prevent liquid contamination on the reflector surface. The results across the '-' side at AFRs 14, 12 give more sensible comparison in Figure 3.33 (b), (c), though the repeatability is poor. As the signal level reduces at AFR=28, the data did not seem physically plausible. The reason behind the selection of the corner cube lay in its unique advantage of parallel incident and emerging beams, making mechanical signal collection feasible, however this advantage can normally be only exploited with a reflector having a diameter of the order of, say 10 mm, as commercially distributed. The tiny dimension of the reflector adopted here proved to be too problematic in relation to the beam steering problem and showed little promise in this application.

3.5 CONCLUDING REMARKS

The retrieval of spatially resolved soot volume fraction profiles has been demonstrated in a representative gas turbine combustor. The sight probe shows particular promise in its application, in both mechanical operation and data interpretation. The reflecting probe proved

less encouraging in measurements in a practical combustor, suffering excessive position-dependent noise at the current, relatively low, absorption levels. The advantage of its improved aerodynamic performance is overturned by the difficulties in signal treatment. Given the restricted size and optical access of the tubular combustor, the sight probe provided more satisfactory results.

Little perturbation is imposed locally on the measurement volume by the sight probe, on the evidence of the water flow visualization test. The measured soot volume fraction distribution suggests an annular development of the sooting region, following the fuel atomization history, with a clearly defined minimum on the combustor centre line. These profiles compared favourably quantitatively with other measurements using probe sampling method.

Combustor operating conditions have a profound effect on the soot concentration level; higher air inlet temperatures inhibit overall soot production, principally by affecting the fuel vaporisation process and subsequent mixing process and shifts in the balance between formation and oxidation. This is in line with gaseous fuel sooting processes reported in the literature. Higher pressures promote soot production as expected.

Multi-phase flow in the primary zone has hampered the soot measurement there. No satisfactory method has been developed insofar for the discrimination of the effect of liquid droplet scattering and particulate soot absorption on path-integrated extinction measurements. In view of the fuel droplet contamination in the primary zone, measurements at higher pressures were confined to the dilution zone station.

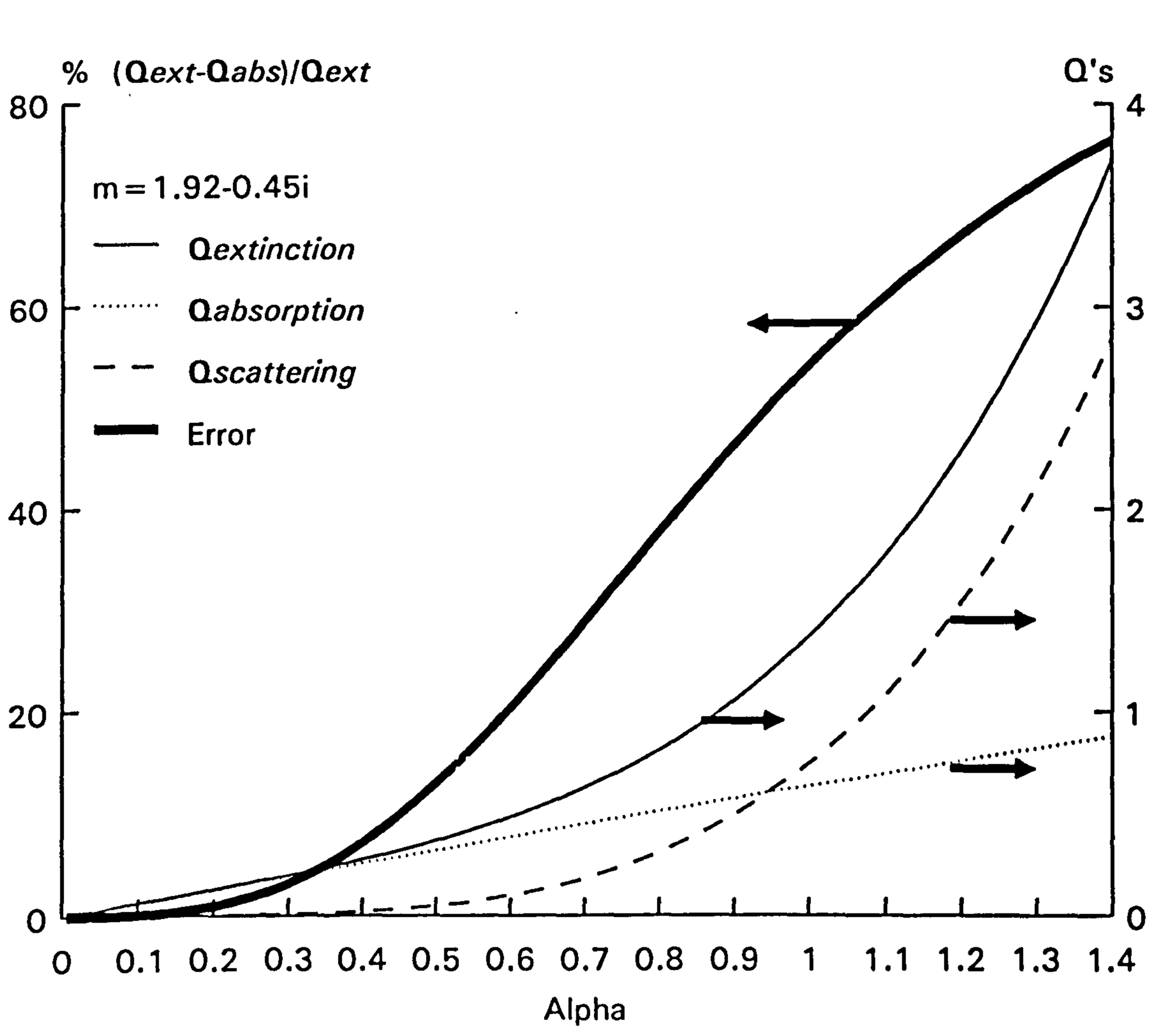

Figure 3.1 Percentage deviation between Rayleigh formula (Eq. 3-6) and the exact value (Eq. 3-3). (m=1.92-0.45i)

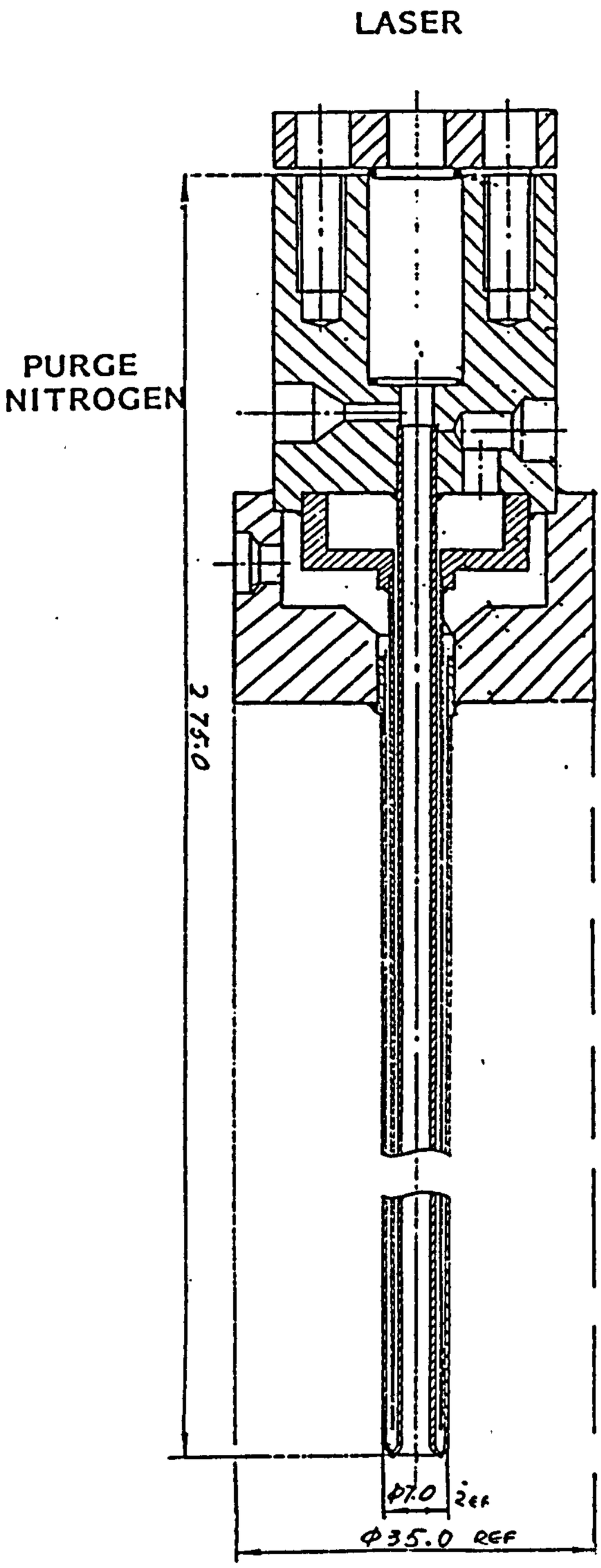

Dimensions in mm

Tube	I.D.	O.D.
Inner	3.28	4.06
Central	4.55	5.45
Outer	6.00	7.00

Figure 3.2 The traversable sight probe

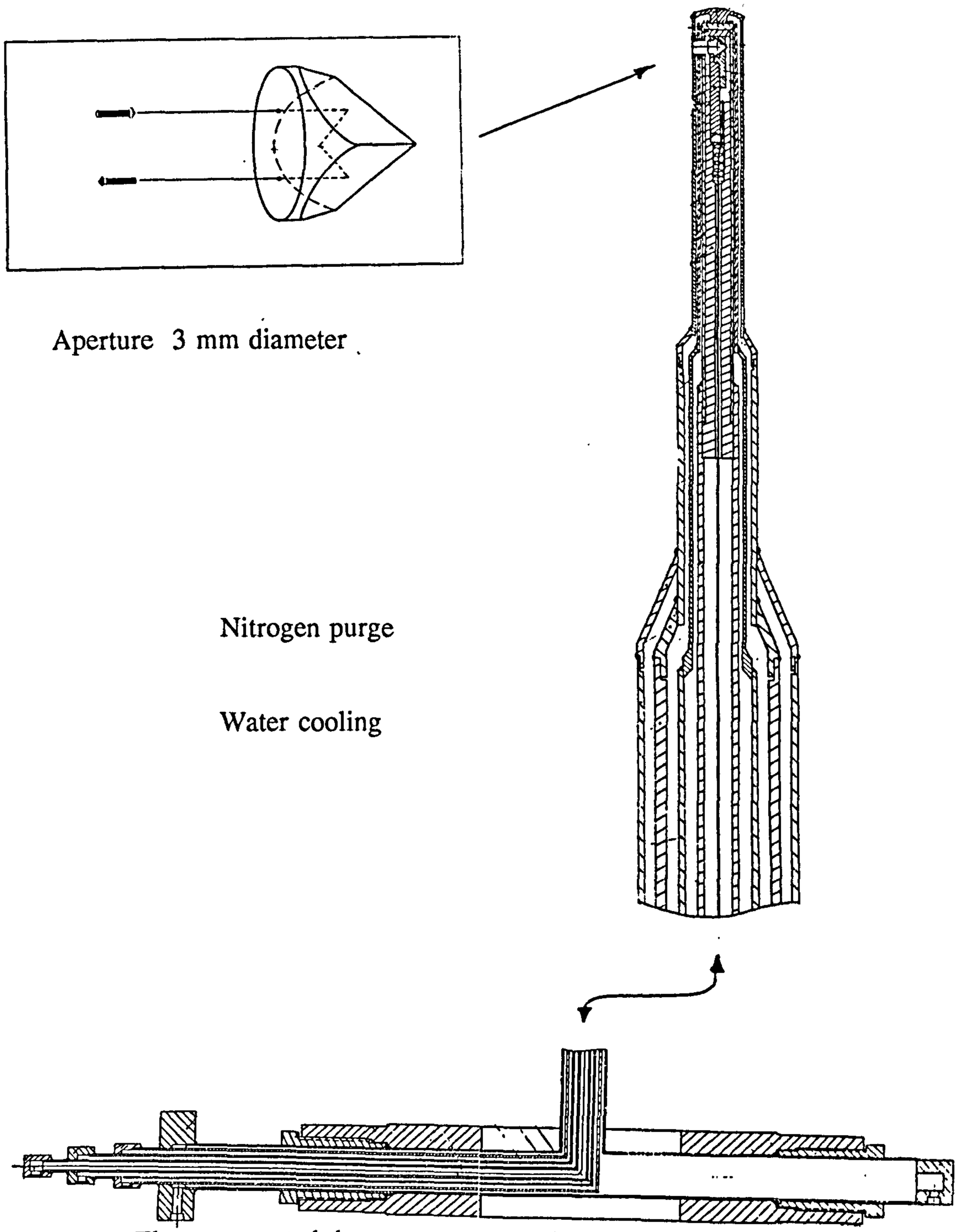

Figure 3.3 The corner cube, reflecting probe

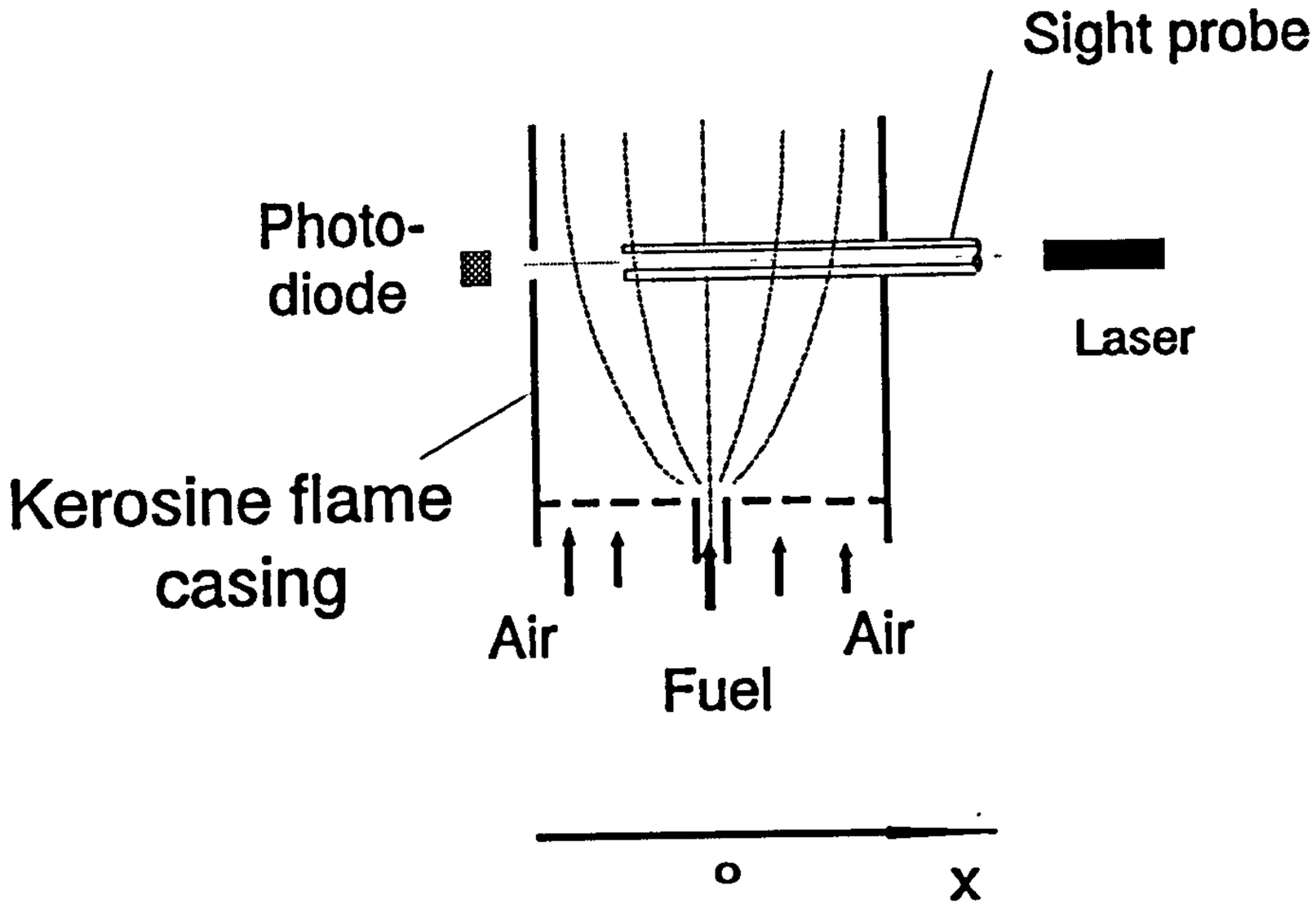

(a) Sight probe in kerosine jet flame

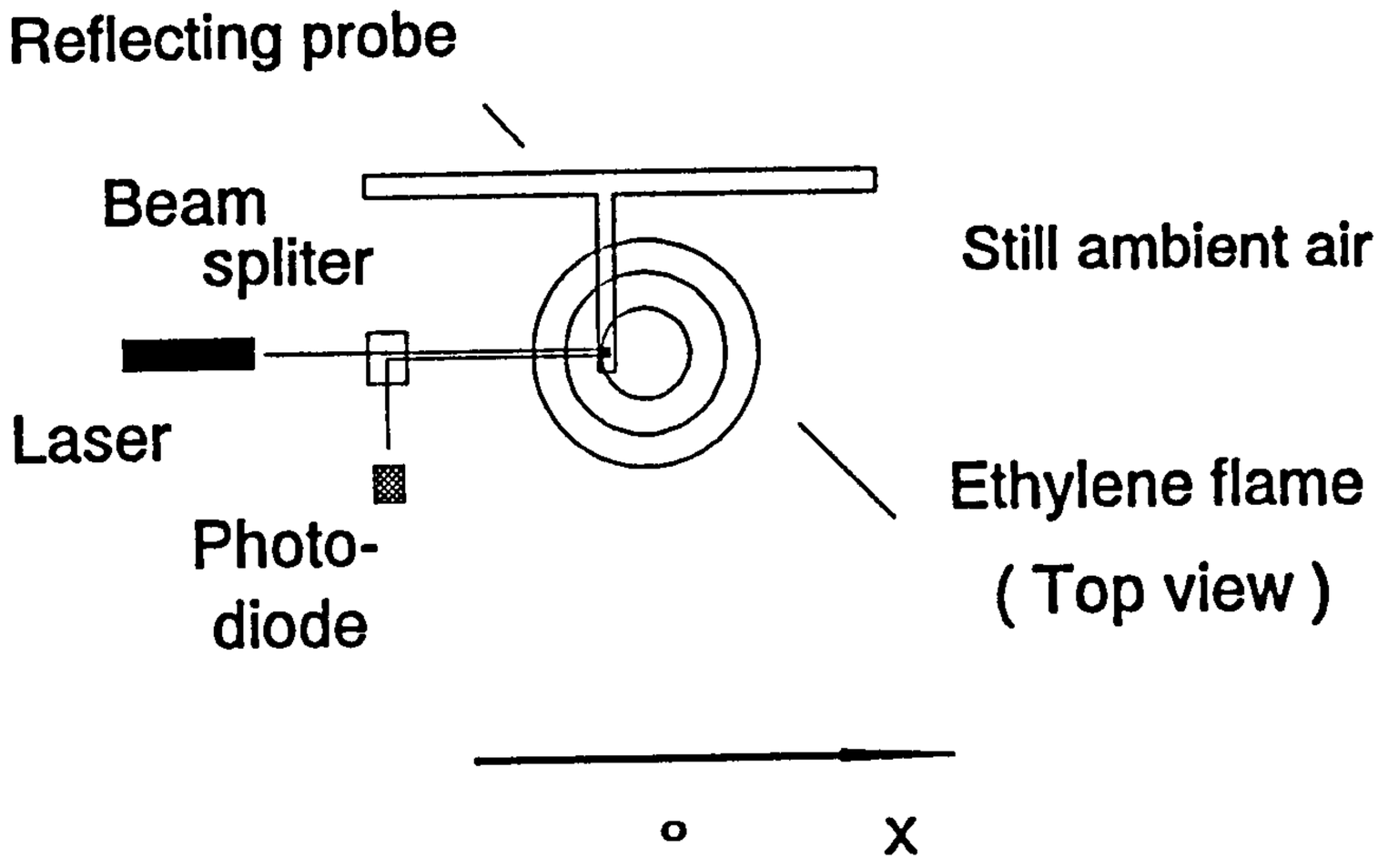

(b) Reflecting probe in ethylene jet flame

Figure 3.4 Probe and optics arrangement in jet flames. (a) Kerosine jet flame for sight probe, (b) Ethylene flame for reflecting probe

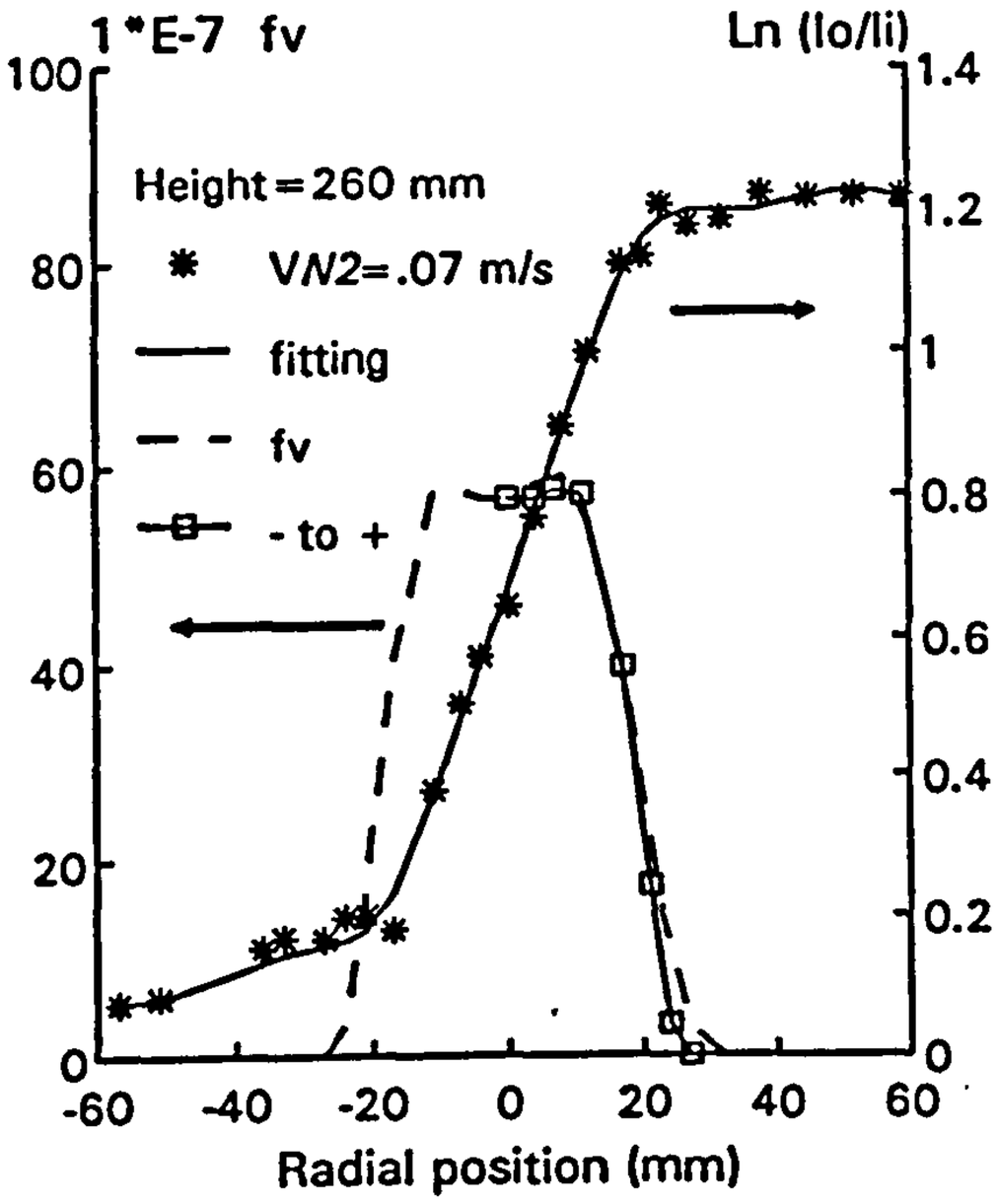

(a)

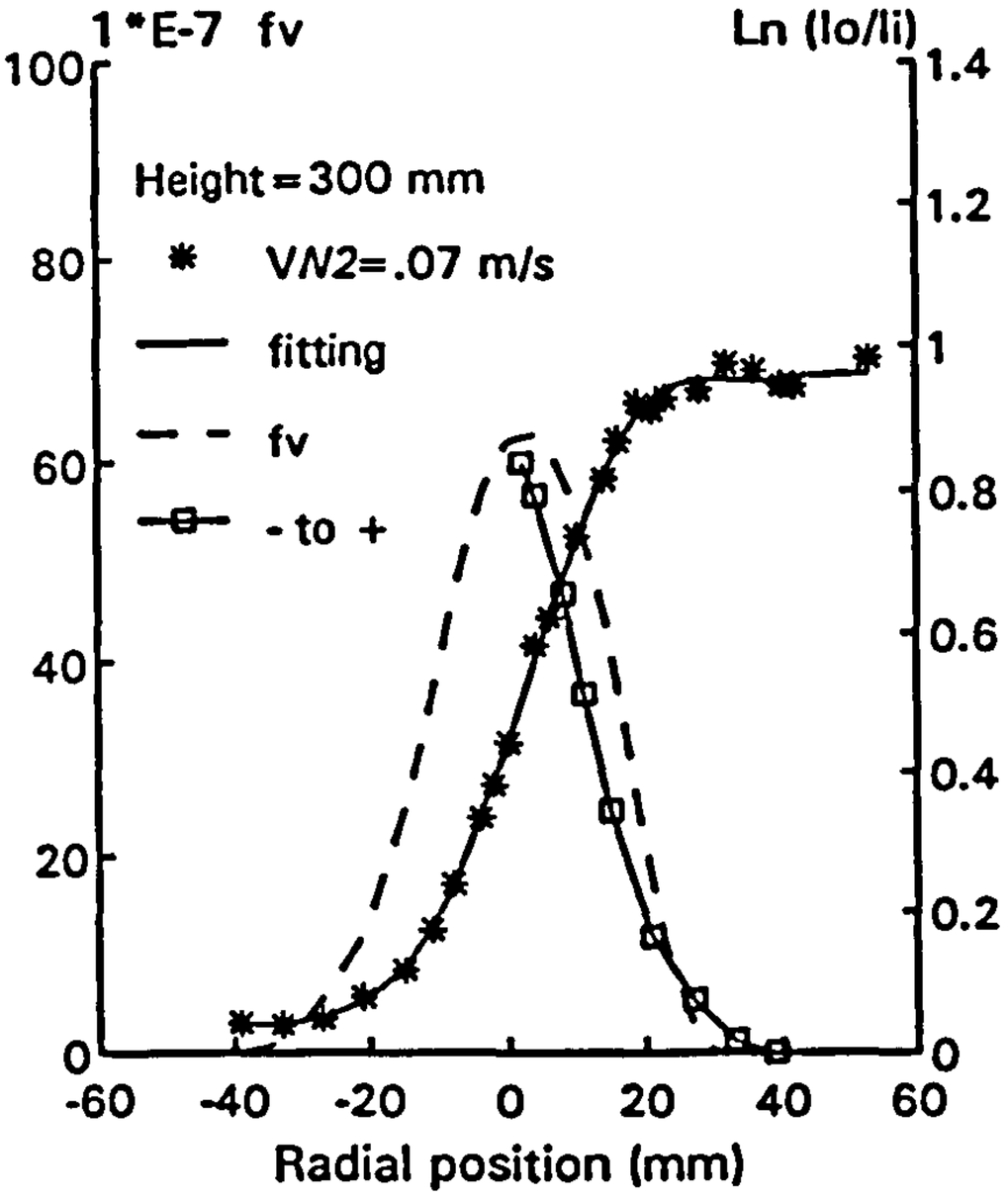

(b)

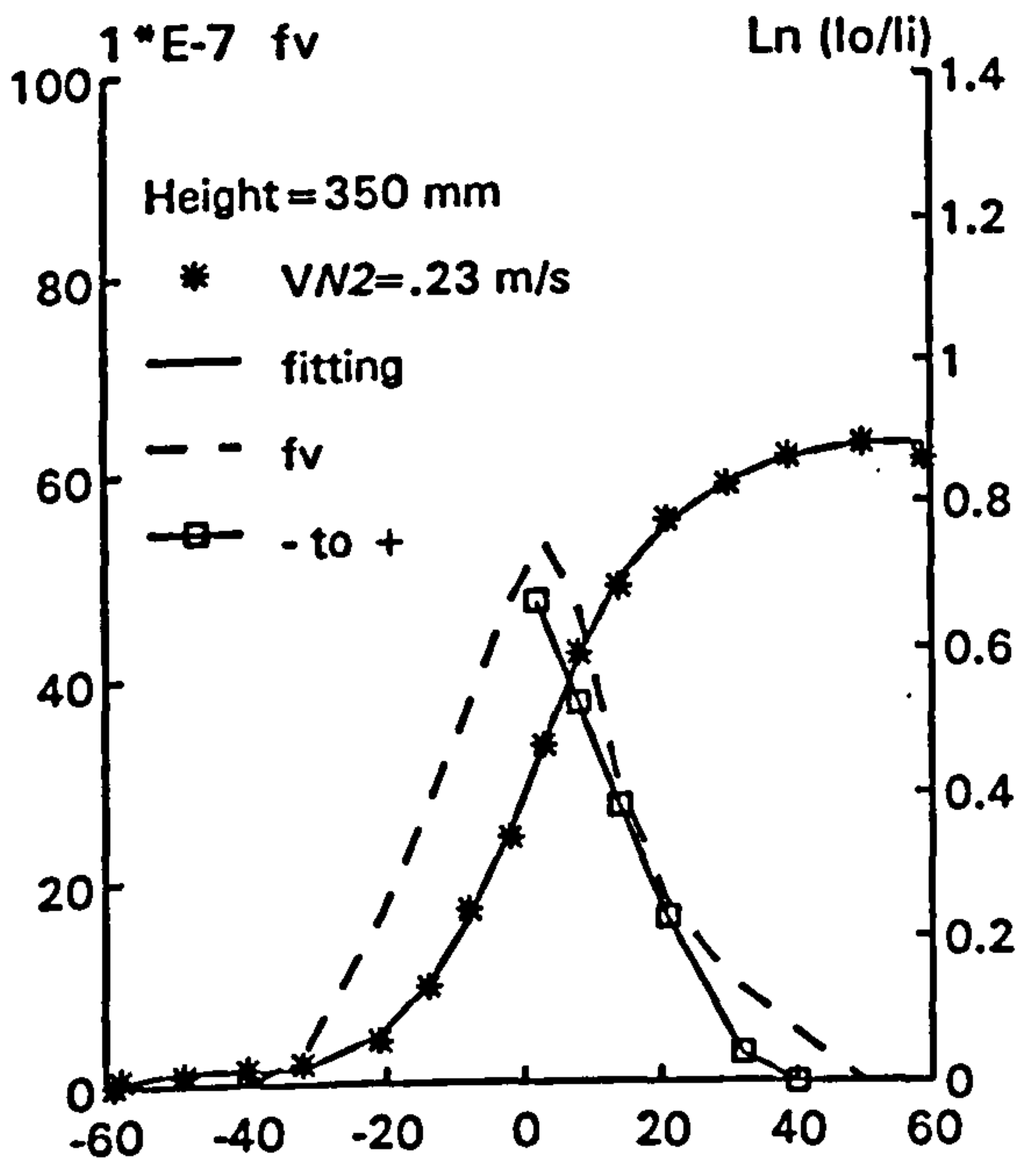

(c)

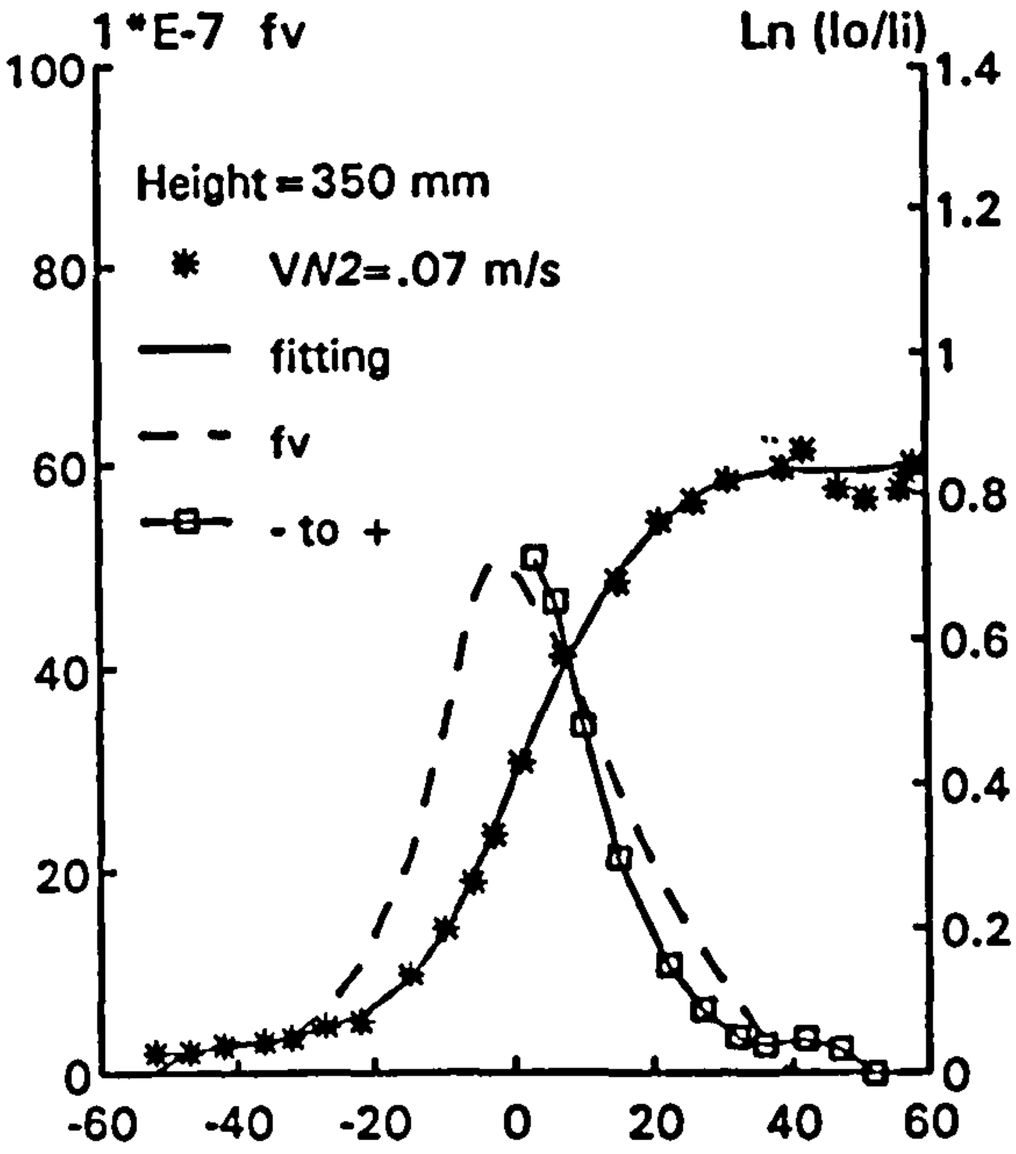

(d)

Figure 3.5 Raw data of laser absorption and soot volume fraction measured by sight probe in the kerosine flame at heights: (a) 260 mm, (b) 300 mm, (c) and (d) 350 mm

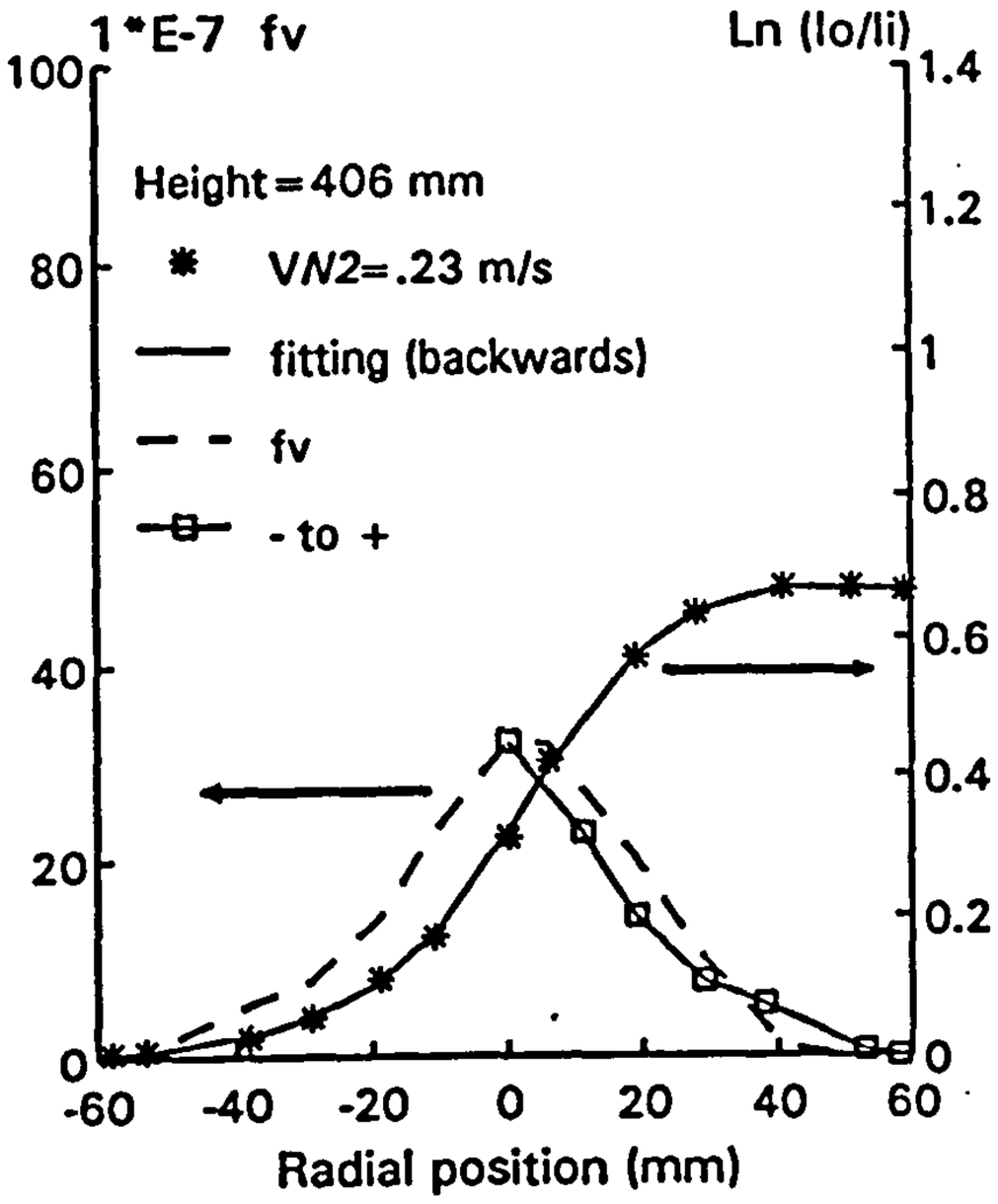

(a)

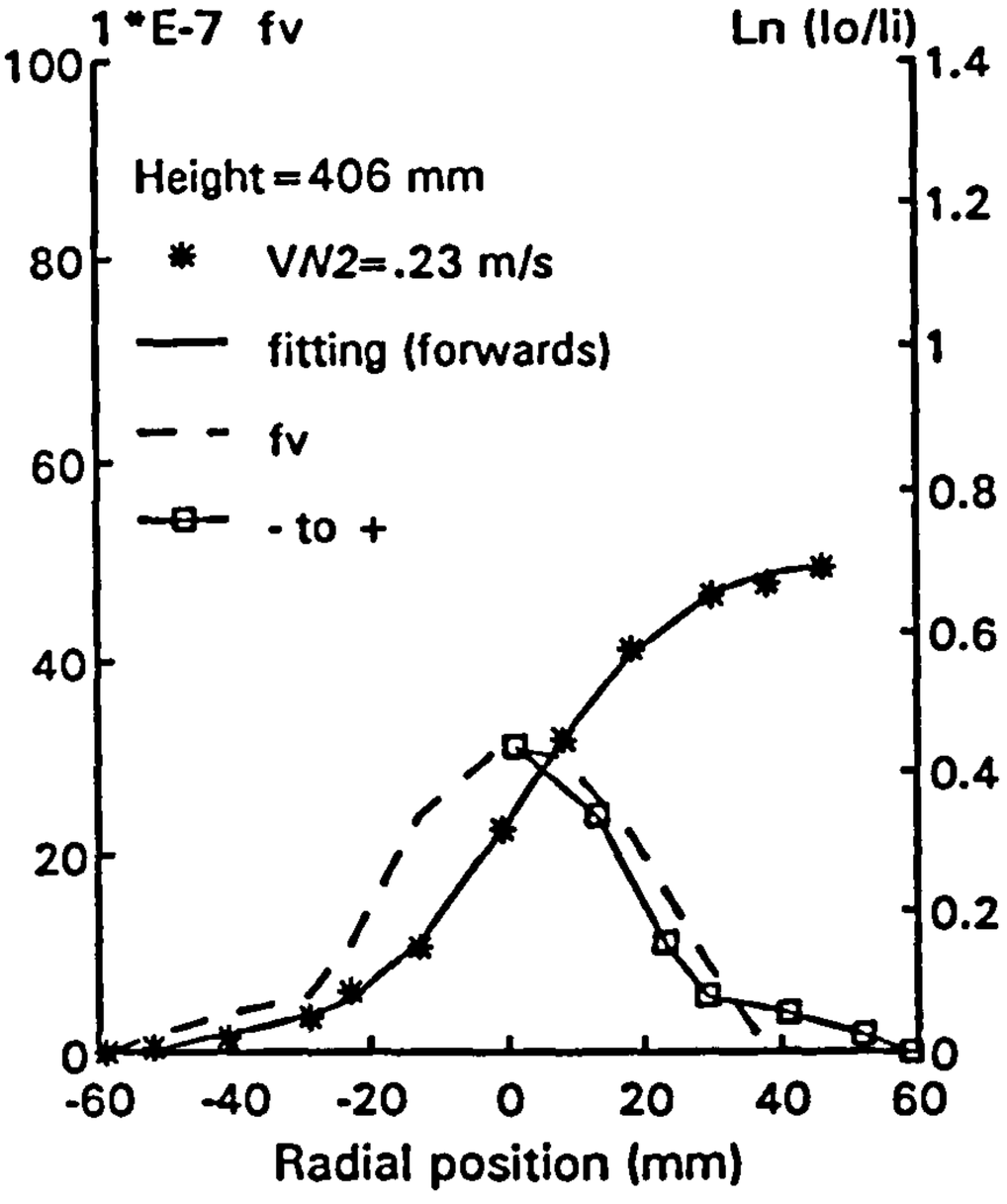

(b)

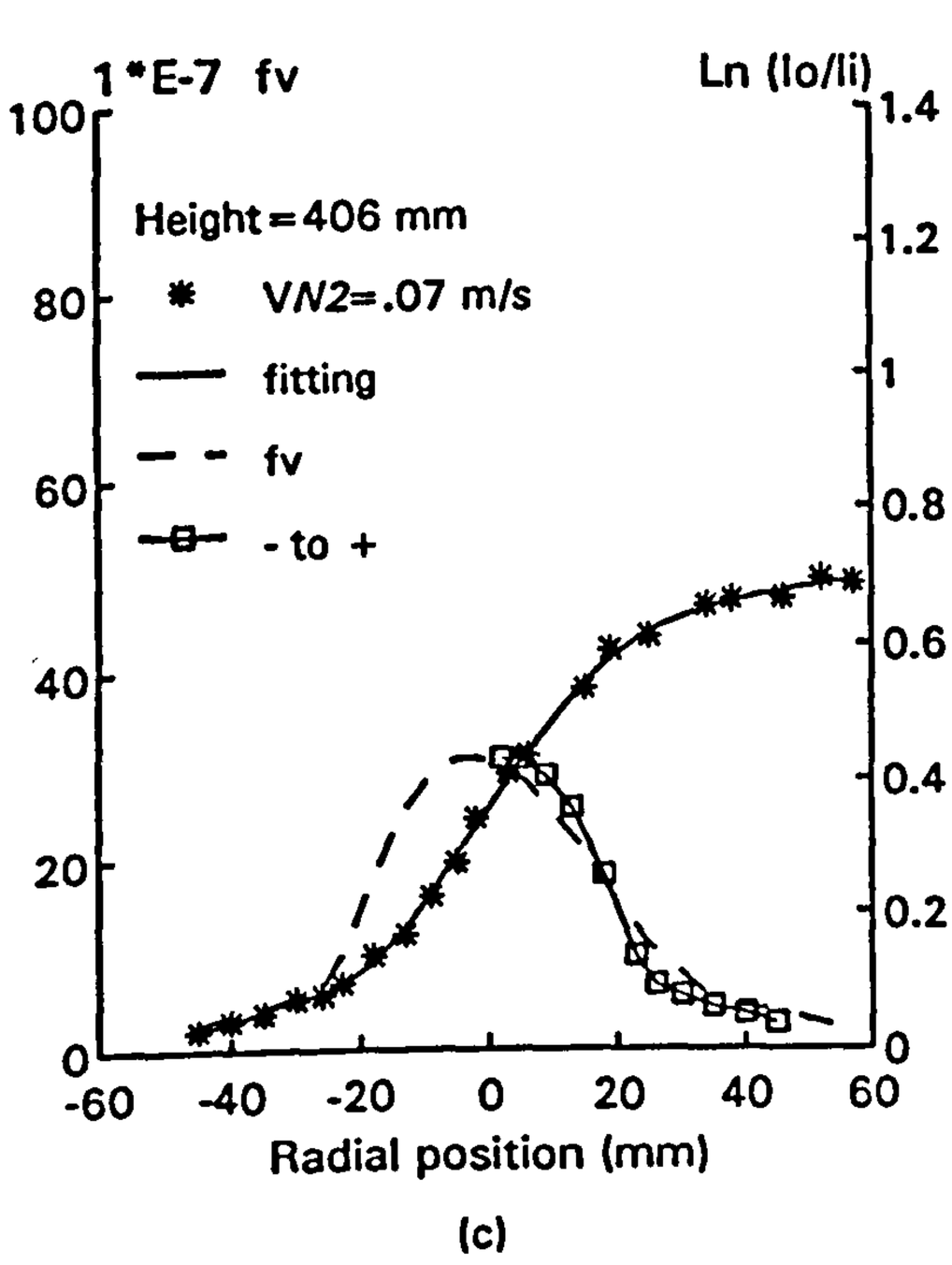

(c)

Figure 3.6 Raw data of laser absorption and soot volume fraction measured by sight probe in the kerosine flame at height 406 mm with: (a) (b) different probe traversing direction and (c) Different nitrogen purge rate

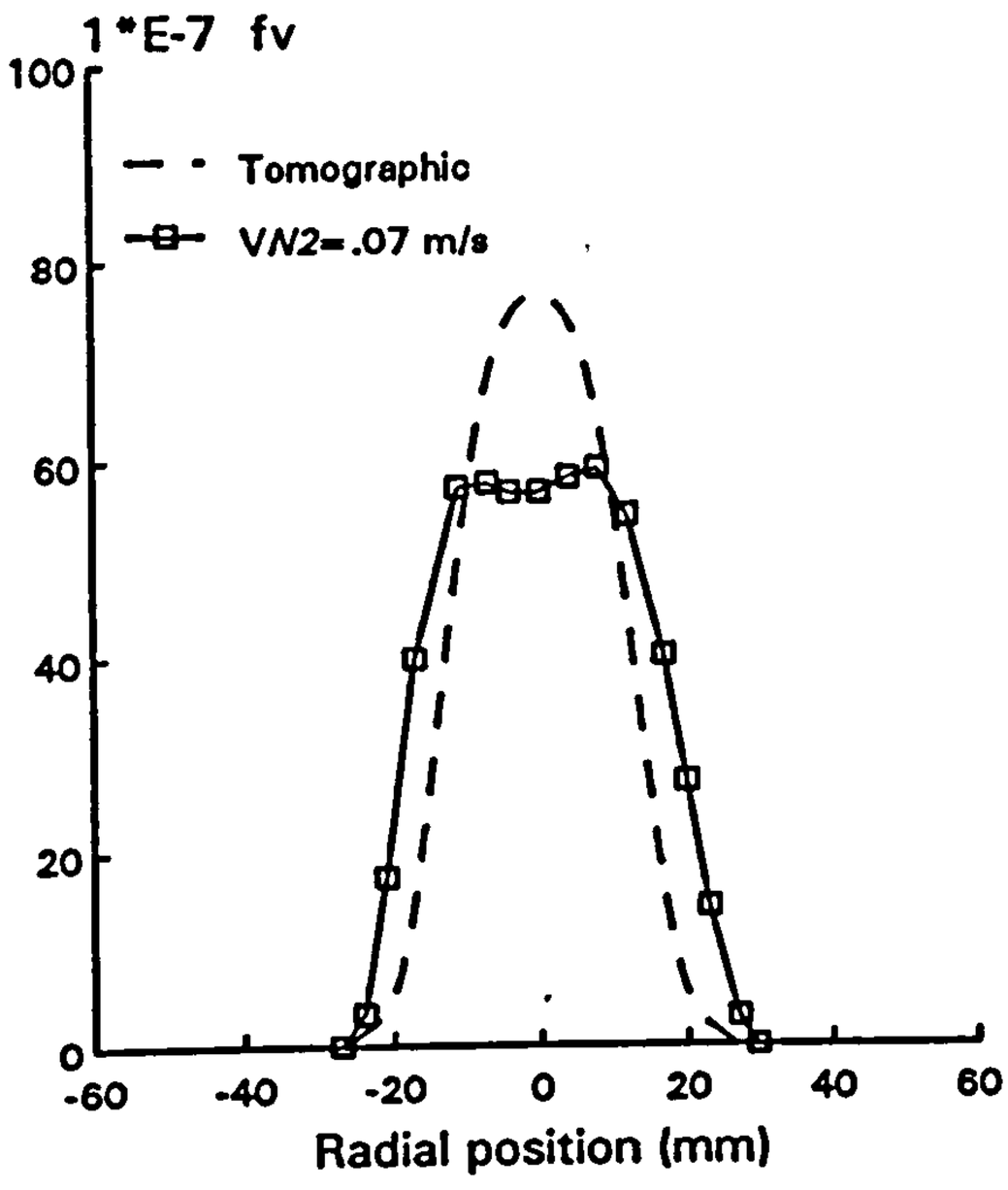

(a) H=260 mm

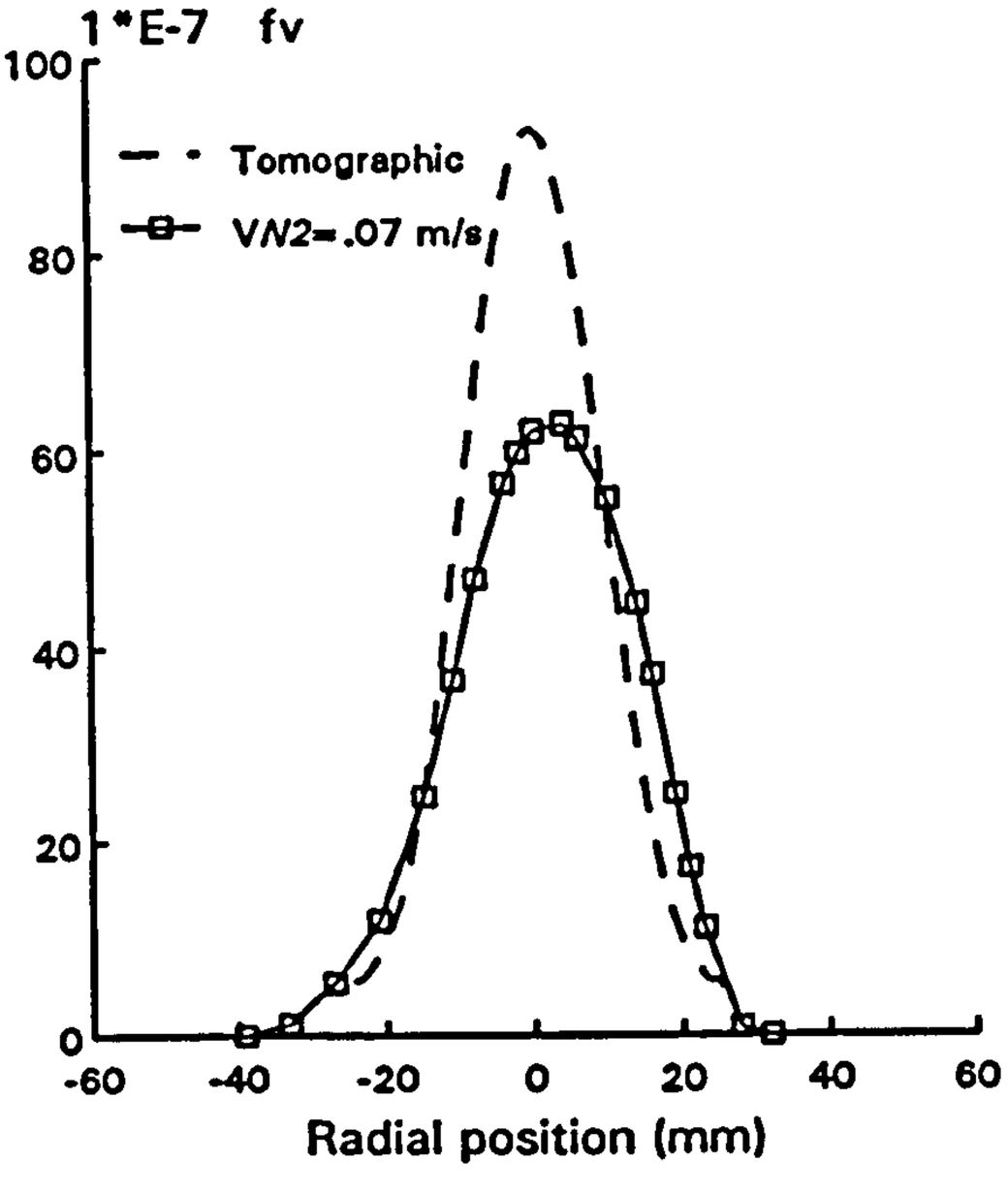

(b) H=300 mm

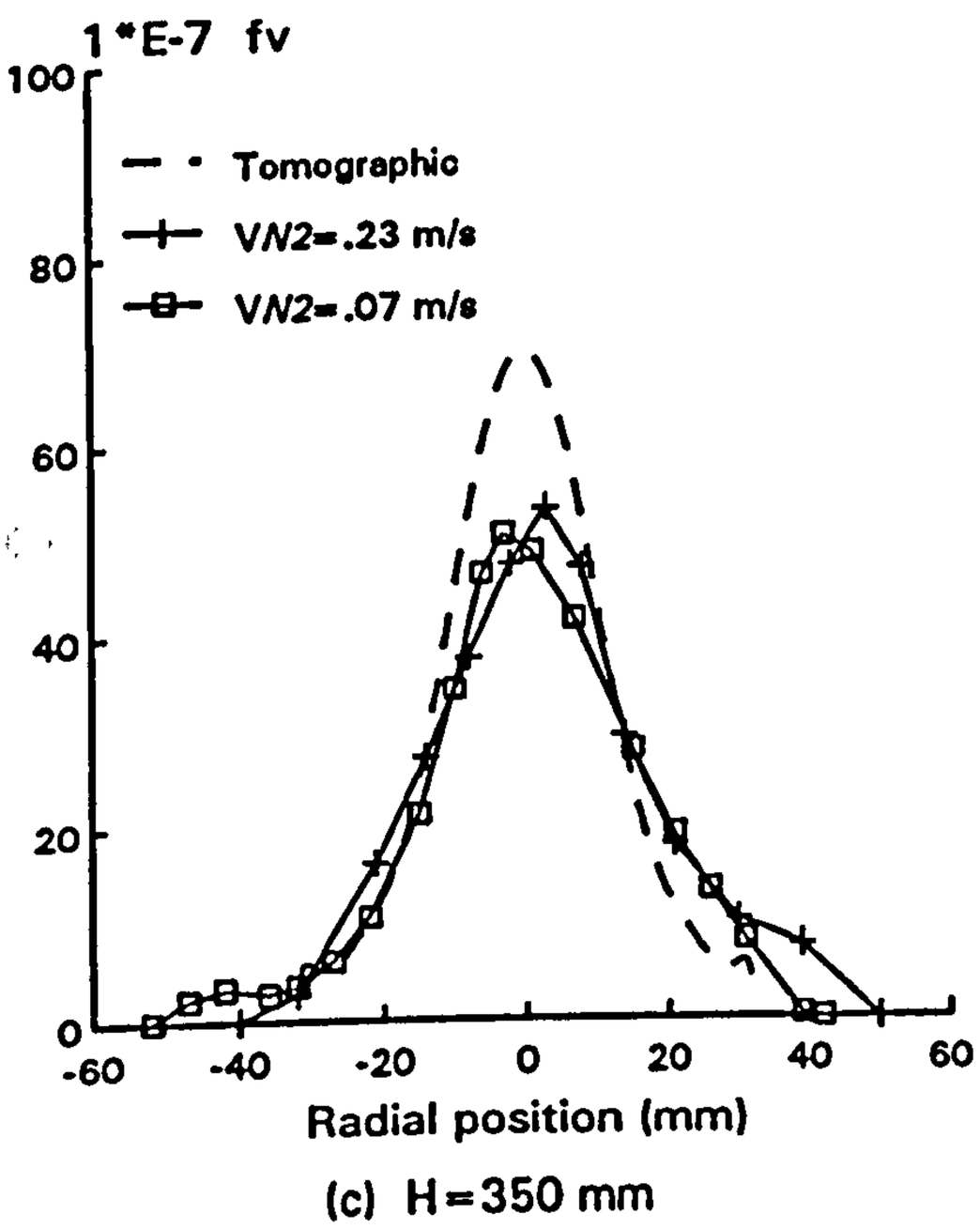

(c) H=350 mm

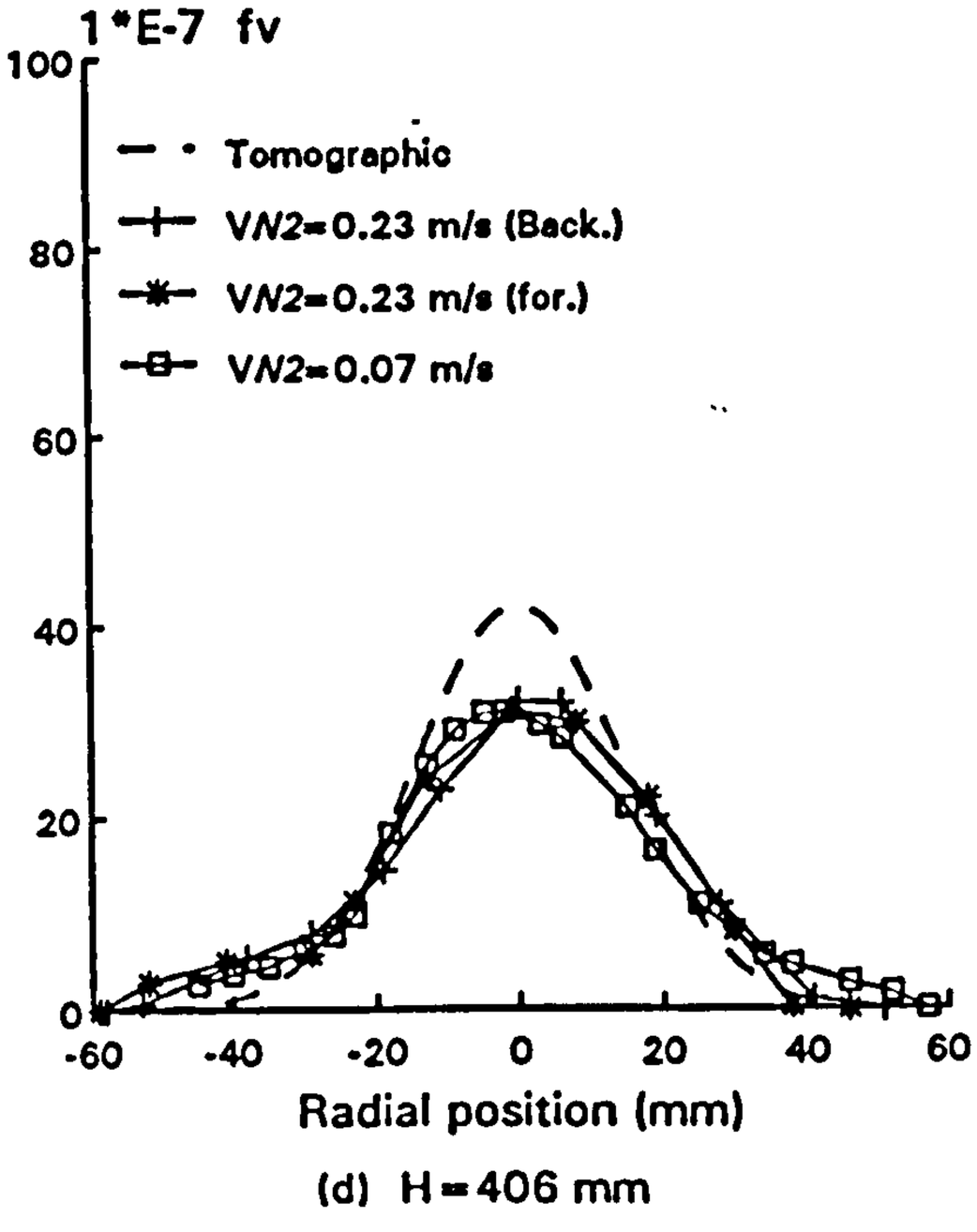

(d) H=406 mm

Figure 3.7 Comparison of soot volume fraction in the kerosine flame measured by probing and the non-intrusive tomographic technique for heights: (a) 260, (b) 300, (c) 350 and (d) 406 mm

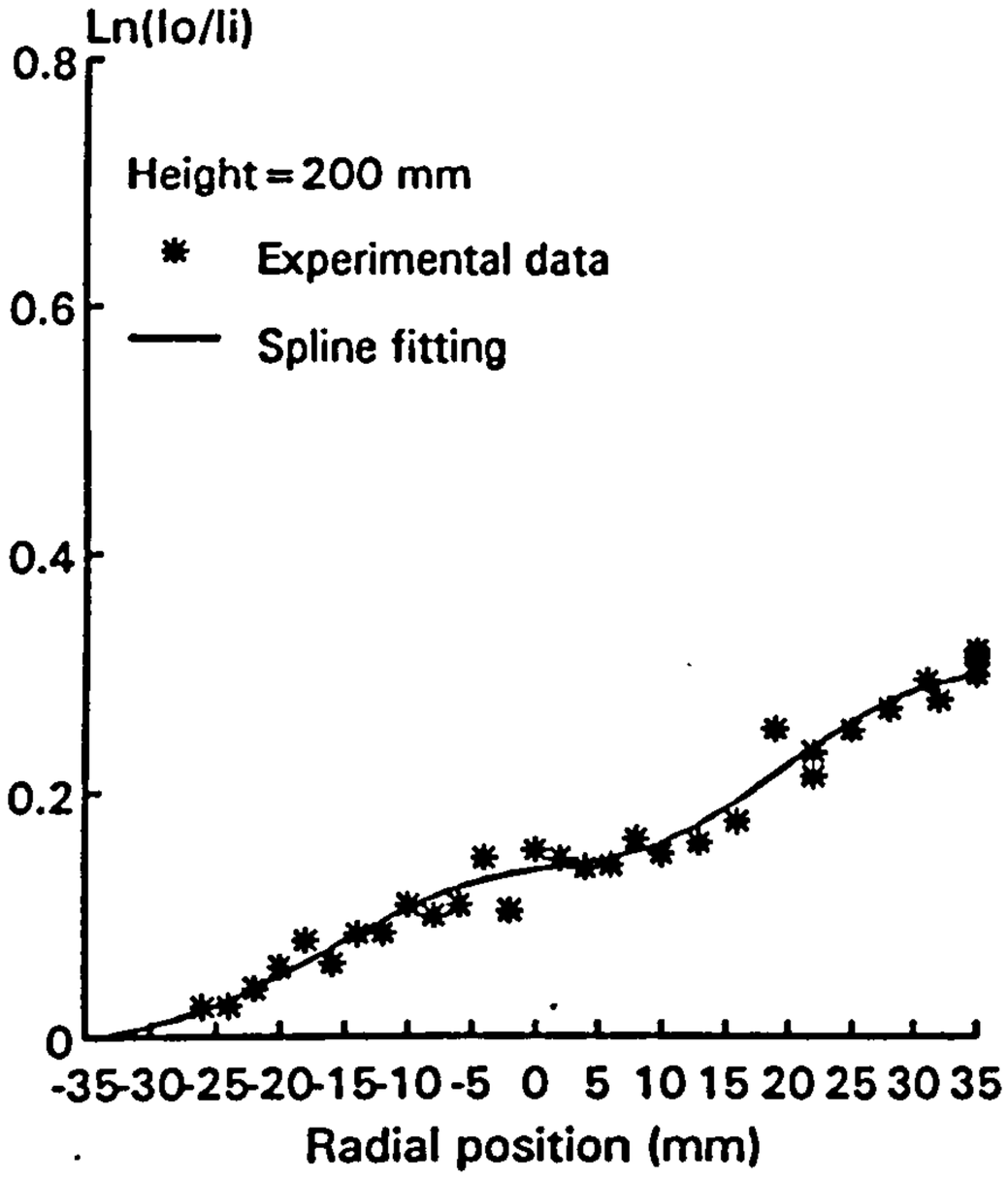

(a)

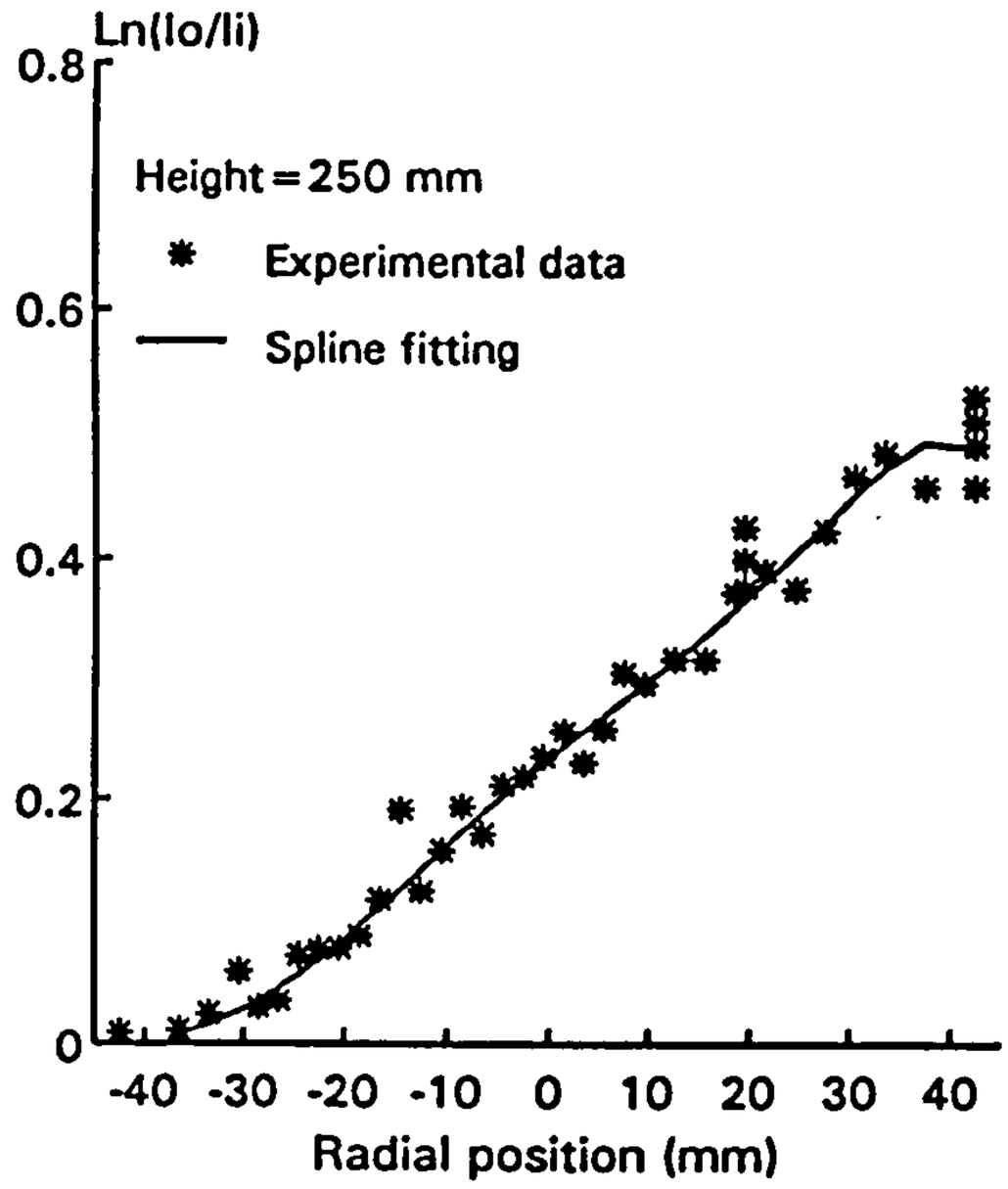

(b)

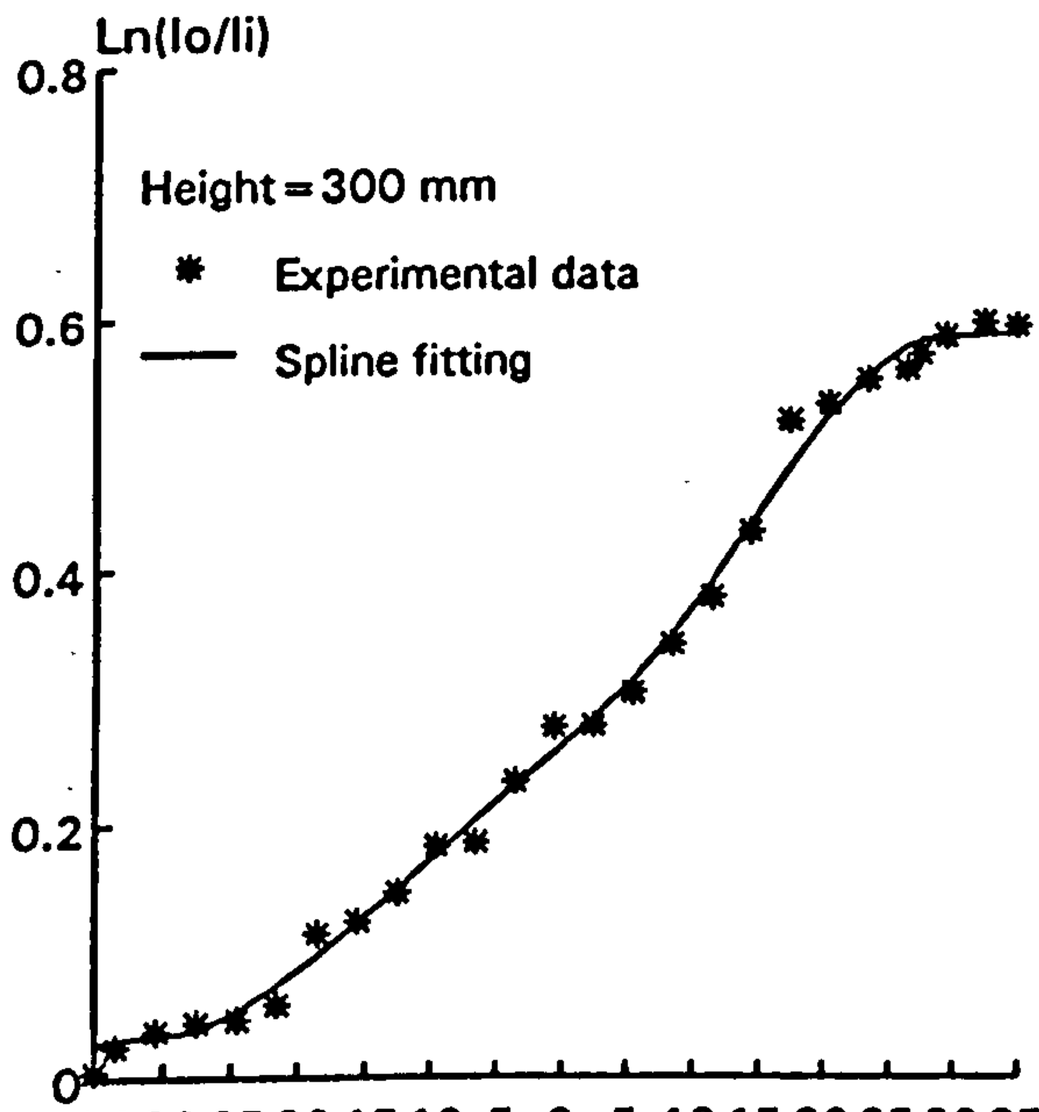

(c)

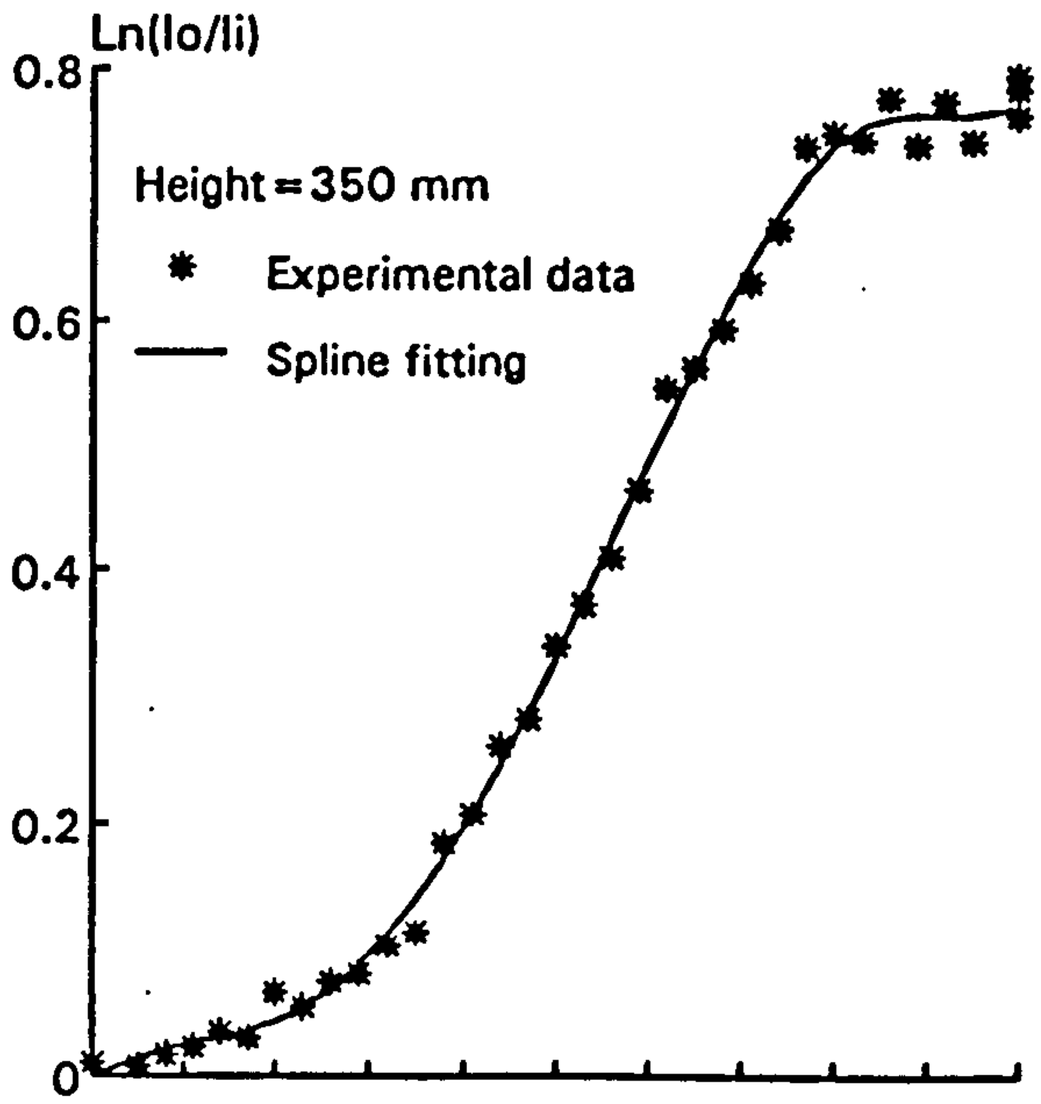

(d)

Figure 3.8 Raw data of laser absorption measured by reflecting probe in the ethylene flame at heights: (a) 200, (b) 250, (c) 300 and (d) 350 mm

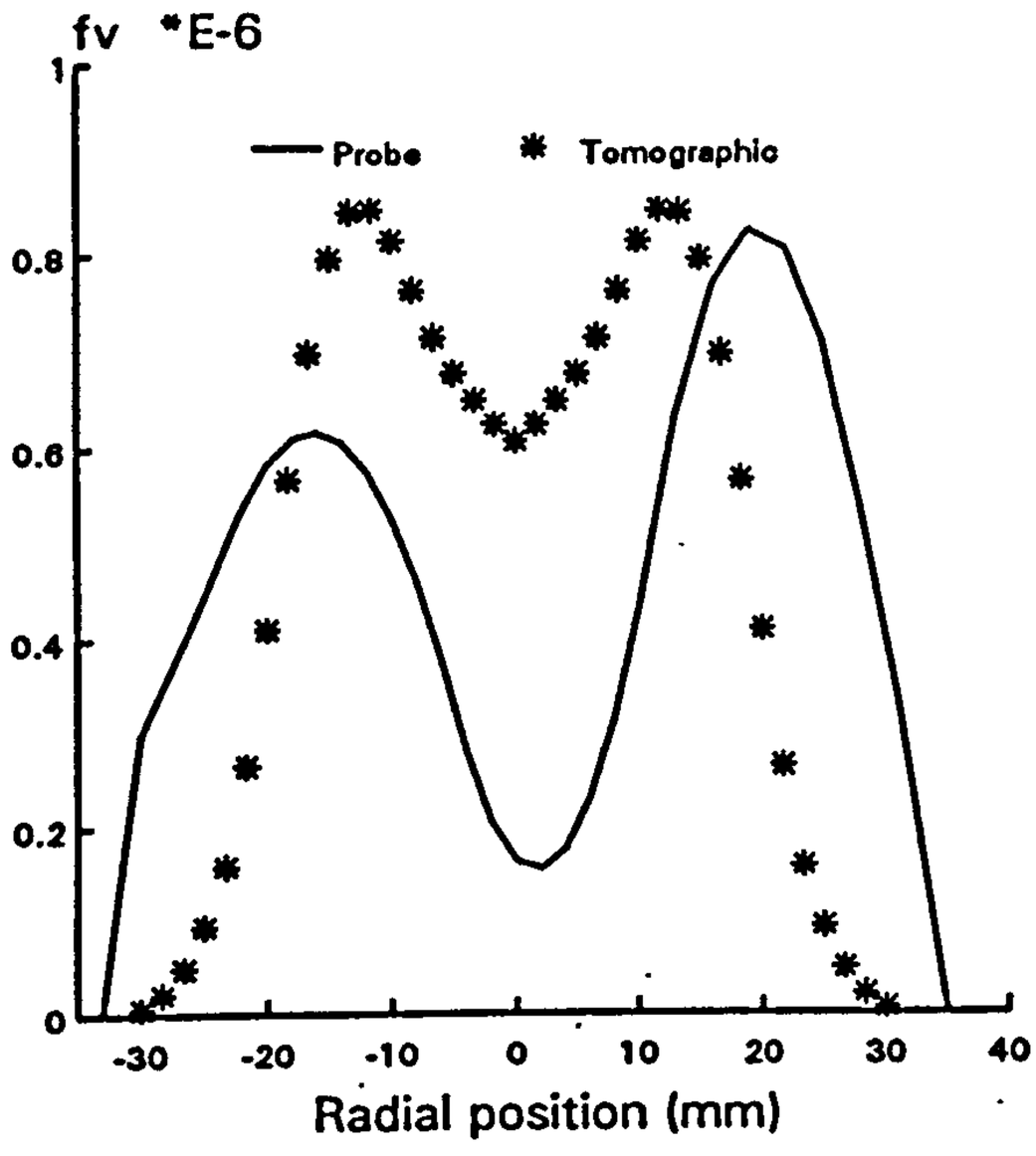

(a) Height = 200 mm

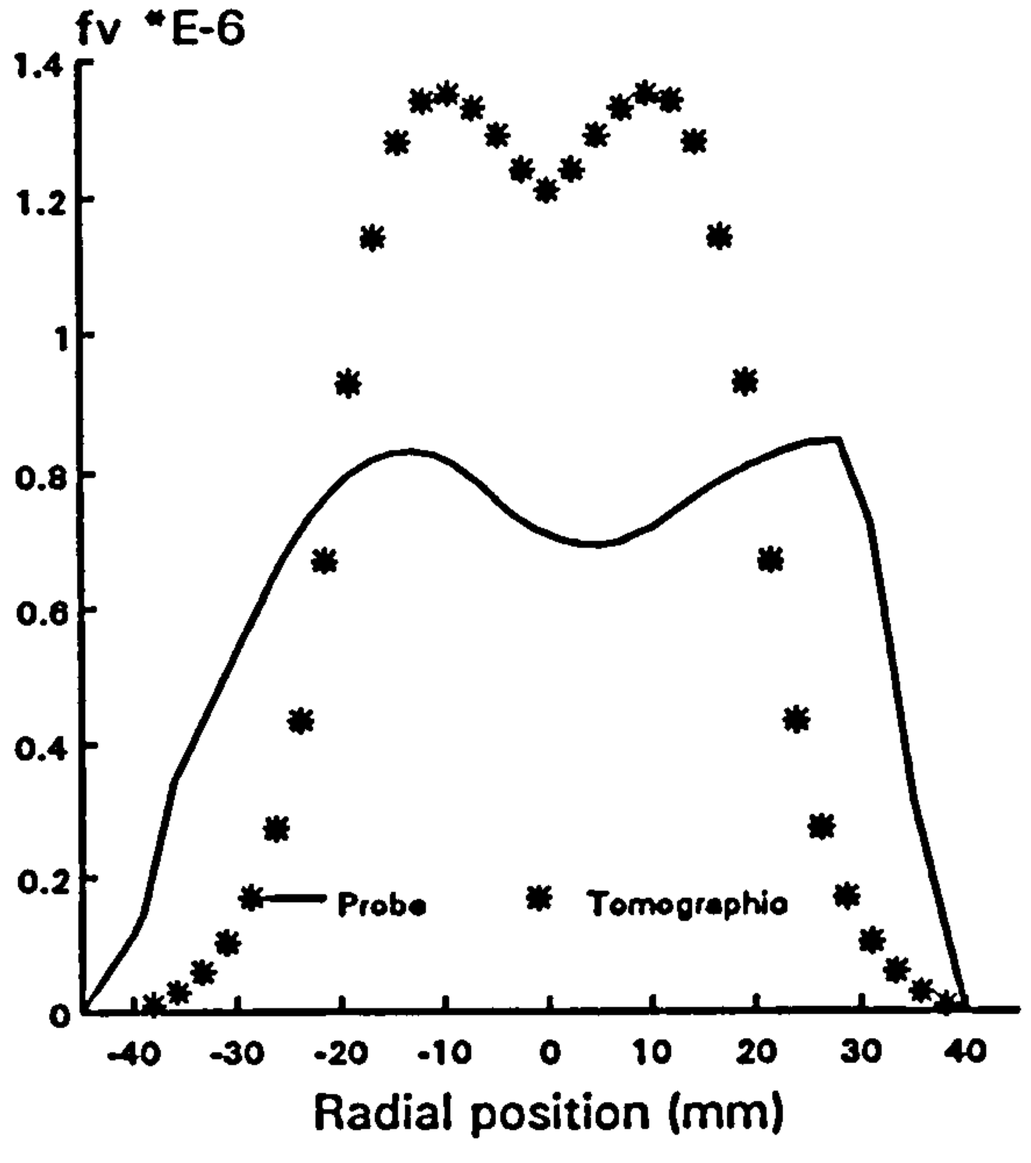

(b) Height = 250 mm

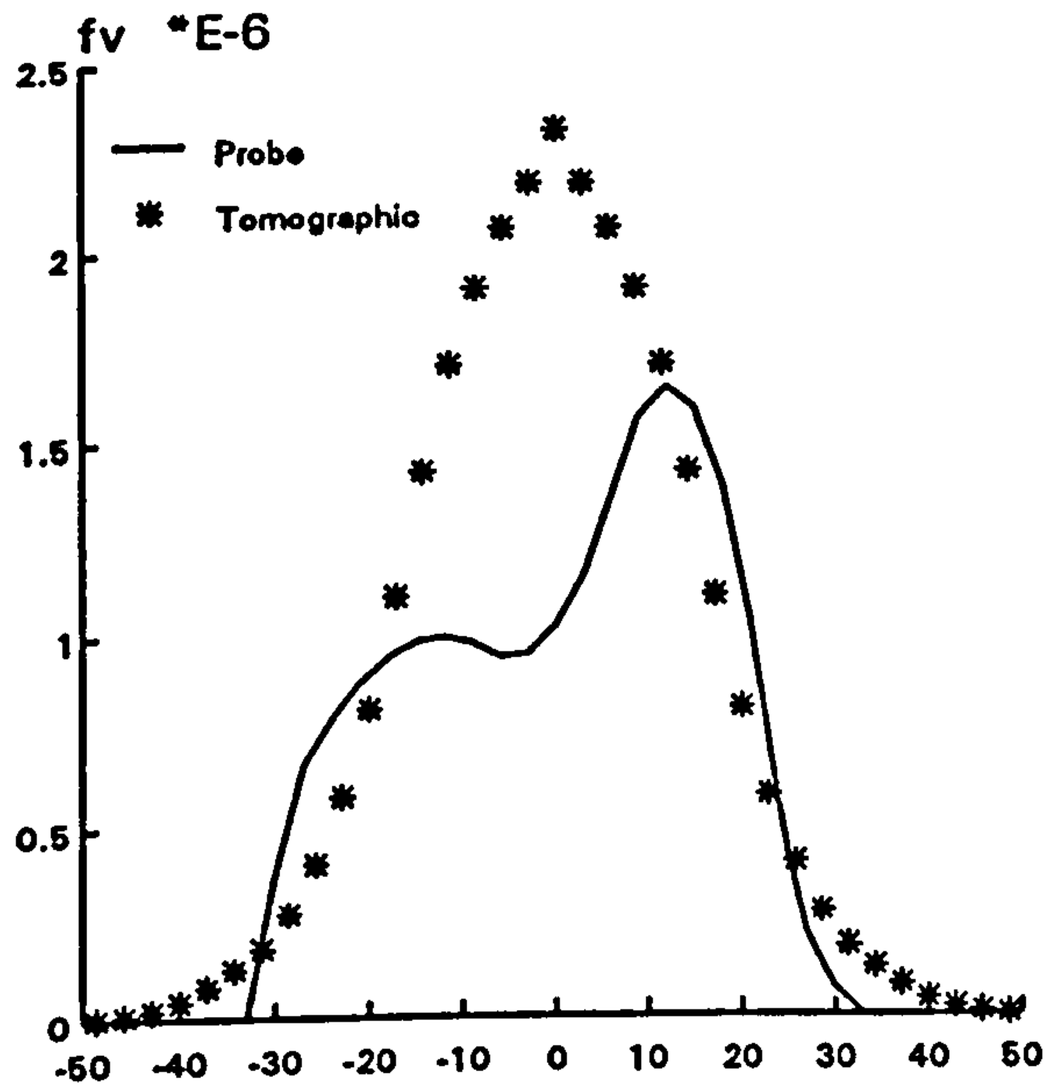

(c) Height = 300 mm

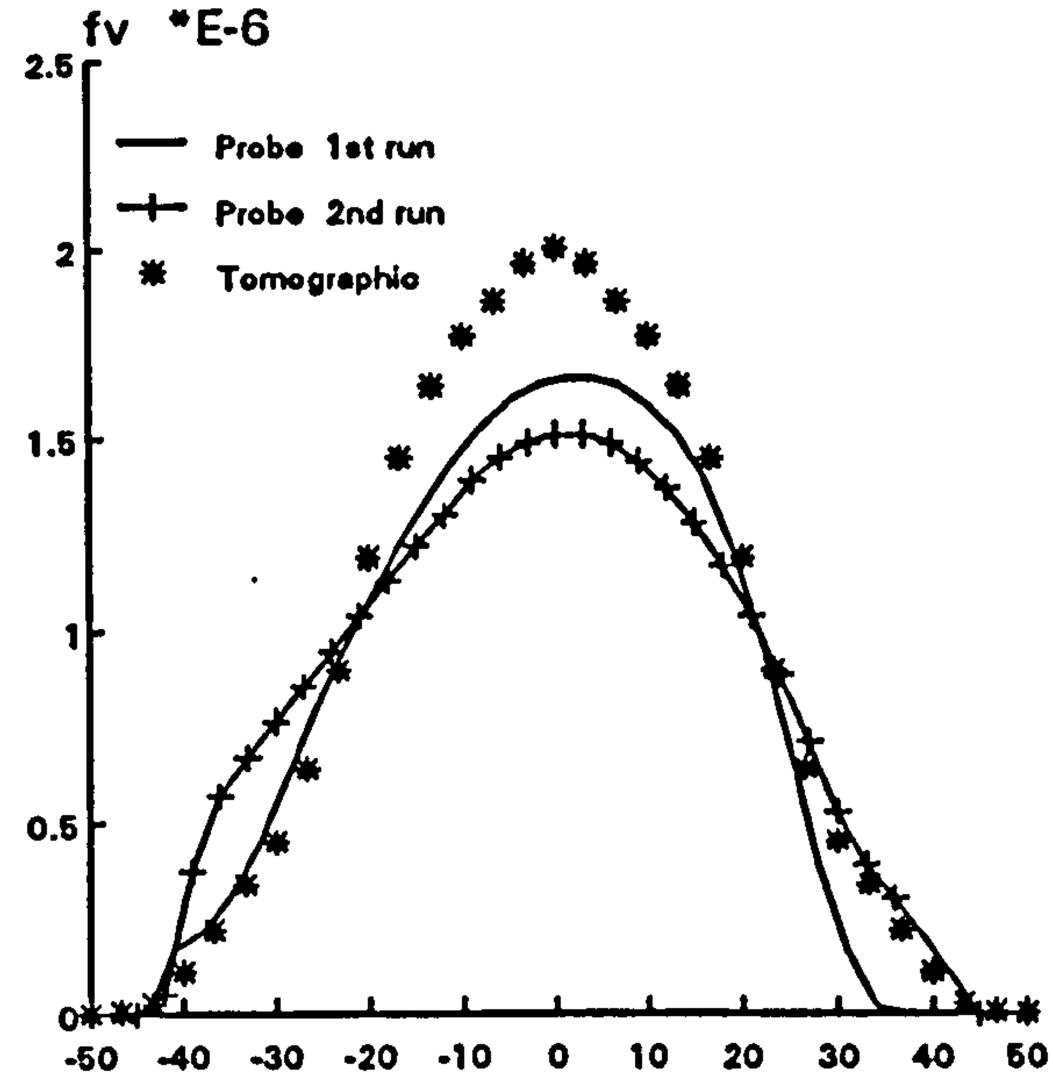

(d) Height = 350 mm

Figure 3.9 Comparison of soot volume fraction measured by probing (reflecting probe) and non-intrusive tomographic techniques in the ethylene flame at various heights

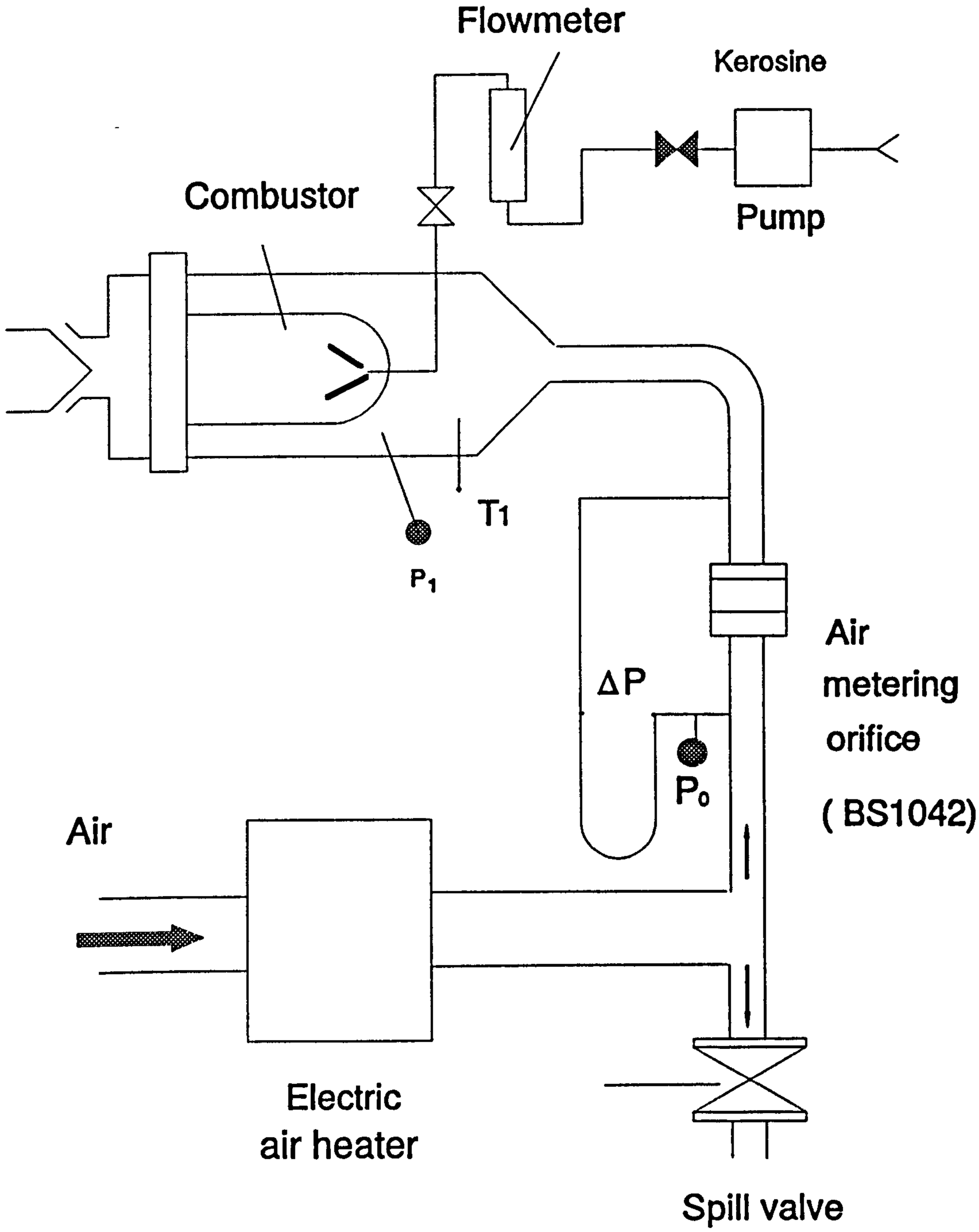

Figure 3.10 Schematic of experimental rig and its installation

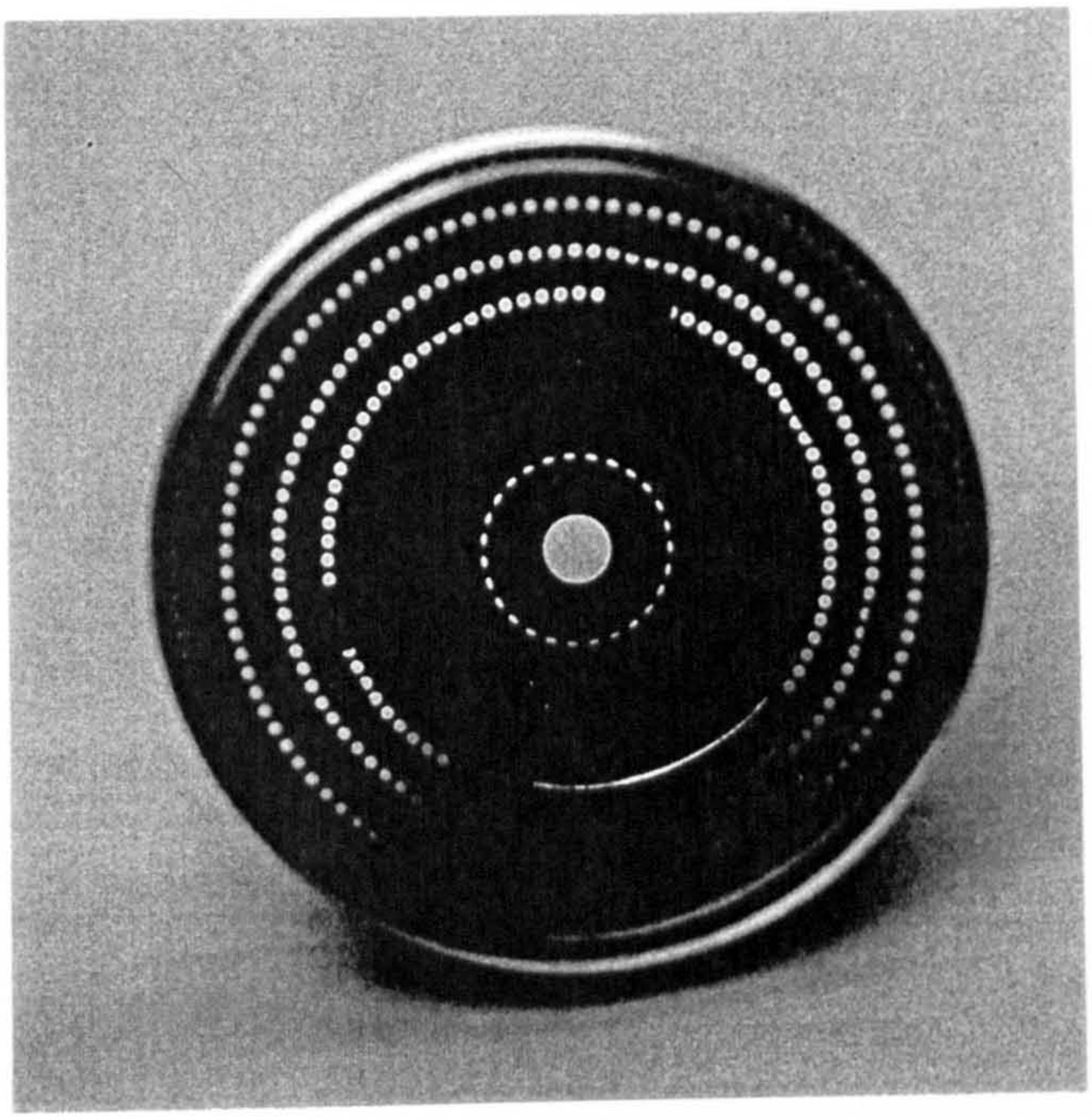

End view

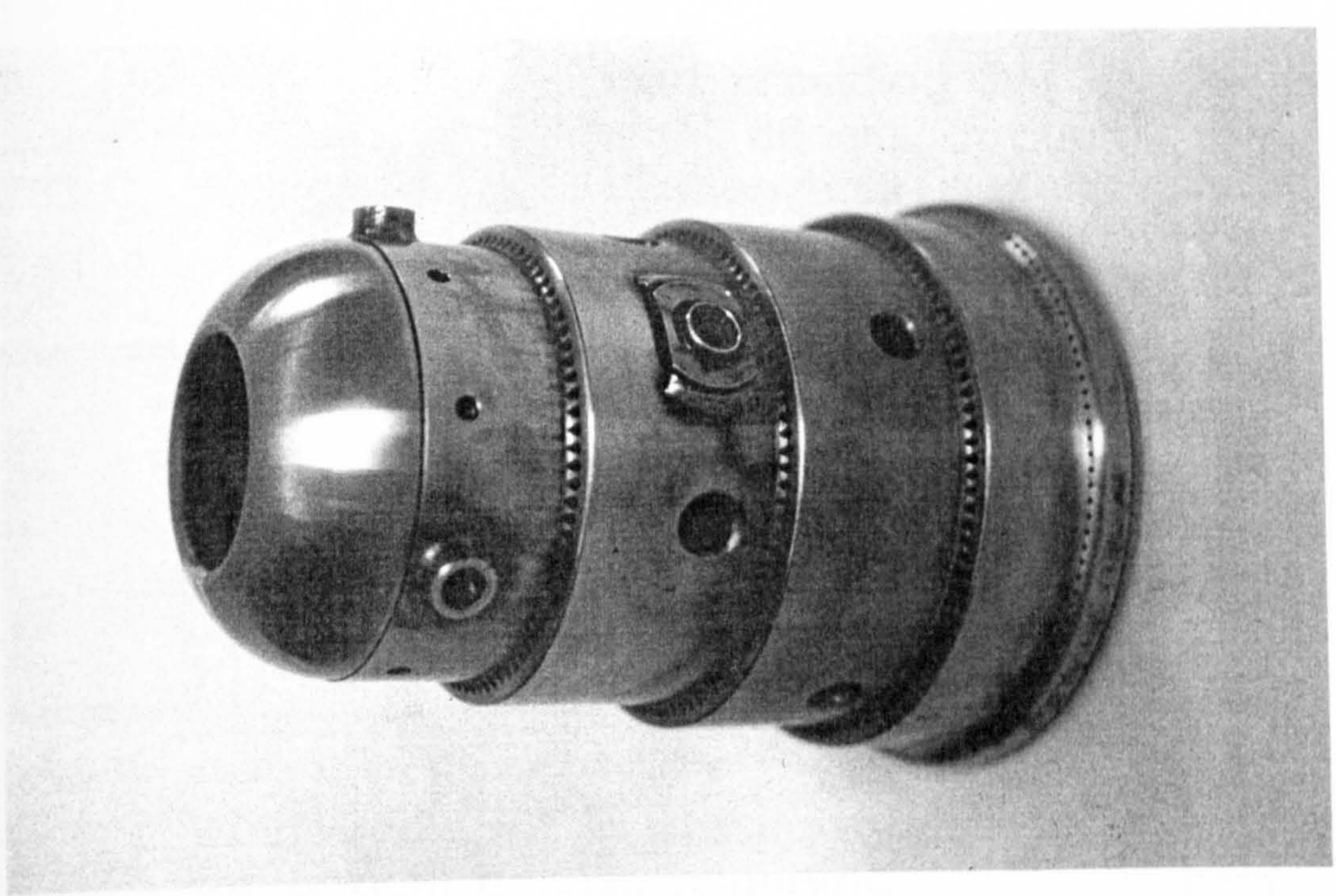

Side view

Figure 3.11 Research gas turbine combustor

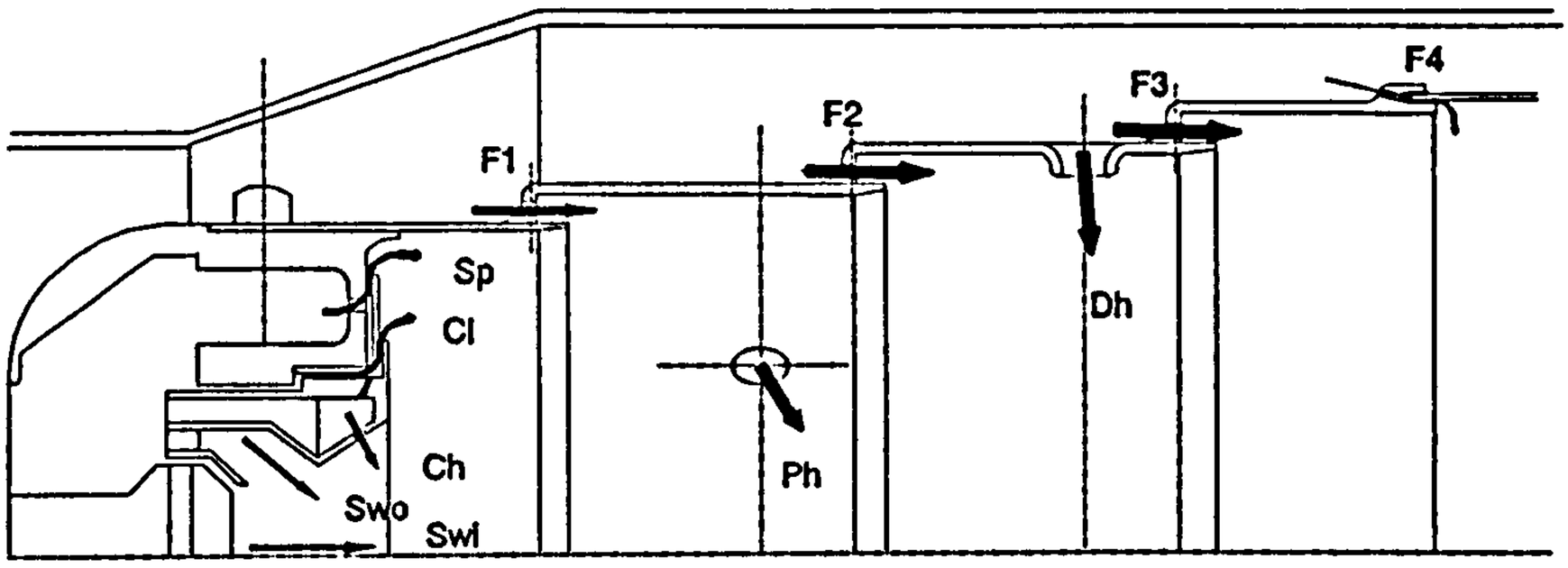

Air flow Distribution (% of total mass flow)

F1 : 1st film cooling : 18%
F2 : 2nd film cooling : 18%
F3 : 3rd film cooling : 20%
F4 : 4th film cooling : 2%
Ph : Primary holes : 14%
Dh : Dilution holes : 12%
Swi : inner swirler : 1%
Sw0 : outer swirler : 5%
Ch : cup holes : 6%
Cl : cup lip : 1%
Sp : splash plate : 3%

Figure 3.12 Air flow distributions in the combustor (after Join-Lambert (1992))

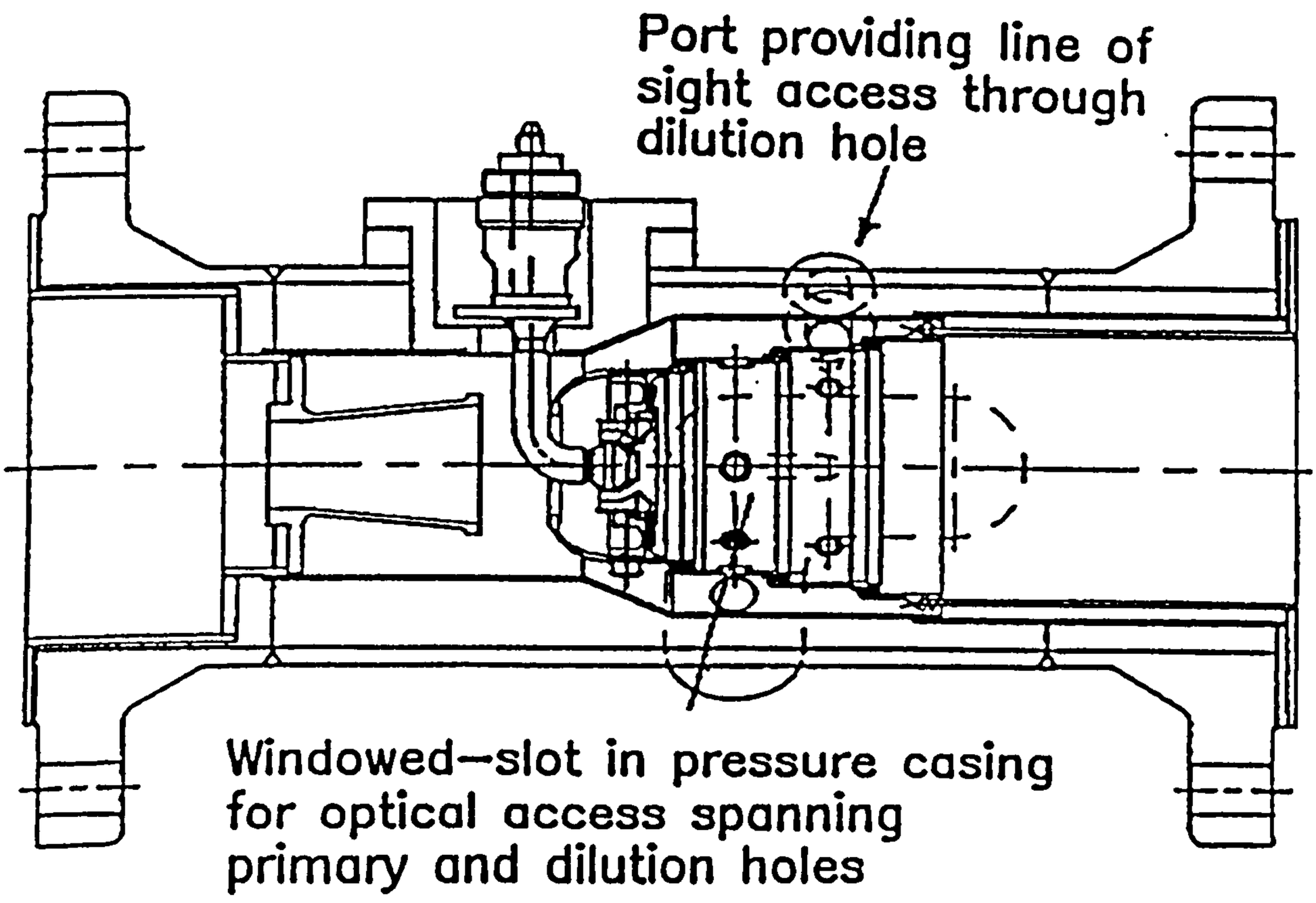

Figure 3.13 Combustor assembled inside the pressure casing

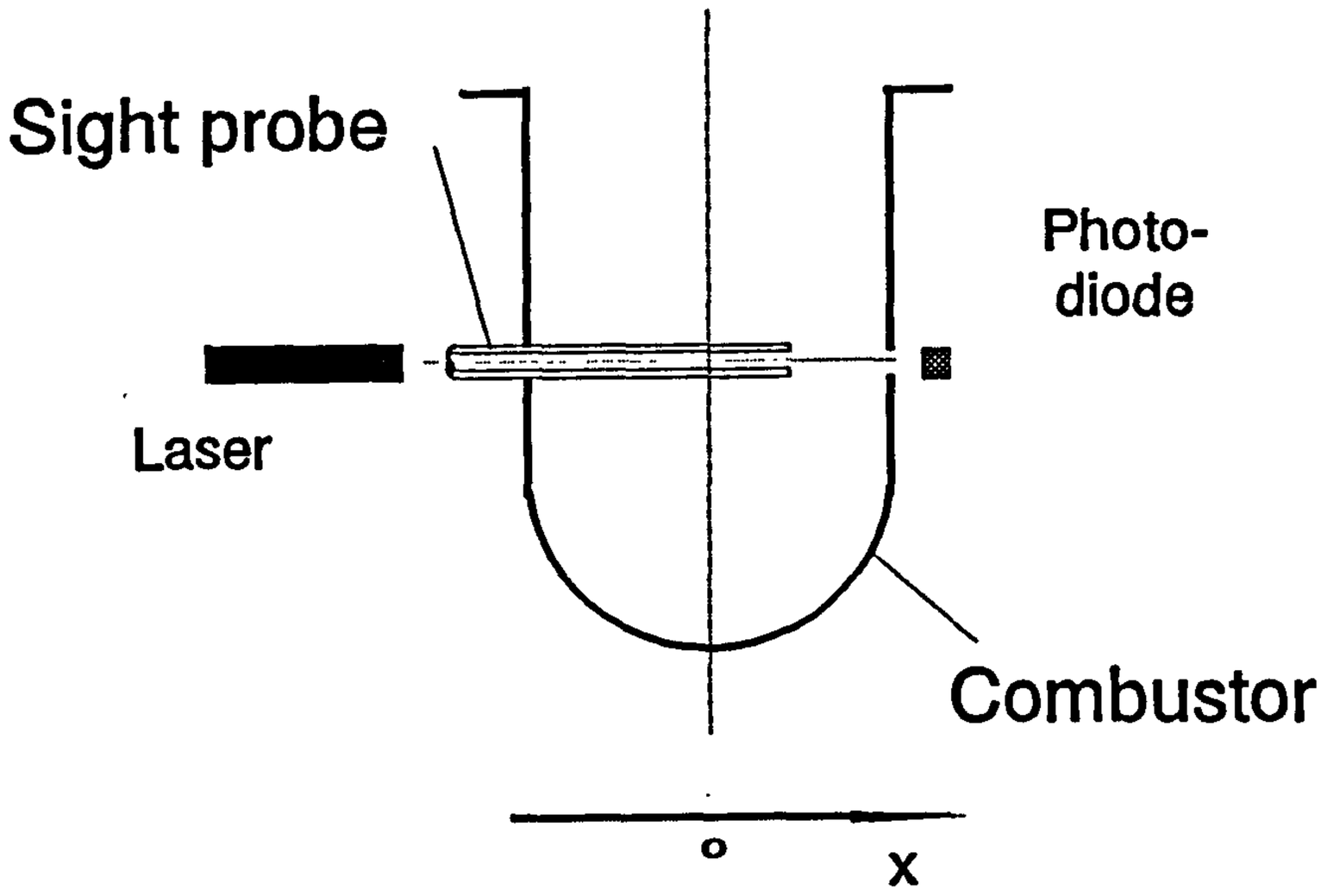

(a) Sight probe

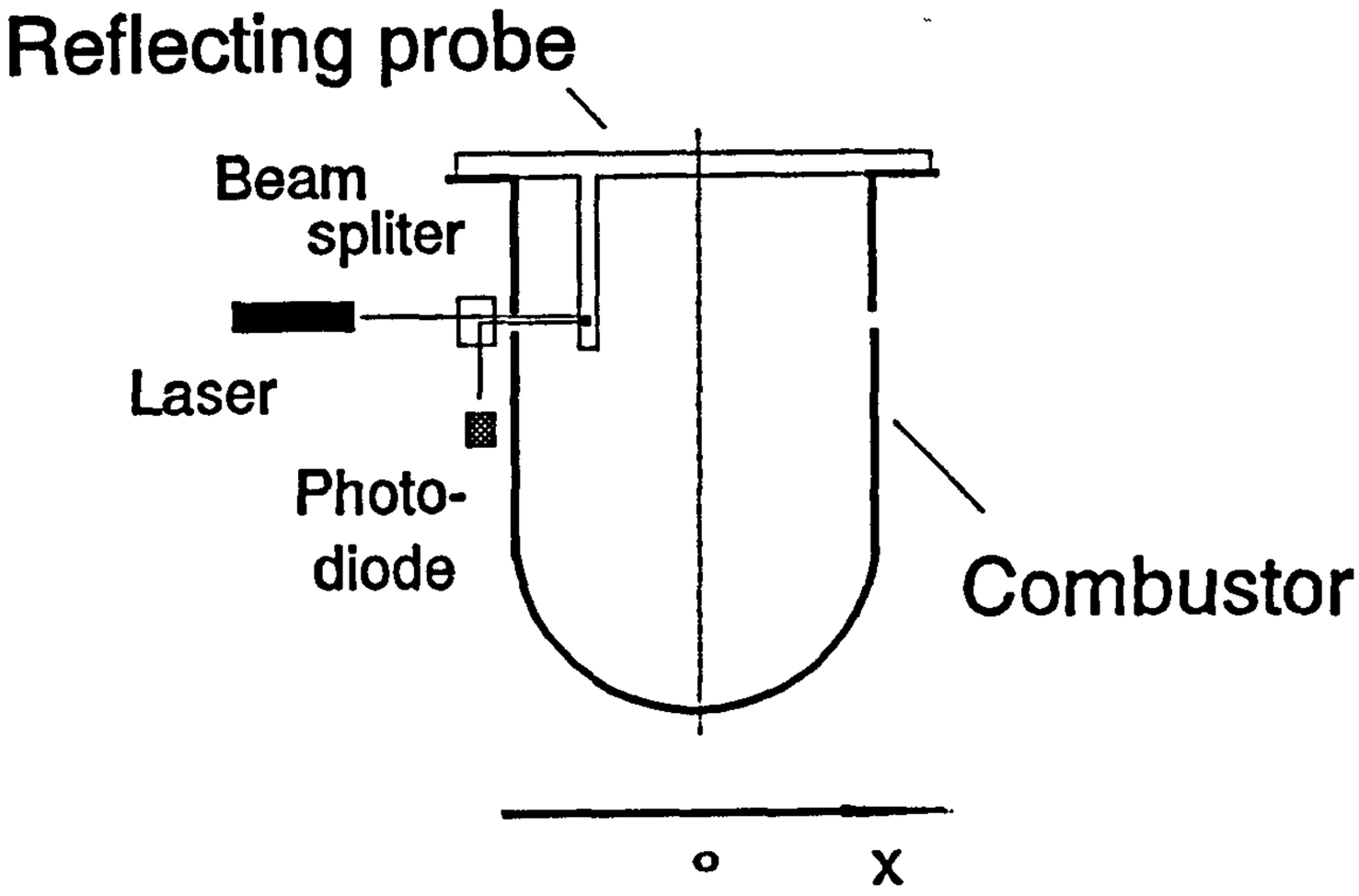

(b) Reflecting probe

Figure 3.14 Alternative configurations in the combustor for (a) Sight probe (b) Reflecting probe

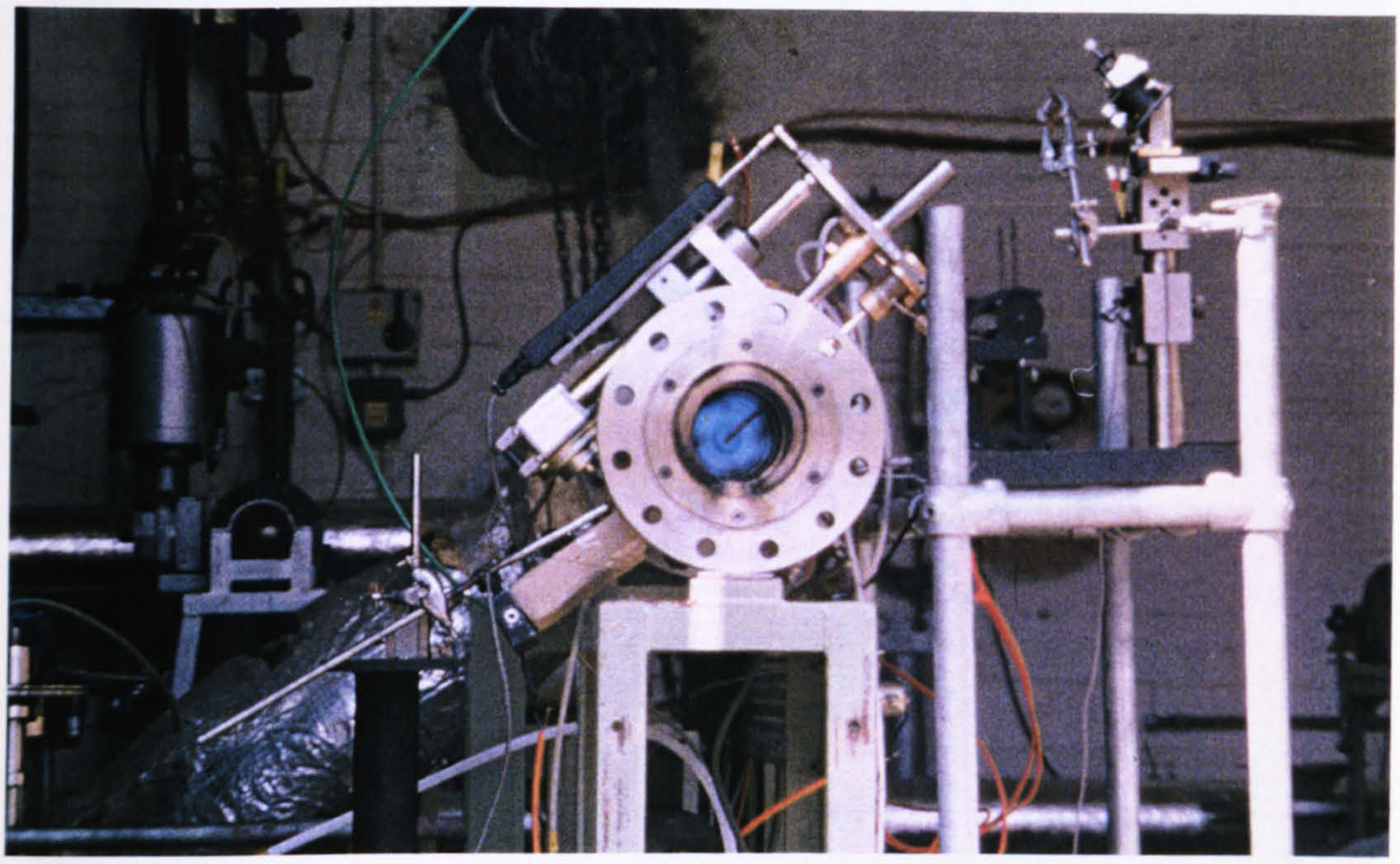

Figure 3.15 Atmospheric pressure combustion: Sight probe experiment at dilution hole station, probe tip on centre-line (AFR-45)

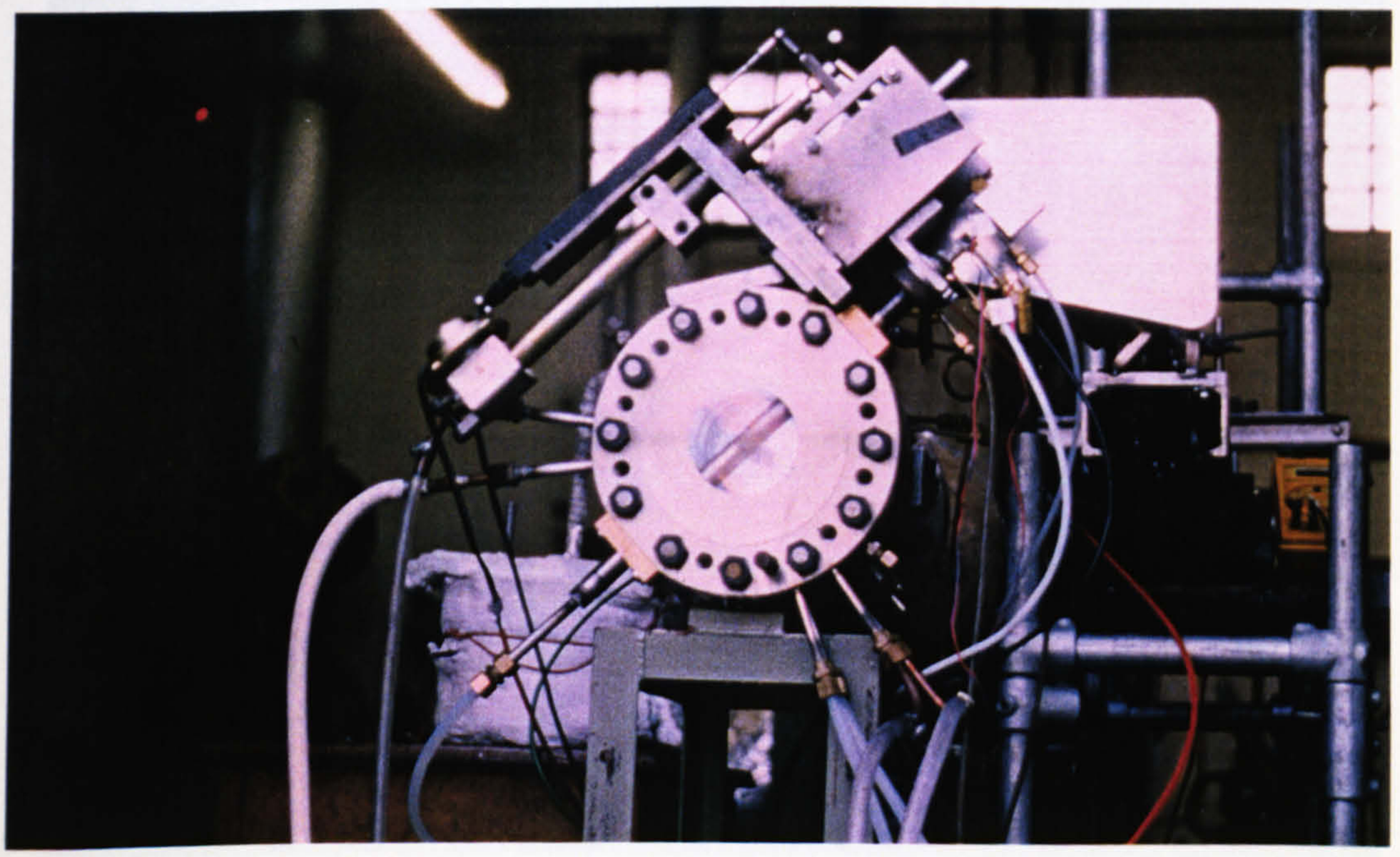

Figure 3.16 Atmospheric pressure combustion: reflector probe experiment at dilution hole station (AFR-16)

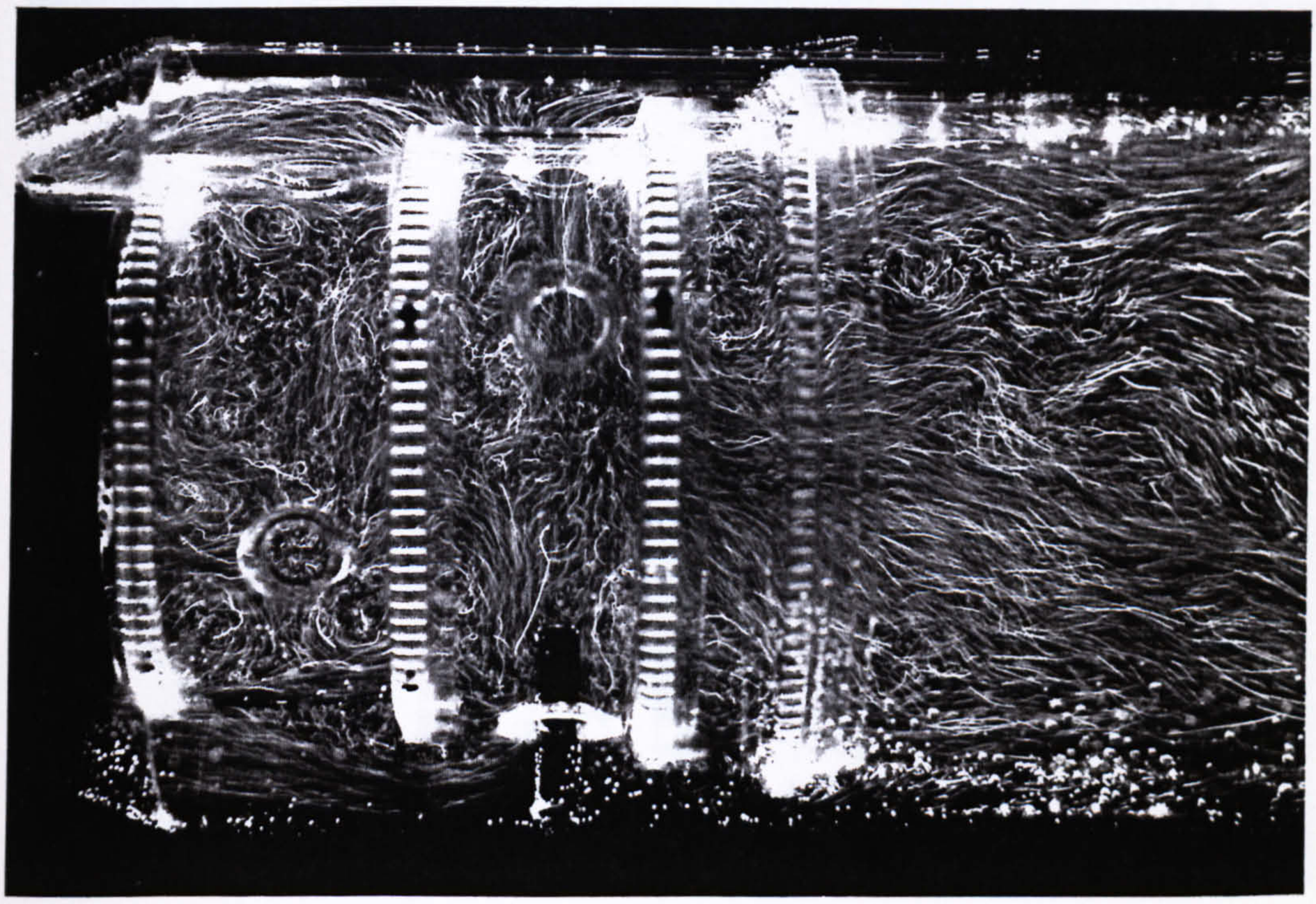

(a) Dilution zone with the presence of sight probe

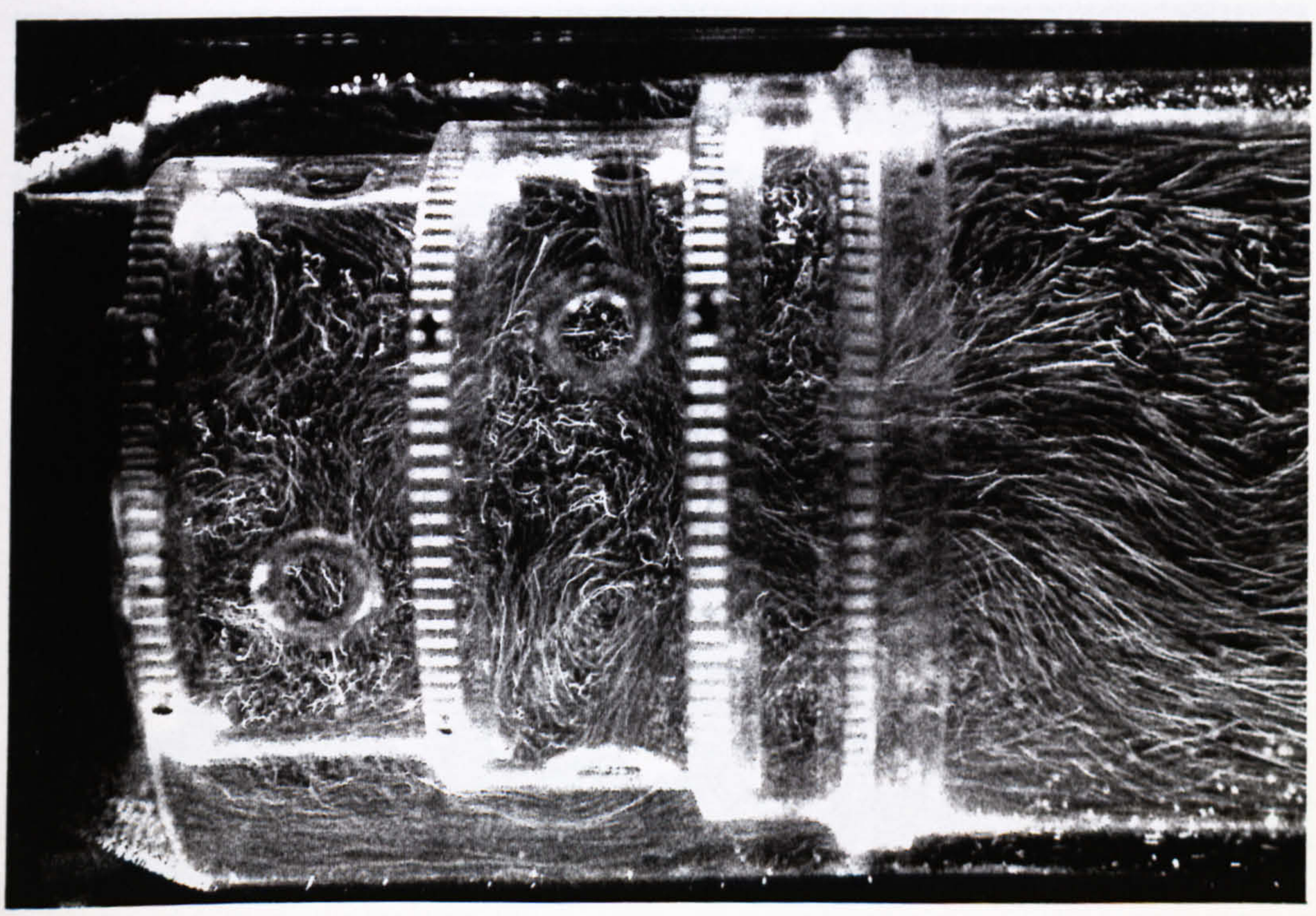

(b) Dilution zone without the presence of sight probe

Figure 3.17 Comparison of the combustor flowfield with and without probe perturbation

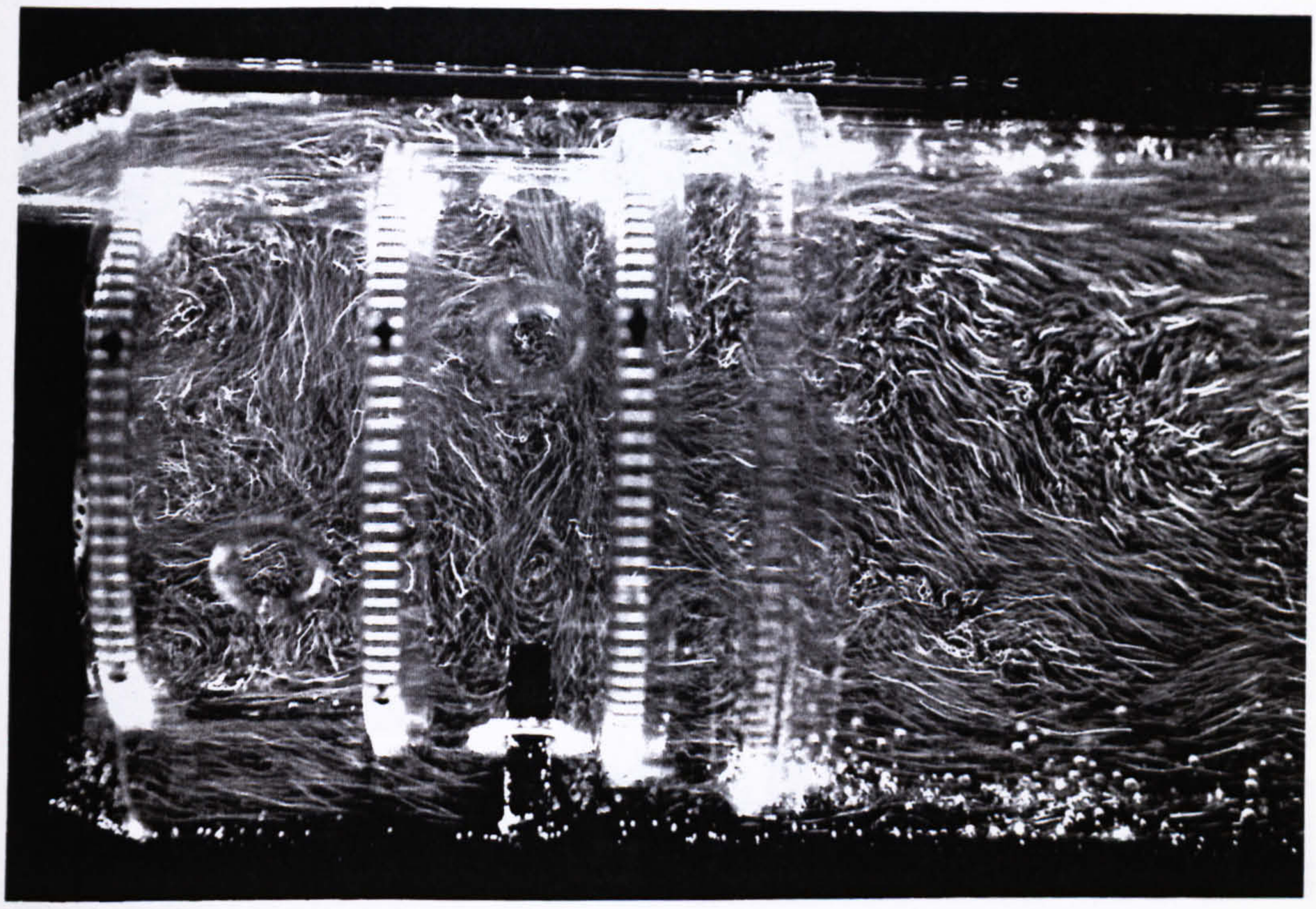

(a) Flowfield image of time t1

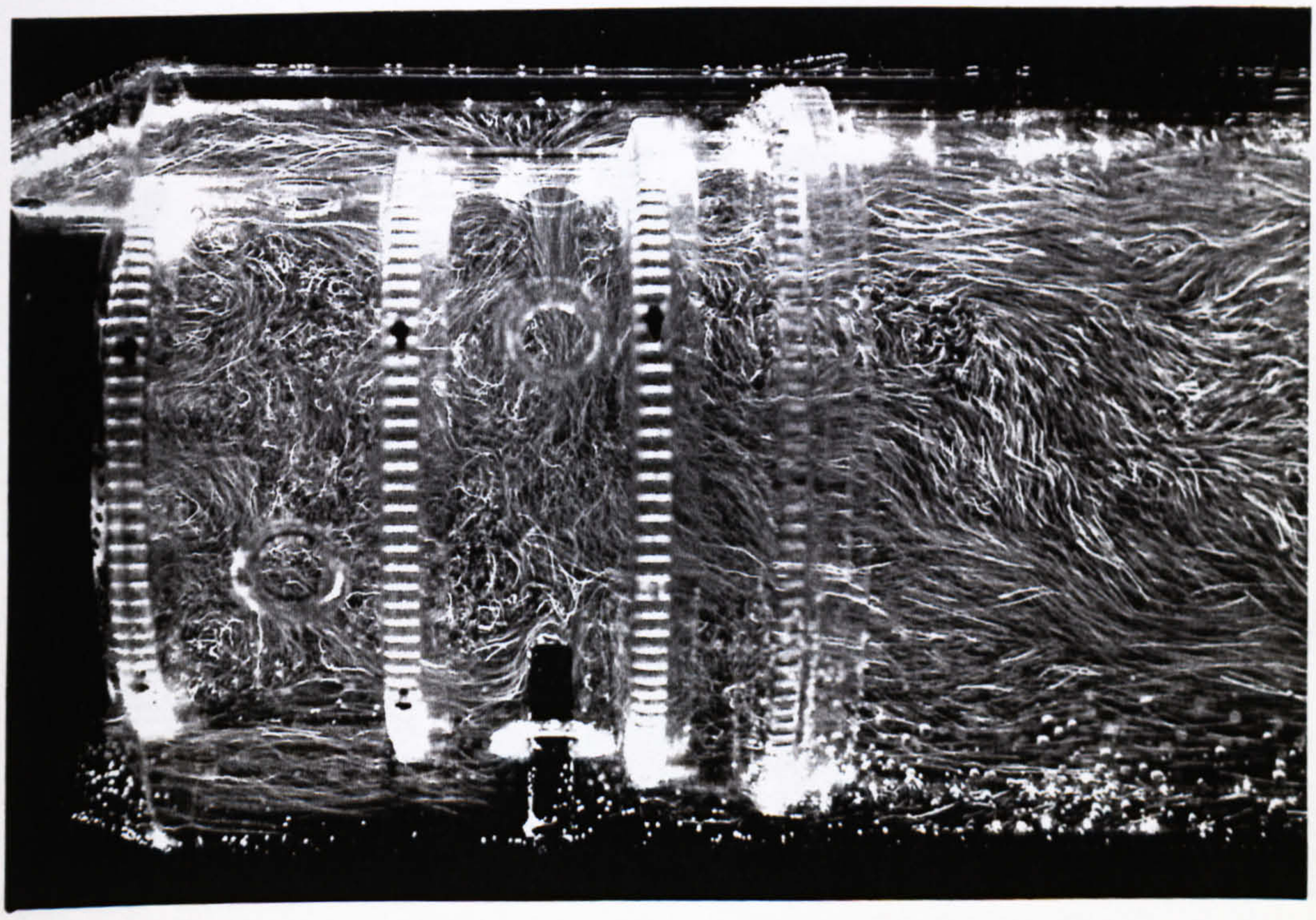

(b) Flowfield image of time t2

Figure 3.18 Combustor flowfield with probe perturbation at different time series

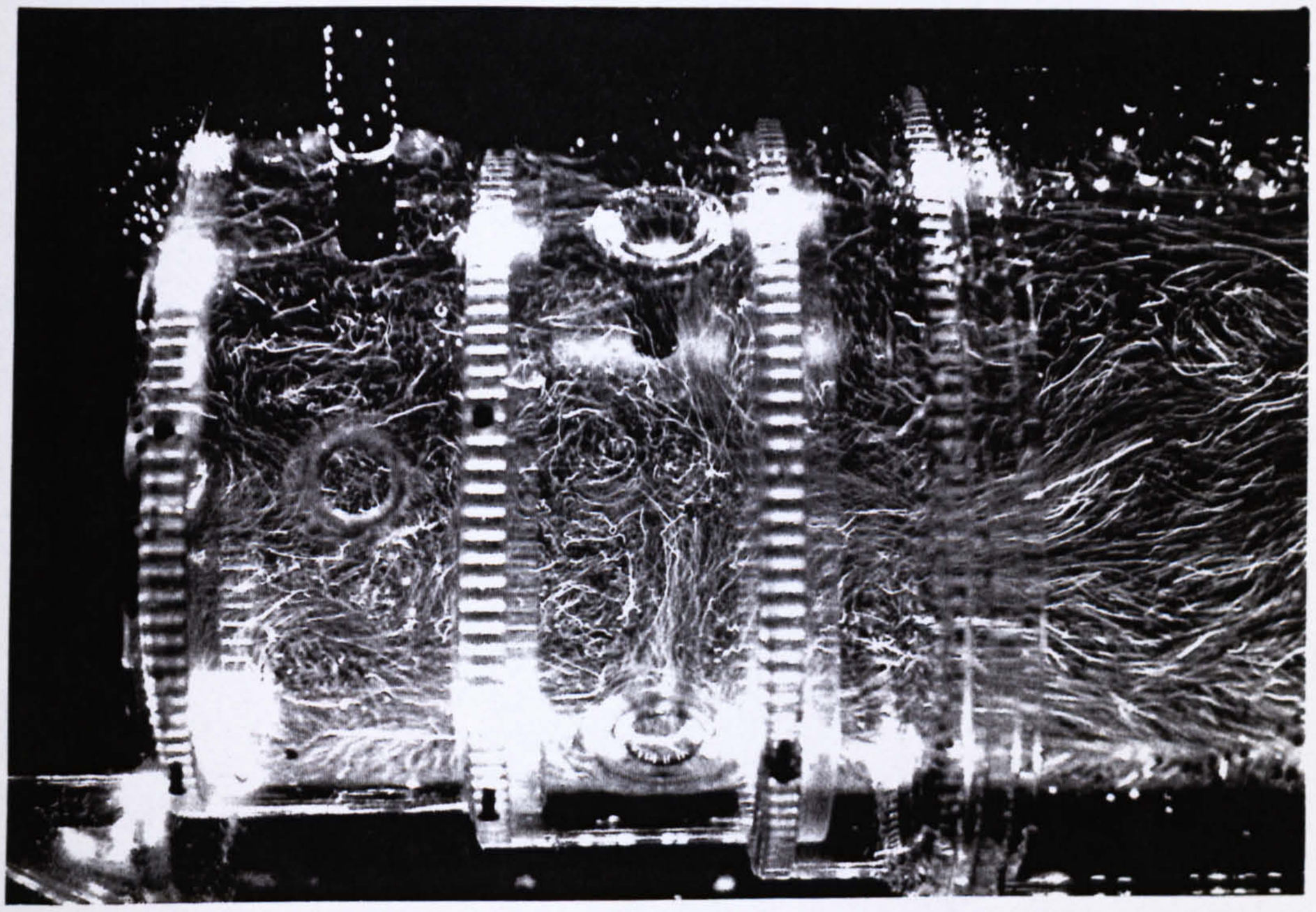

(a) Dilution zone flowfield with probe blockage; the probe is positioned at the neighbouring dilution hole (orthogonal to the paper)

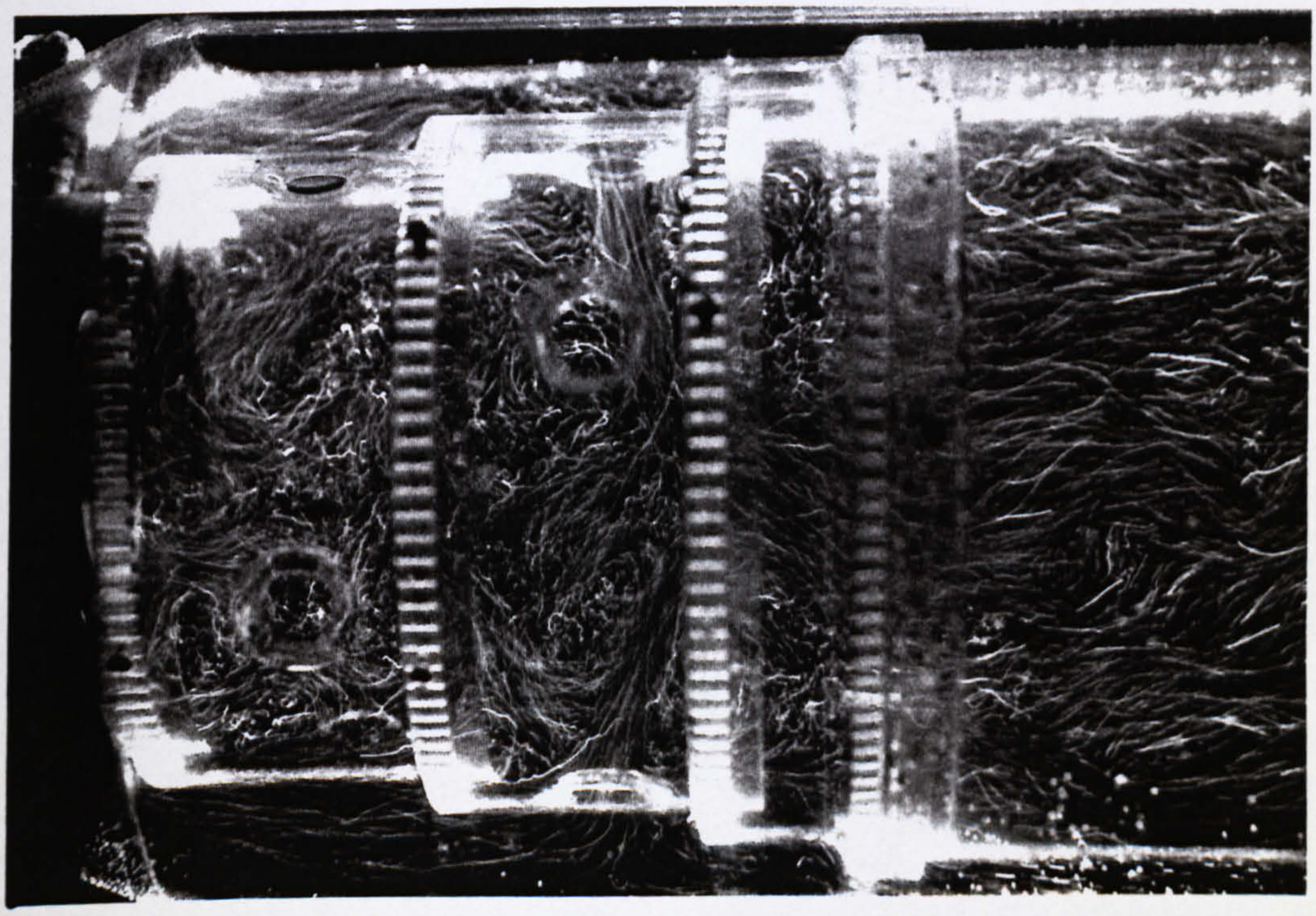

(b) Flowfield without probe (same hole position as (a))

Figure 3.19 Comparison of combustor flowfield with and without probe perturbation (neighbouring holes to that blocked by the probe, 4 holes in the dilution zone)

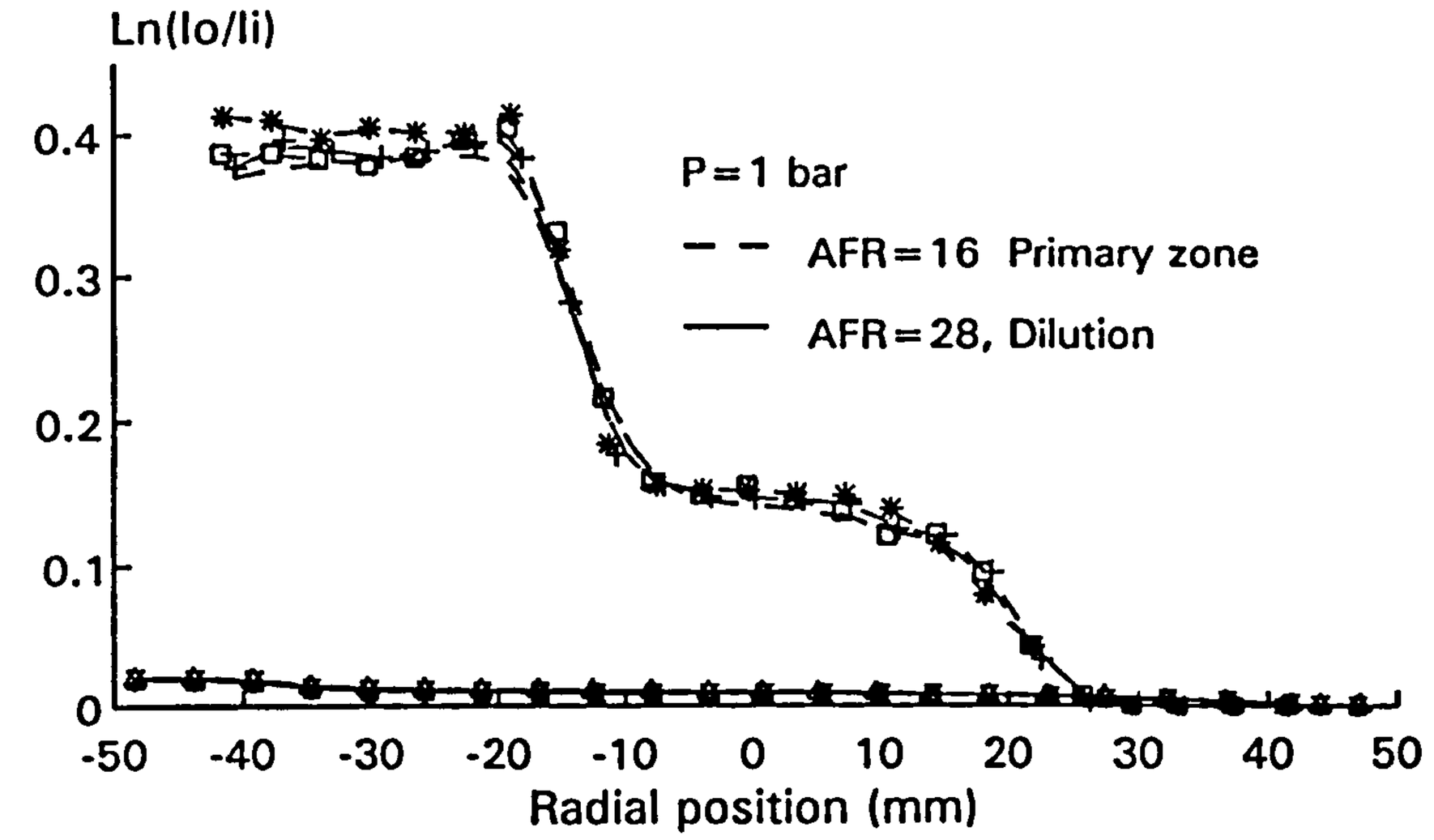

Figure 3.20 Illustrative extinction data from sight probe traversing between primary and dilution holes (four set of data for each condition)

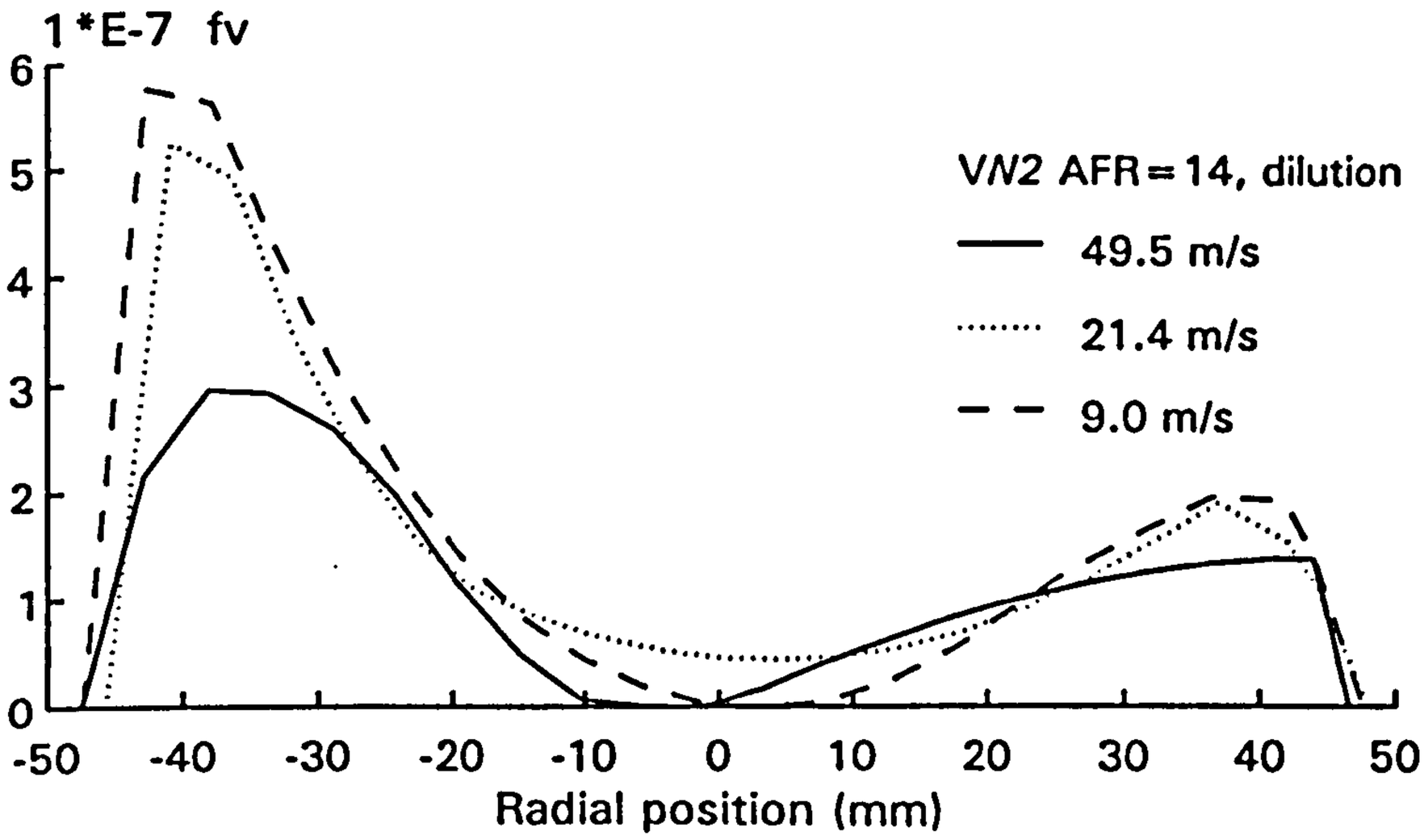

Figure 3.21 Influence of N_2 purge flow rate (velocity) on the measured radial profile of soot volume fraction

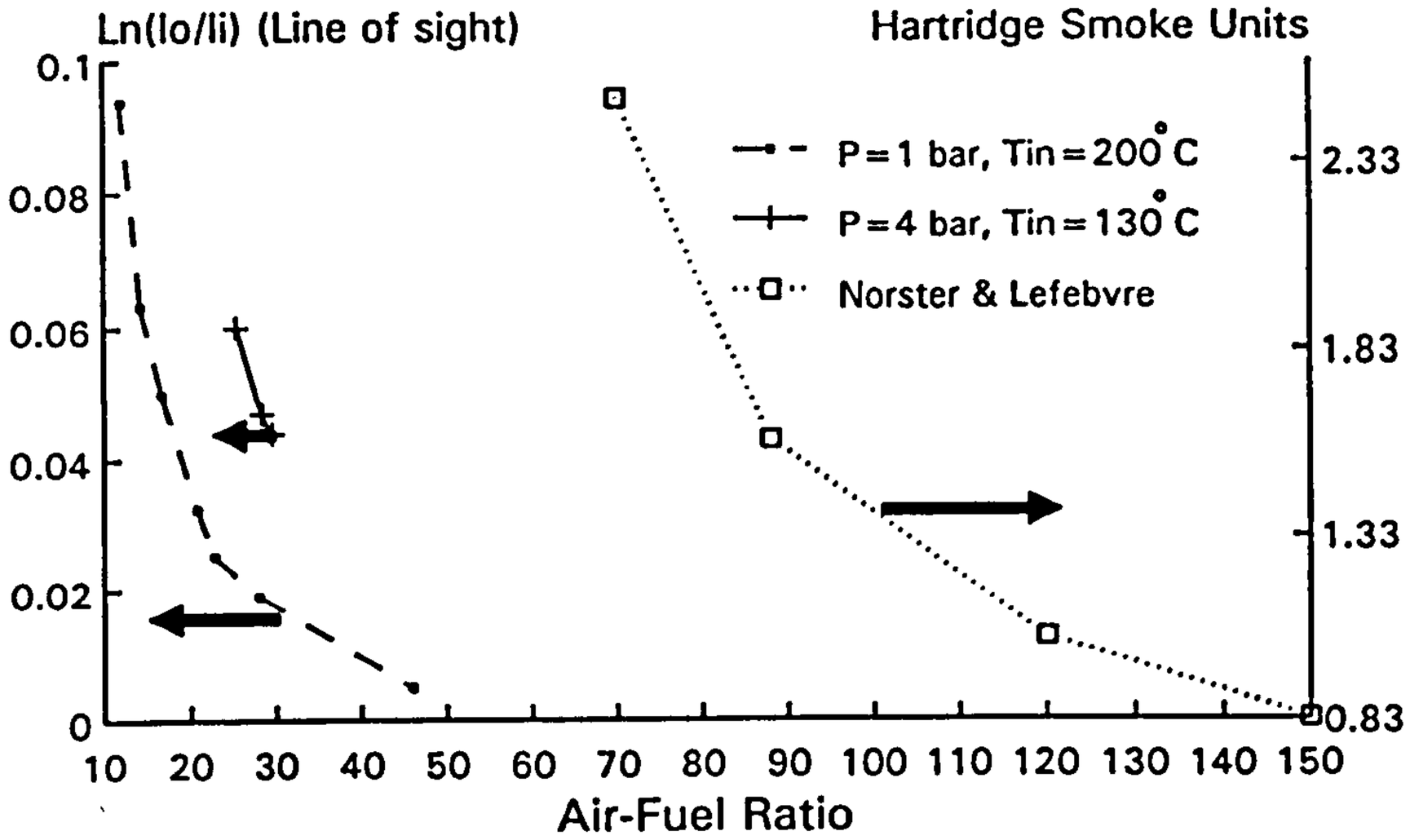

Figure 3.22 Path-integrated absorption measurements at the dilution zone station over a range of AFRs; 1 bar and 4 bar pressure. Also shown is the combustor exhaust smoke number from Norster & Lefebvre (1972)

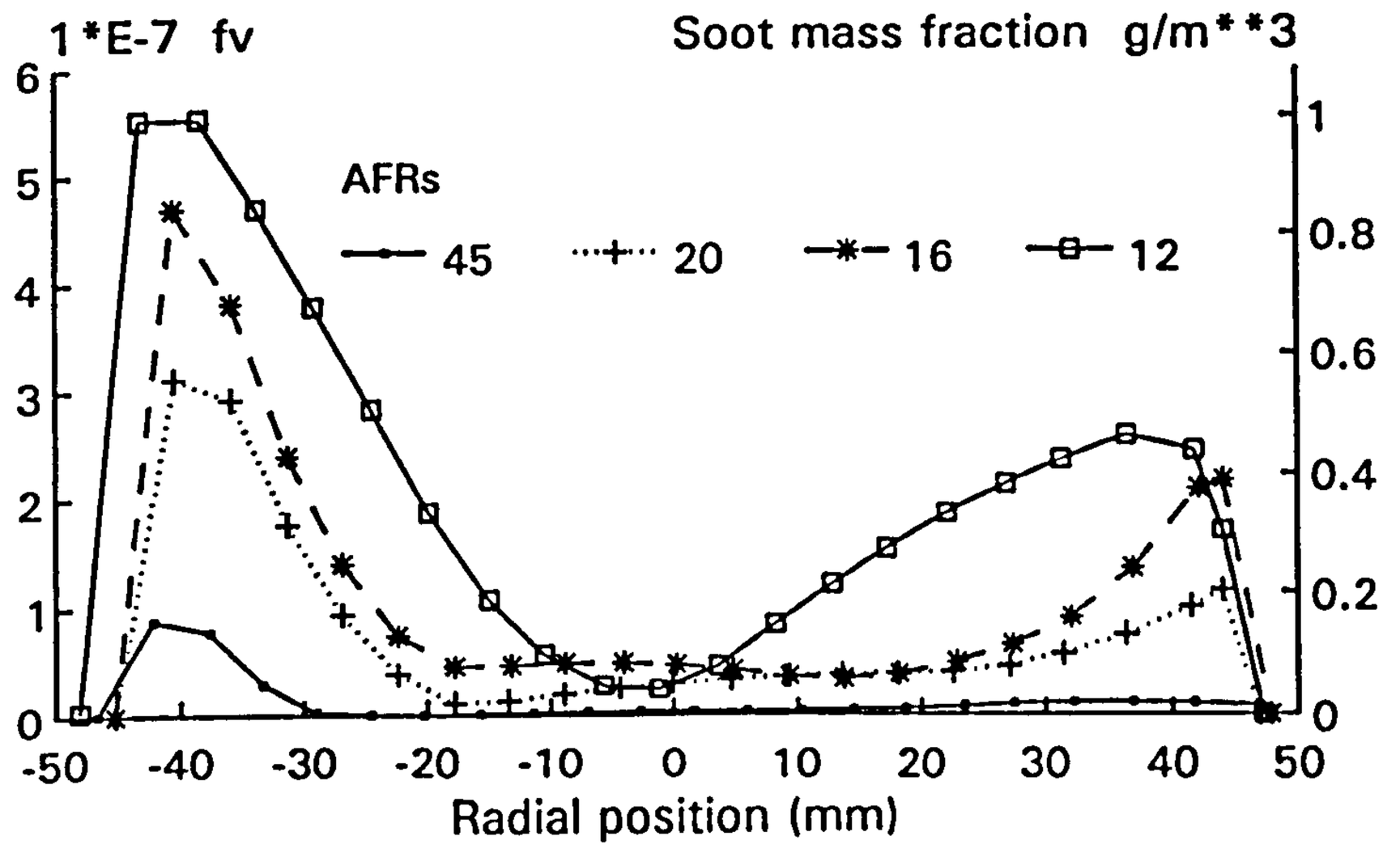

Figure 3.23 Radial profiles of soot volume fraction for varying AFRs; dilution zone location, atmospheric pressure operation

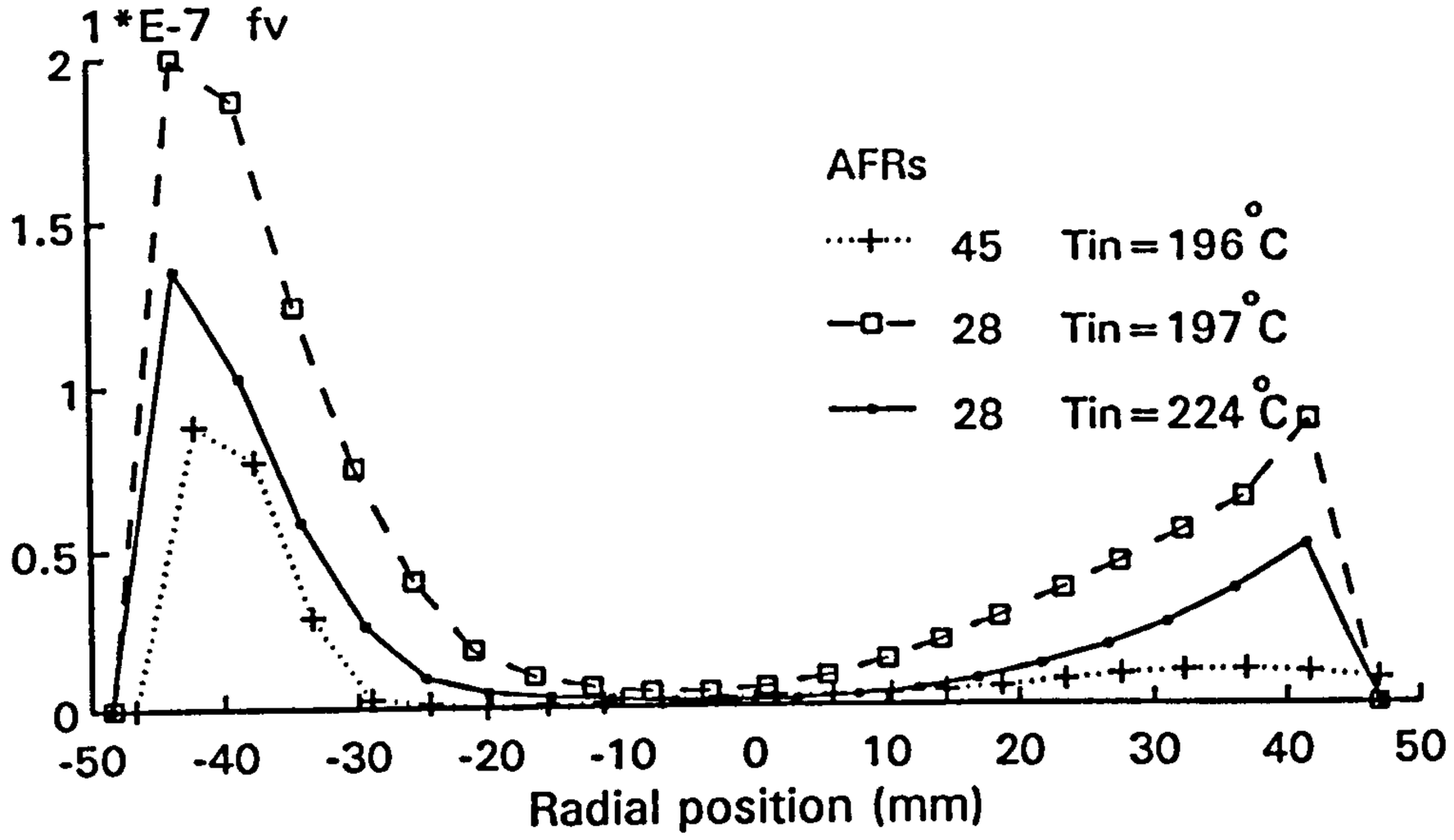

Figure 3.24 Effect of air inlet temperature on soot concentration level; dilution station, P=1 bar

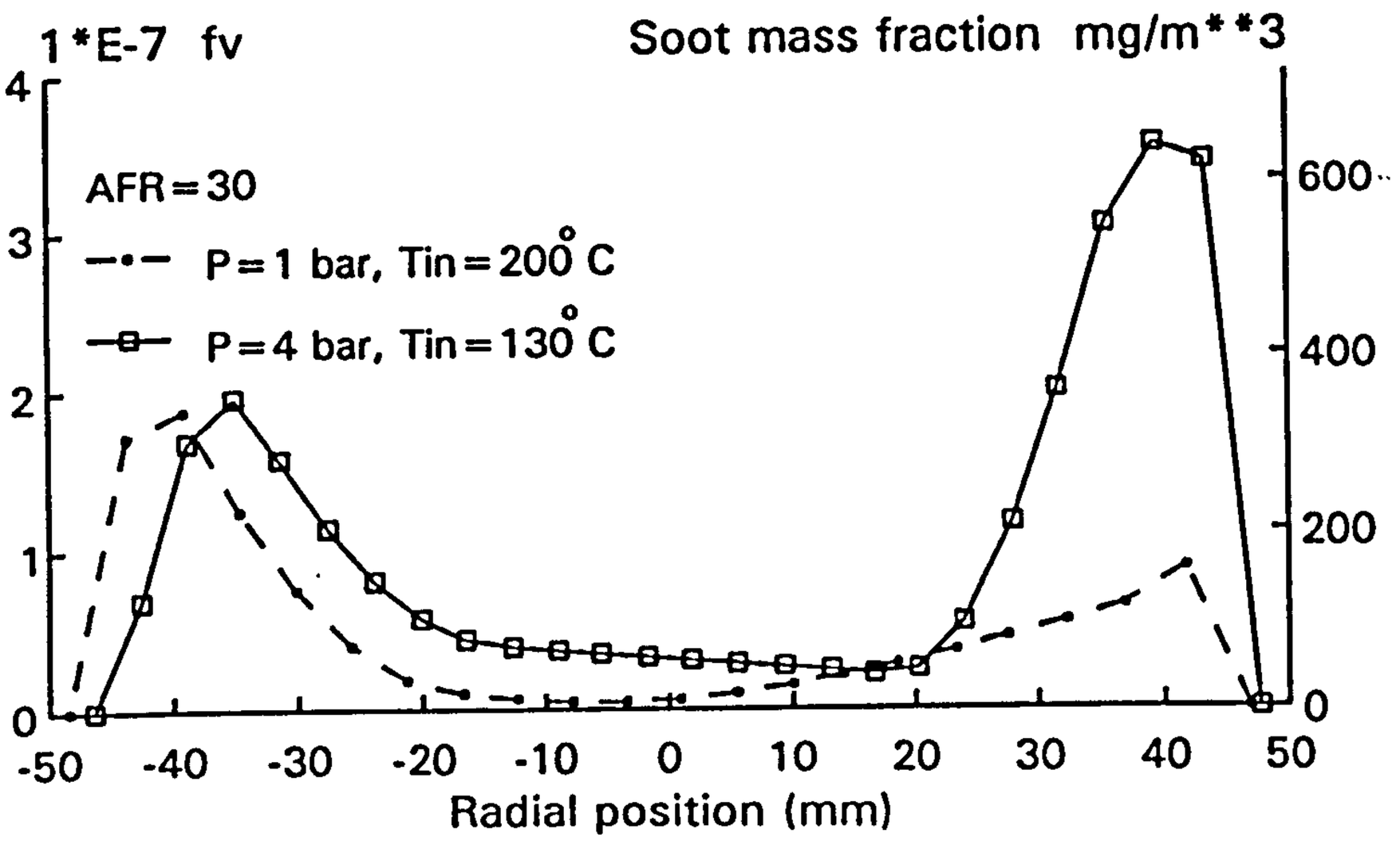

Figure 3.25 Soot volume fraction profiles at pressures 1 and 4 bar; dilution zone

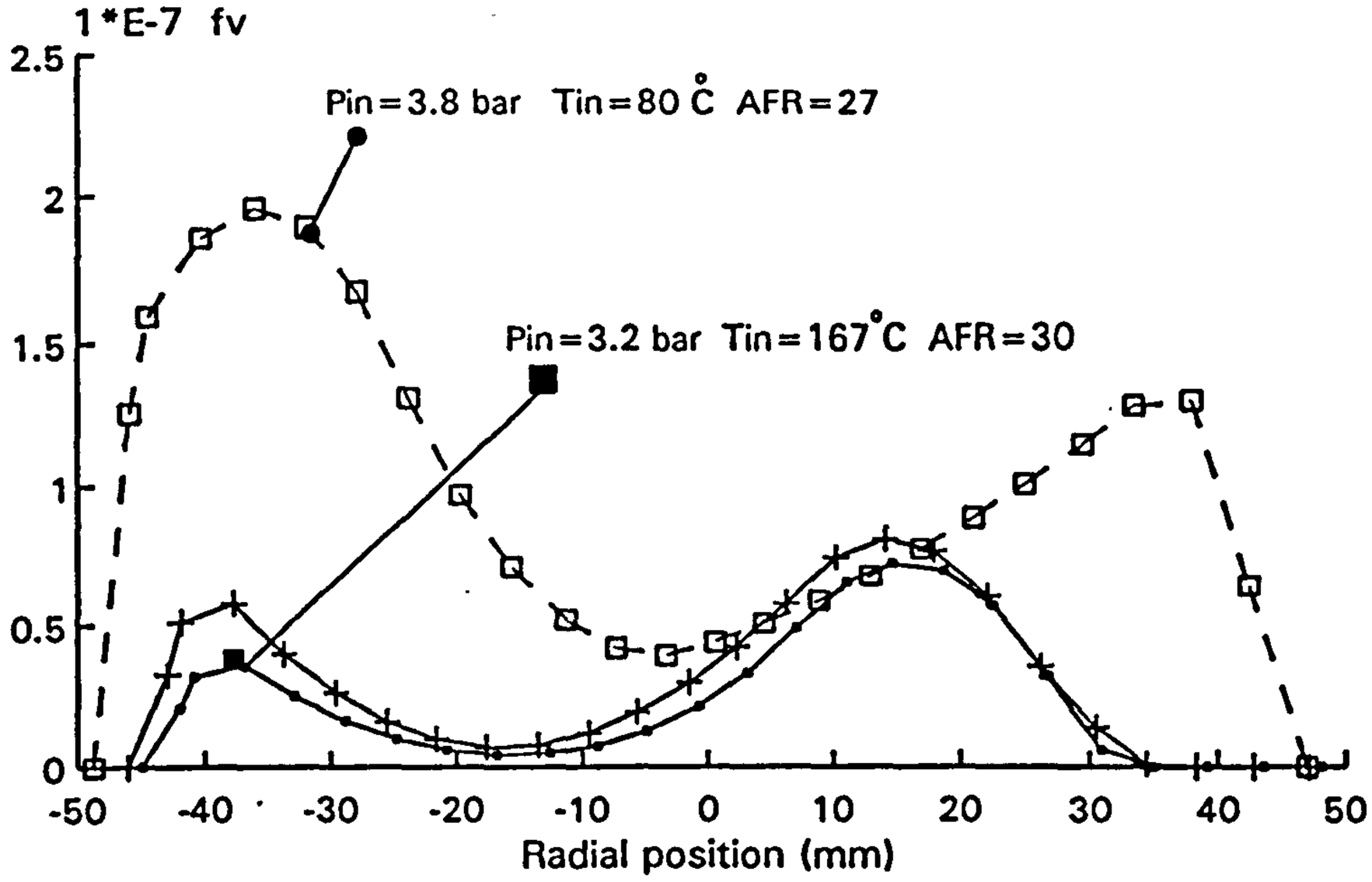

(a)

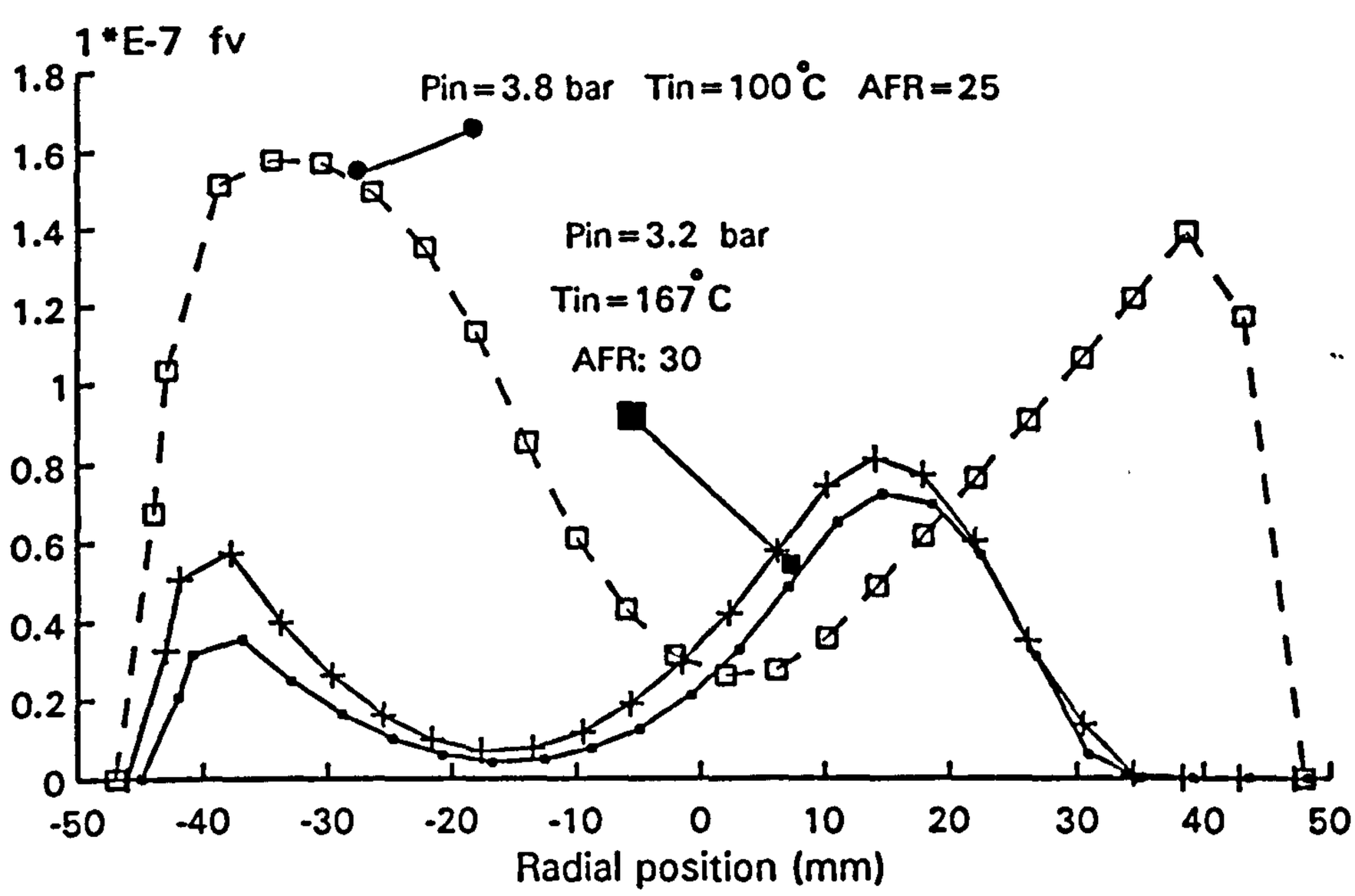

(b)

Figure 3.26 Radial profiles of soot volume fraction at pressures up to 4 bar; dilution zone location

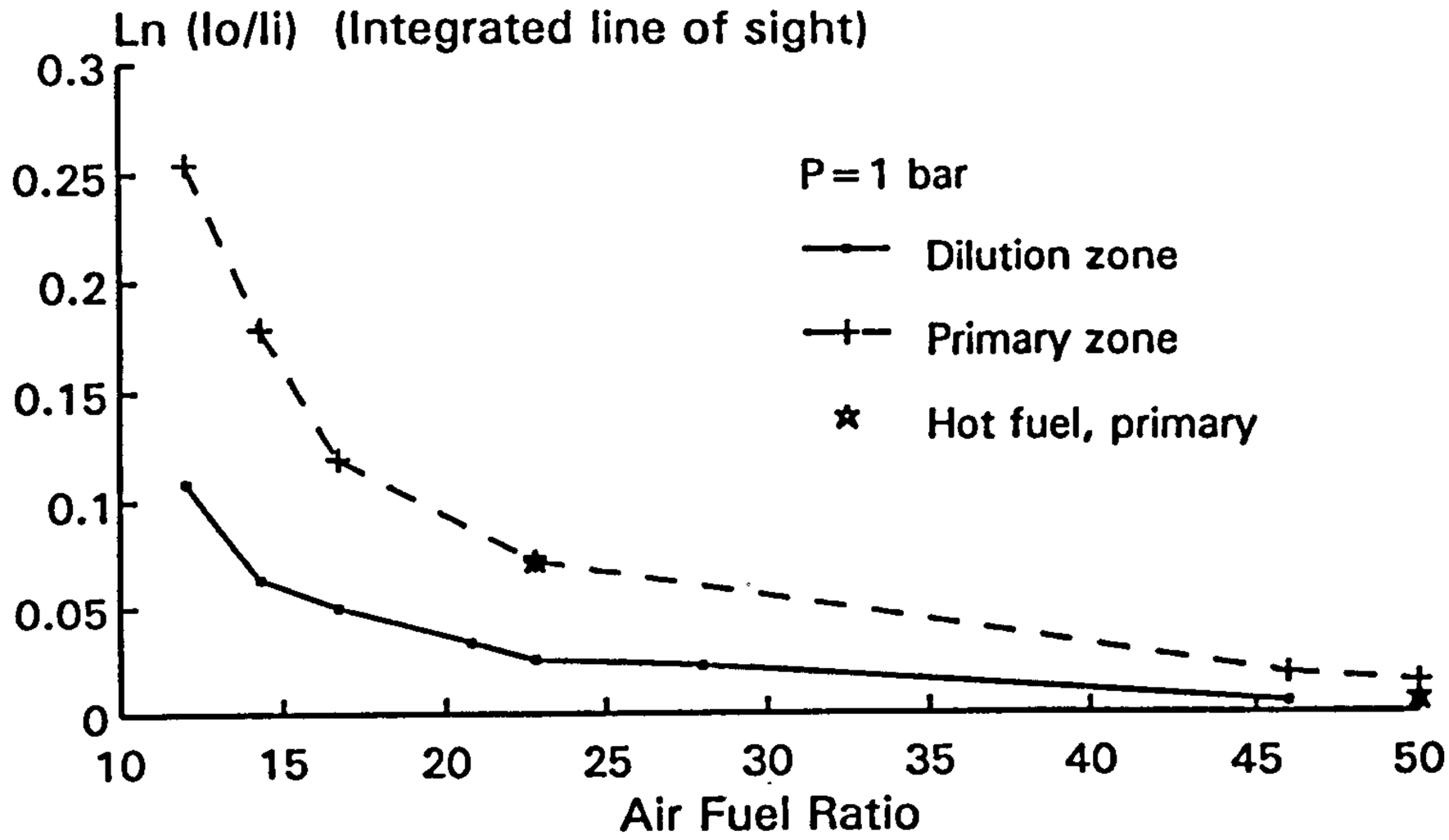

Figure 3.27 Primary and dilution zone station comparisons of path-integrated extinction with varying AFR

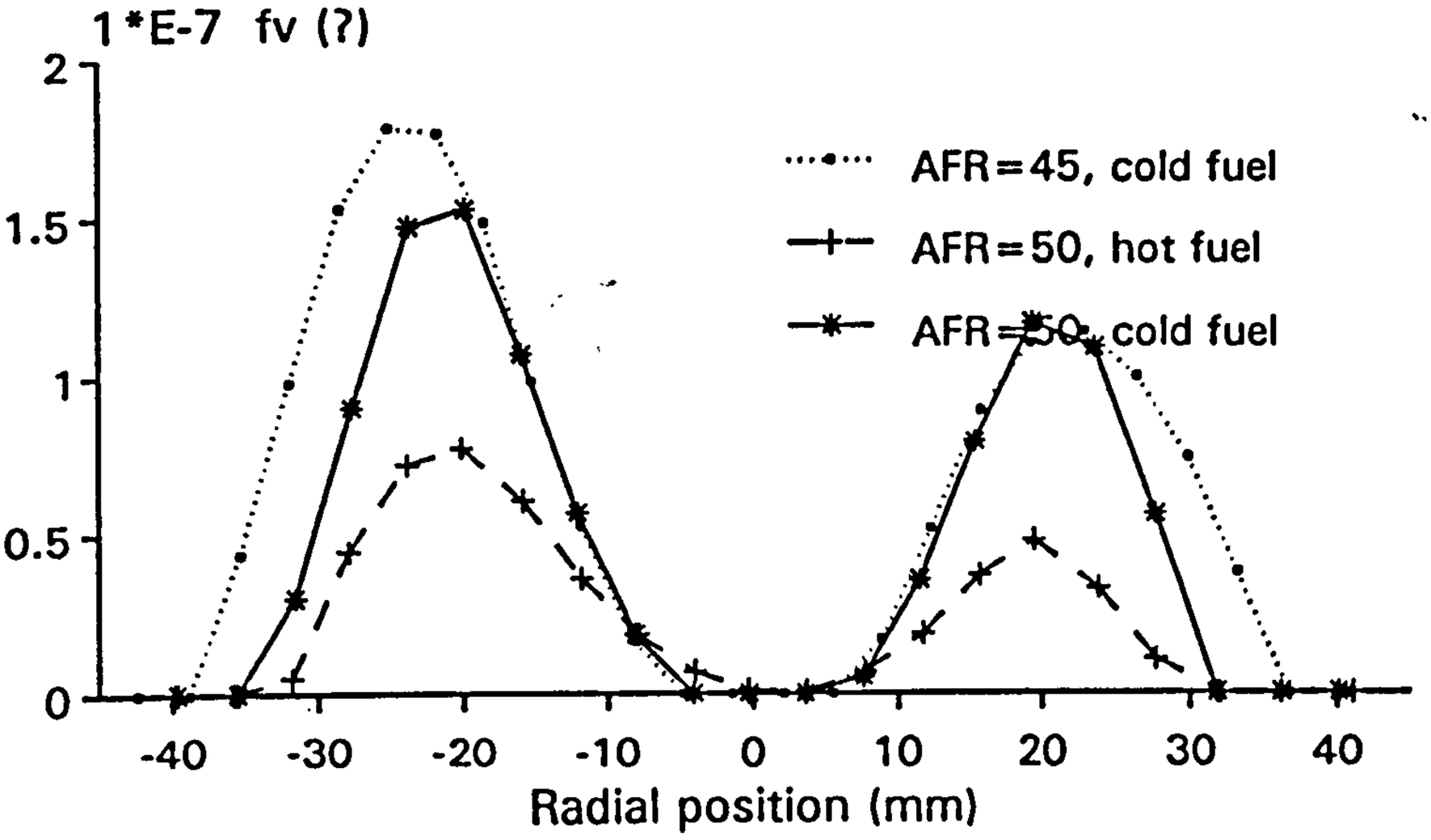

Figure 3.28 Influence of fuel pre-heating up to 115 °C on 'apparent' primary zone soot volume fraction profiles; atmospheric pressure operation

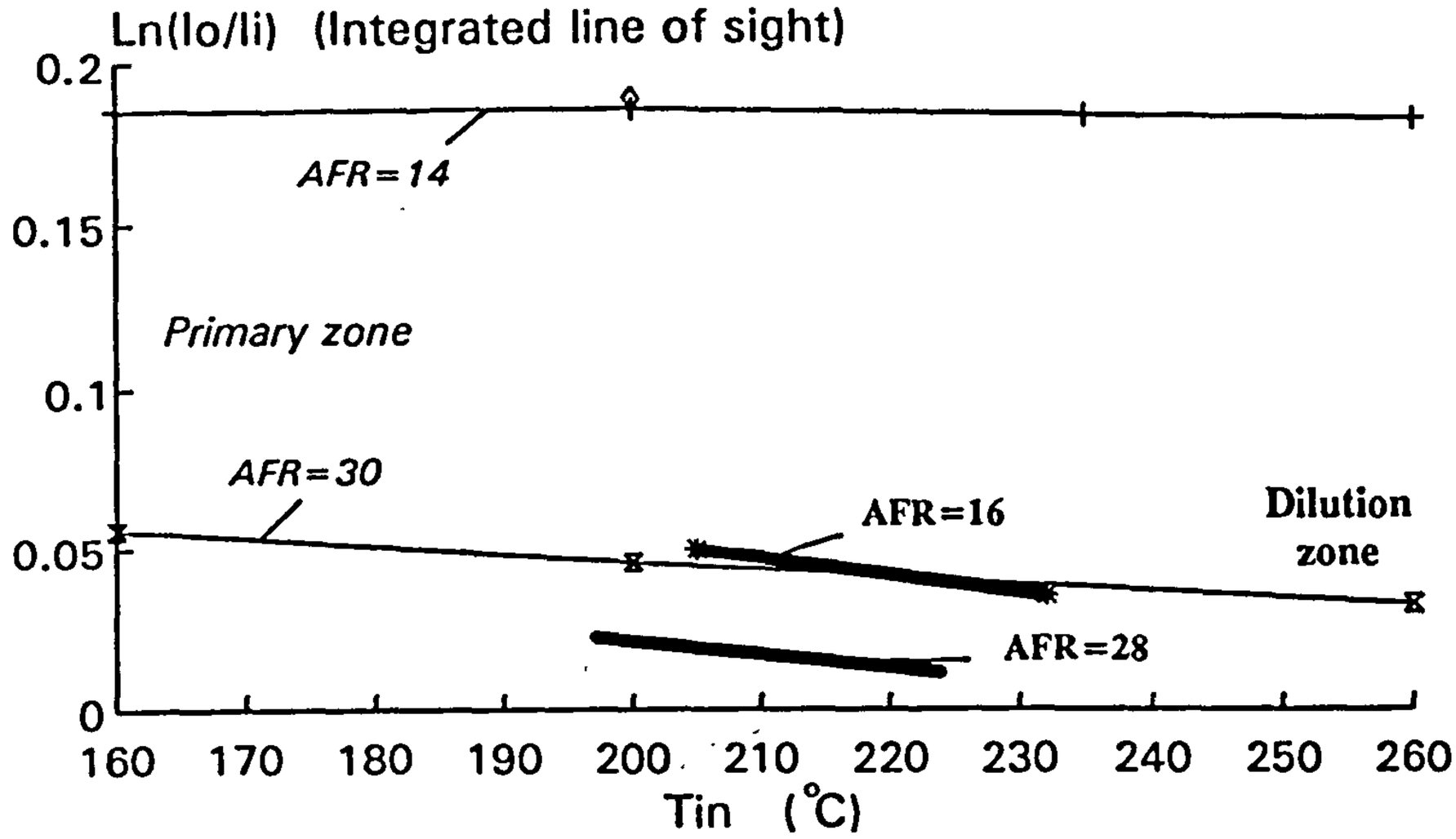

Figure 3.29 Effect of inlet air temperature on path-integrated extinction measurements in the primary and dilution zones; atmospheric pressure operation

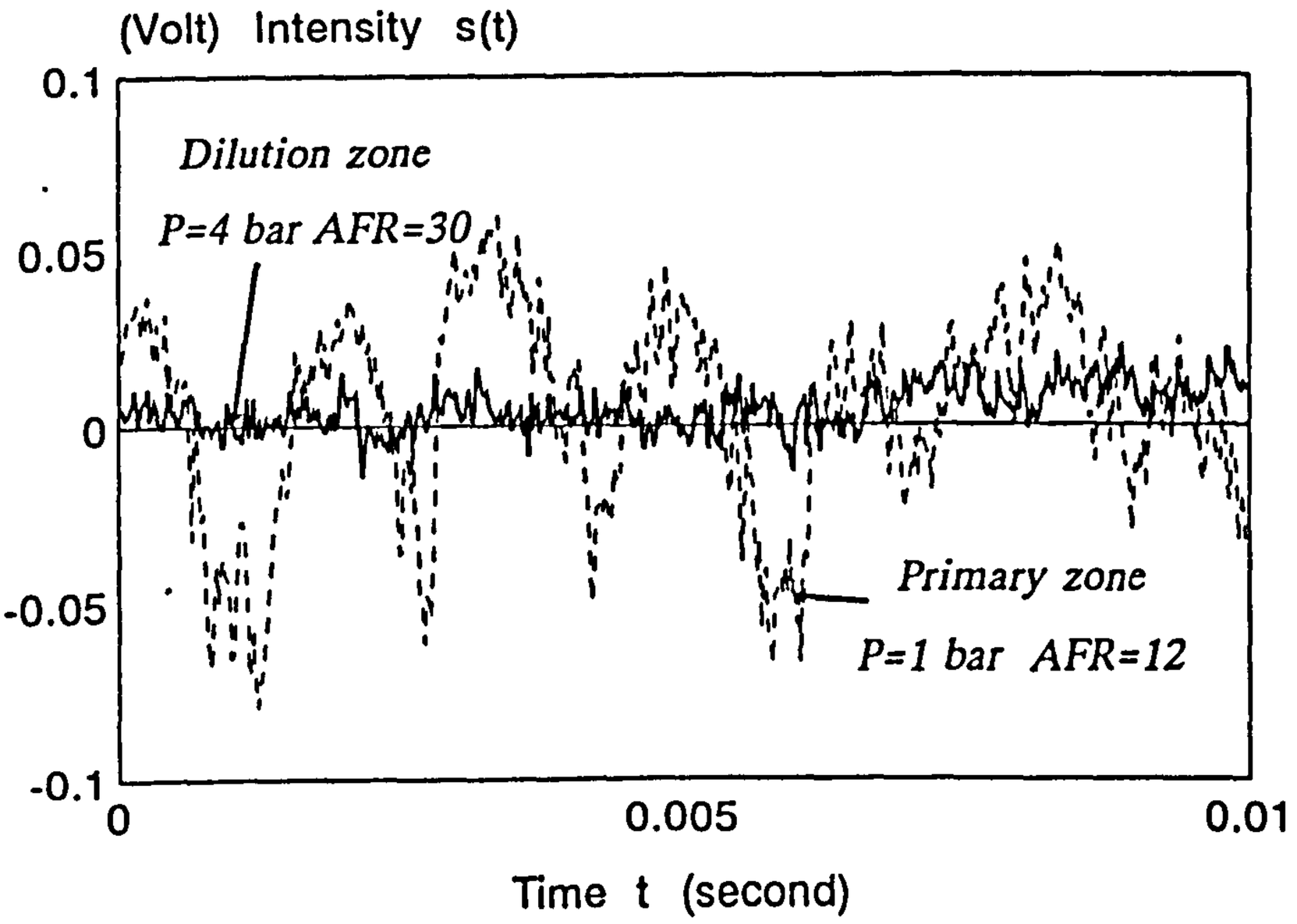

Figure 3.30 Real time data of line-of-sight integrated absorption intensities (transmitted signal) from primary zone droplet dominant (dotted line) and dilution zone soot dominant (solid line) flows

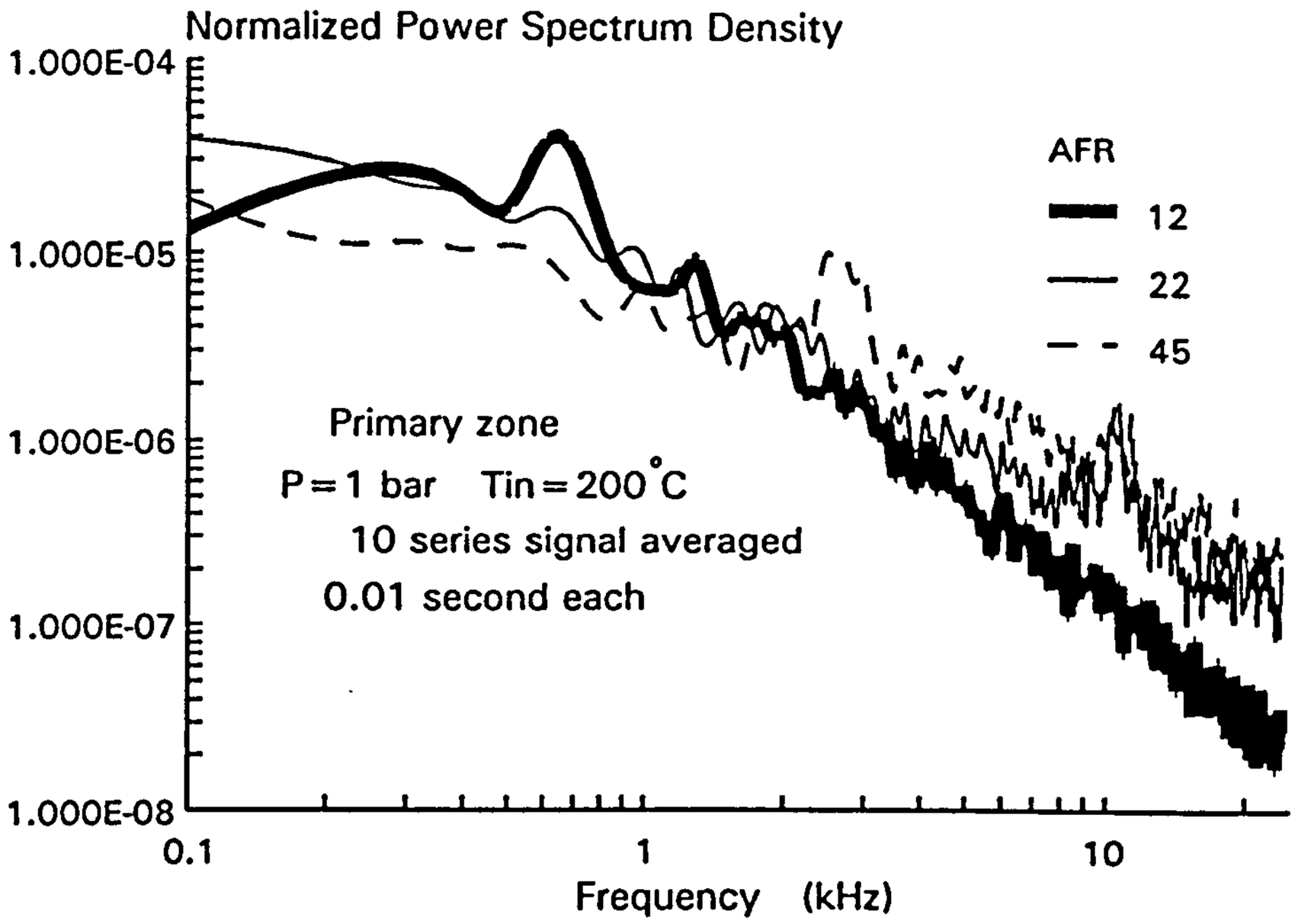

(a)

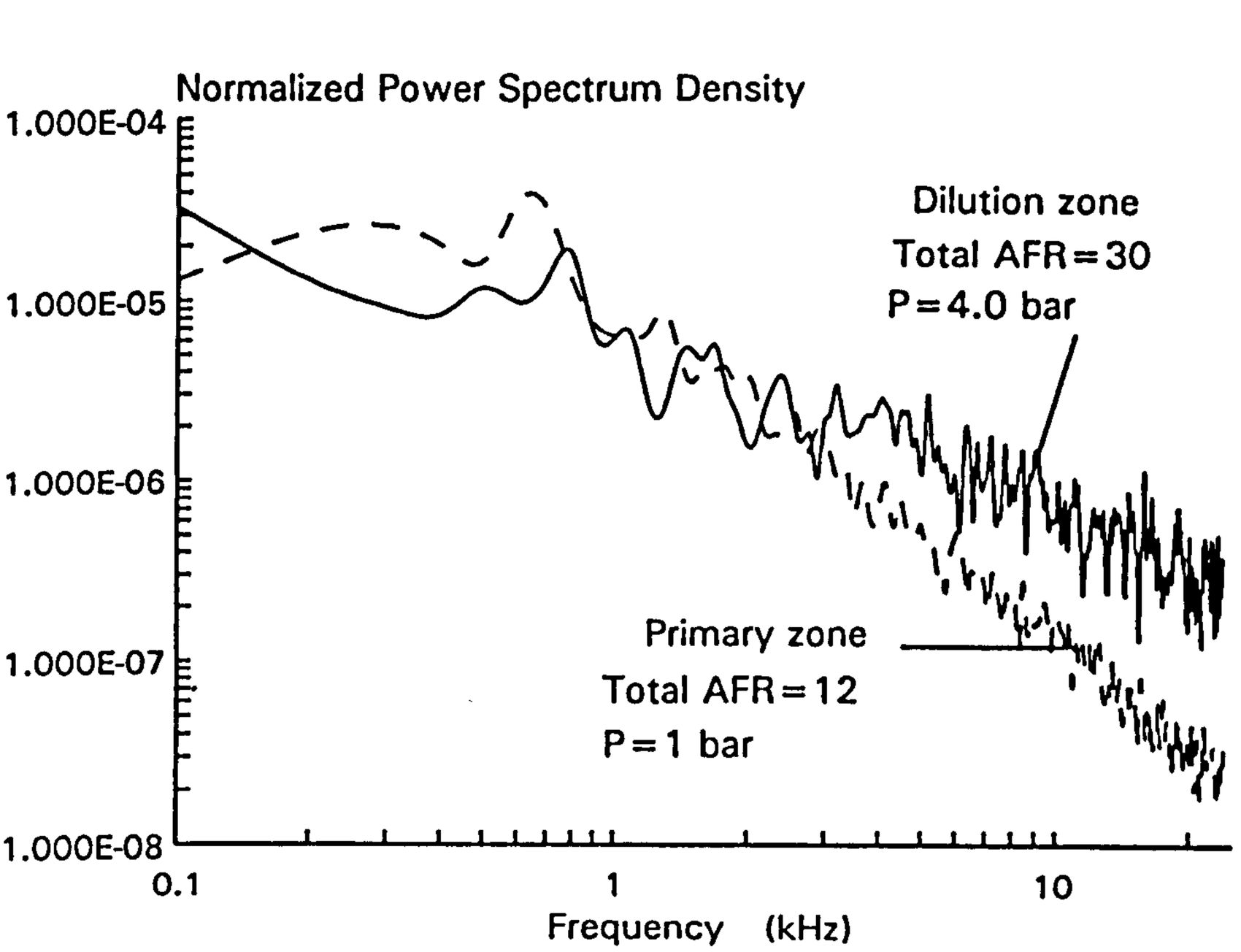

(b)

Figure 3.31 Normalized power spectrum densities of path-integrated extinction data (log-log scale)

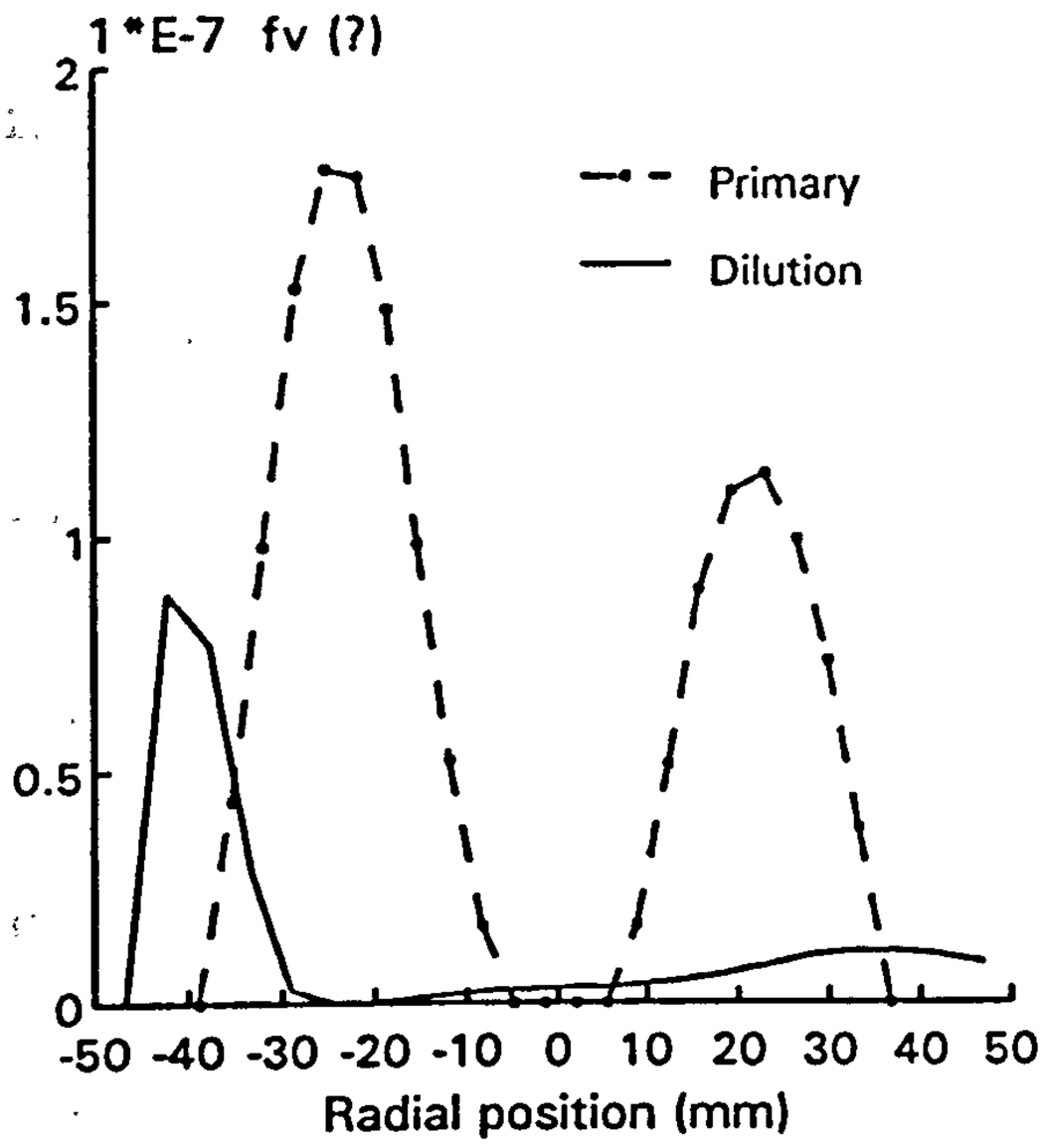

(a) AFR=45

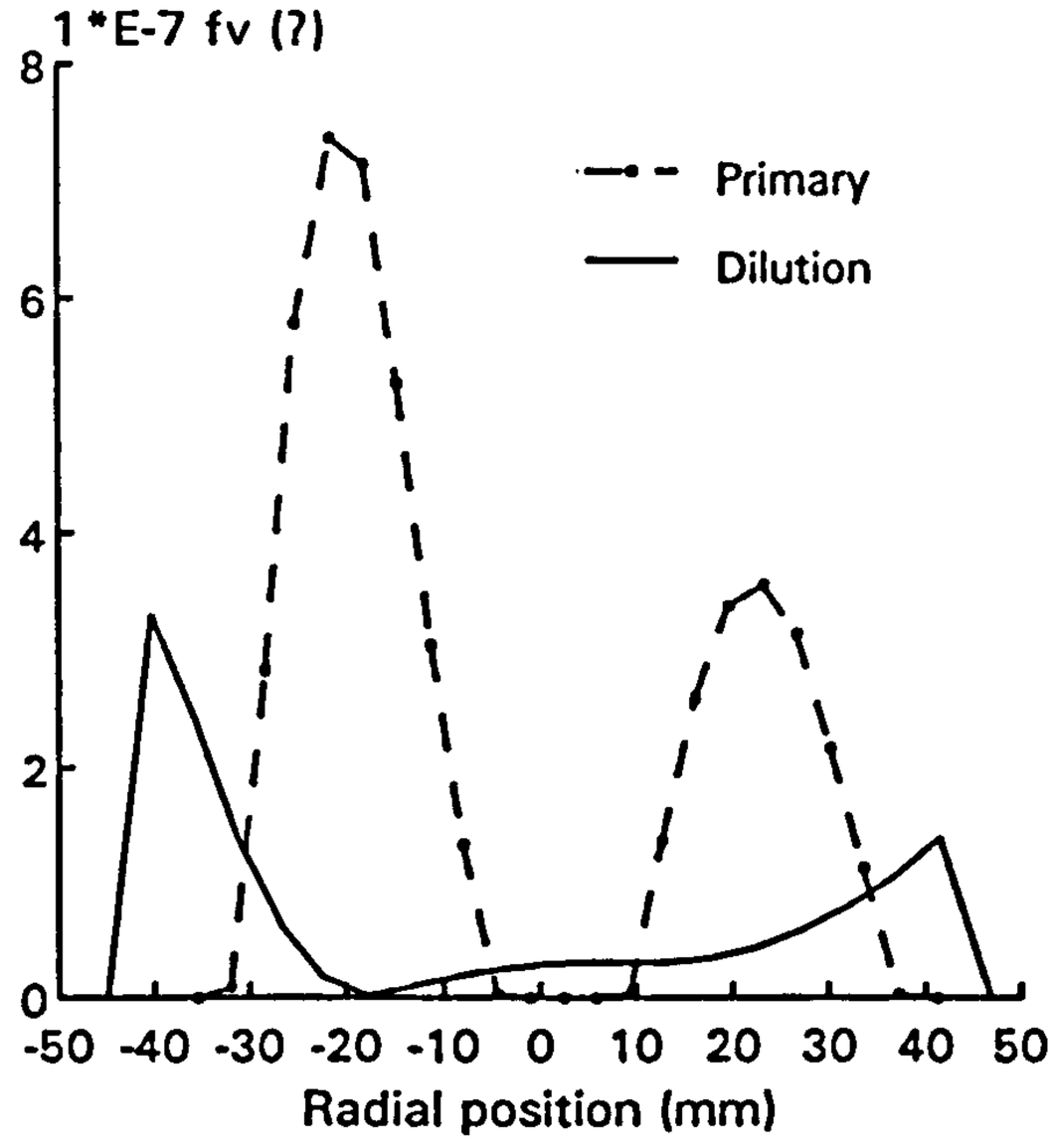

(b) AFR=22

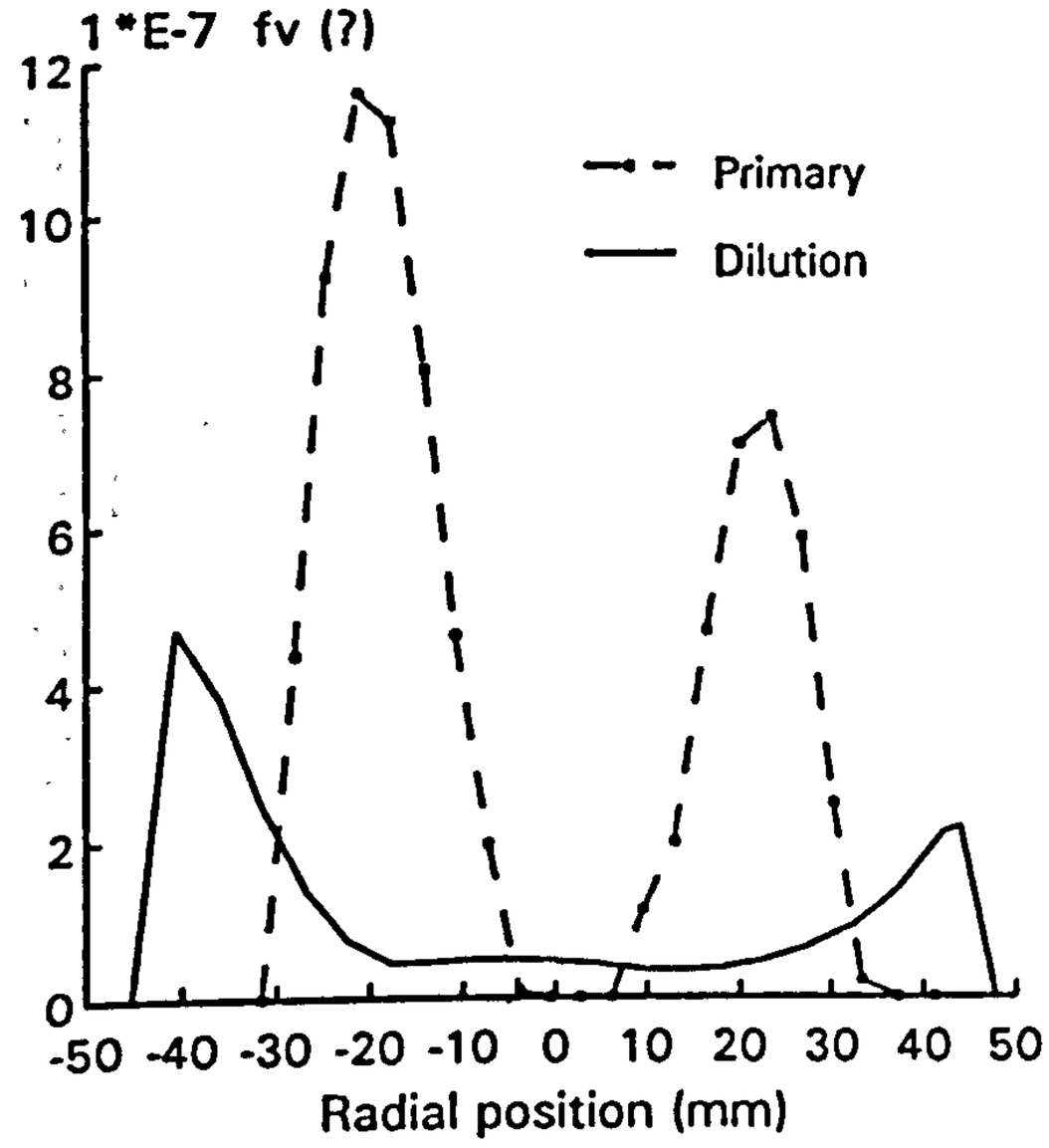

(c) AFR=16

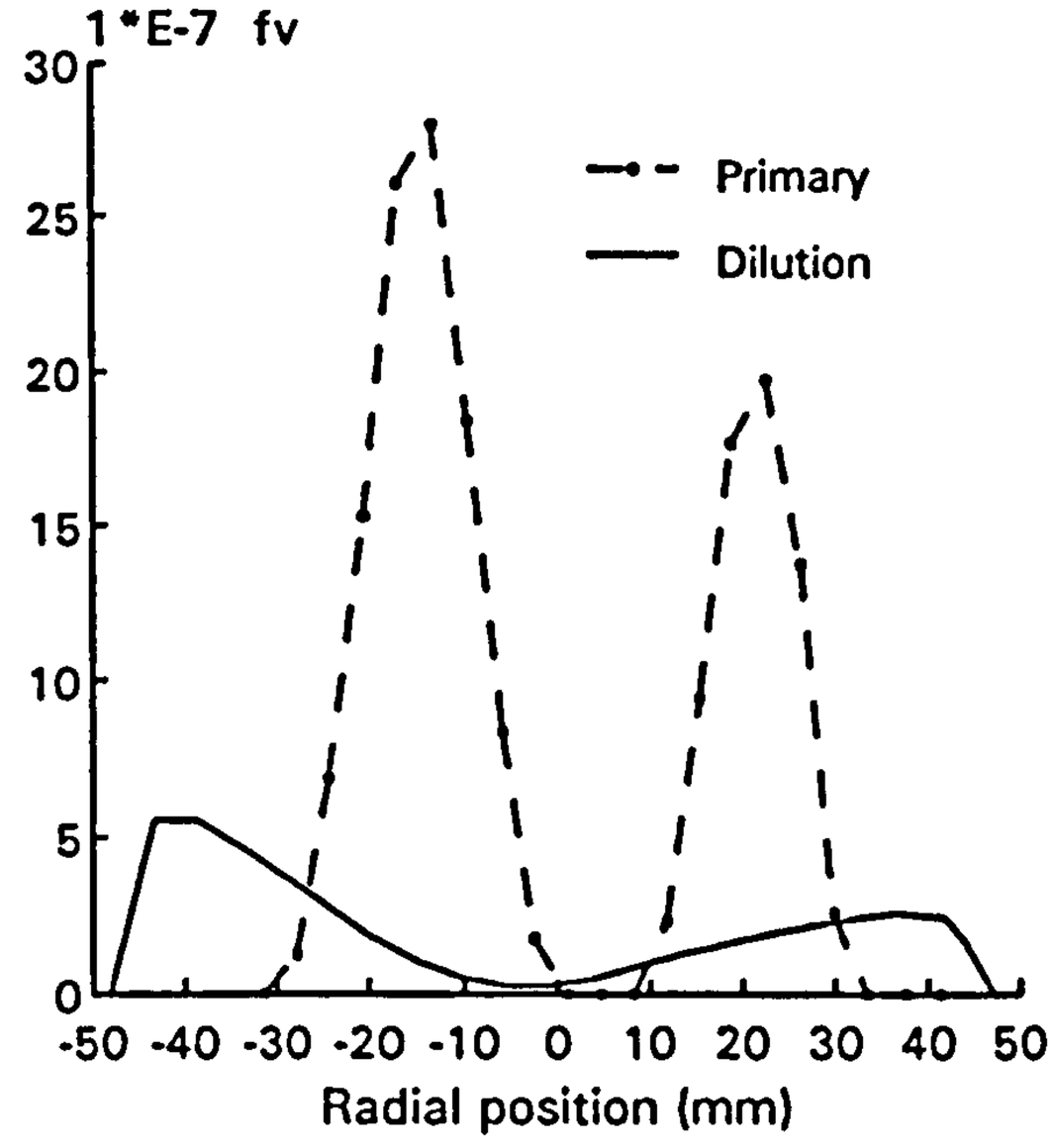

(d) AFR=12

Figure 3.32 Influence of varying AFR on the radial profiles of particulate volume fraction inferred from extinction measurements in the primary and dilution zones at atmospheric pressure

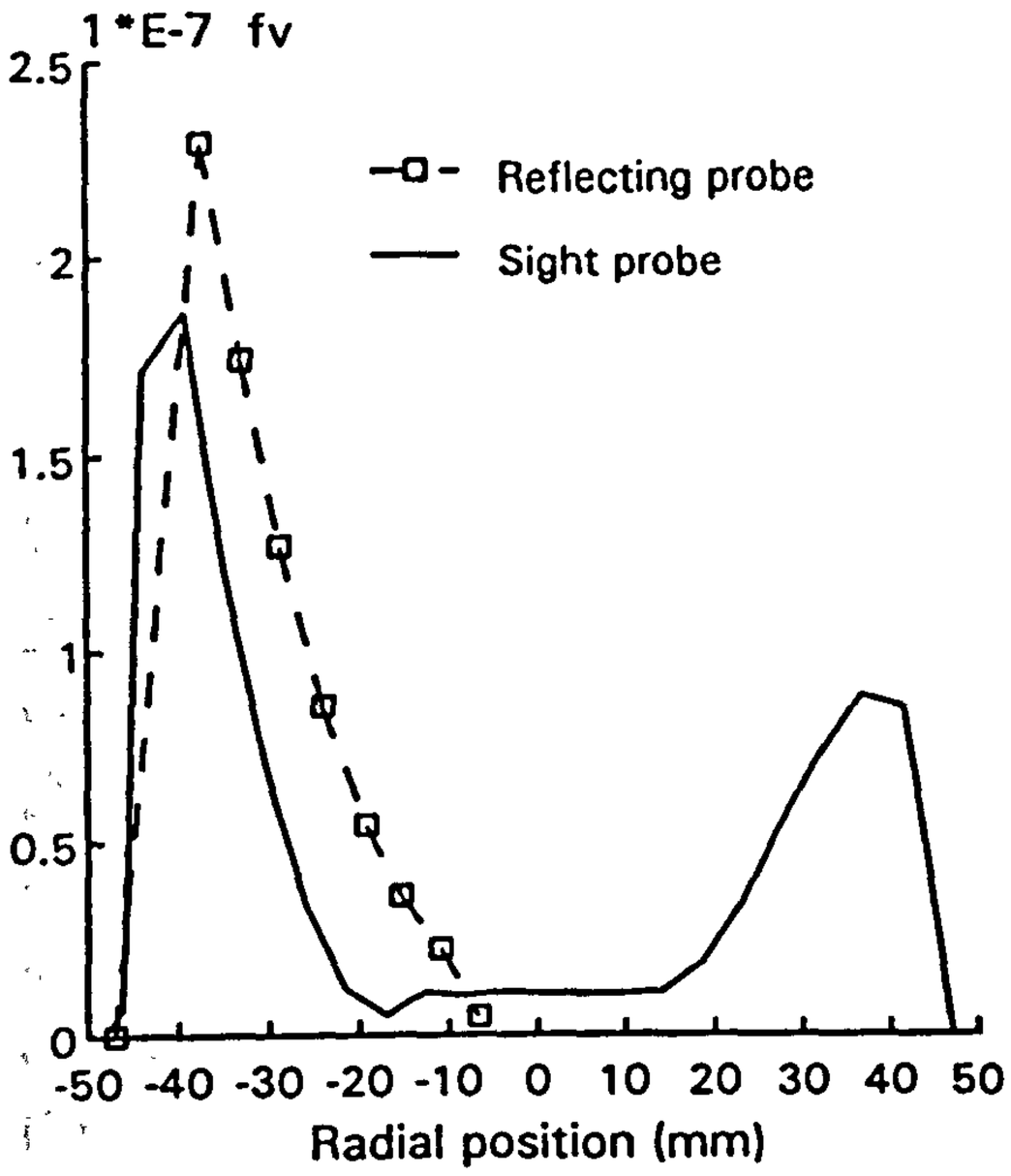

(a) AFR = 28

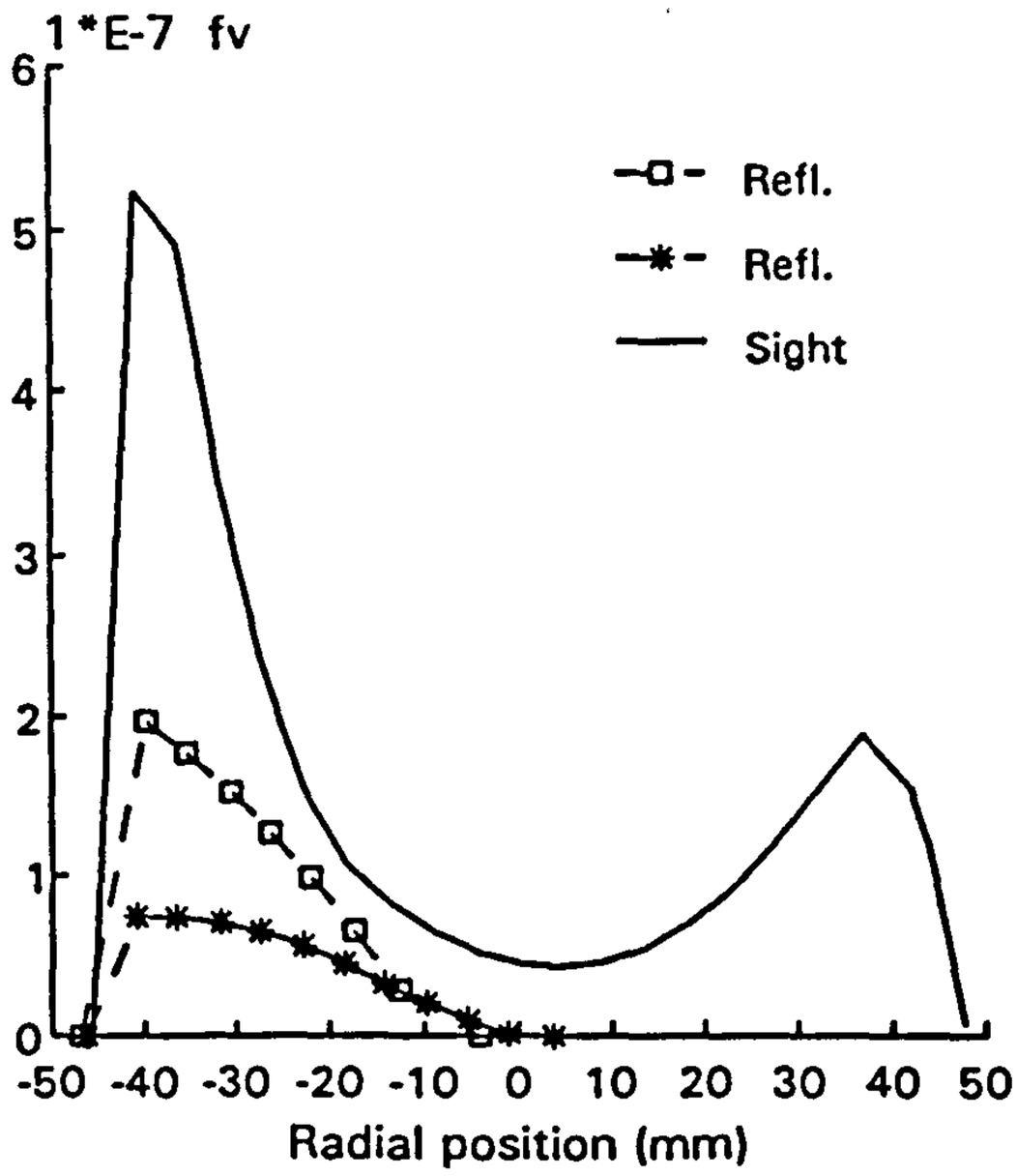

(b) AFR = 14

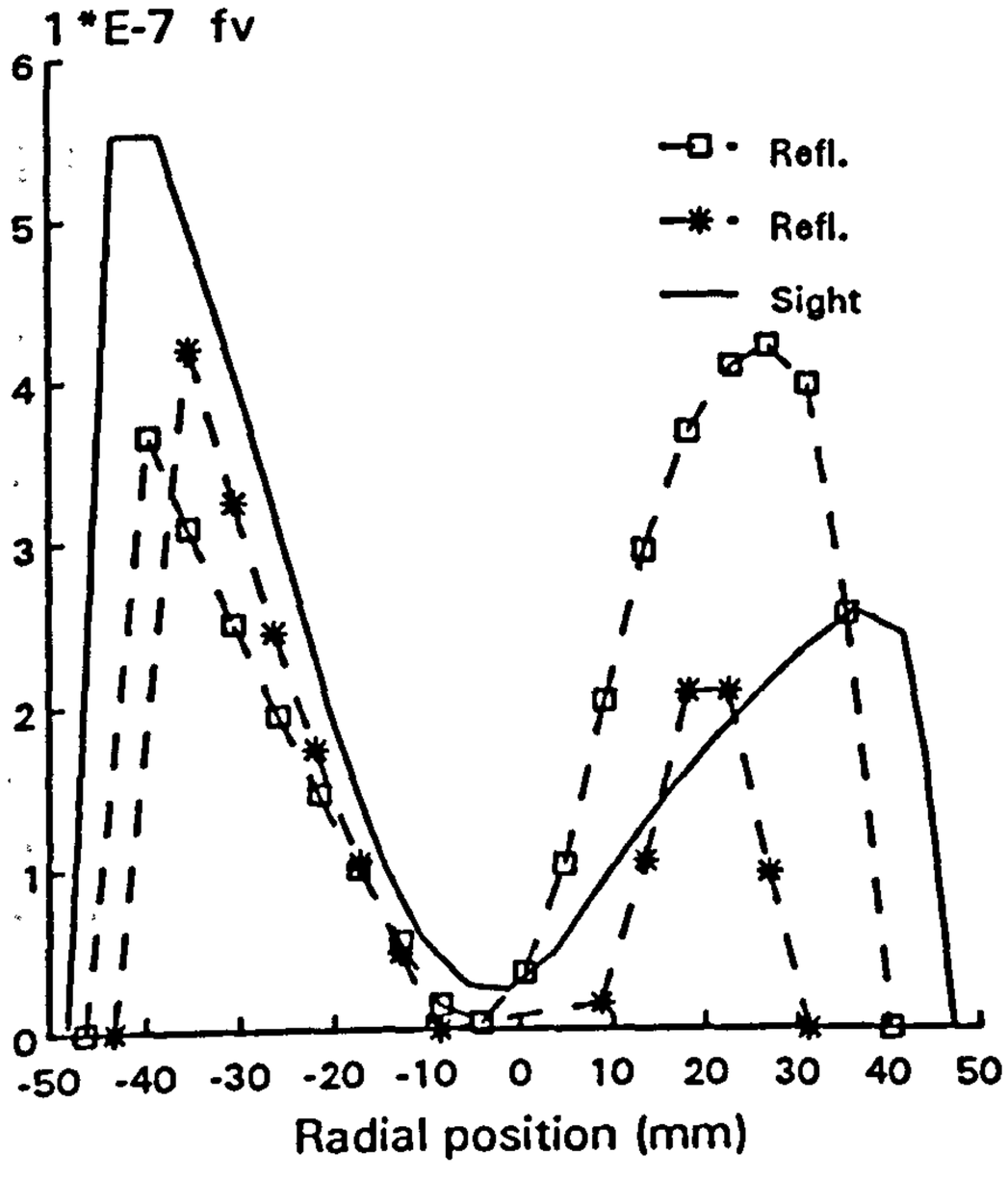

(c) AFR = 12

N_2 purge velocity

Sight probe 10 m/s

Reflecting probe 49 m/s

Figure 3.33 Comparisons of reflecting and sight probe measurements of soot volume fraction in the dilution zone for varying AFR; P=1 bar, varying nitrogen purge flow velocity

Chapter 4 Gaseous Species Analysis in the Combustor

4.1 INTRODUCTION

In a gas turbine combustor soot particles are mainly formed during fuel break-up into low carbon number hydrocarbons, especially acetylene and the major precursor PAH, in the gas phase and near the fuel spray in the primary zone. The rates of soot formation, a process consisting of nucleation, coagulation and surface growth, is determined by chemical kinetics and physical mechanisms and is therefore dependent on local temperature, pressure, fuel composition and mixture fraction (Jander and Wagner (1990)). The soot formation mechanism may involve a relatively high activation energy step, that inferred from soot formation during combustion are significantly higher than many other chemical reactions (cf. Gilyazetdinov (1972), Tesner et al. (1979) and Mullins et al. (1987)). The whole process of soot production is therefore highly temperature dependent and the occurrence of a critical temperature for soot onset merely emphasises that only above this threshold temperature are the kinetic rates fast enough for soot to be formed (Glassman (1988)).

The mixture fraction distribution or fuel concentration profile in the combustor is primarily determined by combustor geometry and in particular the air split and fuel preparation. The regions where the mixture can form soot is very narrow; only those rich pockets, typically for the mixture fraction > 0.1, and high temperatures are candidates for soot formation. There has been comparatively little detailed analysis of soot formation/destruction in combustors largely due to the lack of soot measurements together with appropriate thermal and aerodynamic information, for example, temperature distributions and mixture fraction profiles.

Measurements of the flow properties in gas turbine combustors have been reported by a number of authors, including Jones and Toral (1983) and Heitor and Whitelaw (1986). These studies provided a deeper understanding of the combustion process taking place inside the combustor but their emphasis was mainly on thermophysical aspects of combustion and did not include particulate soot. The combustion conditions investigated, mostly fuelled by gaseous propane and operated at low pressures, are however not representative of those arising in gas turbine engines. Although the flame shape and species concentration profiles in the turbulent kerosine spray flames are generally indistinguishable from those obtained in propane diffusion flames (Onuma et al. (1975, 1977)), the fuel type is vitally important in relation to soot production (Glassman (1988) and Haynes and Wagner (1981)). This is also clearly demonstrated in the two-step model evaluation where the soot formation activation energies

differ significantly for different parent fuels (Stewart et al. (1991)). The present experiments on a tuboannular combustor, fuelled by aviation kerosine through an airblast atomizer, at pressures up to 4 bar are more closely representative to that of the practical gas turbine combustion.

Investigations of the combustion process often require spatially resolved measurements of species concentration and temperature. These are key parameters in describing the combustion performance in terms of thermal efficiency and pollutant emission levels. Recently, an extended laminar flamelet approach - based on a conserved scalar, normally referred to as mixture fraction ζ - has shown a potential method of analysis for soot production in laminar and buoyant flames (Syed (1991)) and turbulent jet flames (Fairweather et al. (1992), Young (1993)). The local mixture fraction in combustors is primarily affected by two processes: fuel distribution, determined by spray atomization quality, and turbulent mixing between the fuel and injected air. Most of the mixture fraction measurements in combustors simply rely on isothermal flow tracing of an inert contaminant, helium gas injected through fuel passage for example (Heitor and Whitelaw (1986)). This can often provide an overestimation of mixing. Representative results can be obtained by sampling most of the combustion species and evaluating mixture fraction from the major species concentrations (cf. Jones and Wilhelmi (1989)). A more direct technique, employed successfully in this group (Syed (1991) and Young (1993)), is that of probe sampling for the local mixture, its complete catalytically-assisted oxidation and subsequent analysis by mass spectrometer to determine the carbon and nitrogen element ratio. The mixture fraction can then be inferred from this ratio. This method is adopted in the combustor measurement here, with only minor modification to that conducted previously in laminar and turbulent non-premixed flames.

The mixture fraction measurements are complemented by a limited range of combustion species. Gaseous species, like CO_2, NO/NOx have been measured in a conventional manner using probe sampling and commercial instrument analysis. These data offer opportunities for both the evaluation of computational fluid dynamics predictions and also environmental emission predictions. It would also be instructive to measure CO and UHC (unburned hydrocarbon) but unfortunately the scale limits of the instrumentation employed restricts CO data.

In this study, soot particulate temperature is of particular interest. In principle soot temperature can be measured by optical techniques, for example by the two colour method or filament brightness temperature (Lewis and von Elbe (1987)). These techniques are based on the thermal radiation from soot particles, particularly at visible wavelengths. They are typically integrated line of sight measurements in combustors as demonstrated by Norgaron (1971), and

the relatively low soot concentration level (as illustrated in the previous chapter) implies low radiation levels for which the techniques are unsuitable. Some optical temperature experiments reported in Chapter 5 demonstrate these features. Temperature measurements inside combustors normally focus on gaseous properties, measuring gas temperature by thermocouple for example. Typical soot particle sizes are sufficiently small (sub micron) that it is reasonable to assume that soot is locally thermo-equilibrated with the gaseous mixture and therefore the difference between their temperatures is expected to be negligible. Pagni and Okoh (1984) suggested such differences to be $\leq$ 10 K, a figure less than 1% compared with the local temperature. Whilst the accuracy of the above claim is questionable given the level of experimental uncertainty generally, the broad magnitude should be close to the real situation. The thermocouple is thus considered, based on these factors, to be the most suitable method to retrieve spatially resolved temperature information in the present study.

The results presented here, consistent with the soot volume fraction measurements, are taken from the same tuboannular (can-type) combustor at pressures up to 4 bar with the preheated air inlet temperature up to 200 °C. The following section provides details of the flows investigated and of the instrumentation used. Gaseous species analysis will follow for mixture fraction, CO_2, temperature and NO/NOx respectively. Thermal properties are coupled with soot measurements to provide a complete picture of soot production in the combustor dilution zone location. Attempts have been made to generate state relationships of time-averaged scalars including temperature, CO_2 and soot volume fraction vs the time mean conserved scalar, or mixture fraction, with some comparisons from computational laminar flamelet predictions and equilibrium calculations. The conclusions from these data are presented in the final section.

4.2 GASEOUS SPECIES, MIXTURE FRACTION AND TEMPERATURE MEASUREMENT DETAIL

The SNECMA designed combustor was operated at the same flow conditions as employed for the soot volume fraction measurements. The extremely rich conditions (overall Air-Fuel-Ratio 14 or so) were not repeated here since these are not representative of normal gas turbine operations. At atmospheric pressure, the Air-Fuel-Ratio was controlled between 45 to 22 and, for the elevated pressure of 4 bar, from 45 to 30, the latter limit was set by the limitation of the un-cooled pressurising tail pipe on the rig and also the running cost.

The sight probe, described earlier, was adapted for extracting gas samples and also

supporting the thermocouple. Gas sampling in laboratory flames normally employs isokinetic probes to ensure that the aerodynamic properties (especially velocity) of the sampled gas be kept the same as that in the surrounding flow field. This is easy to achieve in a simple, predictable flow field, for example, in jet flames. In the gas turbine combustor however the three dimensional flow introduces a complicated streamline pattern and gas sampling can only be performed under representative conditions. Uncertainties related to isokinetic sampling for gas analysis might arise when using the sight probe without modification. It is suggested that isokinetic sampling can reduce sampling disturbance considerably because this avoids preferential segregation of light and heavy patches in the flame (Bilger (1977 b)). The water flow visualization test in the replica combustor suggested that the swirling component of the fluid velocity had diminished almost completely at the dilution zone section and therefore the flow in this region was broadly two dimensional and the streamlines were not parallel to the probe axis (Join-Lambert (1992)). The sight probe was thus redesigned with its sampling axis parallel to the combustor axis to more nearly satisfy the needs of isokinetic sampling. Comparisons of the resulting isokinetic and non-isokinetic sampling have been conducted and will be demonstrated in the later section.

Temperature

Gas temperature was measured by conventional fine wire thermocouple (Pt-Pt 13% Rhodium) of mineral insulated type with a platinum sheath of outside diameter of 1.0 mm. The thermocouple was primarily supported by a stainless steel tube, of inside diameter 1.1 mm and outside diameter 1.5 mm, mounted inside the sight probe, to eliminate the catalytic effect of the platinum sheath on the gas sample. The distance between the tips of the thermocouple and the probe was 6.0 mm, this 6.0 mm spatial difference was taken in to account in data reduction (Figure 4-1 (a)).

The recorded temperature was actually the thermocouple metal sheath temperature not the local gas temperature. There exist conduction, convection and radiation heat transfer between the sheath, gas and combustor liner. Only when thermocouple and surrounding gas are locally equilibrated then the recorded temperature was truly the same as that of gas. In practical situations, like the combustor here, the thermocouple temperature was normally higher that the combustor liner temperature and lower than that of gas, hence there was radiation loss from thermocouple to the liner. The measured temperature needs to be compensated against radiation loss, under the heat transfer balance between convection and radiation (conduction was much less important than these two). The maximum compensation was estimated to be 124 K for 1 bar and 117 K for 4 bar pressures (for detailed compensation calculations, see Appendix

C: Thermocouple compensation). The rig exit temperature, at the position of 112 mm down stream from combustor liner exit, was measured by fine wire thermocouple (K-type) of mineral insulated type with outside diameter of 3.0 mm. It was also compensated for the same effect of radiation loss.

Gaseous species concentration

A sketch illustrating the application of the original probe is shown in Figure 4.1 (a), where sample gas was extracted along the path from the tip of the probe. To achieve near isokinetic sampling, the inlet of the probe was adjusted to be parallel to the combustor axis (Figure 4.1 (b)). The diameter of the entrance hole of the isokinetic probe was 1.0 mm. Whilst this will certainly improve the sampling quality, the new tip of the gas inlet was 5.0 mm upstream from the dilution hole centre line, where soot and temperature measurements were performed. This spatial discrepancy complicated the interpretation of the measurements, especially in the dilute jet penetration region, where the axial gradient of the gas property was high, and the influence of the 5 mm off-set was not negligible.

Gas extracted through the probe was analyzed simultaneously for the compositions of CO_2, NO and NOx. Figure 4.2 outlines diagrammatically the instrumentation set up for the analysis. Gaseous samples were cooled immediately after being extracted into the probe. A freezing trap was used to achieved fast quench for the sample by observing the sensitivity of results to the cooling water flow rate; some illustrations will be shown in the following results section. Liquid water, condensed on the cooling line, was deposited in a dryer to allow the remaining gas to pass to instruments. A bypass was introduced to maintain the required sampling flow rate. Norster and Lefebvre (1972) reported that the measurement for NO/NOx above 10 ppm level will not be disturbed by the presence of liquid water. In this study, the influence of liquid water on NO, NOx detection was tested by passing span gas (NO 30 ppm) through a water sink. It was confirmed that there was no effect on the output of the instrument. The CO_2 concentration was measured by an infrared analyzer (ADC type 517-MK3 dual gas analyzer for CO and CO_2) at a sample rate (combustion product plus oxidant dilute required by the instruments) of 1.5 litre/minute and NO/NOx by Rack-Mounted Chemiluminescent NO-NOx Gas Analyzer (Thermo Electron Model 10A) at a sampling rate of 0.04 litres/min, required by the instrument reaction chamber. The suction velocities of sight and isokinetic probes were 20.0 and 32.1 m/s, respectively, at the entrance of the probe under the sampling rate of 1.22 litre/minute in the sample line. The upper limits of the instrument for CO_2 is 15% and 0.25% for CO, the latter was found too low for CO measurement inside the combustor. All these measurements were made on a dry basis.

The uncertainties of these analyzers were within 2% at full scale. The use of a stainless steel probe in some experiments (Allen (1975), Kyokuo et al. (1980)) was likely to give some undesirable catalysis effects (mainly NO to NO_2 conversion). The NO_2 concentrations measured here were relatively low and this problem was not taken into account. The measured gaseous species concentrations by probe sampling are arguably close to density weighted averages and within 10% of the true values (Heitor and Moreira (1993)) and can thereby be compared directly with numerical predicted values. Exit plane gaseous mixtures were extracted by a water cooled stainless steel probe of 9 holes drilled to give an area weighted spacing, each hole being of 1.0 mm diameter. The exit sample was measured independently on the same line by switching from dilution zone to exit station or vice versa.

Mixture fraction

The mixture fraction ζ may be defined (Spalding (1963))

$$\zeta = \frac{Y_{fuel}}{Y_{air} + Y_{fuel}}$$

$$= \frac{1}{1 + (air/fuel)_{mass}} \qquad (4\text{-}1)$$

which, for the complete reaction of kerosine with air, may be written

$$\zeta = \frac{1}{1 + 2.665 (N_2 / CO_2)^*_{mole}} \qquad (4\text{-}2)$$

The determination of mixture fraction was achieved by the measurement of $(N_2 / CO_2)^*_{mole}$, based on carbon and nitrogen element conservation. By passing the extracted mixture and excess oxygen through a platinum catalyst chamber, which was electrically heated to about 800 °C, all the species containing the carbon element are converted into CO_2.

The $(N_2 / CO_2)^*_{mole}$ was measured by Mass Spectrometer (VG Quadruples) with less than 3% uncertainty, following the instrument repeatability analysis. The mass spectrometer was capable of detecting the relative concentration of individual gaseous species, for a span gas (normally 10% CO_2 by volume and N_2 balanced) the ratio of molecular weight 44 (related to CO_2 mass spectrum) over 14 (related to the N_2 mass spectrum) was a function only of measured chamber pressure. A calibration curve can be obtained for such a relationship and by passing the sample gas into the mass spectrometer, the $(N_2 / CO_2)^*_{mole}$ was detectable under particular chamber pressures according to the calibration curve. The calibration is instrument-dependent, and usually changes when the mass spectrometer is turned on and off; thus the spectrometer had

to be calibrated on each experiment date.

Mixture fraction measurements in laminar and turbulent jet flames have used quartz tubes for mixture extraction (Moss et al. (1987), Young (1993)), but in the combustor environment the quartz probe was considered too fragile and stainless steel was utilised here. The mixture fraction probe (hypodermic tube) was accommodated inside both the original and modified sight probe. The mixture passage was electrically heated over 500 °C to keep the wall temperature well above the boiling points of both water and kerosene to prevent any condensation in the line.

The consequences of probe presence in the flow may be important in composition measurements since it may disturb the scalar concentration gradients in the vicinity of the probe as a result of the streamline distortion, but no attempts have been made to quantify the effect of probe disturbance. Sivathanu and Gore (1991) reported that the maximum errors in the local CO_2 mean concentration measurements due to the presence of optical probes were less than 5% (of the mean concentration) in a jet flame. It is expected that such error in the combustor measurement should also be small.

In turbulent flow fields of practical interest the chemical reactions are comparatively fast so that the combustion process may be mixing controlled. The classical approach to the solution of these problems has been to describe the mixing by obtaining the solution for a conserved scalar. Mixture fraction is chosen as such a conserved scalar since it is readily inferred from the ratio of mass concentrations of molecular carbon and that of nitrogen. In flames combustion equilibrium calculations (Gordon and McBride (1971)) are based on the fast chemistry assumption and the instantaneous scalars, like molecular species and free radical concentrations and temperatures, are then functions only of mixture fraction. The local equilibrium state in the combustor has been calculated from the measured mixture fraction profiles on a dry basis to be consistent with the measured species. An indication can then be found as to how far the local values are from complete chemical equilibrium.

The percentage of soot formed from carbon elements in the kerosine fuel was calculated from the measured soot volume fraction using

$$\eta_{C\,soot}(\%) = \frac{f_v \cdot \rho_s}{\zeta \cdot 0.858 \cdot \rho_{mix}} \cdot 100 \qquad (4\text{-}3)$$

where ρ_s is the soot density, taken as 1800 kg/m^3 (to be consistent with previous works within the group), ρ_{mix} was gas mixture density. Measured soot volume fractions in this combustor

have not exceeded 1.0 ppm locally and therefore the particle-laden gas can be assumed to be ideal, without introducing significant error with respect to the soot particles. ρ_{mix} is determined from the measured gas temperature via the equation of state.

Another measure of combustion completeness was provided by the fraction of carbon in carbon dioxide, originating in the kerosine fuel, following

$$\eta_{CO_2}(\%) = \frac{X_{CO_2} \cdot \rho_{CO_2}}{\zeta \cdot 0.858 \cdot \rho_{mix}} \cdot 100 \qquad (4\text{-}4)$$

X_{CO2} was the CO_2 concentration (volume fraction). If the densities of CO_2 and the mixture are assumed to be simply linear functions of their respective molecular weights from the state equation, Eq. 4-4 can be re-written as

$$\eta_{CO_2}(\%) = \frac{X_{CO_2} \cdot 12.0}{\zeta \cdot 0.858 \cdot 28.9} \cdot 100 \qquad (4\text{-}5)$$

4.3 RESULTS AND DISCUSSION

The soot volume fraction measurements discussed in Chapter 3 provide information from the dilution hole station only. The following gaseous species and temperature measurements are therefore reported in the same region to establish a limited data base for this combustor. Although it is clearly desirable to have a full data map of the combustor, including the primary zone which is the predominant combustion regime for a gas turbine combustor, the focus on the soot production process here has influenced the data collection. For this reason all the work in this and the following chapter are concentrated at the station of the dilution holes, although, as indicated earlier, under the comparatively rich conditions investigated with AFR~22 this is often more characteristic of the zone inbetween primary and dilution than of a conventional dilution zone.

Whilst measurement points are essentially unlimited for radial traversing, in order to reduce the combustor operation cost, experiments were performed at selected radial positions, especially in the region where soot concentration peaks were found (eg. R≈-35, +30 mm), with fewer points in the centre part where properties tend to exhibit lower radial gradients. Of the instruments employed the mass spectrometer responded particularly slowly and thus controlled the whole sampling process. It normally took several minutes for one point, and both the temperature and CO_2 output were observed to remain steady during the mixture fraction measurement. For each flow condition the measurement traverse is repeated at some radial

position and showed good repeatability. Since the carbon monoxide concentration in most radial positions exceeded 0.25%, the upper limit of the instrument, detailed distributions of CO are not available. The CO concentrations at the rig exit (about 100 mm downstream of the combustor exit plane) however are all below that limit and these results are presented.

4.3.1 Sampling by sight and isokinetic probes

The comparison of non-isokinetic and isokinetic sight probe applications for mixture fraction in Figure 4.3 shows that the discrepancy in the two methods is more significant near R=+40 mm. This reflects the dilution air impingement which is detectable by the sight probe (traversing on the axis of the dilution hole centre line) but is missed by the isokinetic probe, due to the 5 mm spacial displacement of the sampling tip (the radii of the dilution holes are 4.9 mm). The profiles at R=-50~-40 mm for both Air-Fuel-Ratios of 45 and 28 are in good agreement since the axial gradient is negligible in this region because of both the high axial velocity, hence short residence time, and the absence of a dilution effect due to hole blockage by the probe.

The profiles in the combustor centre differ from 15% to 20% for AFRs 45 and 28, respectively. While experimental uncertainties should be taken into account, the decreasing in mixture fraction may indicate a progressive mixing along the combustor axis. Since mixture fraction reflects flow unmixedness, it will approach the overall value of mixture fraction - 0.022 and 0.035 for AFRs 45 and 28, respectively.

The unmodified sight probe extracted gas samples existing at the vicinity of the probe tip (Figure 4.1 (a)), and higher density (high molecular weight) components in the mixture have relatively higher momentum than the low density components, whereas the latter are more likely to be sampled by the sight probe. Bilger (1977 b) has shown that high suction rate (velocities) may cause a bias towards the lower density components. Carbon dioxide (44) may have therefore less chance to be extracted than other species, like H_2O (18), CO (28), N_2 (28), O_2 (32). The carbon dioxide distributions (Figure 4.4) near the probe entry side agree very closely from the two probes. In this region there is no dilution effect and the gas velocity is also relatively high, compared with that around centre part, and so the axial concentration gradient will be negligible as the results indicate. The suction rate employed in the present experiment was therefore considered appropriate. The CO_2 discrepancy at R=+40 mm is obviously due to the probe spacial displacement as discussed for the mixture fraction measurements. In the low velocity region near the combustor axis, the long residence time may promote CO_2 production and the carbon dioxide concentration is expected to exhibit a positive gradient. Such

a gradient will result in higher concentrations downstream and the 5 mm probe tip displacement between the two probes can no longer be assumed negligible. Both the distributions in Figure 4.4 for AFRs 45 and 28 show the higher CO_2 concentrations 5 mm downstream. For the richer case at AFR=28, local mixture fraction profiles are closer to stoichiometry and thus the combustion zone has extended to the "dilution" hole section, resulting in larger gradient of CO_2 concentration.

From these comparisons, it is obvious that the measurements by the sight probe seems more representative to the local flow field acrose the dilution holes, where soot volume fraction and temperature have been measured, than that by its isokinetic counterpart in the present study. The main disadvantage of the isokinetic sampling is its 5 mm axial displacement that complicates the correlation of mixture fraction with the soot volume fraction and temperature measurements. The probing comparison helps to determine the result quality by using the sight probe and also the selection of proper probing data set. It was found that the measured species in a tubular combustor were independent of the suction velocity in the range from 6 to 20 m/s by using sampling method similar to the present sight probing (Heitor and Whitelaw (1986) and Heitor and Moreira (1993)). The suction velocity employed by the sight probe, about 20 m/s, is believed to be adequate for the present measurement. Subsequent analysis associated with mixture fraction, temperature and soot volume fraction will thus base on the sight probe results from the above conclusions except for CO_2 where the iso-kinetic data are used.

4.3.2 Mixture fraction and Carbon Dioxide

The conditions prevailing at the dilution hole position are clearly inhomogeneous and difficult to predict on the basis of global features (for example overall Air-Fuel-Ratio). The stoichiometric mixture fraction of the Avtur aviation kerosine is 0.0638 (1/(1+14.67)). For an overall Air-Fuel-Ratio of 45, the averaged mixture fraction across the dilution hole station is naturally below the stoichiometric value (Figure 4.5 (a)). From the flamelet state relationship predicted by Askri-Sardhai (1987) and Lindstedt (1992), unburned fuel kerosine or hydrocarbon can only exist at conditions of mixture fraction $>$ 0.0638. During the experiments, condensed fuel can be smelt from the sampling spill valve at richer flow conditions, ie. AFR=28, 22, but not at AFR=45. These results suggest that there is little fuel or UHC remaining in this zone at AFR=45 at 1 bar pressure. With pressure increased to 4 bar (Figure 4.5 (b)) the maximum mean mixture fraction is still in the lean mixture side for AFR=45.

Since the gas turbine combustor is designed to operate at AFRs near 45 with combustion efficiency close to 100%, the combustor aerodynamic configuration must meet the requirement

of fulfilling complete heat release from the fuel-air reaction when approaching dilution zone thereby achieving high combustion efficiency. The higher peak of mixture fraction at the probe entry side at AFR=45 shows that even with the air penetration blocked the dilution station is still below stoichiometric. This should be representative of situations at the dilution station but circumferentially displaced from the dilution holes, or without local air penetration. The air impingement on the opposite side dilutes the mixture towards much leaner levels as expected. These measurements suggest that the fuel in this flow condition has been completely consumed, consistent with high combustion efficiency.

As the fuel mass flow rate is increased, with the overall Air-Fuel-Ratio decreasing to 28 and then 22, the flow field becomes locally richer and the mixture fraction exceeds stoichiometric value (Figure 4.5 (a) and (b)). At the elevated pressure of 4 bar, the mixture fraction showed broadly the same feature. The peak positions in these profiles again reflect the fuel atomization characteristics. Wheras experimental errors may be responsible for the small differences in the profiles of mixture fraction at AFR=30, with air pre-heating of 130 °C and 200 °C (Figure 4.5 (b)), such difference may also indicate the different mixing processes. Higher inlet air pre-heating can, as observed by Bicen et al. (1990), increase the flow field temperature substantially due to the exponential dependence of reaction rate on temperature. The accordingly increased velocity, or reduced residence time, may shorten the mixing process for the same geometric length up to the dilution section. This can lead to higher mixture fraction relative to the overall value of 0.032 due to the poorer mixedness.

The nearly identical distribution of mixture fraction at the different pressures of 1 and 4 bar for both AFR=45 and 28 (30) (although the similarity for AFR=30 is not as close as AFR=45) in Figures 4.6 (a), 4.7 (a) showed the comparative insensitivity of the mixing process to pressures up to 4 bar in dilution zone. The profiles are globally plausible since the integration of the two profiles tends to give the same total Air-Fuel-Ratio, although the combustor flow field is actually asymmetrical hence scalar distributions are two-dimensional not linear. It would be instructive to establish whether at pressures even higher than 4 bar the profile will still remain the same.

The peaks of mixture fraction for AFR=45 at both 1 and 4 bars are both below stoichiometric (Figure 4.6 (a)). Experimental data from kerosine-fuelled combustors has suggested a critical equivalence ratio range for soot formation, ie. only when mixture fraction is above about 0.16 (Prado et al. (1977)) could soot formation proceed. A similar range is reported by Moss et al. (1991) in laminar flames (ζ : 0.07 - 0.20). The function of the dilution zone is essentially to dilute the hot gas with cold air, permitting only limited further chemical

reaction. In terms of soot formation, this is evidently achievable since gas turbine combustors operate at conditions near AFR=45 and no soot will be formed after dilution station. The combination of mixture fraction and soot volume fraction measurements confirm the speculation in Chapter 3 that the soot volume fraction in the dilution zone may be a direct indicator of exhaust smoke levels under representative conditions although the final smoking level is determined primarily by the balance of soot formation and oxidation rates.

The carbon dioxide profiles for AFR=45 at pressures 1 and 4 bars (Figure 4.6 (b)) are also identical, similar to the mixture fraction. As increased pressure will promote chemical reaction which should generate CO_2 more rapidly, the results appear to confirm that at this AFR, the combustion process is nearly complete in the dilution zone and further increase in pressure will not change CO_2 concentration levels further. For AFR=28 at 1 bar and AFR=30 at 4 bar in Figure 4.7 (b), where the AFR is about 6% different, it is not clear from this figure whether the mixture enrichment from AFR=30 to 28 is competitive with the effect of pressure drop on the CO_2 concentration, as the profiles are close to each other. However, when the air inlet temperature is reduced by 70 K, the reaction rate is decreased and the CO_2 levels also decrease as shown in the figure. These comparisons for different conditions, for example inlet temperature and pressure, may not be conclusive since any such change can result in different flame structure inside the combustor and one physical location can not represent the whole flow field feature. A whole map of flow properties are naturely more capable of showing the broad combustion flow structure. The limited data in this study however may serve for qualitative analysis.

Figures 4.8 and 4.9 compare the measured CO_2 concentration together with the calculated equilibrium CO_2 concentration based on the measured mixture fraction (Gordon and McBride (1971)). Relative to pollutant formation, for example those of NOx and soot, CO_2 formation is associated with fast chemistry and thus does not, in principle, need long residence time to reach equilibrium. Some parts of the dilution station appear closer to equilibrium than others. The radial positions of those regions close to equilibrium are not consistent with the AFR reduction. At higher pressures the reaction rate for CO to CO_2 is faster and the CO_2 level is expected to be higher than that at low pressure, unless such conversion is already complete as implied for the AFR=45.

Included in these comparisons are the combustor exit CO_2 concentrations, based on overall AFR, with highlighted bar. The exit concentration rises significantly from half of the dilution station level at AFR=45 to about 80% at AFR=22. Schoenung and Hanson (1981) suggested that carbon monoxide conversion to CO_2 can only take place at temperatures above

1500 K. The maximum mean temperatures for AFRs 45, 28, 22 are 1450, 1700, 1800 K respectively. For AFR=45, there is no CO_2 formation down stream from dilution zone and due to the dilution air addition the CO_2 concentration at exit is much lower than that at dilution station. For AFR=22, the CO_2 levels at the two locations are closer, there might be some CO_2 formation between the two positions since it is the combination of the formation rate and dilution rate which determine the exit level. When the combustor is operated at AFR=22, it is expected that CO_2 continues to be formed after the dilution station and chemical reaction dominates the limited dilution air quenching effect. This trend is also exhibited at elevated pressure (Figure 4.9).

Analysis of exit CO_2 against overall Air-Fuel-Ratio is shown in Figure 4.10 (a), together with the results from an uncooled sampling probe. The purpose of performing the uncooled probing measurement is to check the influence of water cooling rate on the sampling results and, by gradually increasing the water flow rate, an optimum rate may be established to quench sufficiently any reaction in the sampling line. At AFR=45, water cooling had no effect on CO_2 concentration which suggested there is no further conversion of fuel or carbon monoxide to carbon dioxide at this location indicating all the fuel had been converted to carbon dioxide, possibly as early as in the dilution zone. This is also an indication of complete combustion. With the overall air-kerosine mixture being adjusted towards richer conditions, there is more unburned hydrocarbon or CO left in the exit plane which contributed to the higher CO_2 level from the uncooled probing.

Figure 4.10 (b) illustrates the exit CO against overall Air-Fuel-Ratio. For the conditions of AFR=45 there is little CO conversion to CO_2 so the CO result is not influenced by cooling water flow rate in the sampling probe, whereas the quenching effect is obvious for AFRs of 28, 22. The combination of Figures 4.10 (a) and (b) reveals that at AFR=45, the kerosine/air reaction has almost completed and few intermediate fuel species like CO are left downstream from the dilution zone. With enriched flow conditions more CO is left incompletely oxidized, as a result of the enlarged reaction zone and correspondingly reduced residence time. High pressure will promote such chemical reaction and the exit CO level is lower than that at 1 bar.

The CO_2 concentration at 4 bar is slightly higher than that of 1 bar. As the comparison in Figures 4.6 (b) and 4.7 (b) reveals the nearly identical profile of CO_2 at different pressures with the same Air-Fuel-Ratio, 45 or 30, the exit CO_2 level shows that at high pressure there is still fuel or CO conversion to CO_2 from the dilution station to exit plane probably owing to the higher temperature, whereas for AFR=30 there will be more such conversion than for leaner

conditions. At 4 bar and AFR=30, with air inlet temperature dropped from 200°C to 130 °C, the carbon dioxide level decreased as well, exhibiting the same trend as in the dilution zone.

4.3.3 Temperature

The temperature profiles in Figure 4.11 are relatively flat in the middle, with good temperature traverse quality (or pattern factor). Although such a term is normally referred to the combustor exit assessment, the temperature profile should only smooth further at the exist and uniformity improve due to the progressive heat convection. From the water flow visualization test (Join-Lambert (1992)), it is believed that the circumferential velocity component (swirling component) has vanished by the time the flow reaches the dilution zone and that this establishes a high traverse quality.

With fuel enrichment, the temperature profiles for AFR=28 (30) are flatter than that at AFR=45 in Figure 4.11. This is in contrast with the trend from a propane-fuelled combustor reported by Heitor and Whitelaw (1986). The contradiction may stem from the different phases of the original fuel. It has been experimentally observed by Ehalil and Whitelaw (1976) that flames fuelled by propane and by liquid kerosine have properties which are similar in general but significantly different in detail. They found the temperature traverse quality of kerosine flame is better than propane flame. Gaseous fuel tends to mix with air much faster than liquid fuel. The prolonged evaporation and subsequent mixing of fuel drops in the flow field can expand the combustion zone inside the combustor. With the overall mixture being adjusted from AFR=45 to AFR=28, there are more stoichiometric patches in the regime near the combustor centre line as shown in Figure 4.5. The broadening of combustion zone raises the temperature in the corresponding region, thereafter, improve the temperature traverse quality.

In the field of dilution air penetration, R=+35~+50, the temperature persists with the different AFRs and pressures, partly because of the upstream film cooling effect but mostly because of the air impingement. Of AFR=45, the temperature at 4 bar is about 150 K higher than that at 1 bar, while for AFR=30 the difference is about 200 K. These differences are very high compared with equilibrium from which pressure has little influence on temperature between 1 and 4 bar. This may be attributed to both the increased reaction rates at the elevated pressure and the reduced thermal radiation loss from the combustion products to the hotter wall at higher pressure. Changes in the flame structure at elevated pressures may also change the local properties at a fixed geometric location, like the dilution zone station.

Comparisons of measured temperature and equilibrium temperature, calculated from the

measured mixture fraction, are shown in Figures 4.12 and 13. The gas temperatures in the dilution zone are about 80% of equilibrium values in general, similar to CO_2 concentrations. It should be emphasised that such comparisons are only qualitative in a sense that they are based on time-averaged data and only instantaneous scalars have functional relationships if the combustion is mixing controlled. This issue will be discussed in more detail later. The exit averaged temperature is higher at elevated pressure than at low pressure with AFR=28, 22 (Figure 4.14 (a)) but for AFR=45, the temperature remains the same for different pressures. Recalling the characteristics of CO_2 concentration in Figures 4.8 and 4.9, the continuous reactions at richer conditions which raise the temperature may dominate the dilution effect and thereafter result in higher exit temperature at rich conditions. Additional temperature information is given for the duct wall (the stainless steel pipe connecting the combustor liner and rig flange) in Figure 4.14 (b). Since there is no additional cooling air available, the temperature increases with both the decreasing AFR and increasing pressure.

4.3.4 NO/NOx

Like soot production, NO/NOx formation is a comparatively slow chemical process and therefore is reaction rate controlled in combustors. Nitric oxide is mainly generated in the vicinity of the primary zone where high temperature and near-stoichiometric mixtures prevail. Figures 4.15 and 4.16 show NO/NOx distributions at the dilution station compared with local equilibrium calculations. Equilibrium is only attained if the residence time is infinitively long but the residence time in a practical gas turbine combustor, typically of a few milliseconds, can never reach this level. As expected, the measured profiles are much lower than the equilibrium ones. With the increase in residence time from the dilution station to the exit, the NOx level increased still further as shown by the exit NOx concentrations. NOx mainly comprises NO and NO_2 and in most flames the 'thermal NO' is the principle source. The NO_2 concentrations in Figures 4.15 and 4.16 are considered too high for combustion temperatures about 1450 K and may be due to the prolonged sampling time with low temperature. The NOx levels inside this combustor, about 20 ppm at 1 bar, are however similar to the propane-fuelled combustors as reported by Jones and Toral (1983), Heitor and Whitelaw (1986) and also by Hori (1986).

Increased ambient pressure has raised the NOx concentrations as shown in Figure 4.16. Correa (1993) has suggested that NOx scales approximately as $p^{0.5}$ in non-premixed combustors in which the overall residence time is held constant (mass flow vary linearly with pressure, as performed in the present study). The doubled NOx concentrations at 4 bar, about 40 ppm, reveal the same pressure dependence. The absolute concentration levels are similar as those measured at elevated pressures by Drennan et al. (1993).

At the combustor exit, spatially averaged NO/NOx concentrations are lower than the equilibrium values, and decrease when the overall Air-Fuel-Ratio is increased (Figure 4.17 (a)). At a pressure of 1 bar the exit NOx level is higher that NO level, while at elevated pressure of 4 bar there is little difference between NO and NOx. The NOx is strongly affected by air inlet temperature - higher temperatures enlarge the hot region inside the combustor and enhance NO/NOx formation. A similar trend has been reported by Roffe and Venkataramani (1978), Correa (1993) and Drennan et al. (1993). The pressure exponent dependence of exit NOx concentration at AFR=45 agrees to the figure of 0.5, however such dependence is weaker at richer conditions.

4.3.5 Correlation of scalars with local mixture fraction

It is suggested that in the gas turbine combustion chamber the fuel breakdown reactions seem to be physically rather than kinetically limited (Jones and Toral (1983)). It is likely that laminar flamelet may exist in the combustor flow field where the combustion features a non-premixed mode. There is however no experimental evidence confirming such existence, mainly due to the lack of instantaneous mixture fraction distributions. The limited data from the present study, for example the time-averaged temperature, CO_2 and mixture fraction profiles at the dilution station, may indicate the scalar state relationships even though such relationships are more meaningful based on the construction of instantaneous data. State relationships for both temperature and carbon dioxide vs mixture fraction, based on measurements, are compiled in Figures 4.18 (a), (b) and 4.19. They are compared with both equilibrium and laminar flamelet profiles, the latter is constructed from stretched laminar flame predictions of counter flow diffusion flame with strain rate 100 1/s (the details of such calculations are discussed in Appendix E: Kerosine-air reaction prediction). Since the flamelet calculations are evaluated in terms of instantaneous properties whilst the experimental data are time-averaged, there will be some degree of discrepancy in the comparison due to the scalar fluctuation.

The carbon dioxide and mixture fraction measurements show an encouraging consistency with flamelet description at Air-Fuel-Ratio 45 (Figure 4.19 (a)). Certain degree of scatter may be caused by the scalar fluctuation which has not been represented by the measurements. The effect on CO_2 by hydrodynamic stretch has been demonstrated by Liew (1985) in diffusion flame predictions where higher strain rate can suppress burning significantly, thereafter, result in lower CO_2 concentration. Local stretches in the flow field are not uniform and such scatter may be inevitable, even for instantaneous data correlations. Similar to the CO_2 concentration, temperature and mixture fraction correlation based on measurements show broadly consistency with the flamelet calculation, with some data points scatter further away from the main

correlation. While the stretch has a larger influence on temperature than gaseous species, for example CO and CO_2 (Liew (1985)), which may explain the greater degree of scatter, uncertainties related to sampling techniques and flow condition variation can also make contributions. It is not possible from the present study to separate all these factors, ie. scalar fluctuation, flow field stretch and experimental uncertainty, in the combustor flow field.

At richer operating condition of AFR=28 (30), the relationships of both temperature and carbon dioxide concentration are less consistent with laminar flamelet description. Experimental results at conditions of overall AFR=23.7 without air preheating, as reported by Jones and Wilhelmi (1989), indicated that in propane-fuelled combustor the functional relationship between gaseous species, such as unburned fuel C_3H_8 and CO, and mixture fraction is only very weakly dependent upon strain rate. They speculated that the only way a laminar flamelet description can be reconciled with measurements is if it is presumed that local strain rates are sufficiently large to suppress burning completely for a fraction of the time in the fuel rich regions. It should be emphasised that at these conditions which are richer than operation the combustion zone has extended beyond the primary zone as the mixture fraction profiles show in Figure 4.5. The higher scalar fluctuation due to the increased combustion generated turbulence may contribute to the large scatter in the scalar state relationships at AFR=28 (30). On the other hand, flow conditions may have profound influence on the combustion, for example Bicen et al. (1990) suggested that with the air preheated to the temperature of 523 K, the kinetic limitation on the propane-air combustion inside a combustor can be reduced and conserved scalar approach may be appropriate. It is important to distinguish between the turbulence effect, represented by the scalar fluctuation, and the detailed combustion process (such as the controlling steps by either chemical reaction or physical mass diffusion) in clarifying the applicability of the conserved scalar/laminar flamelet approach in gas turbine combustions.

The time averaged temperature-mixture fraction correlations from jet flame data in Figure 4.18 (c) give a well defined relationship. The combustion in the downstream regions (260-406 mm from the fuel source) of the pre-vaporized kerosine jet flame is characteristically similar to that in a fire (Young (1993)). Its local reaction zones should be essentially laminar-like, with limited small-scale interaction between the turbulence and microscopic molecular processes. Fire-like jet flames have generally modest strain rate as suggested by Bilger (1977 a). The consistency of time-averaged measurement with a laminar flamelet description in Figure 4.18 (c) from the jet flame may imply a low degree of both hydrodynamic stretch and turbulent fluctuation. The same feature is also illustrated in the next soot volume fraction-mixture fraction correlations.

The correlations of soot volume fraction f_v vs mixture fraction ζ from both this combustor and in jet flames (Young (1993)) are illustrated in Figure 4.20. The non-premixed kerosine jet flame exhibits a more or less linear state relationship between f_v and mixture fraction at each vertical position as displayed in Figure 4.20 (b). Results from a liquid pool fire (Koylu and Faeth (1991)) also generates a largely linear relationship between f_v and ζ. The measurement in the combustor however does not show a clear functional curve. In non-premixed flames, as in the cases of jet flames and gas turbine combustions, universal state relationship may only exist when the mixing rate is much lower than the reaction rate, or the Damköhler number (the ratio of the two rates) is larger. The situation in the combustor is generally quite different from that in the jet flame in relation to the mixing-reaction process.

The turbulent jet flame fuelled by vaporised kerosine has the similar characteristics of the buoyant fire where the mixing time is comparatively longer than the reaction time. Soot formation involves finite chemical kinetics, and the soot volume fraction in turbulent jet flames has been found dependent on the residence time in the lower flame regime but dependent in the upper regime where soot oxidation is dominant (Kent and Honnery (1987)). Kent and Bastin (1984) reported measurements concerning effects of residence time on soot concentrations in a turbulent acetylene-air diffusion flame. They observed that at large residence times, soot volume fractions exhibited relatively little change at fixed positions. As the residence time was reduced, this plateau condition eventually ended and a regime was reached where further reductions in residence time caused a progressive reduction in soot volume fractions. A similar independence has also been reported by Koylu and Faeth (1991) where the residence time is much longer (>200 ms) than that in a gas turbine combustor (typically of the order of a few milliseconds).

Because of the vigorous mixing occurring in the highly turbulent flow inside the combustor, the characteristic Damköhler number in relation to soot formation may not be as high as in the jet flames and the soot volume fraction-mixture fraction correlations in the combustor may not follow a universal relationship. The residence time dependence has been addressed by relating the soot formation rate, rather than the soot concentration, to local conserved scalar. This extended laminar flamelet concept has been used successfully in fires (Syed (1991)) and turbulent jet flames (Fairweather et al. (1992)) and will be applied to the combustor soot modelling in Chapter 6.

The elliptic flow in a typical combustor, including reverse recirculating flow and transverse jet penetrations, complicates the definition of the residence time and it is difficult to describe the soot-time history from the limited experimental data. Further more, soot formation

rate is kinetically controlled by temperature which in turn dependents on local conserved scalar, the scatter in the time-averaged temperature-mixture fraction correlations in Figure 4.19 (a) and (b) may partly explain the time-averaged f_v-mixture fraction correlations in Figure 4.20 (a) where no clear relationship between f_v and ζ exists. Uncertainties arising from experiments, for example the difference in sampling technique and instantaneous flow condition variation as discussed in Section 3.4.1, may also be responsible for the scatter in the f_v-mixture fraction correlations.

From the spatial profiles of mixture fraction, soot volume fraction and temperature an estimate of mass fraction of soot carbon generated from fuel carbon is shown in Figure 4.21, together with the generation factor of carbon dioxide from fuel carbon in the dilution station. It is clear that most of the carbon is turned into CO_2, over 95% in the centre part of the combustor, and only a few percent is converted to particulate soot. The positions of maximum soot conversion at all the flow conditions are shifted from where the peak soot volume fractions locate. The 70% mass fraction of soot carbon from fuel carbon in kerosine, burning in a confined jet flame, indicates poor fuel-air mixing (Young (1993)). Their better mixing in the combustor substantially reduces the soot levels there. The maximum 3.4% appears at AFR=28 and 1 bar and the rest are below 1%, a moderate level at such low power flow conditions compared with the 5% at high pressure, high temperature conditions (Tilston (1992)). It is difficult from the curves to draw a clear trend from lean to rich conditions, or from low to high pressure conditions. For various AFRs, rich mixtures tend to promote soot formation, so local f_v and ζ both increase. At the elevated pressure, the mixture fraction profiles do not change as much as those of f_v do, thus the profile is more f_v dependent. The figures in terms of absolute percentage in the present study are however considered only qualitatively informative given the uncertainties related to the flow condition repeatability and local flow field variations caused by the two different probing techniques, where nitrogen purge was used for soot volume fraction and the 'opposite' gas suction was used for mixture fraction measurement.

Aviation fuel normally contains a blend of hydrocarbons including paraffins, naphthenes, aromatics and limited proportions of olefins. In laminar diffusion flames, smoke point measurements suggest a trend to increasing propensity to soot of the form (Schalla and Hibbard (1959))

paraffins < olefins < acetylenes < aromatics < naphthalenes.

The above general trend has been supported by the experimental results in a model gas turbine combustor (Bowden and Pearson (1984)). It is however not possible from the limited data to identify which constituent in the kerosine is the major contributor to the soot formation at the present low conversion rate of fuel carbon to soot. Such identification may point out the

relative importance of these various hydrocarbon constituents in soot formation and thus highlight the sooting tendency of fuel with varying hydrocarbon structure.

4.4 CONCLUSION REMARKS

In addition to soot volume fraction measurements, a data set for the gaseous species properties at the dilution zone station have also been obtained to aid interpretation of soot production in the gas turbine combustor. The present experiments conducted in the SNECMA designed tubular combustor suggest the following:

(1) At representative gas turbine operating conditions (AFR near 45), the mixture fraction distribution at the dilution zone does not change in either the profile or peak value at atmospheric and elevated pressures up to 4 bar. The maximum mean values are below stoichiometric. Under this condition soot formation may not occur down stream from the dilution zone which confirms that f_v in the dilution zone may be a direct indicator of exhaust smoke levels.

(2) The CO_2 conversion rate is high in centre part of the combustor owing to the effective mixing, in the region of dilution air penetration and film cooling the reaction is quenched and the conversion rate drops. Temperatures at 4 bar are higher than at 1 bar, the physical mixing and chemical reaction are strongly influenced by pressure. The increased temperature also benefits from less thermal radiation loss from combustion products to the combustor liner.

(3) Conserved scalar approach to describe the scalar state relationships for the time-averaged CO_2 concentrations against mixture fraction present well defined functional curves at representative combustor flow condition. The relationships of temperature vs mixture fraction exhibit more scatter in the correlation. Scalar fluctuations may have profound influence in these relationships which are based on time-averaged measurements. Instantaneous properties are clearly required to validate the laminar flamelet concept in the gas turbine combustion. The detailed profiles of scalar dissapation rates in the combustor flow field may also influence the correlations. Correlations of soot volume fraction with mixture fraction do not show a clear relationship, mainly due to the highly turbulent and three dimensional flow field.

(4) The level of soot carbon converted from the carbon element in kerosine is typically below 4% locally. The peak position of the conversion is shifted relative to the f_v peak

position. The low conversion rate reflects the good mixing characteristics of this combustor.

(5) Aside from the soot formation, additional NOx measurements show that the pressure exponent dependence ($\sim P^{½}$) of NOx scales in this combustor is in close agreement with reported in the literature.

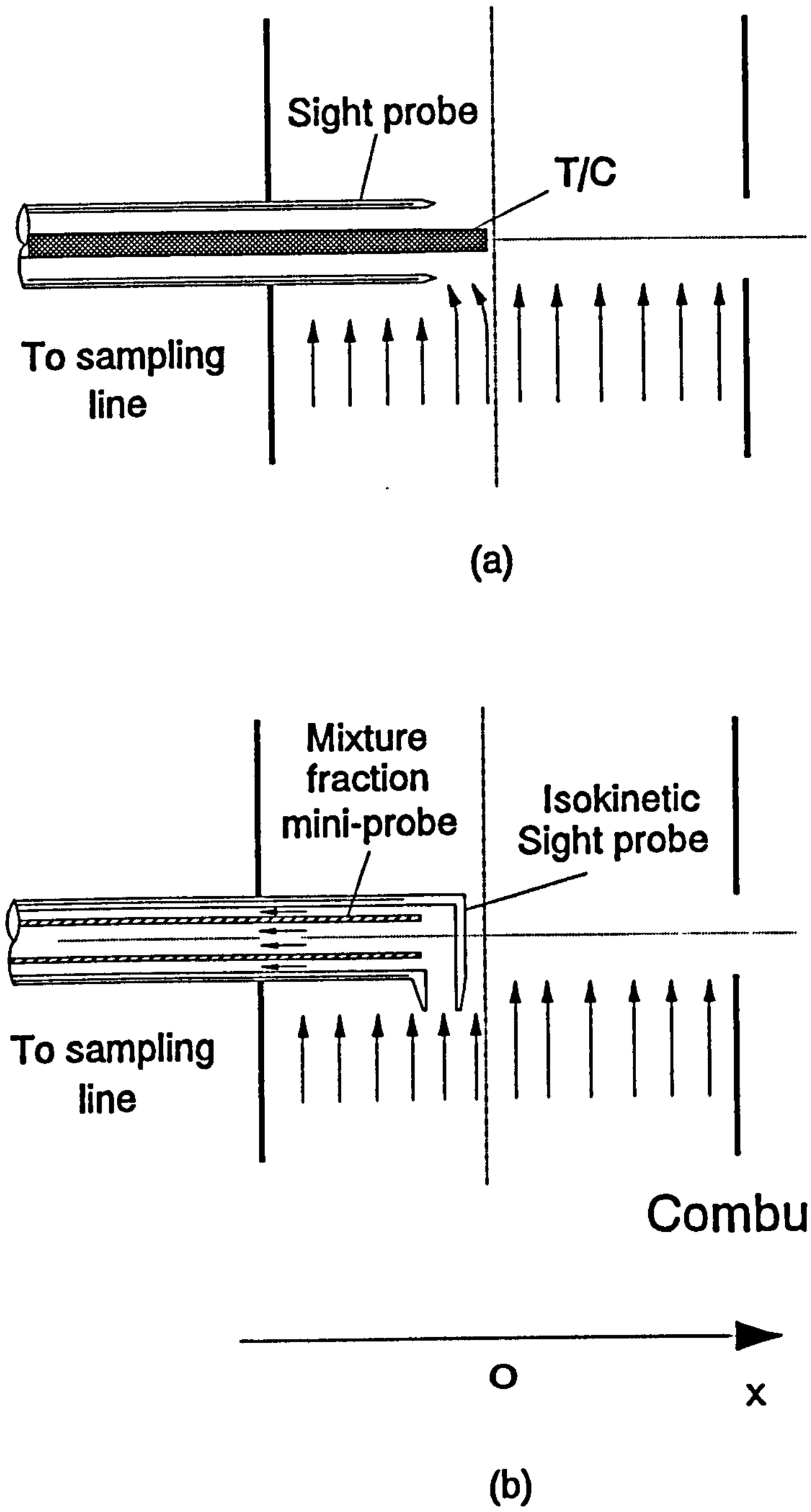

Figure 4.1 Gas sampling probes set up. (a) Original sight probe, with thermocouple, (b) Isokinetic probe, with mixture fraction miniature probe

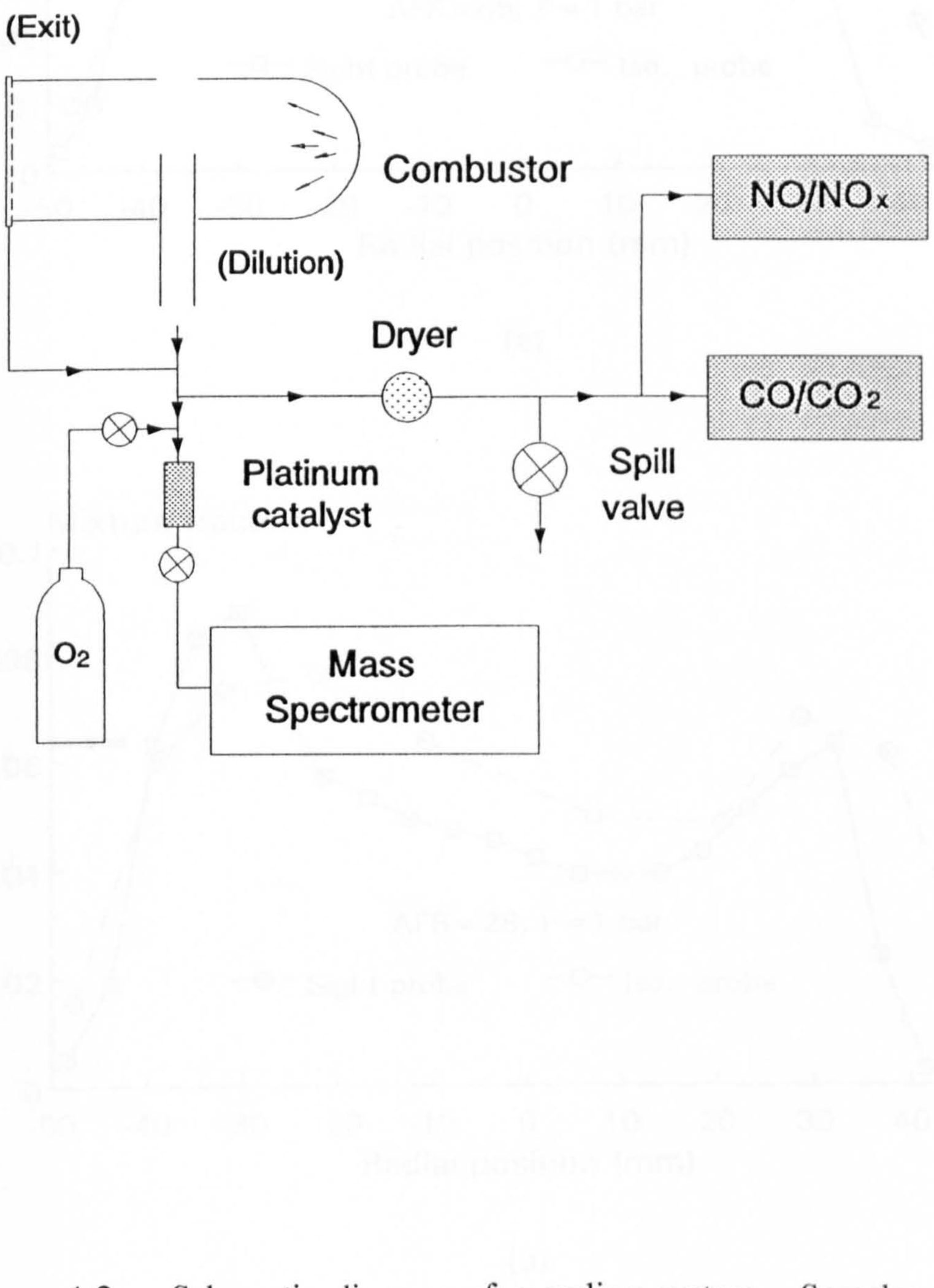

Figure 4.2 Schematic diagram of sampling system. Samples from dilution zone and exit plane were measured independently by switching on one of the lines.

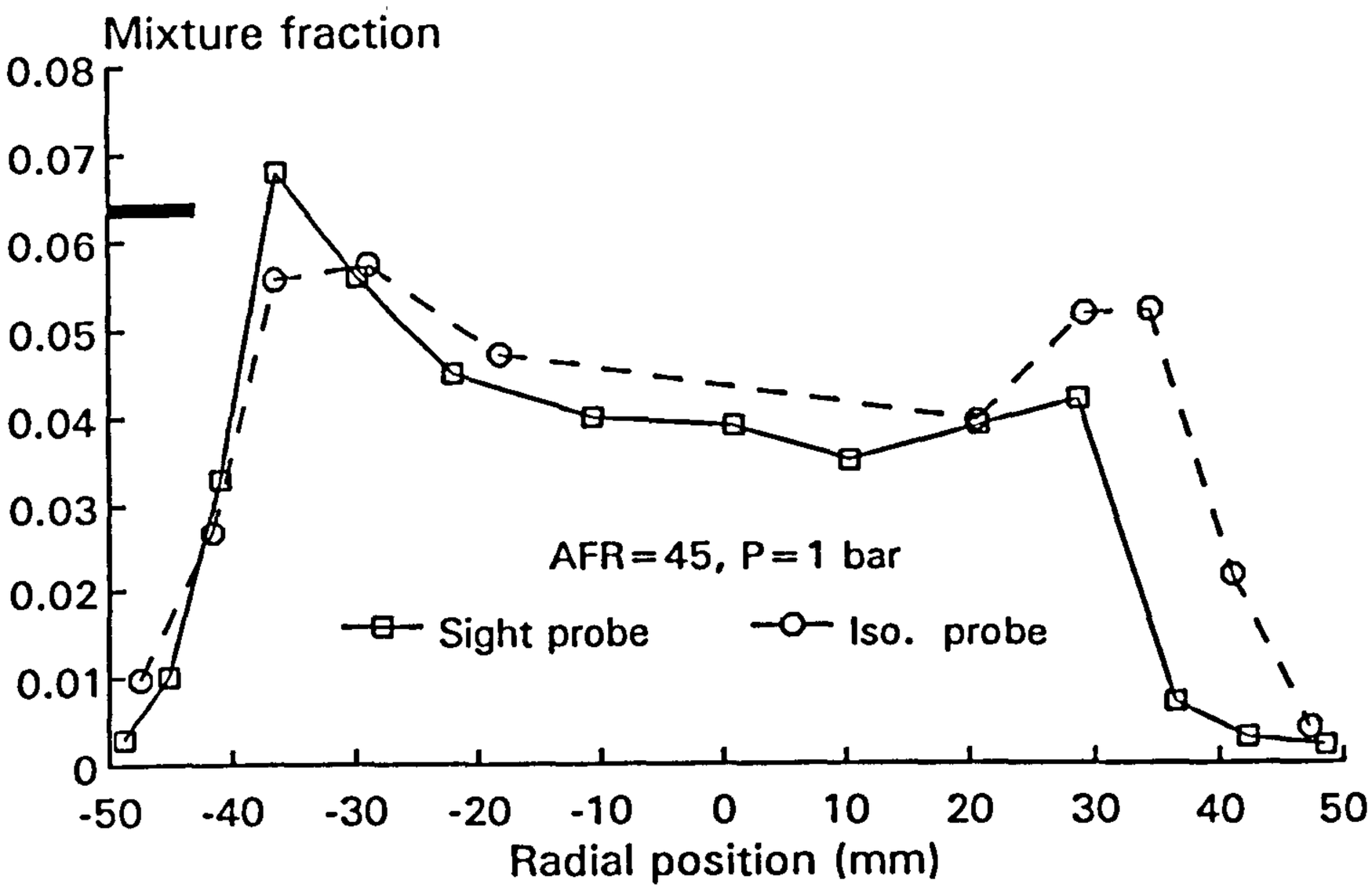

(a)

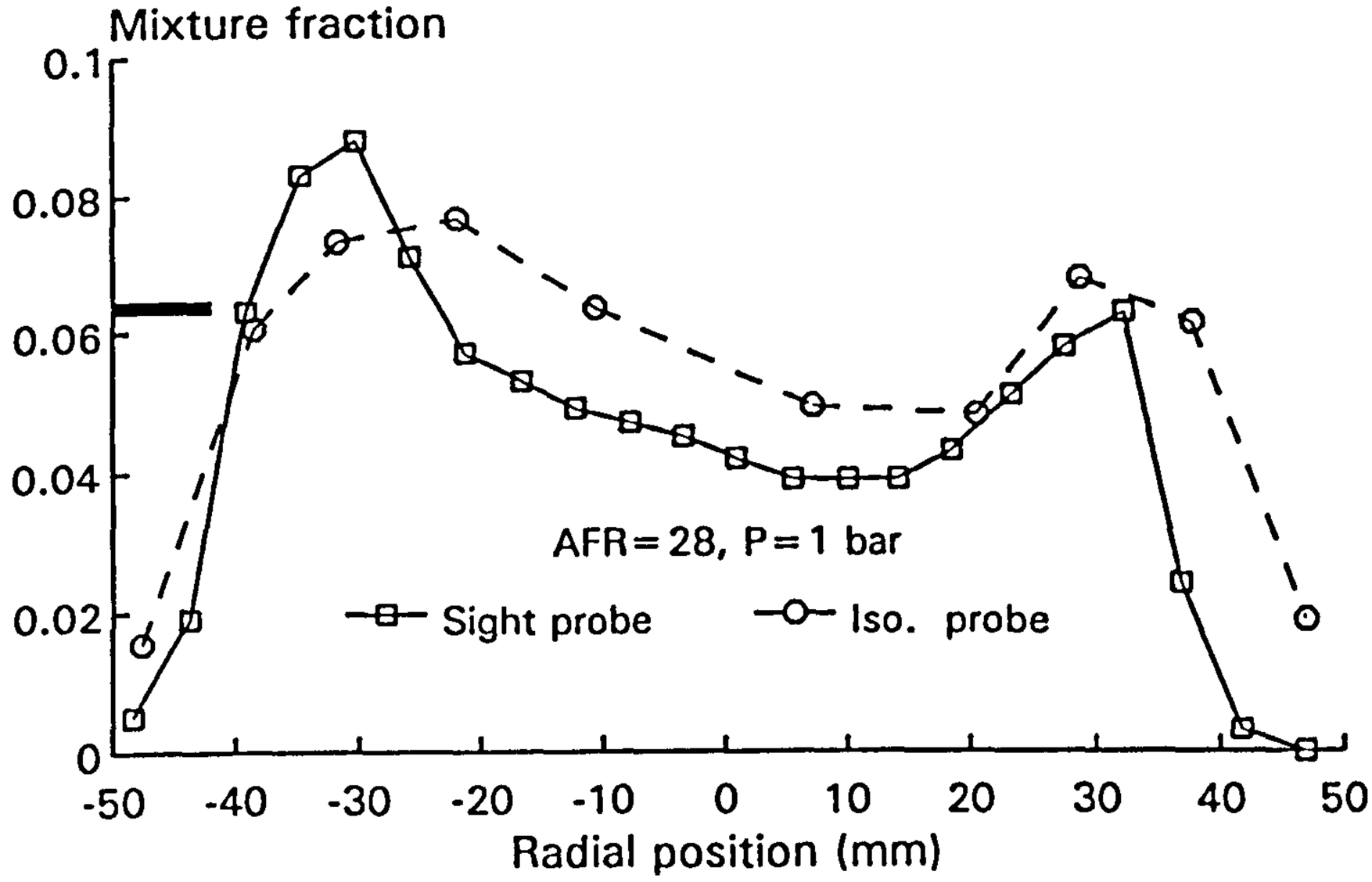

(b)

Figure 4.3 Comparison of mixture fraction measurements by sight and isokinetic probes, (a) AFR=45, P=1 bar; (b) AFR=28, P=1 bar. Highlighted bar indicates stoichiometric value

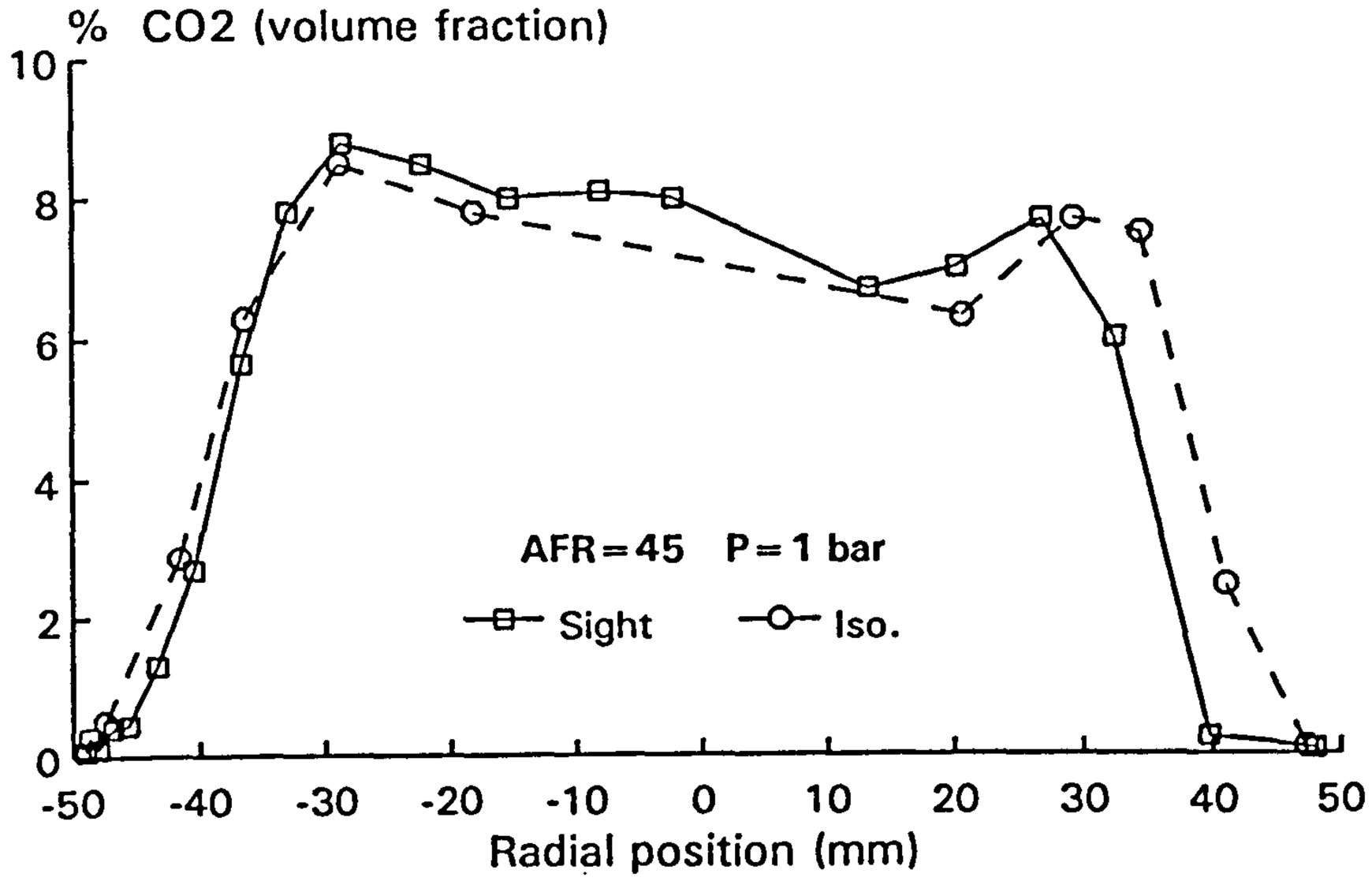

(a)

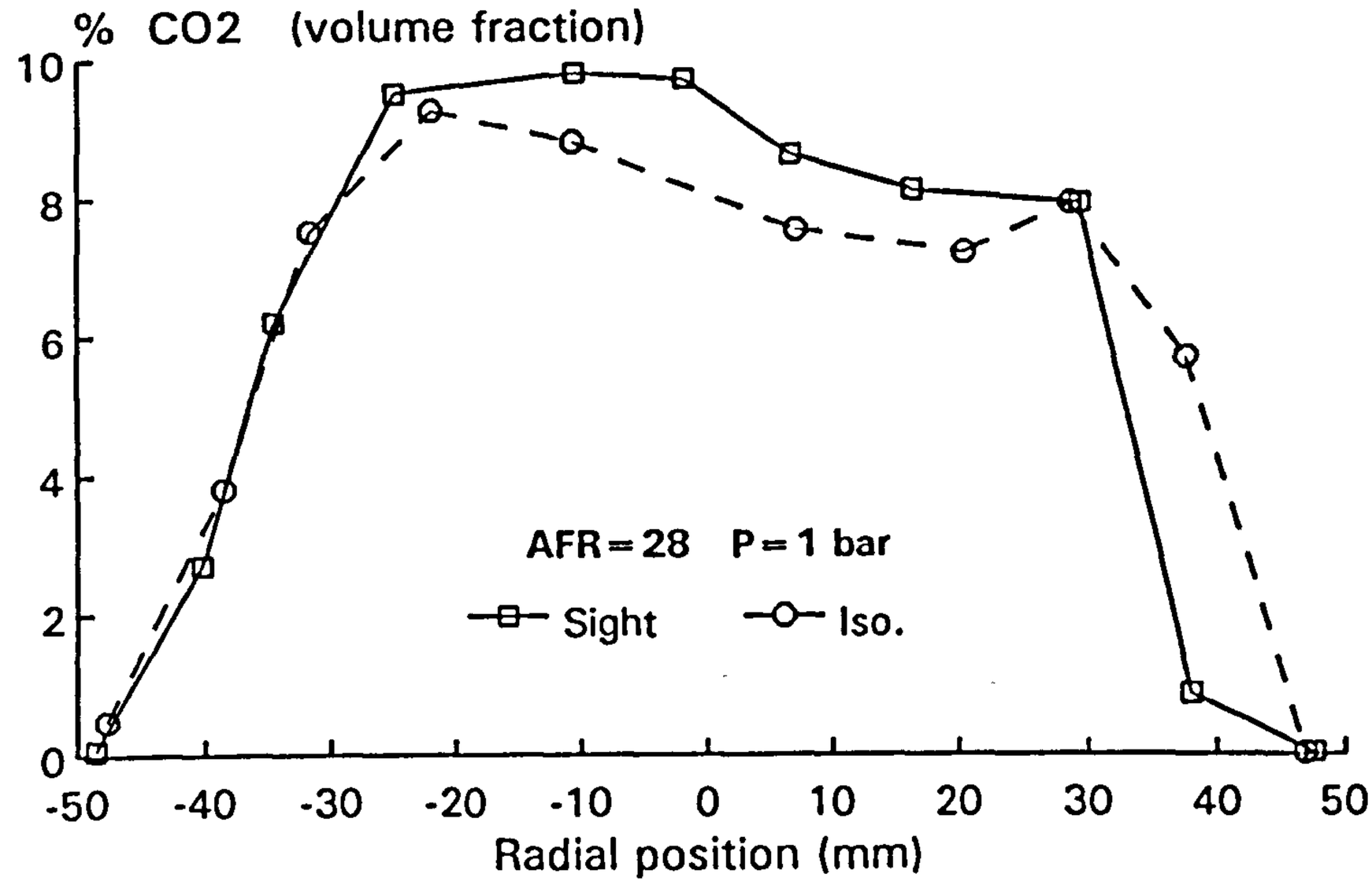

(b)

Figure 4.4 Comparison of carbon dioxide concentrations measured by sight and isokinetic probes; P=1 bar, (a) AFR=45, (b) AFR=28

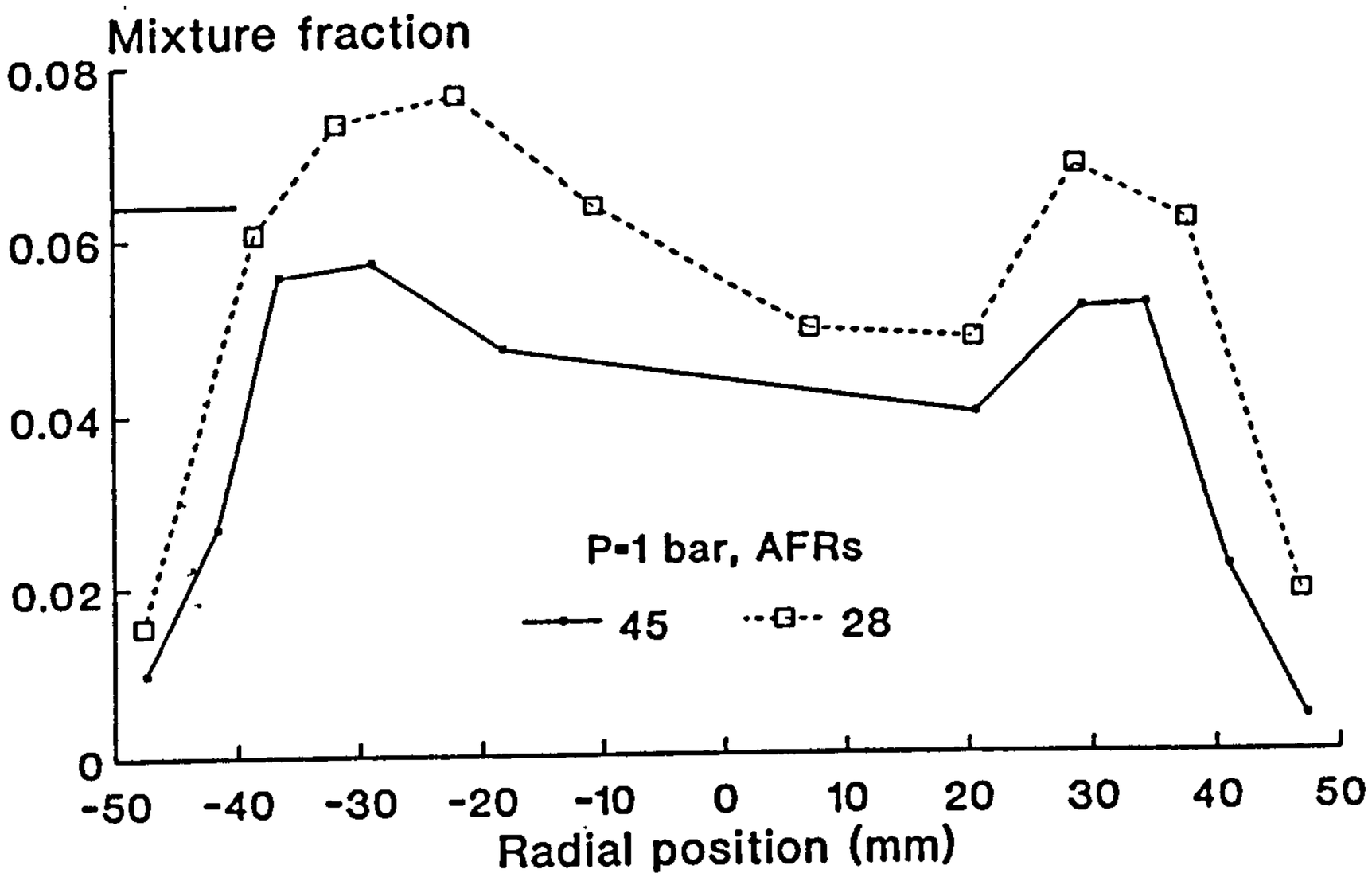

(a)

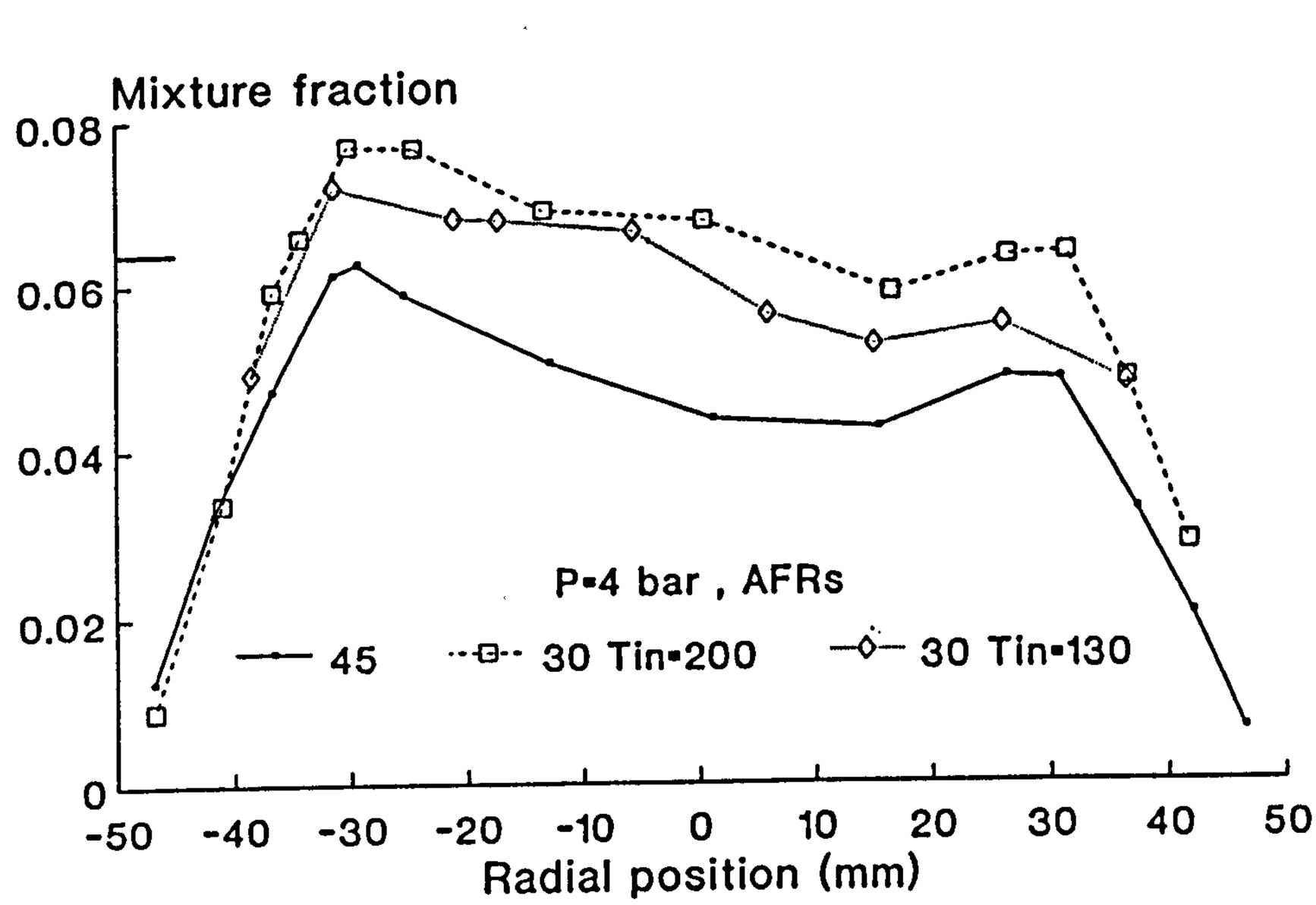

(b)

Figure 4.5 Mixture fraction distributions at different conditions. (a) AFR=45, 28, P=1 bar, (b) AFR=45, 30 (Tin=200, 130 °C), P=4 bar

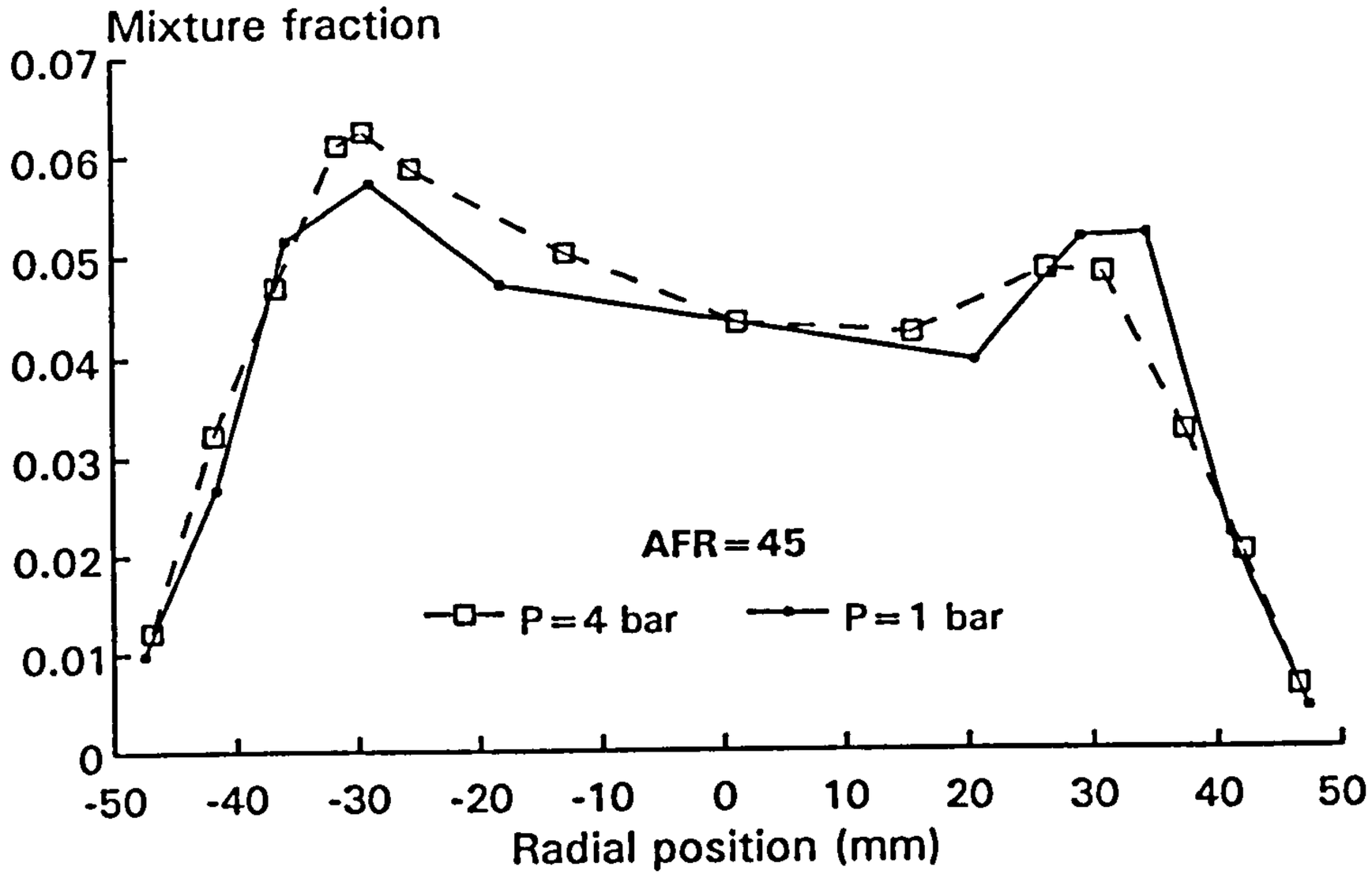

(a)

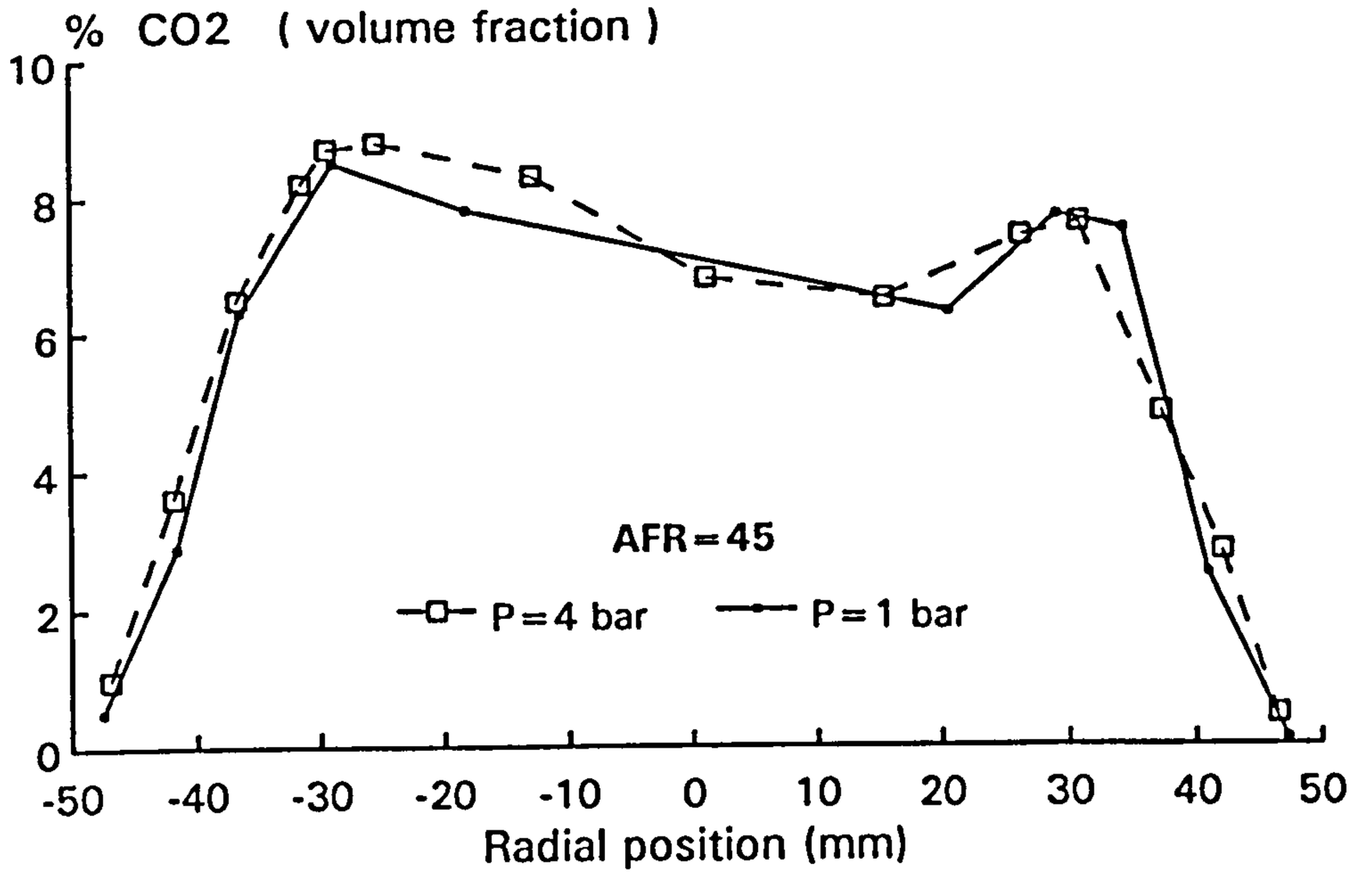

(b)

Figure 4.6 Comparison of: (a) mixture fraction, and (b) CO_2 distributions at AFR=45, P=1 and 4 bar

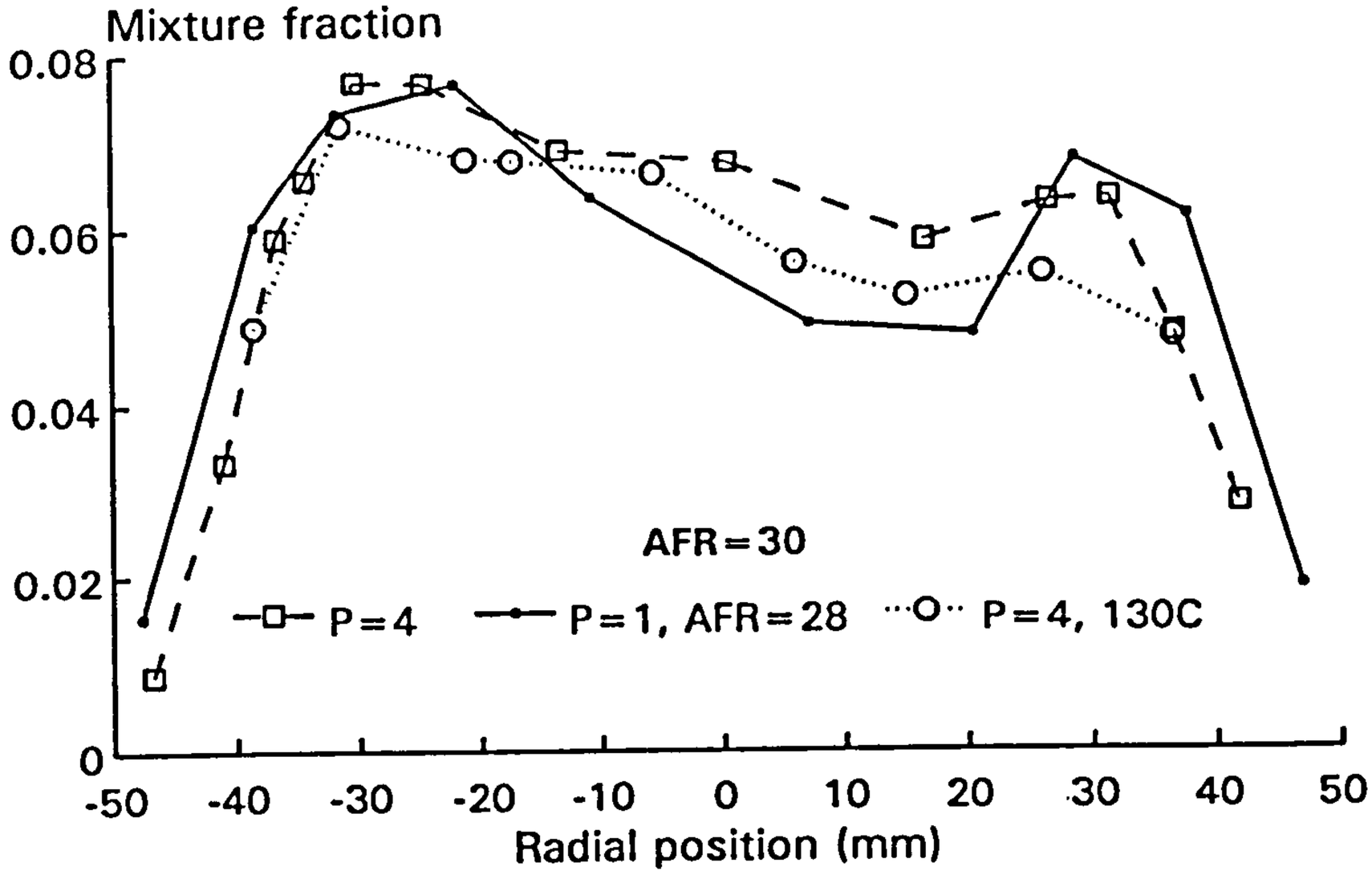

(a)

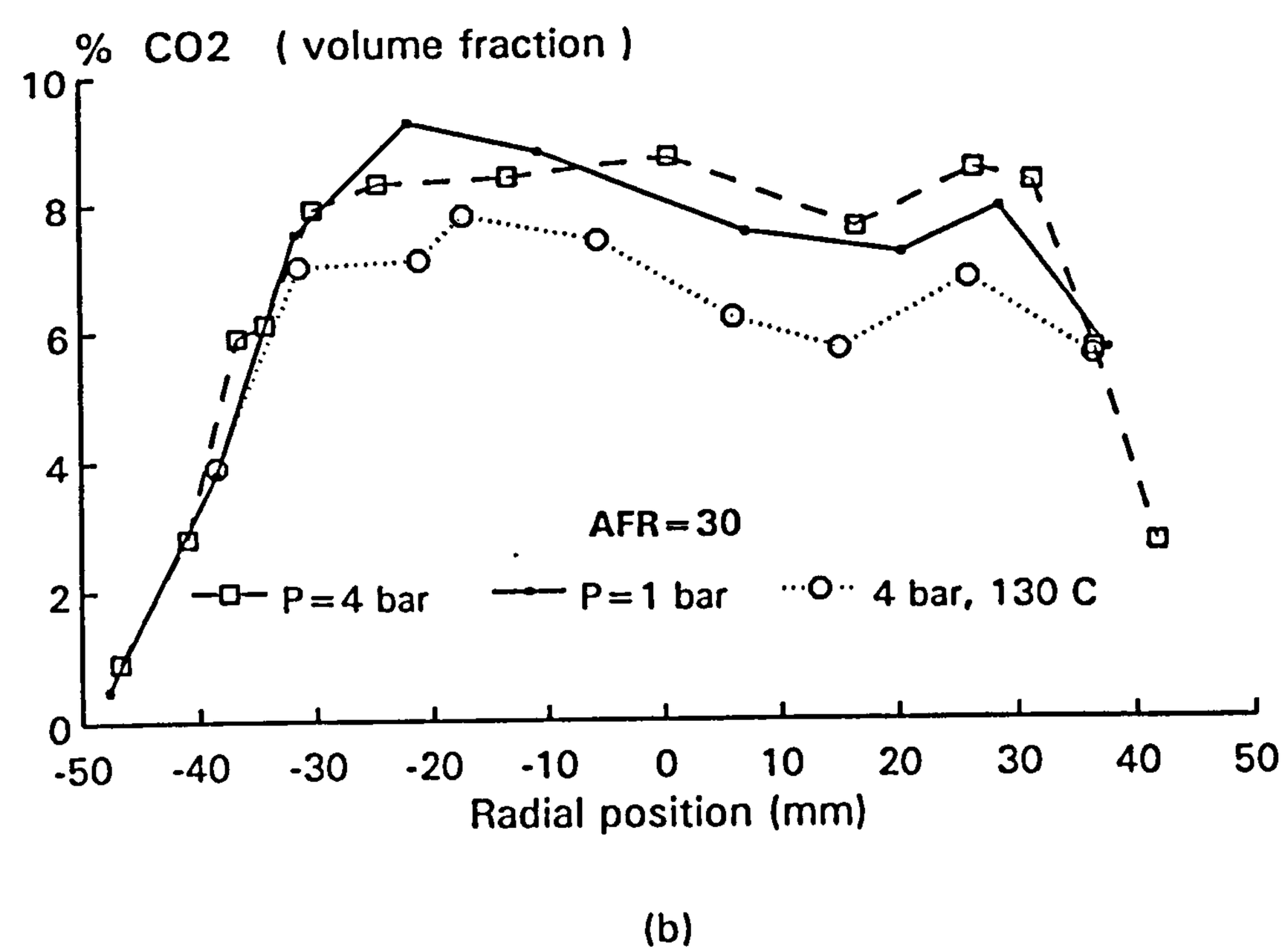

(b)

Figure 4.7 Comparison of: (a) mixture fraction, and (b) CO_2 distributions at AFR=30, P=1 and 4 bar

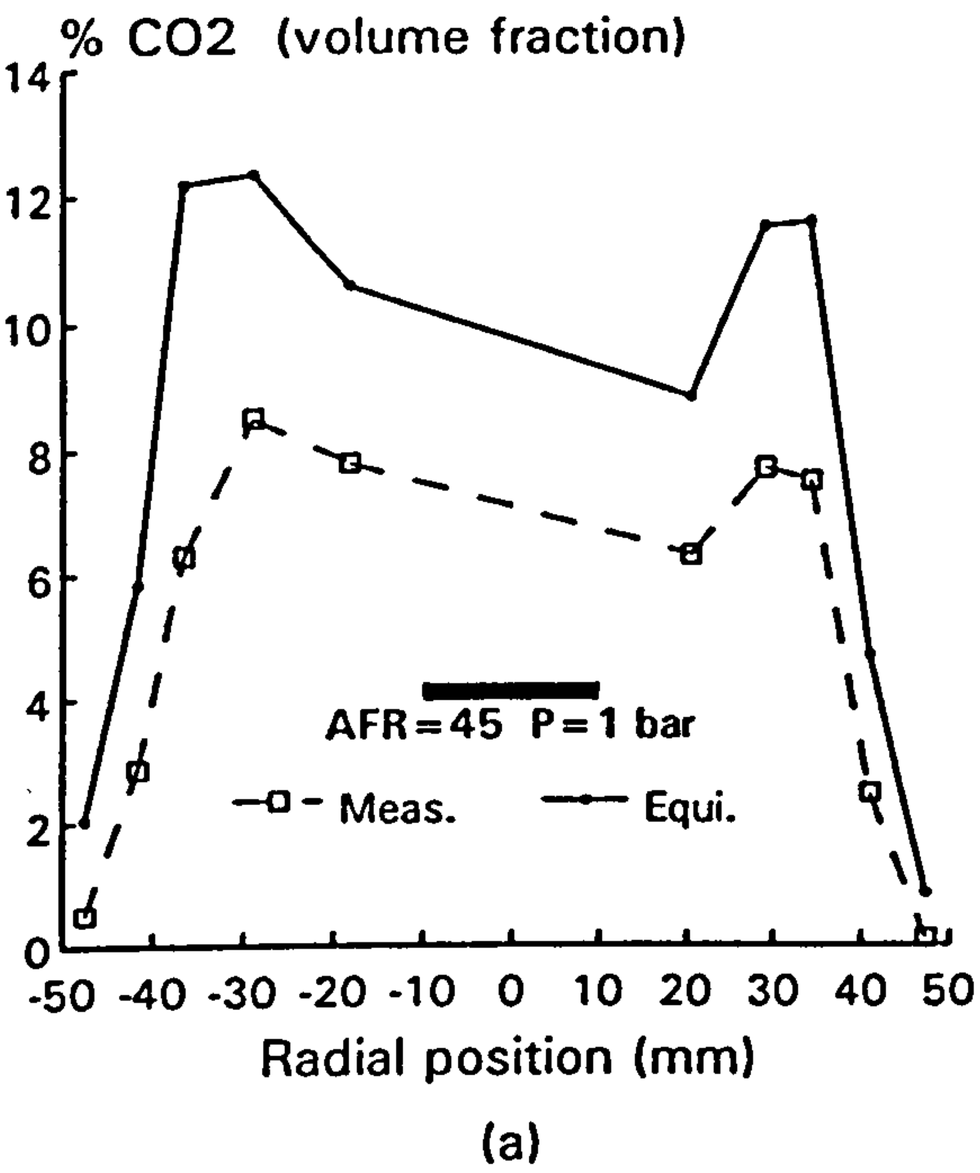

(a)

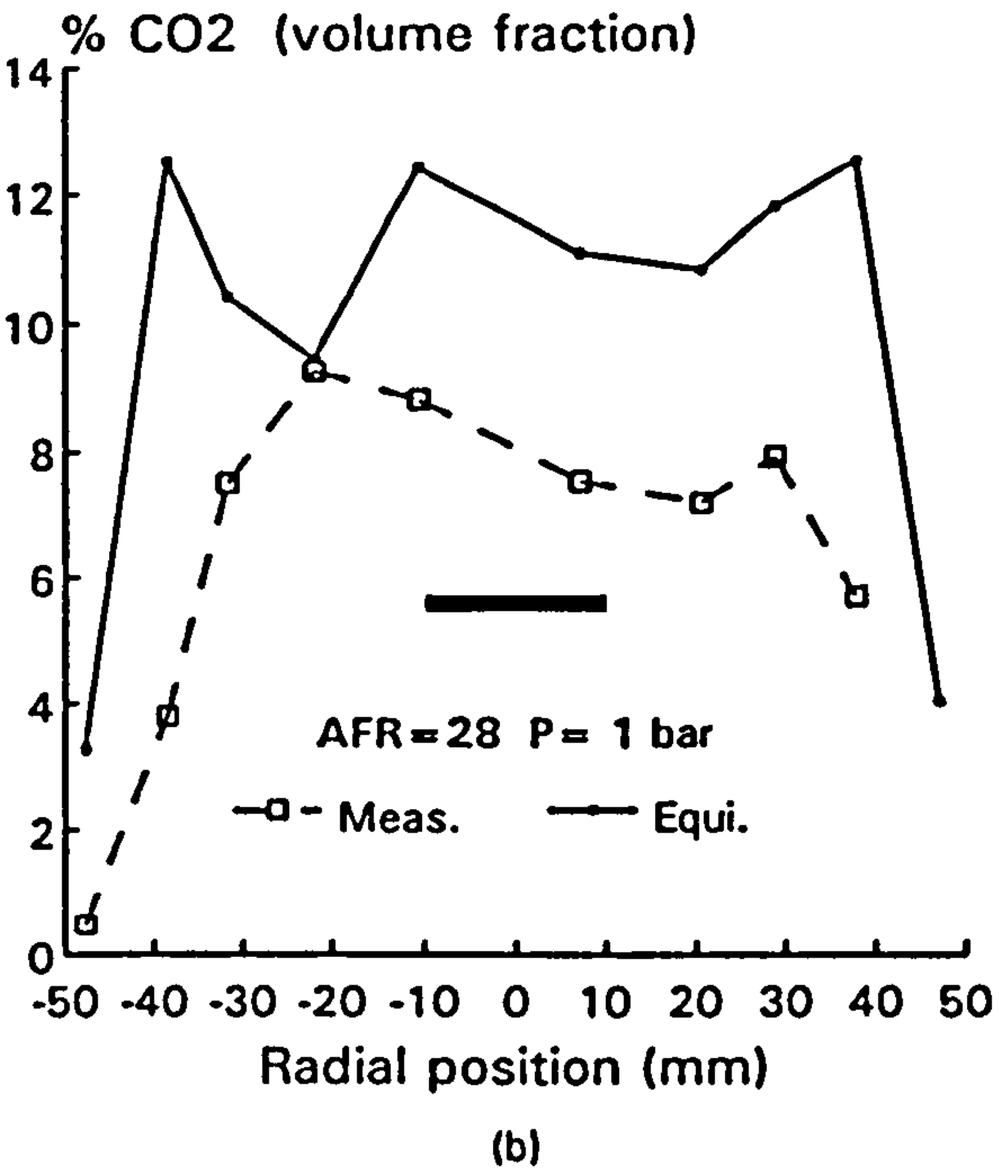

(b)

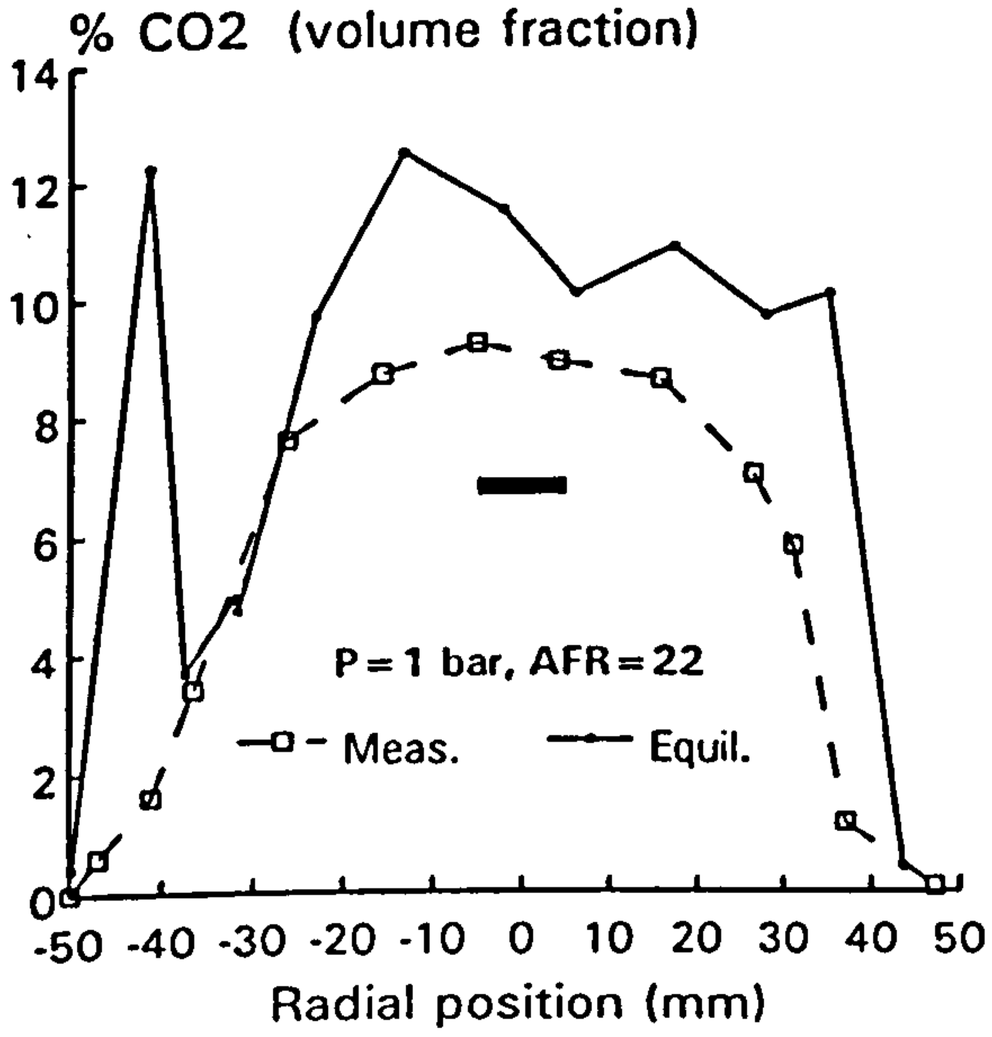

(c)

Figure 4.8 Carbon dioxide concentration profiles with comparison of equilibrium calculation; P=1 bar, AFR=45, 28, 22. (Exit CO_2 averaged concentration also shown)

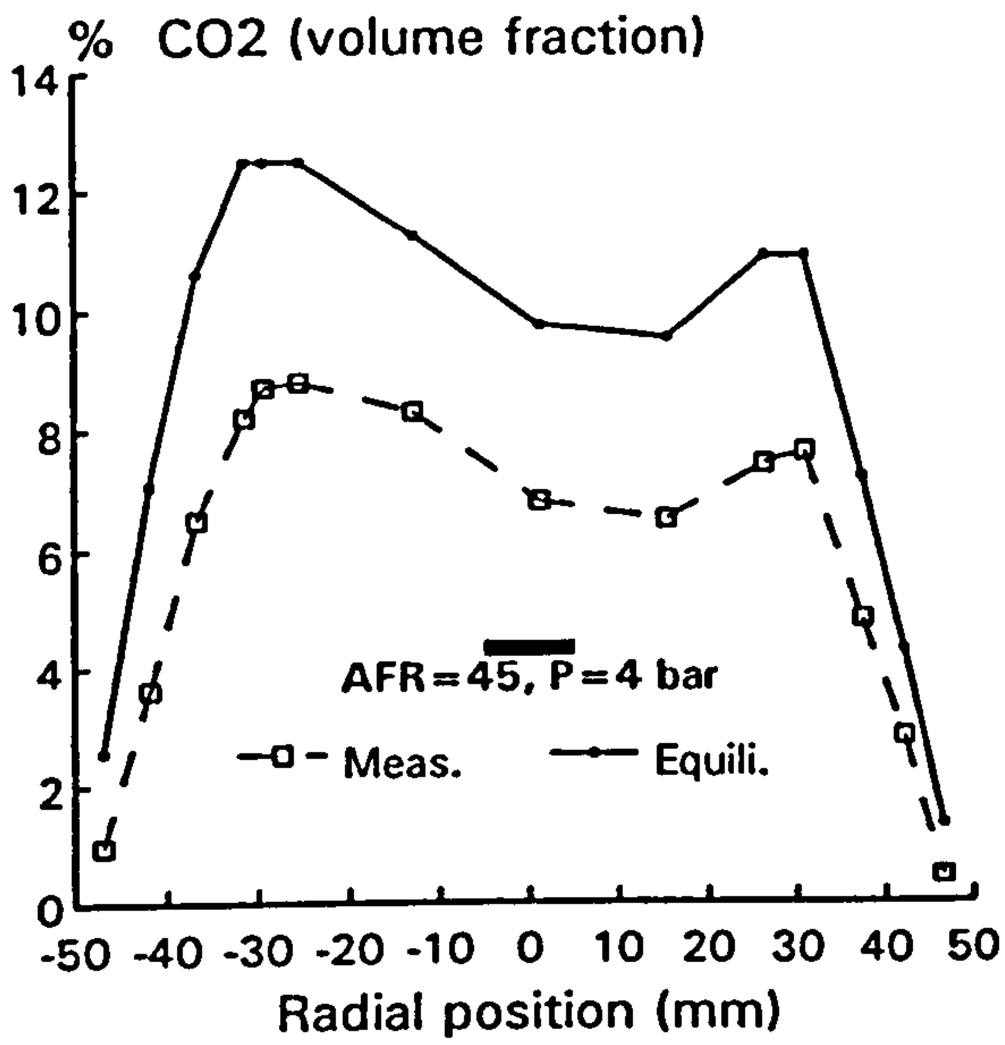

(a)

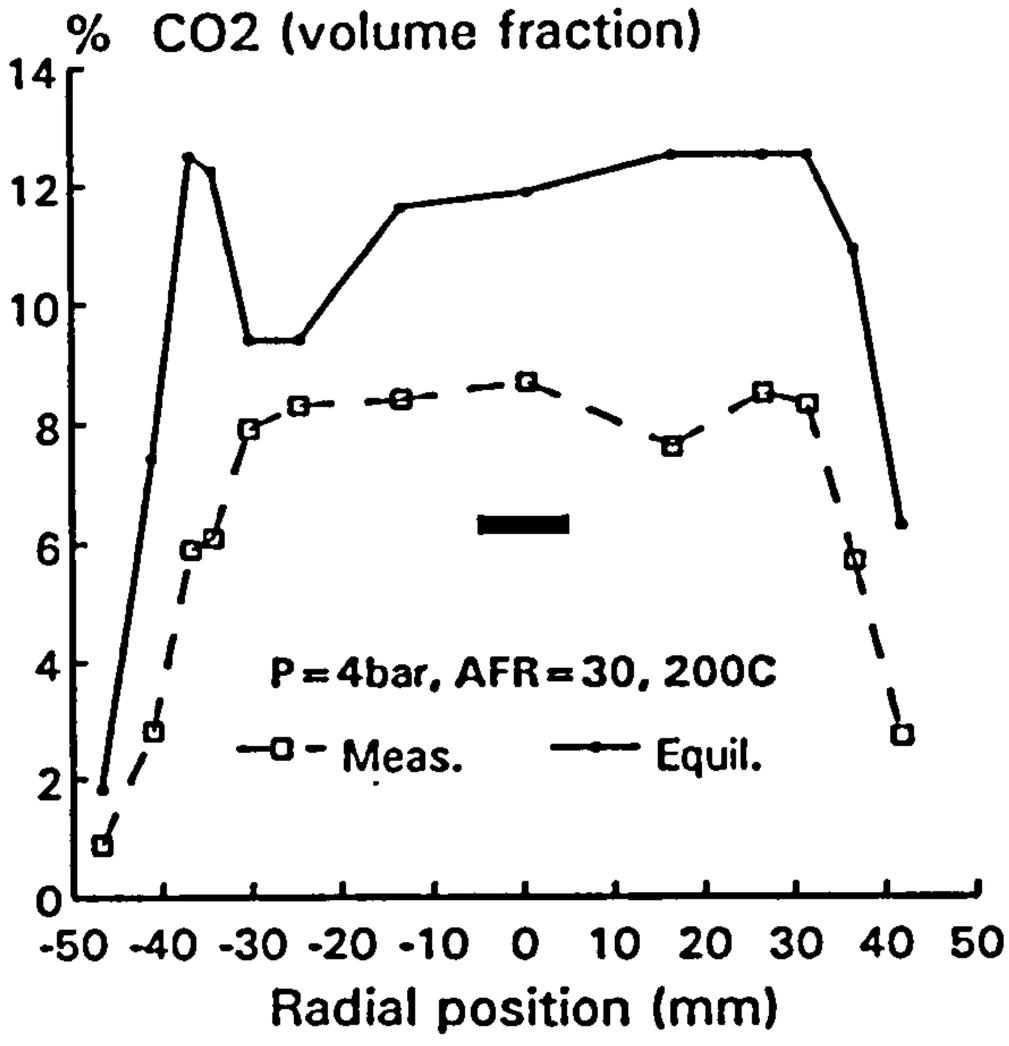

(b)

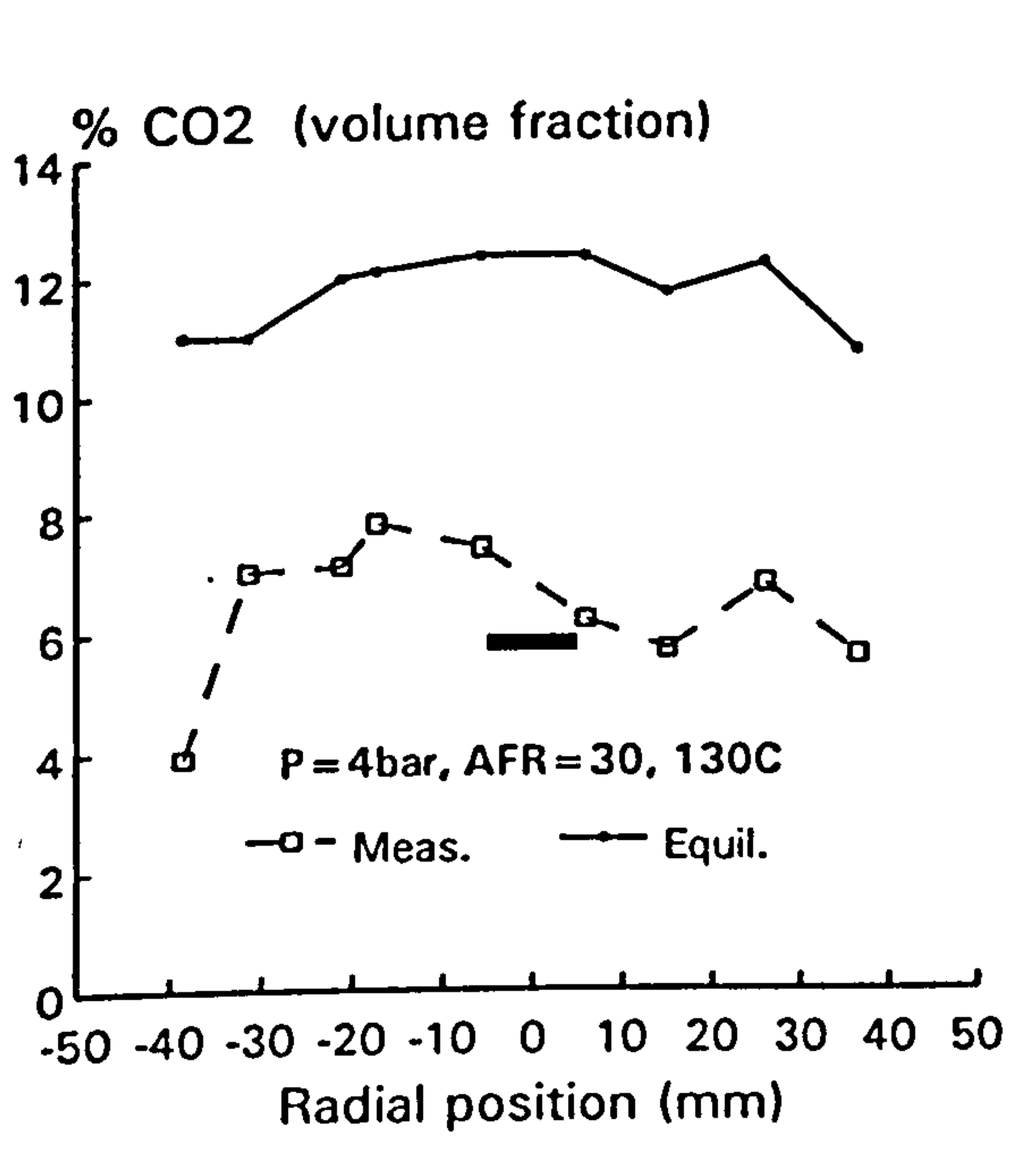

(c)

Figure 4.9 Carbon dioxide concentration profiles with comparison of equilibrium calculation; P=4 bar, AFR=45, 30. (Exit CO_2 averaged concentration also shown)

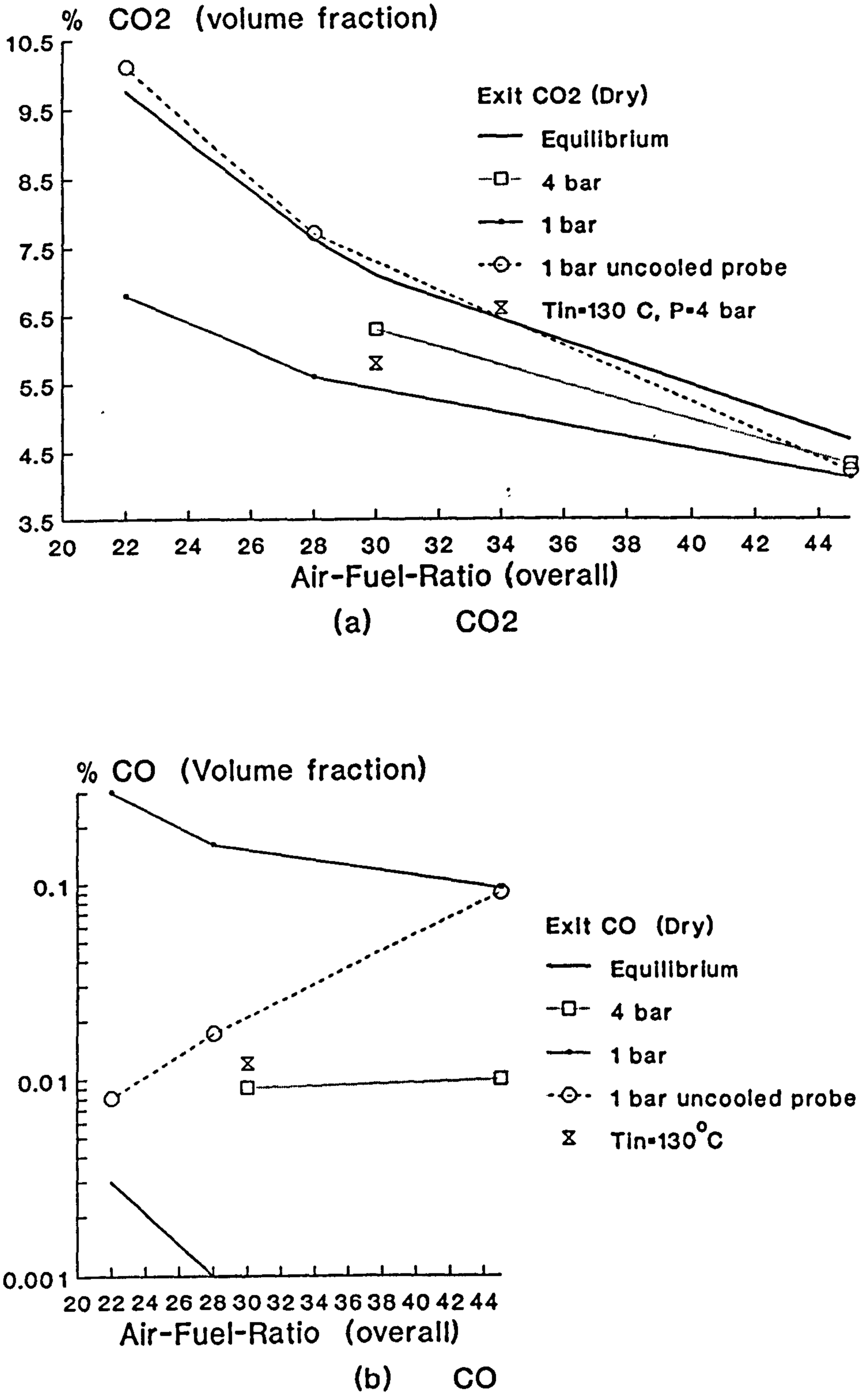

Figure 4.10 (a) Exit CO_2 and (b) CO averaged concentrations with comparison of equilibrium; also shown the results from uncooled probe

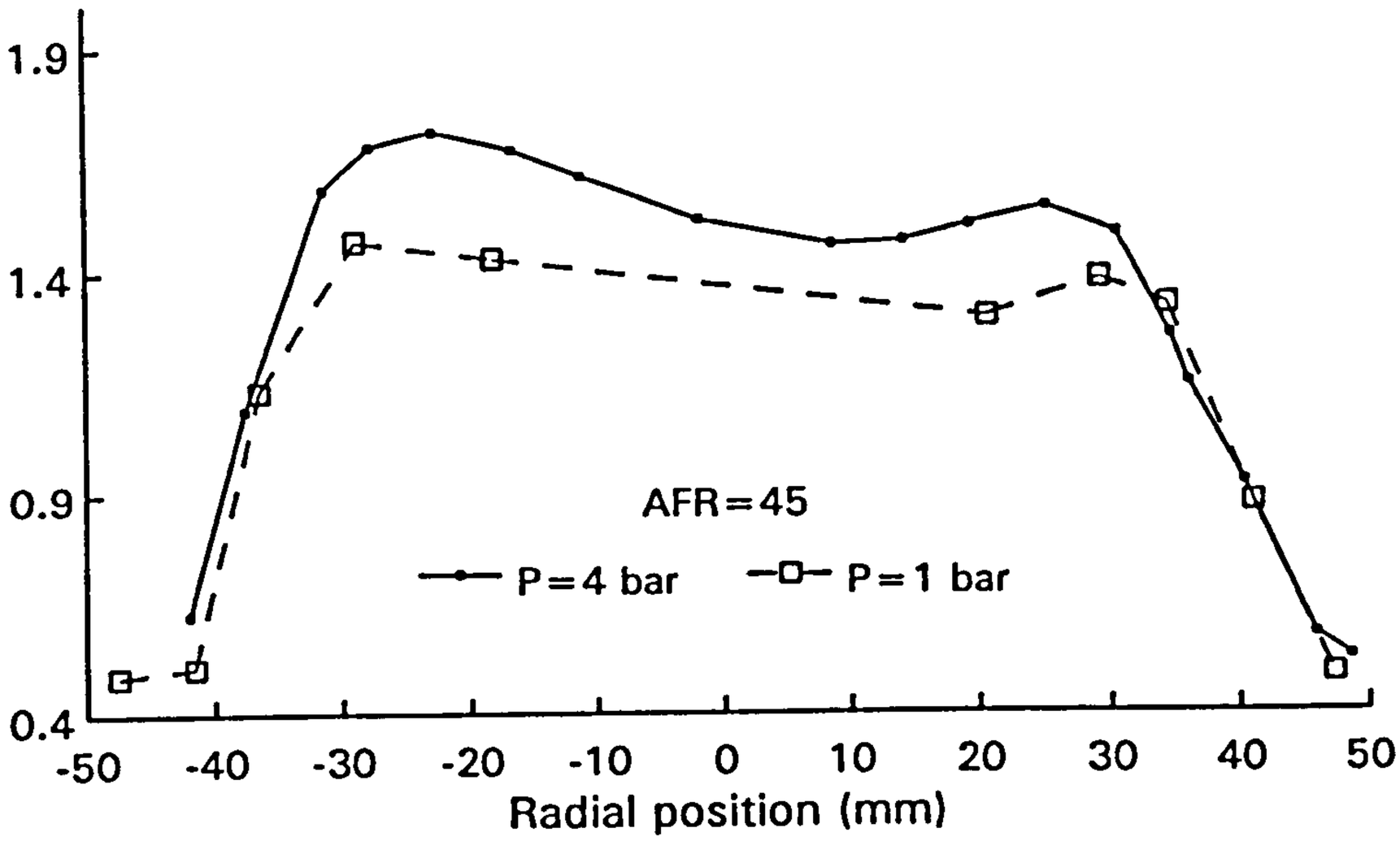

(a)

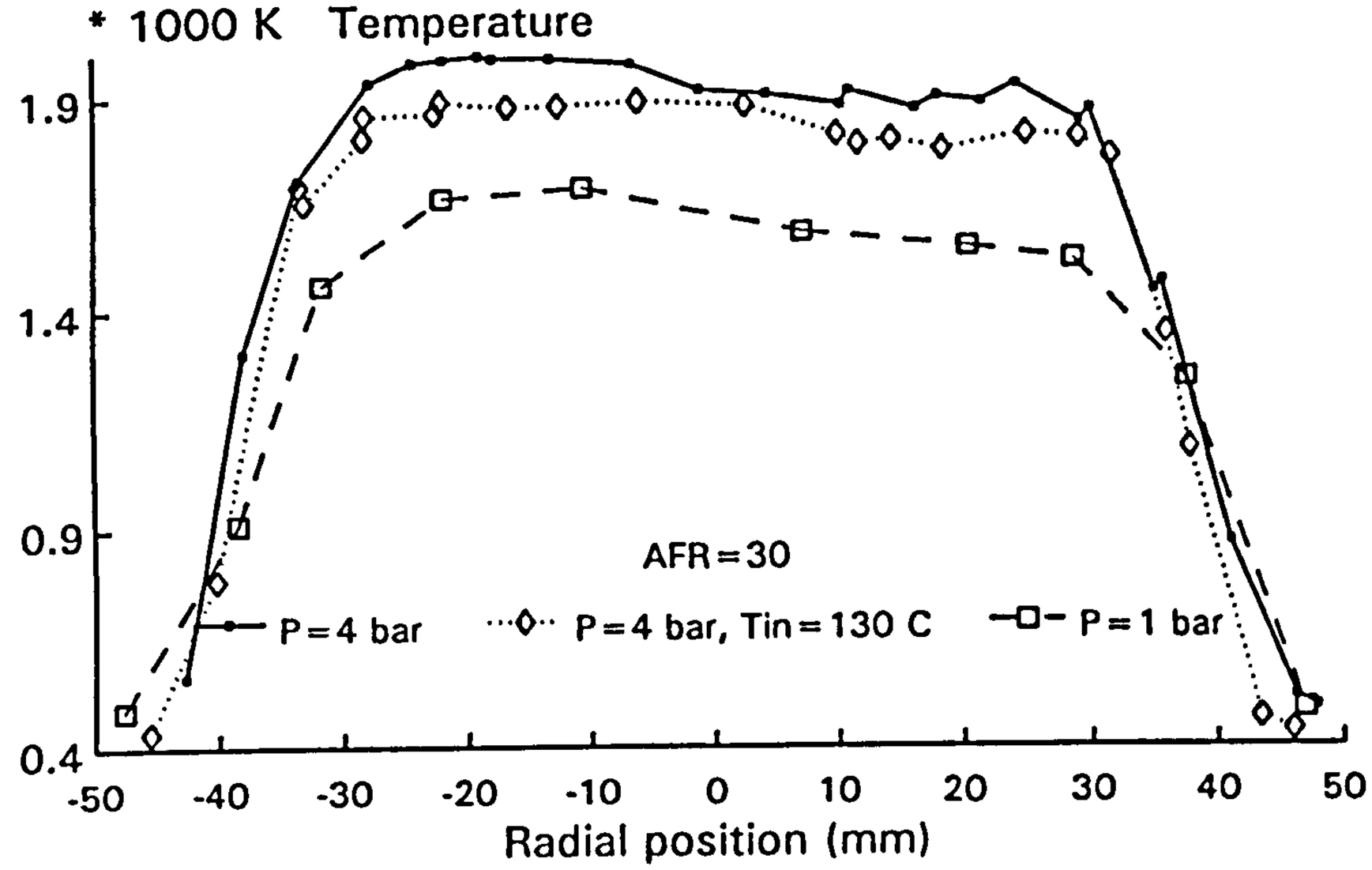

(b)

Figure 4.11 Comparison of temperature profiles at pressures 1 and 4 bar; (a) AFR=45, (b) AFR=30

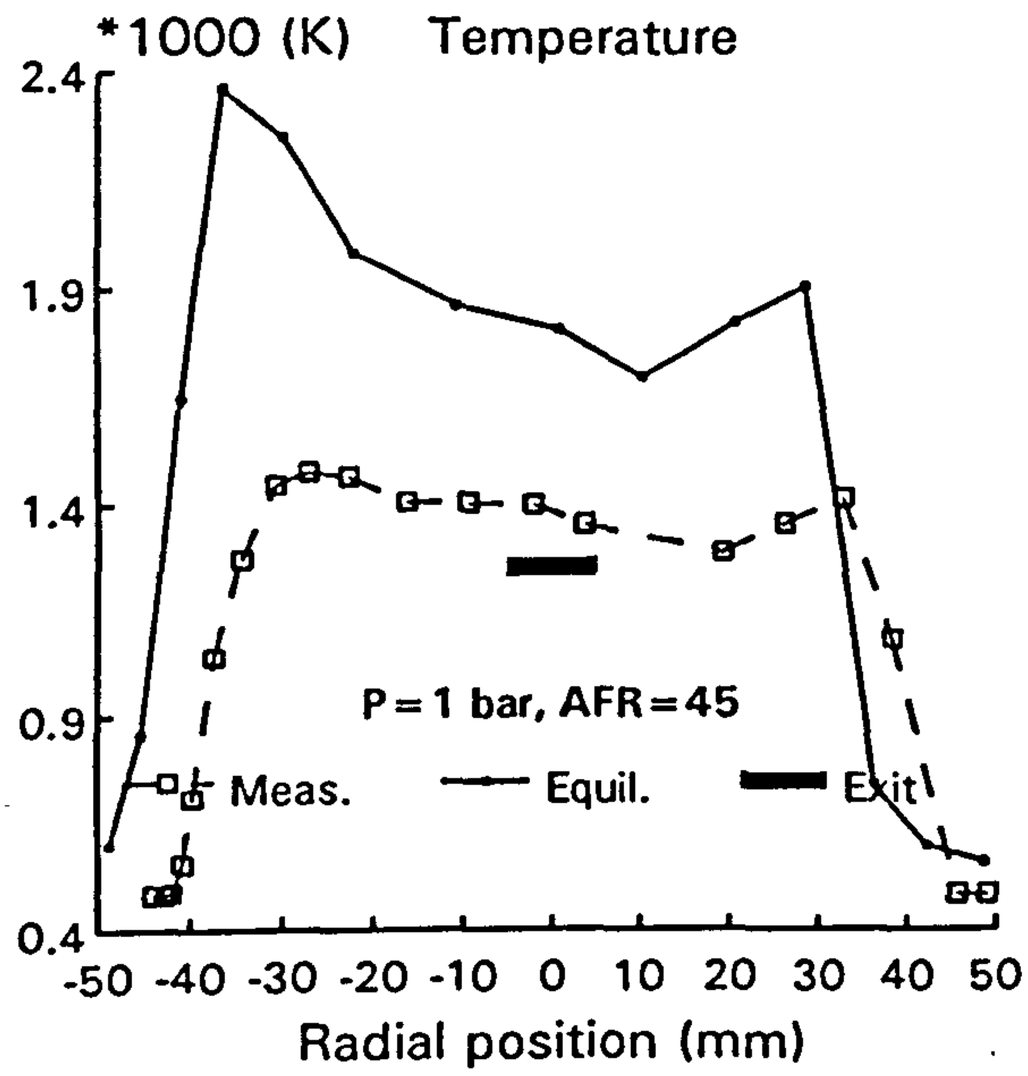

(a)

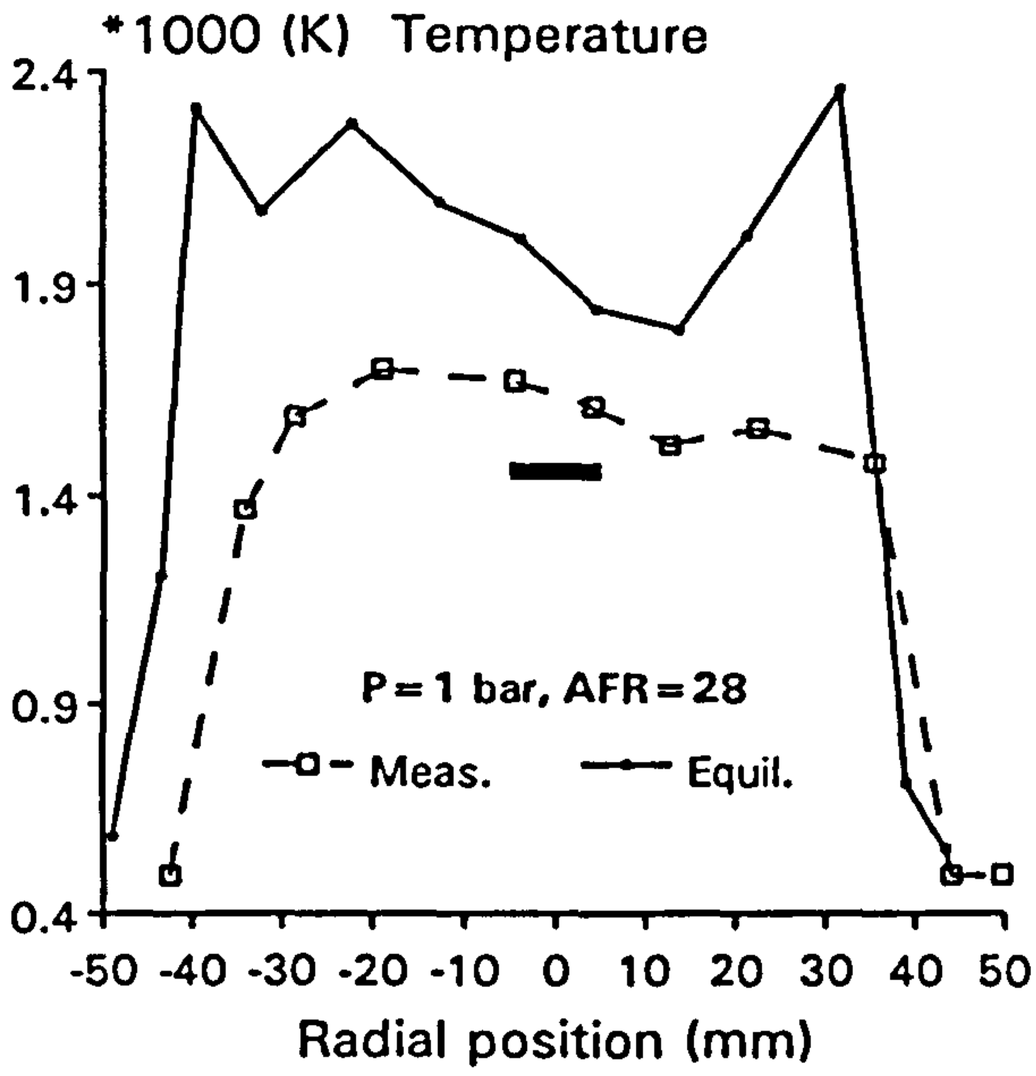

(b)

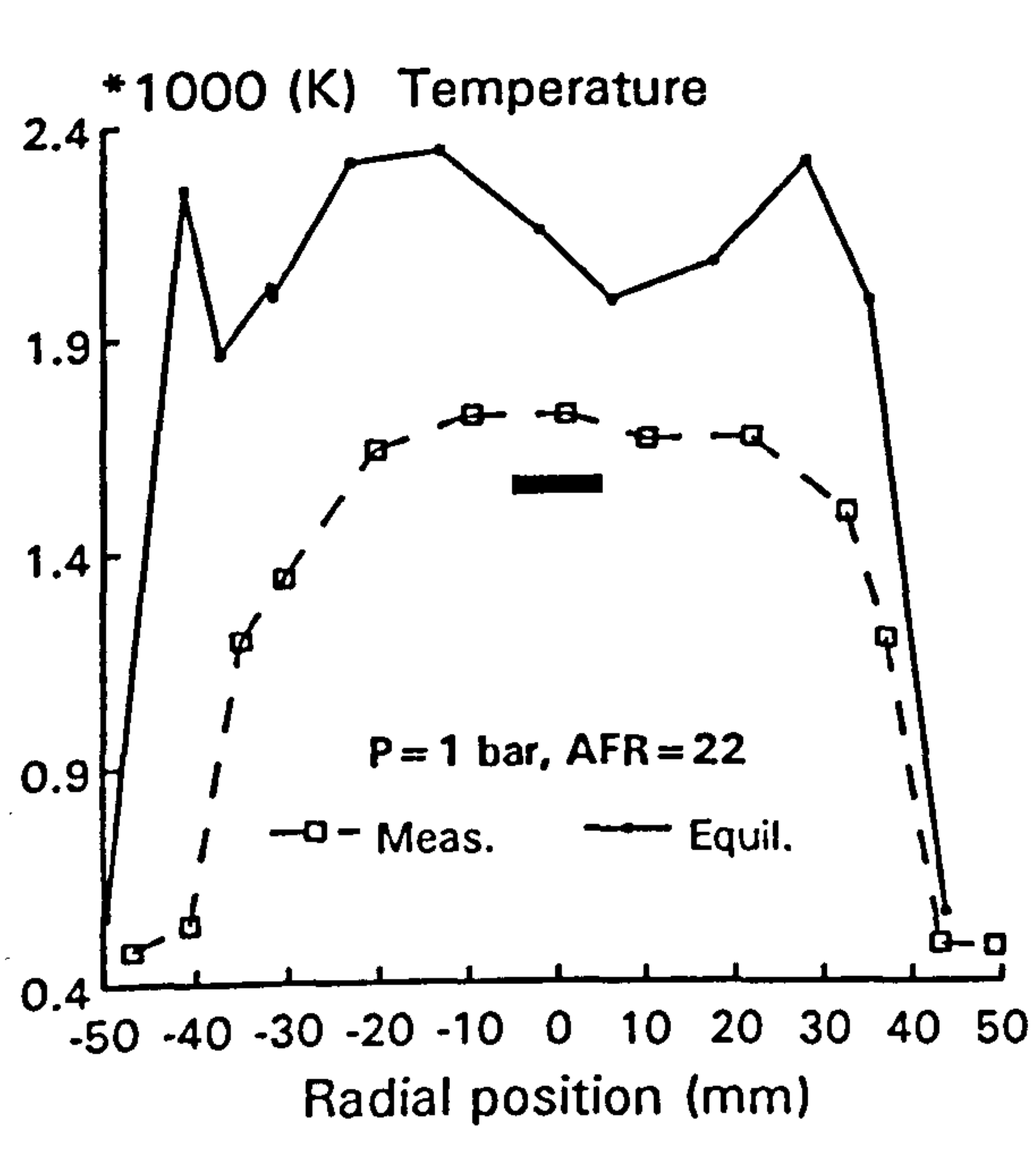

(c)

Figure 4.12 Temperature profiles with comparison of equilibrium calculations; P=1 bar, AFR=45, 28, 22. (Exit temperature also shown)

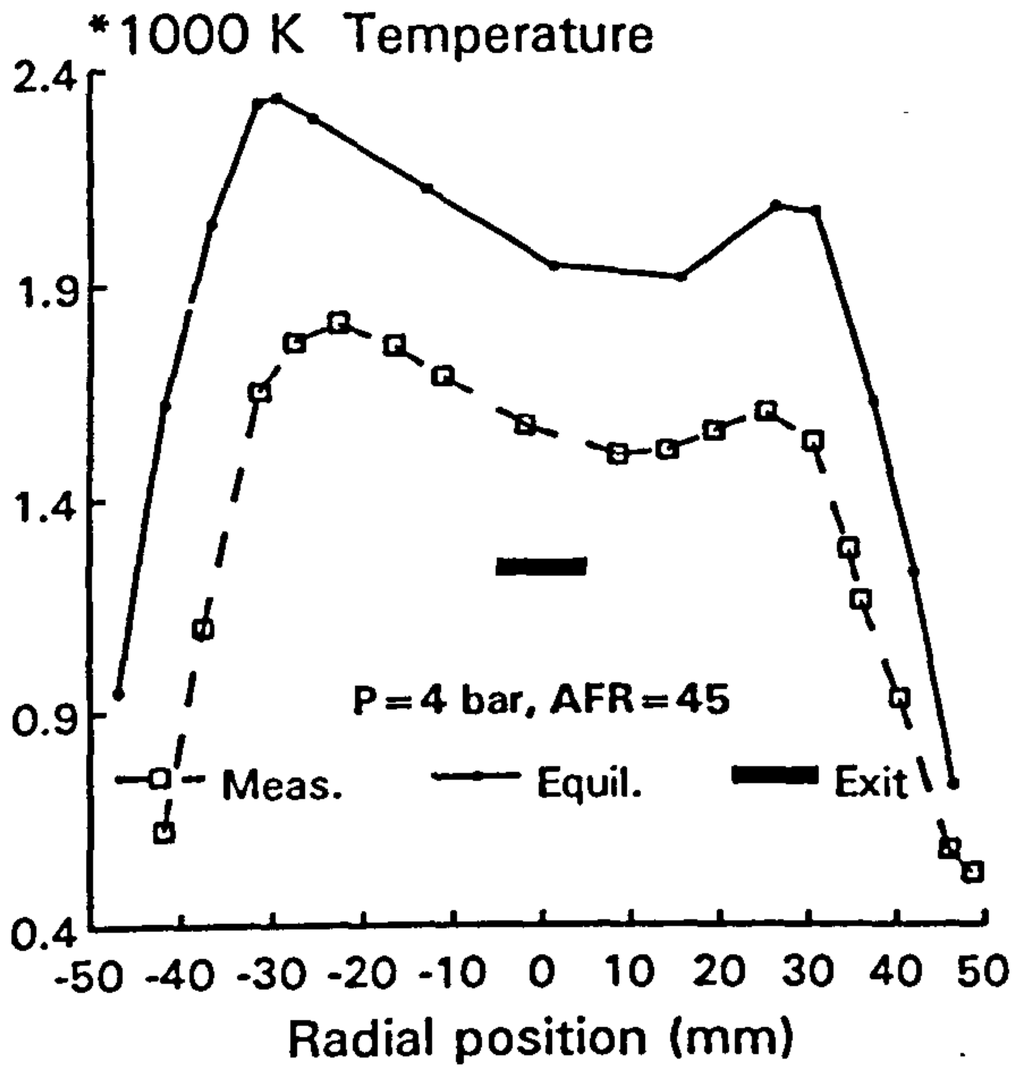

(a)

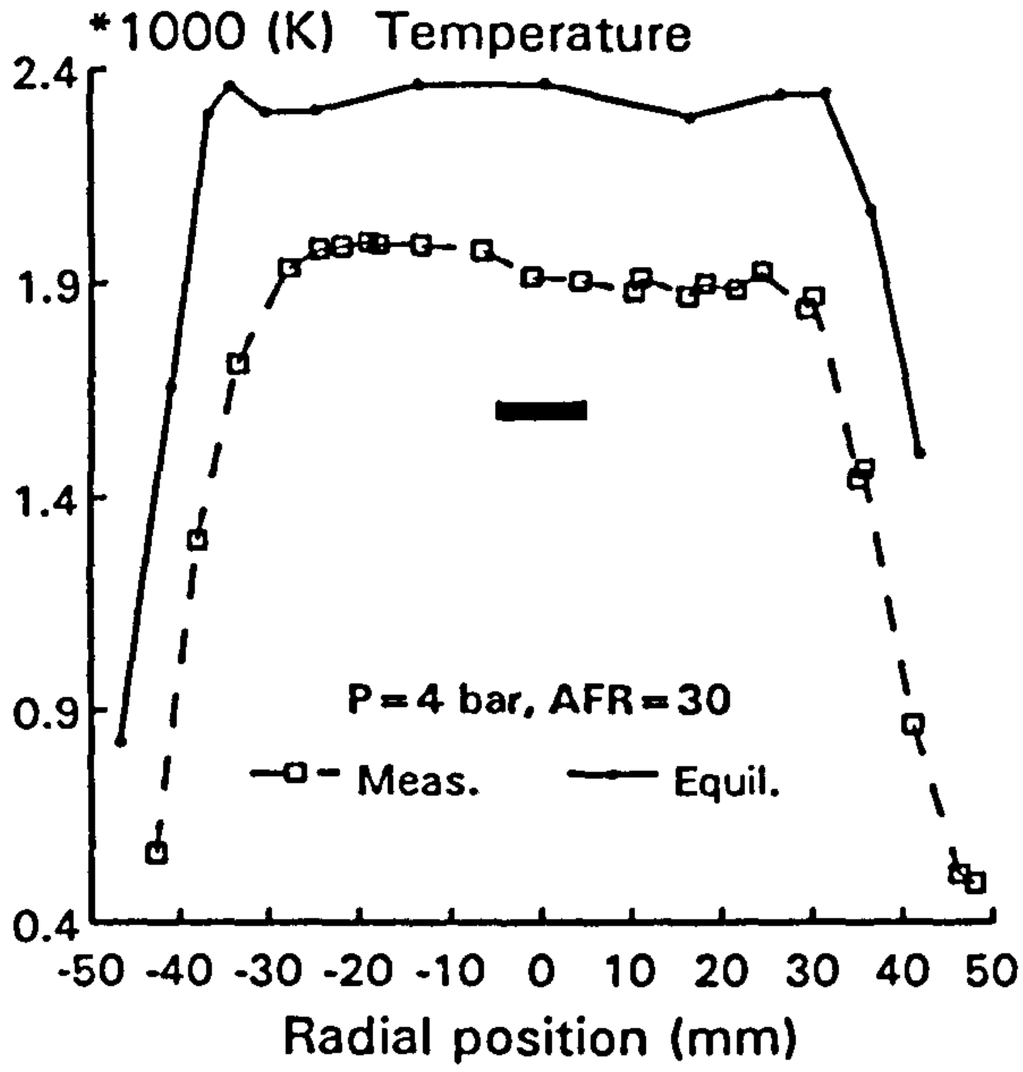

(b)

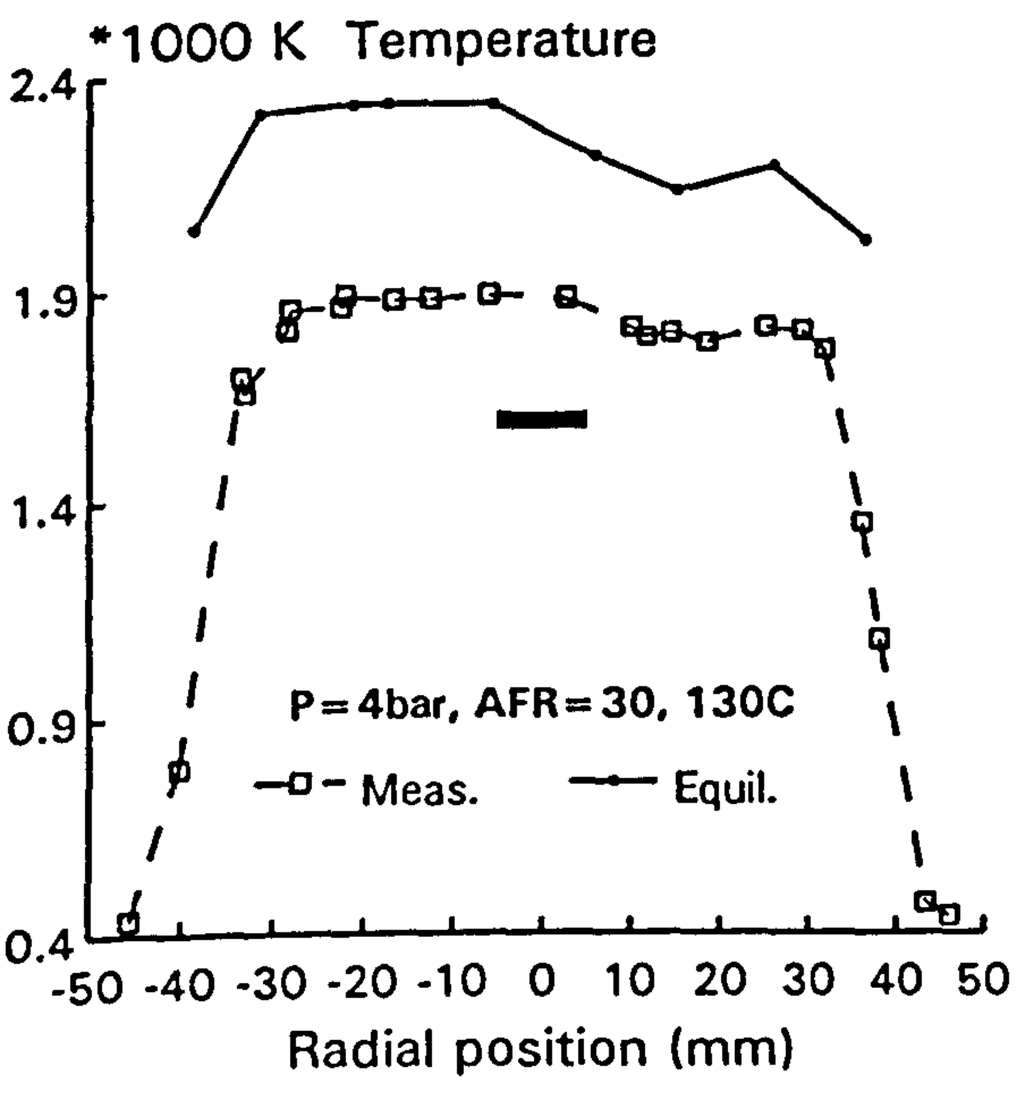

(c)

Figure 4.13 Temperature profiles with comparison of equilibrium calculations; P=4 bar, AFR=45, 30. (Exit temperature also shown)

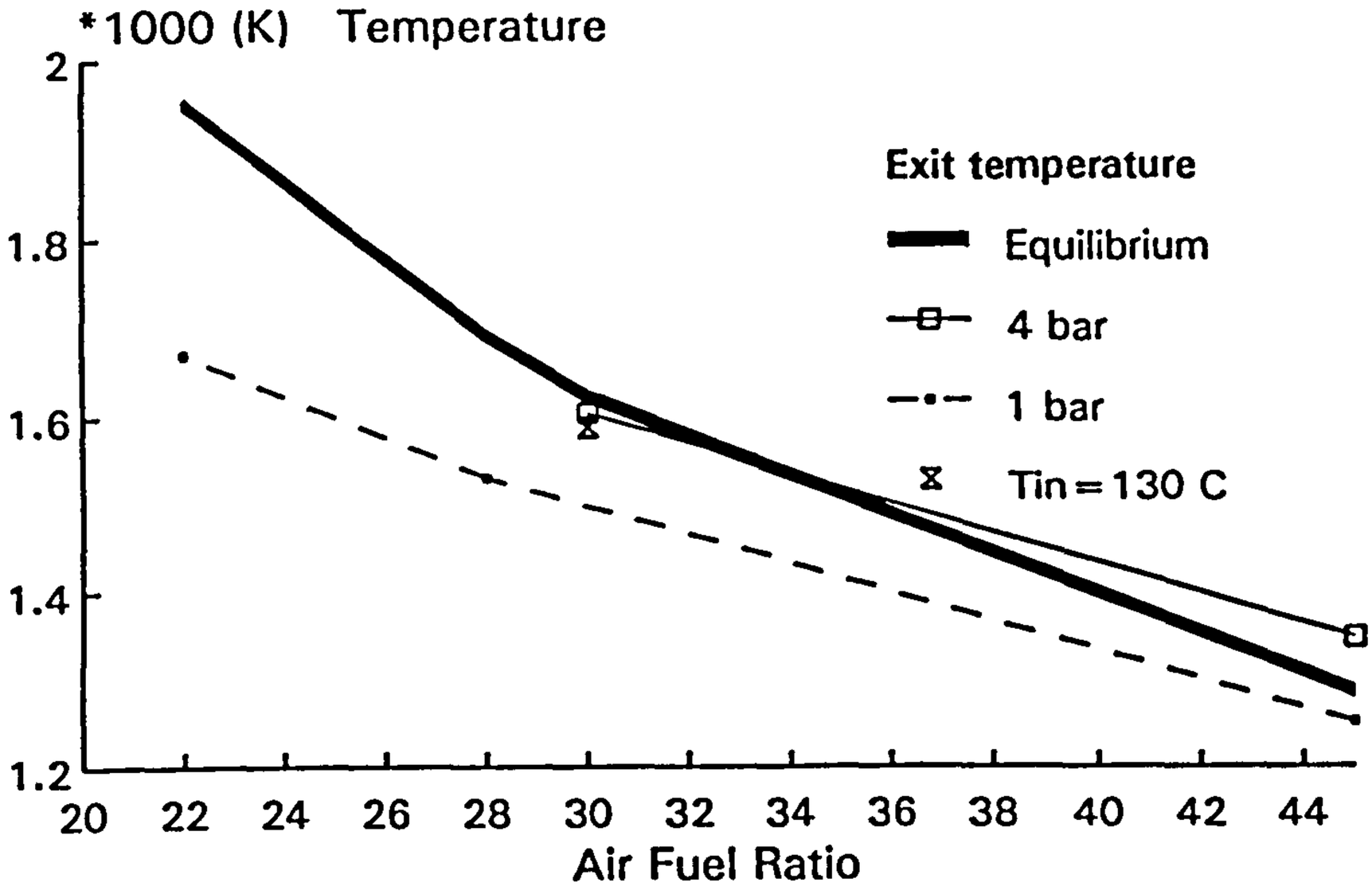

(a)

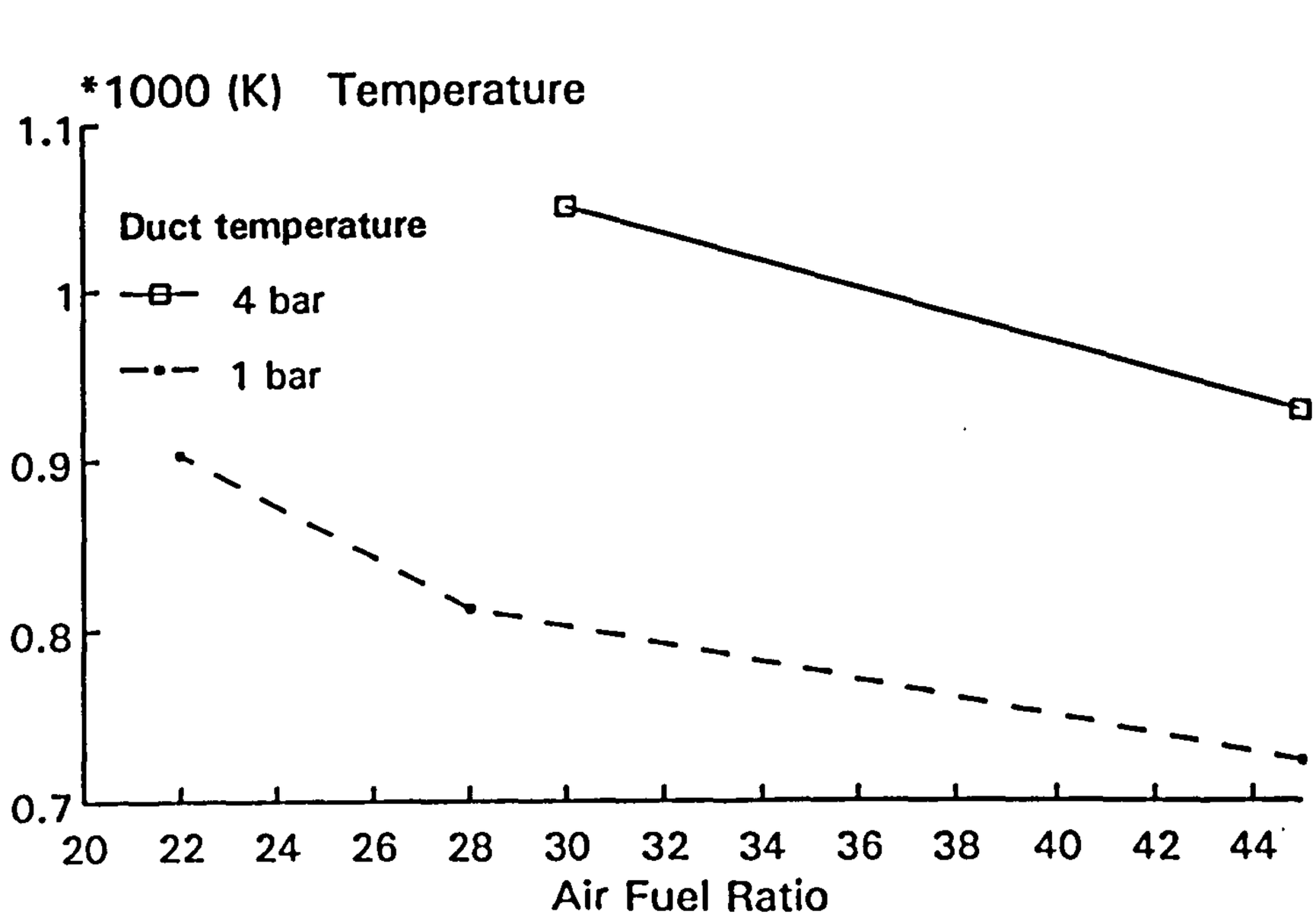

(b)

Figure 4.14 (a) Exit temperature with the comparison of equilibrium calculation and (b) duct wall temperature

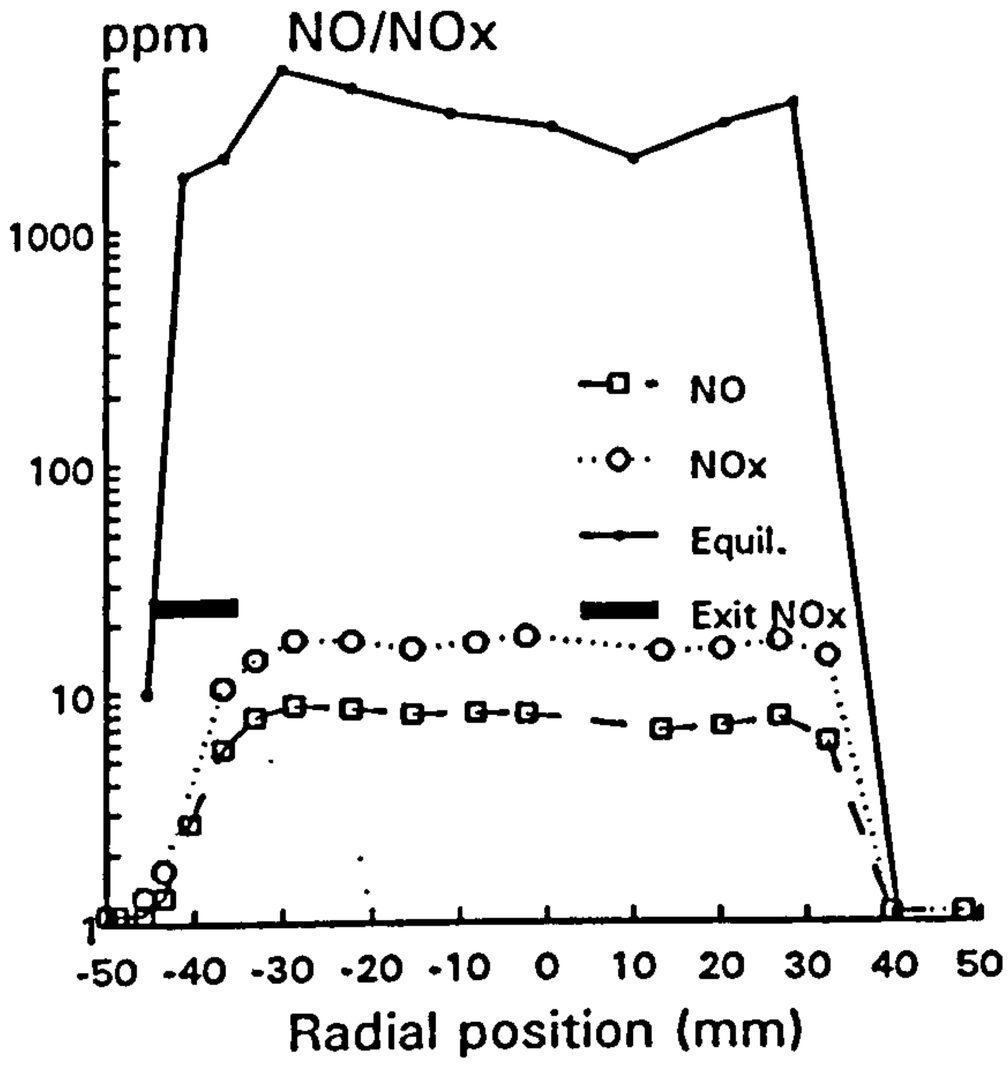

(a) P = 1 bar, AFR = 45

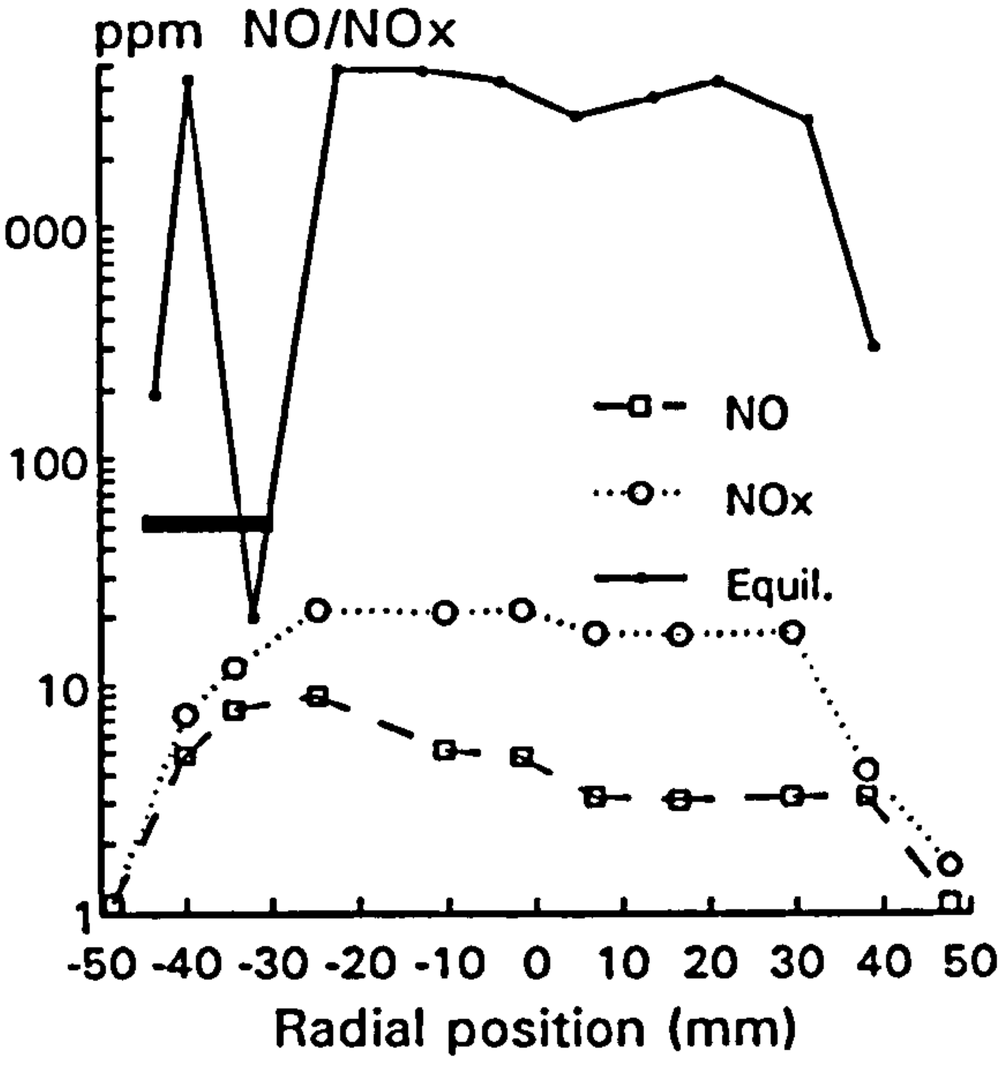

(b) P = 1 bar, AFR = 28

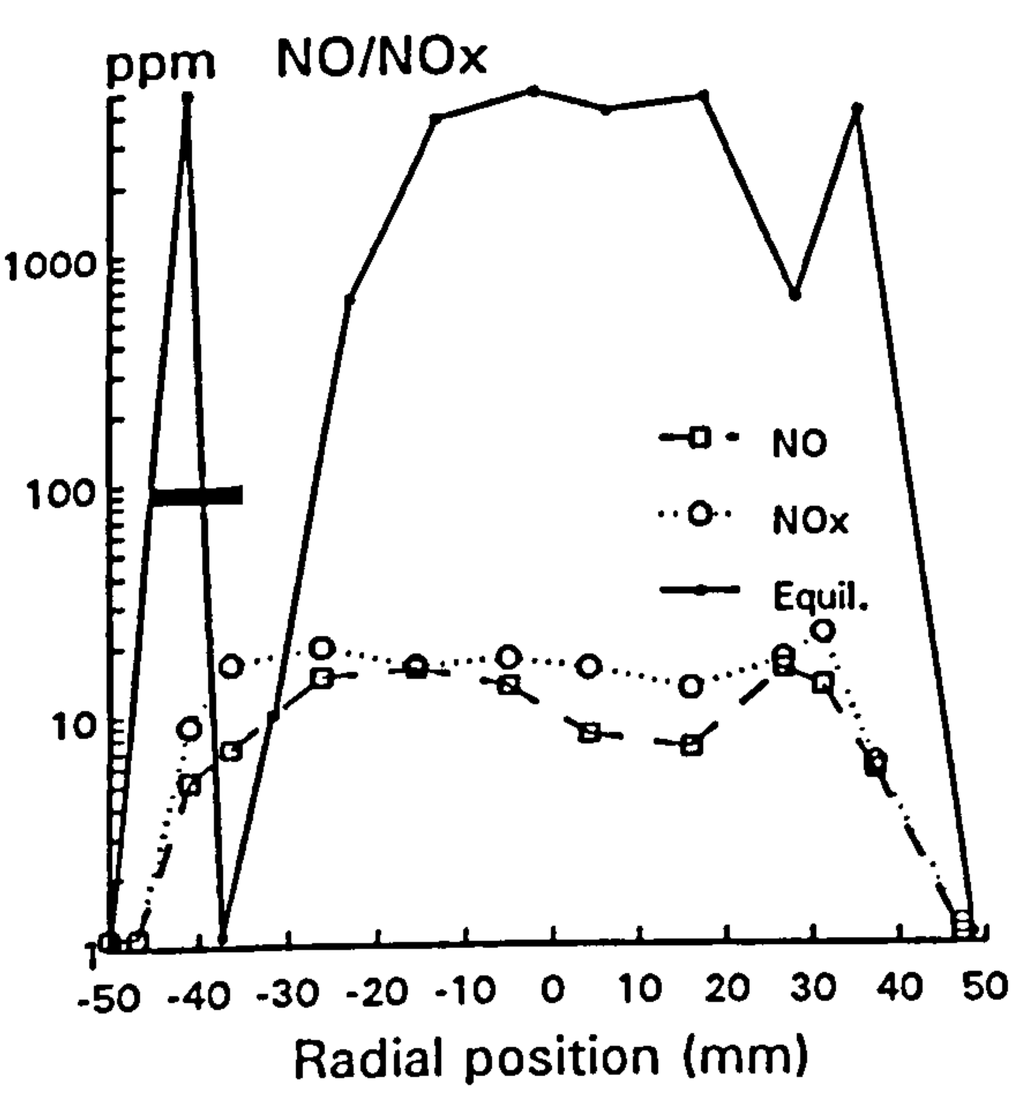

(c) P = 1 bar, AFR = 22

Figure 4.15 NO/NO_x concentration profiles with comparison of equilibrium calculation; P=1 bar, AFR=45, 28, 22. (Exit NO_x averaged concentration also shown)

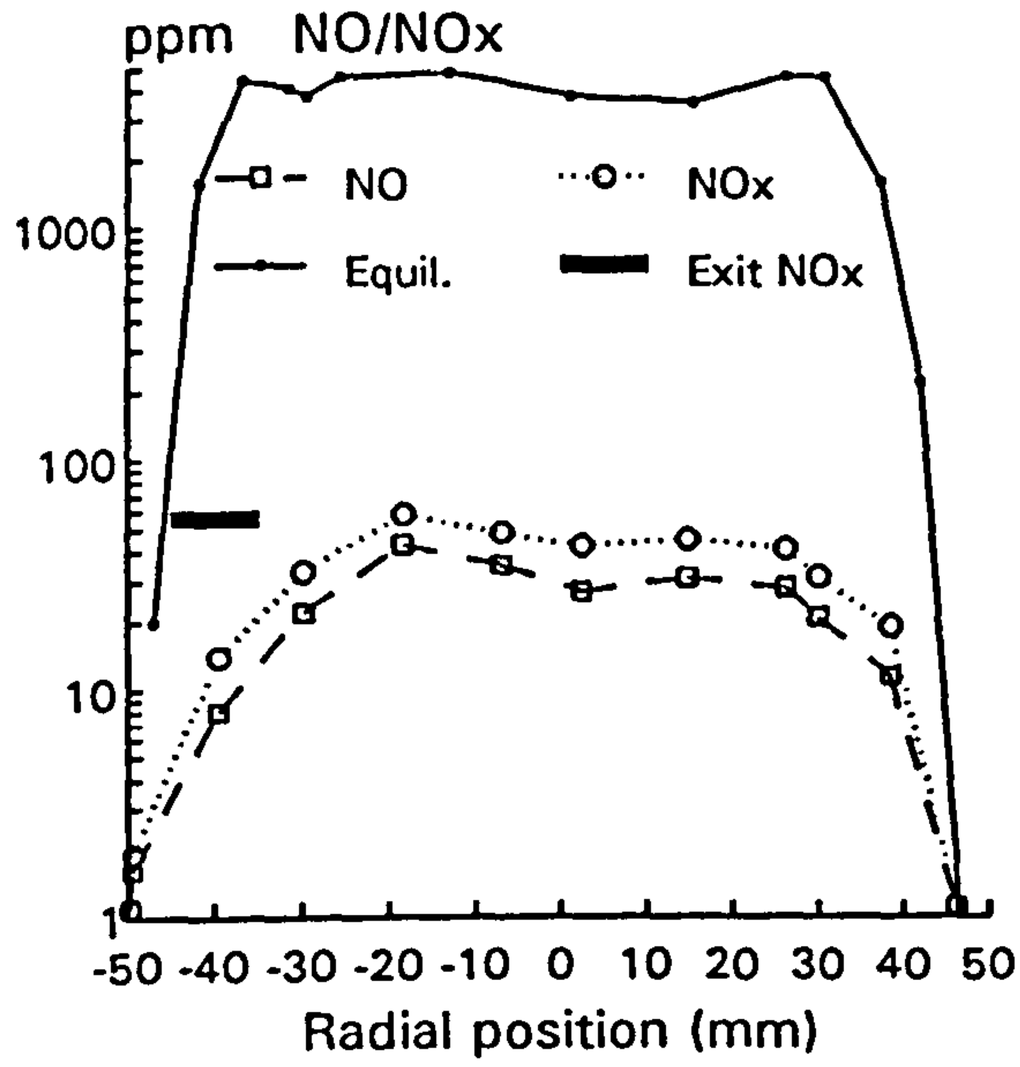

(a) P=4 bar, AFR=45

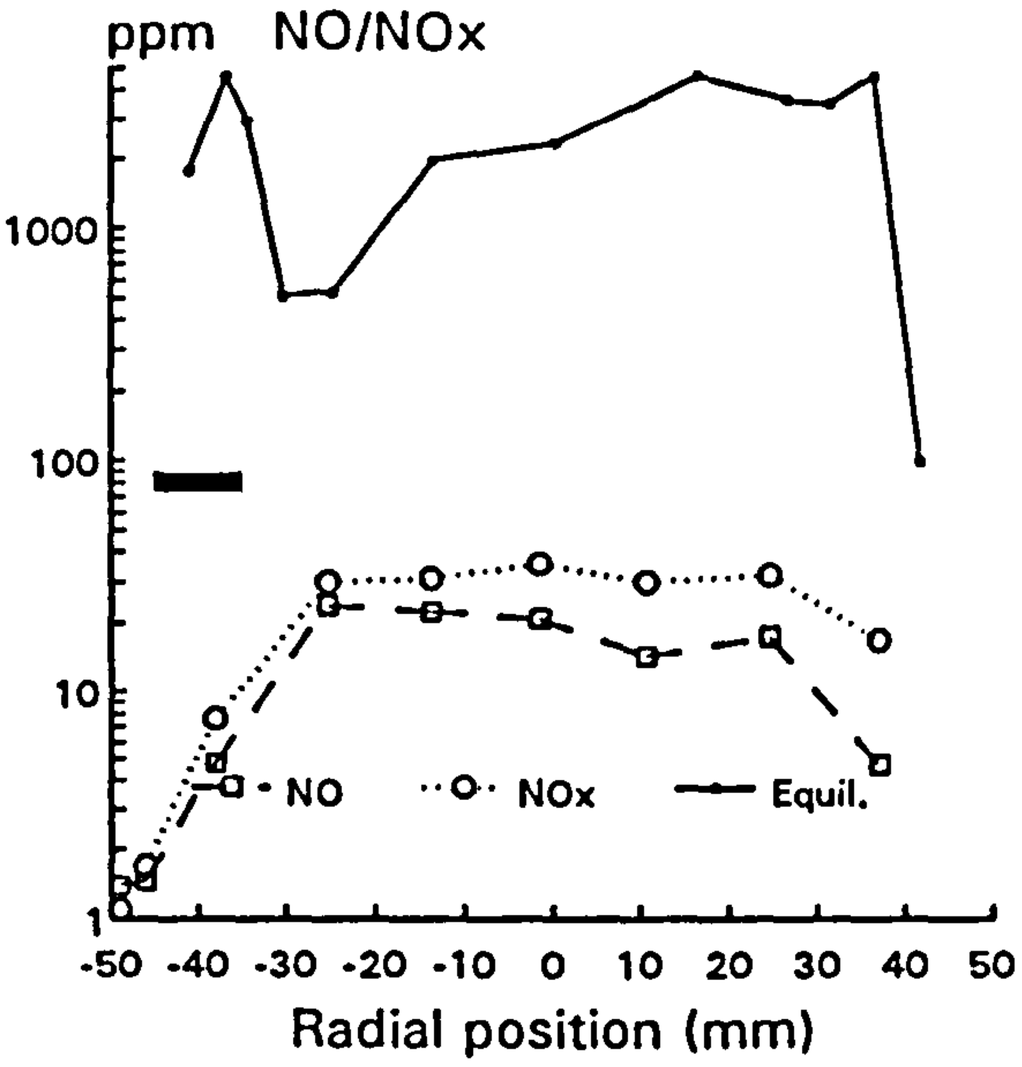

(b) P=4 bar, AFR=30

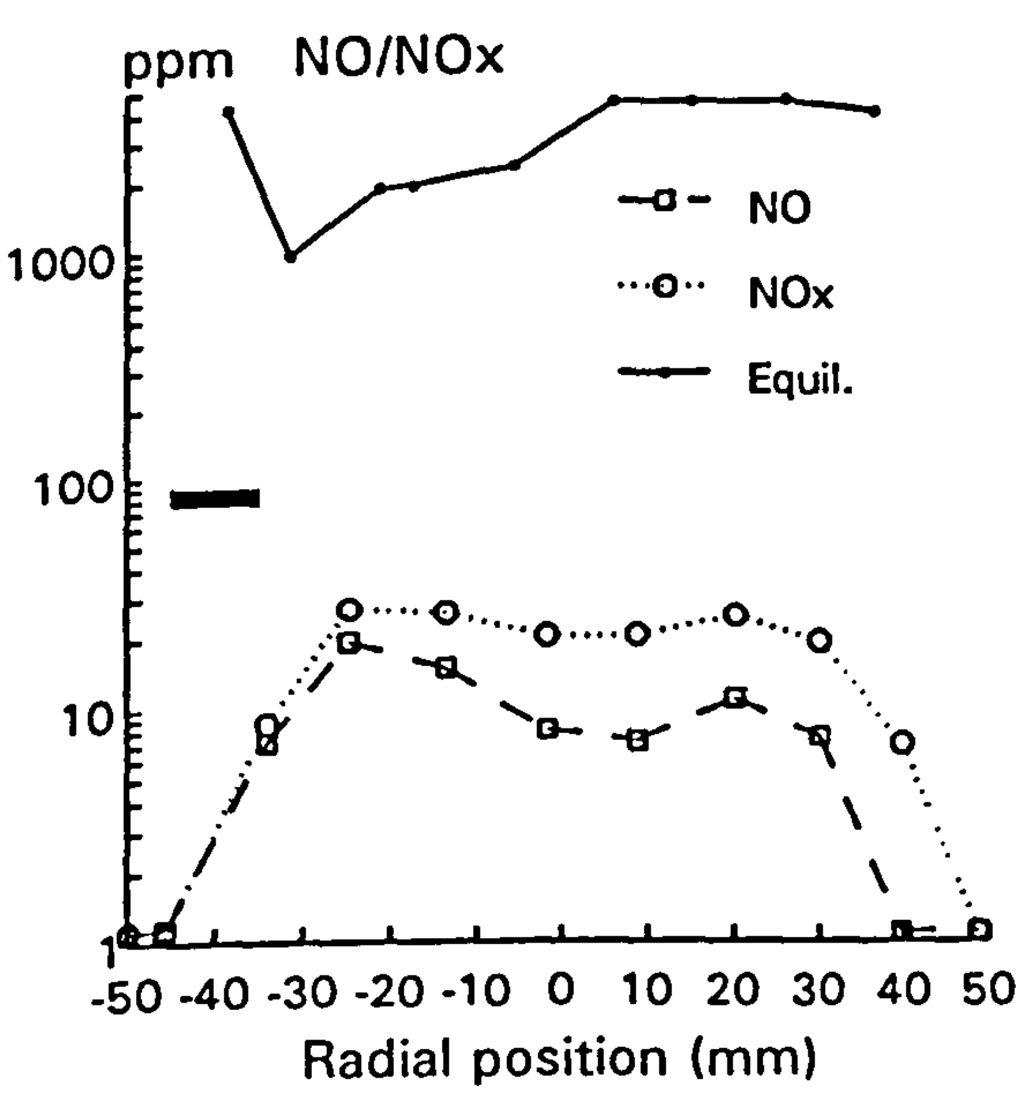

(c) P=4 bar, AFR=30, Tin=130 C

Figure 4.16 NO/NO_x concentration profiles with comparison of equilibrium calculation; P=4 bar, AFR=45, 30. (Exit NO_x averaged concentration also shown)

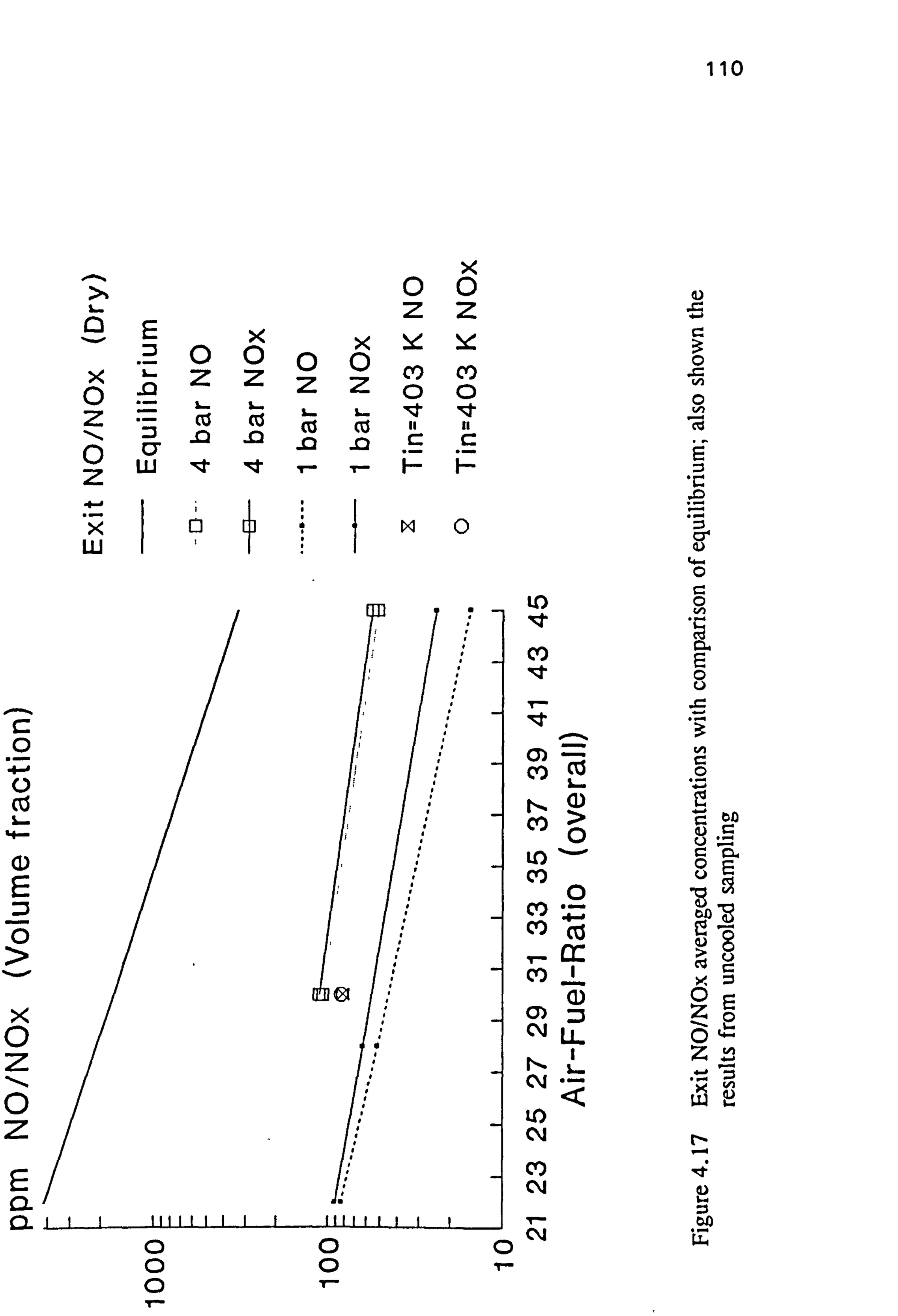

Figure 4.17 Exit NO/NOx averaged concentrations with comparison of equilibrium; also shown the results from uncooled sampling

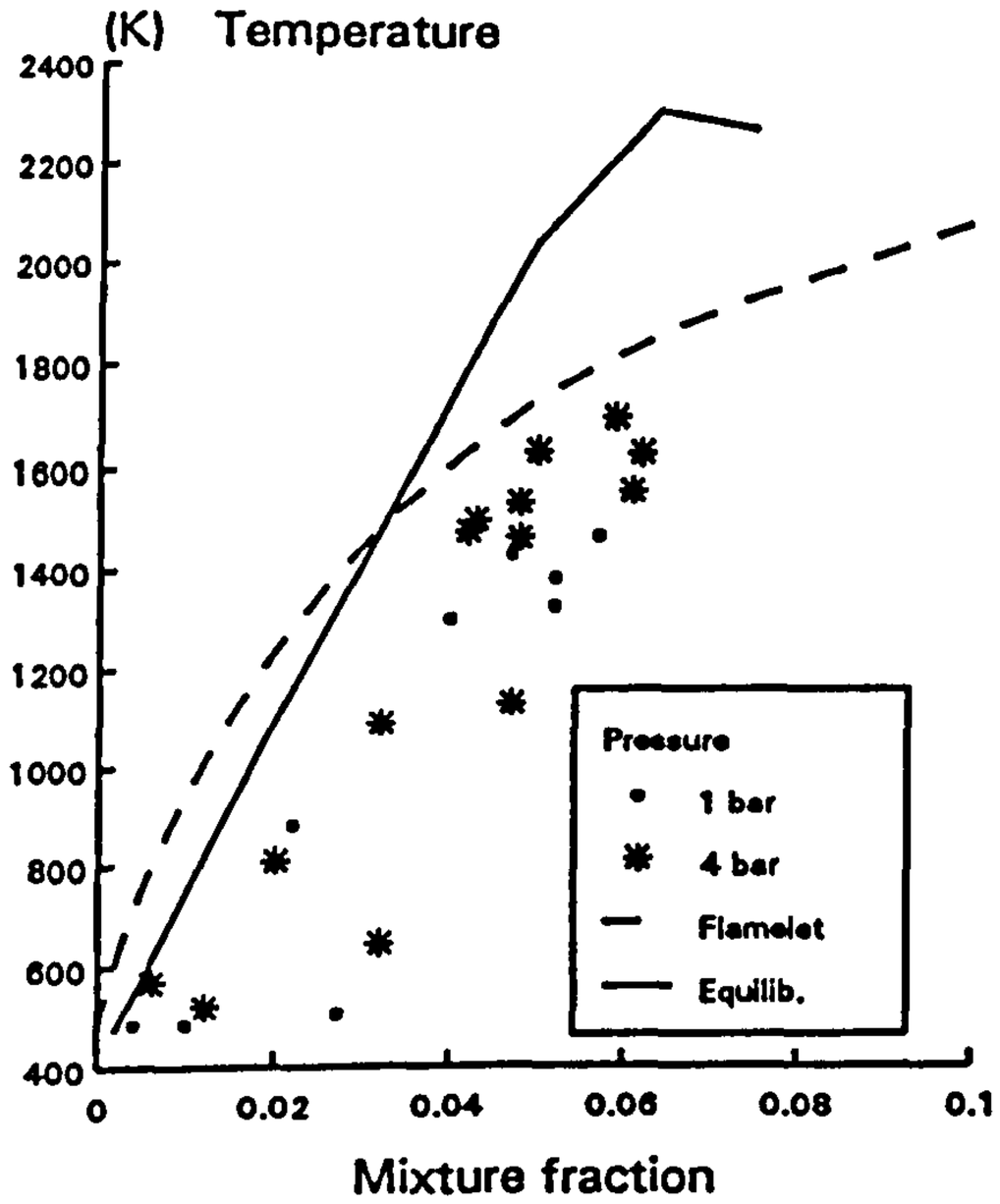

(a) AFR=45, Tin=200 C

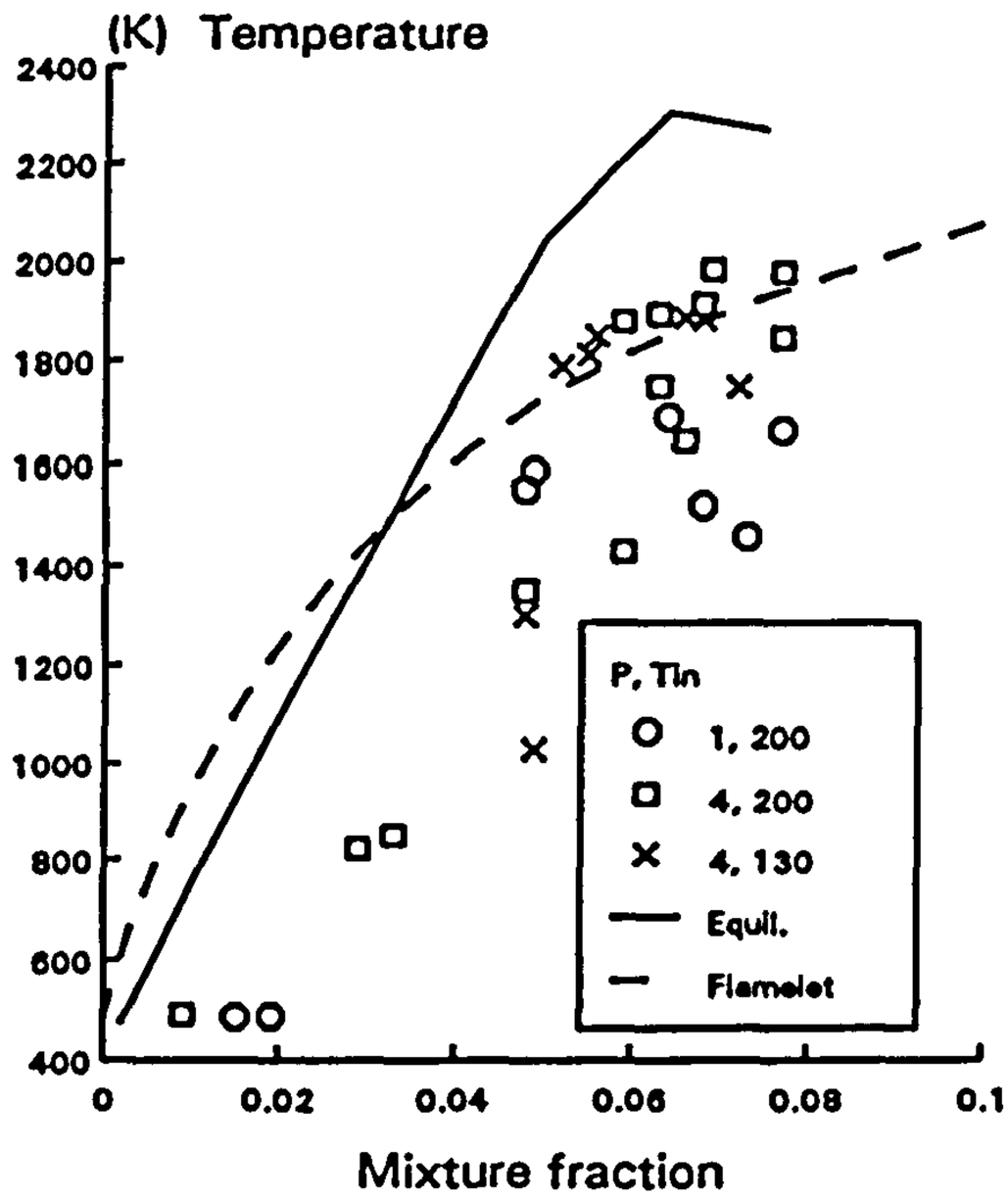

(b) AFR=(28) 30

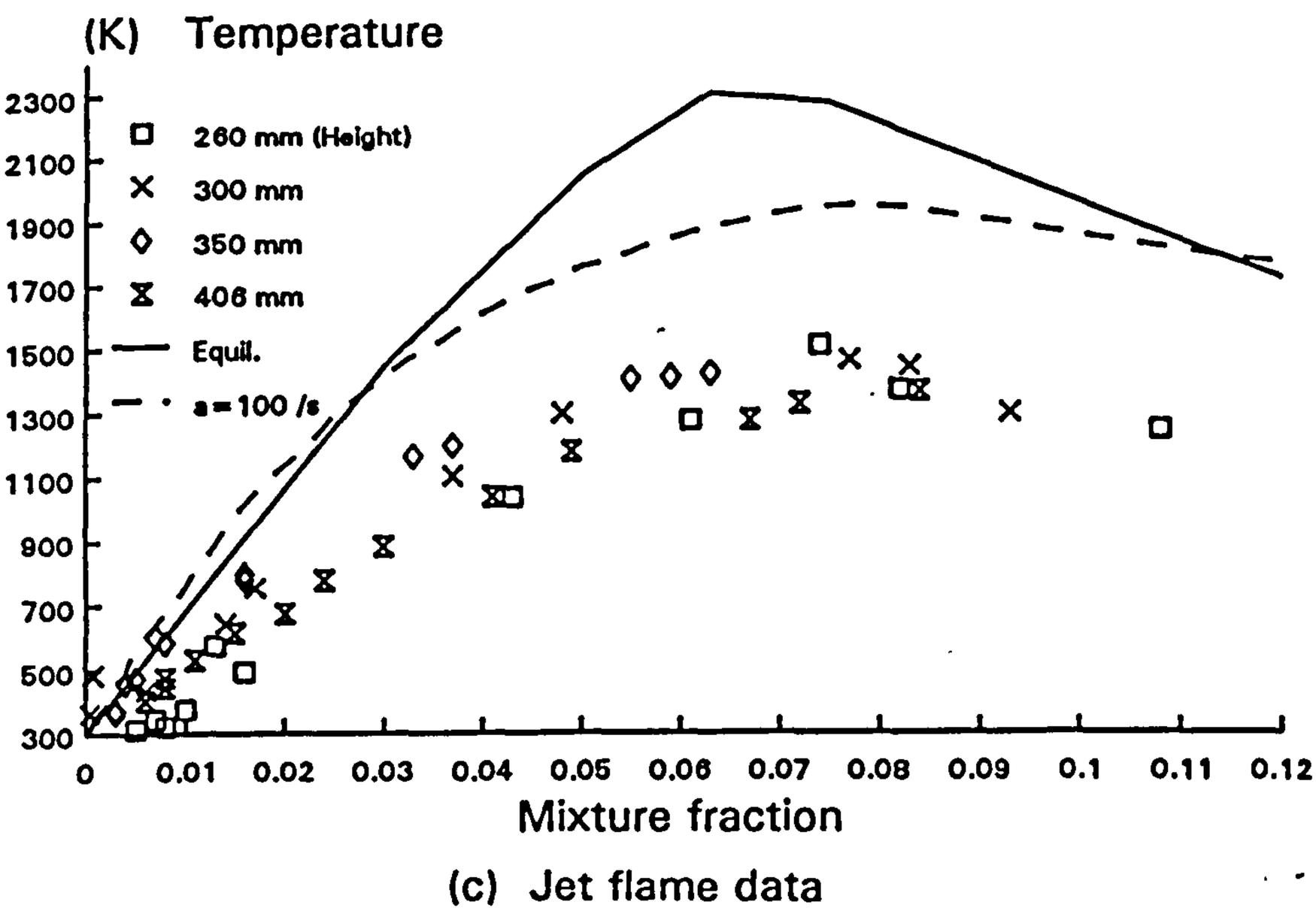

(c) Jet flame data

Figure 4.18 State relationships for temperature vs mixture fraction. (a) present combustor measurements, AFR=45 (b) AFR~30 and (c) jet flame data compiled from Young (1993)

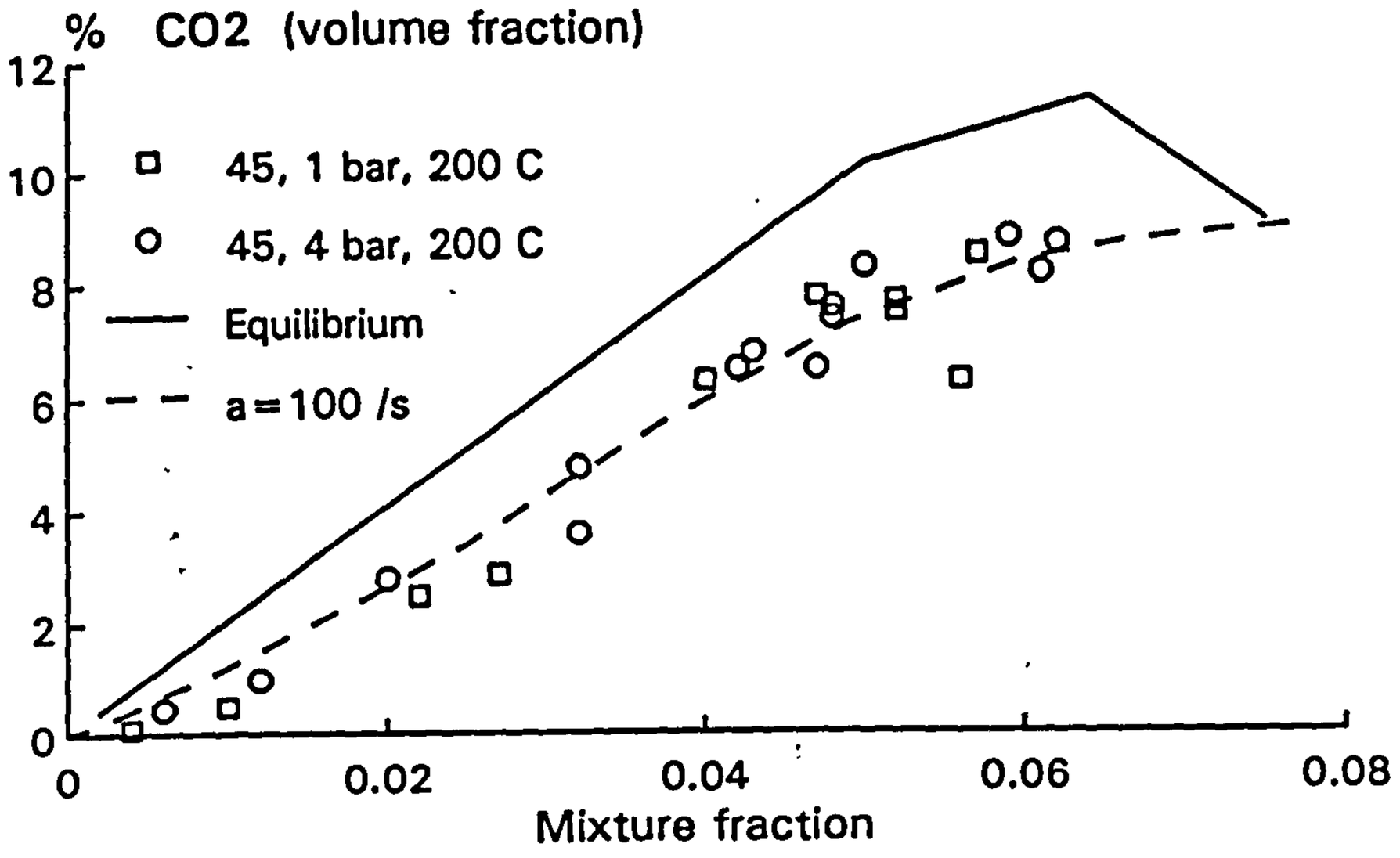

(a)

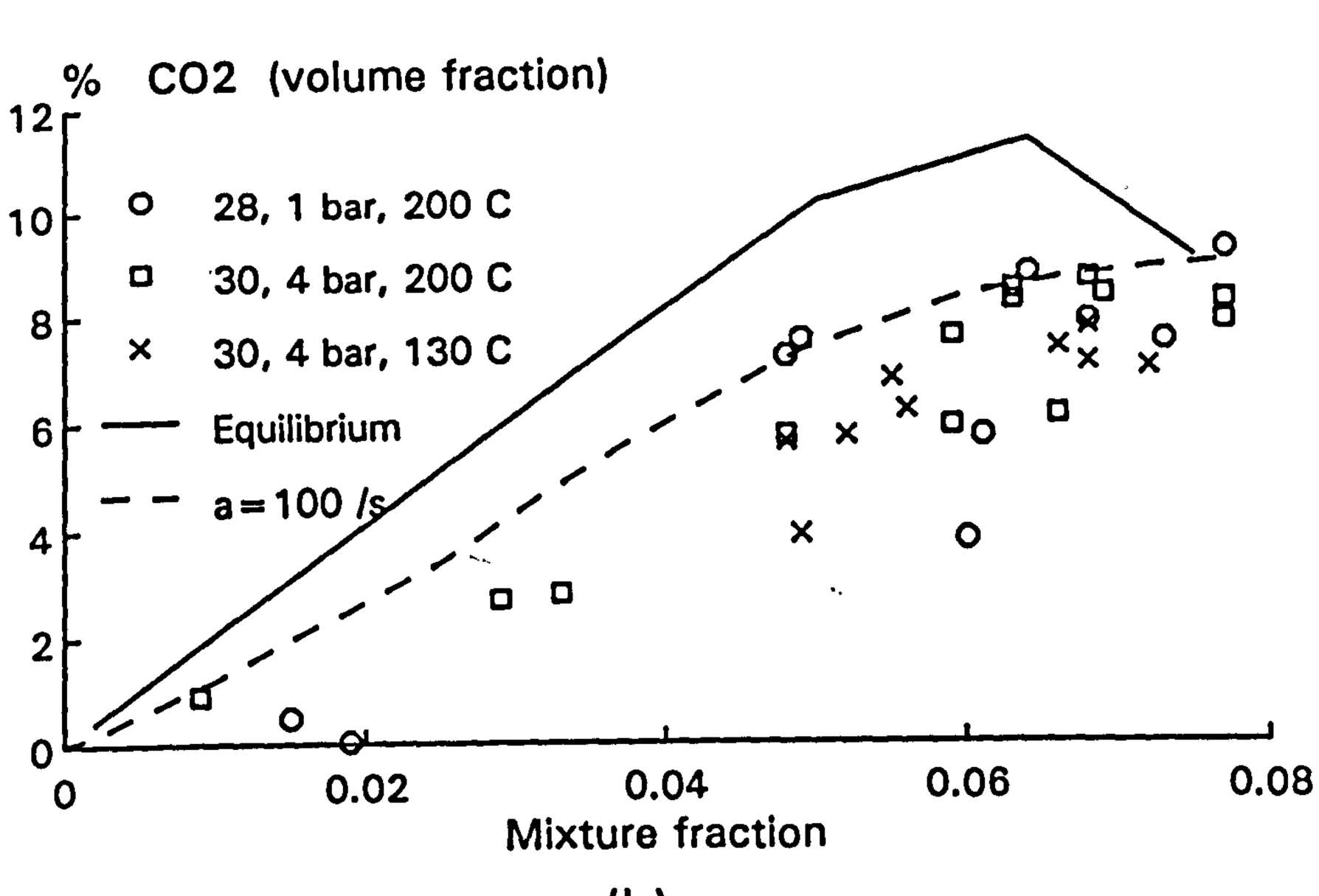

(b)

Figure 4.19 State relationships of CO_2 concentrations vs mixture fraction in combustor (a) AFR=45 and (b) AFR~30

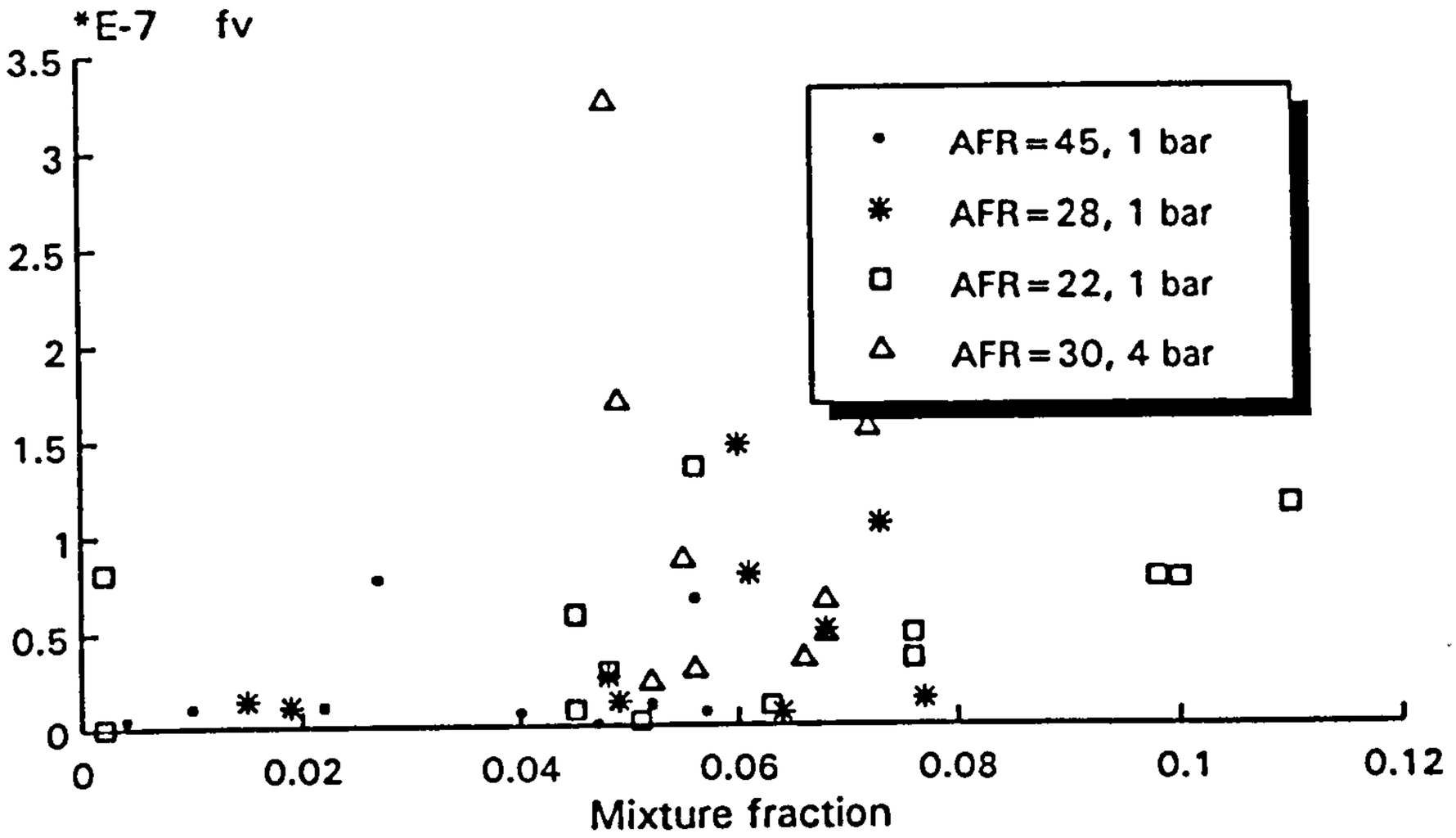

(a) fv vs mixture fraction in combustor

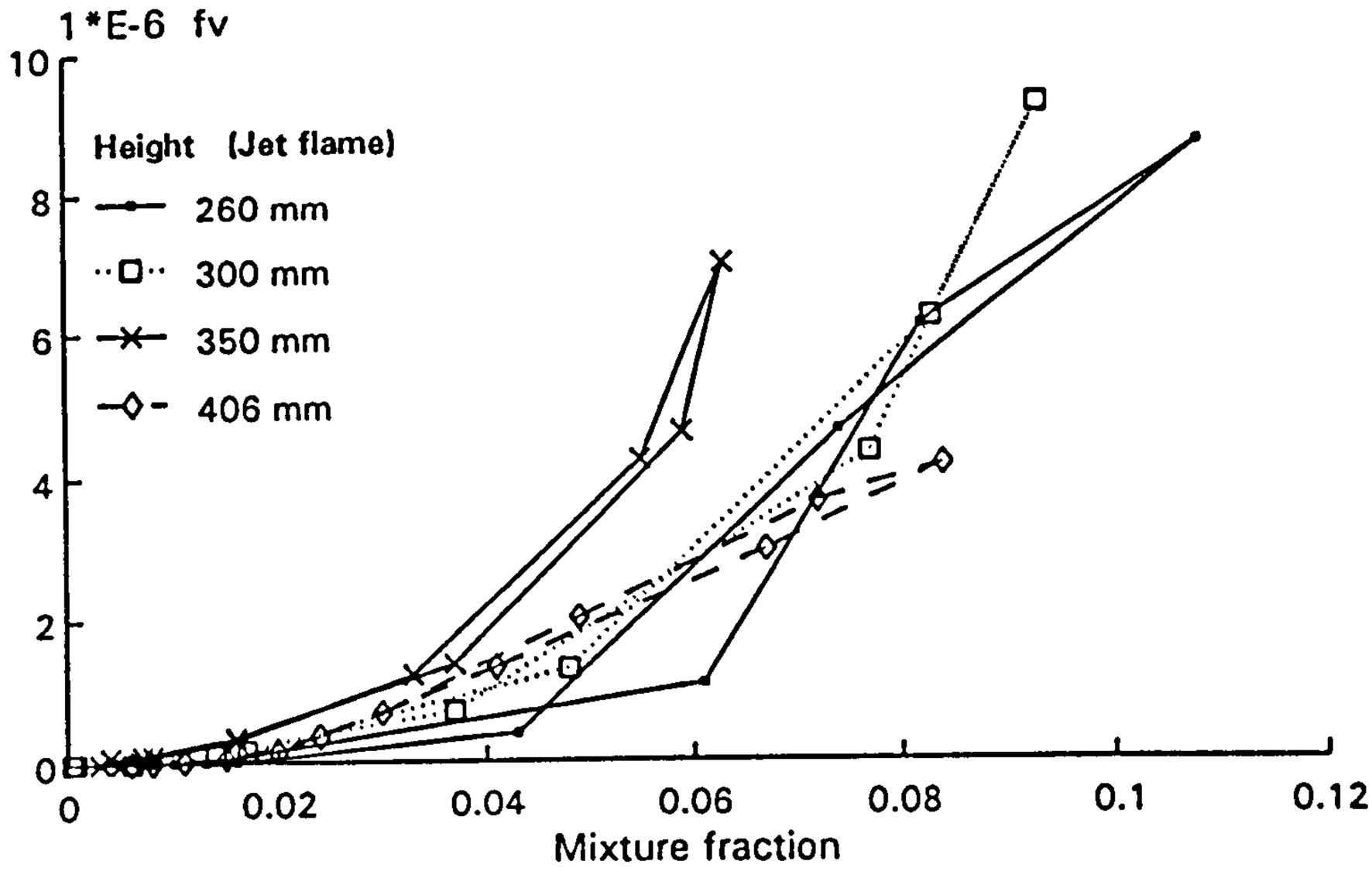

(b)

Figure 4.20 Scalar state relationship of soot volume fraction against mixture fraction. (a) combustor, (b) jet flame data compiled from Young (1993)

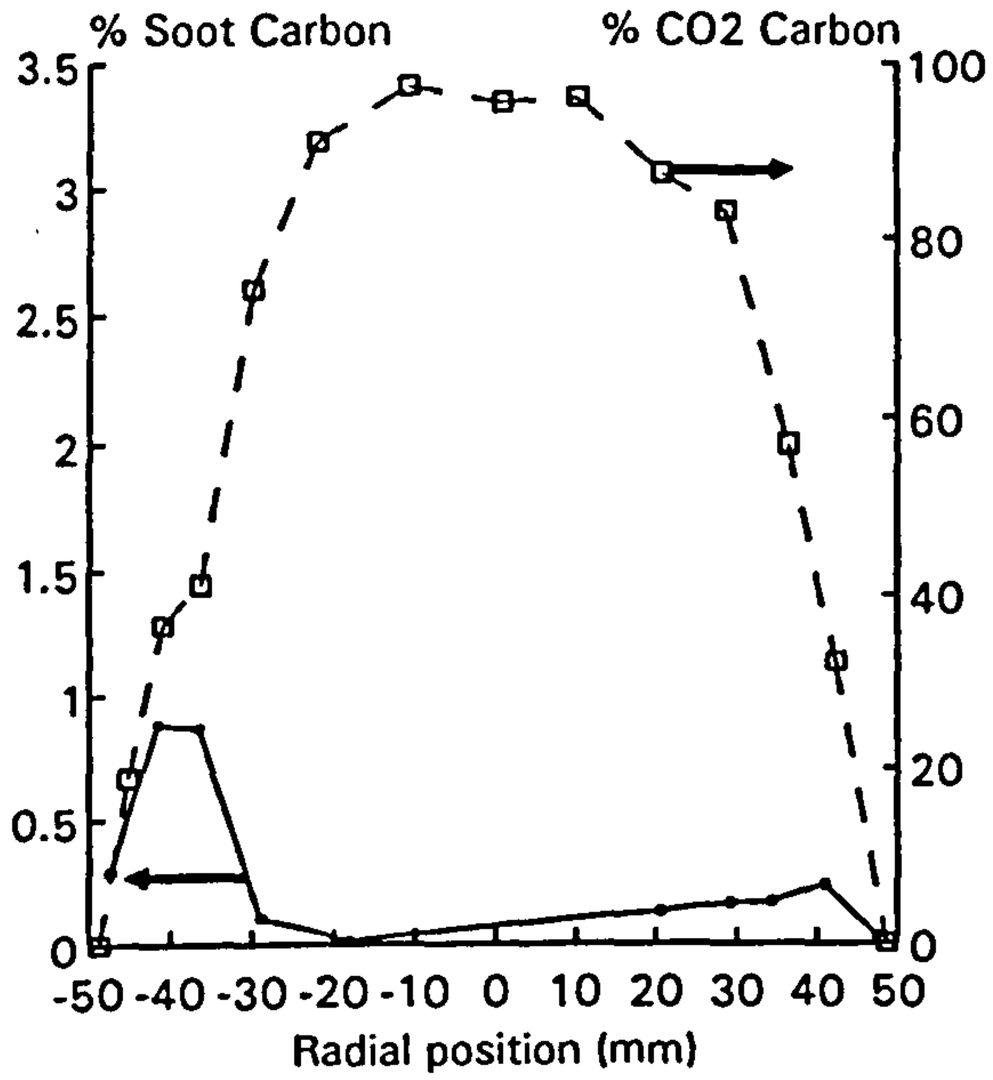

(a) AFR-=45, P=1 bar

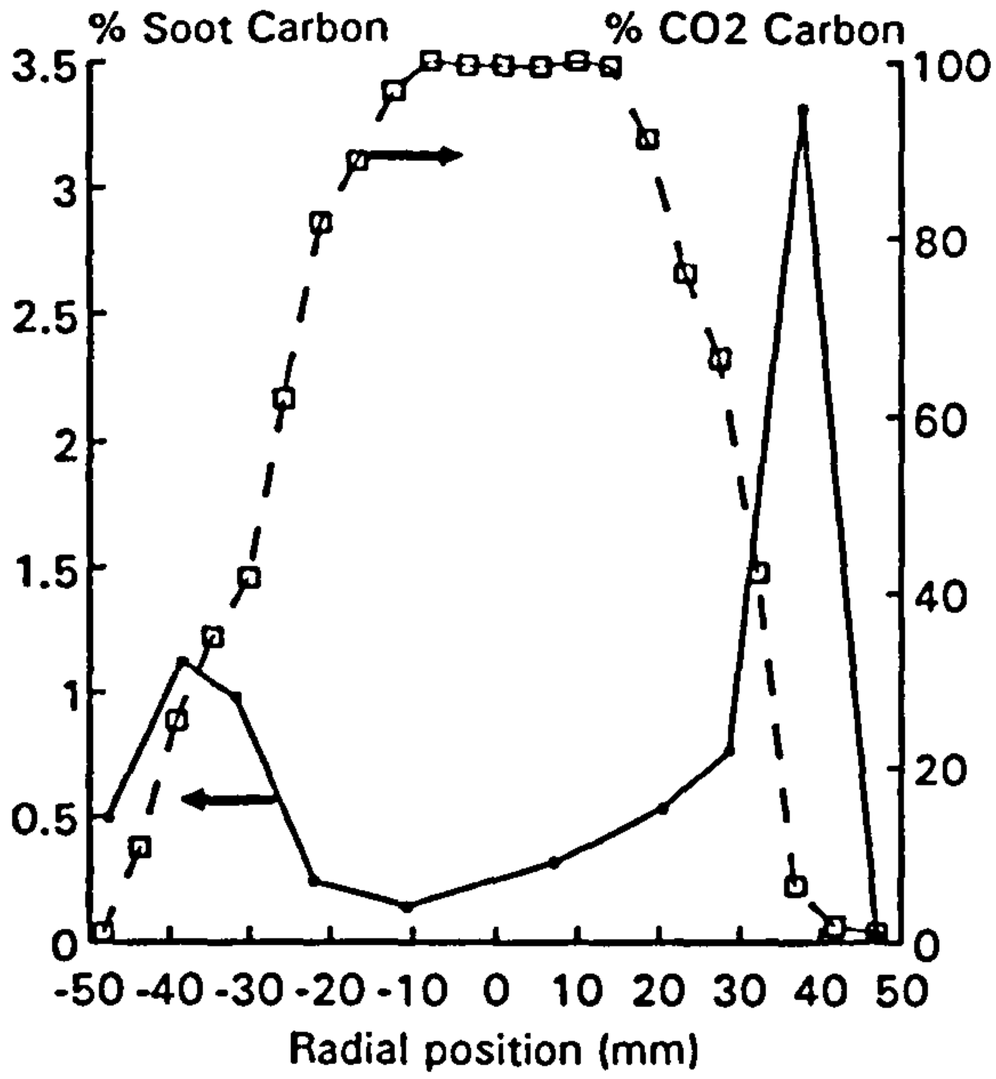

(b) AFR=28, P=1 bar

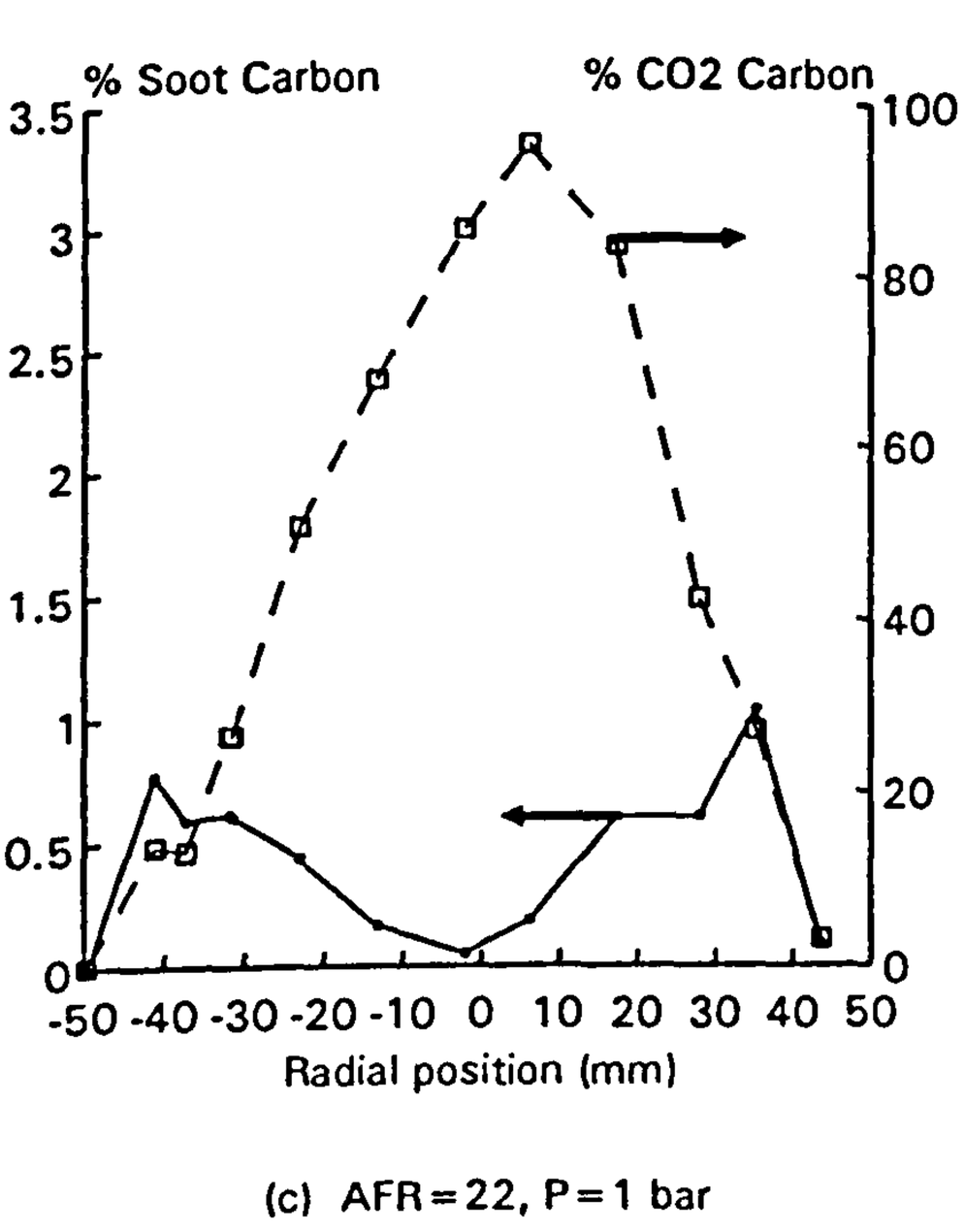

(c) AFR=22, P=1 bar

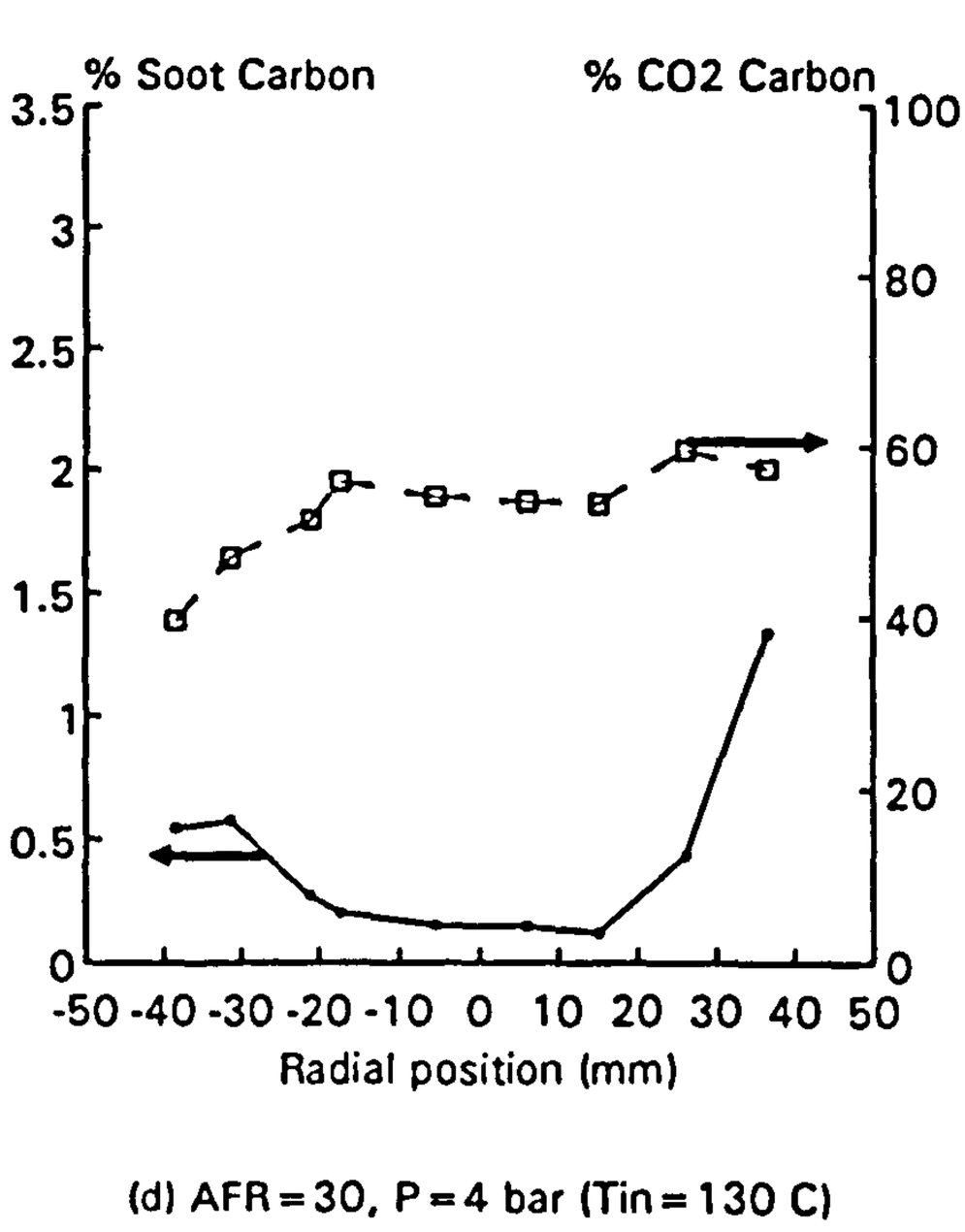

(d) AFR=30, P=4 bar (Tin=130 C)

Figure 4.21 (a) Soot particle and (b) CO_2 generation rates based on carbon conservation (Eqs. 4-3 and 4-5)

Chapter 5 Spectral Radiation Measurement

5.1 INTRODUCTION

Thermal radiation plays an important role in the process of heat transfer from the combustion products, gaseous and particulate, to the surrounding environment, the corresponding spectrum of thermal energy flux lies in the wavelength from 0.1 to 100 μm, including the visible range from 0.35 to 0.75 μm. Radiance from hot gaseous species distributes energy at distinct infrared wavelengths featuring narrow band spectra. Soot particles, by comparison, emit thermal radiation energy in a continuum, from visible to infrared, depending on the particle temperature and size. Particulate soot is an effective radiative emitter, such that, when the size of soot reaches certain diameter, it will behave like a blackbody with emissivity unity. Also, at high soot concentration, the obscuration rate becomes so high that no light can be beamed through the mixture and as a result the absorptivity (or emissivity) approaches unity.

High soot levels are generally caused by poor fuel-air mixing, eg. in the turbulent jet diffusion flame (Young (1993)). The mixing process in a gas turbine combustor is significantly enhanced by various means, most notably by the primary and dilution jet penetrations into the combustion zones. Measured soot concentrations in the SNECMA designed combustor are typically an order of magnitude lower than those in jet flames. In the "dilution" zone, the volume fraction is lower than 10^{-6} under the operating conditions reported in Chapter 3. The presence of soot particles, even with relatively low concentration, contribute to most of the visible radiation heat exchange and the mechanism has been the subject of many investigations. Claus (1981) has identified, in experiments on a JT8D can-type combustor, that soot contributes typically from 70 to 80% of the total radiation in the primary zone, from 50 to 70% in the intermediate zone and from 35 to 50% in the dilution zone. Such trend reflects the combustion development within the combustor as both temperature and soot concentration levels continuously decrease downstream, due to the air dilution and soot destruction process.

The relative proportions of radiation and convection heat transfer depend upon the geometry and operating conditions of the gas turbine engine, and typically radiation accounts for 30 to 50% of the overall heat flux to the walls in the present combustors. Fuel characteristics and, more particularly, future fuel degradation, will also have some impact on the radiation due to the possible higher sooting tendency. Attempts to predict the soot radiance

flux in the combustor are hampered by the lack of both temporally and spatially-resolved soot profiles. Theoretical developments have continued more rapidly in laboratory flames as described in the review by Viskanta and Mengüc (1987).

It is well understood that in gas turbine combustors radiation is the major component of heat flux to the liner walls (Lefebvre (1984)). Excessive thermal radiation from either gas or soot particles is not desirable since it will heat the combustor wall and substantially reduce the liner durability. The application of film cooling on the wall is the most common engineering response to the radiation heating to reduce the liner temperature. The drawback associated with film cooling is that temperature pattern factor is often worsened and excessive cooling air leads to the decrease of combustion efficiency at low power settings. To achieve the minimum cooling air distribution combustor designers have to understand the detailed process of flame radiation in the combustor. It is particularly critical to the development of combustion strategies like rich-burn-quick quench which tend to generate high radiative flux from the high soot levels.

Although a general framework has been established for the different behaviour of gas (non-luminous flame) and soot (luminous flame) radiation, no completely satisfactory model has yet been found to theoretically predict the fully-coupled radiative heat transfer, even in laboratory flames of simple flow geometry. In relation to soot, the obstacle is partly the distributed presence of soot which is both emitting and absorbing body, especially when the soot concentration is high. Radiative heat flux at the combustor liner wall from the flame is strongly affected by the detailed radial temperature and soot concentration distributions (Ferguson and Mellor (1979) and Mengüc et al. (1986)). The spatially resolved soot volume fraction and temperature profiles in the SNECMA combustor therefore provide a useful tool to predict the radiation from soot particles, although they are simply time-averaged properties. Theoretical calculations applying time-mean data usually underestimate the spectral/total radiation intensity in fires (Syed (1991) and Sivathanu et al. (1991)) and jet flames (Faeth et al. (1987)) due to the influence of turbulent fluctuations. To fully evaluate the quality of the predictions based on mean properties in the combustor, experimental data is required from spectral radiance measurement.

In connection to the soot radiation measurement, a related study of optical temperature measurement was conducted. The application of fine wire thermocouples in sooty flames suffers, in particular, from soot particle deposition on the thermocouple bead. The measurement uncertainty of the bead contamination can possibly be overcome by rapidly inserting method to minimise the particle deposition time. It however introduced other

questions of how to determine the true temperature since the thermocouple reading may drop continuously during the measurement as the particles build onto the bead. On the other hand, some flames may have such high temperatures that no thermocouple wire can survive in the flame. The development of a non-intrusive technique has considerable advantages with respect to the above limitations. Recent developments of the CARS technique show potential for accurate gas temperature determination with adequate spatial resolution, however its application to sooty flames is very limited whilst the hardware implementation and subsequent analysis required for these measurements are relatively complex.

By contrast, conventional optical soot temperature measurement is simply dependent on the flame emission from hot soot particles, usually at visible wavelengths. The techniques often applied include brightness (Kurlbaum), Schmidt and two colour temperature measurements. The first one is quite straight forward since it use a blackbody light source (typically a blackbody lamp or furnace) as a reference which is calibrated against a detector, eg. PhotoMultiplier Tube. When the combined lamp plus flame radiance signal at the detector is the same as the lamp signal alone, the flame temperature is equal to the source brightness temperature according to Kirchhoff's law. This technique has been used in sooty laboratory flames (Kent and Bastin (1984)), however this method is not suitable for applications in highly turbulent flames where there are difficulties in identifying the signal from flame plus lamp in the fluctuating flow with that of lamp alone. Hence, only the latter two techniques are chosen for temperature measurements on the combustor. The results from these two methods only indicate line-of-sight averaged values, representative of the temperature in the soot-laden region. This possesses a more serious problem in turbulent, rather than laminar flames, since the temperature profile is not homogeneous along the optical path in turbulent flames.

The radiation measurement in this chapter is performed in the "dilution" zone of the SNECMA-designed combustor. Optical temperature measurements were first performed in a sooty laminar flame to examine the technical feasibility of the Schmidt and two-colour methods. Based on the development in the laminar sooty flame, the optical system was then used in the combustor for absolute radiance flux detection. The small dimension laminar flame introduces its own uncertainty in relation to the spatial resolution which has substantial influence on the signal quality, the detailed discussions can be found in Appendix D: Optical Temperature Measurements. The measured absolute spectral radiation intensity from the combustor is compared with that predicted using the measured time-averaged soot volume fraction and temperature profiles reported in the previous chapters.

5.2 EXPERIMENTAL DETAILS

5.2.1 Radiation fundamentals

The spectral distribution of a blackbody emission was first determined by Planck (1959). For a physical non-blackbody, with temperature T, emissivity ε_λ, spectral radiation intensity $I_{e\lambda}$ at wavelength λ can be defined as

$$I_{e_\lambda} = \frac{Cos\,\theta}{\pi} \cdot \varepsilon_\lambda \cdot e_{b_\lambda}\,, \quad \frac{W}{\mu m \cdot m^2 \cdot str} \tag{5-1}$$

where $e_{b\lambda}$ is the spectral blackbody emission

$$e_{b_\lambda} = \frac{C_1}{\lambda^5 [\exp(\frac{C_2}{\lambda T}) - 1]}\,, \quad \frac{W}{\mu m \cdot m^2} \tag{5-2}$$

where the first and second radiation constants are $C_1 = 3.742 \times 10^8$ W.$\mu m^4/m^2$ and $C_2 = 1.439 \times 10^4$ μm.K, θ is the solid angle. [When the viewing direction is normal to the radiation surface, Cosθ is equal to 1.] This intensity distribution is illustrated in Figure 5.1, with radiation flux from blackbody ($\epsilon = 1.0$) and gray body ($\epsilon = 0.1$) of arbitrarily assigned temperatures 2800 and 2000 K respectively. It should be noticed that for most flames generated from hydrocarbon-air combustion the radiation will peak in the infrared region, and the intensity increases monotonously in the shadowed visible spectrum. This is also illustrated by Wien's displacement law (Holman (1990))

$$\lambda_{max} T = 2897.6, \quad \mu m \cdot K \tag{5-3}$$

and when the temperature is below 3220 K the radiation peak intensity fall in the spectrum $\lambda > 900$ nm.

According to Kirchhoff's identity, the emissivity of a body is identical to its absorption coefficient when the mixture is in radiative equilibrium. Combined with the Beer-Lambert law of Eq. 3-1, emissivity of a soot-bearing medium is directly dependent on soot volume fraction following

$$\varepsilon_\lambda = 1 - \exp[-\frac{36\pi F(\lambda) L}{\lambda} \cdot f_v] \tag{5-4}$$

Yuen and Tien (1977) have shown that this equation represents an excellent approximation (within 7%) to exact closed-form expressions for soot emissivity based on non-gray analysis. When soot concentration f_v is very high, ε_λ will approach unity according to Eq. 5-4.

Two optical techniques have been applied for the soot temperature measurement. One is based on the radiation energy flux intensity from the flame and the measured soot volume fraction f_v, which is directly related to flame emissivity ϵ_λ, from which we infer flame temperature T, using Eq. 5-1. This is similar to the Schmidt temperature measurement (Schmidt (1909)), except that the emissivity ϵ_λ is evaluated from f_v following Eq. 5-3, which is derived from more advanced laser extinction measurement. The alternative is the so-called "two colour" measurement, based on the radiation intensities at two different wavelengths λ_1, λ_2,

$$I_{e_{\lambda_1}} = \frac{Cos\,\theta}{\pi} \cdot \frac{C_1 \cdot \epsilon_{\lambda_1}}{\lambda_1^5 [\exp(\frac{C_2}{\lambda_1 T}) - 1]} \qquad (5\text{-}5\ (a))$$

$$I_{e_{\lambda_2}} = \frac{Cos\,\theta}{\pi} \cdot \frac{C_1 \cdot \epsilon_{\lambda_2}}{\lambda_2^5 [\exp(\frac{C_2}{\lambda_2 T}) - 1]} \qquad (5\text{-}5\ (b))$$

Since $\exp(C_2/\lambda T) \gg 1$, we may re-arrange Eqs. 5-5 (a) and (b), such that the expression for temperature T can be derived of the form

$$T = \frac{C_2 (1/\lambda_1 - 1/\lambda_2)}{\ln(\frac{C_1}{\pi} \cdot \frac{\epsilon_{\lambda_1}}{\lambda_1^5 I_{e_{\lambda_1}}}) - \ln(\frac{C_1}{\pi} \cdot \frac{\epsilon_{\lambda_2}}{\lambda_2^5 I_{e_{\lambda_2}}})} \qquad (5\text{-}6)$$

in this case f_v is also needed to calculate the spectral emissivity $\epsilon_{\lambda i}$, i=1,2.

5.2.2 Combustor and instrumentation

The model tubular combustor, together with the experimental rig, was the same one employed in the earlier soot volume fraction measurement and gas analysis experiment. The flow conditions repeated those employed in Chapter 4, ie. AFR=45~22 with air preheating up to 200 °C at pressures 1 and 4 bar. A fused quartz window of effective diameter 10 mm was mounted on the detecting side of the rig to provide radiative optical access.

Red He-Ne laser light (at 632.8 μm, the same laser tube used in the combustor soot volume fraction measurement) was used for optical alignment. Two apertures, of 6.5 mm hole diameter, were positioned between the burner and the detector to define the spatial resolution (Figure 5.2). This diameter is much bigger than the one, 1.0 mm, used in the optical temperature measurement laminar flame. The selection of the 6.5 mm size follows the

conclusion from the laminar flame experiments that bigger aperture size, aside from higher responsivity of radiation detector, is required to increase the radiation signal level and therefore improve the measurement (cf. Appendix D). The aperture diameter chosen here was a compromise between small target size, or better spatial resolution essentially due to the scalar gradients in the combustor flow field, and high signal to noise ratio.

The calibration light source was a blackbody furnace (Spembly Technical Products Ltd. 10 K.V.A high temperature furnace). The radiating element inside the blackbody furnace was a graphite ball which was electrically heated in a nitrogen filled environment. The blackbody temperature of the emitting graphite element was monitored by measuring the total radiation intensity from the element through a Calcium fluoride window of 0.2 inch thick by a Land Continuous Optical Pyrometer (type MQO 7/50/10 EW, Instrument No. 40102) according to the calibration table No. Q431 for the pyrometer. This calibration table is supplied by the pyrometer manufacturer.

The radiation intensity from the flame, or the furnace, was focused by an optical lens onto the entrance slit of the spectrometer. The grating spectrometer (Spex make) was manually scanned to divide the emission intensity into spectral profiles at individual wavelength and then refocused on to a photomultiplier tube (PM tube). For a given spectral emission $I_{e\lambda}$, the PM tube voltage output V and $I_{e\lambda}$ normally had the following linear relationship

$$I_{e_\lambda} = a_\lambda V + b \tag{5-7}$$

where a_λ, b were wavelength dependent constants of the PM tube. The calibration curve of the PM Tube output voltage against the furnace radiation was shown in Figure 5.3. The constants a_λ, b were instrument dependent and therefore had to be calibrated prior to the measurement. The radiation flux measurements initially provided voltage signal from the PM tube, such voltage can then be converted to absolute radiation intensity using the calibration in Eq. 5-7.

Once the radiation intensity was obtained, optical temperature can be readily calculated. Since the solid angle in this experiment was considered to be 0, the Schmidt temperature can be determined following

$$T = \frac{C_2}{\lambda} \cdot \frac{1}{\ln\left[\frac{C_1}{\pi} \cdot \frac{\epsilon_\lambda}{\lambda^5 (a_\lambda \cdot V + b)} + 1\right]} \tag{5-8}$$

and the two-colour temperature can be obtained from Eqs. 5-6 and 5-7 as

$$T = \frac{C_2(1/\lambda_1 - 1/\lambda_2)}{\ln[\frac{C_1}{\pi}\cdot\frac{\epsilon_{\lambda_1}}{\lambda_1^5(a_{\lambda_1}V+b)}] - \ln[\frac{C_1}{\pi}\cdot\frac{\epsilon_{\lambda_2}}{\lambda_2^5(a_{\lambda_2}V+b)}]} \tag{5-9}$$

Emissivity $\epsilon_{\lambda i}$ in Eqs. 5-8 and 5-9 were related to soot absorption in Rayleigh limit

$$\epsilon_M = 1 - \exp[\ln(\frac{I}{I_o})\cdot\frac{F(\lambda_i)}{F(632.8)}] \tag{5-10}$$

where $\ln(I/I_o)$ was measured by laser extinction at 632.8 nm. Selection of soot refractive indices from different workers will introduce some discrepancy in the results. Details of this issue will be discussed in the following sections.

5.2.3 Data acquisition

The visible radiation flux from the luminous flame was focused on to the entrance slit of the spectrometer, and measured by the PM tube. The width of the entrance slit was adjusted at about 1.0 mm to provide enhanced signal strength, whereas the spectral resolution was about 5 nm halfwidth which was determined at the wavelength of 632.8 nm by the He-Ne laser light. The spectrum range, employed in this study from 514.5 to 850 nm, was limited by the effective response range of the PM tube (Burle make, model 4832) from about 185 to 930 nm, and the lower limit was also related to the signal-to-noise ratio. The absolute responsivity of the PM tube is typically about 60 mA/W. The voltage output from the PM tube was sent through an Analog-Digital Convertor to BBC micro-computer, whose measuring range was set at 0~20 mV. The experimental procedure involved collecting 10,000 samples from the flame at the sampling frequency of 14.3 kHz. The uncertainty arising from the optical detecting system was less then 3 percent, which was estimated during the calibration of the PM tube against the furnace.

As mentioned before, the selection of soot refractive indices will introduce some discrepancy in the results. The data reported by Lee and Tien (1981), Dalzell and Sarofim (1969) and Mullins and Williams (1987) suggested that soot refractive index is largely insensitive to the composition and structure of the parent fuel. It is noticeable that this conclusion was only based on gaseous fuels of pure composition. The values of such soot properties from kerosine flames reported by Batten (1985) are significantly different (See Appendix A: Survey of Soot Refractive Index). Since it is value of $F(\lambda)/\lambda$, $F(\lambda)$ is the complex function of refractive index, that is used in the data processing, the uncertainty of the temperature measurement depended on this value. Such value suggested by Batten (1985) is

typically about 20% lower than that by Lee and Tien (1981). Spectral emissivity ϵ_λ is proportional to $F(\lambda)/\lambda$ (cf. Eq. 5-4) and temperature inferred by using Batten's data will thereafter be higher than that using Lee and Tien's following Eqs. 5-8 and 5-9.

5.2.4 Radiation prediction based on experimental data

The equation of radiative heat transfer describes the spectral radiation intensity $I_{e\lambda}$ in a medium of spectral extinction coefficient k_λ along a non-homogeneous path, x_i, as

$$\frac{dI_{e_\lambda}}{dx_i} = -k_\lambda(x_i)\left[I_{e_\lambda}(x_i) - \frac{e_{b,\lambda}}{\pi}\right] \tag{5-11}$$

$e_{b,\lambda}$ is the spectral blackbody emission at λ (Eq. 5-1). In the combustor "dilution" zone, scattering by soot particle and fuel droplet were assumed to be negligible, as the parametric size of soot $\pi d/\lambda \ll 1$ and the number density of fuel droplets was considered to be low. Therefore the extinction was entirely attributed to absorption. Integrating Eq. 5-11 for the spatial distance from $-D_d/2$ to $+D_d/2$, where $D_d = 98$ mm was the dilution zone diameter, gave

$$I_{e_\lambda}(D_d/2) = I_{e_\lambda}(-D_d/2)\tau_\lambda(D_d/2) - \int_{-D_d/2}^{D_d/2} k_\lambda(x_i)\frac{e_{b,\lambda}(x_i)}{\pi}\tau_\lambda(x_i)\,dx_i \tag{5-12}$$

where the transmittance $\tau_\lambda(x_i)$

$$\tau_\lambda(x_i) = \exp\left(-\int_{D_d/2}^{x_i} k_\lambda(x'_i)\,dx'_i\right) \tag{5-13}$$

the absorption coefficient $k_\lambda(x_i) = 36\pi F(\lambda) fv(x_i)/\lambda$ was that employed in Eq. 3-9, and the blackbody emission $e_{b,\lambda}(x_i)$ was defined by Eq. 5-2. The boundary $x = -D_d/2$ (at the combustor wall) was always free of soot thus $I_{e\lambda}(-D_d/2) = 0$. The soot concentrations were very low ($f_v < 4\times10^{-7}$) at the present flow conditions. Applying the optical thin assumption, ie. $\tau_\lambda(x_i) = 1$, will cause, in the case of most sooty condition AFR=30 at 4 bar, less than 5% difference in the integrated line-of-sight radiation predictions. Eq. 5-12 is for the prediction of radiative emission from turbulent flame which normally requires a detailed knowledge of the variation in both time and space of temperature and radiating species. In the present experiment the soot particles were the major emission source in the spectrum from 514.5 to 850 nm. All the experimental data, for example radiation intensity, temperature and soot concentration, however were time averaged. The measured radiation intensities were compared with the predictions from Eq. 5-12 based on the measured mean properties.

5.3 RESULTS AND DISCUSSION

The PM tube voltage against spectral wavelength at various flow conditions is shown in Figure 5.4, the signals are much higher than 1 mV, a threshold of sensitive signal level as discussed in Appendix D, and thus the PM tube voltage should be in the linear part of its calibration, ie. Eq. 5-7 applies to all the measurements. The corresponding spectral radiation intensities at these flow conditions (Figure 5.5) have been calculated based on the calibration in Figure 5.3.

One distinct feature of the profiles in Figure 5.5 is that there is a high peak at the wavelength near 515 nm. This is the narrow banded emission from C_2 at the Swan band since C_2 has very strong emission at 516 nm (Gaydon (1974)) which is within the half-width of the spectrometer set-up. The higher C_2 emissions at increased soot levels from the measurement (Figure 5.5 (c), (e) and (g)) may imply a simultaneous increase in the C_2 concentrations. There is however no such distinct emission reported in other sooty flames, for example those fuelled by methane (Crauford et al. (1985)). The role of C_2 in soot formation has often been analytically excluded given the recent more evident role of PAH/C_2H_2 in the soot nucleation. It was suggested by Tesner et al. (1971) and Jensen (1974) that C_2 fragment might be the kinetic equivalent of condensed "nuclei". Natural C_2 radicals are non-thermally excited products from as yet unidentified chemical reactions. Its concentrations in hydrocarbon flames are often very low, even in rich acetylene/oxygen flames at temperatures above 3000 K, the mole fractions of C_2 are of the order of $10^{-4} \sim 10^{-3}$ as measured by Baronavski and McDonald (1977). The distinct peak observed here in a combustion enviroment where the mean temperature is lower than 2000 K may be attributed to a high C_2 concentration. The emission data here may indicate the C_2 connection with soot formation.

The radiation intensity at AFR=45 and 1 bar is also very interesting as it implies that the low level of laser extinction measured in Chapter 3 is mostly due to soot particle absorption and the aerosol is not dominated by droplets. This is because that liquid droplets will not emit any visible radiation energy. Although droplet contamination has not been clarified quantitatively, the low number density and small size of droplets in the dilution zone suggest that, even with the fuel droplets present, it will be optically thin to the radiation and therefore will not disturb the soot volume fraction measurement at this particular flow condition.

The maximum temperature in the "dilution" zone of the combustor was measured to be 1960 K at the present flow conditions (cf. Chapter 4). Soot particles, at these temperature levels, would exhibit a peak radiation at a wavelength longer than 1478 nm from Wien's displacement law (Eq. 5-3). The radiation intensity curves show a monotonic increase in the present spectral range, in line with the classical theory.

Predictions based on time mean properties, namely temperature and soot volume fraction profiles, are compared with the measured radiation data. For conditions of atmospheric pressure, the predictions all underestimate the mean flame emission whilst at AFR=30 and 4 bar the prediction is about 50% higher than the measurement. The underestimation may reflect the ignorance of turbulent fluctuations in the flame structure which features turbulent/radiation interactions. The inadequacy of this mean-property calculation for thermal radiation flux has been reported by Jeng et al. (1984), Syed et al. (1990) and Sivathanu et al. (1991) in fires and jet flames by Faeth et al. (1987). Experimental uncertainties, for example the variation of flow conditions for the different measurements and the measurement accuracies of the f_v and T, may affect the radiation prediction which is correlated from the f_v and T data. Fundamental impacts, for example the detailed distributions of f_v and T and the scalar fluctuations, can be important and will be assessed in more detail.

In jet flames, the high soot concentration regime is often associated with high temperature and the major radiation source is comparatively easy to locate. In the gas turbine combustor mixtures of high soot volume fraction does not necessary have high temperature, as for example shown in Figure 5.5 (b), (d), (f) and (h). It is thus difficult to define from these time-averaged properties which part along the line of sight is the main emitting body. A strong dependence of radiation flux on the detailed soot concentration and temperature distributions in the combustor has been observed in their prediction by Mengüc et al. (1986).

Furthermore, temperatures greater than the time-average value are expected to contribute more to the mean emission than the average temperature because of the exponential dependence of the radiation intensity on temperature in Eq. 5-1. The turbulent intensity which can be defined as T_{RMS}/T_{mean}, T_{RMS} is the root-mean-square temperature, has been found the highest in the combustor about 13% at atmospheric pressure by Heitor and Whitelaw (1986). Similar level of temperature fluctuation has also been reported by Zhu et al. (1993). Assuming the temperature fluctuation scale in the SNECMA designed combustor has the similar level near the dilution jets and a lower level, 10%, in the centre part of the combustor, instantaneous temperature profiles may be represented as $T_{mean}+T_{RMS}$ (the lower temperature $T_{mean}-T_{RMS}$ is not as influential as the higher one in the contest of mean radiation prediction). The predictions based on the "instantaneous" temperature show a closer agreement with the measurements. No such demonstration has been made for the condition of AFR=30 at 4 bar. The close agreement at 4 bar may reflect a low degree of scalar fluctuation whilst the over-prediction may stem from the droplet contamination in the extinction measurement which give an over-estimation of f_v (Figure 5.5 (g)). The importance of the scalar fluctuation, especially temperature fluctuation, in the mean radiation prediction is clearly illustrated for flow conditions at atmospheric pressure

while at elevated pressures such radiation/turbulence interaction may diminish.

The estimated optical temperature is based on the integrated radiation intensity and integrated laser extinction measurements. The extinction value at AFR=45 of 4 bar is interpolated from Figure 3.22. The Schmidt and two colour optical temperature calculations are compared for all the different conditions. The temperatures inferred at each condition are fairly constant over the spectrum (Figure 5.6 (a)), except at 600 nm where the signal to noise levels are relatively low and give a sharp change. At the commonly used wavelength of 632.8 nm, at which soot volume fraction is measured, the line of sight mean temperatures indicate the logical change of temperature as fuel flow rate increases at both 1 and 4 bar pressures.

The discrepancy arising from the choice of soot refractive index is illustrated in Figure 5.6 (b), where two set of index are applied for the two colour temperature estimation. The most commonly cited data of Lee and Tien (1981) lead to the lower temperature (about 100 K) than using Batten's (1985) data. The Schmidt temperature is higher at conditions of low soot concentration (AFR=45 and 28, P=1 bar). Spatial temperature profile in Chapter 4 indicates the difference for pressures 1 and 4 bar at AFR=45 is about 150 K. The Schmidt value shows such difference of about 50 K and two colour about 230 K using Lee and Tien's data.

To verify the optical temperature measurement, all results from Schmidt and two colour have been drawn in Figure 5.7 to compare with the thermocouple value. The bars indicate the span generated by the two different techniques and selection of refractive index. The line of sight temperatures are close to the ones in the centre of the combustor. The temperatures compare favourably for each flow condition which implies that radiation predictions may have an encouraging agreement with line-of-sight radiation flux measurements if the prediction is based on the line-of-sight soot concentration data. The prediction is linearly proportional to the soot volume fraction as illustrated in Eq. 5-13 and the f_v fluctuation may be mildly influential compared with the temperature fluctuation as revealed in the temperature comparisons in Figure 5.7.

5.4 CONCLUDING REMARKS

Radiation measurements have been conducted in the tubular combustor, complementing the previously reported soot volume fraction and temperature measurements.

Spectral radiations at 514.5 nm (of 5 nm halfwidth) have distinct peak which may be

contributed from C_2 emission, and the such emission increases with more sooty flame inside the jet kerosine-fuelled combustor. The detailed connection of C_2 to the soot formation need further experimental investigation given the comparatively limited information in the literature.

Spectral radiation intensities in the combustor are in poor agreement with that predicted using the measured time-mean, spatially resolved soot volume fraction and temperature profiles. In the highly turbulent flow inside the combustor, property fluctuations, especially temperature fluctuation, can not be ignored since the radiative intensity is a strong function of temperature. Using the temperature profiles, including the fluctuation, in the combustor can improve the prediction significantly as shown in the present study. To have more precise prediction a more detailed description of the turbulent/radiation interaction, or instantaneous properties may be necessary using, for example stochastic method, for flow conditions at low pressures.

Optical soot temperatures inferred from line-of-sight soot extinction and radiation measurements are close to the gas temperatures which occur at the positions of low average soot concentration and much higher than the time-averaged temperatures corresponding to the high soot loading region near the dilution holes (or combustor wall). The fluctuations of both temperature and soot concentration in this region are relatively high and are probably the most important source of the discrepancy in the predictions.

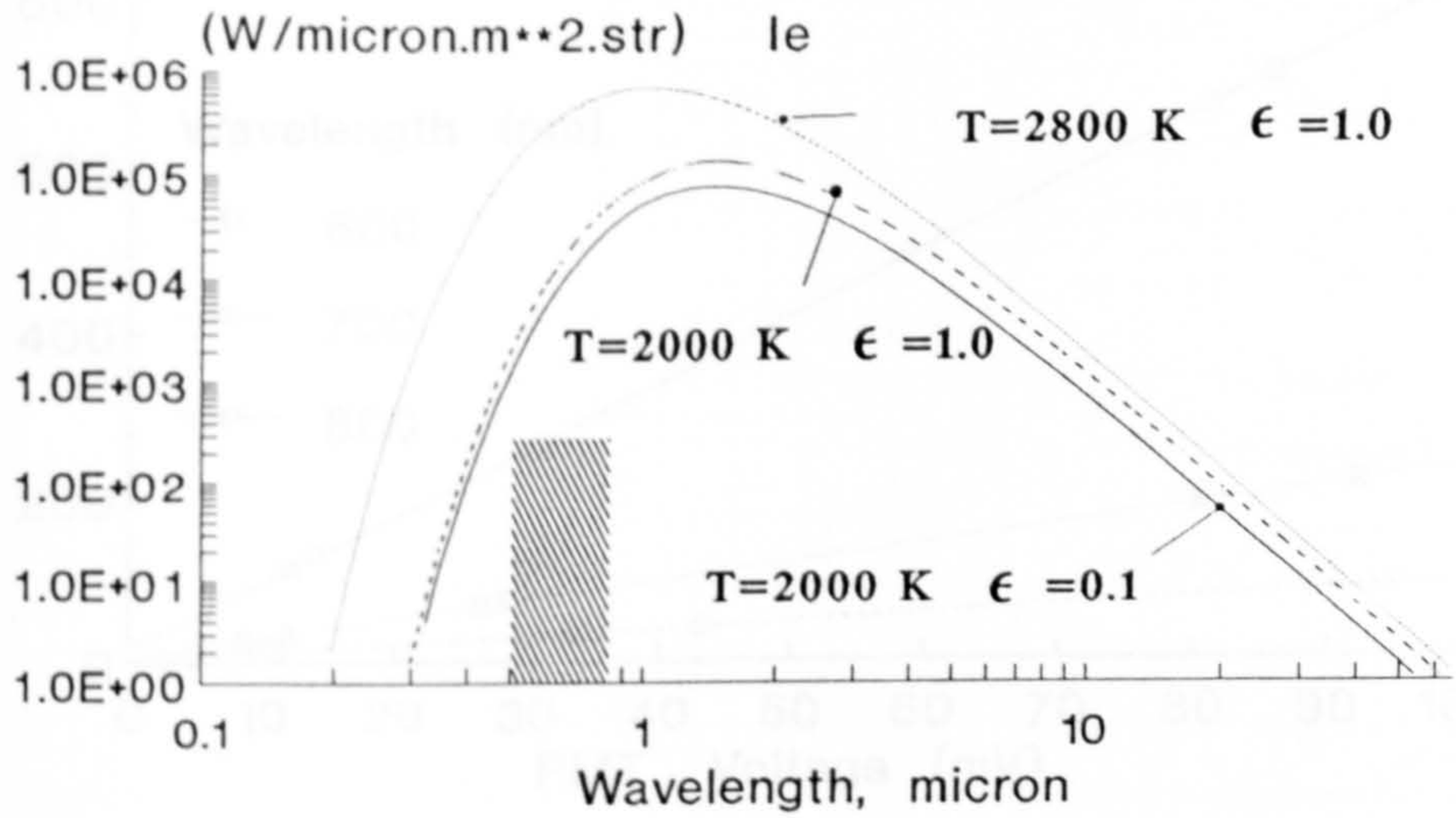

Figure 5.1 Spectral distribution of radiation energy flux intensity (from Eq. 5-1)

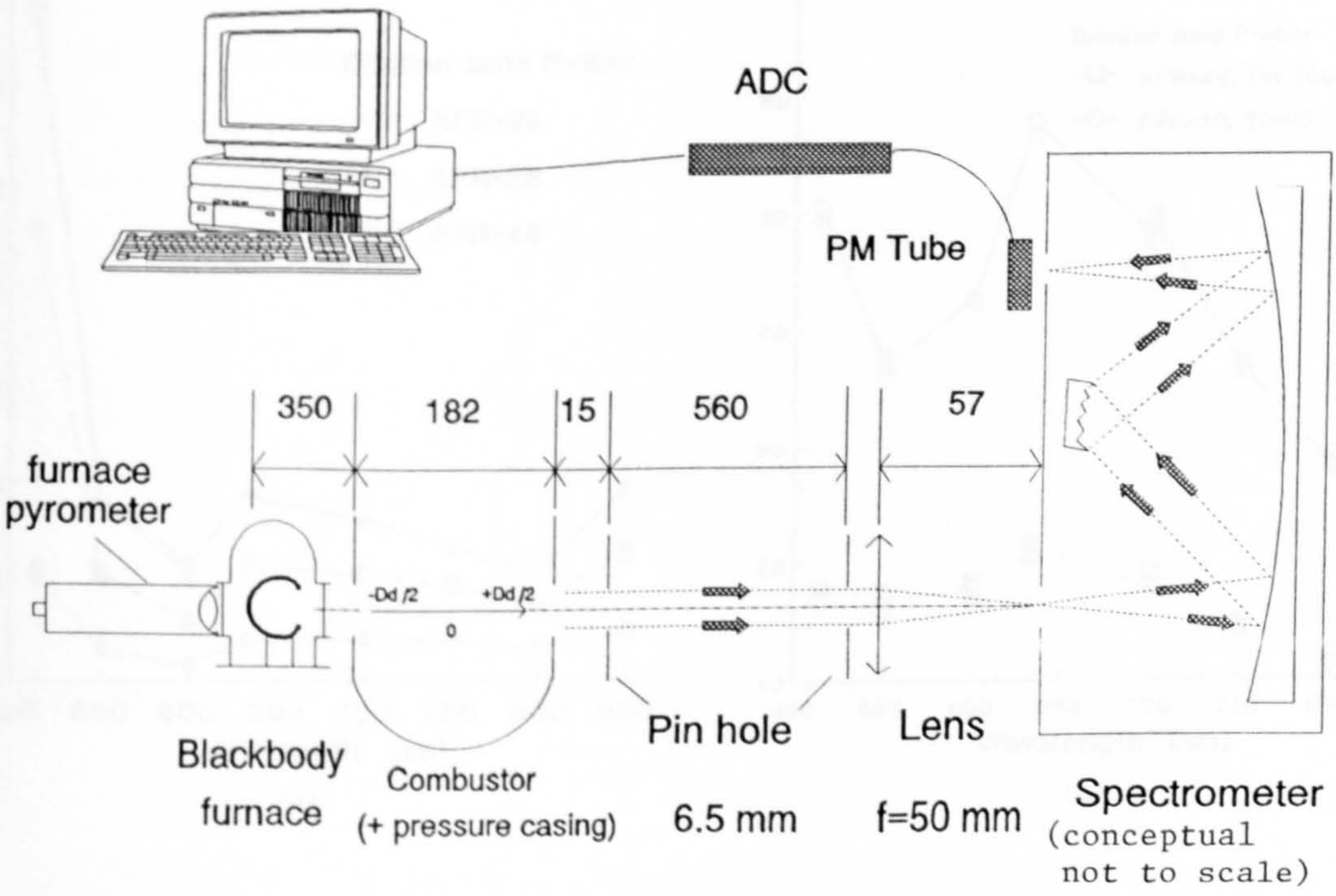

Figure 5.2 Optical set-up for radiation measurement in the combustor (calibration by furnace)

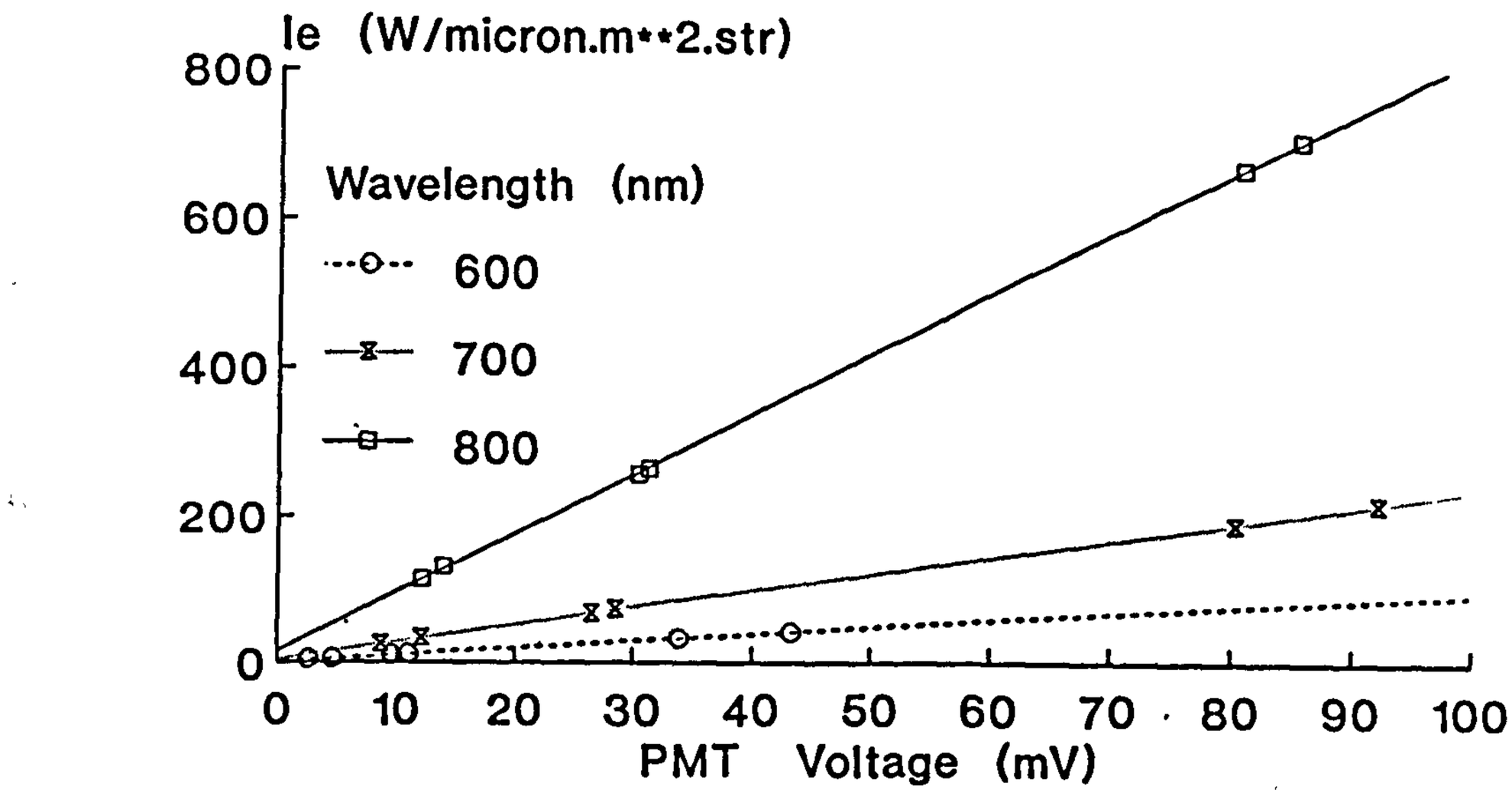

Figure 5.3 PM tube calibration against blackbody furnace radiation

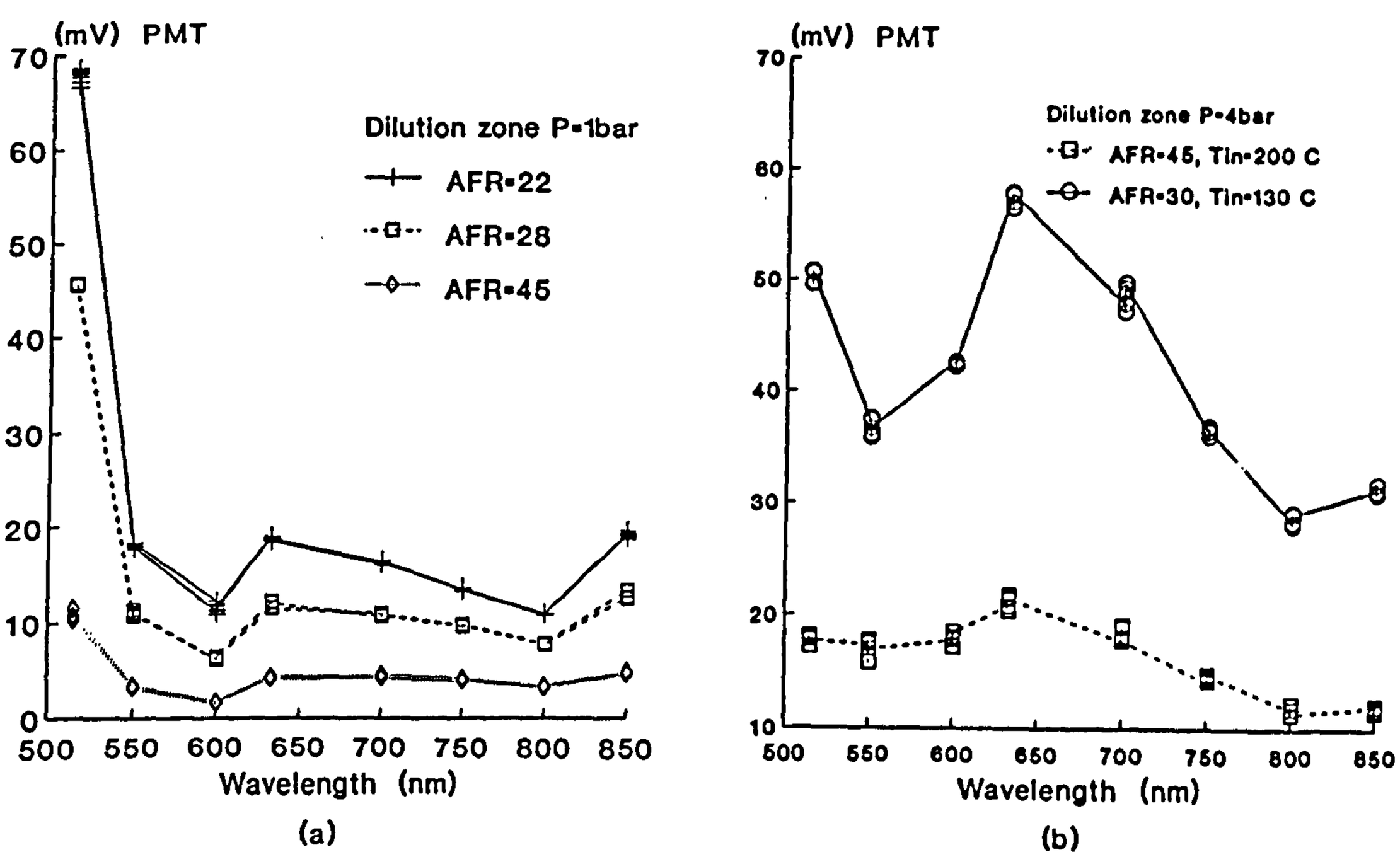

Figure 5.4 Raw voltage data of radiation measurements for different AFRs at pressures (a) 1 and (b) 4 bar

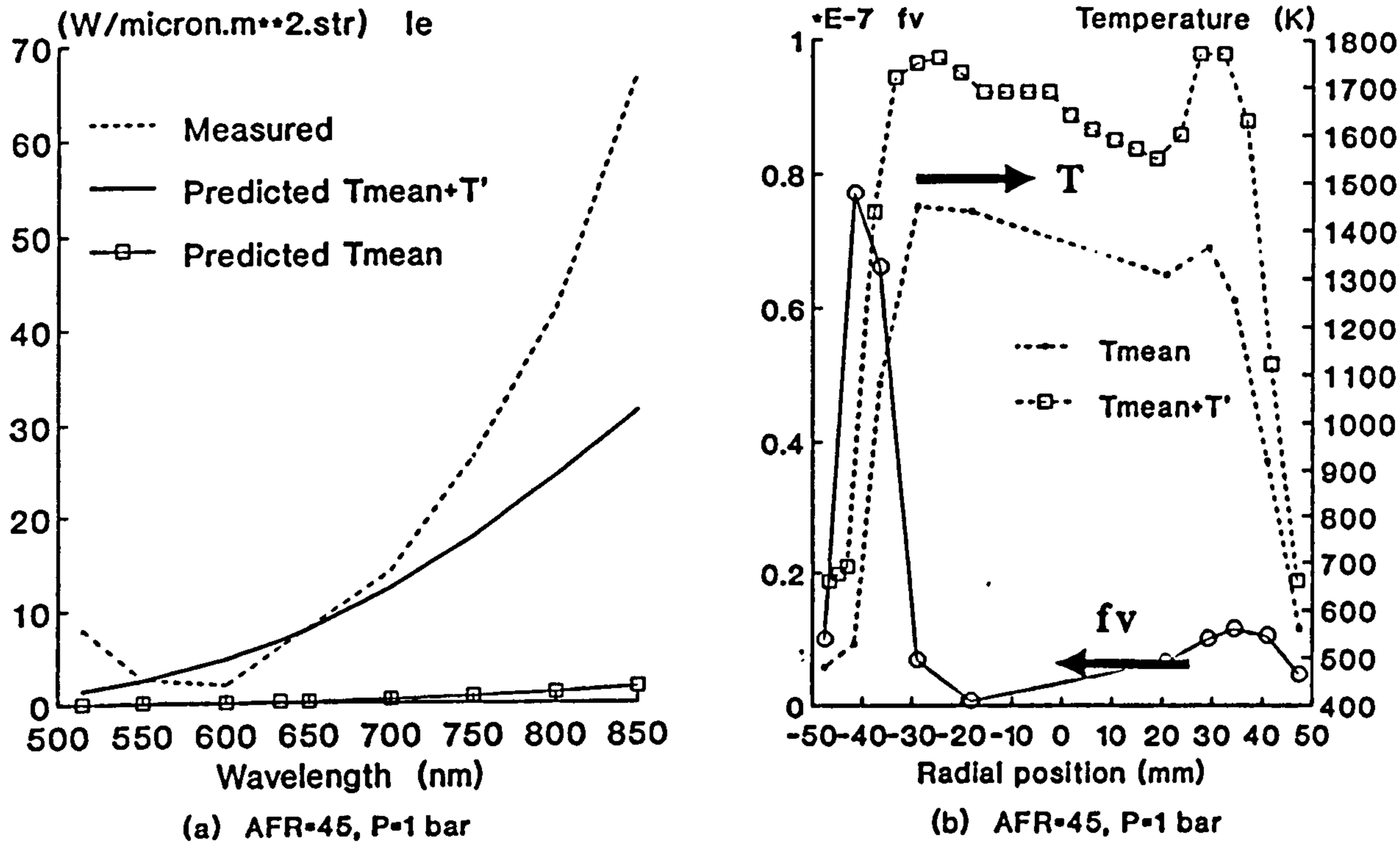

(a) AFR=45, P=1 bar

(b) AFR=45, P=1 bar

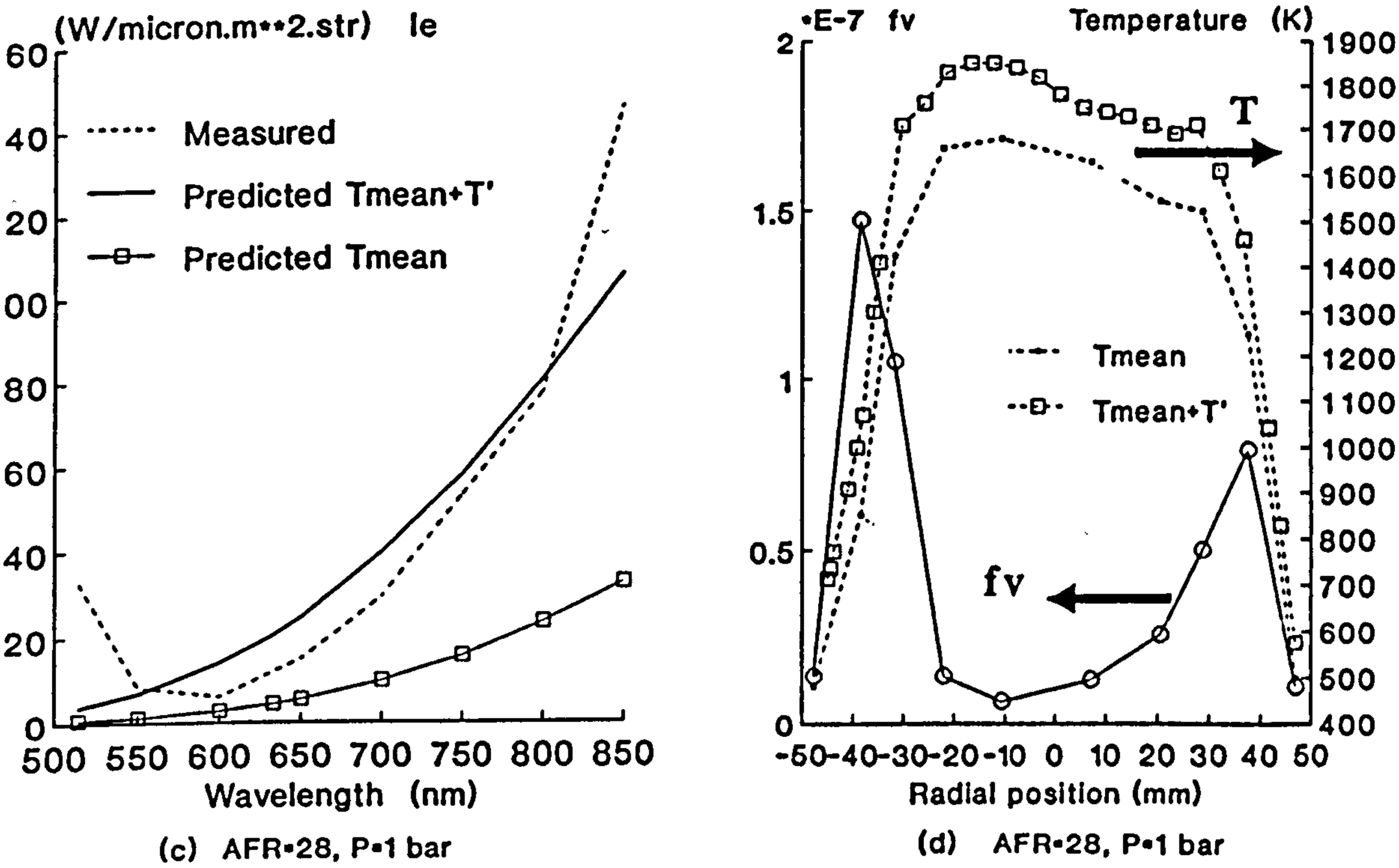

(c) AFR=28, P=1 bar

(d) AFR=28, P=1 bar

Figure 5.5a Comparison of measured and predicted spectral radiation flux for (a) (b) AFR=45 and (c) (d) AFR=28, P=1 bar with the effect of temperature fluctuation on the prediction

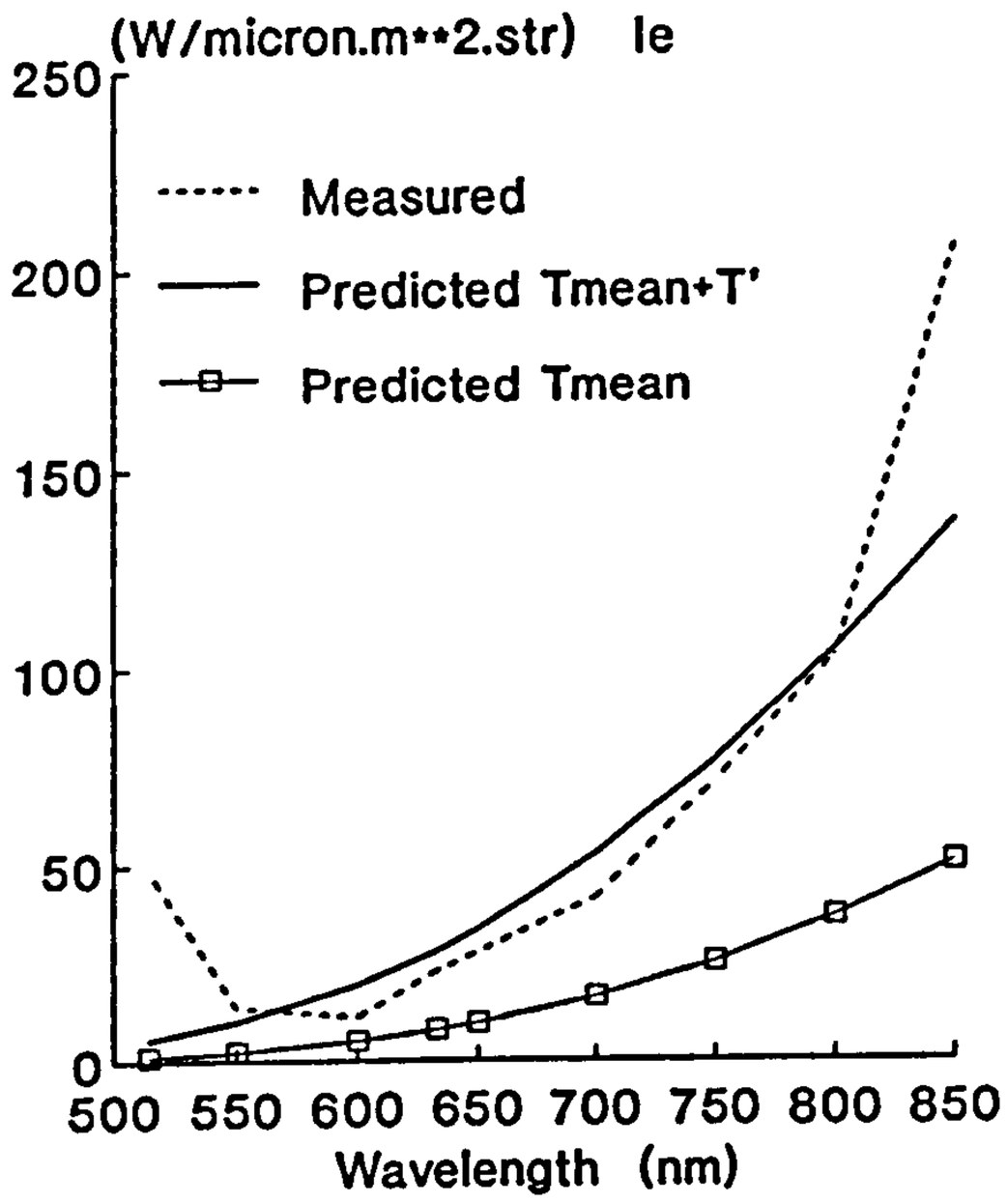

(e) AFR=22, P=1 bar

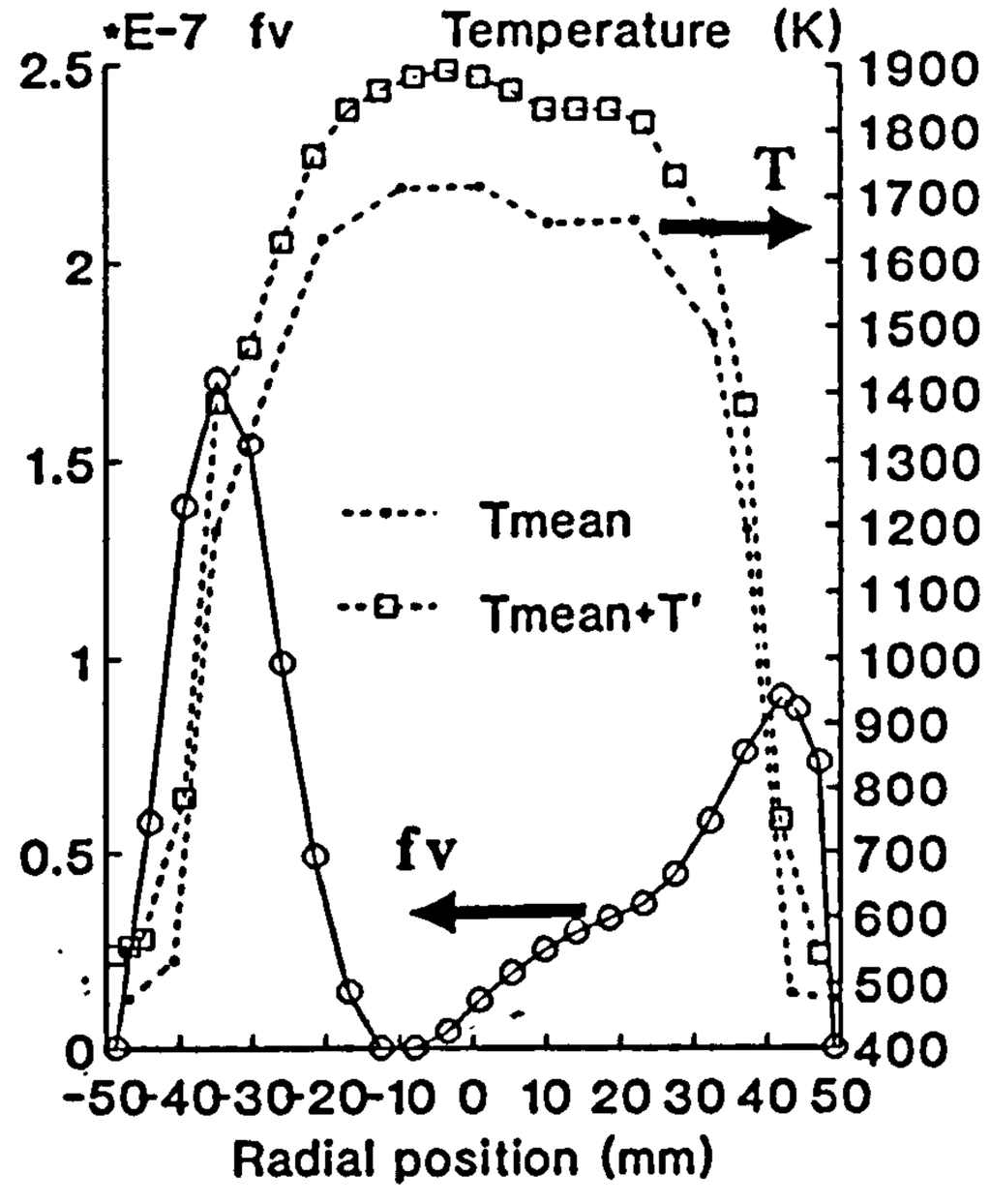

(f) AFR=22, P=1 bar

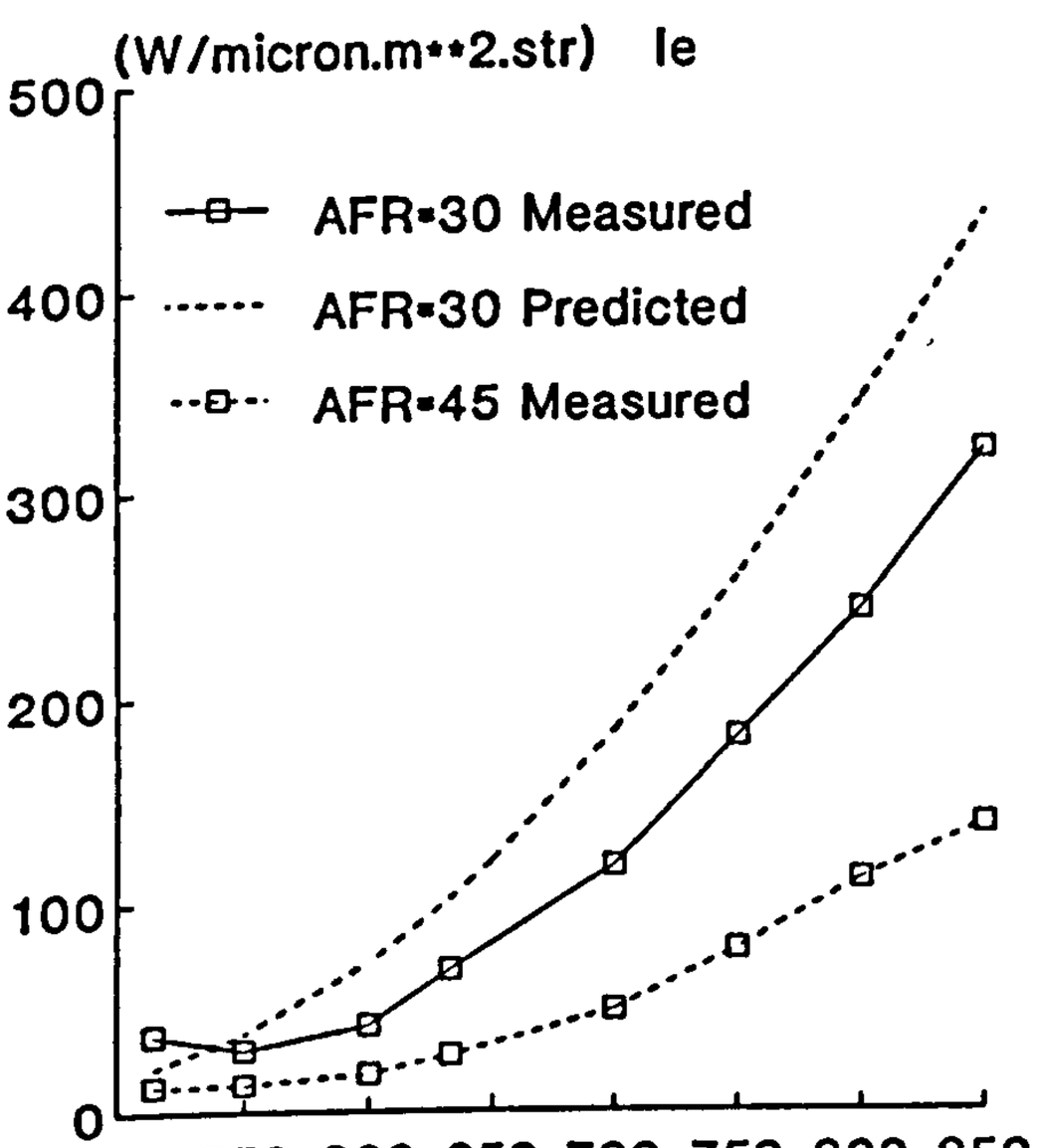

(g) P=4 bar

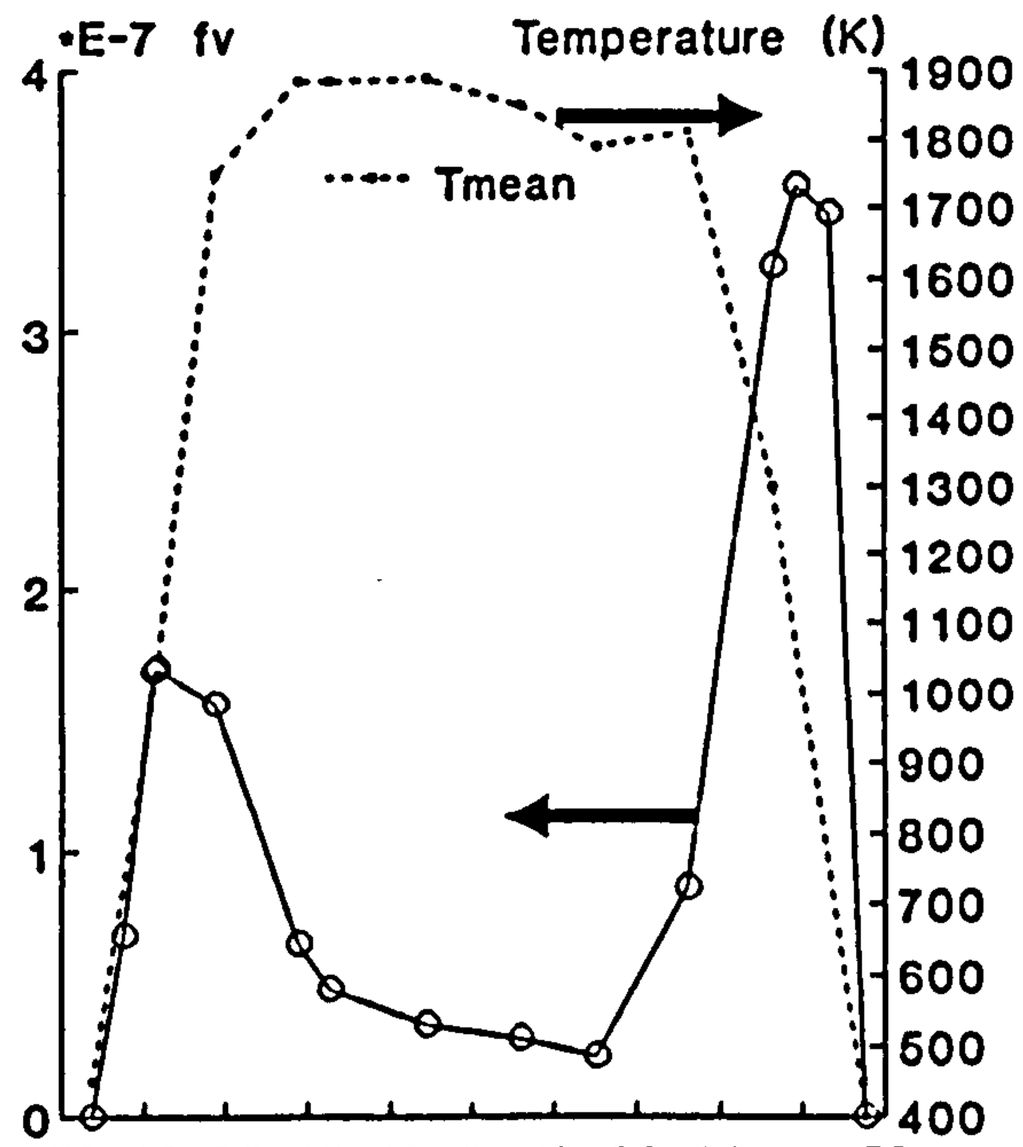

(h) AFR=30, P=4 bar (Tin=130 °C)

Figure 5.5b Comparison of measured and predicted radiation flux for (e) (f) AFR=22, P=1 bar and (g) (h) AFR=30, 4 bar, with the effect of temperature fluctuation on the prediction

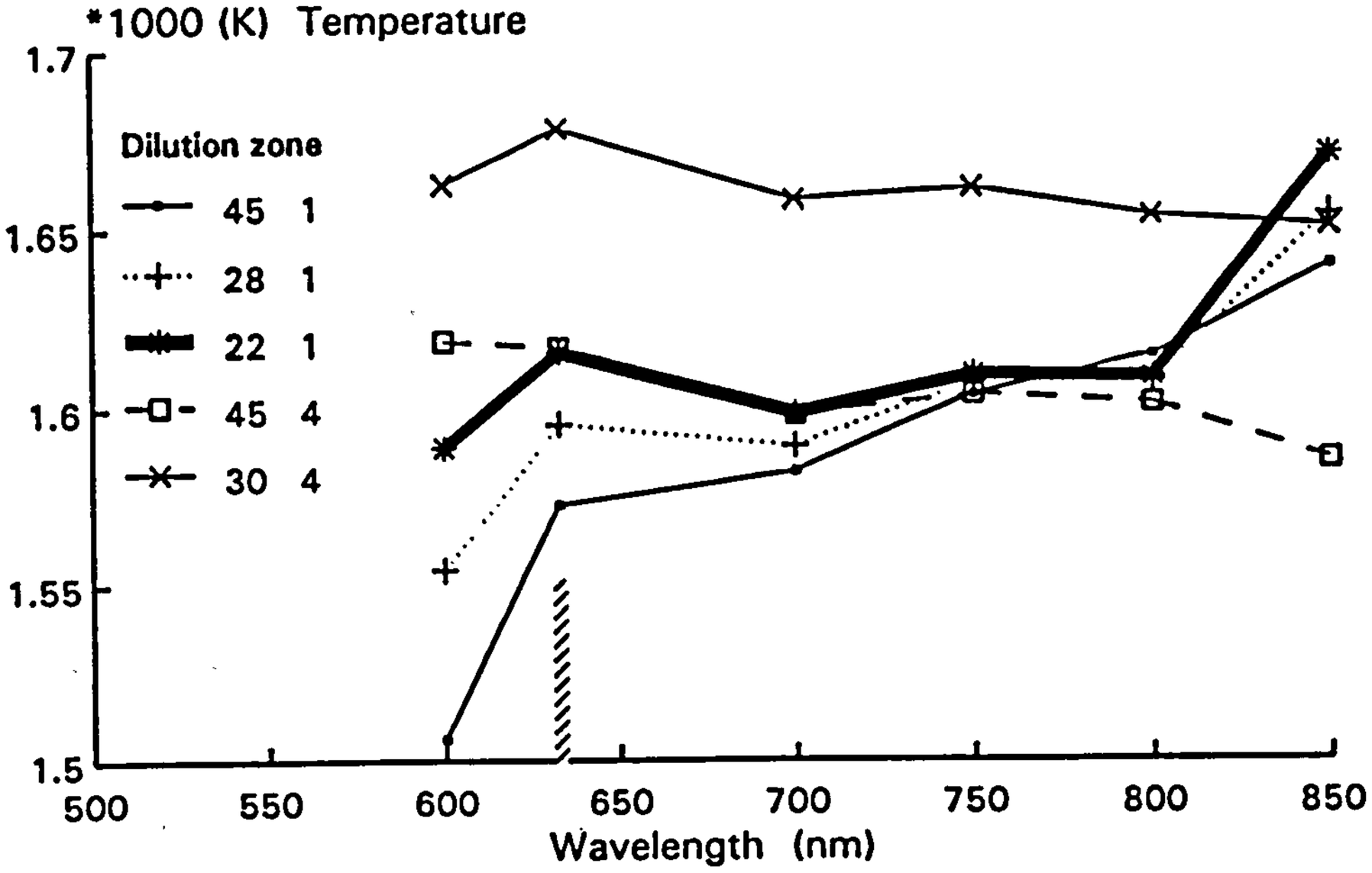

(a)

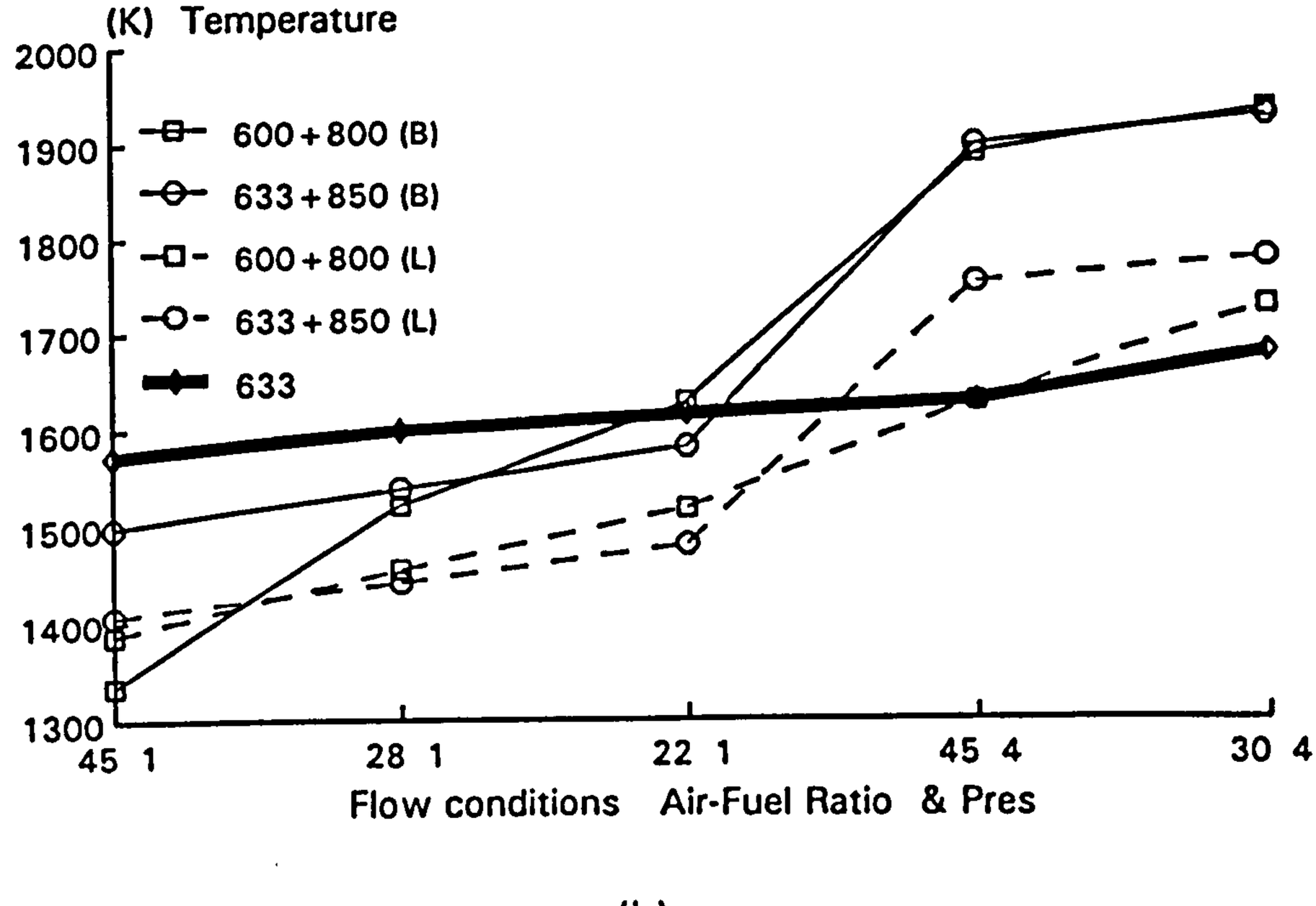

(b)

Figure 5.6 Averaged temperature based on (a) schmidt and (b) two colour methods from integrated radiation and soot volume fraction (I/I_o) measurements

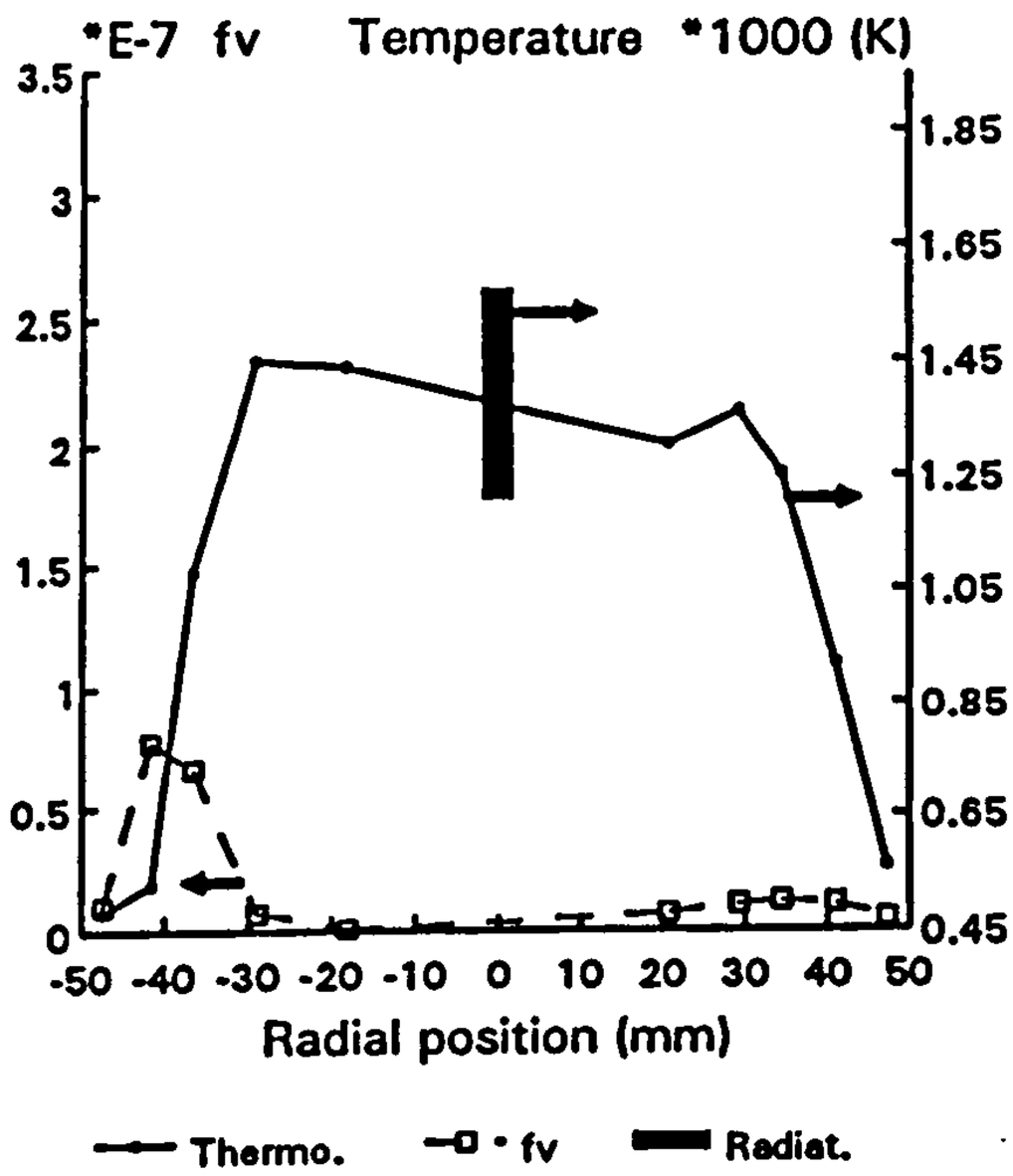

(a) AFR = 45, P = 1 bar

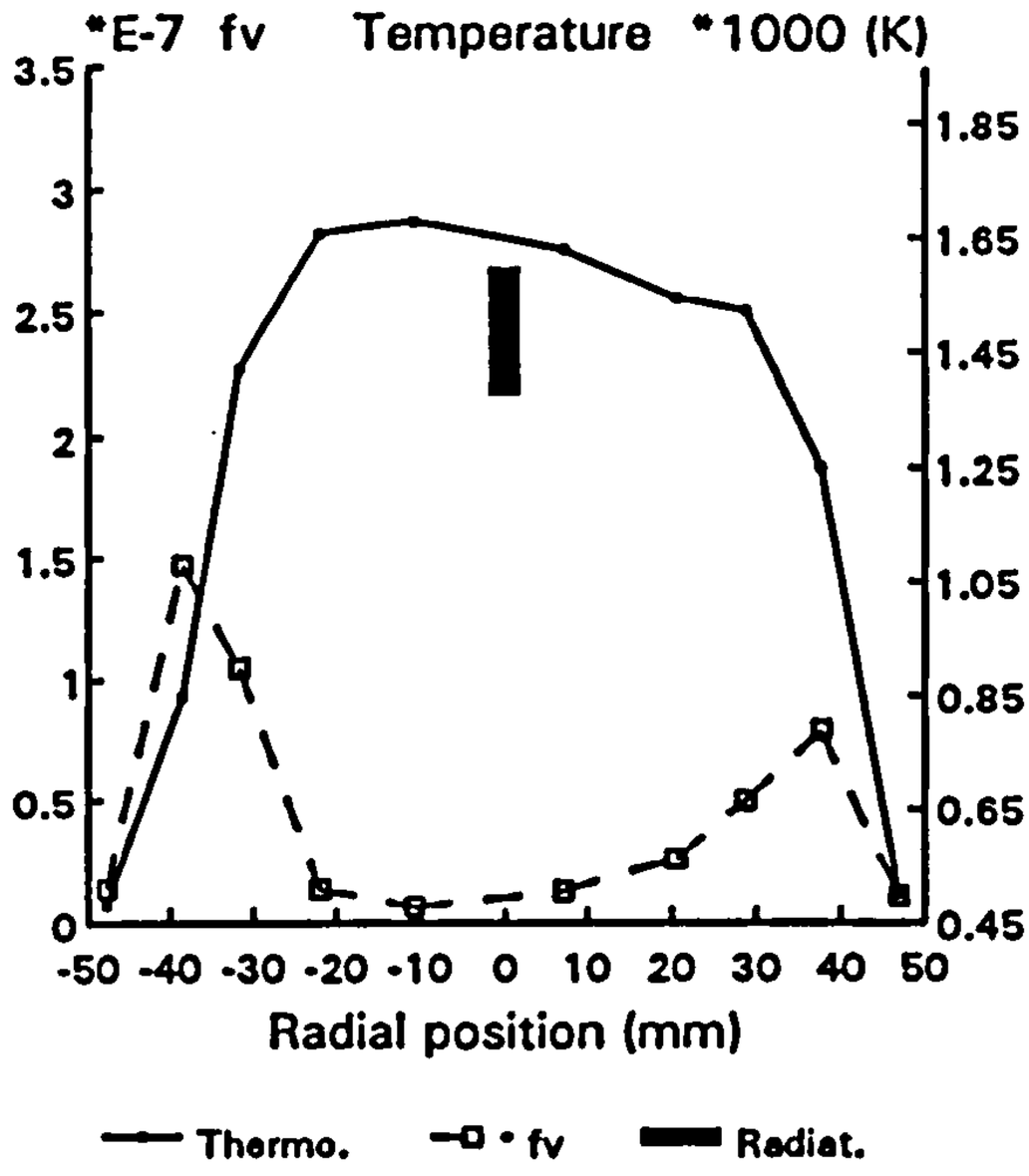

(b) AFR = 28, P = 1 bar

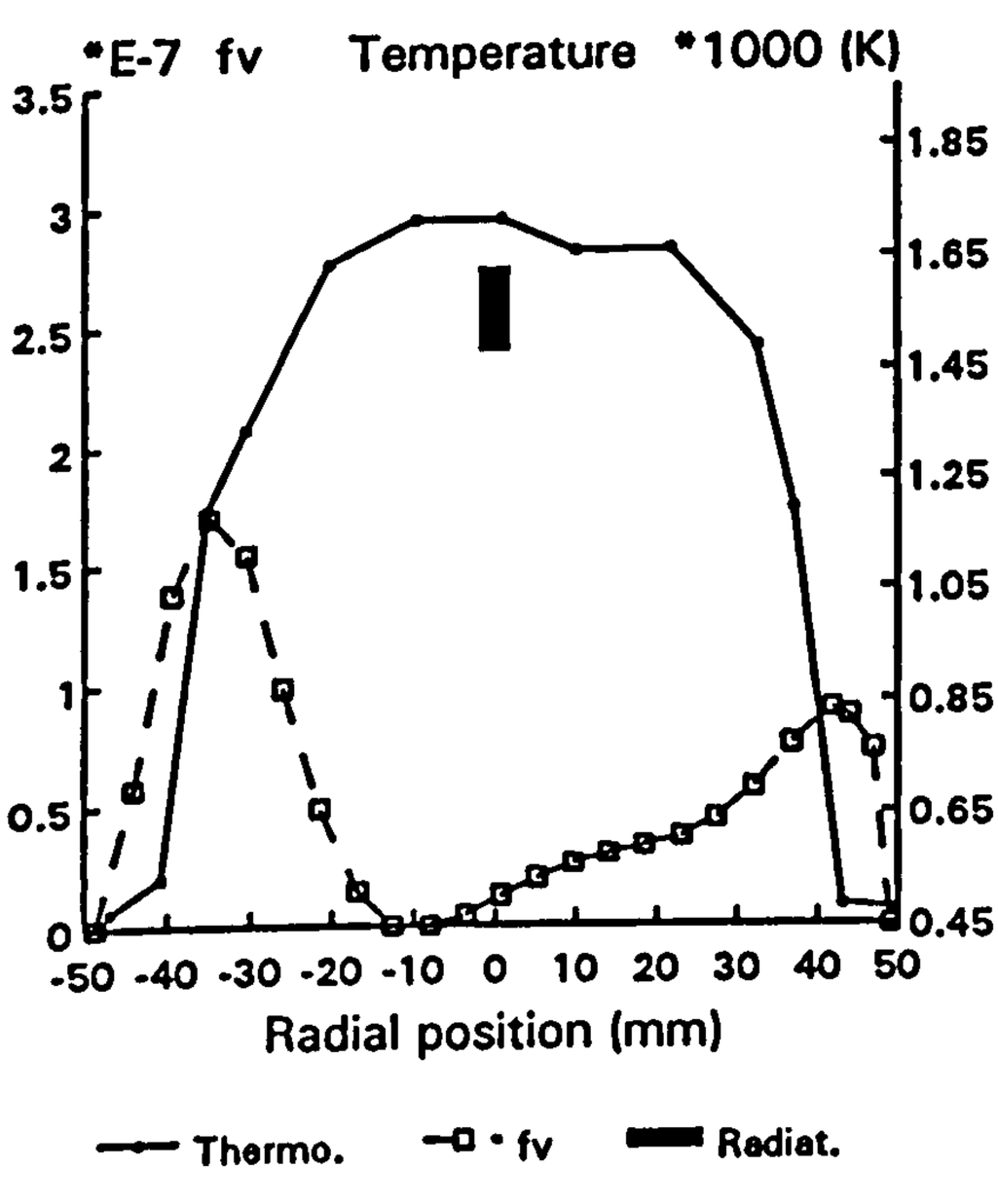

(c) AFR = 22, P = 1 bar

Figure 5.7a Comparison of temperature by thermocouple and optical measurements, P=1 bar. Highlighted bars indicate possible range of integrated temperature

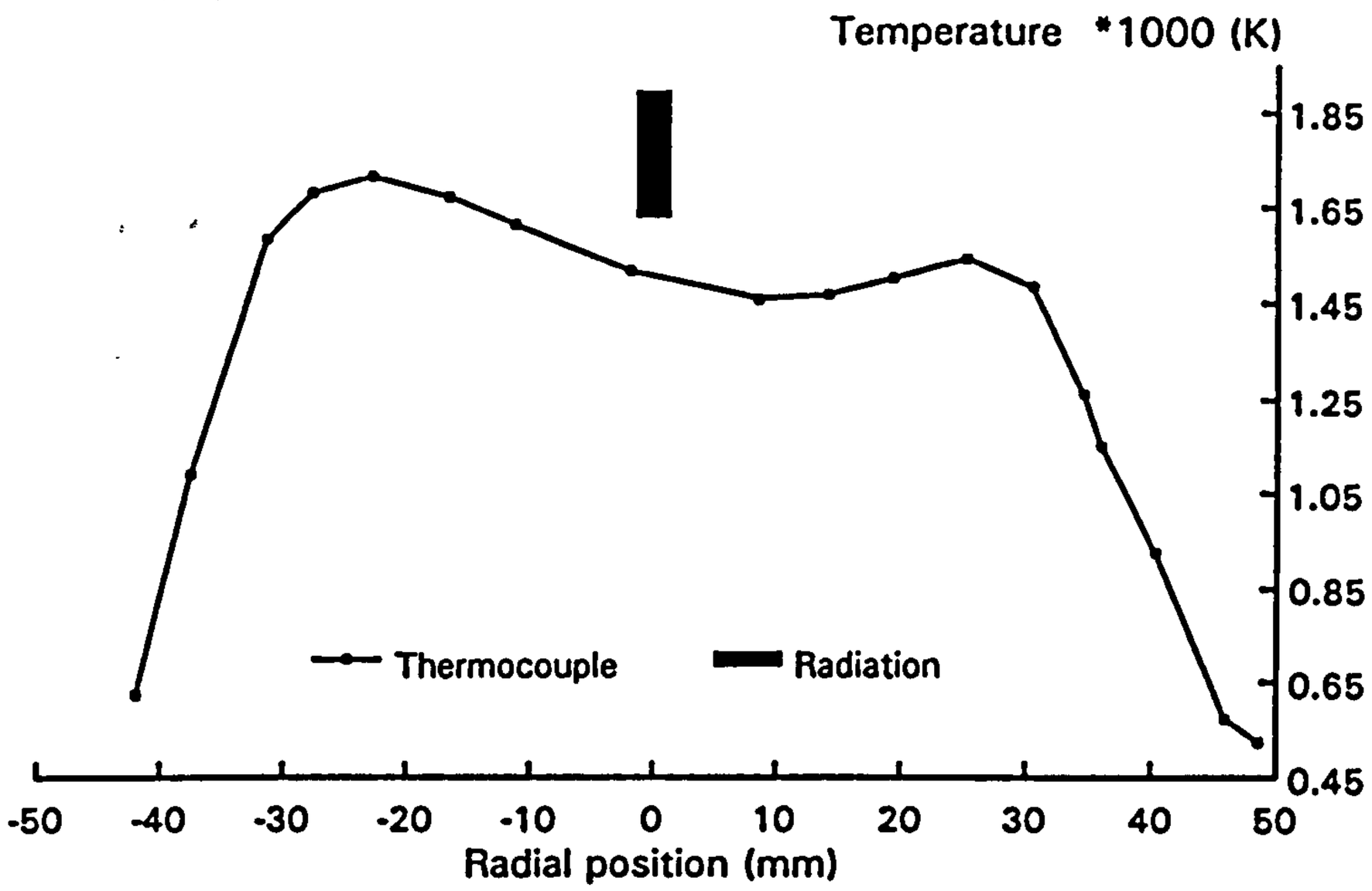

(a) AFR=45, P=4 bar

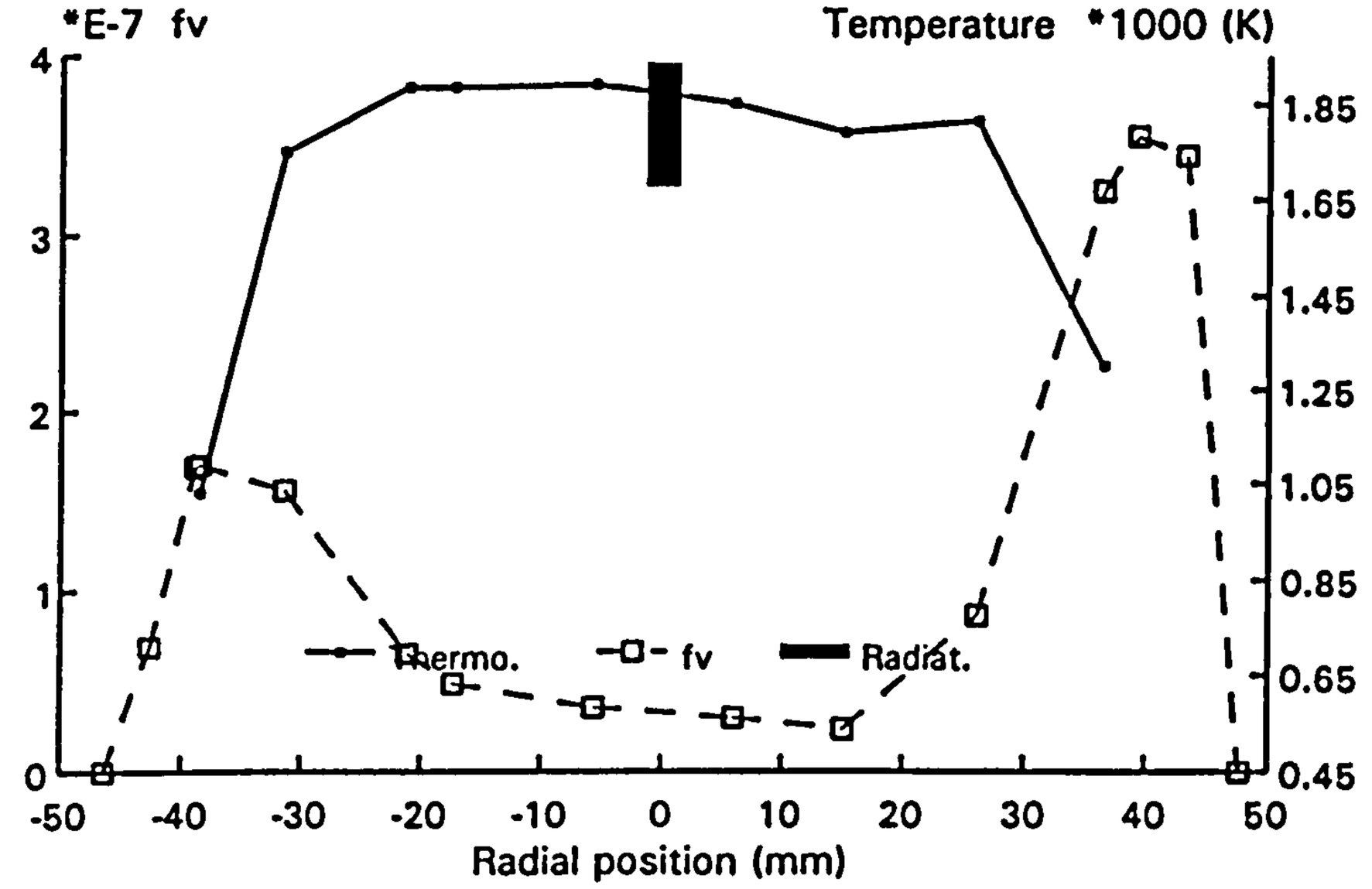

(b) AFR=30, P=4 bar (Tin=130°C)

Figure 5.7b Continued. P=4 bar

Chapter 6 Modelling Soot in the Combustor Flow Field

6.1 INTRODUCTION

Gas turbine combustor designs have evolved through largely empirical development in the past, where the general combustor performance can be estimated from correlations with fairly acceptable accuracy, for example those of exit plane temperature pattern and combustion efficiency. The more demanding challenge embodied in pollutant emission reduction, for smoke and NOx in particular, needs information from within the combustion chamber since these species are not simple equilibrium products due to the comparatively slow chemistry. The numerical predictions for these species must therefore be extended into the combustor.

The present understanding of the turbulence, the detailed chemistry of the multi-component fuel (kerosine) combustion and their interaction is very poor. Mathematical models describing these phenomena are at present incapable of simulating the combusting flow with sufficient accuracy. Further more, the highly complex shape of a modern combustion chamber in conjunction with the irregular flow boundary, for example primary and dilution jets and film cooling near the wall, introduces other numerical difficulties related, for example, to grid generation (Correa and Shyy (1987)). While the computational techniques for flows in the gas turbine combustor are continuously moving forward, improved approaches for non-equilibrium chemistry and for soot modelling also need to be established.

The two-equation soot formation model, based on the early work of Gilyazetdnov (1972) and developed by Moss et al. (1987, 1988), has been incorporated in an extended laminar flamelet concept for soot prediction in buoyant fires (Syed (1991)). The model characterises the governing steps in soot production, namely nucleation, surface growth, coagulation and oxidation. This essentially global mechanism is, from computational viewpoint, tractable since it introduces only two additional variables in relation to soot properties, ie. particle number density and volume fraction. This approach has been tried in a tubular combustor flow whose geometry is similar to the present SNECMA designed one, however, there was no experimental soot data to compare with the numerical simulation (Alizadeh (1993)).

The intention of the work outlined in this chapter is to apply the existing soot model to the combustor flow and evaluate the predictions by comparison with the limited soot concentration and other scalar properties which are readily accessible. While the soot model

may need further refinement for a particular flow, the preliminary computation here is to apply directly the model developed for laboratory flames. The measured data profiles, at one axial position, are treated only as guidance for assessing the soot model capability since a whole property map is clearly required for mathematical model validation.

6.2 COMPUTATIONAL DETAILS FOR THE COMBUSTOR

The modelling work was carried out on a commercial CFD code - PHOENICS - version 1.6. The calculation was performed on a SUN SPARC +1 work station. Numerical tests of the geometrical representation for the combustion chamber showed that the proposed grid generation led to plausible predictions for water flows in the combustor when compared with water flow visualization experiments (Perrin (1992)). The modelling strategy for combustion employed here was the extended laminar flamelet approach, which has been used by Alizadeh (1993) for a similar combustor flow field predictions. The following sections describe only briefly the computational details and the reader is referred to the above works for more detail.

6.2.1 The PHOENICS code

The PHOENICS computer code consists of three main component programs, namely SATELLITE, EARTH and PHOTON. Input data relating to the computations, including grid generation, boundary conditions, etc., are fed to the SATELLITE through a Q1 file which is written in a special, Fortran-like CFD language. The numerical calculations for the property balance equations, including the effects of chemical reaction and turbulence interactions, are conducted by the EARTH which can be manipulated by the GROUND file. The third PHOTON program produces graphic output for data analysis.

The balance equations 2-1～2-4 are solved by the code using finite volume methods. The turbulence model selected for the present study was the "classical" two-equation model, namely κ-ϵ model. Although this turbulence model may provide an appropriate description for flows in the combustor dilution section, its application in the highly turbulent primary zone is often far from satisfactory (Jones and Whitelaw (1984) and Correa and Shyy (1987)). Its choice reflects the compromise between accuracy and computational cost. The flow variables solved and subsequently used in the combustion calculations are mean density and mixture fraction mean and variance. Mixture fraction is a conserved scalar and its implementation in Eq. 2-4 does not contain a source term. Once the mixture fraction Favre mean and variance are obtained, scalars relevant to chemical reactions, for example temperature and gaseous species

concentrations, are readily determined through post processing by applying the prior constructed state relationships for laminar flamelet burning.

6.2.2 Laminar flamelet approach

The chemical source term closure in Eq. 2-4 was achieved by using the laminar flamelet approach. Gas turbine combustion is usually considered to be non-premixed and the flame inside the combustor is normally assumed to be controlled by the physical mixing rate and drop evaporation rate, in the case of liquid fuel burning. Distributions of mixture fraction in the flow field reflect the fuel-air mixing process. Other scalars are linked to the conserved scalar - mixture fraction - through unique state relationships. Laminar flamelet calculations were employed to establish such relationships.

Satisfactory calculations for laminar liquid kerosine-air combustion are not available at present, partly due to the two phase flow but the main difficulty is the extreme complexity of the detailed chemistry which is not yet tractable (cf. Appendix E: Kerosine-Air Flame Prediction). Gaseous propane is often considered to be broadly representative of kerosine since they have some similar thermo-chemical properties. Propane has therefore been used to simulate the combustion of vaporized kerosine fuels in an annular gas turbine combustor (Wear and Jones (1973)). In the present study, the flamelet calculation was based on propane-air burning at the initial conditions appropriate to the inlet conditions in the combustor, for example air and fuel inlet temperatures of 473 K and 300 K, respectively, at atmospheric pressure.

The reaction mechanism employed comprised 26 steps involving 44 species. The calculation was performed with a one-dimensional counter-flow code and incorporated strain rate of 100 1/s. It is entirely conceivable that the hydrodynamic strain in the whole combustor flow field may not be uniform. On the other hand, profiles of strain rate in the complex three dimensional flow are inaccessible at present through either computational or experimental study. The prediction of a combustor flow using the same laminar flamelet method for a single strain rate 100 1/s showed general good agreement with measurements in an earlier study (Alizadeh (1993)). This modest stretch level was therefore applied for the present combustor flow field on the basis of computational simplicity. The laminar flamelet was essentially adiabatic and no radiation heat loss was incorporated.

In the context of soot modelling, formation rates in Eq. 2-8 were treated as functions of mixture fraction only. The rate constants used here were taken from those evaluated for a turbulent ethylene jet flame (Young (1993)) where

$C_\alpha = 1.7 \times 10^{8}$ $m^3\ kg^{-2}\ K^{-½}\ s^{-1}$

$C_\beta = 9.0 \times 10^{19}$ $m^3\ K^{½}\ s^{-1}$

$C_\gamma = 1.26 \times 10^{-11}$ $m^3\ K^{-½}\ s^{-1}$

$C_\delta = 144.0$

and the activation temperatures

$T_\alpha = 46.1 \times 10^{3}$ K

$T_\gamma = 12.6 \times 10^{3}$ K

The application of the rate constants from the ethylene flame are expected to underpredict the sooting level in kerosine flames as reported by Stewart et al. (1991). Whereas the rate constants for a pre-vaporised laminar kerosine-air flame may be significantly different from the values above, the present selection of rate constants was only intended to initiate the modelling campaign in the SNECMA designed combustor with fewer variables. Based on the relationships of the various formation rates against mixture fraction, the balance equations (Eq. 2-12) were solved and the time-averaged soot number density n and soot volume fraction f_v determined by a post processing computation.

6.2.3 Boundary conditions

A cylindrical polar-type grid generation was employed for the combustor in which the flow field was assumed to be axially symmetric and the computational mesh was constructed for one quarter of the cross section (90 degree in the angular IX direction). There were in total 43120 (IX×IY×IZ=28×28×55) cells created for the combustor domain (Figure 6.1). The air flow split was based on the data supplied by the combustor designer, SNECMA (cf. Figure 3.12). The computations were performed for one flow condition, ie. air mass flow rate of 0.12 kg/s and Air-Fuel-Ratio of 45 at atmospheric pressure with air preheated to 200 °C. Radial profiles of experimental data at one axial location in the dilution section were compared with the predictions.

All the measured scalars, for example soot volume fraction and mixture fraction, were obtained by the physical probing method in which one of the dilution holes was partially blocked (cf. Figure 3.14 and 3.17). Such hole blockage was not simulated in the numerical prediction under the constraint of computational time, potentially requiring a full 360° simulation. This may introduce ambiguities in the data interpretation. Other flow inlet characteristics, for example the staged liner film cooling, were prescribed in the calculation. Whilst the casing and combustor flow field is not entirely axially symmetric, on the evidence of the flow visualization test and the measured scalar profiles, such a flow feature has not been reproduced in the boundary condition definition.

The fuel injector employed in the experiments was of an airblast type. In practice, liquid fuel inside the atomizer is dispersed in a manner in which the thin film is formed first (pre-filming) and the liquid sheet subsequently interacts with the blasting air. Two schemes, representing the fuel injection, were tested in the absence of a comprehensive model of two phase flow. The first one simply treated the injector as entirely full of propane (Figure 6.2 (b)). To closely describe the airblast injection, the second scheme located the fuel near the wall of the injector, similar to the pre-filming effect (cf. Figure 6.2 (a) and (c)). Due to the cell number constraint, three radial cells (IY=1~3) were used for the injector (cf. Figure 6.1). In the second scheme the fuel flow occupied one third of the injector mesh. The second scheme is inexact given the coarse grid resolution, it is however expected to be more in accord with the real injector. Results from the two schemes will be compared in the following section.

6.3 RESULTS AND DISCUSSION

A complete map of flow properties inside a combustion chamber may serve as a CFD validation data base, the transverse scalar profiles at one axial station (ie. the dilution hole section) reported in the previous chapters can only be treated as a guide to the modelling development. Whereas a number of flow field variables can be retrieved from the prediction, for example the three velocity components and mean density field, only those relevant to soot modelling are presented in the following discussions.

The predicted mean mixture fraction is shown in Figure 6.3. Data from three angular positions are used, namely IX=1 (the longitudinal plane containing the primary hole), IX=7 (the plane containing no primary or dilution hole) and IX=14 (the plane containing the dilution hole) (cf. Figure 6.1). Data at plane IX=7 for the dilution section is considered as representative of that measured by the probes on the probe blocked-side (ie. radial position: -50~0 mm). The predicted mixture fraction has a higher peak of 0.13 and low values near the combustor axis (Figure 6.3 (a)). The predicted combustion zone appears to exhibit a much narrower radial domain than the measurements. The positions of the peak mixture fractions are however in good agreement.

The principle reasons for the different flame structures accompanying propane and kerosine combustion might be their different transport (by convection and turbulent diffusion) and the influence of droplet evaporation. Such differences have been observed in turbulent propane and liquid kerosine flames by Ehalil and Whitelaw (1976) where the length of a kerosine flame is increased due to extended fuel evaporation. The prolonged evaporation in the

combustor flow field can clearly influence the mixing and quenching of chemical reaction effects by the surrounding high velocity gas stream. Recent experimental evidence suggest that even where the spray flame is consistent with group combustion theory, small individual droplets do exist outside of the combustion zone (McDonell and Samuelsen (1991)). The envelopes of droplet burning can also contribute to the spread of the combustion zone.

Similarly in the temperature profiles, the 'pattern factor' of the prediction differs significantly from the measurements (Figure 6.4). In particular, the predicted temperatures are generally higher than measurement. The calculated mean temperature is essentially post-processed, based on adiabatic laminar flamelet burning. In the combustor, the wall temperature is significantly lower than the hot gas temperature, the maximum temperature of the duct, which is not cooled by air filming, is 900 K at the present flow condition (cf. 4.14 (b)). Under these conditions the radiation loss from the combustion product can reduce the temperature. The adiabatic temperature at stoichiometry for a laminar kerosine-air burning is about 2100 K (instantaneous), the maximum mean temperature measured is only 1450 K at 1 bar (Figure 4.18 (a)).

Included in the figures for comparison purposes are the temperature distributions in the primary zone, where measurements by CARS and other CFD predictions based on equilibrium are shown (Figure 6.4 (c)). The CARS temperature are obtained through two opposing primary holes while the other two holes are blocked (Magre et al. (1991), cf. Table III in chapter 3 for combustor geometry), the consequent flow pattern may therefore be altered due to the hole blockage. The flamelet predictions are nevertheless very close to the measurement around the combustor centre line whereas near the wall the present calculations over predict temperature. The over prediction may be partly attributed to the fuel boundary definition, as the second injection scheme in the calculation clearly shows such an effect. Replacing the kerosine with propane as fuel may also be responsible. The lower peak temperature from the present prediction is influenced by the finite rate chemistry employed in the flamelet which departs from full chemical equilibrium.

Since the rich mixtures in the prediction are confined in a narrow regime with high temperature, which is favourable for soot formation, the soot volume fraction profiles are, not surprisingly, over predicted (Figure 6.5). Again the positions of peak soot volume fractions are in good agreement and the profiles from the predictions are broadly similar in shape to the measurement. The contribution of OH oxidation to the soot volume fraction at the dilution section is insignificant. Indeed, the mixture fractions down to the dilution zone are as high as 0.1 in the sooting region (radial positions:-40 ~ -30 mm). Recalling the soot oxidation rate in

Figure 2.1, the rates are very low at mixture fraction fractions higher than, say 0.08. Therefore applying the higher burnout rate by OH radicals does not influence the calculation. This reflects the character of the predicted flow field rather than the true relative importance of the O_2 and OH oxidation mechanisms. With the improvement of the prediction for mixture fraction and temperature, the soot formation rate is expected to decrease and the calculated soot concentrations may be close to the measured ones.

Carbon dioxide concentrations are shown in Figure 6.6. Because of the lower carbon to hydrogen ratio in the propane, its combustion tends to generate less CO_2 than kerosine, the difference is about 12% under equilibrium conditions. Adding this percentage to the predicted CO_2 concentrations, the peak values agree with the experiments. The lower distributions on the centre-line are attributed to the primary jet penetration which reduces the level of mixture fraction.

Fuel injection schemes 1 and 2 only exert influence near the combustor centre-line where all the scalar distributions are affected. At angular plane IX=7, where neither primary nor dilution jets penetrate through the combustor liner, the fuel boundary condition has less influence on the scalar profiles than the plane IX=1 where the primary jets are located (Figure 6.3~6 (b)). This may imply that if any difference exists due to the fuel injection, it will strongly affect the primary zone. In a gas turbine type combustor fuelled by propane, Noyce et al. (1981) reported that, for their combustor geometry, relatively small differences are seen between the results downstream of the primary air ports using two different fuel injectors. Indeed, fuel-air combustion conventionally takes place in the primary zone, the mixing and chemical reaction there is strongly dependent on the fuel injection. The downstream domain is more influenced by convection and dilution which is essentially determined by the combustor geometry, for example the jet penetration.

The whole flow field map from the CFD predictions demonstrates such characteristics. The recirculation zone is smaller under the fuel injection scheme 2 compared with the size in scheme 1 (Figure 6.7 (a) and Figure 6.8 (a)). The aerodynamic flow fields downstream exhibit little difference. Under the scheme 1, rich mixtures travel down to the dilution zone (Figure 6.7 (b)). As a result, the combustion zone extends to the dilution zone and the cold primary jet penetrates deep to the combustor axis (Figure 6.7 (d)). Such penetration is reduced in the injection scheme 2, with the effect of a smaller recirculation zone (Figure 6.8 (d)). Without experimental data, it is difficult to judge which scheme is more realistic although the second one seems more representative of the airblast atomization.

A large proportion of soot particles exist outside the primary zone (Figure 6.7 and 6.8 (e)). While the soot formation rate may be high in the primary zone, as shown in Figure 6.7 and 6.8 (f), the soot concentration does not necessary reach its maximum levels there. This is consistent with the slow sooting chemistry where in the combustor the overall residence time is only 2~3 ms and the zone is inhomogeneous. It is also interesting to note that the predicted formation rate is higher along the fuel trajectory, rather than in the slow velocity and high temperature, but leaner mixture, recirculation zone. Whether this is representative of kerosine combustion can not be verified at present. The formation rate is virtually zero near the combustor axis, downstream from the primary zone. Therefore the soot particles in the centre part of this domain are not formed by chemical reaction but by turbulent diffusion from the neighbouring sooting region. This may imply that soot properties, for example particle size and mass (or volume) fraction, in the combustor centre-line as reported by Prado et al. (1977) and Eckerle and Rosfjord (1988), can not represent the detailed sooting processes in the combustor flow field.

Soot oxidation rates peak near the dilution zone and the rate in primary zone is, as expected, very low (Figure 6.7 and 6.8 (g)). This explains the results in Figure 6.5 where oxidation by OH does not exert significant influence on the soot volume fraction at the dilution hole station. Additional information on soot number density is shown in Figure 6.8 (h). Unlike the laboratory flames where the range of soot number density normally lies between 10^{15}~10^{16} $1/m^3$ (Jander and Wagner (1990)), the number density here, maximum of 1.75×10^{14} $1/m^3$, is an order of magnitude lower. This may be attributed to the vigorous mixing in the combustor flow field and also the comparatively low power flow conditions. Alizadeh (1993) predicted soot number densities above 10^{15} $1/m^3$ at conditions of air inlet temperature 800 K and pressure of 8 bar. Figure 6.9 shows the soot volume fraction predicted using the particle consumption rate by OH radicals. Compared with the soot volume fraction maps in Figure 6.8 (e), the effect of increased oxidation rate is more obvious at the combustor exit than at the dilution zone (Figure 6.9 (a)), since such rate is significantly higher from the dilution zone to the exit plane (cf. Figure 6.8 (g) and 6.9 (b)).

6.4 CONCLUSIONS

An extended conserved scalar approach, based on the laminar flamelet concept, has been applied to the modelling of soot production in a tubular gas turbine combustor at conditions of atmospheric pressure and limited pre-heat inlet temperature. Predicted scalar profiles are compared with the measurements and the following conclusions drawn:

1) The descriptions of the gaseous fuel burning inside the gas turbine combustor need to be extended to incorporate spray combustion, especially at low power conditions such as those which have been used in this study. Given the present incomplete understanding of turbulence in complex flows, of the chemistry of combustion for complicated fuels, in particular kerosine, and the interaction of these phenomena, it is not possible to distinguish which is the dominant factor in the discrepancies between the predictions and measurements.

2) Computational calculations, at least for the thermal and aerodynamic properties of the flow field, must be representative of the real combustor flow for the purposes of soot model development in the gas turbine combustion. Soot predictions in the tubular combustor are substantially influenced by the flow field simulation. Whilst the model can predict soot concentration profiles broadly similar to the limited measured data, to evaluate the global soot model for the combustor flow, a complete soot data map is required. Given the uncertainties in the flow field predictions, the application of this two-equation soot model in the highly turbulent and complex flow field seems promising.

3) Soot is distributed from primary to dilution zones with the formation rate highest in the primary zone and the oxidation rate peaking near the dilution zone. In the stream-wise planes between primary jets the soot concentration continues to increase into the dilution zone. Soot particles near the combustor centre-line are transported from off-axis sooting region, rather than formed by chemical reactions. Under the present flow condition, soot consumption in the primary zone is insignificant and applying OH oxidation rate exerts little influence on the soot concentration at dilution zone. Such effect is more obvious at the combustor exit plane which is directly related to combustor smoke emission.

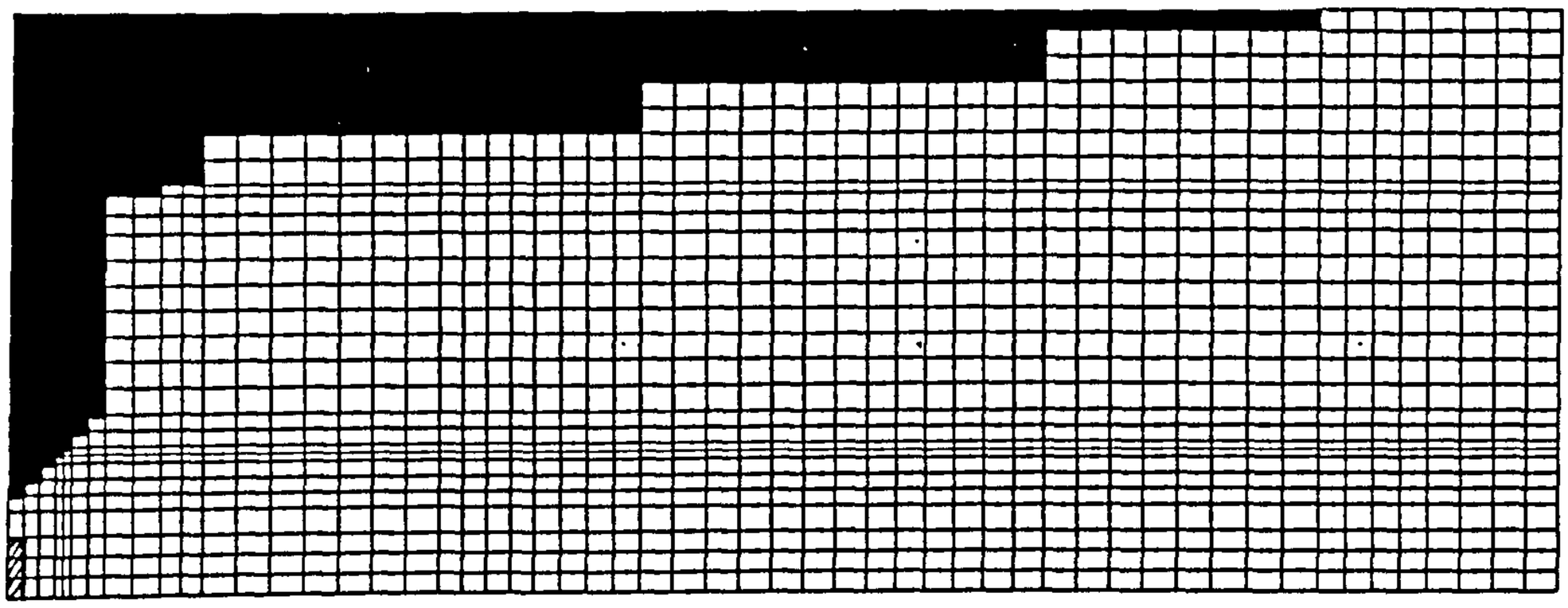

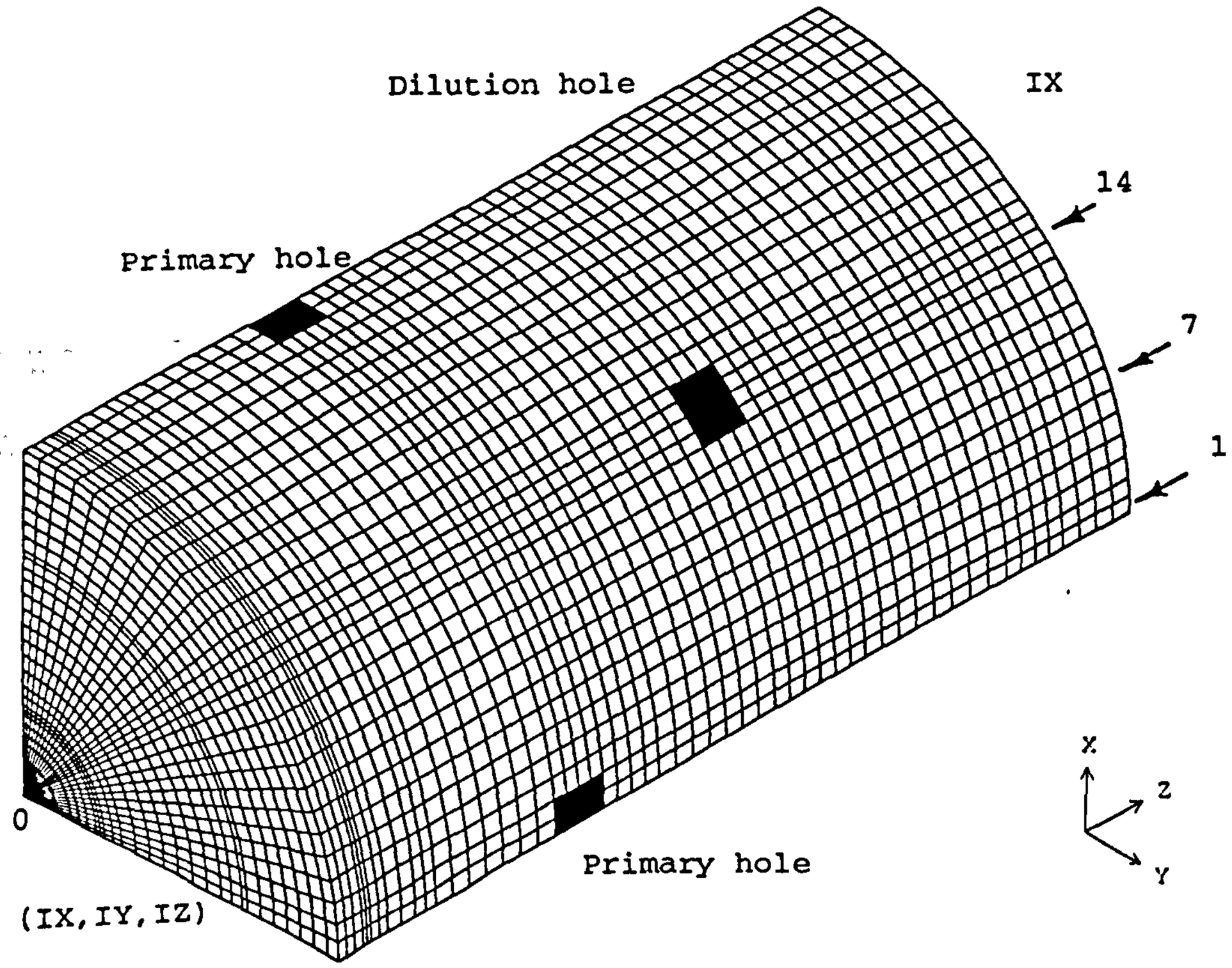

Figure 6.1 Mesh generation for the tubular combustor

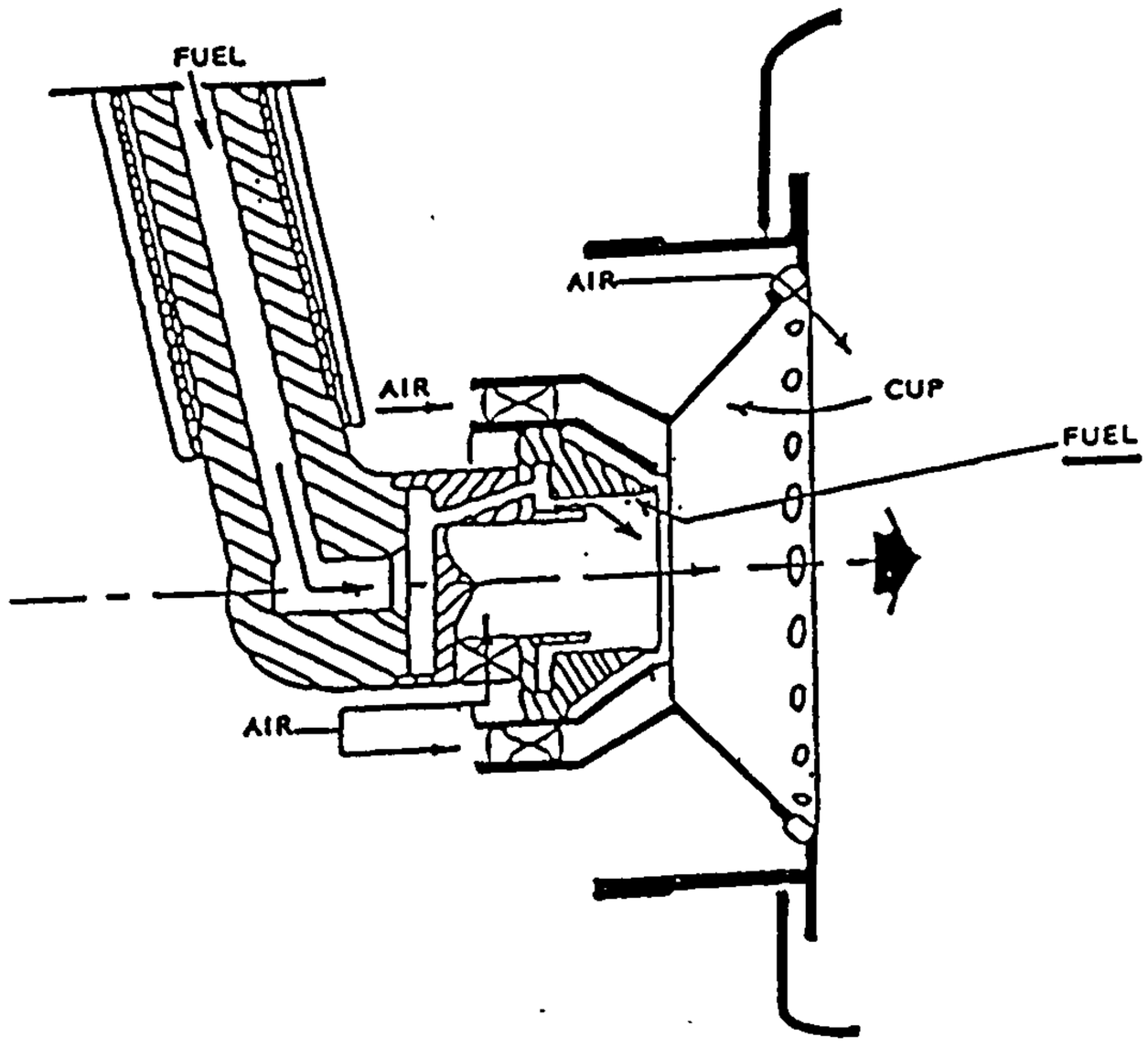

(a) Original design

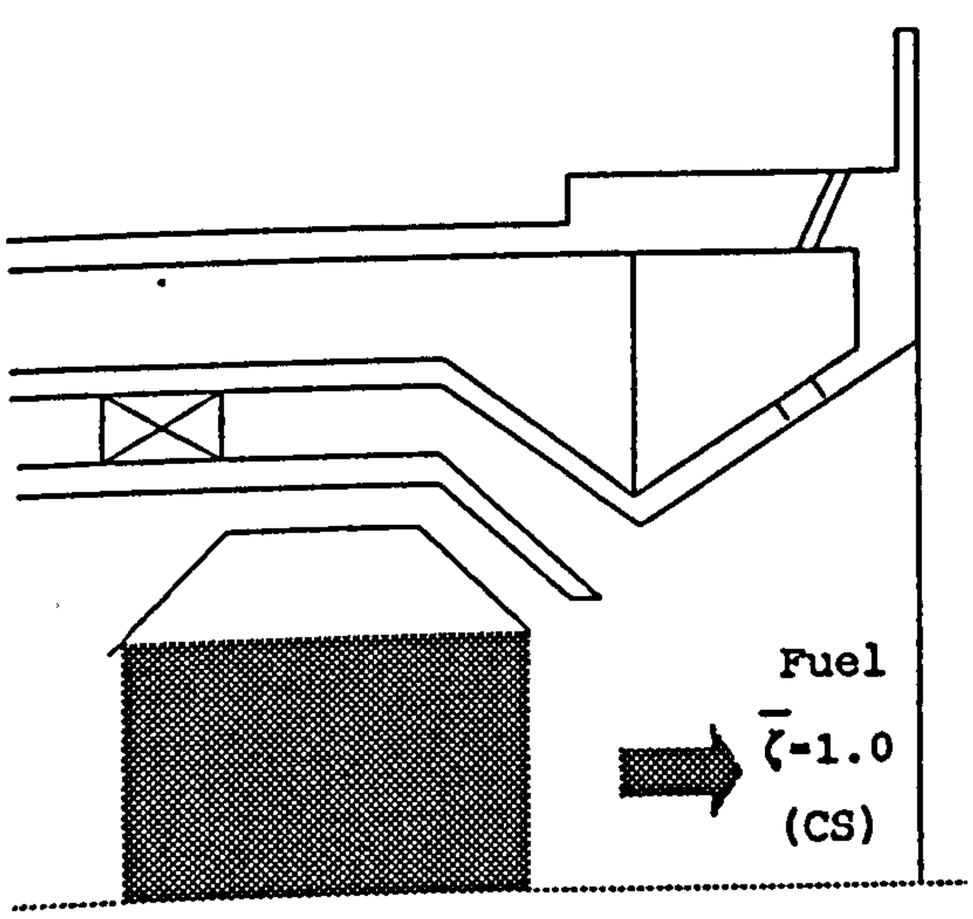

Atomization scheme I

(b) fuel injection only

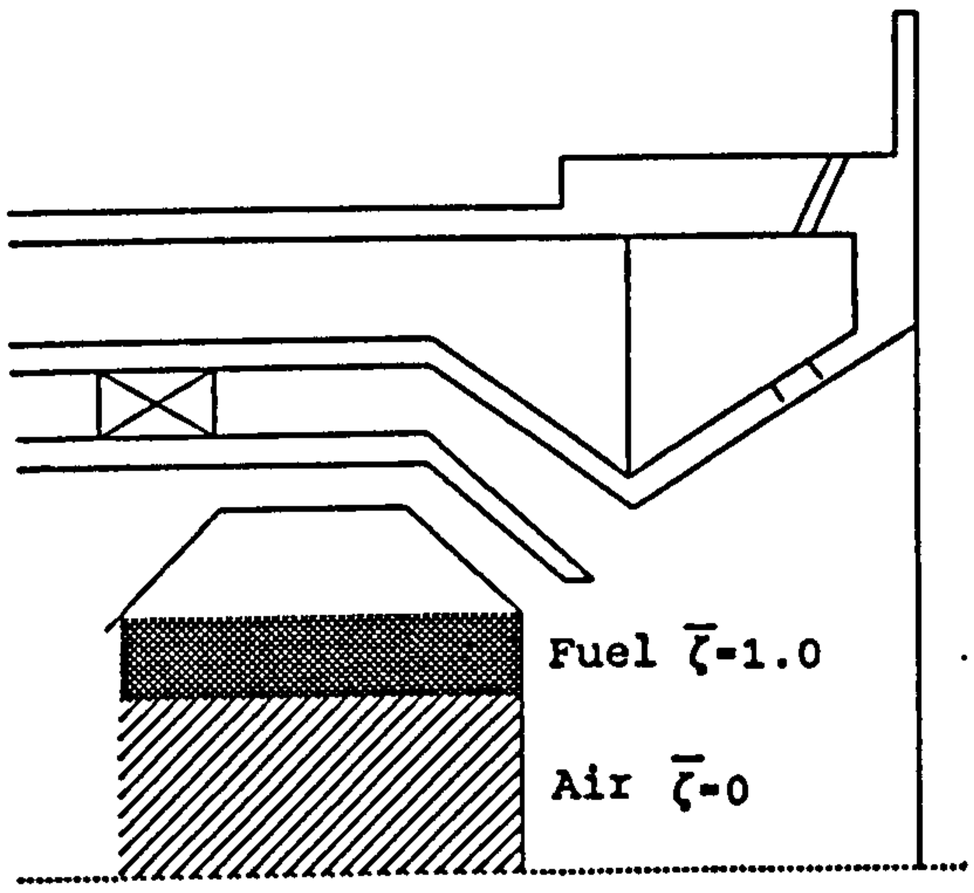

Atomization scheme II

(c) fuel+air injection

Figure 6.2 Two schemes representing fuel inlet boundary conditions

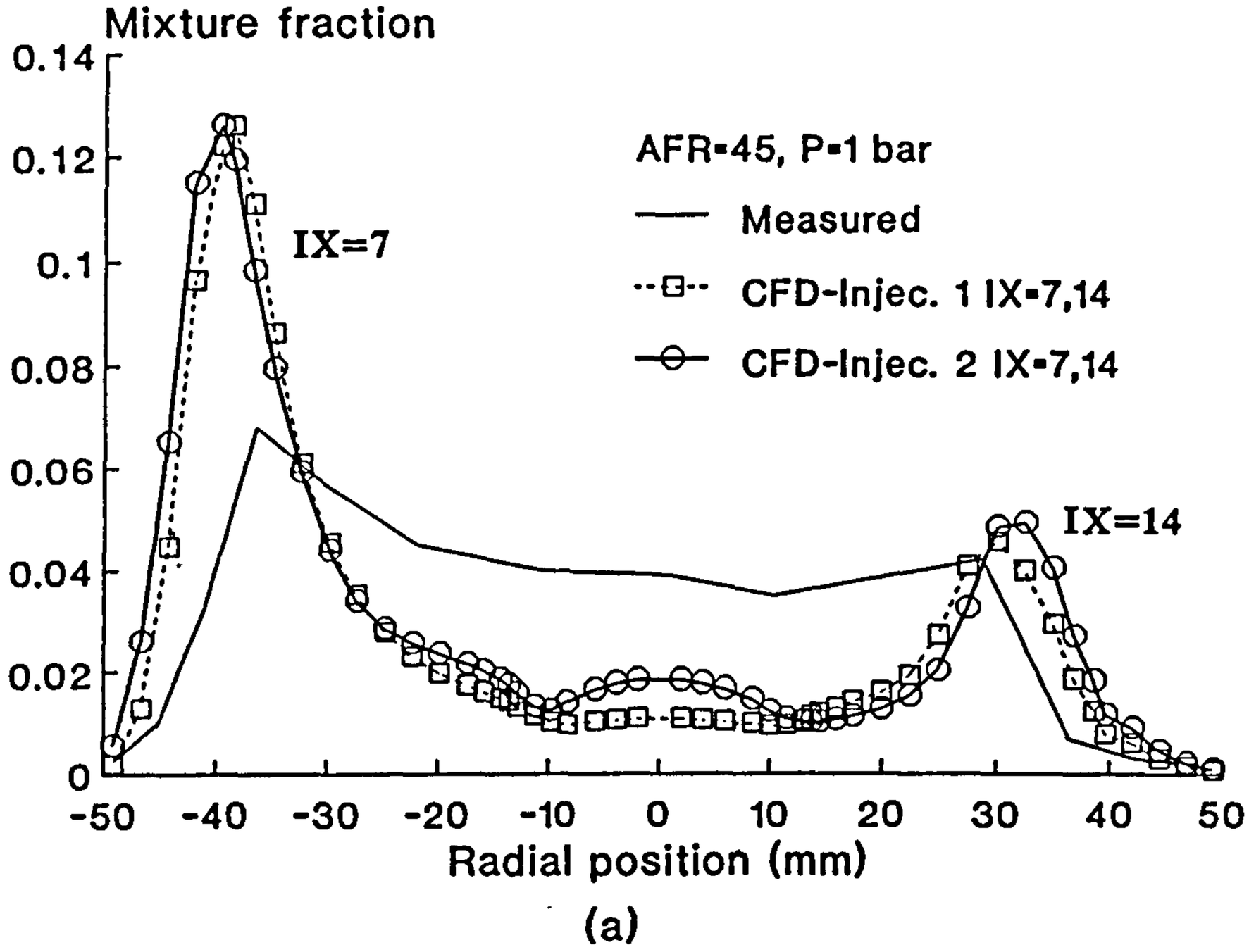

(a)

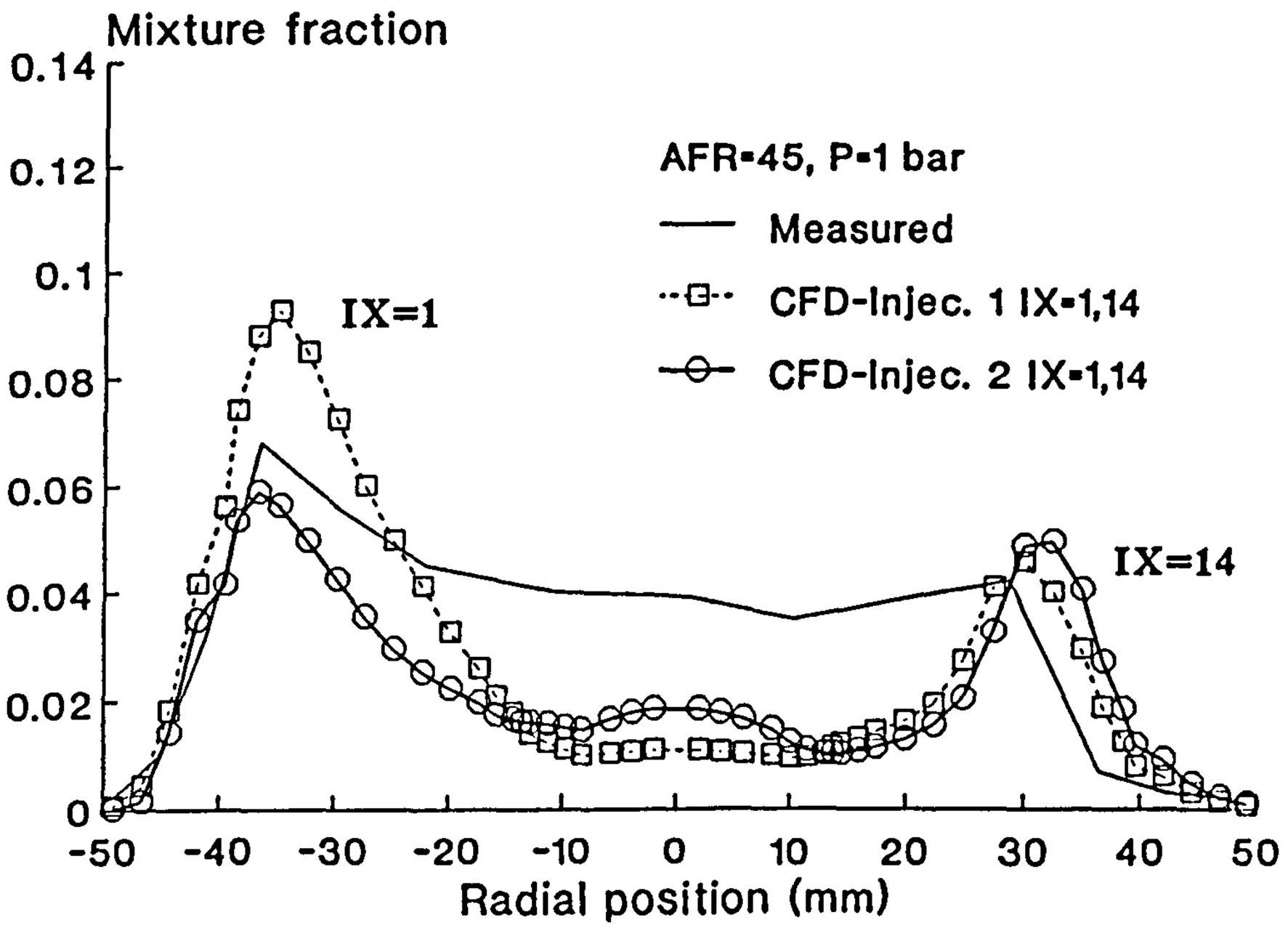

(b)

Figure 6.3 Predicted and measured mixture fraction profiles at the dilution zone station.

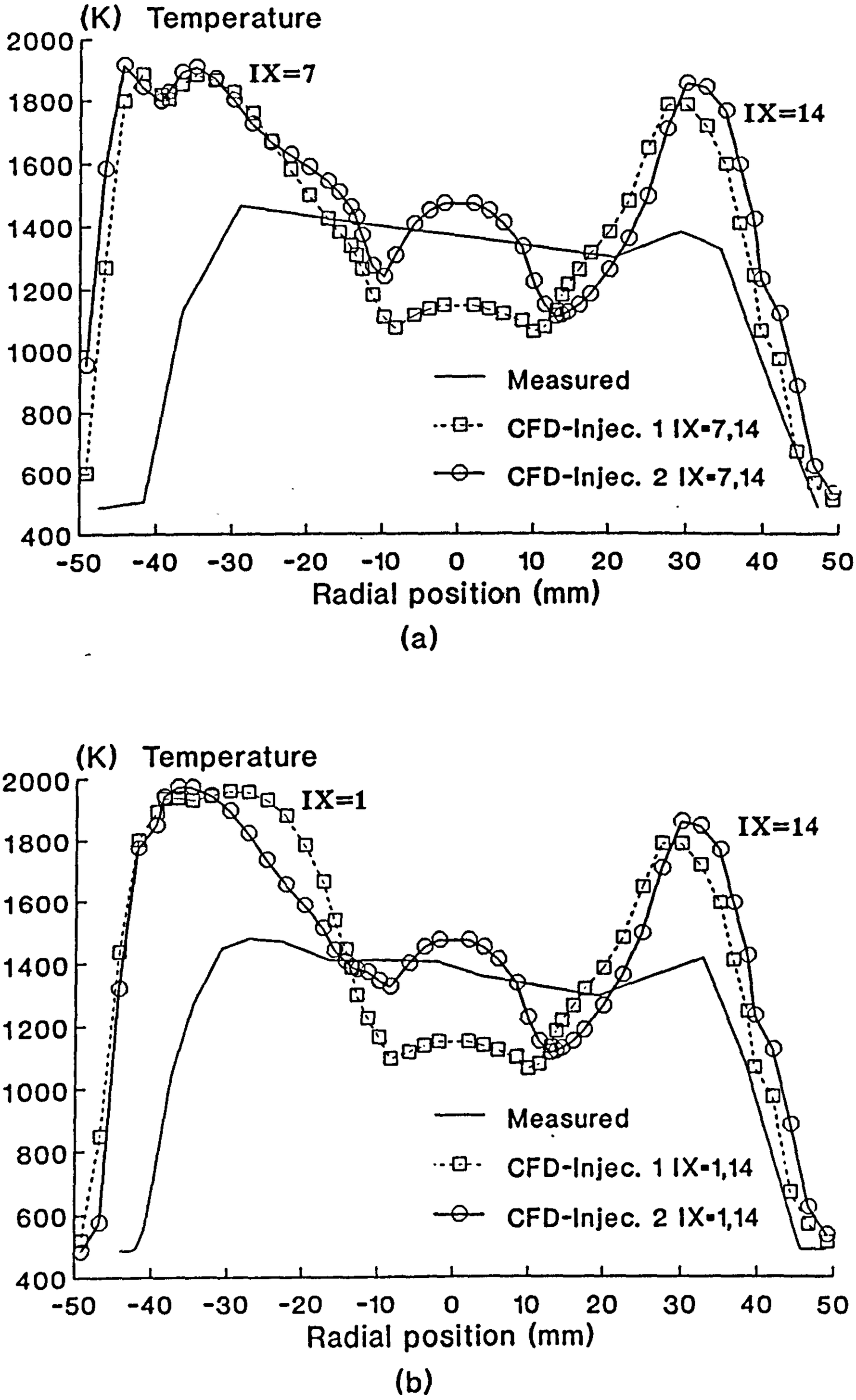

Figure 6.4 Predicted and measured temperature profiles at the dilution zone station.

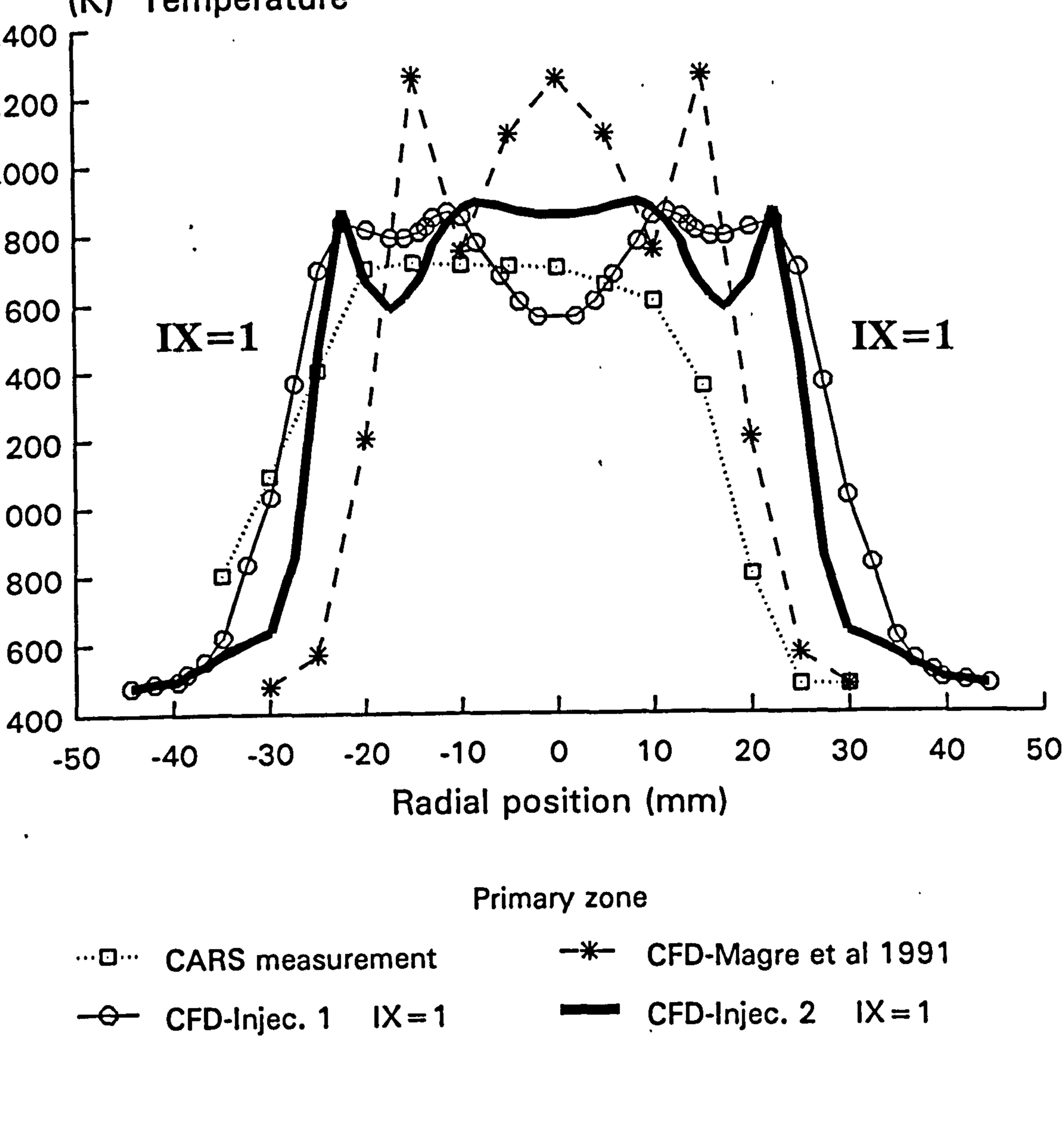

Figure 6.4 (c) Temperature profiles at the primary zone. Comparison of CARS measurement and CFD predictions by equilibrium (Magre et al (1991)) and the present laminar flamelet approach.

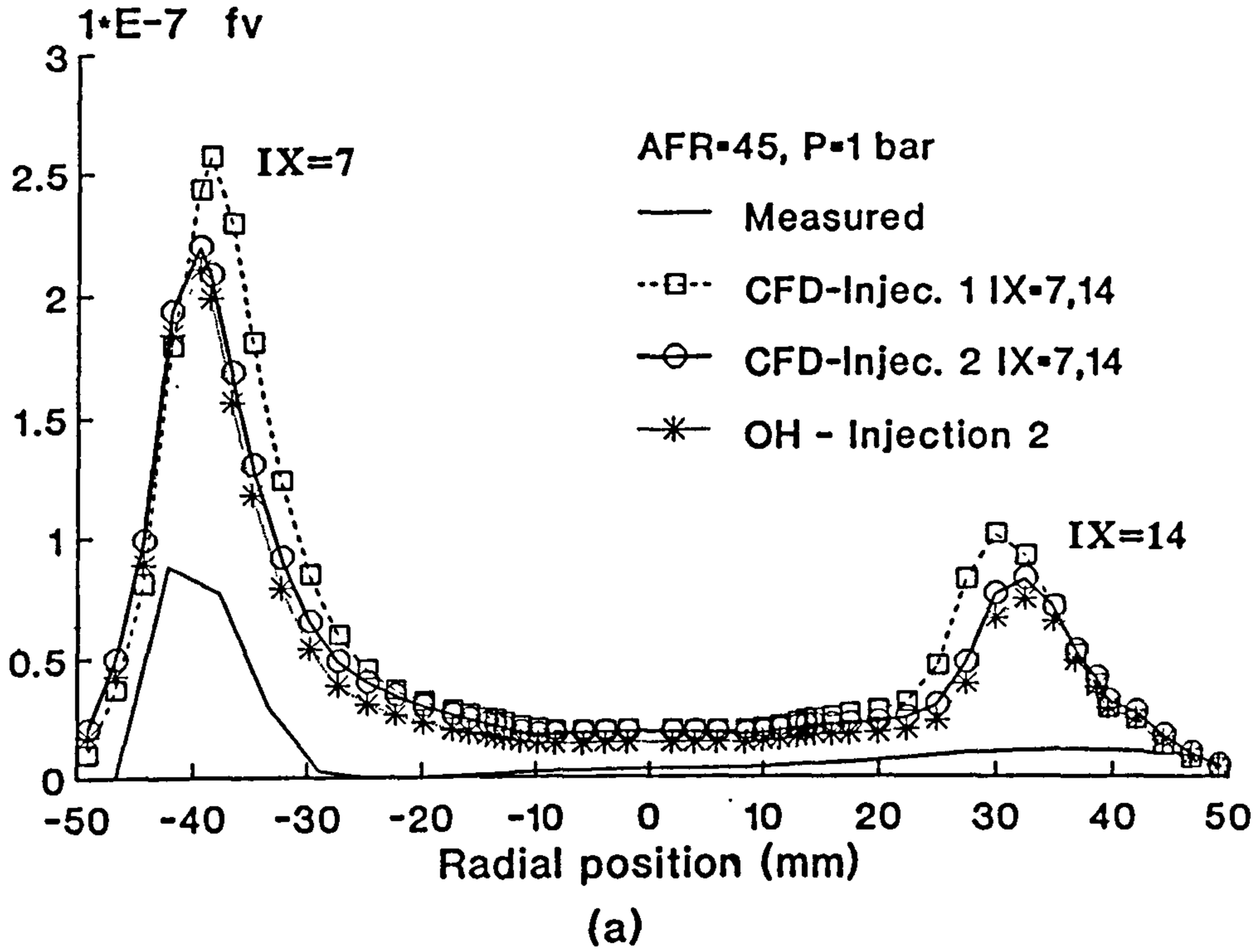

(a)

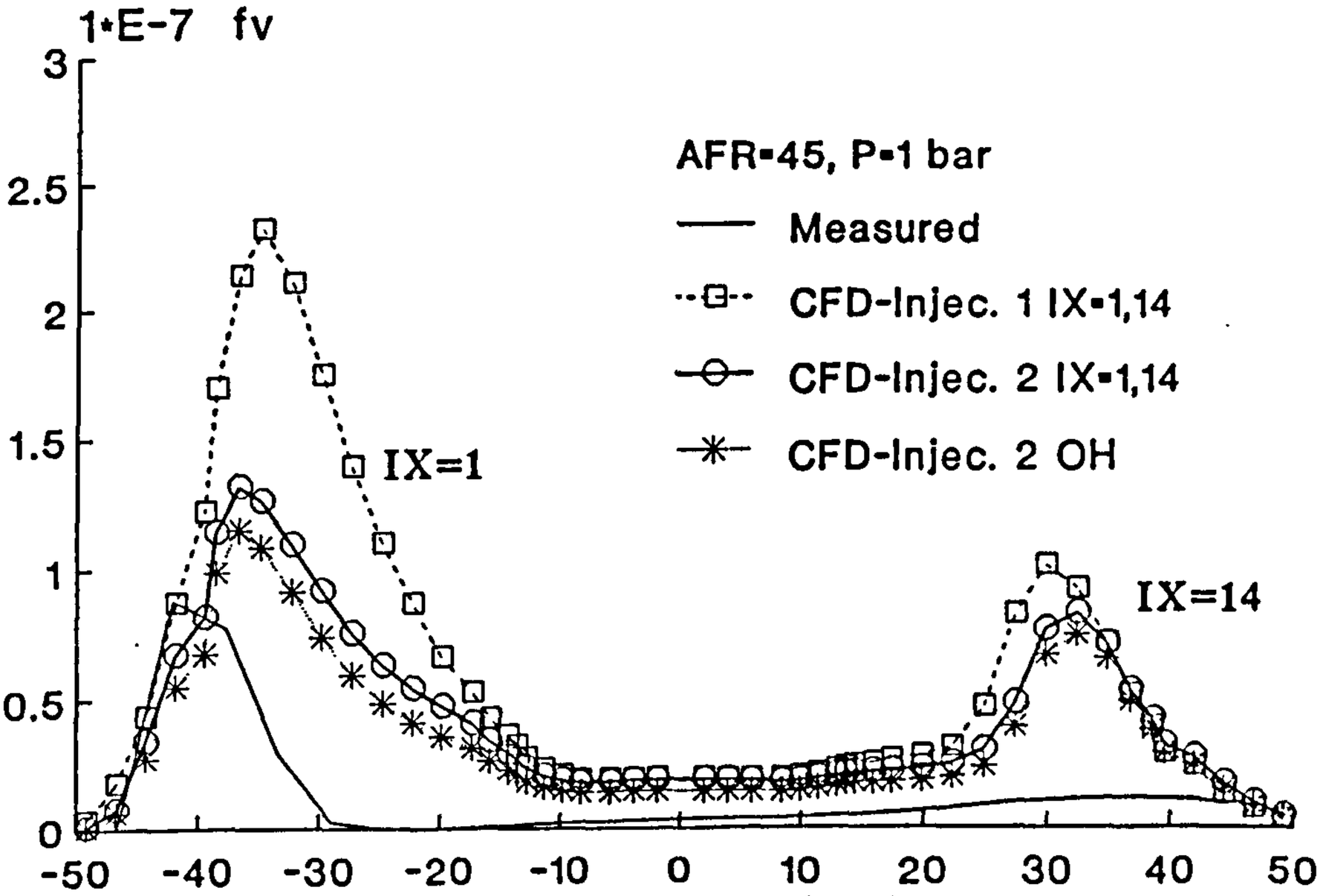

(b)

Figure 6.5 Predicted and measured soot volume fraction f_v profiles at the dilution zone station.

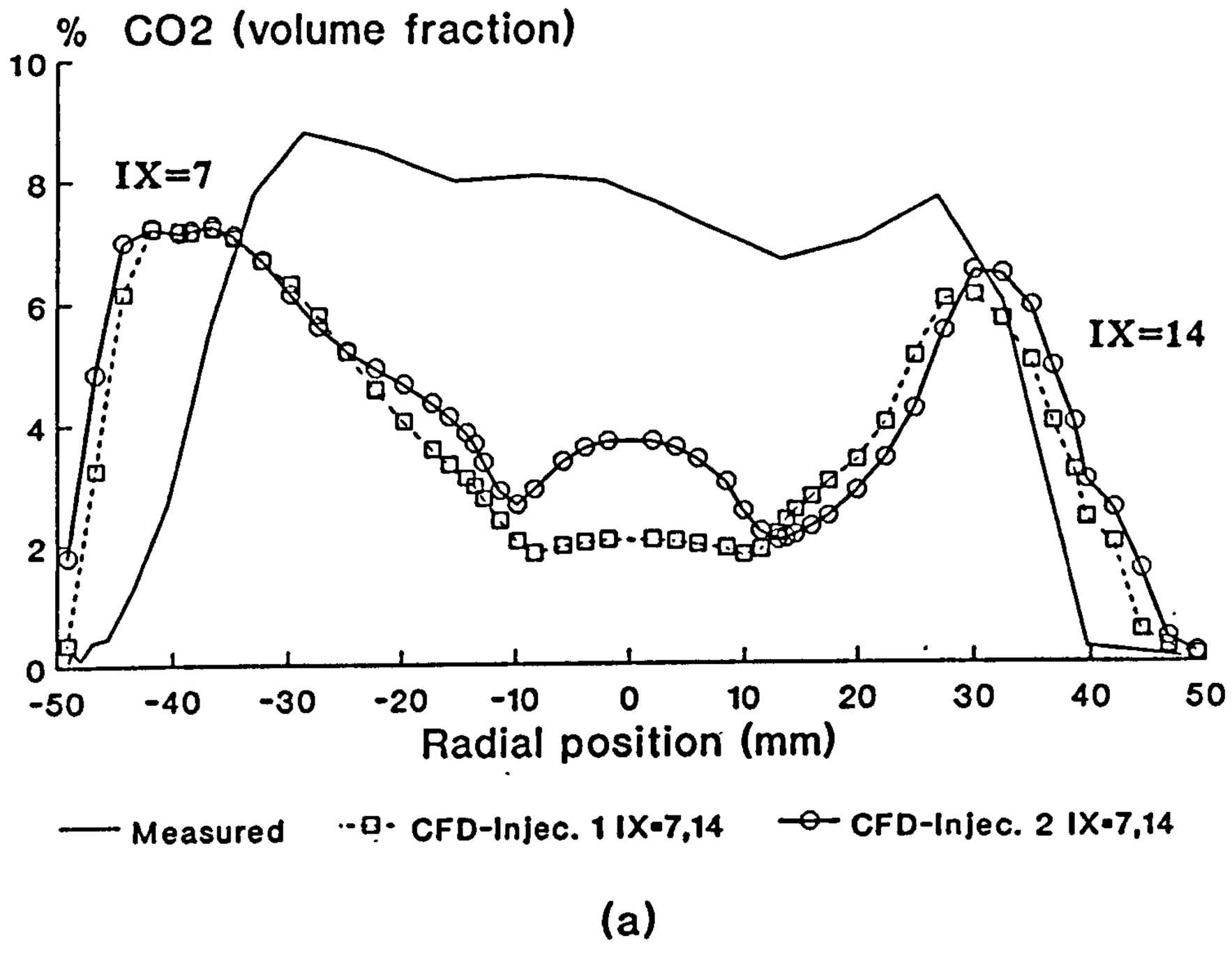

(a)

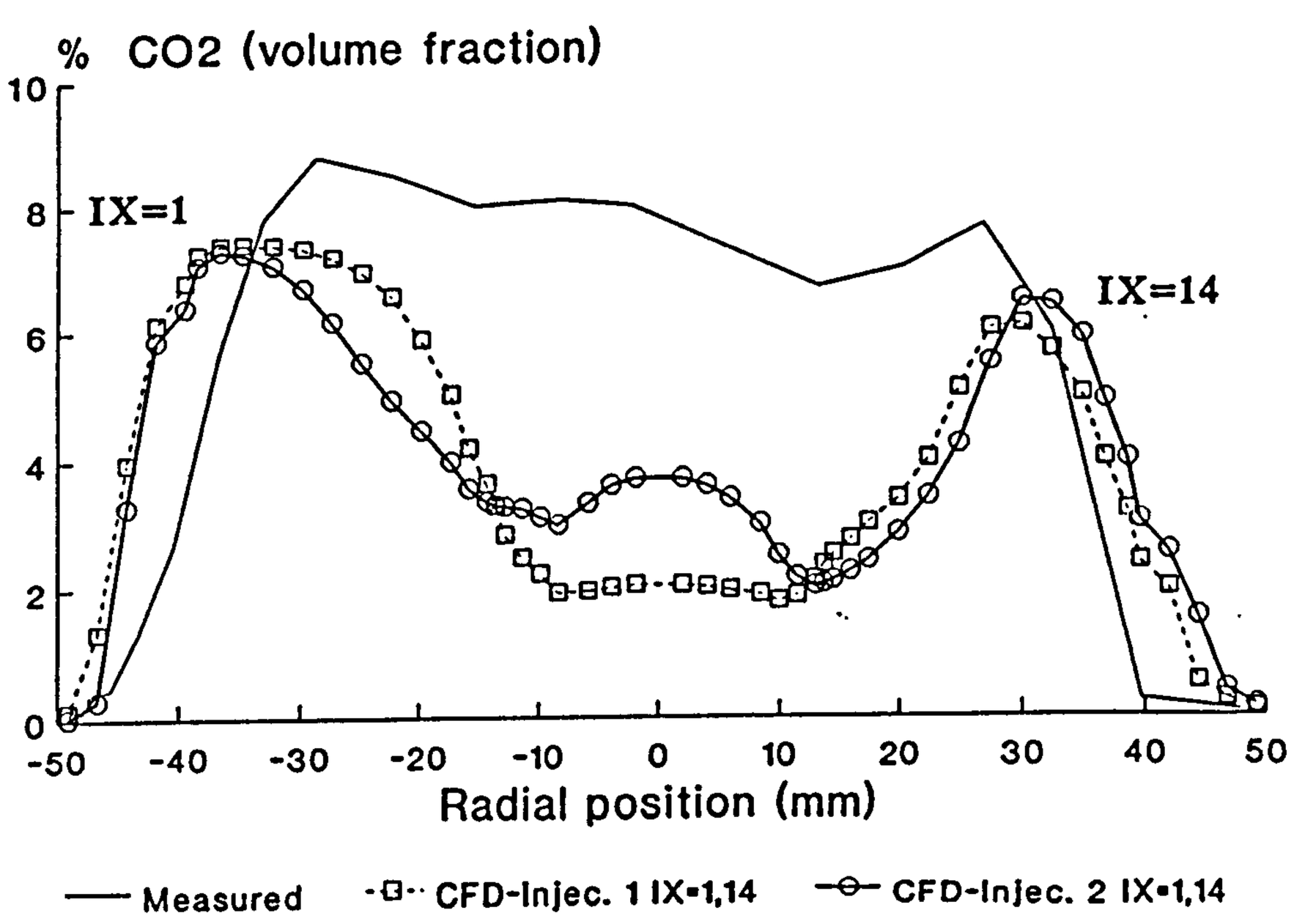

(b)

Figure 6.6 Predicted and measured carbon dioxide concentration profiles at the dilution zone station.

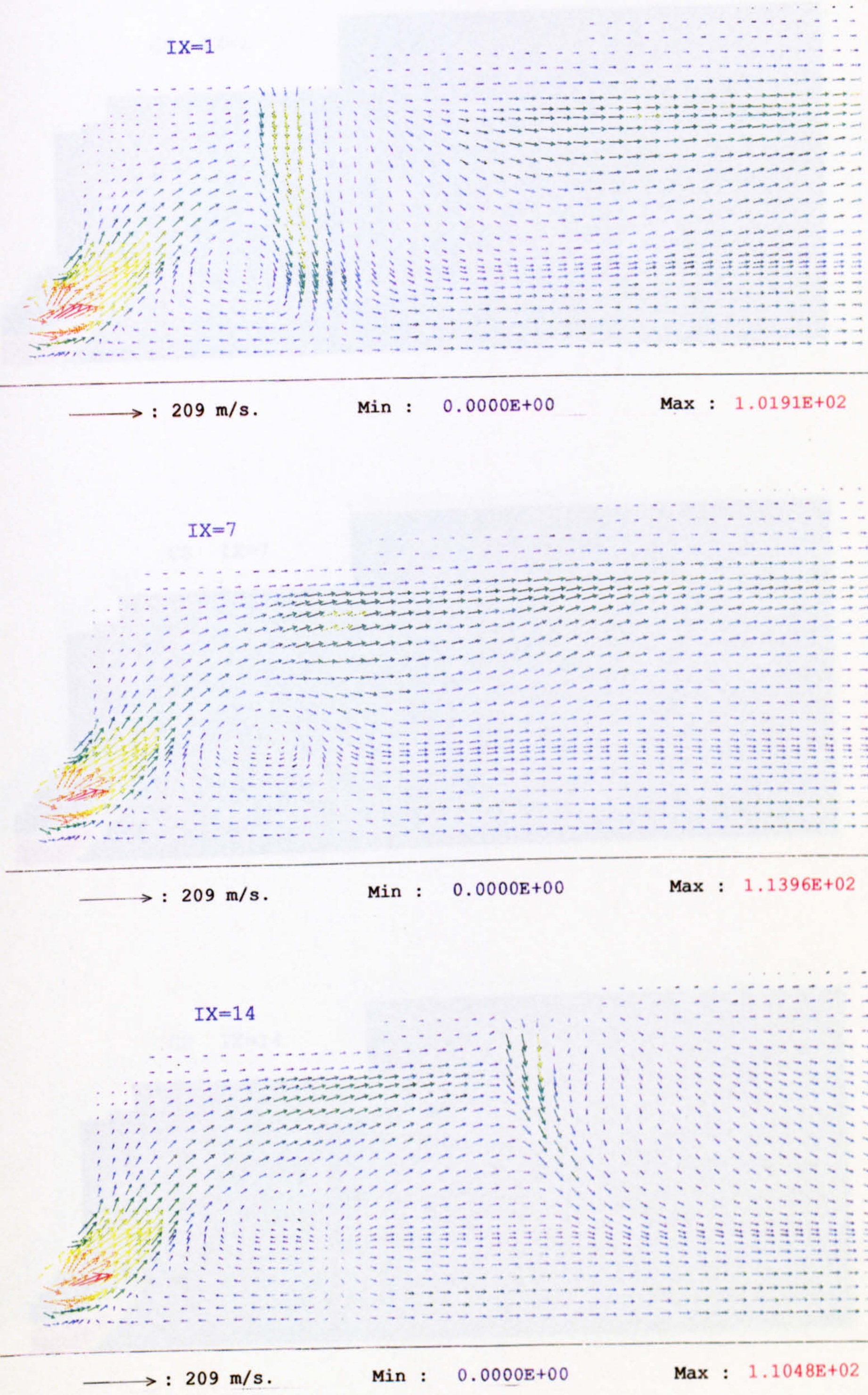

Figure 6.7 (a) Velocity vectors (Injection scheme I)

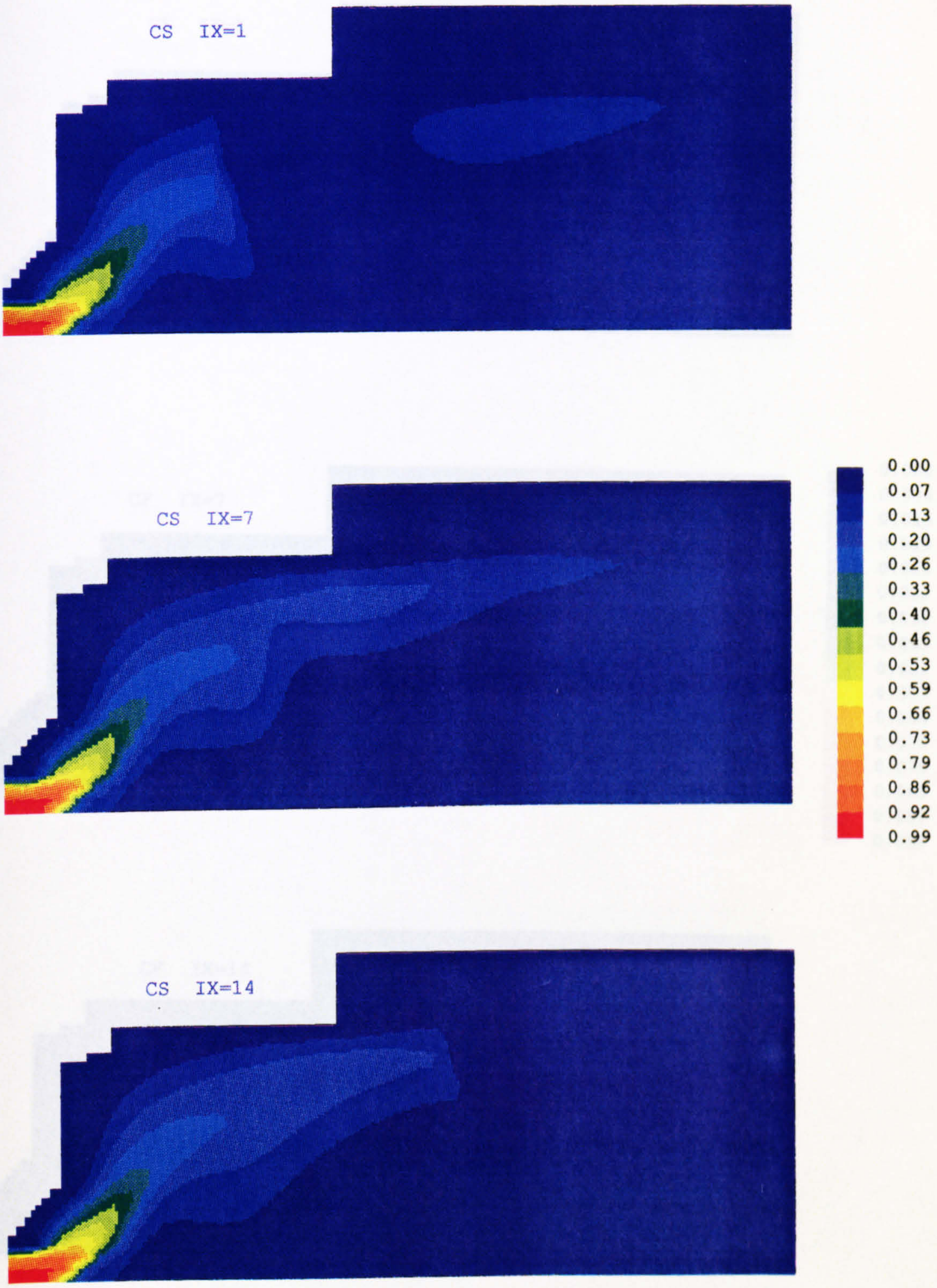

Figure 6.7 (b) Mean mixture fraction contours (Injection scheme I)

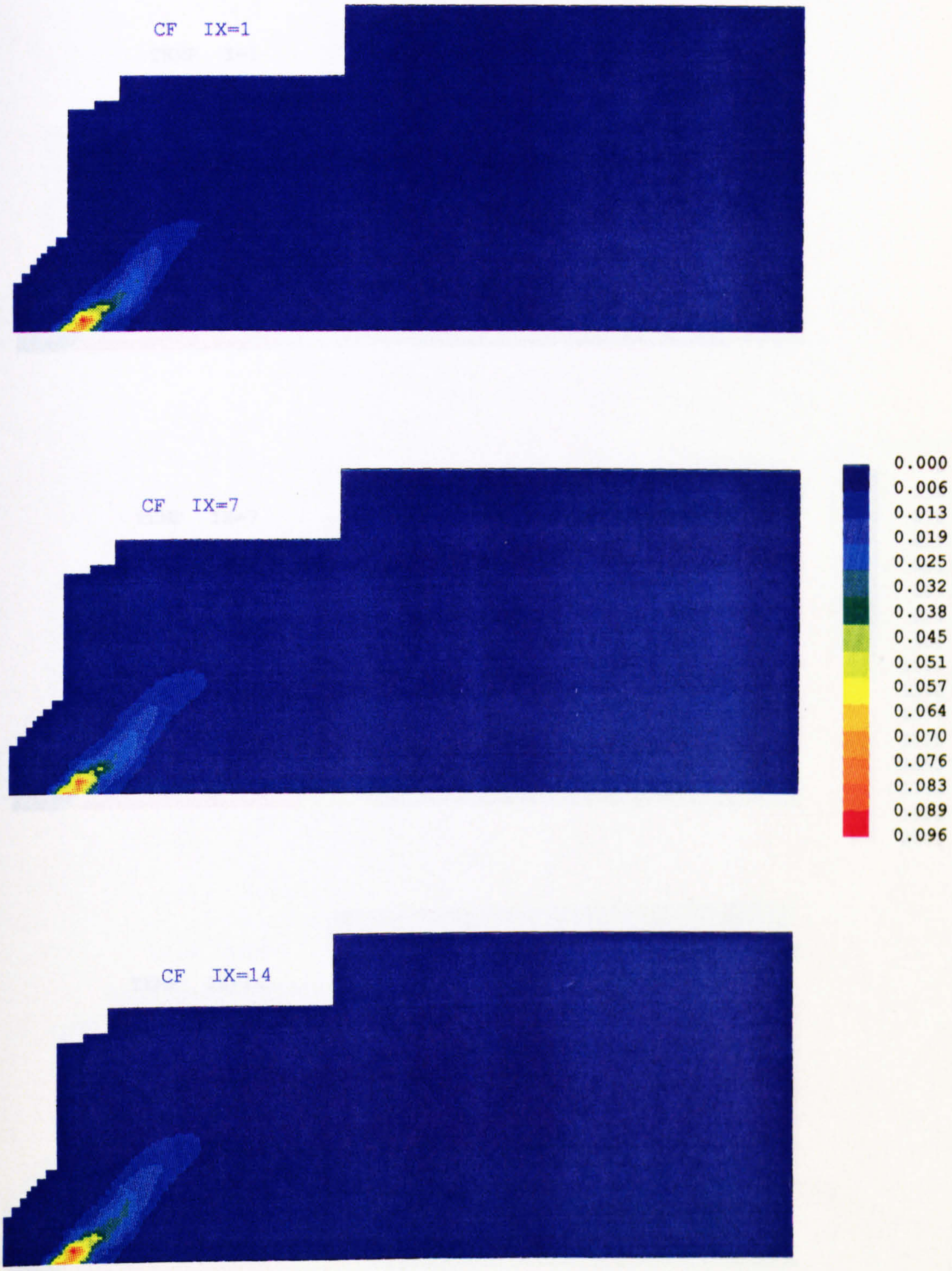

Figure 6.7 (c) Contours of mixture fraction fluctuation (Injection scheme I)

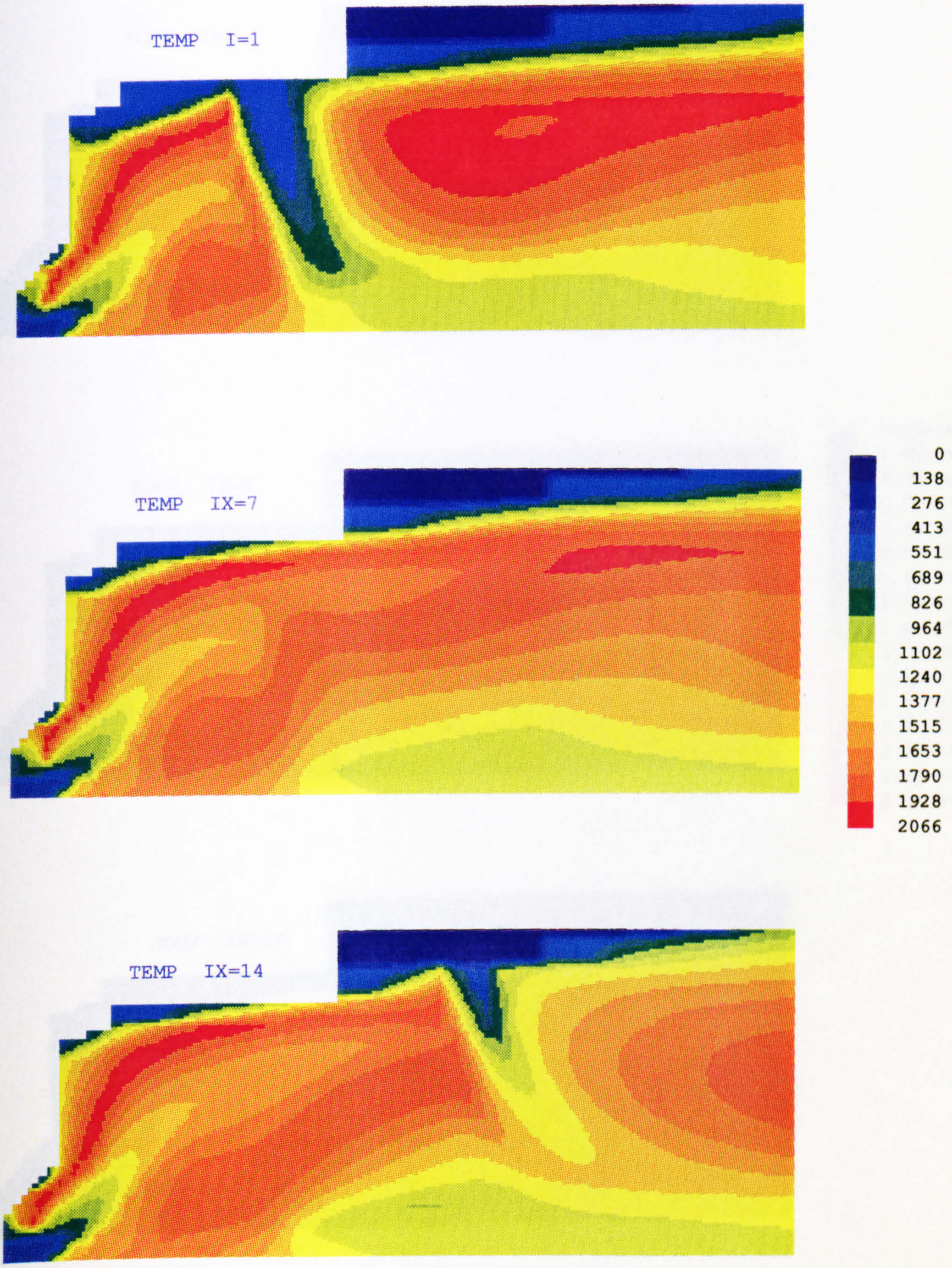

Figure 6.7 (d) Mean temperature contours (Injection scheme I)

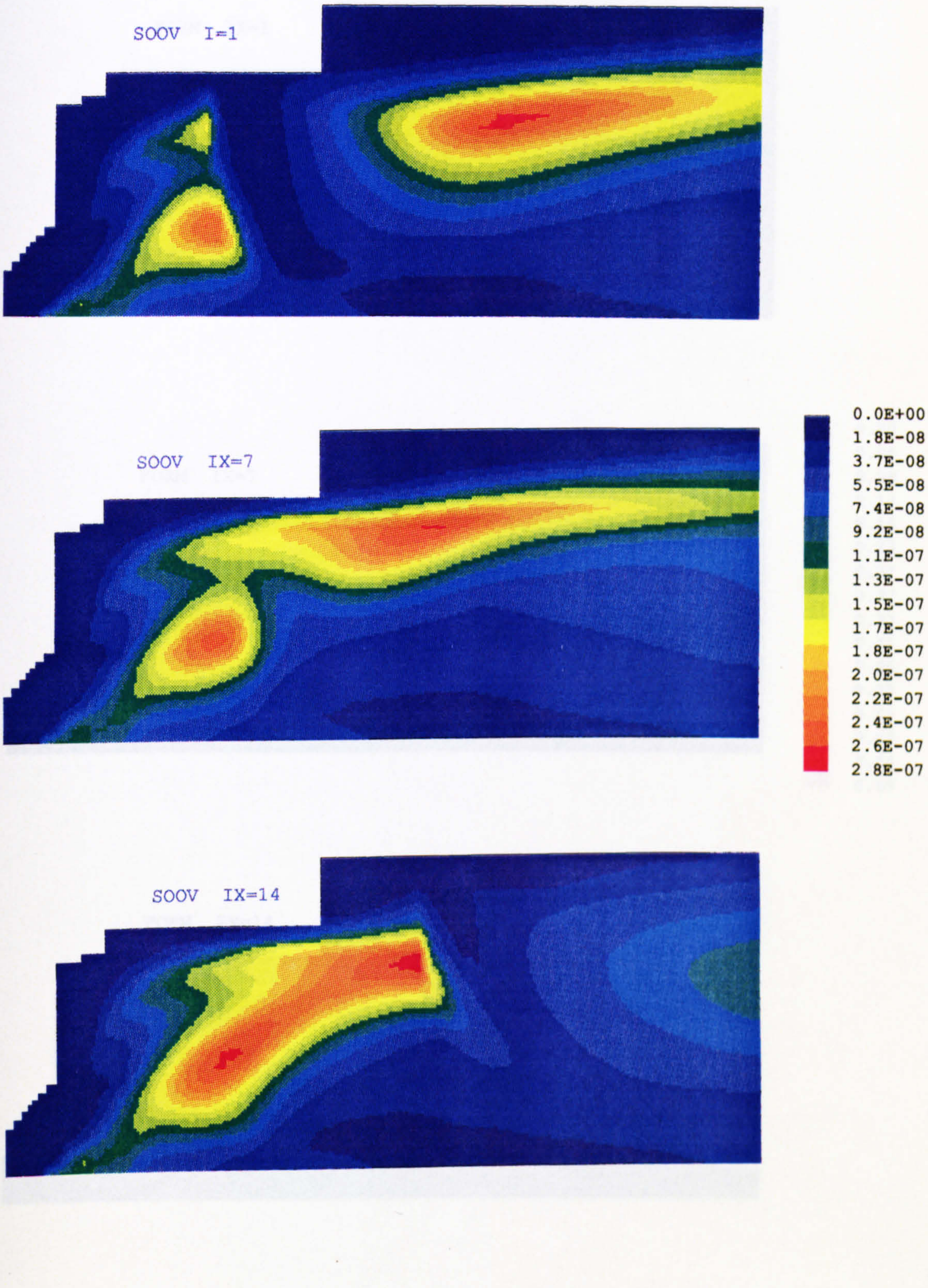

Figure 6.7 (e) Contours of soot volume fraction (Injection scheme I)
(oxidation by O_2 - Nagle and Strickland-Constable formula)

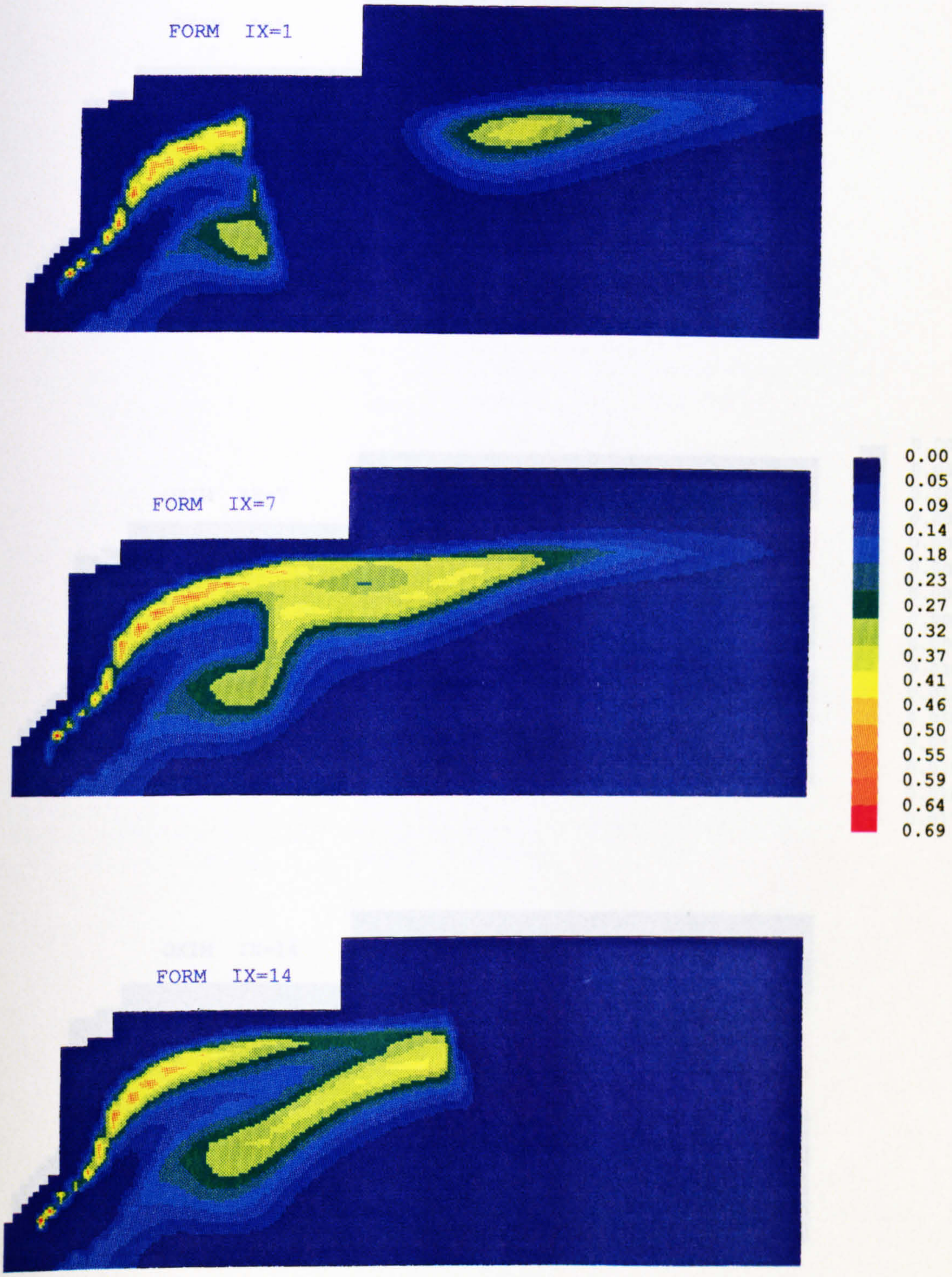

Figure 6.7 (f) Contours of soot formation rate (Injection scheme I)

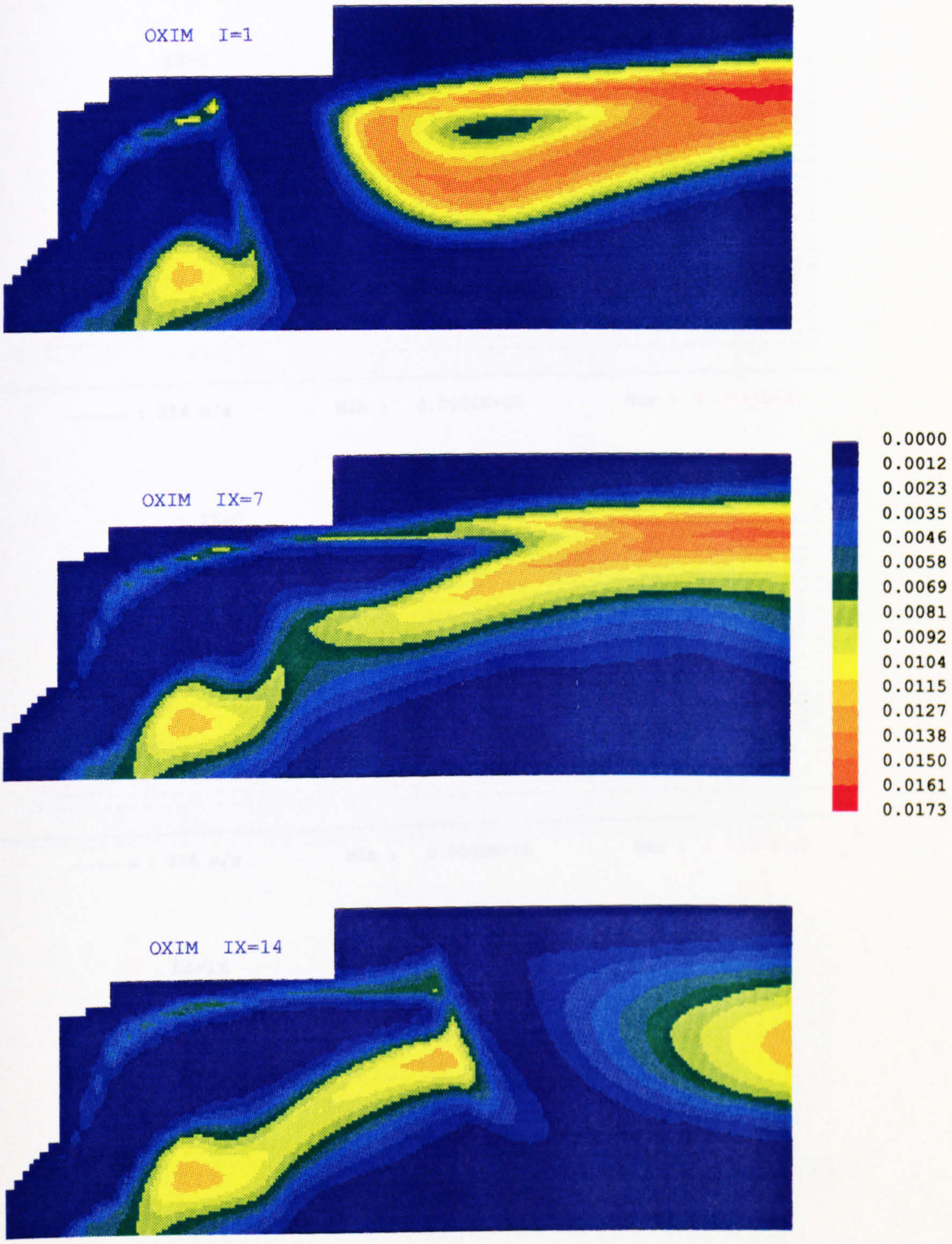

Figure 6.7 (g) Contours of soot oxidation rate (Injection scheme I)
(oxidation by O_2 - Nagle and Strickland-Constable formula)

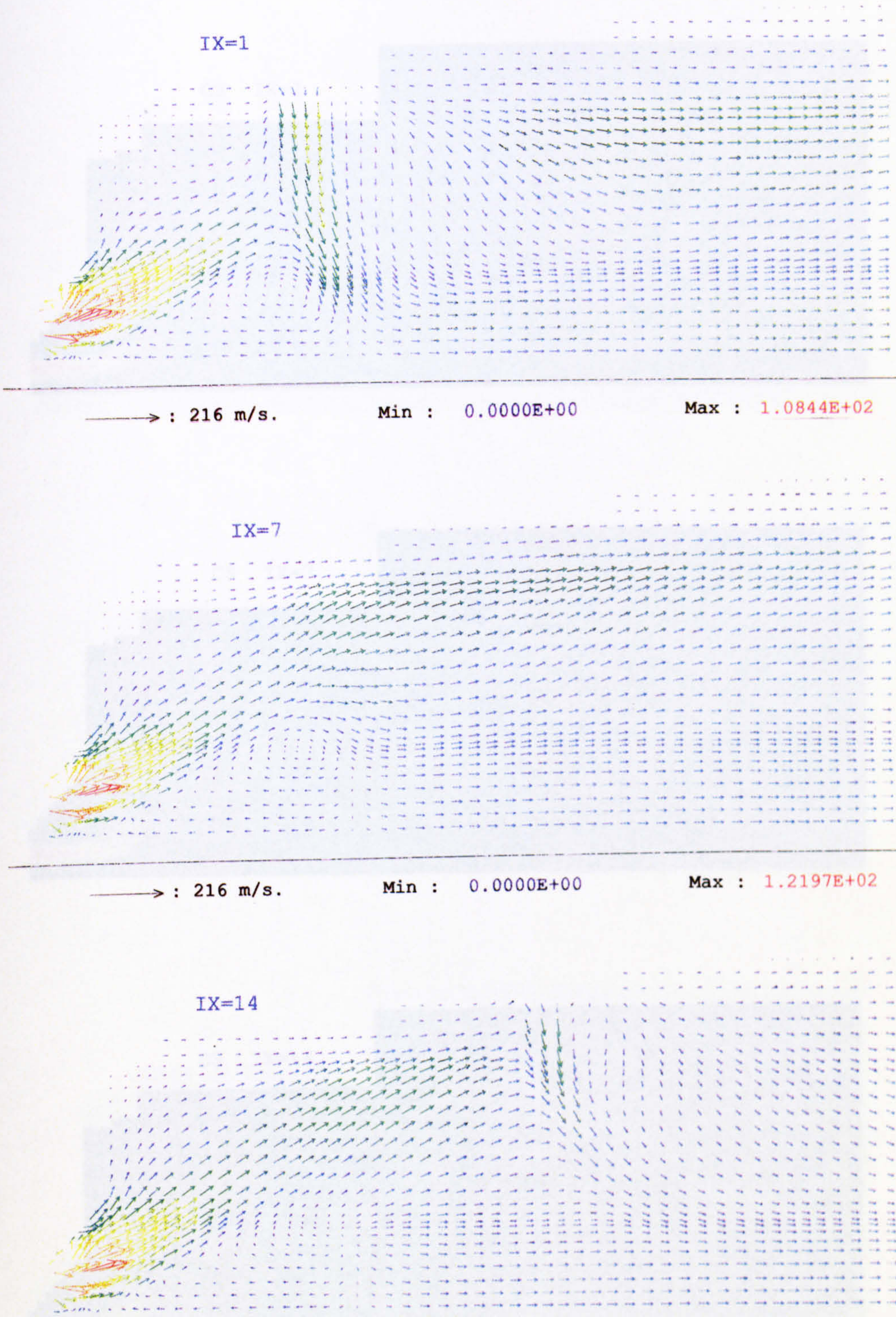

Figure 6.8 (a) Velocity vectors (Injection scheme II)

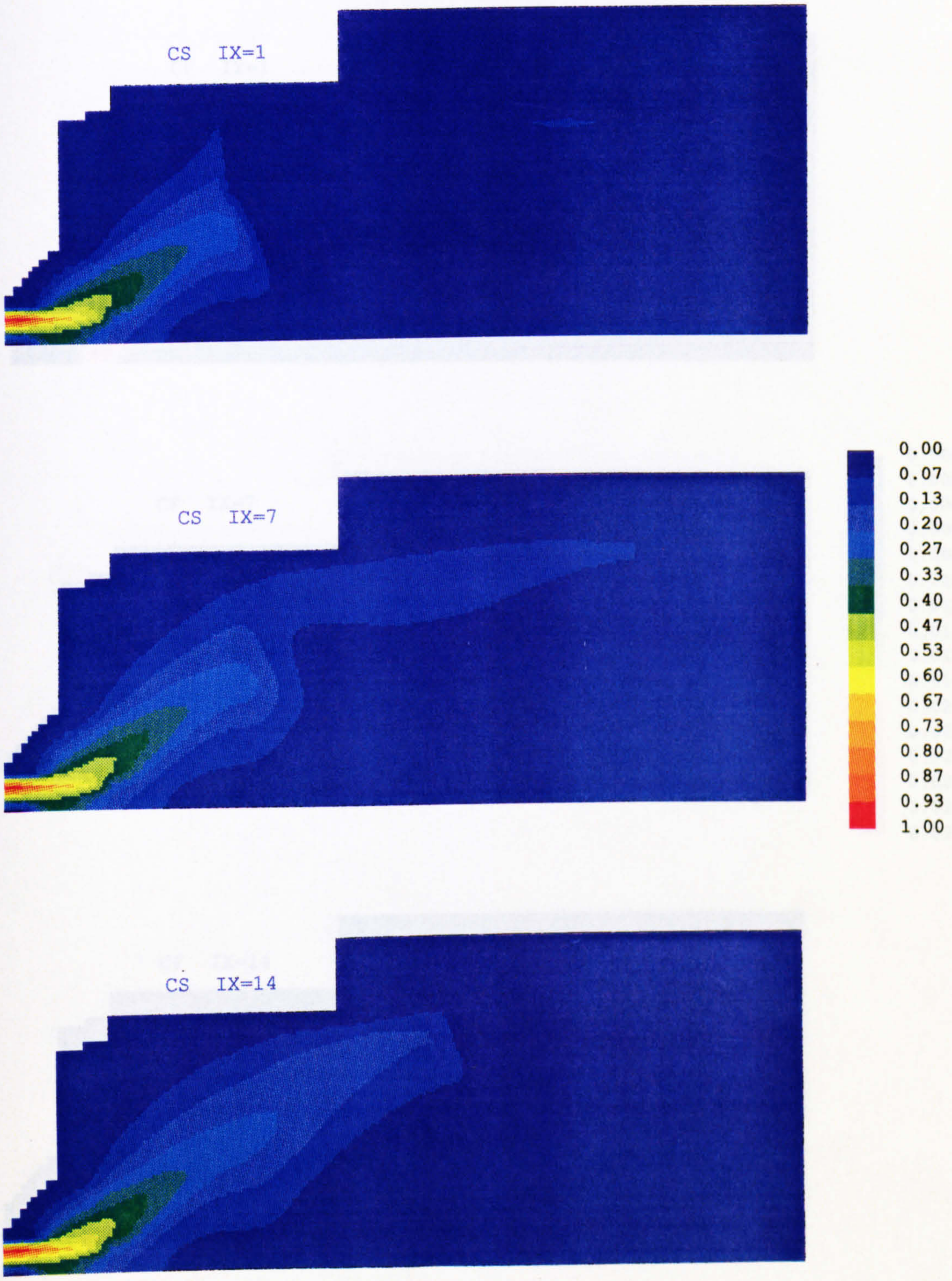

Figure 6.8 (b) Mean mixture fraction contours (Injection scheme II)

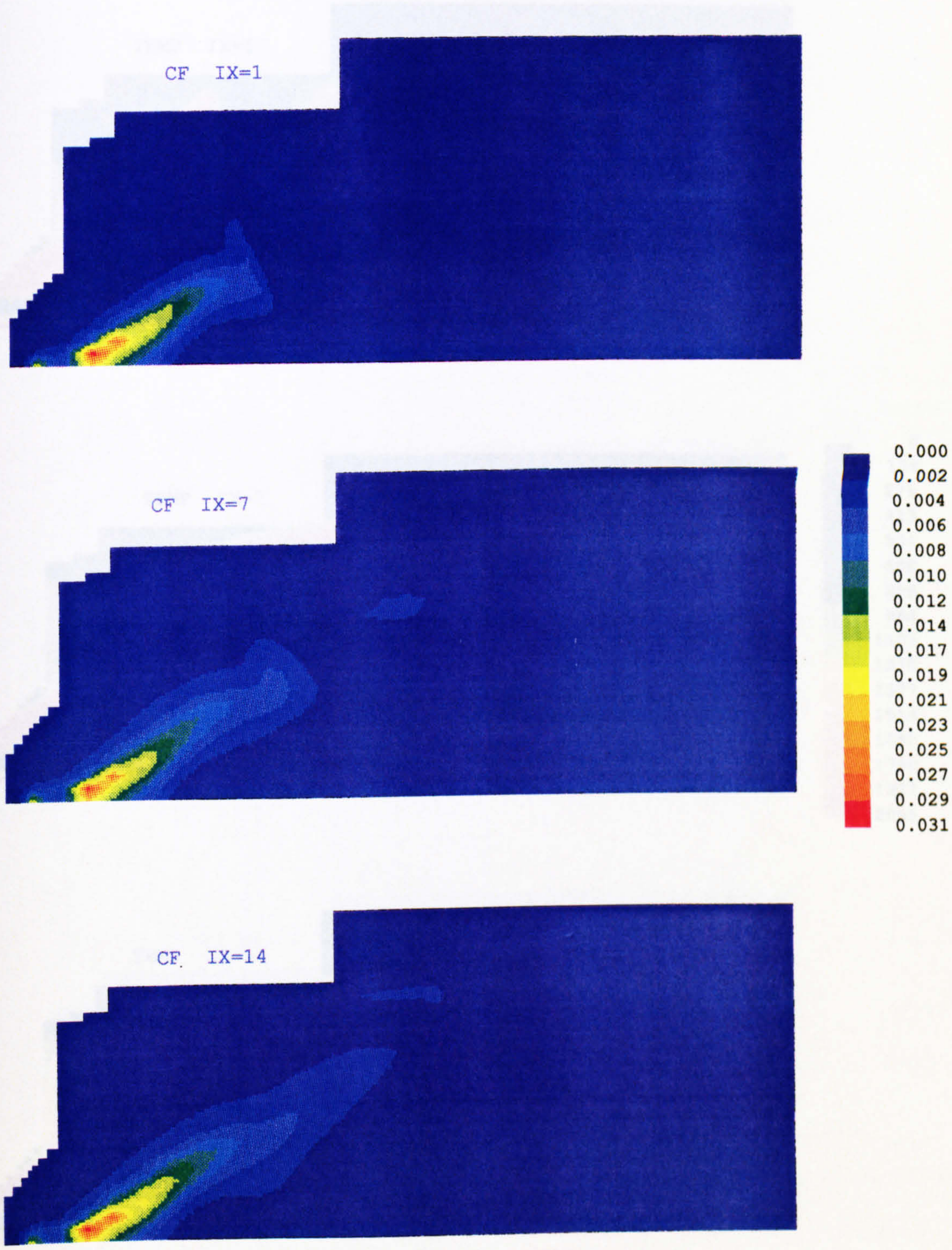

Figure 6.8 (c) Contours of mixture fraction fluctuation (Injection scheme II)

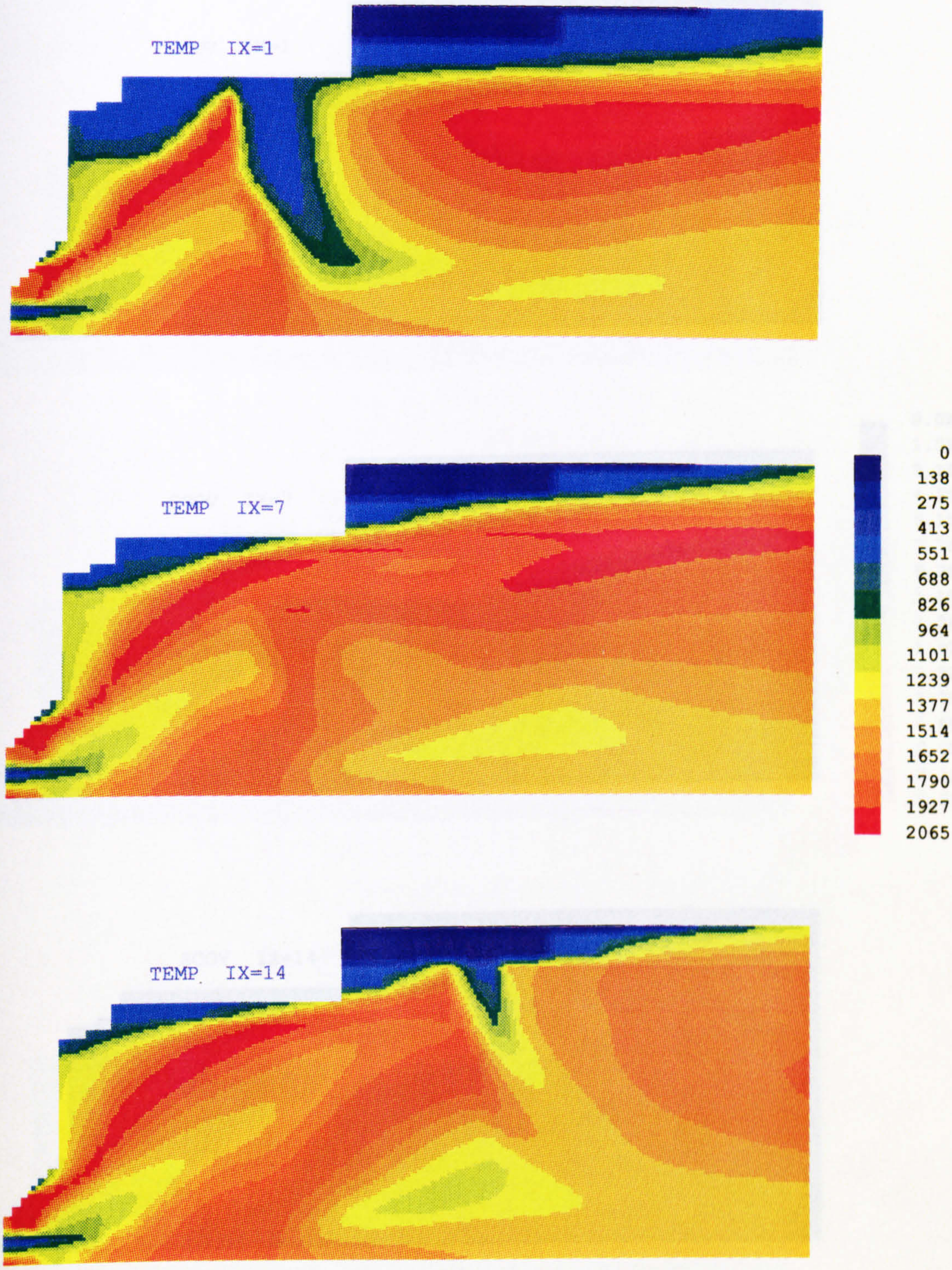

Figure 6.8 (d) Mean temperature contours (Injection scheme II)

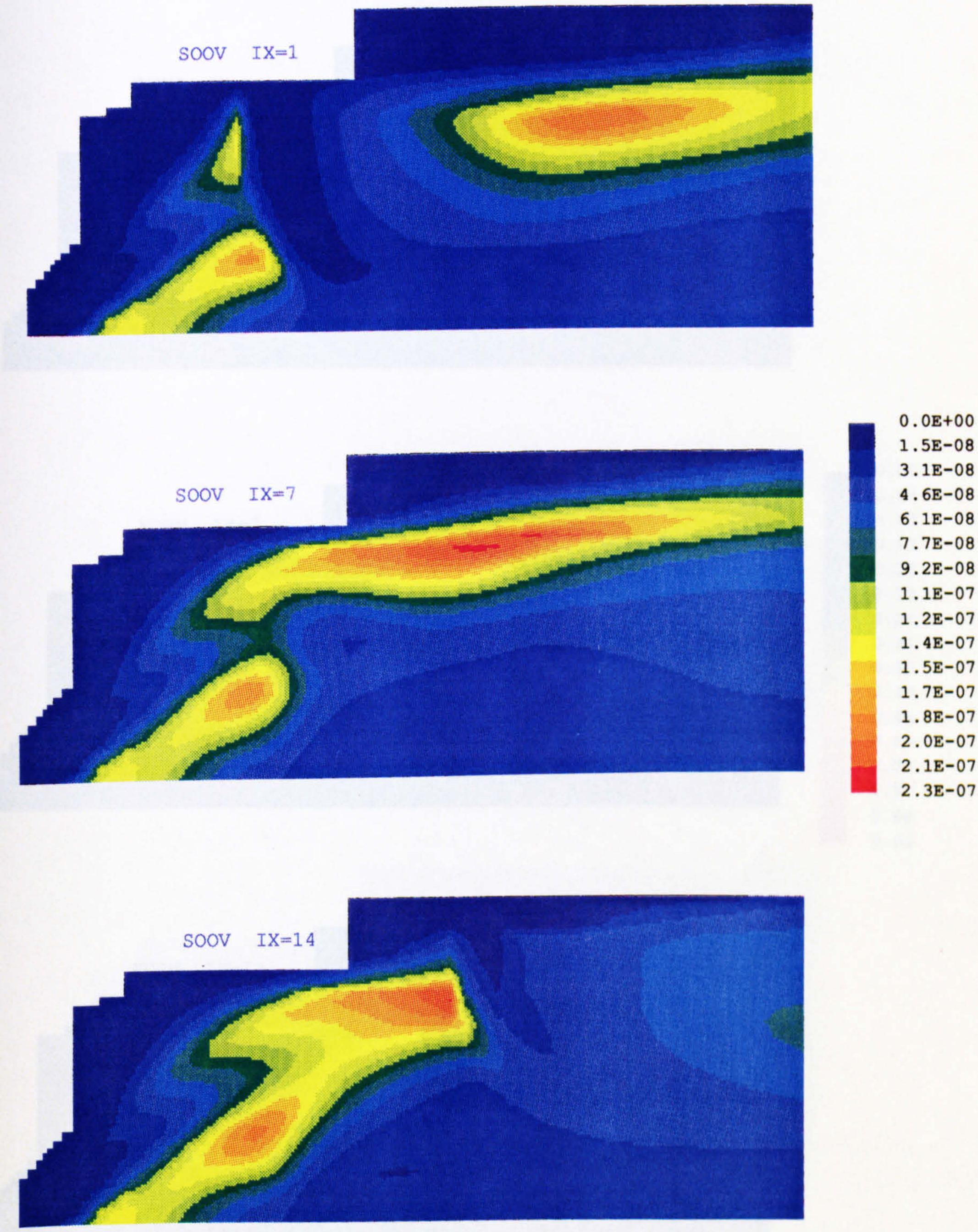

Figure 6.8 (e) Contours of soot volume fraction (Injection scheme II)
(oxidation by O_2 - Nagle and Strickland-Constable formula)

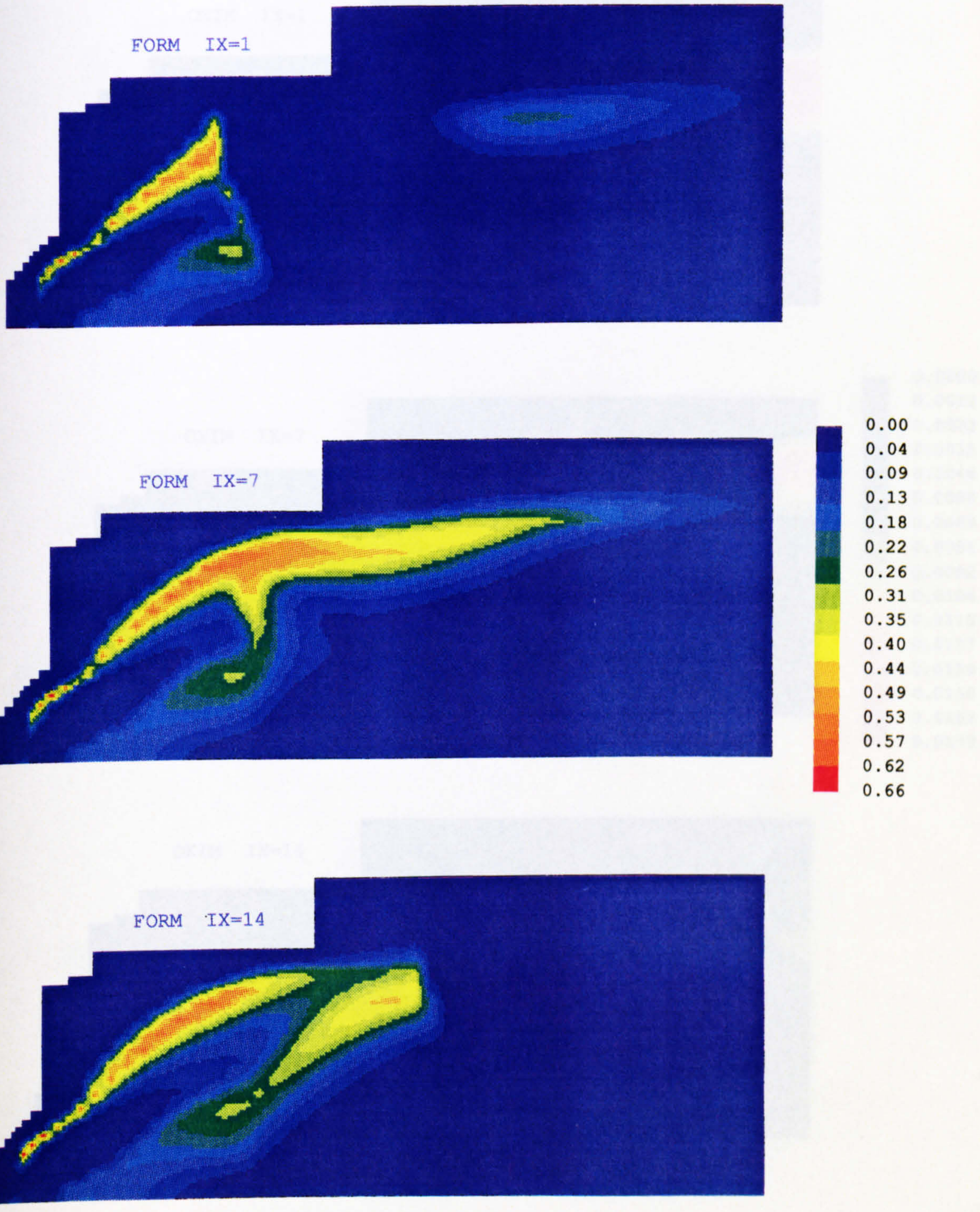

Figure 6.8 (f) Contours of soot formation rate (Injection scheme II)

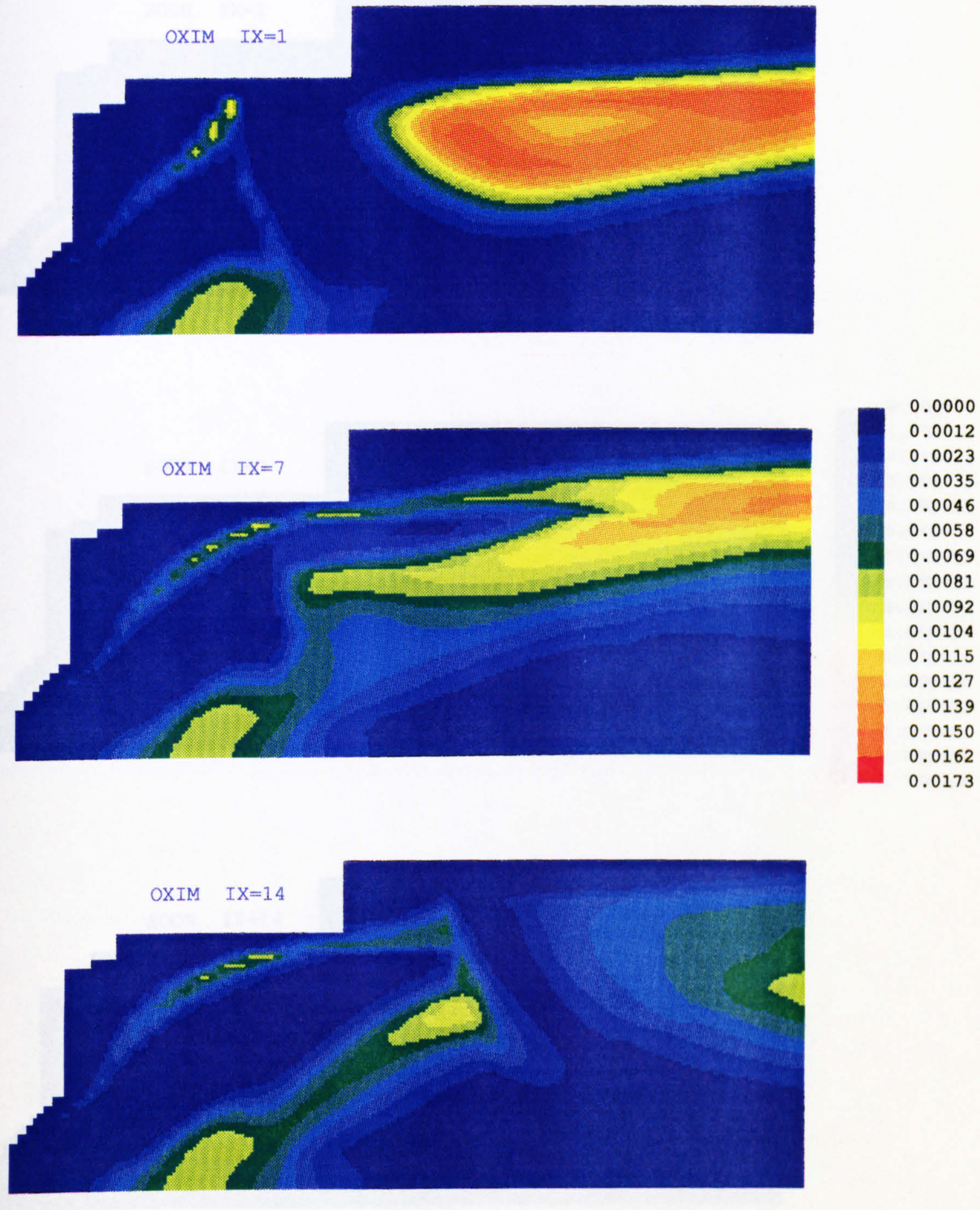

Figure 6.8 (g) Contours of soot oxidation rate (Injection scheme II)
(oxidation by O_2 - Nagle and Strickland-Constable formula)

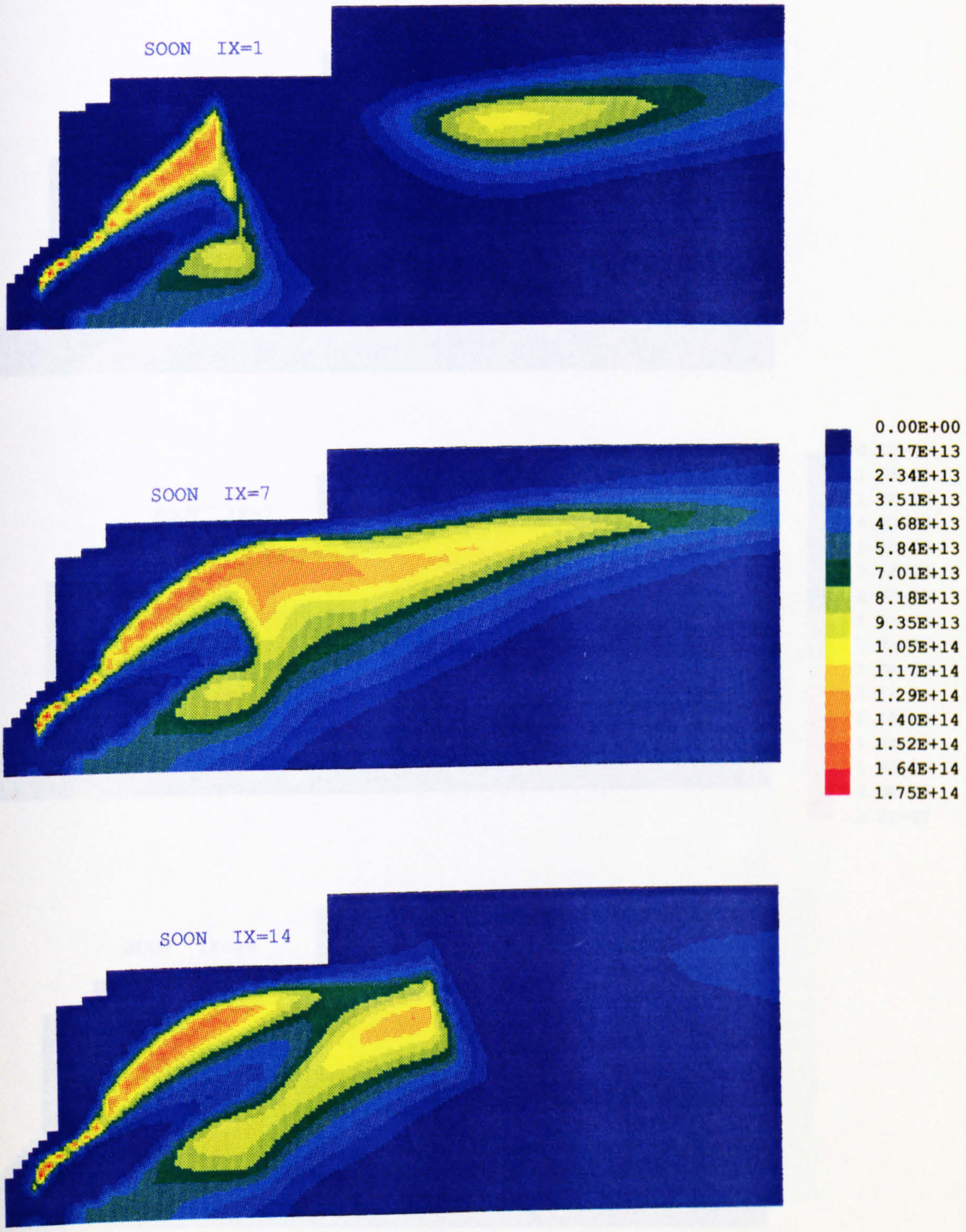

Figure 6.8 (h) Contours of soot number density ($1/m^3$) (Injection scheme II)

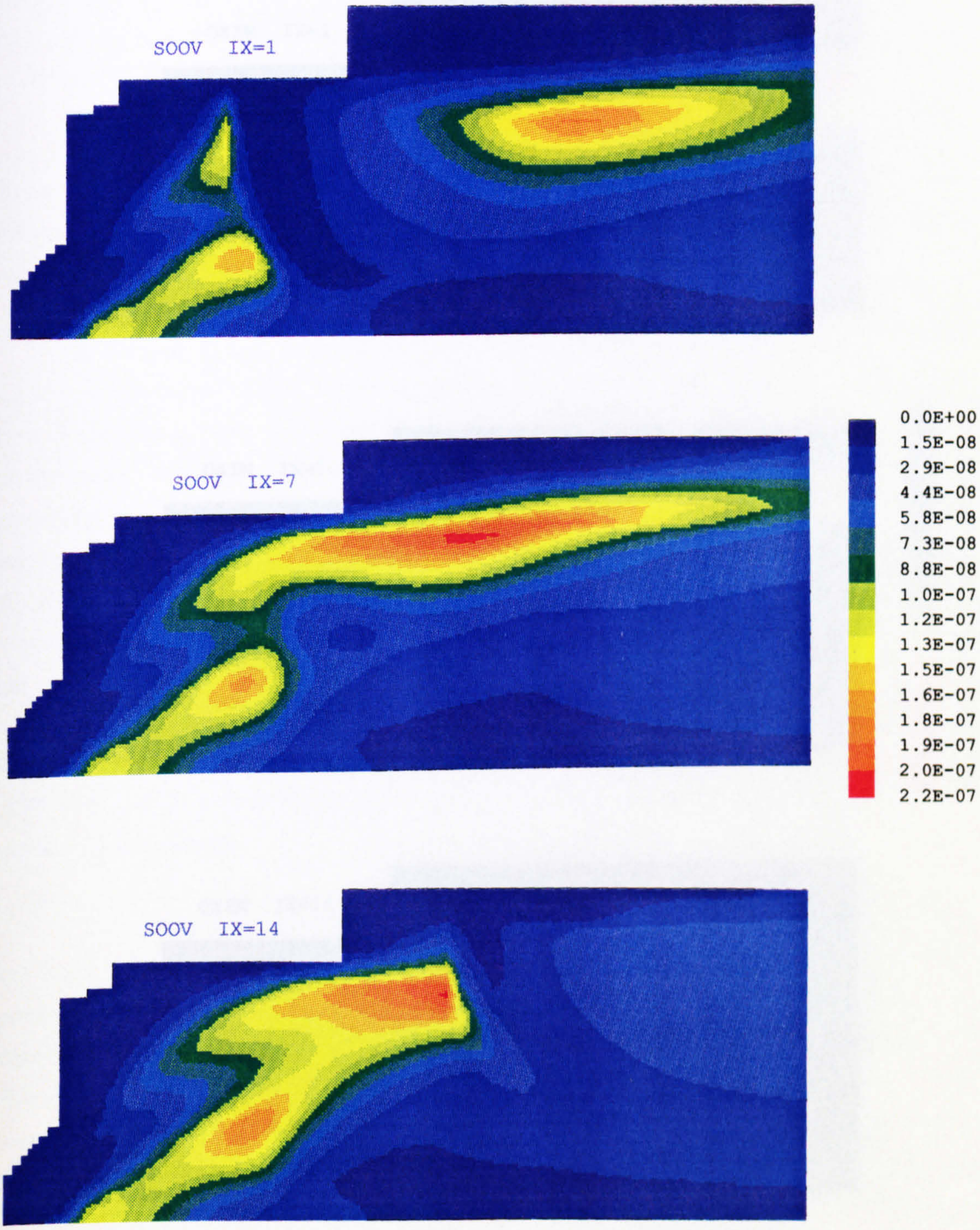

Figure 6.9 (a) Contours of soot volume fraction (Injection scheme II) (oxidation by OH - Fenimore and Jones formula)

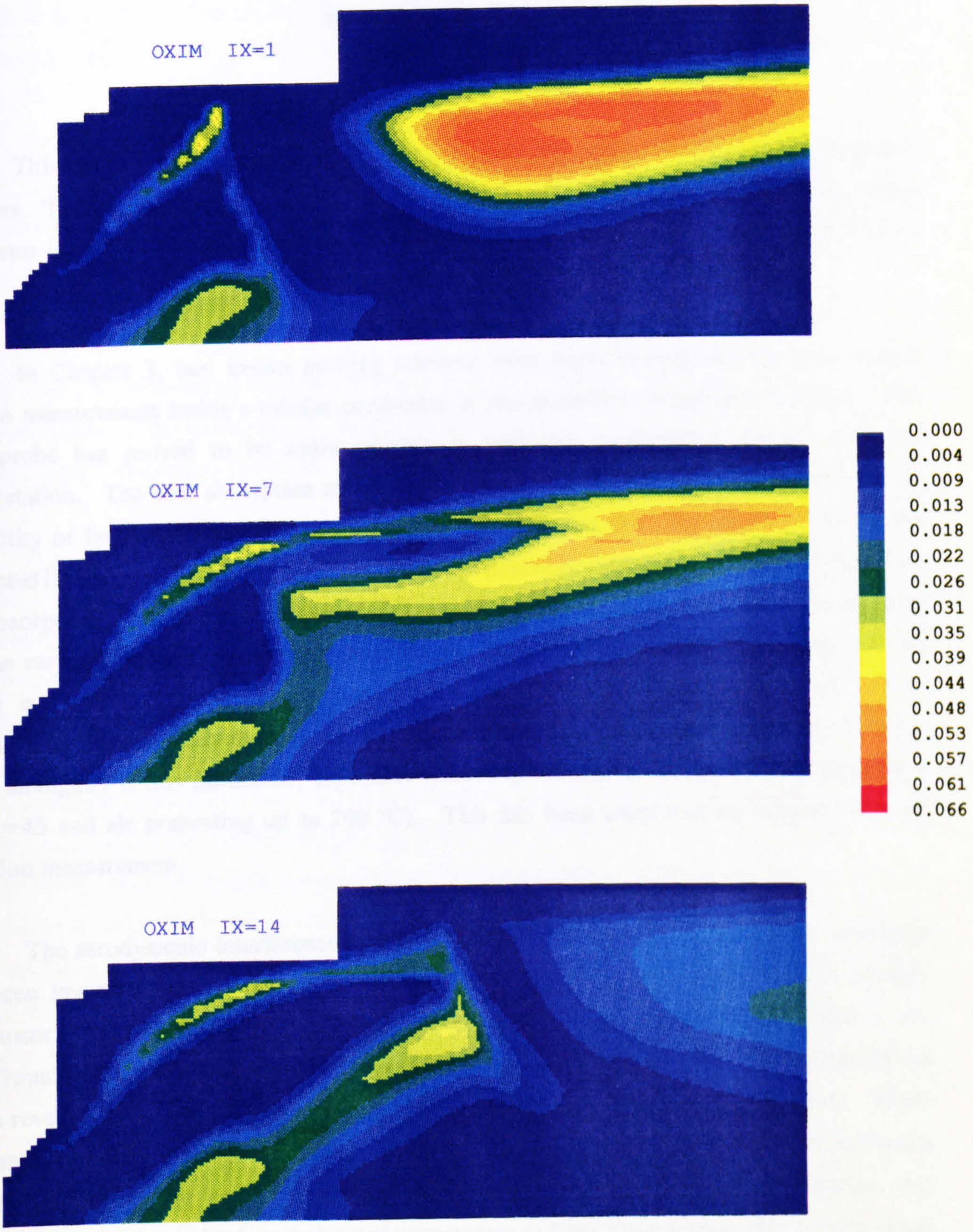

Figure 6.9 (b) Contours of soot oxidation rate (Injection scheme II)
(oxidation by OH - Fenimore and Jones formula)

Chapter 7 Conclusions and Recommendations for Further Investigations

This chapter draws conclusions from the experimental study reported in the preceding Chapters. The application of the laminar flamelet approach to soot modelling in the gas turbine combustor is also discussed. Finally some recommendations for further investigations will be made.

In Chapter 3, two in-situ probing schemes have been investigated for soot volume fraction measurement inside a tubular combustor at representative operating conditions. The sight probe has proved to be more reliable in both the mechanistic analysis and data interpretation. The soot absorption measurements in the primary zone are hampered by the possibility of fuel drop scattering in the multi-phase flow domain. Spectral analysis of the integrated line-of-sight extinction signal shows little discernible difference between the scattering and absorption signals. One difficulty with regard to the spectrum is that, as the probing volume varies from being soot dominant to droplet dominant, the flow field may also change and it is essential to separate the flow fluctuation from the extinction spectrum. Soot measurements in this study thereby are only performed in the dilution section, where the two-phase ambiguity is less influential, especially under representative combustor flow conditions (AFR=45 and air preheating up to 200 °C). This has been supported by separate thermal radiation measurement.

The aerodynamic interference due to the presence of the sight probe in the combustor has been investigated with the aid of a water flow visualization test in a replica perspex combustor. Such disturbance is believed to be localised and the whole flow field is not significantly affected. Evaluation of the probing/absorption technique in a small diameter jet flame reveals that the probing data is very similar to other non-intrusive measurement. While the necessary inert gas purge may alter the local soot properties near the probe tip, the influence can be minimised by employing a minimum purge rate. The spatially-resolved soot concentrations at atmospheric and elevated pressure up to 4 bar show comparable sooting levels with other reported experiments at similar flow conditions (Clark (1982)). The peak soot volume fractions follow the fuel trajectory, the skewed soot distributions reflect in part the asymmetry of the combustor flow field. Peak soot concentrations are located off-axis, whereas near the combustor centre line small particle concentrations are found. An increase in the air inlet temperature results in lower sooting levels, the trend is consistent with other combustor

measurements where spray evaporation, rather than soot formation, is significantly affected (Naegeli et al. (1983)). The reflecting probe showed less promise in the context of combustor measurement, where the small size optical reflector restricted probe performance.

The scalar profiles reported in Chapter 4 provide complementary information in relation to soot production in practical gas turbine combustion. The detailed scalar distributions for liquid kerosine burning are different from other published works which have typically used gaseous propane as fuel. The kerosine flame has spread more widely and consequently the temperature traverse quality is better than the propane flame. At fixed air mass flow rate, increasing the fuel kerosine flow rate has extended the flame further downstream from the primary zone, as indicated by the time-averaged mixture fraction distributions at the combustor dilution section. The temperatures are much lower than those predicted from equilibrium considerations, but close to the stretched laminar flamelet values.

The correlation of time-averaged carbon dioxide concentrations with the time-averaged conserved scalar, mixture fraction, shows a very clear functional curve which can be prescribed by laminar flamelet relationship. Similar correlations of time-averaged temperature with mixture fraction do not show this relationship as clearly as the CO_2. The detailed correlations are dependent on the flow conditions, and more scatter appears in the relationship when the flame is richer overall. Scalar fluctuations may be responsible for the scatter in the correlations and the scalar dissipation rate may also be important in the balance between finite rate chemistry and transport, especially for temperature as implied by turbulent jet flame calculations (Liew et al. (1984)). Soot loading in this tubular combustor is characteristically low under the flow conditions used here. The low sooting level is attributed to many factors, including low power flow conditions, vigorous fuel-air mixing and short residence time. No unique state relationships have been observed for mean soot volume fraction against mixture fraction, due probably to fluctuation levels and augmented fuel-air mixing and to the underlying more kinetically controlled soot formation process.

Thermal radiation from soot particles has been measured in the visible spectrum. One distinct peak at wavelength near 516 nm persists throughout the measurement. This narrow band spectrum is believed to be contributed by the C_2 radical emission. Whereas C_2 may be related to the soot formation process as proposed in some early work, the detailed chemistry is poorly understood at present. The spectral radiation distributions are generally in accord with classical radiation theory. Predictions of radiation flux, based on measured time-averaged soot concentrations and temperatures, generally gave underestimations when compared with the measured radiation. The levels of temperature fluctuation may be the major source of this

discrepancy. Predictions which included temperature fluctuation show good agreement with measurements in the spectral radiation distributions. With the low sooting level in this tubular combustor under the flow conditions employed, the optical thin assumption can be used without introducing large discrepancies in the predictions. Optical temperatures inferred from measured thermal radiation and soot absorption are close to values measured by thermocouple. These comparisons suggest a strong dependence of radiation intensity on temperature, following an exponential function as formulated in Eq. 5-11, but with only weak dependence on the soot concentration.

Numerical calculations of soot formation in the combustor using an extended laminar flamelet approach generated broadly similar soot concentration profiles. The peak soot volume fraction predicted are consistent with the measurements. The accuracy of predictions in terms of the absolute values suffered from various computational limitations, for example the descriptions of turbulence, spray combustion and the lack of satisfactory boundary conditions, especially for fuel inlet conditions. In this study gaseous propane is used as the fuel and the resulting flame is concentrated in a narrow regime and is thereby influenced by the high inlet air momentum. The predicted scalar profiles reveal such features when compared with the measurements. The soot volume fraction is consequently over-predicted. With improvement in the flow field calculation, the soot concentration level can be expected to lie closer to the measurements.

Particulate soot is usually formed in the combustor primary zone, which is shown in the computational test in Chapter 6. Information in relation to soot properties in the primary zone is crucial to understanding the detailed soot formation process. In this study, the multi-phase flow in the primary zone restricts the absorption measurement under the low-power flow conditions. With increased inlet air temperature, the probing domain may be extended further upstream but the exact axial location limit will depend on the flow field structure. It is desirable to discriminate the droplet scattering from the extinction measurements and analysis of the spectral extinction signal may be an option.

At present, only time-averaged scalar distributions inside a gas turbine combustor can be obtained. Given the experimental limitations, scalar fluctuations must be taken into account when applying the conserved scalar/laminar flamelet concept. Although a clear state relationship can be constructed for carbon dioxide which involves comparatively fast chemistry, more measurements for other species, for example carbon monoxide and the parent fuel, are required to verify the existence of flamelet structures in the combustor flow field.

Mean thermal radiation flux is strongly dependent on temperature fluctuations at low power operating conditions. Whether this holds at higher power conditions needs further experimental investigation.

The soot formation model characterised by two equations, for volume fraction and number density, shows encouraging performance in predicting soot production in the combustor. Computational improvement for overall flow field simulation is necessary however for further development of the soot model in its application to gas turbine combustion.

Reference

Alizadeh, S. (1993) "Flow field prediction of NOx and smoke production in aircraft engines" Ph.D thesis, Cranfield University

Allen, J.D. (1975) "Probe sampling of oxides of nitrogen from flames" *Combustion and Flame*, Vol. 24, p. 133

Ang, James A. Pagni, Patrick J. Mataga, Thomas G. Margle, Janice M. and Lyons, Valerie J. (1988) "Temperature and velocity profiles in sooting free convection diffusion flames, *AIAA Journal*, Vol. 26, No. 3, March, pp. 323-32

Appleton, John P. (1973) "Soot oxidation kinetics at combustion temperatures" AGARD CP-125

Askari-Sardhai, A. (1987) "Laminar flamelet modelling of turbulent combustion chemistry for practical fuels" Ph.D thesis, Cranfield Institute of Technology

Babikian, D.S. Edwards, D.K. Karam, S.E Wood, C.P. and Samuelsen, G.S. (1990) "Experimental mass absorption coefficients of soot in spray combustor flames" *J. Thermophysics*, Vol. 4, No. 1, January pp. 8-15

Baronavski, A.P. and McDonald, J.R. (1977) "Application of saturation spectroscopy to the measurement of C_2, $^3\pi_u$ concentrations in oxy-acetylene flames" *Applied Optics*, Vol 16, pp. 1897-1901

Batten, Carmen E. (1985) "Spectral optical constants of soots from polarized angular reflectance measurements" *Applied Optics*, Vol. 24, No. 8, 15 April, pp. 1193-1199

Bertrand, C. and Delfau, J.L. (1985) "Mechanism of soot formation in hydrocarbon flames" *Combustion Science and Technology*, Vol. 44, p. 29

Bicen, A.F. Tse, D.G.N. and Whitelaw, J.H. (1990) "Combustion characteristics of a model can-type combustor" *Combustion and Flame*, Vol. 80, pp. 111-125

Bilger, R.W. (1976) "Turbulent jet diffusion flames" *Prog. Energy Combust. Sci.*, Vol. 1, pp. 87-109

Bilger, R.W. (1977 a) "Reaction rates in diffusion flames" *Combustion and Flame*, Vol. 30, pp. 277-284

Bilger, R.W. (1977 b) "Probe measurements in turbulent combustion" in Experimental diagnostics in gas phase combustion systems, Zinn, B.T. (Ed.), *Prog. Astronaut. Aernaut.*, Vol. 53

Bilger, R.W. (1980) "Turbulent flows with non-premixed reactors" see Libby and Williams (1980)

Blazowski, W.S. (1978) "Future jet fuel combustion problems and requirements" *Progress in Energy and Combustion Science*, Vol. 4, pp. 177-199

Bockhorn, H. (1993) "Soot formation during combustion: recent developments in mechanisms and models" Proceeding of the Anglo-German Combustion Symposium, Cambridge, pp. 1-9

Bowden, T.T. Pearson, J.H. and Wetton, R.J. (1984) "The influence of fuel hydrogen content upon soot formation in a model gas turbine combustor" ASME 84-GT-6

Bradley, D. Dixon-lewis, G. El-din Habik, S. and Mushi, E.M.J. (1984) "The oxidation of graphite powder in flame reaction zones" *20th Symposium (International) on Combustion*, pp. 931-940

Calcote, H.F. (1981) "Mechanisms of soot nucleation in flames - A critical review" *Combustion and Flame*, Vol. 42, pp. 215-242

Charalampopoulos, T.T. (1992) "Morphology and dynamics of agglomerated particles in combustion systems using light scattering techniques" *Progress in Energy and Combustion Science*, Vol. 18, pp. 13-45

Charalampopoulos, T.T. and Chang, H. (1991) "Agglomerate parameters and fractal dimension of soot using light scattering - effects on surface growth" *Combustion and Flame*, Vol. 87, pp. 89-99

Chigier, N. (1976) "The atomization and burning of liquid fuel sprays" *Progress in Energy, Combustion Science*, Vol. 2, pp. 97-114

Clark, Jim A. (1982) "Measured and predicted soot profiles in a gas turbine combustor" *Combustion and Flame*, Vol. 48, pp. 121-133

Claus, R.W. (1981) "Spectral flame radiance from a tubular can combustor" NASA TP-1722

Coelho, P.J. Farias, T.L. Pereira, J.C.F. and Carvalho, M.G. (1993) "Numerical prediction of turbulent sooting diffusion flames" AGARD CP-536

Correa, S.M. (1993) "A review of NOx formation under gas turbine combustion conditions" *Combustion Science and Technology*, Vol. 87, pp. 329-362

Correa, S.M. and Shyy, W. (1987) "Computational models and methods for continuous gaseous turbulent combustion" *Progress in Energy, Combustion Science*, Vol. 13, pp. 249-292

Crauford, N.L. Liew, S.K. and Moss, J.B. (1985) "Experimental and numerical simulation of a buoyant fire" *Combustion and Flame*, Vol. 61, p. 63

D'Alessio, A. D'anna, A. D'orsi, A. Minutolo, P. Barbella, R. and Ciajolo, A. (1992) "Precursor formation and soot inception in premixed ethylene flames" *24th Symposium (International) on Combustion*, pp. 973-980

Dalzell, W.H. and Sarofim, A.F. (1969) "Optical constants of soot and their application to heat flux Calculations", *Journal of Heat Transfer*, Transaction of ASME, Vol. 91, No. 1, pp. 100-104

Dasch, Cameron J. and Heffelfinger, David M. (1991) "Planar imaging of soot formation in turbulent ethylene diffusion flames: fluctuations and integral scales" *Combustion and Flame*, Vol. 85, pp. 389-402

Dec, John E. (1992) "Soot distribution in a D.I. diesel engine using 2-D imaging of laser-induced incandescence, elastic scattering and flame luminosity" SAE 920115

Desaulty, M. (1991) "Turbine engine combustor design at SNECMA" ISABE 91-7007

Domnick, J. (1992) "Application of LDA in gas-flows", Advanced laser-doppler anemometry short course, UMIST, UK

Drennan, S.A. Peterson, C.O. Khatib, F.M. Sowa, W.A. and Samuelsen, G.S. (1993) "Pollutant emissions from and within a model gas turbine combustor at elevated pressures and temperatures" AGARD CP-536

Eckbreth, A.C. (1988) "Laser diagnostics for combustion temperature and species" Abacus Press

Eckerle, W.A. and Rosfjord, T.J. (1988) "Soot loading in a generic gas turbine combustor" *J. Propulsion*, Vol. 4, No. 1, Jan.-Feb. pp. 89-96

Edelman, R.B. Fortune, O. and Weilerstein, G. (1972) "Some observations on flows described by coupled mixing and kinetics" *Emissions from Continuous Combustion Systems*, ed. by Walter Cornelins and William G. Agrew, Plenum Press, London, pp. 55-87

Ehalil, E.E. and Whitelaw, J.H. (1976) "Aerodynamic and thermodynamic characteristics of kerosine-spray flames" *16th Symposium (International) on Combustion*, pp. 569-576

El Banhawy, Y. and Whitelaw, J.H. (1981) "Experimental study of the interaction between a fuel spray and surrounding combustion air" *Combustion and Flame*, Vol. 42, pp. 253-275

Faeth, G.M (1983) "Evaporation and combustion of sprays" *Progress in Energy, Combustion Science*, Vol. 9, pp. 1-76

Faeth, G.M (1987) "Mixing, transport and combustion in sprays" *Progress in Energy, Combustion Science*, Vol. 13, pp. 293-345

Faeth, G.M. Gore, J.P. and Sivathanu, Y.R. (1987) "Radiation from soot-containing flames" AGARD CP-422

Fairweather, M. Jones, W.P. Ledin, H.S. and Lindstedt, R.P. (1992) "Predictions of soot formation in turbulent, non-premixed propane flames" *24th Symposium (International) on Combustion*, pp. 1067-1074

Fenimore, C.P. and Jones, G.W. (1967) "Oxidation of soot by hydroxyl radicals" *J. Phys. Chem.*, Vol. 71, pp. 593-597

Ferguson, C.R. and Mellor, A.M. (1979) "Radiative heat transfer from gas turbine flames" ASME 79-GT-144

Fischer, S.J. Hardouin-Dupare Benedicte and Grosshandler, W.L. (1987) "The structure and radiation of an ethanol pool fire" *Combustion and Flame*, Vol. 70, pp. 291-306

Flower, W.L. (1989) "Soot particle temperatures in axisymmetric laminar ethylene-air diffusion flames at pressures up to 0.7 MPa" *Combustion and Flame*, Vol. 77, pp. 279-293

Frenklach, Michael and Wang, Hai (1990) "Detailed modeling of soot particle nucleation and growth" *23rd Symposium (International) on Combustion*, pp. 1559-1566

Garo, A. Prado, G. and Lahaye, J. (1990) "Chemical aspects of soot particles oxidation in a laminar methane-air diffusion flame" *Combustion and Flame*, Vol. 79, pp. 226-233

Gaydon, A.G. (1957) "The spectroscopy of flames" Chapman & Hall, London

Gilyazetdnov, L.I. (1972) "The kinetics and formation mechanism of carbon black during the thermal decomposition of hydrocarbons in the gas phase" *Khim. Tverd. Topliva*, Vol. 3, pp. 103-111

Glassman, Irvin (1988) "Soot formation in combustion processes" *Twenty-Second Symposium (International) on Combustion*, pp. 295-311

Gordon, S. and McBride, B.J. (1971) "Computer program for calculation of complex chemical equilibrium compositions, rocket performance, incident and reflected shocks and Chapman-Jouget detonations", NASA SP-273

Greenhalgh, D.G. (1993) "Optical combustion diagnostics, fundamental or practical" Proceeding of the Anglo-German Combustion Symposium, Cambridge, pp. 18-25

Gülder, Ö.L. Glavincevski, B. and Baksh, M.F. (1989) "Fuel molecular structure and flame temperature effects on soot formation in gas turbine combustors" ASME 89-GT-288

Hall, Robert J. and Bonczyk, Paul A. (1990) "Sooting flame thermometry using emission / absorption tomography" *Applied Optics*, Vol. 29, No. 31, pp. 4590-4598

Harris, Stephen J. and Weiner, Anita M. (1983) "Surface growth of soot particles in premixed ethylene/air flames" *Combustion Science and Technology*, Vol. 31, pp. 155-167

Harris, S.J. Weiner, A.M. and Ashcraft, C.C. (1986) "Soot particle inception kinetics in a premixed ethylene flame" *Combustion and Flame*, Vol. 64, pp. 65-81

Haynes, B.S. and Wagner, H.Gg. (1981) "Soot formation" *Progress in Energy, Combustion Science*, Vol. 7, pp. 229-273

Heitor, M.V. and Moreira, A.L.N. (1993) "Thermocouples and sample probes for combustion studies" *Progress in Energy and Combustion Science*, Vol. 19, pp. 259-278

Heitor, M.V. and Whitelaw, J.H. (1986) "Velocity, temperature, and species characteristics of the flow in a gas-turbine combustor" *Combustion and Flame*, Vol. 64, pp. 1-32

Holderness, F.H. and Macfarlane, J.J. (1973) "Soot formation in rich kerosine flames at high pressure" AGARD CP-125

Holman, J.P. (1990) "Heat Transfer", 7th ed., McGraw-Hill Book Company

Hopkins, Tim and Phillips, Chris (1988) "Numerical methods in practice: Using the NAG library" Addison-Wesley Publishing Company,

Hori, Morio (1986) "Experimental study of nitrogen dioxide formation in combustion systems" *21st Symposium (International) on Combustion*, pp. 1181-1188

Hubbard, E.H. (1957) *J. Inst. Fuel*, Vol. 3, pp. 553-576

Jander, Helga and Wagner, Heinz Georg (1990) "Soot formation in combustion", An International Round Table Discussion, Vandenhoeck & Ruprecht, Göttingen, Germany

Jasuja, A.K. and Tam, I.C.K. (1992) "Determination of air blast atomized spray structure using state-of-the-art laser diagnostics" AIAA 92-3232

Jeng, S.-M. Lai, M.-C. and Faeth, G.M. (1984) "Nonluminous radiation in turbulent buoyant axisymmetric flames" *Combustion Science and Technology*, Vol. 40, pp. 41-53

Jensen, D.E. (1974) "Prediction of soot formation rates: a new approach" *Proc. Roy. Soc.* A. Vol. 338, pp. 375-396

Join-Lambert, A. (1992) "Aerodynamic investigation of a tubular combustor", M.Sc Thesis, Cranfield Institute of Technology

Jones, W.P. and Toral, H. (1983) "Temperature and composition measurements in a research gas turbine combustion chamber" *Combustion Science and Technology*, Vol. 31, pp. 249-275

Jones, W.P. and Whitelaw, J.H. (1984) "Modelling and measurements in turbulent combustion" *20th Symposium (International) on Combustion*, pp. 233-249

Jones, W.P. and Wilhelmi, J. (1989) "Velocity, temperature and composition measurements in a confined swirl driven recirculating flow" *Combustion Science and Technology*, Vol. 63, pp. 13-31

Katsuki, M. Mizutani, Y. and Shibuya, K. (1976) "Emissions from gas turbine combustors" *Bulletin of the JSME*, Vol. 19, pp. 1353-1366

Kent, J.H. and Bastin, S.J. (1984) "Parametric effects on sooting in turbulent acetylene diffusion flames" *Combustion and Flame*, Vol. 56, pp. 29-42

Kent, J.H. and Honnery, D. (1987) "Soot and mixture fraction in turbulent diffusion flames" *Combustion Science and Technology*, Vol. 54, pp. 383-397

Kent, J.H. and Honnery, D. (1990) "A soot formation rate map for a laminar ethylene diffusion flame" *Combustion Science and Technology*, Vol. 79, pp. 287-298

Kent, J.H. and Wagner, H.Gg. (1982) "Soot measurement in laminar ethylene diffusion flames" *Combustion and Flame*, Vol. 47, p. 52

Kent, J.H. and Wagner, H.Gg. (1983) "Soot formation in diffusion flames" AGARD CP-353

Kent, J.H. and Wagner, H.Gg. (1984) "Why do diffusion flames emit smoke" *Combustion Science and Technology*, Vol. 41, pp. 245-269

Kerker, M. (1969) "The scattering of light" Academic press, London

Khan, I.M. and Greeves, G. (1974) "A method for calculating the formation and combustion of soot in diesel engines" Afgan, N.H. and Beer, J.M. (ed.), Scripta Book Co.

Klassen, M. Sivathanu, Y.R. and Gore, J.P. (1992) "Simultaneous emission absorption measurements in toluene-fueled pool flames: mean and RMS properties" *Combustion and Flame*, Vol. 90, pp. 34-44

Koch, R. Wittig, S. Feld, H.-J. and Mohr, H.-J. (1991) "In-Situ soot measurements in an operating engine gas turbine combustor" ASME 91-GT-177

Köylu, Ü.Ö. and Faeth, G.M. (1991) "Carbon monooxide and soot emissions from liquid-fueled buoyant turbulent diffusion flames" *Combustion and Flame*, Vol. 87, pp. 61-76

Kuo, Kenneth K. (1986) "Principles of combustion" John Wiley & Sons

Kyukuo, D. Sawada, T. and Nistu, A. (1980) "Pollutant emission levels during transient operations of a small gas turbine" *Combustion Science and Technology*, Vol. 24, p. 43

Lefebvre, A.H. (1983) "Gas turbine combustion" Hemisphere Publishing Corporation

Lefebvre, A.H. (1984) "Flame radiation in gas turbine combustion chambers" *International Journal of Heat and Mass Transfer*, Vol. 27, pp. 1493-1510

Launder, B.E. and Spalding, D.B. (1974) "The numerical computation of turbulent flows" *Comput. Meth. Appl. Mech. Eng.* Vol. 3, pp. 269-289

Laurendeau, N.M. (1978) "Heterogeneous kinetics of coal char gasification and combustion" *Progress in Energy and Combustion Science*, Vol. 4, pp. 221-270

Lee, K.B. Thring, M.W. and Beer, J.M. (1962) "On the rate of combustion of soot in a laminar soot flame" *Combustion and Flame*, Vol. 6, pp. 137-145

Lee, S.C. and Tien, C.L. (1981) "Optical constants of soot in hydrocarbon flames" *18th Symposium (International) on Combustion*, pp. 1159-1166

Lewis, Bernard and von Elbe, Guenther (1987) "Combustion, flames and explosions of gases" 3rd ed., Academic press, Inc., London

Libby, P.A. and Williams, F.A. (1980) "Turbulent reacting flows" Topics in Applied Physics, Vol. 44, Springer-Verlag

Liew, S.K. (1983) "Flamelet models of turbulent non-premixed combustion" Ph.D thesis, Department of Aeronautics and Astronautics, University of Southampton

Liew, S.K. Bray, K.N.C. and Moss, J.B. (1984) "A stretched laminar flamelet model of turbulent non-premixed combustion" *Combustion and Flame*, Vol. 56, p. 199

Lindstedt, R.P. (1992) Unpublished data

Magre, P. Collin, G Ansart, D Baudouin, C and Bouchie, Y. (1991) "Mesures de température par DRASC et validation d'un code de calcul sur foyer de turboréacteur" Proceeding of Third European Propulsion Forum, ONERA, Paris, AAAF, pp. 349-368

Markstein, G.H. (1984) "Measurements on gaseous-fuel pool fires with a fibre-optic absorption probe" *Combustion Science and Technology*, Vol. 39, pp. 215-233

McDonell, Vincent G. and Samuelsen, Scott (1991) "Gas and drop behavior in reacting and non-reacting air-blast atomizer sprays" *Journal of Propulsion*, Vol. 7, No. 5, pp. 684-691

McGuirk, J.J. (1987) "3-D combustor predictions - a comparison of equilibrium and laminar flamelet chemistry models" AGARD CP-422

Mckinnon, J. Thomas and Howard, Jack B. (1992) "The role of PAH and acetylene in soot nucleation and growth" *24th Symposium (International) on Combustion*, pp. 965-971

Megaridis, C.M. and Dobbins, R.A. (1988) "Soot aerosol dynamics in a laminar ethylene diffusion flame" *22nd Symposium (International) on Combustion*, pp. 353-362

Mengüc, M.P. Cummings III, W.G. and Viskanta, R. (1986) "Radiative transfer in a gas turbine combustor" *J. Propulsion*, Vol. 2, No. 3, pp. 241-247

Millikan, R.C. and Foss, W.I. (1962) "Non-equilibrium effects in soot deposition" *Combustion and Flame*, Vol. 6, pp. 210-211

Mizutani, Y. Yasuma, G. and Katsuki, M. (1977) "Stabilization of spray flames in a high-temperature stream" *16th Symposium (International) on Combustion*, pp. 631-638

Moss, J.B. Stewart, C.D. and Syed, K.J. (1987) "Flamelet chemistry modelling of soot formation for radiation prediction in combustor flowfield" AGARD CP-422

Moss, J.B. Stewart, C.D. and Syed, K.J. (1988) "Flowfield modelling of soot formation at elevated pressure" *22nd Symposium (International) on Combustion*, pp. 413-423

Moss, J.B. Stewart, C.D. Young, K.J. and Zheng, Q-P. (1991) "Smoke production in aircraft engine: flow field modelling and experimental validation", Proceeding of Third European Propulsion Forum, ONERA, Paris, AAAF, pp. 333-347

Mullins, J. Simons, B. and Williams, Alan (1987) "Rates of formation of soot from hydrocarbon flames and its destruction" AGARD CP-422

Mullins, Jeremy and Williams, Alan (1987) "The optical properties of soot: a comparison between experimental and theoretical values" *Fuel*, Vol. 66, February, pp. 277-280

Naegeli, David W. Dodge, Lee G. and Moses, Clifford, A. (1983) "Effects of flame

temperature and fuel composition on soot formation in gas turbine combustors" *Combustion Science and Technology*, Vol. 35, pp. 117-131

NAG Fortran Library Manual (1990), Mark 14, The Numerical Algorithms Group Ltd.

Nagle, J. and Strickland-Constable, R.F. (1962) "Oxidation of carbon between 1000-2000 °C" *Proceeding of the Fifth Conference on Carbon*, Pergamon Press, London, pp. 154-164

Nakanishi, K. Kadota, T. and Hiroyasu, H. (1981) "Effect of air velocity and temperature on the soot formation by combustion of a fuel droplet" *Combustion and Flame*, Vol. 40, pp. 247-262

Neoh, K.G. Howard, J.B. and Sarofim, A.F. (1981) "Soot oxidation in flames" *Particulate carbon: formation during combustion*, (ed. Siegla, D. C. and Smith, G. W.), Plenum Press, New York, pp. 261-277

Neoh, K.G. Howard, J.B. and Sarofim, A.F. (1984) "Effect of oxidation on the physical structure of soot" *20th Symposium (International) on Combustion*, pp. 951-957

Nishida, O. and Mukohara, S. (1982) "Characteristics of soot formation and decomposition in turbulent diffusion flames" *Combustion and Flame*, Vol. 47, pp. 269-279

Norgren, C.T. (1971) "Determination of primary-zone smoke concentrations from spectral radiance measurements in gas turbine combustors" NASA TN D-6410

Norgren, Carl T. and Ingebo, Robert D. (1976) "Spectral radiance measurements and calculated soot concentrations along the length of an experimental combustor" NASA TM X-3394

Norster, E.R. and Lefebvre, A.H. (1972) "Effects of fuel injection method on gas turbine combustor emission" *Emissions from Continuous Combustion Systems*, ed. by Walter Cornelins and William G. Agrew, Plenum Press, London, pp. 255-278

Noyce, J.R. Sheppard, C.G.W. and Yamba, F.D. (1981) "Measurements of mixing and species concentrations within a gas turbine type combustor" *Combustion Science and Technology*, Vol. 25, pp. 209-217

Onuma, Y. and Ogasawara, M. (1975) "Studies on the structure of a spray combustion flame" *15th Symposium (International) on Combustion*, pp. 453-465

Onuma, Y. Ogasawara, M. and Inoue, T. (1977) "Further experiments on the structure of a spray combustion flame" *16th Symposium (International) on Combustion*, pp. 561-567

Pagni, P.J. and Okoh, C.I. (1984) "Soot generation within radiation diffusion flames" *Twentieth Symposium (International) on Combustion*, pp. 1045-1054

Palmer, H.B and Cullis, C.F. (1965) "The formation of carbon from gases" *Chemistry and Physics of Carbon*, (ed. Walker, P.L.), Vol. 1, pp. 265-325, Marcel Dekker, New York

Perrin, J. (1992) "Computational study of a tubular combustor" M.Sc Thesis, Cranfield Institute of Technology

Peters, N. (1984) "Laminar diffusion flamelet models in non-premixed turbulent combustion" *Progress in Energy and Combustion Science*, Vol. 10, pp. 319-339

Peters, and Haumond (1991) in *Design of modern turbine combustors*, (ed.) Mellor, A.M., Academic Press, London

Planck, M. (1959) The theory of heat radiation, Dover Publications, New York

Prado, G.P. Lee, M.L. Hites, R.A. Hoult, D.P. and Howard, J.B. (1977) "Soot and hydrocarbon formation in a turbulent diffusion flame", *16th Symposium (International) on Combustion*, pp. 649-661

Presser, C. Gupta, A.K. and Semerjian, H.G. (1993) "Aerodynamic characteristics of swirling spray flames: pressure-jet atomizer" *Combustion and Flame*, Vol. 92, pp. 25-44

Roffe, G. and Venkataramani, K.S. (1978) "Emissions measurements for a lean premixed propane/air system at pressures up to 30 atmospheres", NASA CR-159421

Roth, P. Brandt, O. and von Gersum, S. (1990) "High temperature oxidation of suspended soot paticles verified by CO and CO_2 measurements" *23rd Symposium (International) on Combustion*, pp. 1485-1492

Saito, K. Gordon, A.S. and Stickle, W.F. (1991) "A study of the early history of soot formation in various hydrocarbon diffusion flames" *Combustion Science and Technology*, Vol. 80, pp. 103-119

Schmidt, H. (1909) Ann Physik, 29, p. 971

Schoenung, S.M. and Hanson, R.K. (1981) "CO and temperature measurements in a flat flame by laser absorption spectroscopy and probe techniques" *Combustion Science and Technology*, Vol. 24, pp. 227-237

Sivathanu, Y.R. and Gore, J.P. (1991) "Simultaneous multiline emission absorption measurements in optically thick turbulent flames" *Combustion Science and Technology*, Vol. 80, pp. 1-21

Sivathanu, Y.R. Gore, J.P. and Dolinar, J. (1991) "Transient scalar properties of Strongly Radiating jet flames" *Combustion Science and Technology*, Vol.76, pp. 45-66

Souil, J.M. Vantelon, J.P. Joulain, P. and Grosshandler, W.L. (1986) "Experimental and theoretical study of thermal radiation from freely burning kerosene pool fires" Progress in Astr. & Aero., Vol. 105, (ed.) Bowen, J.R. Leyer, J.-C. and Soloukhin, R.I.

Spalding, D.B. (1963) "Convective mass transfer" Edward Arnold (Publishers) Ltd.

Srivatsa, S.K. (1982) "Computations of soot and NOx emissions from gas turbine combustor: final report" NASA CR-167930

Stewart, C.D. Syed, K.J. and Moss, J.B. (1991) "Modelling soot formation in non-premixed kerosine-air flames" *Combustion Science and Technology*, Vol.75, pp. 211-226

Syed, Khawar J. (1991) "Soot and radiation modelling in buoyant fires" Ph.D thesis, Cranfield Institute of Technology

Syed, K.J. Stewart, C.D. and Moss, J.B. (1990) "Modelling soot formation and thermal radiation in buoyant turbulent flames" *23rd Symposium (International) on Combustion*, pp. 1533-1541

Tesner, P.A. Snegirova, T.D. and Knorre, V.G. (1971) "Kinetics of dispersed carbon formation" *Combustion and Flame*, Vol. 17, pp. 253-260

Tesner, P.A. (1979) "Soot formation during combustion" *Combustion, explosion and shockwaves*, Vol. 15, pp. 111-120

Tilston, J.R. (1992) Unpublished data

Vandsburger, U. Kennedy, I. and Glassman, I. (1984) "Sooting counter flow diffusion flames with varying oxygen index" *Combustion Science and Technology*, Vol. 39, pp. 263-285

Viskanta, R. and Mengüc, M.P. (1987) "Radiative heat transfer in combustion systems" *Progress in Energy and Combustion Science*, Vol. 13, pp. 97-160

Vranos, Alexander (1974) "Turbulent mixing and NOx formation in gas turbine combustors" *Combustion and Flame*, Vol. 22, pp. 253-258

Warnatz, J. (1984) "Rate coeffcients in the C/H/O/system" *Combustion chemistry*, ed. Gardiner, Jr. W.C., Springer-Verlag, New York

Wear, Jerrold D. and Jones, Robert E. (1973) "Comparison of combustion characteristics of ASTM A-1, propane and natural-gas fuels in an annular turbojet combustor" NASA TN D-7135

Weiner, A.M. and Harris, S.J. (1989) "Optical detection of large soot precursors" *Combustion and Flame*, Vol. 77, pp. 261-266

Westbrook, Charles K. and Pitz, William J. (1991) "Numerical modeling of combustion of complex hydrocarbon" in Numerical approaches to combustion modeling, ed. Elaine S. Oran and Jay P. Boris, Vol 135, Progress in Astronautics and Aeronautics, AIAA

Williams, Alan (1990) "Combustion of liquid fuel sprays" Butterworths, London

Wood, C.P. and Samuelsen, G.S. (1984) "Optical measurements of soot size and number density in a spray atomized, swirl-stabilized combustor" ASME 84-GT-153

Young, K.J. (1993) "Soot formation in turbulent, vaporised kerosine - air jet flames at elevated pressure" Ph.D thesis, Cranfield Institute of Technology

Yuen, W.W. and Tien, C.L. (1977) "A simple calculation scheme for the luminous-flame emissivity" *16th Symposium (International) on Combustion*, pp. 1481-1488

Zheng, Q-P. Stewart, C.D. and Moss, J.B. (1993) "In-situ soot concentration measurements in a tubular gas turbine combustor" Proceeding of the Anglo-German Combustion

Symposium, Cambridge, pp. 511-514

Zhu, J.Y. Tsuruda, T. Sowa, W.A. and Samuelsen, G.S. (1993) "Coherent Anti-Stokes Raman Scattering (CARS) thermometry in a model gas turbine can combustor" *J. Eng. Gas Turbines and Power*, Transaction of the ASME, Vol. 115, pp. 515-521

Appendix A Refractive Index of Soot

Refractive index of particulate soot: $m=n-i\kappa$

Complex function of refractive index:

$$F(\lambda)=\frac{n\,\kappa}{(n^2-\kappa^2+2)^2+4\,n^2\,\kappa^2}$$

λ: Wavelength

λ (μm)	n	κ	F(λ)/λ	Fuel	Author(s)
.5145	1.268	.206	.03910	Kerosine	Batten (1985)[a]
	1.892	.523	.05997	[b]	Lee and Tien (1981)[a]
	1.865	.502	.05523	[b]	Lee and Tien (1981)[a]
.5500	1.281	.219	.03857	Kerosine	Batten (1985)[a]
.6000	1.309	.229	.03630	Kerosine	Batten (1985)[a]
	1.850	.476	.04876	[b]	Lee and Tien (1981)[a]
.6328	1.327	.238	.03534	Kerosine	Batten (1985)[a]
	1.100	.370	.06364	"	"
	1.560	.520	.06421		Dalzell & Sarofim (1969)
	1.920	.450	.04130	Propane	Mullins & Williams (1987)
	1.838	.464	.04558	[b]	Lee and Tien (1981)[a]
.6500	1.336	.243	.03492	Kerosine	Batten (1985)[a]
	1.830	.460	.04431	[b]	Lee and Tien (1981)[a]
.7000	1.368	.254	.03315	Kerosine	Batten (1985)[a]
	1.828	.460	.04122	[b]	Lee and Tien (1981)[a]
.7500	1.826	.460	.03853	[b]	Lee and Tien (1981)[a]
.8000	1.824	.469	.03686	[b]	Lee and Tien (1981)[a]
.8500	1.820	.476	.03531	[b]	Lee and Tien (1981)[a]

[a] Extrapolated from published data

[b] Polystyrene & plexiglas

Appendix B Discrete Fourier Transform of Absorption Signal

The line-of-sight transmitted laser intensity is a function of the instantaneous soot concentration. The deviation of the intensity signal depends on the fluctuations of soot particle size and number density. The frequency of the fluctuation can be resolved by Discrete Fourier Transform (DFT) of the absorption signal.

A series of absorption intensity data in the combustor were recorded by microcomputer using OASIS software at the maximum data acquisition speed of 51.2 kHz up to a maximum number of points N=512 for each run. The two data series in Figure 3.30 shows one set exhibiting a distinct low frequency and the other a high frequency spectra. Analysis of the measured signal s(t) by discrete Fourier integral expansions gives

$$S(f_k) = \sum_{t=0}^{T} s(t)\, e^{-j2\pi f_k t} \qquad \text{(B-1)}$$

where t=nT/N is the recording time sequence, T is the total recording time, T=10 ms (512/51,200), n is the sequential number of each point in the data set. f_k is the kth discrete frequency, f_k=k/T, k=1,2,3,...,N. Following Euler's relation

$$e^{-j\theta} = \cos\theta - j\sin\theta, \qquad j = \sqrt{-1} \qquad \text{(B-2)}$$

Eq. B-1 can then be expressed as

$$S(f_k) = a_k - jb_k, \qquad k=1,2,3,\ldots,N \qquad \text{(B-3)}$$

where

$$a_k = \sum_{n=1}^{N} s(n)\cos(2\pi nk/N)$$

$$b_k = \sum_{n=1}^{N} s(n)\sin(2\pi nk/N)$$

with its complex conjugate $S^*(f_k)$

$$S^*(f_k) = a_k + jb_k, \qquad k=1,2,3,\ldots,N \qquad \text{(B-4)}$$

The single sided power spectrum density (PSD) of the Fourier series s(t) is defined by

$$PSD(f_k) = \frac{2}{T} S(f_k) \cdot S^*(f_k)$$

$$= \frac{2}{T}(a_k^2 + b_k^2), \qquad k=1,2,3,\ldots,N/2 \qquad \text{(B-5)}$$

To obtain quantitative comparisons directly from the measured signal of each flow condition, the power spectrum is normalised to eliminate any ambiguity arising from the difference of absolute signal level. The normalised power spectra density NPSD(f_k) is

$$NPSD(f_k)=\frac{PSD(f_k)}{\frac{N}{2T}[s'(t)]^2} \qquad \text{(B-6)}$$

where $[s'(t)]^2$ is the square of turbulent intensity of s(t)

$$s(t)^2=\sum_{k=1}^{N/2}[PSD(f_k)\Delta f_k] \qquad \text{(B-7)}$$

the normalised power spectrum density

$$NPSD(f_k)=\frac{2T}{N}\frac{a_k^2+b_k^2}{\sum_{i=1}^{N/2}[(a_i^2+b_i^2)\Delta f_i]}\ , \quad k=1,2,3,\ldots,N/2 \qquad \text{(B-8)}$$

The absorption signal can then be processed to derive the normalised power spectrum against the fluctuation frequency f_k. Although the highest frequency of data acquisition is 51.2 kHz, the symmetric sine and cosine function of the Fourier series will generate a pair of frequency ranges, ie. 0~25.6 kHz and 25.6~51.2 kHz with identical spectra. Only one pair is necessary for analysis, therefore the effective frequency range of the single sided normalised power spectrum density of the present measurement is taken as 0~25.6 kHz. About ten data sets are averaged to present a smooth curve for each flow condition.

Appendix C Thermocouple Radiation Compensation for Temperature Measurement

Exit plane temperature measurement

A K-type thermocouple has been used which has a stainless steel shield of diameter d_1=4.76 mm, with shield emissivity 0.6. The combustor exit diameter is D_e=113.0 mm. Since the thermocouple bead is close to the tip plane of its shield, assuming the temperatures of the bead and the tip are same, then for gas flowing over a plane plate of diameter d_1 (Figure C.1), the heat transfer balance for the thermocouple tip is

$$Q_{Conv.\ gas-t.c} = Q_{Radi.\ t.c.-wall} \tag{C-1}$$

the convection between gas and thermocouple is

$$Q_{Conv.\ gas-t.c.} = \frac{Nu \cdot k}{d_1}(T_{gas} - T_{t.c.}) \tag{C-2}$$

As the Re number is typically less than 10^5, in the laminar boundary layer near the plate (Holman (1990)),

$$Nu = 0.664 \cdot Pr^{1/3} \cdot Re^{1/2}$$

the radiation from thermocouple to wall is

$$Q_{radi.\ tc-wall} = \varepsilon \cdot \sigma\ (T_{t.c.}^4 - T_{wall}^4) \tag{C-3}$$

At the exit, the duct wall temperature is taken from measured values (cf. Table C-I and Figure 4.14 (b)).

T_{gas} is readily obtained from Eqs. (C-2) and (C-3).

Dilution zone temperature measurement

An R-type thermocouple has been used which has a platinum shield of diameter d_2=1 mm, the shield emissivity depending on platinum temperature (Ang et al. (1988)). The combustor diameter at the dilution zone D_d=98.0 mm. It has been assumed that for the dilution zone the air mass flow rate from the upstream primary zone is 66% of the total air flow (cf. Figure 3.12) and this leads to an average velocity in the dilution zone about 44 m/s, close to that numerically predicted using PHOENICS (cf. Chapter 6).

T_{gas} in this situation can also be calculated from Eqs. (C-2) and (C-3).

Table C-I Temperature measurement compensation for the K-type thermocouple. Stainless steel shield diameter=4.76 mm, Combustor exit diameter=113 mm

P (bar)	m_a (kg/s)	AFR	$T_{t.c}$ (K)	$T_{exit\ wall}$ (K)	T_{gas} (K)	ΔT (K)
1	0.12	45	1180	723	1273	93
1	0.12	28	1370	813	1527	157
1	0.12	22	1480	903	1681	201
4	0.46	45	1289	928	1346	57
4	0.46	30	1490	1050	1593	103
4	0.46 (T_{in}=131℃)	30	1470	890	1583	113

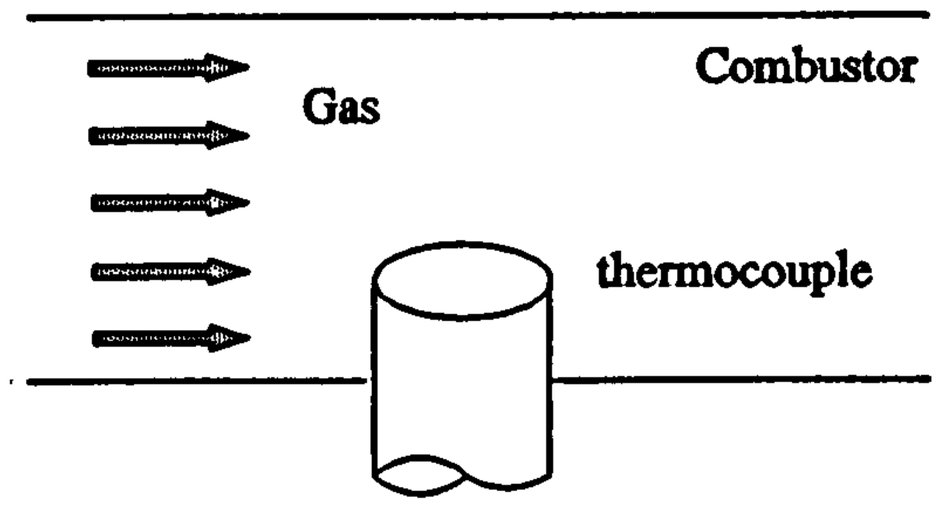

Fig. C-1 Thermocouple heat transfer model

Appendix D: Optical Temperature Measurement in a Sooty Laminar Diffusion Flame

Optical temperature measurements in sooty flames have the advantages over conventional thermocouple due to its non-intrusive nature. Techniques like Schimit and two-colour temperature measurements are in principle based on the flame luminousity and thus are directly related to the flame thermal radiation. The experiment in this section is aimed at assessing the techniques on a sooting flame of small dimension and then develop such techniques for the thermal radiation measurement in a tubular combustor where optical temperature is also inferred (cf. Chapter 5).

BURNER AND INSTRUMENTATIONS

The optical temperature measurement was carried out on a 3 slot Wolfhard-Parker burner. The burner incorporated an inner fuel slot of width 6 mm and two outer air slots each of width 9 mm; the slots were 48 mm long (Figure D.1), the mass flow rates of fuel (ethylene) and slot air were 5.95×10^{-6} kg/s and 8.867×10^{-5} kg/s (or exit velocity 1.8 cm/s and 8.7 cm/s) respectively. The nominal port velocities are deduced from fuel and air flow rates at room temperature. This condition was close to that of Kent and Wagner (1982) and Moss et al. (1987, 1988).

Red He-Ne laser light at 632.8 μm (the same laser tube used in the combustor soot volume fraction and thermal radiation measurements) was used for optical alignment and laser extinction measurement of soot volume fraction, the technique was based on the Beer-Lambert law similar to that detailed in chapter 3. A tungsten strip lamp (GEC make, Model No. 710C, vacuum) served as a calibration light source, its own blackbody temperature was calibrated by National Physical Laboratory. Two pinholes, of 1 mm aperture diameter, were positioned between the burner and detector to define the spatial resolution. The aperture diameter chosen here was a compromise between small target size, or better spatial resolution because of the small dimension of the flat flame, and high signal to noise ratio. The present optical set up gave a biggest spot size of about 1.5 mm in the burner.

The radiation intensity from the flame was focused by an optical lens onto the entrance slit of the spectrometer. Both the signal detecting system, including the spectrometer, PhotoMultiplier tube and a microcomputer, and the subsequent data acquisition process were

identical to that employed for the combustor radiation flux measurement (cf. Section 5.2). The calibration curves for the PM tube against absolute radiation flux is shown in D.2. Here the optical temperatures inferred based on radiation measurement are of primary interest.

RESULTS AND DISCUSSION

The raw data from the flame radiation at heights 8 and 12 mm are shown in Figure D.3 (a) and (b). At the given flow condition, continued soot formation occurs between 8 and 12 mm, similar to the findings by Kent and Wagner (1982) and Moss et al. (1987, 1988). The spectral signal here is expected to be higher at 12 mm. The voltages are very low at the centre of the flame where both soot concentration and temperature are comparatively low, at 8 mm the emission signal is near to the ground level of the PMT output. These voltages can be turned into radiation intensity (Figure D.4) based on the calibration in Figure D.2. The plots of radiation against wavelength in Figure D.5 show smooth curves at each spatial position. As the maximum temperature in the ethylene-air flame (<2180) is much lower than the equilibrium value (about 2395 K) the peak intensity should be located in the infrared spectrum $\lambda > 1200$ nm from Wien's displacement law (cf. Eq. 5-3) and the intensity in the visible wavelength should increase monotonously as the measured curves indicate in Figure D.5.

With the combination of soot volume fraction and thermal radiation intensity the Schmidt temperature at 632.8 nm wavelength has been inferred from Eq. 5-8 (Figure D.6). The inferred temperatures close to the centre line ($x=0$) are unreasonably high. In this flat non-premixed flame the mixture fraction is richer than stoichiometric there, and a typical temperature is 1400 K (Moss et al. (1987, 1988)). The problems encountered in the radiation measurement are mostly affected by instrument hardware limitations since the radiation signals in this regime are particularly low. The reasons for this will be further detailed later. Temperatures in the outer region, although expected to increase, soar rapidly to about 2300 K. The laminar flamelet state relationships constructed from experimental data revealed that the maximum thermocouple temperature was lower than 2180 K in Wolfhard-Parker burner at similar flow conditions (Moss et al. (1988)).

The Kurlbaum brightness temperature method was found to have a limit range of temperature measurement when soot absorption (determined from separate laser extinction measurement) dropped below 10 percent (Kent and Wagner (1983)). The Kurlbaum temperature measurement procedure is somewhat different to that adopted here, nevertheless the methods themselves are fundamentally similar. Applying the same limited range directly to the present experiment at $Y=8$ and 12 mm in Figure D.7, it is shown that the optically measured

temperatures in the absorption > 10% are relatively realistic with respect to the profile shape.

Comparisons of temperatures calculated from spectral emission at various wavelengths are shown in Figure D.7 (a) and (b) for heights 8 and 12 mm respectively. In principle the results should be identical at different wavelengths, the discrepancies arise from uncertainties in experimental procedure and the prescription of the soot refractive index. Two colour temperature inferred from the same radiation data differ from the single wavelength Schmidt temperature (Figure D.7 (c) and (d)). In the sooty part of the flame, the two colour temperature is lower than the Schmidt one and the absolute value is more reasonable. The two-colour technique employs the ratio of two radiation intensities and any uncertainties related to particular measurements might be compensated in the temperature evaluation. The values at 12 mm are not sensitive to the selection of the wavelength pair. Flower (1989) demonstrated that the two colour temperature often differed significantly from the brightness temperature, by up to 150 K, but displayed the same trends with flame conditions and measurement position as the brightness temperature.

The results in the centre part of the flame suffer from low radiation intensity, this low signal is partly limited by the small aperture which is used to define a fine spatial resolution given the small flame size. When radiation intensity is too low that the signal level approaches the detector ground status, output from PM tube does not have a linear relationship with the incident radiation intensity, and Eq. 5-7 can not be applied. The calibration illustrated in Figure D.8 shows the non-linear region of this particular PM tube. When the signal fall off 1 mV, the residual electrons in the PM tube will gave higher output than a linear line should provide, and the dashed curve depart from the solid linear line. When Eq. 5-7 is applied for a PM tube voltages in the experiment, higher than real radiation intensity is estimated for the non-linear region from the linear calibration which is only valid for regions with high voltage signal. A higher radiation intensity, and then high optical temperature is thereafter obtained. Given the present flame configuration, one possible solution to the above difficult is to use a PM tube of higher responsivity, another is to enlarge the aperture size. The latter is more practical but not achievable for the flat flame, however it pin-point the way of improve the experimental technique for the thermal radiation measurements in the tubular combustor. The pin hole size used for the combustor measurement is enlarged to 6.5 mm and satisfactory temperature results have been obtained (cf. Chapter 5).

CONCLUSIONS

Optical temperatures based on radiation measurements have been determined in a sooty

laminar flame and show qualitatively the same profile shape as thermocouple results. The accuracy of the absolute temperature values depend on the soot concentration level, and the optical temperature measurement is more adequate for optically thick flames, typically those of absorption level greater than 10%. Data quality can be improved by increasing the detector responsivity and optical aperture size. Experiments on a combustor using a larger aperture size provide satisfactory optical temperature results.

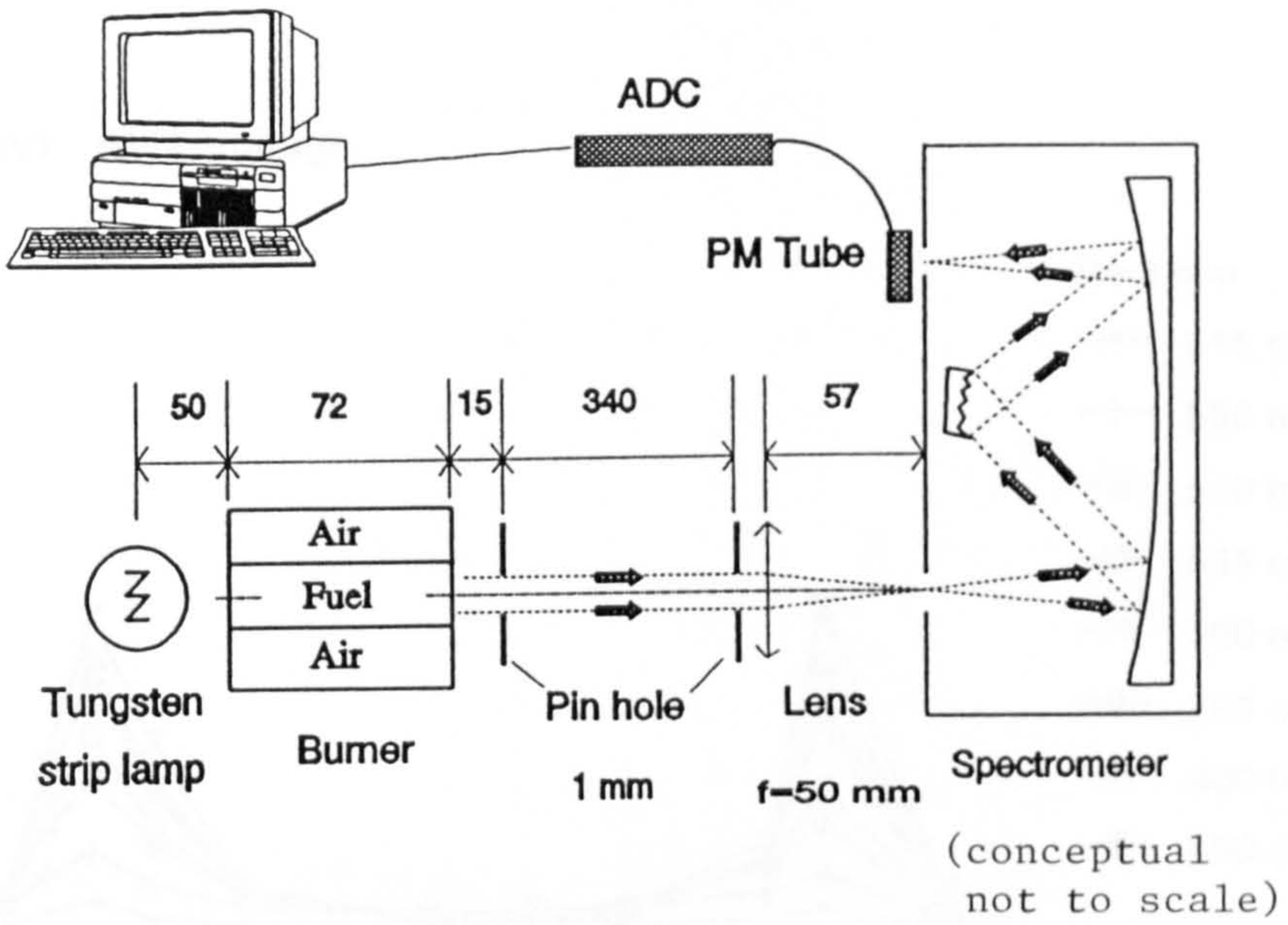

Figure D.1 Optical set-up for radiation measurement in laminar flat flame - Wolfhard-Parker burner. (calibration by lamp)

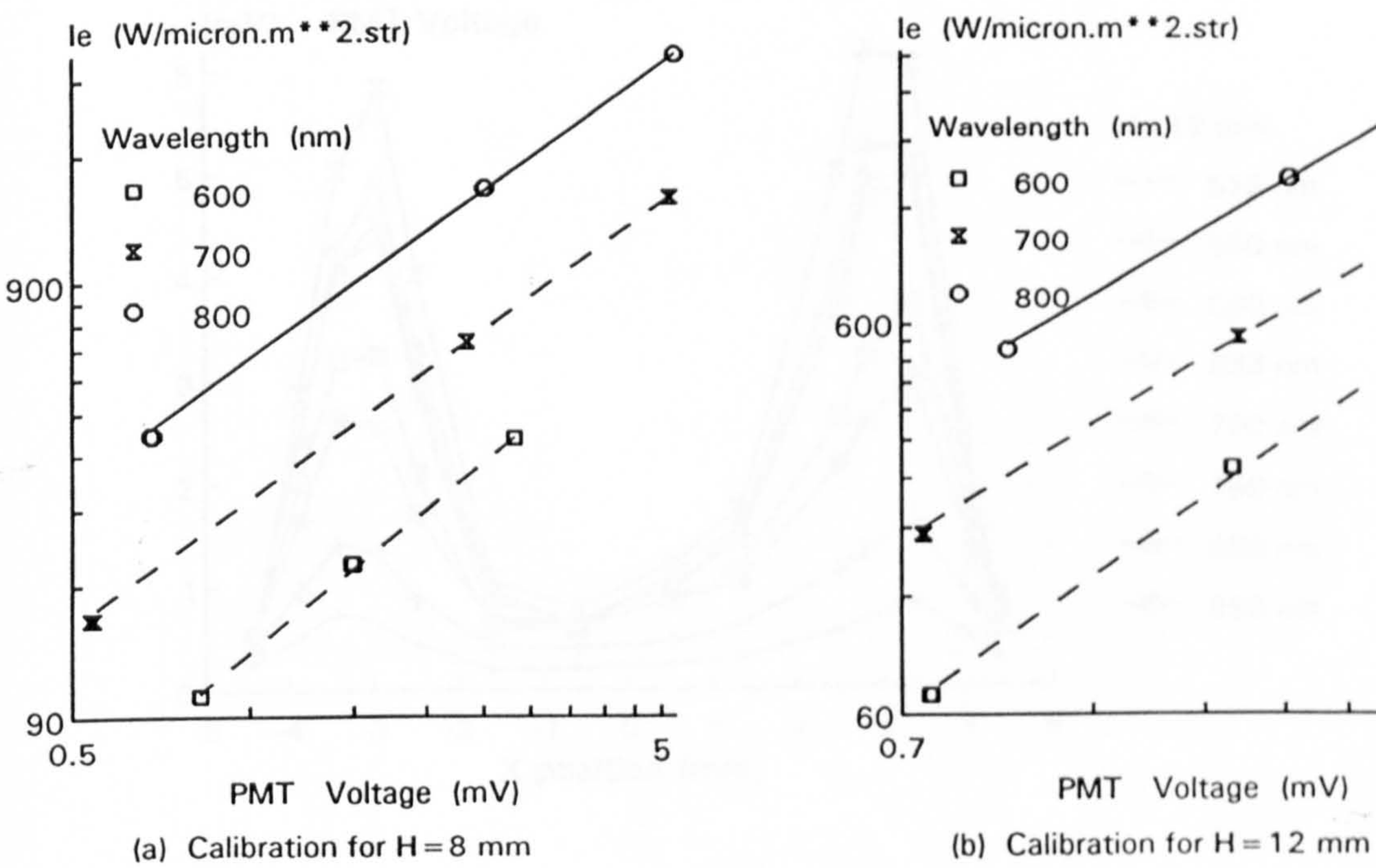

Figure D.2 Calibration curve of **P**hoto-**M**ultiplier **T**ube voltage output against lamp emission (a) Height H = 8 mm, (b) H = 12 mm

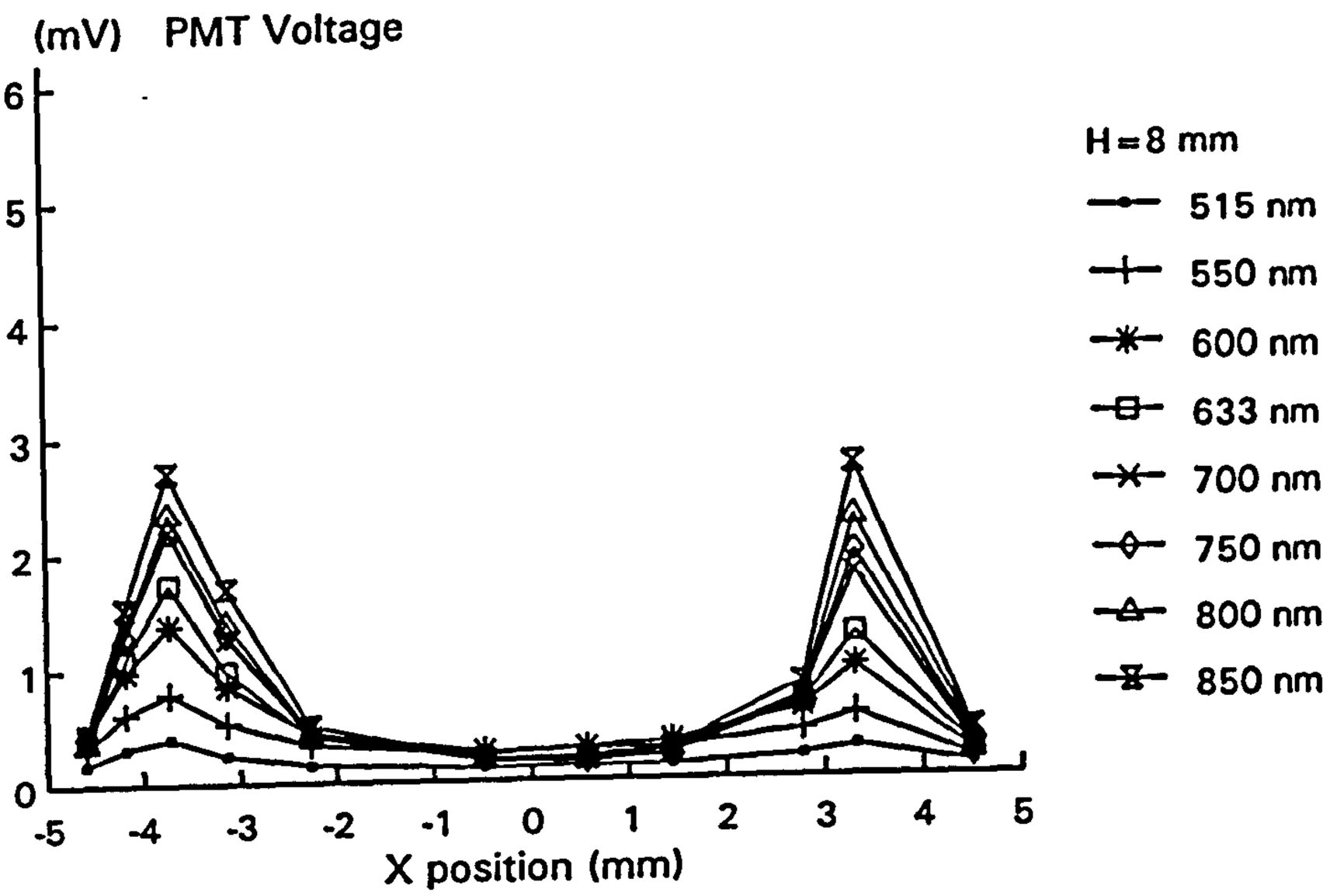

(a)

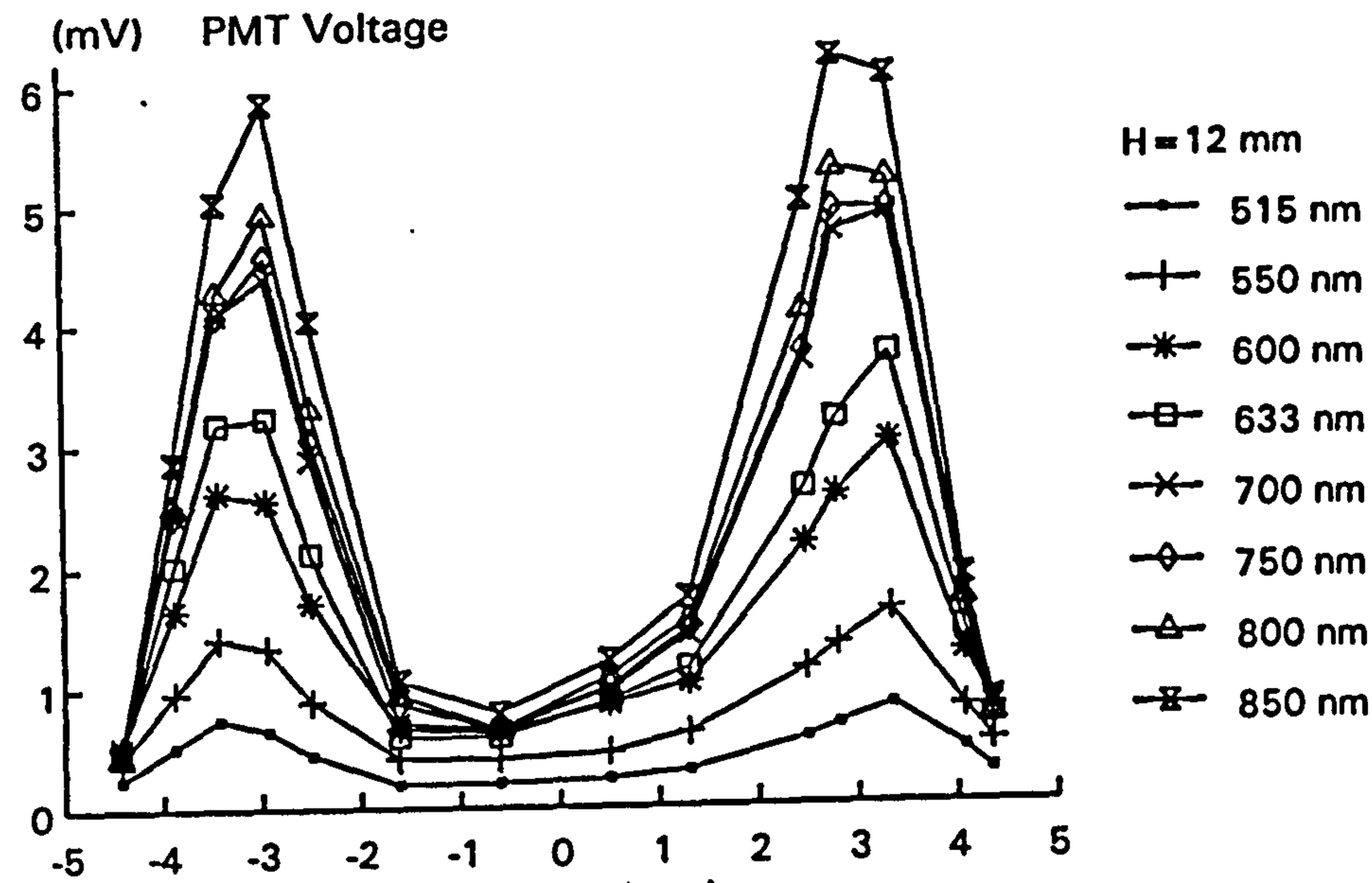

(b)

Figure D.3 Raw data profile (PMT voltage) of measured radiation for heights (a) 8 mm and (b) 12 mm

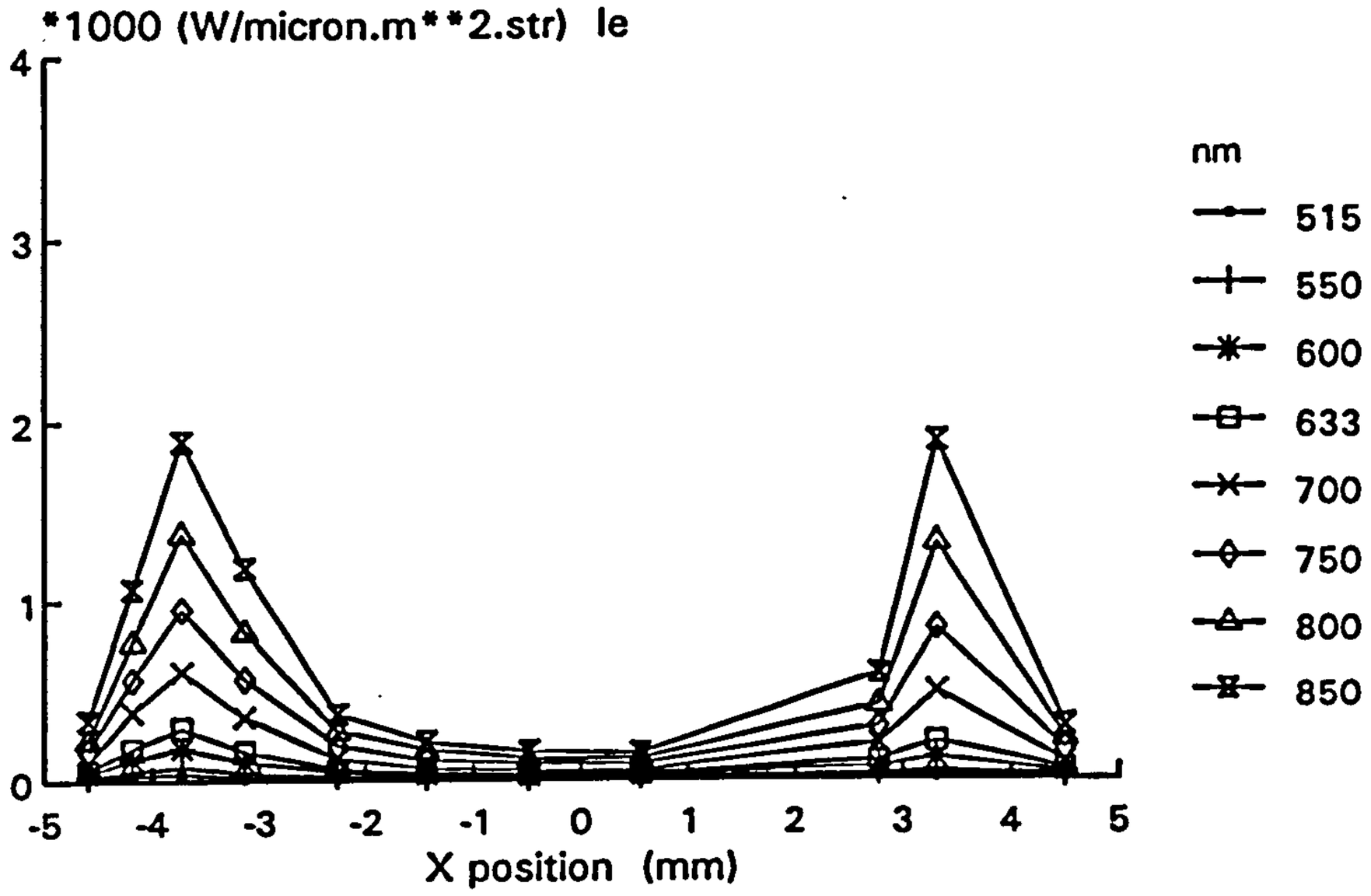

(a) H = 8 mm

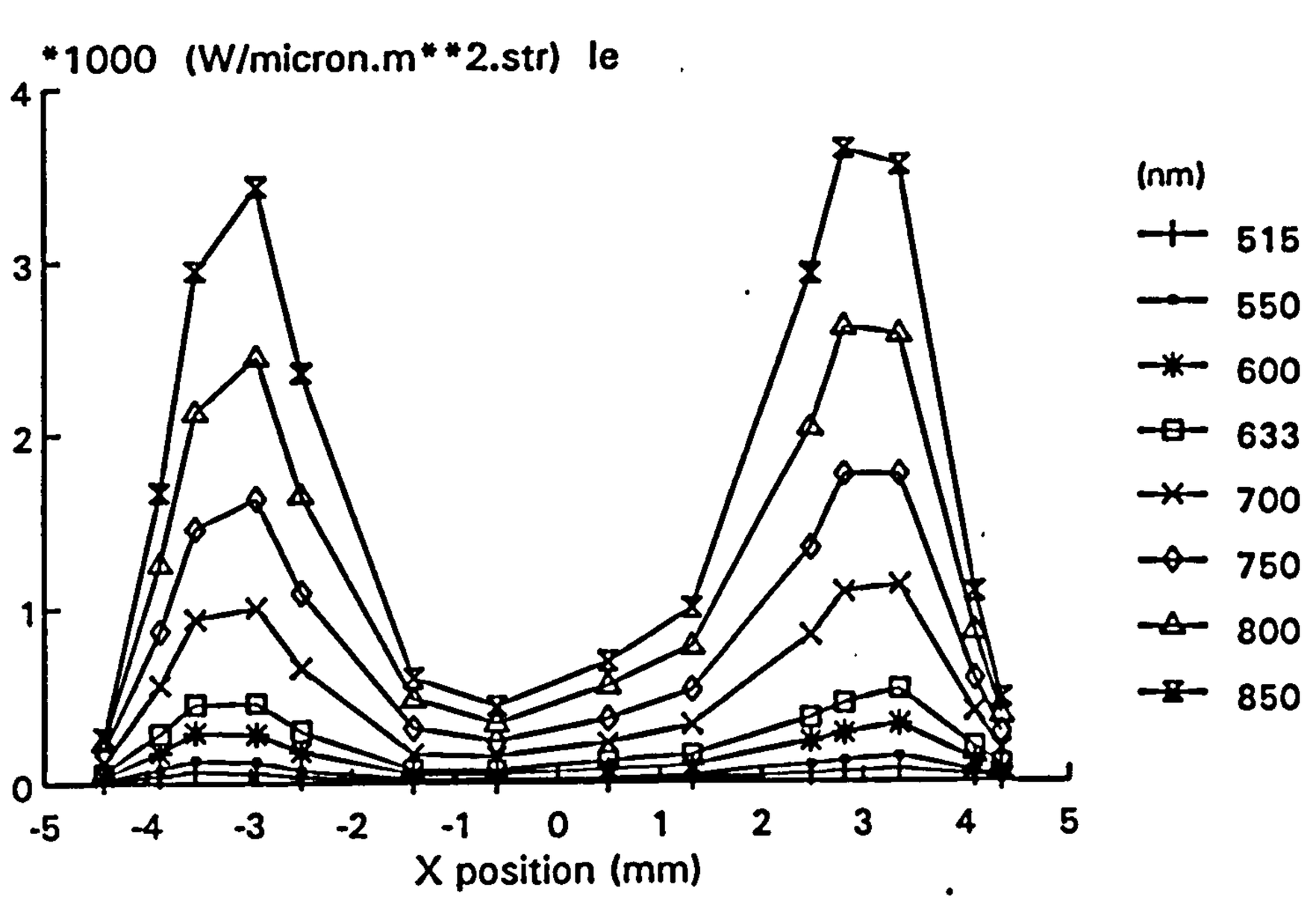

(b) H = 12 mm

Figure D.4 Radiation intensity profiles from wavelength 514.5 to 850 nm at heights (a) 8 mm (b) 12 mm

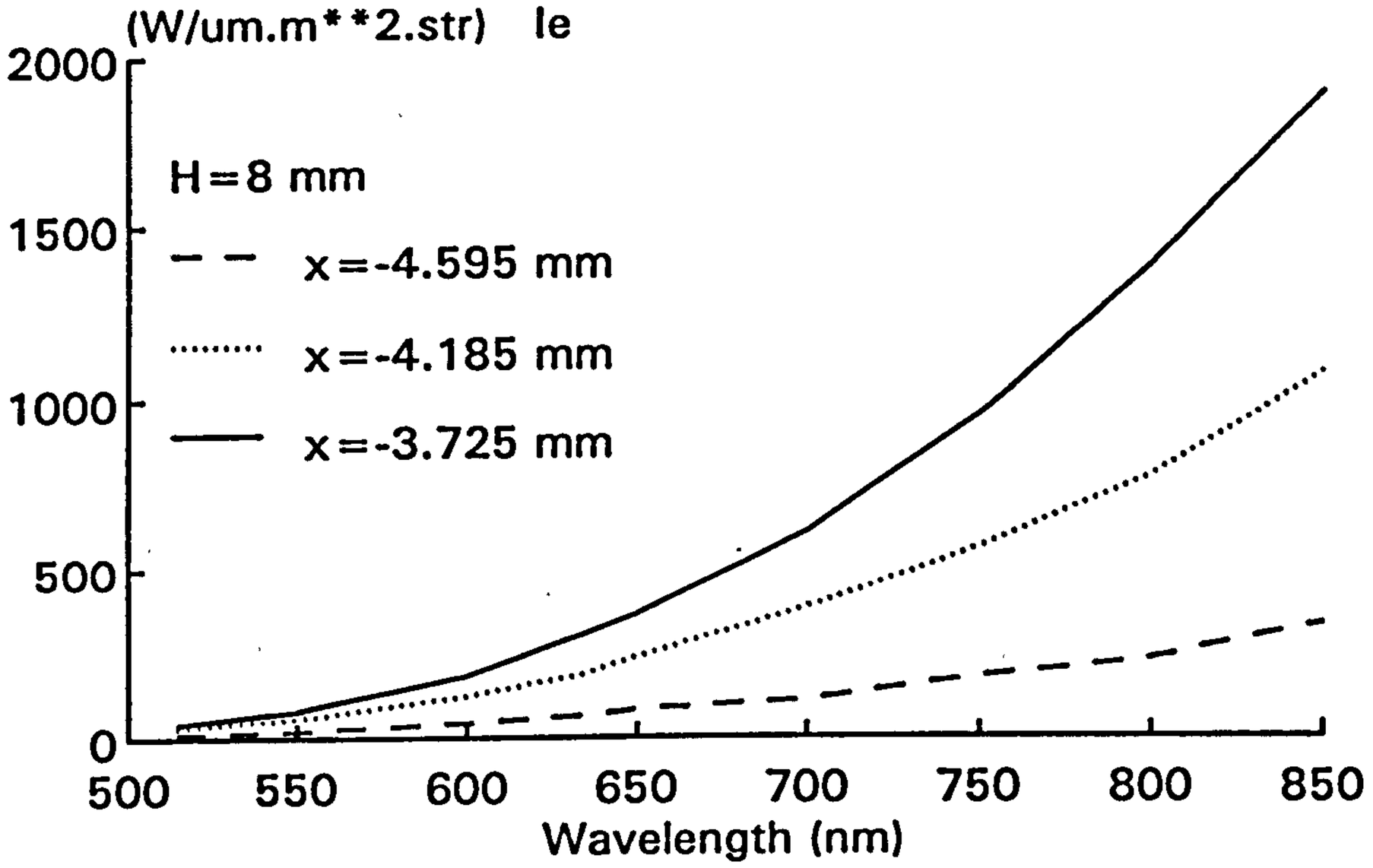

(a)

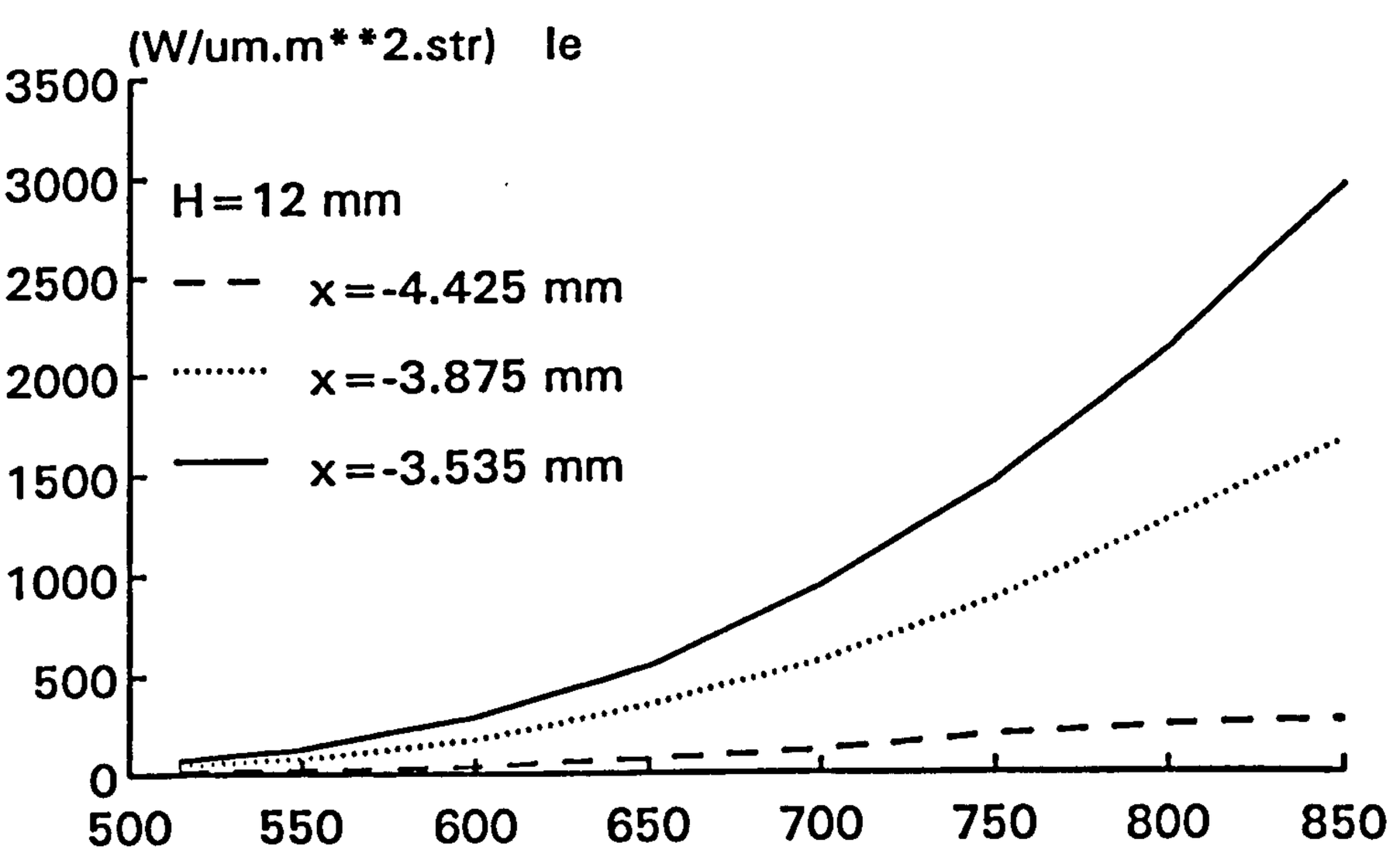

(b)

Figure D.5 Spectral radiation distributions at (a) 8 mm (b) 12 mm from various lateral positions

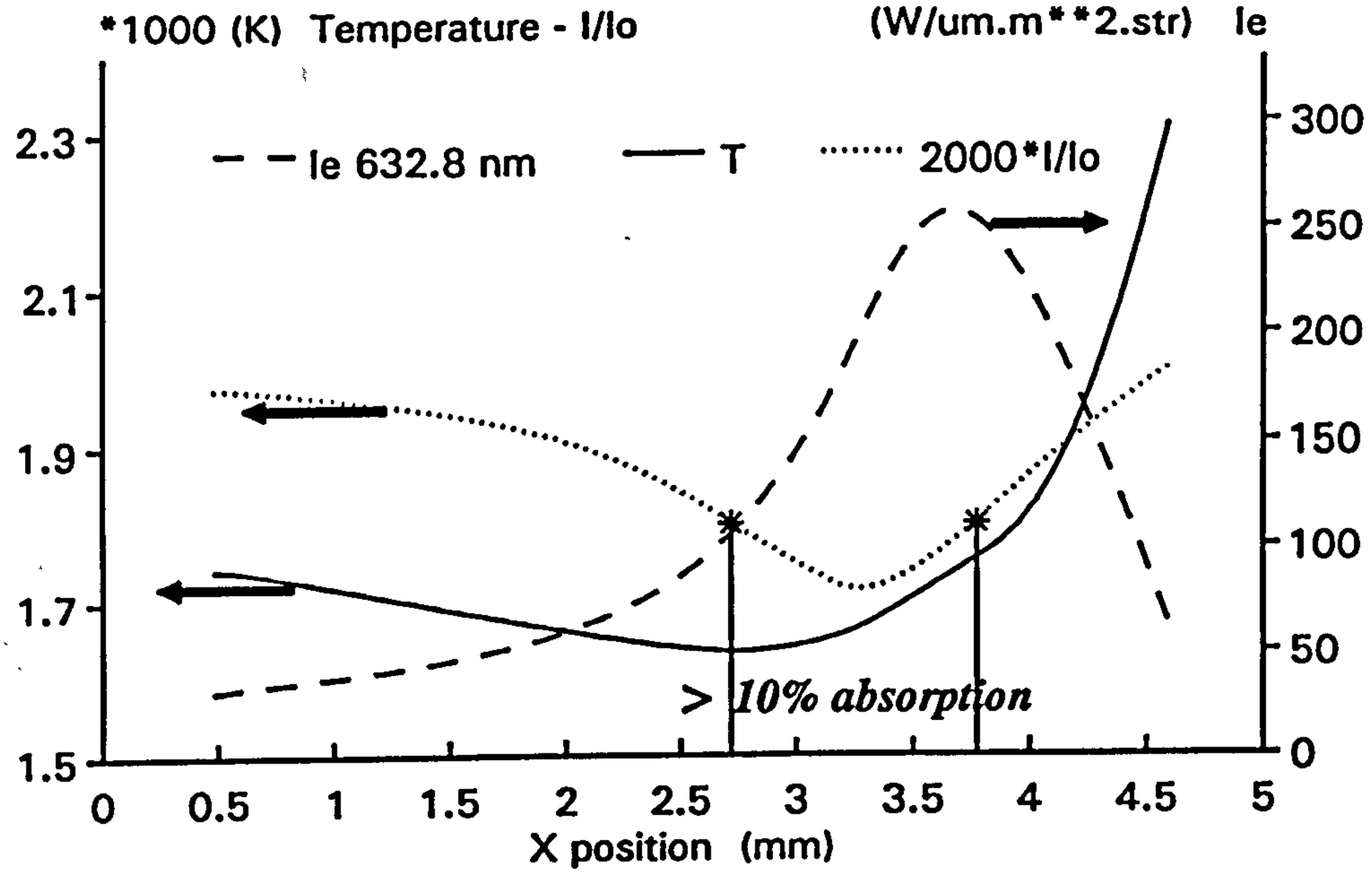

(a) H=8 mm

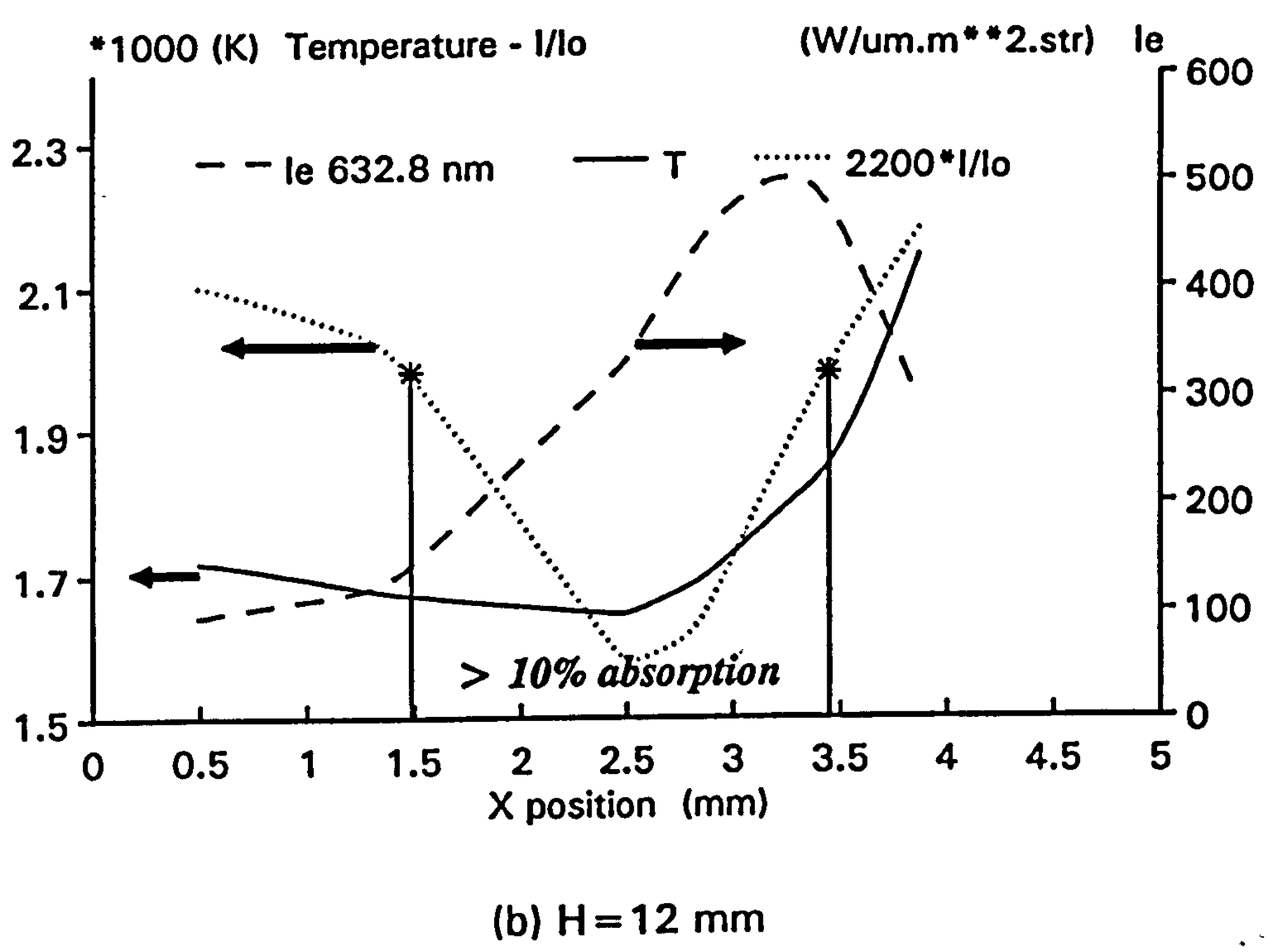

(b) H=12 mm

Figure D.6 Temperature inferred from measured soot volume fraction (illustrated as (I/I_o) for direct input as emissivity) and radiation at 632.8 nm. (a) H=8 mm, (b) H=12 mm

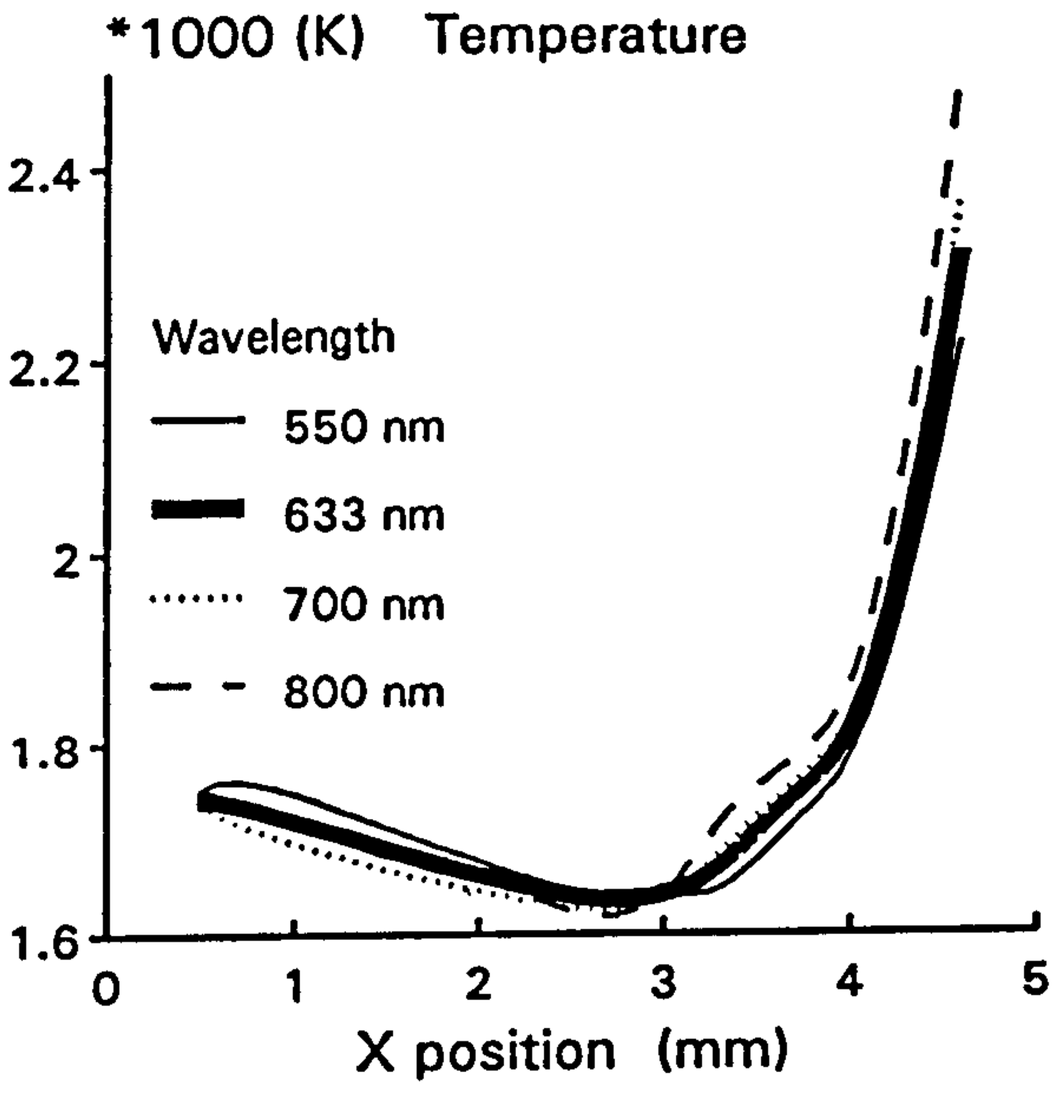

(a) H = 8 mm

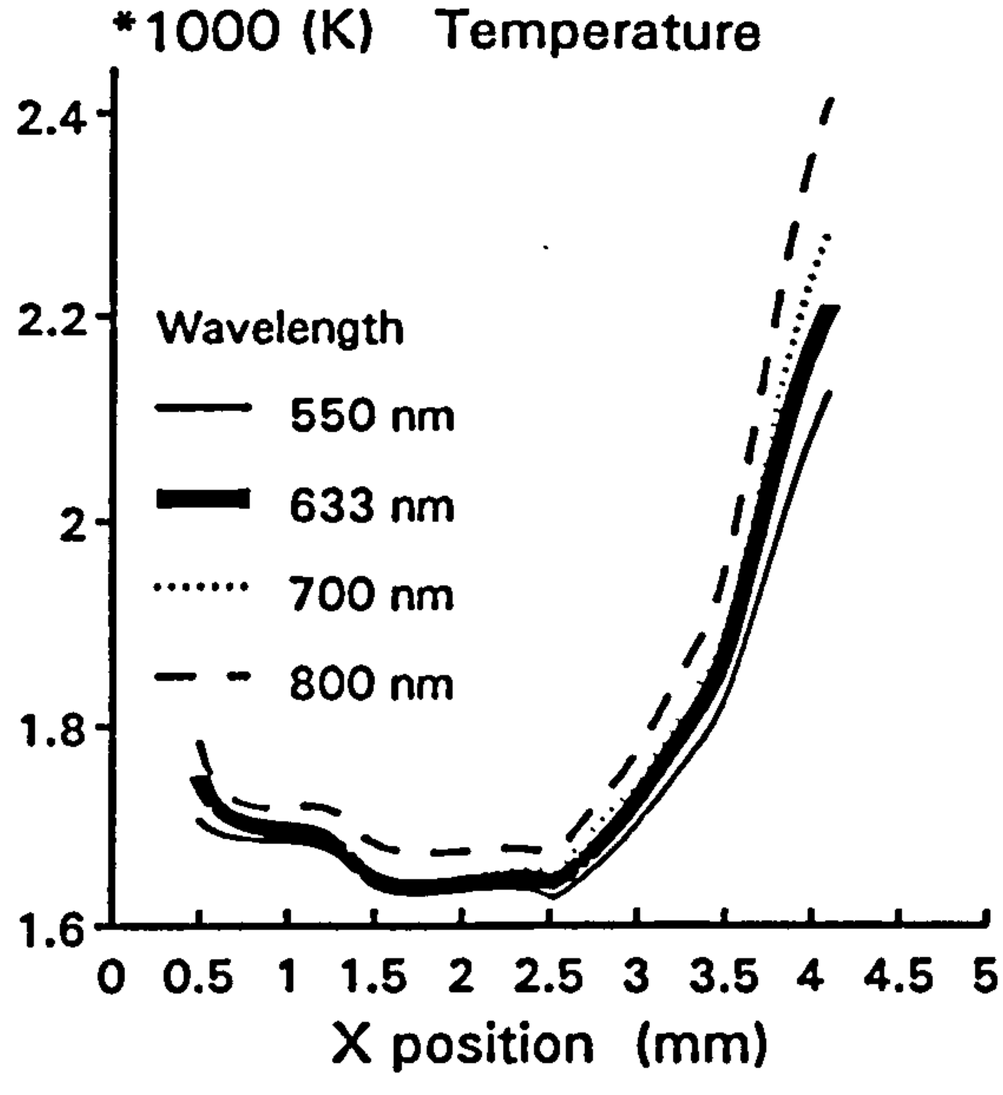

(b) H = 12 mm

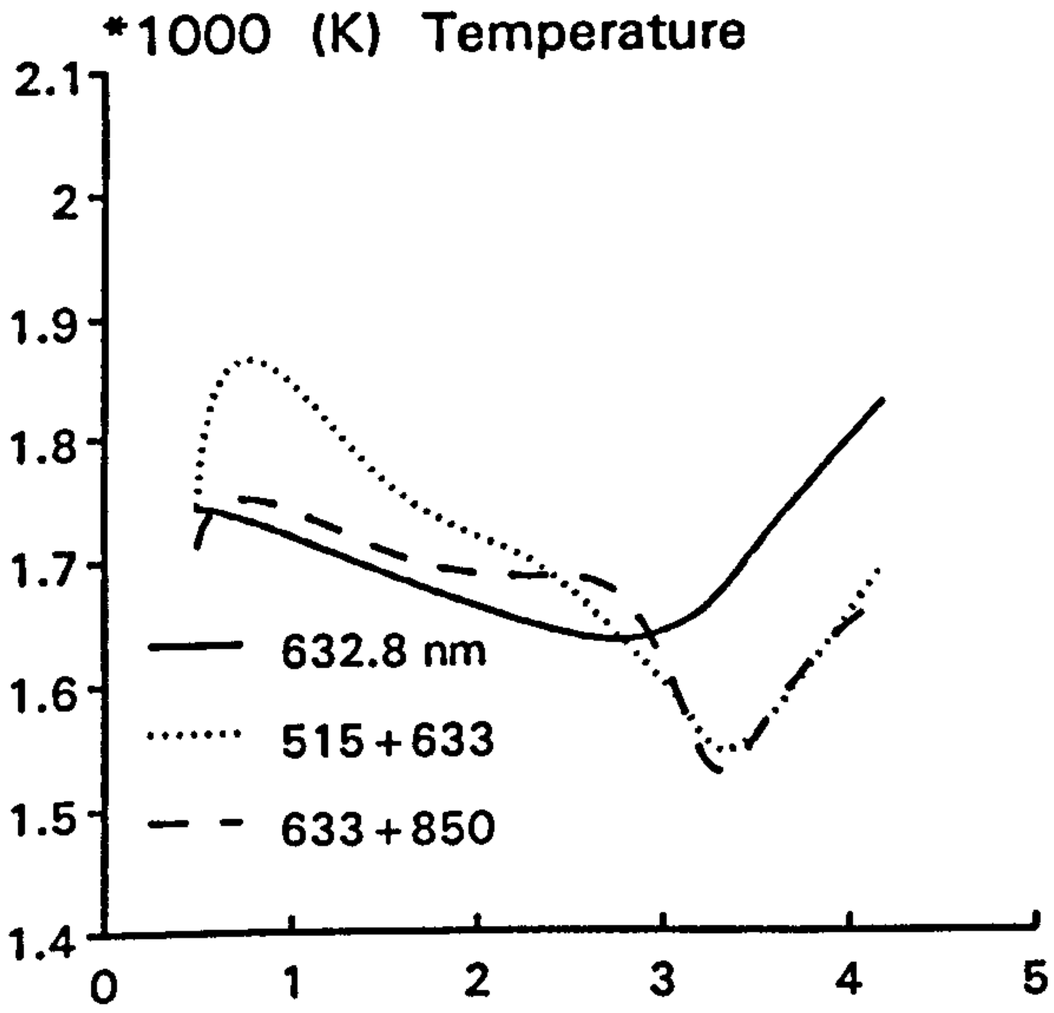

(c) H = 8 mm

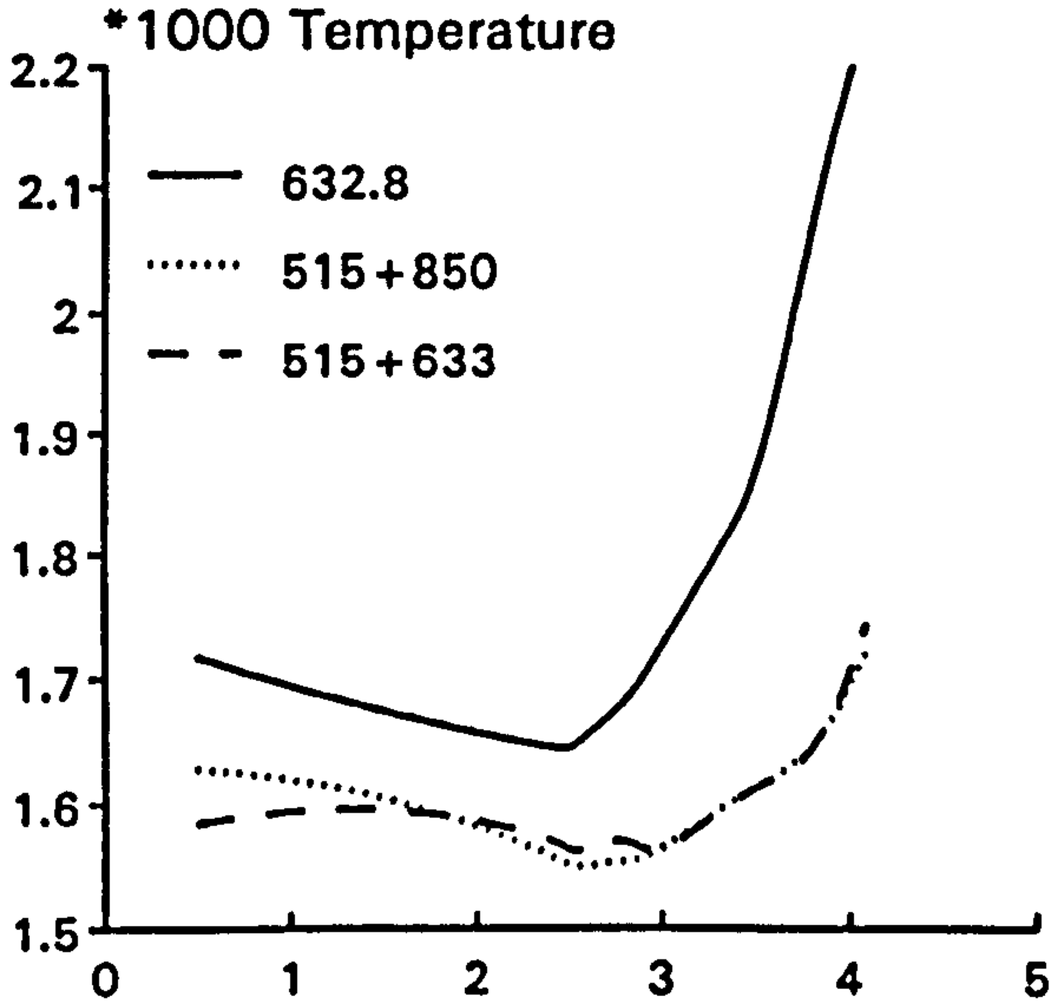

(d) H = 12 mm

Figure D.7 Temperatures inferred from radiation at various wavelengths (a), (b) and two-wavelengths (two-colour) (c), (d)

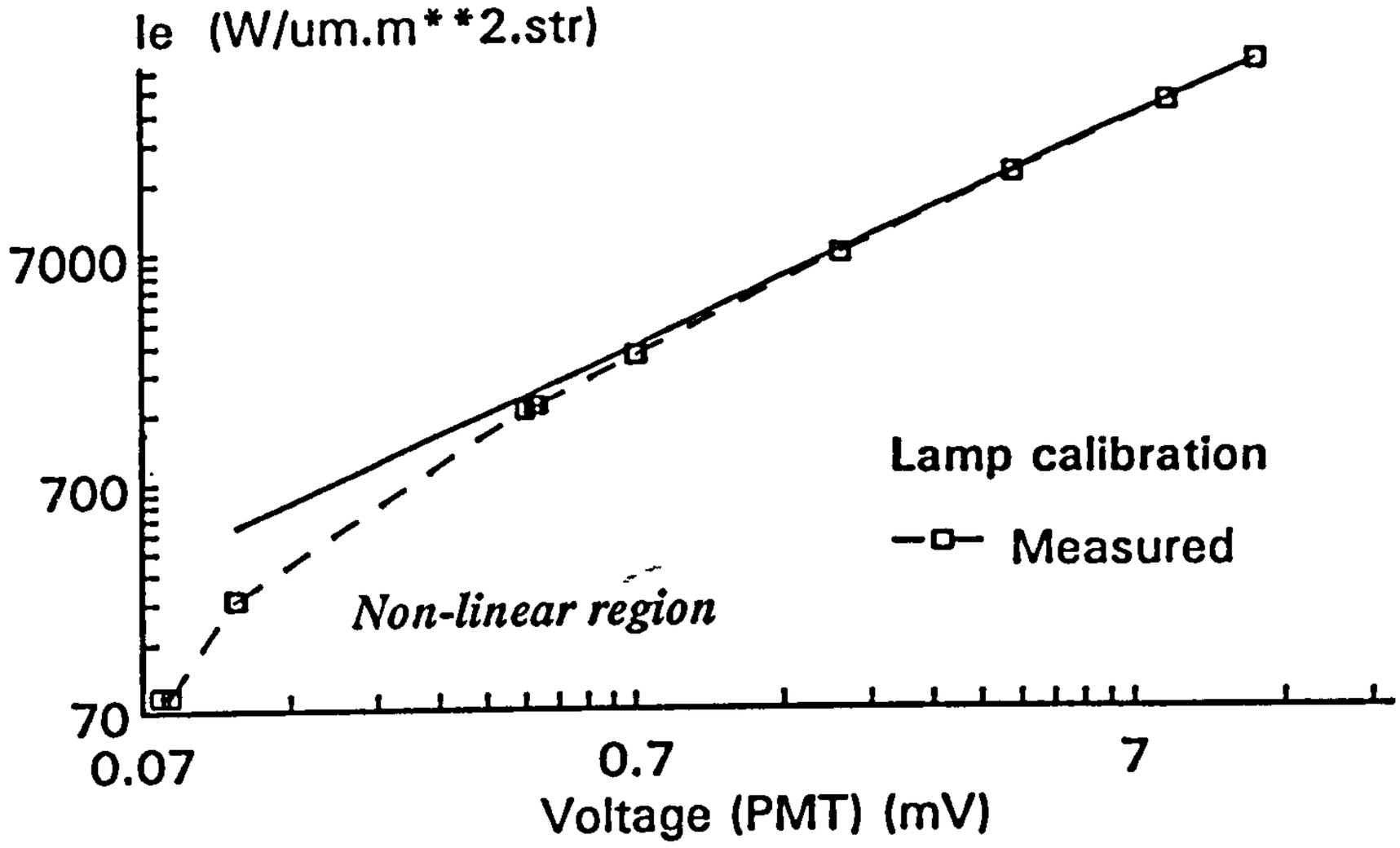

Figure D.8 PM tube calibration against lamp radiation, showing the non-linear relationship at low voltage

Appendix E Kerosine-Air Flame Prediction Using a 1-D Laminar Counter-flow Code

This section briefly outlines a preliminary investigation of laminar flamelet extensions to embrace kerosine-air burning. One of the advantages in applying the laminar flamelet approach to turbulent flame predictions is that the modelling of chemistry/turbulence interaction is simplified through the unique state relationships between the various scalar sets and the chemistry-independent conserved scalar, the mixture fraction. This relationship is vitally important in laminar flamelet-based soot modelling, where particle formation rates are primarily functions of mixture fraction. The detailed scalar relationship can be derived on the basis of complete chemical equilibrium when the chemistry is fast, the time for reaction is infinitely long and the homogeneous mixture burns in an adiabatic environment without any heat loss and work output. Gordon and McBride (1971) have provided a useful program for calculating these equilibrium properties, notably adiabatic temperature and species concentrations.

Most combustion systems however do not meet the adiabatic equilibrium conditions due to some disturbing factors, for example thermal radiation loss and insufficient residence time for all species to attain their equilibrium levels. The departure from equilibrium can, in principle, be addressed by constructing a flamelet library. The library is sometimes established from laminar flame experiments. The most commonly used flame schemes are "flat" flame burners (in Wolfhard-Parker geometry) and counter-flow burner (in porous cylindrical geometry). It has been shown that the steady laminar counterflow diffusion flame exhibits a very similar scalar structure as unsteady distorted mixing layers in a turbulent flow field. Therefore the counterflow geometry has been proposed to be the most representative steady flow field to study chemistry models and molecular transport effects in laminar flamelets (Peters (1984)). Alternatively, it is possible to calculate the flame structure through computation with detailed chemistry.

Combustion reactions for the burning of simple fuel molecules, for example methane CH_4, have been theoretically described that are regarded as accurate reflections of what happens at the molecular level and are in agreement with experiments. Chemistry involved in the combustion of blended fuels, like aviation kerosine, is a very complicated issue. Due to the lack of detailed reaction mechanisms, one approach to resolve the kerosine combustion is to apply a global mechanism, where elementary reactions are replaced by a simple step reaction. This method has been investigated extensively, resulting in the development of a number of

quasi-global finite rate hydrocarbon combustion models (Edelman et al. (1972)). The first step in these models is essentially to describe the break-up of fuel and partial oxidation to hydrogen and carbon monoxide. The drawback is the exclusion of intermediate hydrocarbons which are often important during the combustion. The improvement in the understanding of hydrocarbon - as large as C_8-hydrocarbons (Westbrook and Pitz (1991)) - combustion chemistry in recent years makes it possible to incorporate more elementary mechanisms into the investigation of more practical fuel combustion, with the prospect of kerosine in the near future.

COMPUTATIONAL DETAILS

Parameters which characterise the detailed chemical kinetics, though eliminated in the simplification of flowfield calculation, are the key objects to be determined in the flamelet concept. The study carried out in this thesis is first to identify possible individual molecular processes responsible for kerosine-air combustion and second to determine at what rates these events take place. The computations are performed using a one dimensional counterflow code that has been developed by the research group under Prof. J. Warnatz. Other parameters, such as transport and thermodynamic properties of various species, are normally established through theoretical models. The molecular diffusion coefficients (Lennard-Jones potential parameters) of the fuel, kerosine in the present calculation, are taken from that evaluated by Askari-Sardhai (1987). The NASA format thermochemical polynomials for kerosine which are used to determine the specific heat, enthalpy and entropy of the fuel or other species are also taken from Askari-Sardhai (1987). The properties of other species are contained in the original code which are also available in convenient tabulations.

Elementary reactions available in the numerical code involve species up to C_4-hydrocarbons. The scheme of kerosine break-up is therefore code-restricted, and is assumed to form C_4-hydrocarbon, mainly *n*-butane,

$$C_{12}H_{22} > C_4H_{10} + C_4H_{10} + C_4H_2 \qquad \text{(E-1)}$$

kerosine is defined as $C_{12}H_{22}$ which has the H/C atom ratio of 1.83. The rate coefficients used in the counter-flow code, in the three-parameter form

$$k = A\,T^b \exp(-E/RT) \qquad \text{(E-2)}$$

are estimated for reaction E-1. The temperature-independent part A of the pre-exponential factor is given in units of $cm^3\,mol^{-1}\,s^{-1}$. The exponent b is dimensionless and E is given in units of kJ/mol (R=8.314 J/K mol). Values for A, b and E have been tested and taken as 1.0×10^{12}, 1.0 and 175, respectively. The rate constant A and activation energy E are both higher than that used in global mechanisms ($\sim 10^8$ and 101.43, cf. Edelman et al. (1972)). Subsequent

reactions of C_4 species are relatively well defined by many works, including those of Warnatz et al. (1984). They include 44 steps consisting of 592 elementary reactions. These reactions are used as common subelements for the present task of incorporating new reaction E-1. The initial temperatures for air and fuel are 300 and 655 K, respectively, with strain rate of 100 1/s at atmospheric pressure. The calculated results are compared with equilibrium data and other laminar flamelet predictions for unstrained flames (Askari-Sardhai (1987) using an unsteady one-dimensional code (SNECKS)) and preliminary detailed scheme calculations with strain rate 100 1/s (Lindstedt (1992)) for the same initial conditions.

RESULTS AND DISCUSSION

State relationships of temperature, species concentrations against mixture fraction are shown in Figure E.1. On the fuel lean side below stoichiometry, data from all methods are near identical. The peak temperature of all flamelet results are very close and lower than equilibrium (Figure E.1 (a)). According to Warnatz (1984) hydrocarbon combustion, at least in lean and moderately rich mixtures, is mainly governed by elementary reactions which are not specific for the fuel considered. Thus these well established elementary reactions can describe accurately the kerosine combustion in the lean side. The peak temperature, near stoichiometry, is directly related to the thermal properties of major species, such as CO_2 and H_2O, and is expected to be largely independent of detailed chemistry. On the fuel rich side however, the present calculations underpredict the temperature. The equilibrium calculation does not take the detailed fuel dissociation into account and gives lower temperatures. Chemistry in non-equilibrium flamelet calculations includes some detailed fuel dissociation to lower C-number intermediate. The transport effects which are missing in the equilibrium calculation, also result in higher temperatures at the rich side where the effect is to smooth the scalars gradients.

The fuel concentration in Figure E.1 (b) reveals that the fuel breakup rate is too high and no kerosine is left for mixture fractions below 0.5. This might explain the discrepancy in the temperature prediction. Fuel concentration, as well as hydrocarbon species concentrations, are essential parameters in modelling soot formation mechanisms (cf. Chapter 2) and the present treatment of kerosine combustion chemistry generally does not give satisfactory state relationships in relation to the soot modelling campaign.

Comparisons of relationships for other major combustion products are shown in Figures E.1 (c)~(h). Density and mixture molecular weight are plotted in Figures E.1 (i) and (j). Unlike the temperature and fuel concentration, the present predictions of these properties are very close to other predictions across the whole mixture fraction range. These species are

perhaps more dependent on low C-number hydrocarbon combustion than the parent fuel break-up. For example CO appears as the first product of the hydrocarbon combustion process and is converted subsequently to CO_2, as often implied in global mechanisms. This indicates that a proper fuel break-up mechanism needs to be evaluated for kerosine combustion chemistry.

The present proposal for C_{12}-hydrocarbon breakdown directly to C_4-hydrocarbon seems inadequate, at least for obtaining sensible temperature and parent fuel concentration. Global mechanisms, as well as the present semi-global, semi-elementary mechanism, might produce plausible results for species relating to C_1 or C_2-hydrocarbon combustion, like CO, CO_2, etc. To obtain, for example C_{12} species concentrations for kerosine combustion, more detailed elementary reactions, including those involving more intermediates between C_4 and C_{12}-hydrocarbons, for fuel breakup is a necessity. Such a study lay beyond the scope of the present programme.

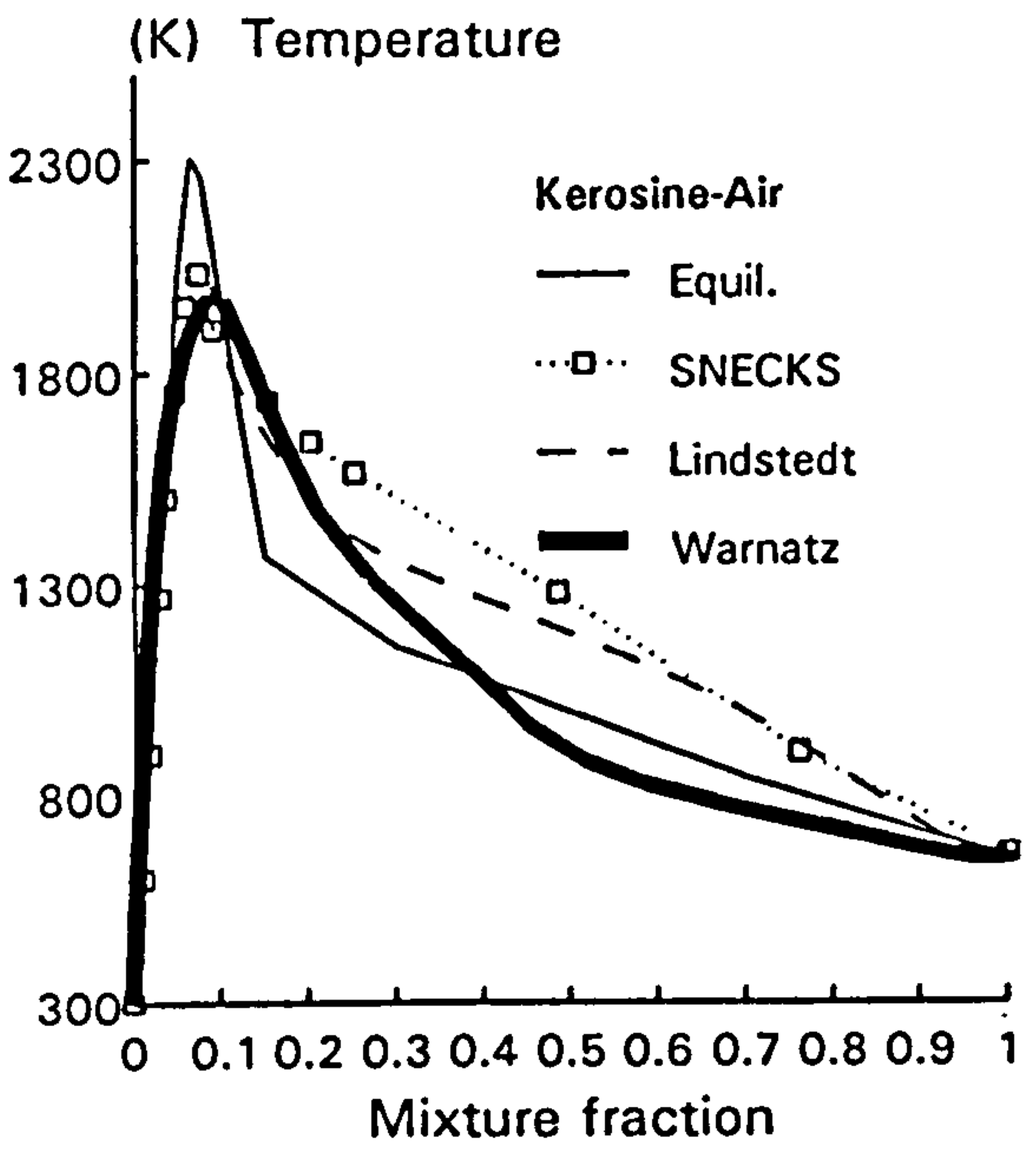

(a)

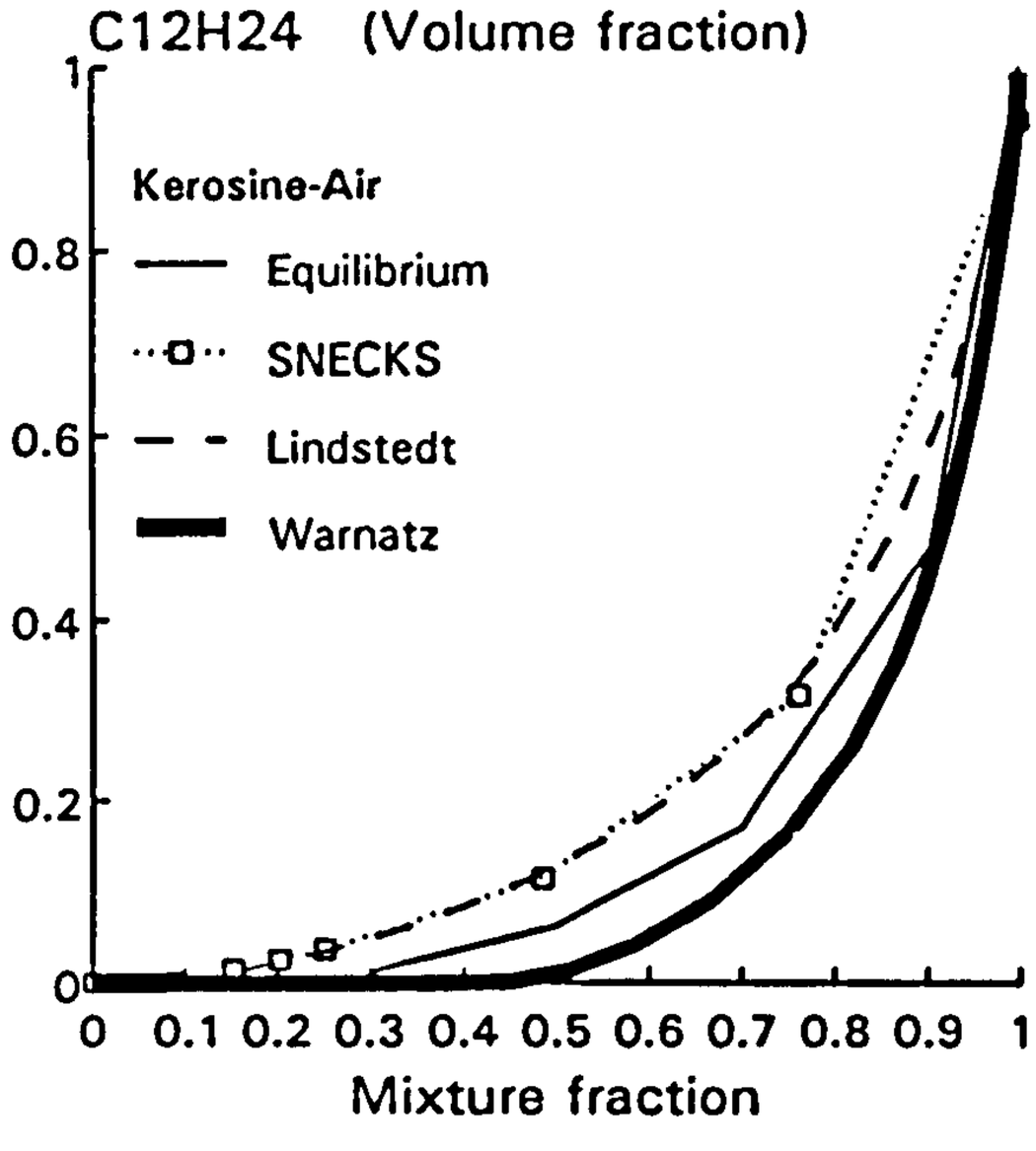

(b)

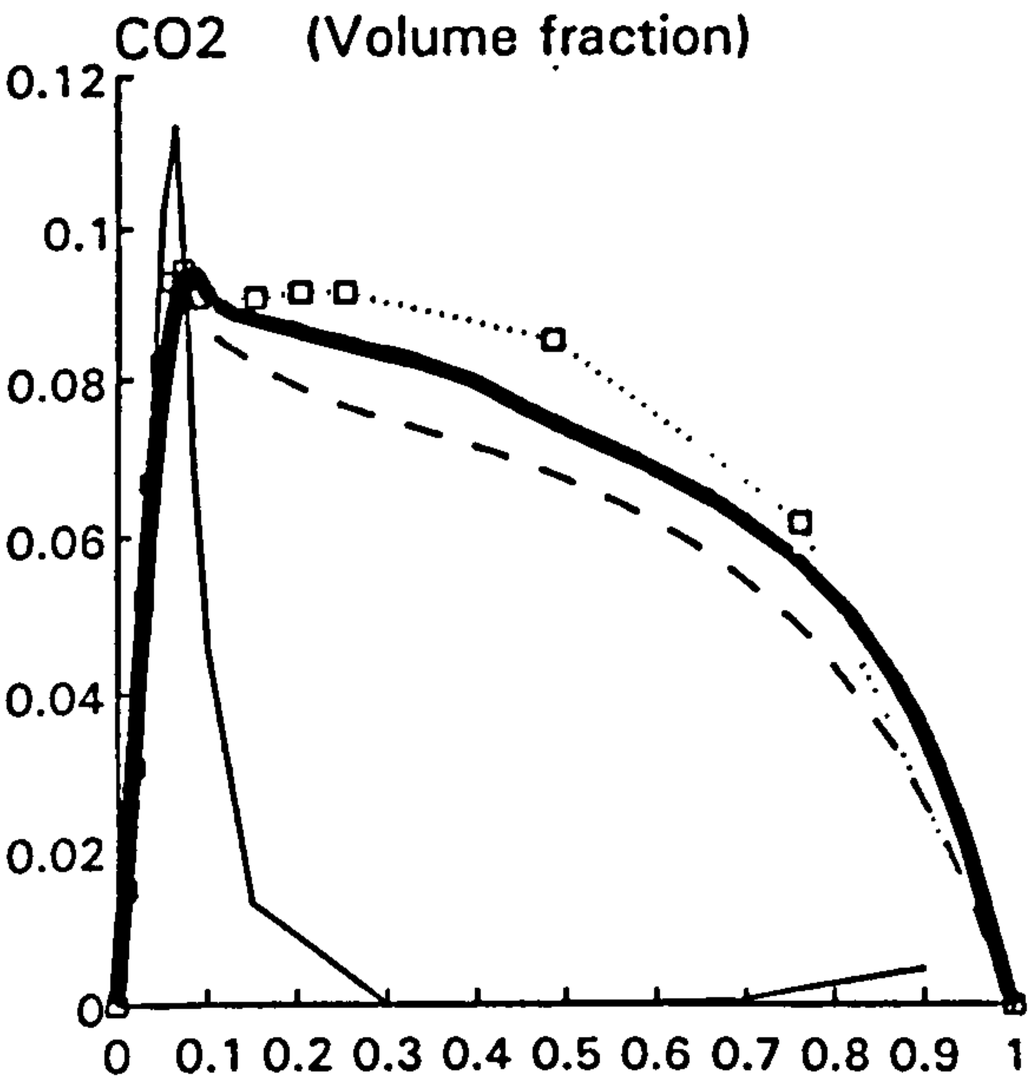

(c)

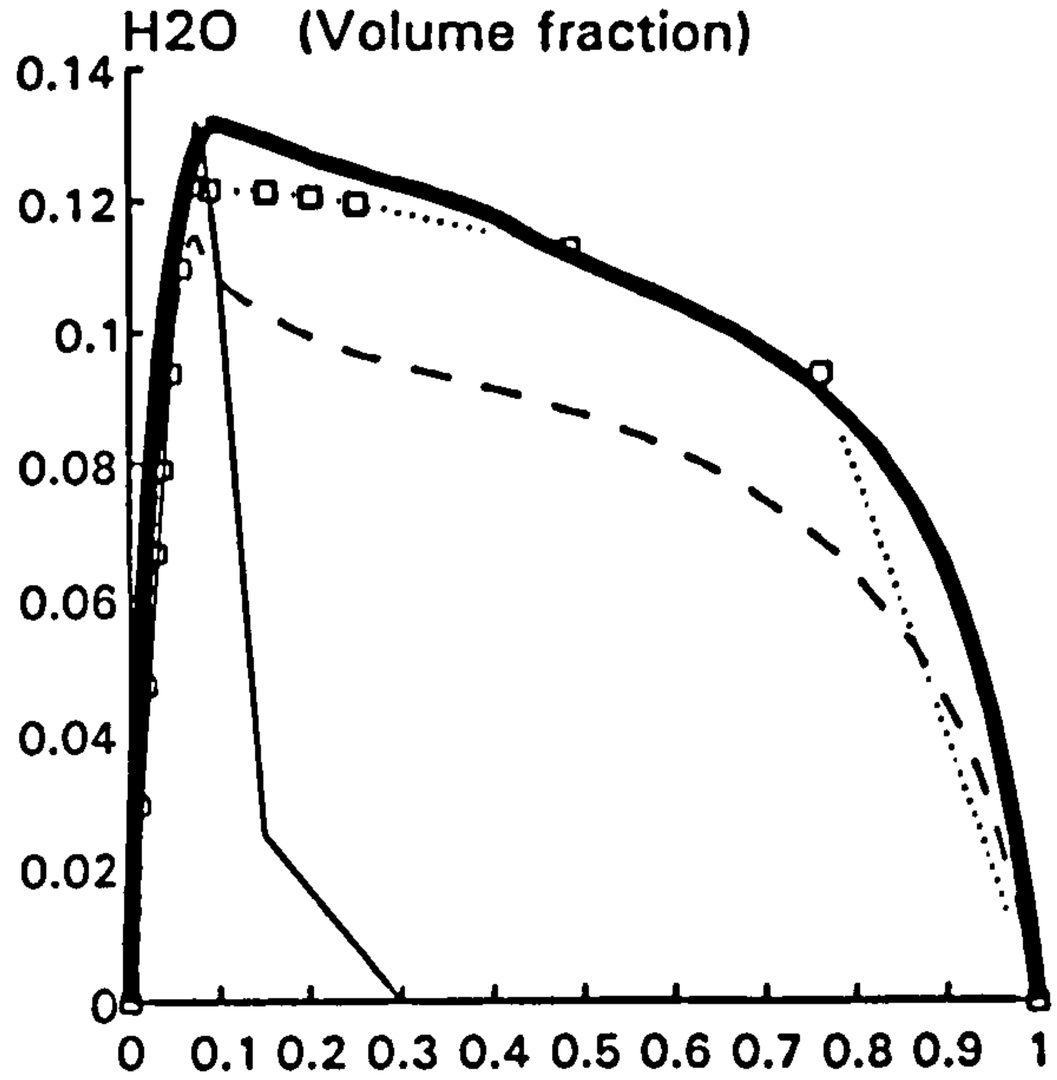

(d)

Figure E.1 Laminar flamelet state relationship of: (a) temperature, (b) Kerosine, (c) CO_2 and (d) H_2O with conserved scalar (mixture fraction) for kerosine-air combustion

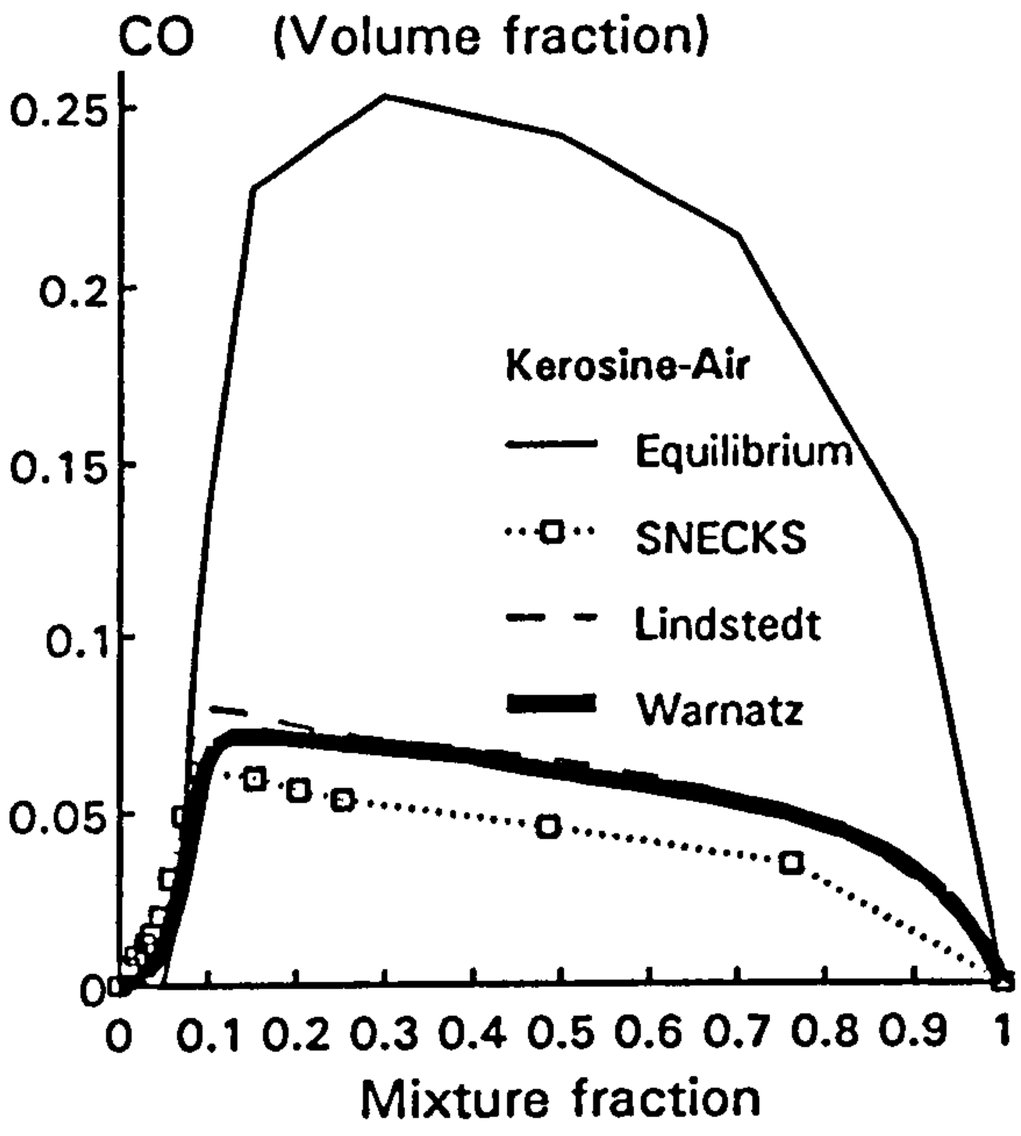

(e)

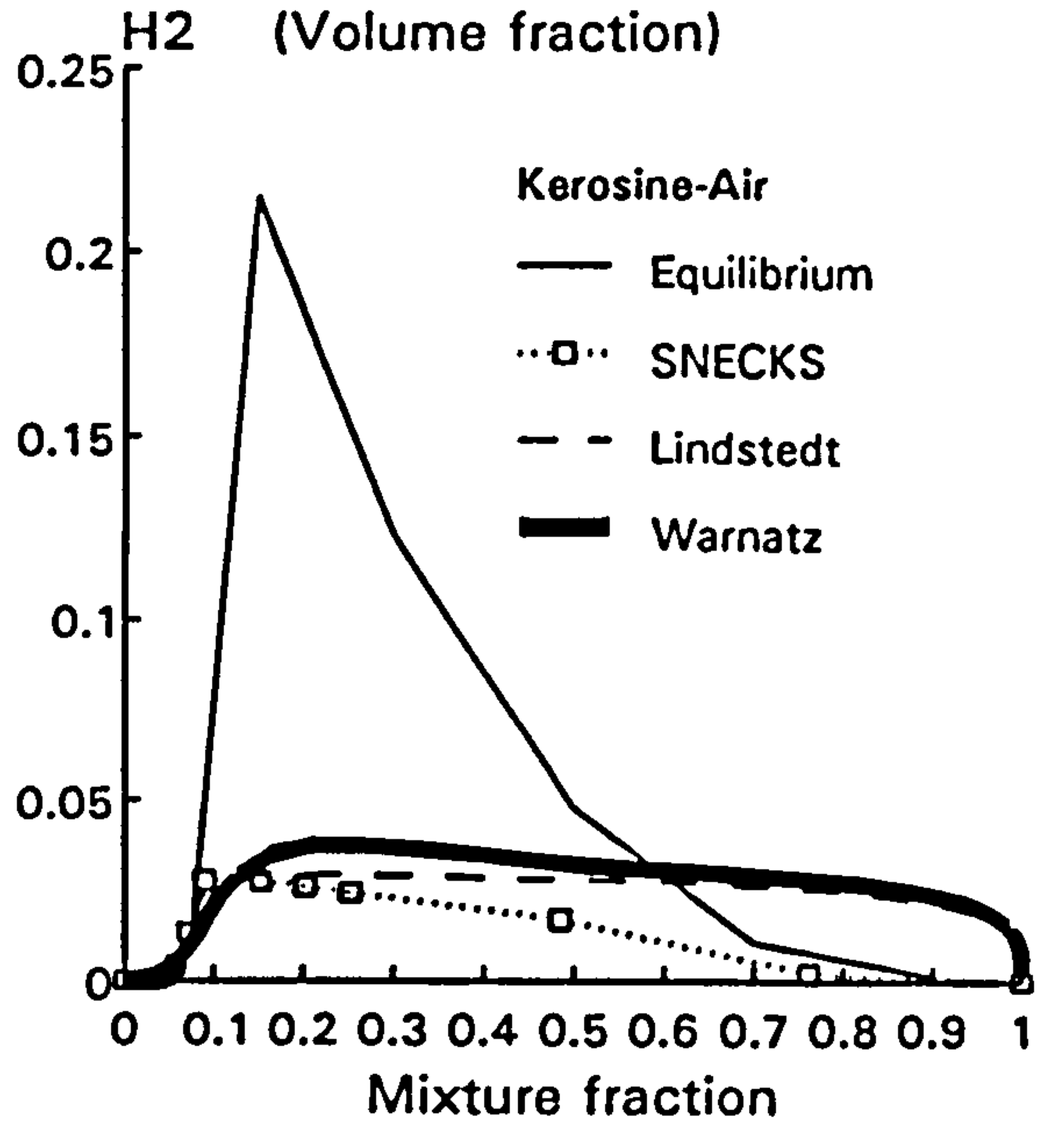

(f)

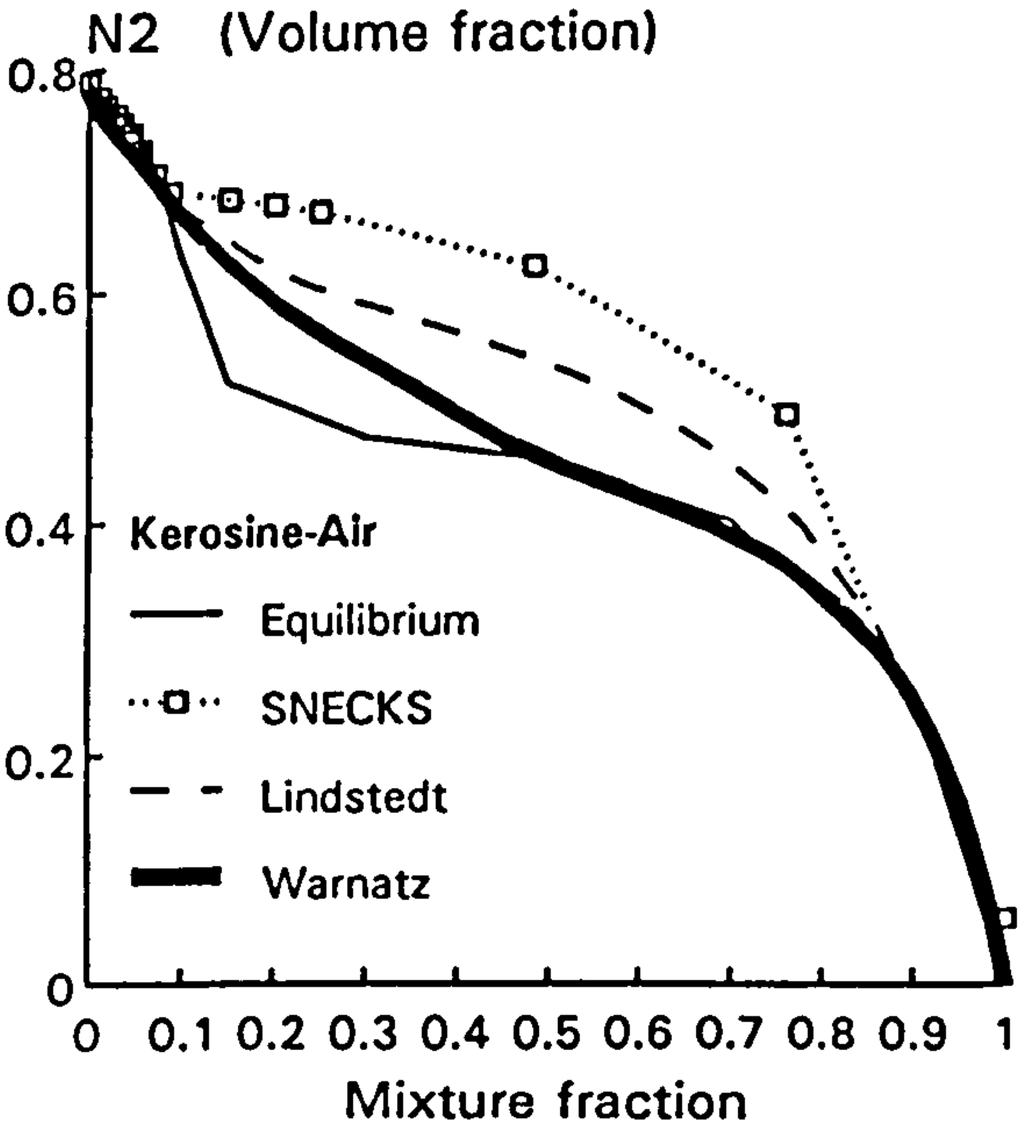

(g)

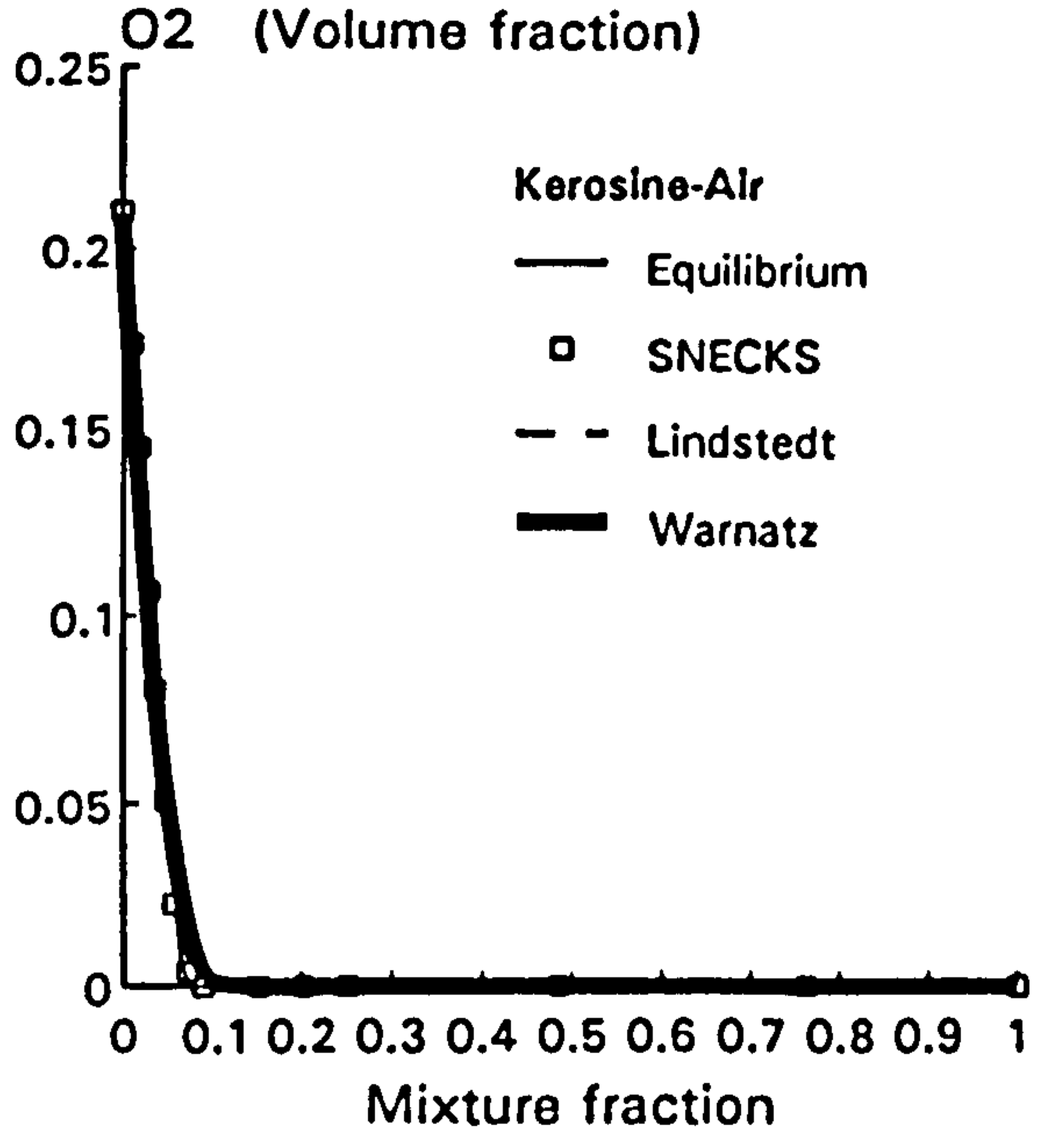

(h)

Figure E.1 Continued. (e) CO, (f) H_2, (g) N_2 and (h) O_2

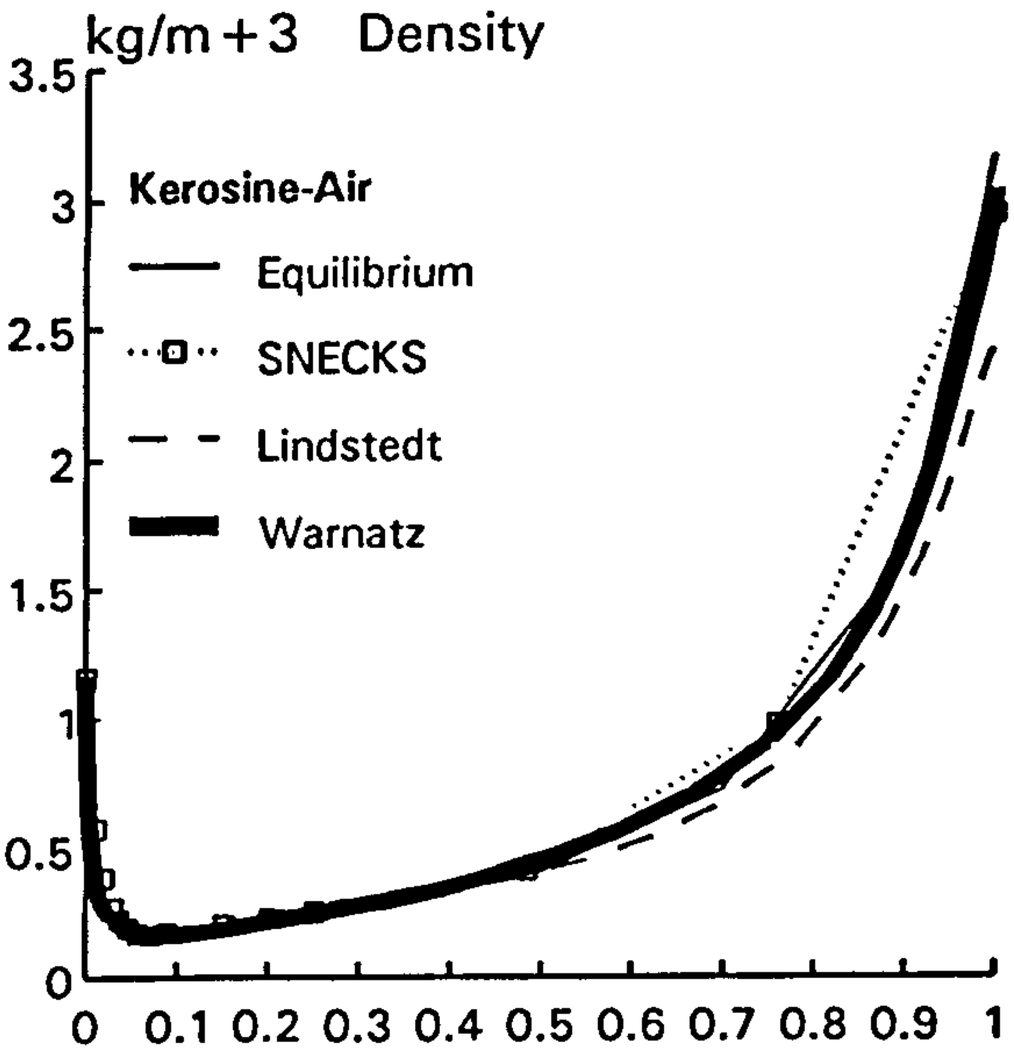

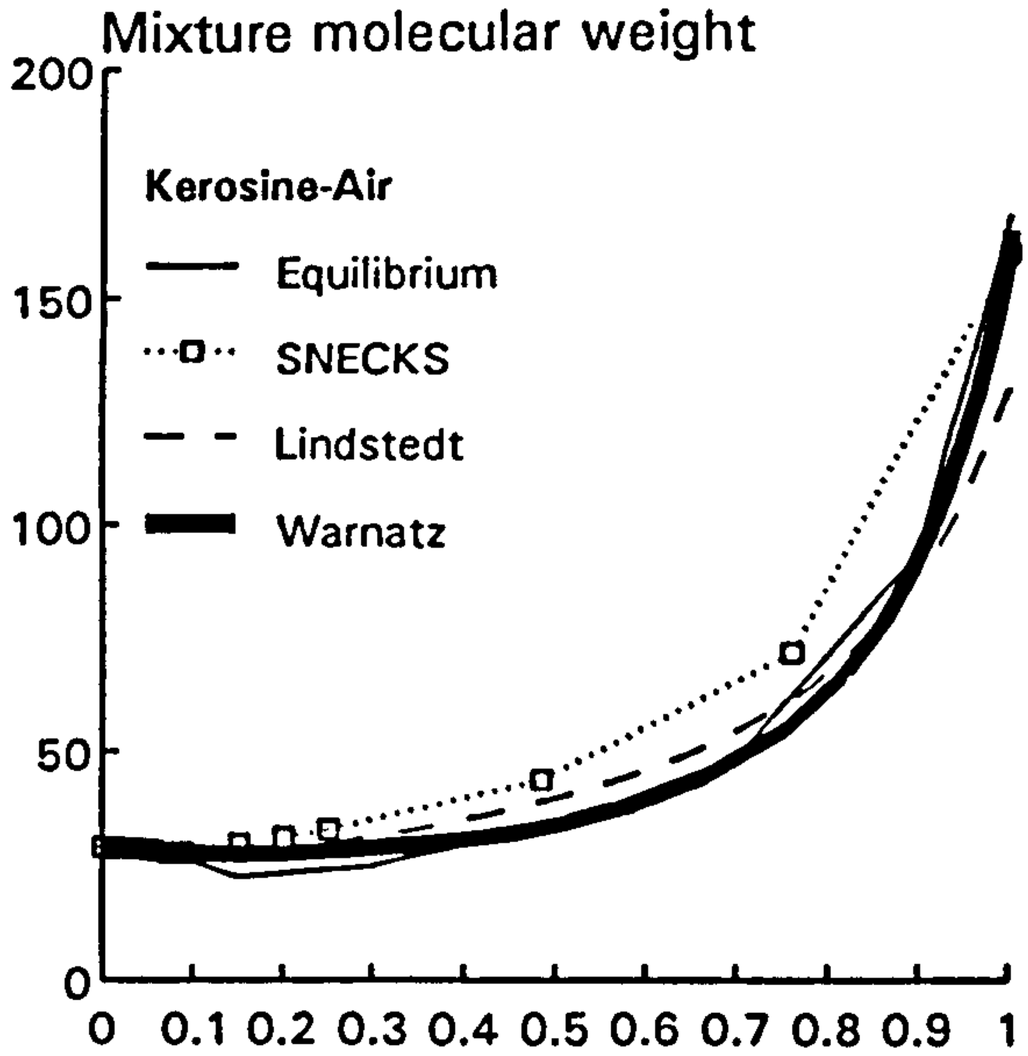

Figure E.1 Continued. (i) Density and (j) Mixture molecular weight